Proceeding of the 8th International Workshop on Biosignal Interpretation (BSI2016)

Edited by Y. Yamamoto, T. Nomura, S. Cerutti, H. Dickhaus, K. Yana

Sessions

November 1, 2016

Tu1
8:30-10:30 Oral session
Biological applications of advanced signal processing

Tu2
11:00 - 13:00 Oral session
ECG and heart rate variability

Tu3
14:30 - 16:30 Oral session
Connectivity and causality

P1
16:30 - 18:00
Poster session 1

November 2, 2016

We1
8:30 - 10:30 Oral session
Analysis of sleep dynamics

We2
11:00 - 13:00 Oral session
Signal processing for human behaviors

We3
14:30 - 16:30 Oral session
Medical decision making

P2
16:30 - 18:00
Poster session 2

November 3, 2016

Th1
9:30 - 12:00 Symposium
From dynamical disease to disease dynamics: Predictive medicine in the era of data science

Th2
13:30 - 15:30 Oral Session
Signal processing for brain computer interface (BCI)

Th3
16:00 - 18:00 Oral session
EEG signal processing

FOREWORD

It is our privilege and pleasure to welcome all of you to Osaka and to the Eighth International Workshop on Biosignal Interpretation (BSI2016). The Workshop is a joint initiative of the International Medical Informatics Association (IMIA), the International Federation for Medical and Biological Engineering (IFMBE), the IEEE Engineering in Medicine and Biology Society (IEEE-EMBS), as well as the Japanese Society for Medical and Biological Engineering (JSMBE) and the Society of Instrument and Control Engineers (SICE).

The Workshop aims at exploring the field of biosignal interpretation, including model-based biosignal analysis, data interpretation and integration, medical decision making extending existing signal processing methods and technologies for the effective utilization of biosignals in clinical environments, as well as for a deeper understanding of biological functions of the whole organism, system, to cellular, protein and gene scales. This Workshop has been held approximately every three years with the site rotationing between Europe, Asia and America. The first one was held in Denmark in 1993 and the most recent one was in Como, Italy, in 2012.

In these last decades the field of biosignal interpretation has undoubtedly developed remarkably, with the topic permeating specialised conferences in biomedical engineering, medical physics, clinical medicine and, due to the advancement of data sciences, in biomedical and health informatics these days.

The scientific program of BSI2016 is organised into 11 single scientific sessions (including one symposium and two poster sessions) which cover the main topics in this fascinating research area. The symposium is dedicated to the dynamical disease concept in the era of data sciences. In addition to the traditional areas of cardiovascular and sensory-motor nervous systems, interesting research topics like Brain Connectivity and Signal Processing for a Brain Computer Interface and for Sleep Studies are considered.

We wish to thank all the important scientific organisations and institutions which have supported the Workshop and also the Members of Program and Scientific Committees who provided great help in organizing the scientific sessions. Many acknowledgements are due to the Local Organizing Committee and the Linkage convention service who have dedicated much time and effort to management, the venue and the interface to attendees. Finally, we hope that the Workshop attendees will bring home wonderful working experiences and memories of the most lively and hearty downtown in Japan, from here, the place called "Naniwa".

Yoshiharu Yamamoto
(General Chair)

Taishin Nomura
(Program Chair)

November 1, 2016

8:30-10:30 Oral session

Biological applications of advanced signal processing

Tu1-1 PDF

Invited lecture

Intrapartum fetal heart rate analysis: From fractal features to sparse feature-selection based classification

Patrice Abry

Ecole Normale Supérieure de Lyon, France

Tu1-2 PDF

Scattering transform of heart rate variability for the prediction of ischemic stroke in patients with atrial fibrillation

Roberto Leonarduzzi[1], Patrice Abry[1], Herwig Wendt[2], Ken Kiyono[3], Yoshiharu Yamamoto[4], Eiichi Watanabe[5], Junichiro Hayano[6]

[1]Univ Lyon, Ens de Lyon, Univ Claude Bernard, CNRS, Laboratoire de Physique, France

[2]IRIT, CNRS UMR 5505, University of Toulouse, France

[3]Osaka Uinversity, Japan

[4]University of Tokyo, Japan

[5]Fujita Health University, Japan

[6]Nagoya City University, Japan

Tu1-3 PDF

Preliminary investigation of instantaneous cardiovascular dynamics from contactless video-photoplethysmography

Gaetano Valenza[1,2], Luca Iozzia[3], Luca Cerina[3], Luca Mainardi[3], Riccardo Barbieri[2,3]

[1]Research Centre E Piaggio, University of Pisa, Italy

[2]Harvard Medical School, Massachusetts General Hospital, USA

[3]Politecnico di Milano, Italy

Tu1-4 PDF

Savitzky-Golay filter-based detrended fluctuation analysis: theory and its application to physiological time series

Yutaka Tsujimoto, Yasuyuki Suzuki, Masanori Shimono, Taishin Nomura, Ken Kiyono

Osaka University, Japan

11:00 - 13:00 Oral session

ECG and heart rate variability

Tu2-1 PDF

Conductive synthetic fabric electrodes: application to ECG measurement

Yeonsik Noh, Sneh K. Sinha, Caitlin Eaton-Robb, Gregory M. Treich, Yang Guo, Mengfang Li, Xiaozheng Zhang, Gregory A. Sotzing, Ki H. Chon
University of Connecticut, USA

Tu2-2 PDF

R-wave magnitude: A control input for ventricular assist devices

Seraina Anne Dual[1], Gregor Ochsner[1], Anastasios Petrou[1], Raffael Amacher[1], Markus Wilhelm[2], Mirko Meboldt[1], Marianne Schmid Daners[1]
[1]ETH Zurich, Switzerland
[2]University Hospital Zurich, Switzerland

Tu2-3 PDF

A method of efficient cardiac risk assessment based on the T-wave morphology changes in Holter ECG recordings

Mitsuki Aihara[1], Saya Nakamura[1], Mami Murakami[1], Kazuo Yana[1], Takuya Ono[2], Tomohide Ichikawa[3], Eiichi Watanabe[3]
[1]Hosei University, Japan
[2]Nippon Medical School, Japan
[3]Fujita Health University, Japan

Tu2-4 PDF

Confounding factors in ECG-based detection of sleep-disordered breathing

Christoph Maier[1], Hartmut Dickhaus[2]
[1]Heilbronn University, Germany
[2]Heidelberg University, Germany

Tu2-5 PDF

Reduced cardiac response to sleep apnea and increased risk of mortality

Junichiro Hayano[1], Emi Yuda[1], Yutaka Yoshida[1], Hiroki Ogasawara[1], Eiichi Watanabe[2]
[1]Nagoya City University, Japan
[2]Fujita Health University, Japan

Tu2-6 PDF

Nonlinearity of heart rate variability induced by respiratory modulation

Yuki Miki[1], Yasuyuki Suzuki[1], Masanori Shimono[1], Eiichi Watanabe[2], Junichiro Hayano[3], Yoshiharu Yamamoto[4], Taishin Nomura[1], Ken Kiyono[1]
[1]Osaka University, Japan
[2]Fujita Health University, Japan
[3]Nagoya City University, Japan
[4]University of Tokyo, Japan

14:30 - 16:30 Oral session

Connectivity and causality

Tu3-1 PDF

Linear and nonlinear functional connectivity methods to predict brain maturation in preterm babies

Mario Lavanga, Ofelie De Wel, Alexander Caicedo, Katrien Jansen, Anneleen Dereymaeker, Gunnar Naulaers, Sabine Van Huffel
KU Leuven, Belgium

Tu3-2 PDF

Quantification of the central-autonomic-network applying normalized shorttime partial directed coherence approach

Steffen Schulz[1], Mathias Bolz[2], Karl-Jürgen Bär[2], Andreas Voss[1]
[1]Institute of Innovative Health Technologies IGHT, Ernst-Abbe-Hochschule Jena, Germany
[2]University Hospital Jena, Germany

Tu3-3 PDF

Transfer entropy analysis of linear model residuals

Fatima Elhamad, Mathias Baumert
University of Adelaide, Australia

Tu3-4 PDF

Connectivity of epileptiform discharges during epileptic seizure in temporal lobe

Hisashi Yoshida[1], Yasuto Yoshioka[2], Masaharu Miyauchi[1], Naoki Nakano[1], Amami Kato[1]
[1]Kindai University, Japan
[2]ROHM semiconductor, Japan

Tu3-5 PDF

Partial correlation-based functional connectivity analysis of the optical intrinsic signals of the mouse neocortex during resting state

Yuto Yoshida, Mitsuyuki Nakao, Norihiro Katayama
Tohoku University, Japan

Tu3-6 PDF

From information flow to microconnectomics

Masanori Shimono
Osaka University, Japan

16:30 - 18:00

Poster session 1

P1-1 PDF

Analysis of facial expression recognition by event-related potentials

Taichi Hayasaka, Ayumi Miyachi
National Institute of Technology, Toyota College, Japan

P1-2 PDF

To assess mental stability using electroencephalography

Yuko Mizuno-Matsumoto
University of Hyogo, Japan

P1-3 PDF

Wavelet-crosscorrelation analysis of abnormal EEG in patients with mental disorders

Kozue Yamaguchi, Yuko Mizuno-Matsumoto
University of Hyogo, Japan

P1-4 PDF

Features of diffuse alpha pattern in electroencephalography

Steven M. A. Carpels, Kozue Yamaguchi, Yuko Mizuno-Matsumoto
University of Hyogo, Japan

P1-5 PDF

Convolutional neural networks using supervised pre-training for EEG-based emotion recognition

Miku Yanagimoto, Chika Sugimoto
Yokohama National University, Japan

P1-6 PDF

An EEG-based communication aid that uses the robot avatar

Ryohei P. Hasegawa, Yoshiko Nakamura
AIST, Japan

P1-7 PDF

Driver fatigue analysis based on binary brain networks

Chi Zhang1, Fengyu Cong[1], Hong Wang[2]
[1]Dalian University of Technology, China
[2]Northeastern University, China

P1-8 PDF

Cortical dipole imaging of visual evoked potential using sigmoid function-based filtering property

Junichi Hori[1], Shintaro Takasawa[1,2]
[1]Niigata University, Japan
[2]Terumo Corporation, Japan

P1-9 PDF

Motion aftereffect direction-specific responses in the steady-state visual evoked potentials

Shiori Arimitsu, Keiko Momose
Waseda University, Japan

P1-10 PDF

Multifractal characteristics of external anal sphincter based on sEMG signals

Paulina Trybek[1,2], Michal Nowakowski[3], Lukasz Machura[1,2]
[1]Silesian Center for Education and Interdisciplinary Research, Poland
[2]University of Silesia, Poland
[3]Jagiellonian University Medical College, Poland

P1-11 PDF

Random point process modeling of the spike trains in response to sinusoidally modulated pulsatile electric stimuli in auditory nerve fiber models

Hiroyuki Mino
Kanto Gakuin University, Japan

P1-12 PDF

Activity analysis of neuronal networks with altered excitatory/inhibitory balance

Shoko Iida[1], Kenta Shimba[1,2,3], Kiyoshi Kotani[1,4], Yasuhiko Jimbo[1]

[1]The University of Tokyo, Japan
[2]Tokyo Institute of Technology, Japan
[3]Japan Society for the Promotion of Science, Japan
[4]JST PRESTO, Japan

P1-13 PDF

sEMG power spectrum after rectal cancer surgery

Lukasz Machura[1,2], Paulina Trybek[1,2], Michal Nowakowski[3]

[1]Silesian Center for Education and Interdisciplinary Research, Poland
[2]University of Silesia, Poland
[3]Jagiellonian University Medical College, Poland

P1-14 PDF

The relationship between recovery from muscle fatigue of the skeletal muscle and magnetic stimulation

Yuya Yokota, Atsuo Nuruki
Kagoshima University, Japan

P1-15 PDF

A microsaccade detection method by using an order-statistic time-window analysis

Shohei Ohtani, Takeshi Kohama, Sho Kikkawa, Hisashi Yoshida
Kindai University, Japan

P1-16 PDF

Simulation of spike propagation in neural network

Shun Sakuma[1], Yuko Mizuno-Matsumoto[1], Yoshi Nishitani[2], Shinichi Tamura[3]

[1]University of Hyogo, Japan
[2]Osaka University, Japan
[3]NBL Technovator Co., Ltd., Japan

November 2, 2016

8:30 - 10:30 Oral session

Analysis of sleep dynamics

We1-1 PDF

Invited lecture

Signal recording and non-linear processing in sleep research

Thomas Penzel

Charite-Universitatsmedizin Berlin, Germany

We1-2 PDF

Markov modeling of sleep stage transitions and ultradian REM sleep rhythm: A simulation study

Akifumi Kishi, Ikuhiro Yamaguchi, Fumiharu Togo, Yoshiharu Yamamoto

The University of Tokyo, Japan

We1-3 PDF

Wake-sleep transition from the perspective of cortico-thalamo-cortical loop: Electroencephalogram data analysis and simulation

Ikuhiro Yamaguchi, Akifumi Kishi, Fumiharu Togo, Toru Nakamura, Yoshiharu Yamamoto

The University of Tokyo, Japan

We1-4 PDF

Time delay between beta EEG and heart rate variability during sleep transitions: Comparison of insomnia patients and normal controls

Hyunbin Kwon[1], Jaewon Choi[2], Yujin Lee[2], Do-Un Jeong[2], Kwangsuk Park[1]

[1]Seoul National University, Korea

[2]Seoul National University Hospital, Korea

11:00 - 13:00 Oral session

Signal processing for human behaviors

We2-1 PDF

Heart rate and heart rate variability monitoring during sleep using 24-GHz microwave radars located beneath the mattress on the bed

Masayuki Kagawa, Kazuki Suzumura, Ayako Hashizume, Takemi Matsui
Tokyo Metropolitan University, Japan

We2-2 PDF

Automatic two-channel sleep-staging using a predictor-corrector method

Shirin Riazy[1], Tilo Wendler[1], Jürgen Pilz[2]
[1]HTW Berlin, Germany
[2]Alpen-Adria university Klagenfurt, Austria

We2-3 PDF

Activation pattern of extensor digitorum brevis muscle during child walking

Annachiara Strazza[1], Michela Sara Palmieri[2], Alessandro Mengarelli[1], Sandro Fioretti[1], Laura Burattini[1], Ornella Orsini[2], Antonio Bortone[2], Francesco Di Nardo[1]
[1]Università Politecnica delle Marche, Italy
[2]Centro ambulatoriale di Riabilitazione Santo Stefano, Italy

We2-4 PDF

Intermittent control properties of car following: Driving simulator experiment

Ihor Lubashevsky, Hiromasa Ando
University of Aizu, Japan

We2-5 PDF

Application of empirical mode decomposition to mother and infant physical activity: Synchronization of circadian rhythms is associated with maternal mental health symptoms

Etsuko Shimizu[1], Toru Nakamura[1,2], Jinhyuk Kim[3], Kazuhiro Yoshiuchi[1], Yoshiharu Yamamoto[1]
[1]The University of Tokyo, Japan
[2]JST, PRESTO, Japan
[3]National Center of Neurology and Psychiatry, Japan

We2-6 PDF

Preceding psychological factors and calorie intake in patients with type 2 diabetes: Investigation by ecological momentary assessment

Shuji Inada[1], Yoko Iizuka[1], Ken Ohashi[2], Hiroe Kikuchi[3], Yoshiharu Yamamoto[1], Takashi Kadowaki[1], Kazuhiro Yoshiuchi[1]
[1]The University of Tokyo, Japan
[2]National Cancer Center Hospital, Japan
[3]National Center of Neurology and Psychiatry, Japan

14:30 - 16:30 Oral session

Medical decision making

We3-1 PDF

Atomic force microscopy for bladder cancer detection

Eugene Demidenko[1], Igor Sokolov[2], John Seigne[3]

[1]Dartmouth College, USA
[2]Tufts University, USA
[3]Dartmouth-Hitchcock Medical Center, USA

We3-2 PDF

A normalized non-stationary wavelet based analysis approach for computer assisted classification of laryngoscopic high-speed video recordings

Mona K. Fehling[1,3], Jakob Unger[2], Dietmar J. Hecker[3], Bernhard Schick[3], Jörg Lohscheller[1]

[1]Trier University of Applied Sciences, Germany
[2]University of California, USA
[3]Saarland University Hospital, Germany

We3-3 PDF

Fetal heart rate classification: First vs. second stage of labor

Jiri Spilka[1], Roberto Leonarduzzi[2], Vaclav Chudáček[1], Patrice Abry[2], Muriel Doret[3]

[1]CIIRC, Czech Technical University in Prague, Czech Republic
[2]Univ Lyon, Ens de Lyon, Univ Claude Bernard, CNRS, Laboratoire de Physique, France
[3]Femme-Mère-Enfant Hospital, France

We3-4 PDF

Assessment of cardiovascular oscillations in amnestic mild cognitive impairment

Nicola Toschi[1,2], Gaetano Valenza[1,3], Luca Citi[4], Maria Guerrisi[1], Stefano Orsolini[5], Carlo Tessa[6], Stefano Diciotti[5], Riccardo Barbieri[2,7]

[1]Massachusetts General Hospital-Harvard Medical School, USA
[2]University of Rome "Tor Vergata", Italy
[3]University of Pisa, Italy
[4]University of Essex, UK
[5]University of Bologna, Italy
[6]Versilia Hospital, Italy.
[7]Politecnico di Milano, Italy

We3-5 PDF

A study of an evaluation method for analgesic level using fuzzy inference based on multiple analgesia indices during general anesthesia

Shotaro Taniguchi[1], Yujing Cao[1], Eiko Furutani[1], Toshihiro Takeda[2], Gotaro Shirakami[2]

[1]Kyoto University, Japan
[2]Kagawa University, Japan

We3-6 PDF

An adaptive and automatic parameter selection method based on rational dilation wavelet transform for wheeze type classification

Sezer Ulukaya[1], Gorkem Serbes[2], Yasemin P. Kahya[3]

[1]Bogazici and Trakya University, Turkey
[2]Yildiz Technical University, Turkey
[3]Bogazici University, Turkey

16:30 - 18:00

Poster session 2

P2-1 PDF

Effect of body posture on LF/HF in ambulatory ECG

Yutaka Yoshida[1], Yuki Furukawa[1], Hiroki Ogasawara[1], Emi Yuda[1], Junichiro Hayano[1], ALLSTAR Study Group[2]

[1]Nagoya City University, Japan
[2]Allostatic State Mapping by Ambulatory ECG Repository Study Group

P2-2 PDF

On the heart-rate signal provided by the Zephyr BioHarness 3.0

Daniele Nepi, Angela Agostinelli, Elvira Maranesi, Agnese Sbrollini, Micaela Morettini, Francesco Di Nardo, Sandro Fioretti, Laura Burattini

Università Politecnica delle Marche, Italy

P2-3 PDF

Ambulatory physical activity monitoring to know healthy life expectancy

Emi Yuda[1], Yutaka Yoshida[1], Hiroki Ogasawara[1], Junichiro Hayano[1], ALLSTAR Study Group[2]

[1]Nagoya City University, Japan
[2]Allostatic State Mapping by Ambulatory ECG Repository (ALLSTAR) project

P2-4 PDF

Estimation method of amount of swallowed water from swallowing sounds

Masataka Imura[1], Hiroki Nakafuji[2], Shunsuke Yoshimoto[2], Osamu Oshiro[2]

[1]Kwansei Gakuin University, Japan
[2]Osaka University, Japan

P2-5 PDF

An integrated data format for the long term ECG recordings

Hidenao Nagai[1], Toyohito Shibui[1], Yoshiki Kinukawa[1], Satoshi Wakabayashi[1], Kazuo Yana[1], Takuya Ono[2]

[1]Hosei University, Japan
[2]Nippon Medical School, Japan

P2-6 PDF

Physiological variation during drowsy driving

Masashi Kitagawa, Shima Okada

Kindai University, Japan

P2-7 PDF

Pharmaceutical benefit assessment for involuntary exerciser patient by image processing

Masaya Kimachi, Shima Okada

Kindai University, Japan

P2-8 PDF

The preliminary study of core temperature estimation with external auditory meatus temperature sensor while exercising

MyungJun Koh, SooYoung Sim, KwangMin Joo, Kwangsuk Park

Seoul National University, Korea

P2-9 PDF

Validating stability of components extracted by nonnegative matrix factorization via clustering

Tianyi Zhou[1,2], Guoqiang Hu[1,2], Reza Mahini[1], Xiao-Feng Gong[1], Qiu-Hua Lin[1], Fengyu Cong[1,2]

[1]Dalian University of Technology, China
[2]University of Jyväskylä, Finland

P2-10 PDF

A simple method for monitoring integration of pore-forming protein into lipid bilayer

Kenta Shimba[1,2,3], Yoshitaka Miyamoto[1], Tohru Yagi[1],

[1]Tokyo Institute of Technology, Japan
[2]Japan Society for the Promotion of Science, Japan
[3]The University of Tokyo, Japan

November 3, 2016

9:30 - 12:00 Symposium

From dynamical disease to disease dynamics: Predictive medicine in the era of data science

Th1-1

Invited Review

Dynamical diseases: Insights into the etiology and treatment of medical emergencies

John G. Milton

The Claremont Colleges, USA

Th1-2

Invited Review

Detection of pre-disease states by DNB (dynamical network biomarkers) toward predictive medicine

Kazuyuki Aihara

The University of Tokyo, Japan

Th1-3

Heart rate dynamics predicting adverse clinical events

Junichiro Hayano[1], Ken Kiyono[2], Eiichi Watanabe[3], Yoshiharu Yamamoto[4]

[1]Nagoya City University, Japan
[2]Osaka University, Japan
[3]Fujita Health University, Japan
[4]The University of Tokyo, Japan

Th1-4

Intermittency and loss of intermittency during human motor control in health and disease

Taishin Nomura[1], Yasuyuki Suzuki[1,2], Fu Chunjiang[1], Ken Kiyono[1]

[1]Osaka University, Japan
[2]Carnegie Mellon University, USA

Th1-5

Early warning signals for dynamical phase transitions into addictive behavior

Jerome C. Foo[1], Hamid R. Noori[2], Ikuhiro Yamaguchi[1], Valentina Vengeliene[2], Alejandro Cosa-Linan[2], Toru Nakamura[1], Kenji Morita[1], Rainer Spanagel[2], Yoshiharu Yamamoto[1]

[1]The University of Tokyo, Japan
[2]Heidelberg University, Germany

13:30 - 15:30 Oral Session

Signal processing for brain computer interface (BCI)

16:00 - 18:00 Oral session

EEG signal processing

Th3-1 PDF

The estimate of mental workload induced by the use of different processors in a cochlear implant during word recognition in a noisy environment

Giulia Cartocci[1,2], Anton Giulio Maglione[1,2], Dario Rossi[1,2], Enrica Modica[1,2], Paolo Malerba[3], Gianluca Borghini[2], Gianluca Di Flumeri[2], Pietro Aricò[2], Fabio Babiloni[1,2]

[1]Sapienza University of Rome, Italy
[2]BrainSigns srl, Italy
[3]Cochlear s.r.l. Italy

Th3-2 PDF

Online detection of auditory attention in a neurofeedback application

Rob Zink[1,2], Annelies Baptist[1,2], Alexander Bertrand[1,2], Sabine Van Huffel[1,2], Maarten De Vos[3]

[1]KU Leuven, Belgium
[2]iMinds Medical IT, Leuven, Belgium
[3]Oxford University, United Kingdom

Th3-3 PDF

Alpha and low-beta oscillatory patterns extracted with canonical polyadic decomposition relate to LDA classifier performance in real-life mobile EEG

Rob Zink[1,2], Borbála Hunyadi[1,2], Sabine Van Huffel[1,2], Maarten De Vos[3]

[1]KU Leuven, Belgium.
[2]iMinds Medical IT, Belgium.
[3]Oxford University, United Kingdom

Th3-4 PDF

Tracking the poles of an AR time-variant model for EEG studies

Giulia Tacchino, Anna M. Bianchi
Politecnico di Milano, Italy

Th3-5 PDF

Automatic artifacts correction: improving on-line EEG analysis

Stefania Coelli, Giulia Tacchino, Anna Maria Bianchi
Politecnico di Milano, Italy

Th3-6 PDF

Cluster aggregation for analyzing event-related potentials

Reza Mahini[1], Tianyi Zhou[1,2], Peng Li[3], Asoke Nandi4, Hong Li[3], Fengyu Cong[1,2]

[1]Dalian University of Technology, China
[2]University of Jyvaskyla, Finland
[3]Shenzhen University, China
[4]Brunel University, UK

Invited lecture

Intrapartum fetal heart rate analysis: From fractal features to sparse feature-selection based classification

Patrice Abry

Ecole Normale Supérieure de Lyon, France

Abstract

Fetal Heart Rate (FHR) monitoring is routinely used in clinical practice to help obstetricians assess fetal health status during delivery. However, early detection of fetal acidosis that allows relevant decisions for operative delivery remains a challenging task, receiving considerable attention. The present work renews FHR analysis and fetal acidosis detection in two ways. First, fractal based features are shown to constitute relevant tools for the assessment of cardiac variability, that significantly outperform and thus satisfactory replace other traditional assessment of cardiac variability such as LF/HF ratio, that relies either on the splitting into a priori chosen frequency bands of the spectral contant of data, or on spectral and DFA based scaling exponents. Second, fetal acidosis detection is commonly formulated as a pH based classification problem. Our original proposition is to promote Sparse Support Vector Machine classification that permits to select a small number of relevant features as well as to achieve efficient fetal acidosis detection. Concepts and tools are illustrated at on a large (1288 subjects) and well documented database, collected at french public academic Hospital in Lyon. It is shown that the automatic selection of a sparse subset of features achieves satisfactory classification performance (sensitivity 0.73 and specificity 0.75, outperforming clinical practice). The subset of selected features receive simple interpretation in clinical practice. A second large database collected in Czech Republic is further used to show the generalization ability of both fractal features and Sparse Support Vector Machine classification.

Scattering Transform of Heart Rate Variability for the Prediction of Ischemic Stroke in Patients with Atrial Fibrillation

Roberto Leonarduzzi[1], Patrice Abry[1], Herwig Wendt[2], Ken Kiyono[3], Yoshiharu Yamamoto[4], Eiichi Watanabe[5], Junichiro Hayano[6]

[1]Univ Lyon, Ens de Lyon, Univ Claude Bernard, CNRS, Laboratoire de Physique, F-69342 Lyon, France;
[2]IRIT, CNRS UMR 5505, University of Toulouse, France;
[3]Division of Bioengineering, Graduate School of Engineering Science, Osaka Uinversity, Toyonaka, Japan;
[4]Educational Physiology Laboratory, Graduate School of Education, University of Tokyo, Tokyo, Japan;
[5]Dept of Cardiology, Fujita Health University School of Medicine, Toyoake, Japan;
[6]Dept of Medical Education, Nagoya City University Graduate School of Medical Sciences, Nagoya, Japan;

Abstract

Atrial fibrillation is an identified risk factor for ischemic strokes. Thus, the dynamics of heart rate under fibrillation might provide a useful predictor for strokes. The complex, nonlinear and multiscale nature of the heart rate calls for the use of powerful signal processing techniques. We explored the application of a novel tool, the scattering transform, to discriminate and predict ischemic strokes from heart rate dynamics. We found that groups of scattering coefficients, at several time scales, were significantly higher (p-value < 0.05) in patients who developed ischemic strokes than in those who did not. We also found significant differences in predictive power (C-statistic) between scattering coefficients and the CHA_2DS_2-VASc score. Results suggest the use of scattering coefficients for the analysis of patients with atrial fibrillation.

Keywords *Atrial fibrillation, ischemic stroke, heart rate variability, scattering transform, multiscale analysis.*

1 Introduction

Atrial fibrillation. AF is a supraventricular tachyarrythmia characterized by uncoordinated atrial activation [1]. In this condition, the sinus node loses its ability to govern ventricular response [2], and, instead, the atrium is depolarized by a chaotic pattern of rapid and random impulses with two main consequences. First, the atrial tissue contracts in an unsynchronized and erratic way, causing the atrial wall to quiver rather than contract [1]. Second, the random pulses that reach the atrioventricular node cause high irregularity in the ventricular response RR intervals [3]. In consequence, the ventricular response is characterized by a white-noise-like nature in the high and low frequency bands (2.5 s to 25 s), and more complex and organized dynamics in the very-low and ultra-low bands (25 s to more than 300 s), which reflect circadian rhythms and AV node properties mediated by the autonomous nervous system [1, 2].

Ischemic stroke. The impaired mechanical function of the atrium decreases blood flow rates within, and thus favors thrombus' formation and embolic events [1]. Thus, AF is identified as an important risk factor for ischemic strokes (IS) [1]. In fact, treatment of AF patients with oral anticoagulants is a mainstay of current clinical practice [1]. In consequence, a robust risk stratification scheme of stroke likelihood in AF patients would be of great clinical value, aiding in the decisions for prophylaxis and allowing to reduce the exposure of low-risk patients to bleeding complications.

Related work. To date, a standard risk stratification metric to guide antithrombotic therapy in AF patients is provided by the CHA_2DS_2-VASc score [4]. This score groups many risk factors: congestive heart failure, hypertension, age ≥ 75 years (doubled), diabetes, stroke (doubled), vascular disease, age 65–74 years, and gender [4]. On a different approach, risk factors have been obtained from the irregular dynamics of the ventricular response RR intervals, since their irregularity shares a common origin with atrial mechanisms that favor thrombogenesis. In [5], the authors used traditional time-domain statistical measures and entropies to characterize irregularity, and showed that they are associated with an increased risk of mortality. More recently, an explicit connection between irregular RR-interval dynamics and IS was explored in [6], where the authors showed that multiscale sample entropy constitutes a useful predictor of ischemic strokes from AF patients.

Goals, contributions and outline. In this contribution, we propose to explore the potential of a recently introduced signal processing tool to predict ischemic strokes from the RR interval irregularity of AF patients. This tool, referred to as the scattering transform [7, 8], is a nonlinear multiscale transform that provides a stable and informative characterization for processes with complex multiscale dynamics. It has been successfully used, e.g., for audio classification [8] and acidosis detection from

This work was supported by CNRS grant PICS 7260.

fetal heart rate [9–11]. A brief introduction to the scattering transform is provided in Sec. 2. A database of 173 AF patients from a hospital in Aichi, Japan, is then described in Sec. 3. Next, the potentials and benefits of the scattering transform for prediction of ischemic strokes from AF patients are discussed in Sec. 4.

2 Scattering transform

Wavelet coefficients. Let $X(t)$ denote the signal to be analyzed. Let also $\psi(t)$ denote a complex analytic mother wavelet, that is, a band-pass filter supported over positive frequencies. Let $\psi_j(t) = \{2^{-j}\psi(2^{-j}t) \;\; j \in \mathbb{N}\}$ denote the collection of templates of ψ dilated at scales 2^j. The complex dyadic wavelet transform computes the downsampled convolutions $X \star \psi_j(2^j k)$ for all times $t = 2^j k$ and scales 2^j.

Scattering transform. First-order scattering coefficients $S_1(j_1)$ are defined as the average amplitude of the modulus of wavelet coefficients $X \star \psi_{j_1}(t)$, for any $1 \leq j_1 \leq J$:

$$S_1(j_1) = 2^{-j_1} \sum_{k=1}^{2^{j_1}} |X \star \psi_{j_1}(2^j k)|. \qquad (1)$$

The average in (1) looses all information related to the time evolution of $|X \star \psi_j(t)|$. This information can be recovered by computing a second level of wavelet coefficients: $|X \star \psi_{j_1}(t)| \star \psi_{j_2}(t)$, for all scales 2^{j_2} such that $j_1 \leq j_2 \leq J$. Since their amplitude is proportional to that of previous level coefficients, they need to be renormalized to avoid spurious dependence. Thus, second-order scattering coefficients are defined, for $j_2 > j_1$, as:

$$S_2(j_1, j_2) = \frac{2^{-j_2}}{S_1(j_1)} \sum_{k=0}^{2^{j_2}} ||X \star \psi_{j_1}| \star \psi_{j_2}(2^{j_2} k)|. \qquad (2)$$

Interpretation. Second-order coefficients can be interpreted as providing a nonlinear representation of the multiscale dynamics of the wavelet coefficients of X at scale j_1. In this work we focus only on the first two orders of scattering coefficients, since they carry most of the energy in X, as shown in [7, 9]. Information contained in first-order scattering coefficients $S_1(j_1)$ is related to the second-order statistics (correlation, spectrum) of X [7], and thus called *linear* in the following. In contrast, second-order scattering coefficients depend on the higher-order moments of X (and thus characterize X beyond spectral properties) [7, 9], and will thus be termed *nonlinear*.

Illustration. Fig. 1 illustrates this property of scattering coefficients. It shows the (log of) coefficients $S_1(j_1)$ and $S_2(j_1 = 10, j_2)$, averaged over realizations of fractional Gaussian noise (fGn, [12]), a processes defined entirely by its second order moments, and the increments of multifractal random walk (MRW, [13]), a process with nontrivial higher-order statistics. Realizations of both processes where synthesized to have the exact same covariance structure. In consequence, Fig. 1 (left) shows that linear scattering coefficients $S_1(j_1)$ are unable to distinguish both processes. In contrast, Fig. 1 (right) shows that

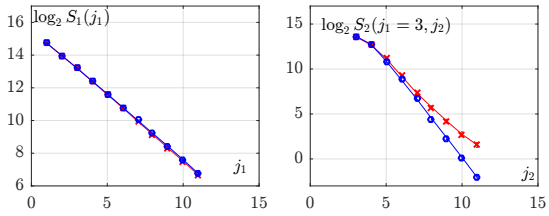

Figure 1: Coefficients $\log_2 S_1(j_1)$ (left) and $\log_2 S_2(j_1 = 3, j_2)$ (right), for two synthetic processes with the same second-order moments but different higher-order moments.

nonlinear coefficients $S_2(j_1, j_2)$, for a particular choice of j_1, are able to discriminate them based on their higher-order statistics.

Software. We computed scattering coefficients using the ScatNet software package for Matlab, available at `http://www.di.ens.fr/data/software/scatnet/`, using a Morlet analytic wavelet.

3 Database

Data collection. We analyzed 24-hour Holter records from patients suffering from permanent AF, defined as AF of more than one year of duration, with no evidence of sinus rhythm, and with no planned sinus rhythm restoration. We excluded patients with complete AV block, sustained ventricular tachycardia, ventricular ectopy $> 5\%$, cardiac pacemakers, paroxysmal AF, valvular AF or prosthethic heart valves, with more than 5% of the Holter record corrupted by artifacts or noise, taking rhythm control drugs, or that had acute coronary syndrome, strokes, hemodynamic instability or undergone surgery in the preceding 6 months. Application of these criteria led to a total of 173 subjects. The CHA_2DS_2-VASc score was recorded for each patient as a baseline measurement of the stroke risk [4].

Patients underwent a follow-up period of 47 ± 35 months. During this period, the diagnosis of ischemic stroke was made by a neurosurgeon. Ischemic strokes were observed in 22 patients.

The study was approved by the ethics committee of Fujita Health University and conformed to the principles outlined in the declaration of Helsinki. All patients provided written informed consent at the time of Holter recording.

Recordings. The 24-hour-long Holter ECGs were recorded with a 2-channel digital recorder (Fukuda Denshi, Tokyo) and digitized at a 125 Hz sampling frequency and 12 bit resolution. RR-intervals were detected automatically, with a manual review and edition by experts.

Preprocessing. All RR time series were preprocessed for outliers, excluding all RR intervals smaller than 350 ms, and larger than 3500 ms or 2.5 times the local 90% percentile. Then, each RR time series was interpolated and resampled at 2 Hz with a linear interpolation scheme, since the wavelet procedure that we applied requires a uniformly sampled time series.

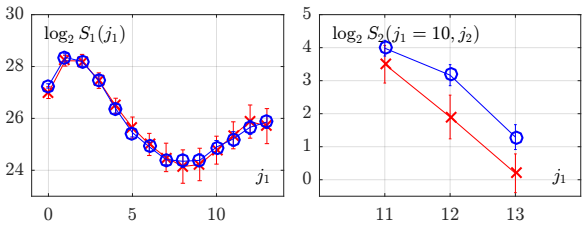

Figure 2: Coefficients $\log_2 S_1(j_1)$ (left) and $\log_2 S_2(j_1 = 10, j_2)$ (right), for the RR time series of patients that did (red crosses) and did not (blue crosses) develop ischemic strokes (median and 95% confidence intervals).

Clinical information. All records are complemented by clinical information, including the reference CHA_2DS_2-VASc score and the administration of antithrombotic drugs such as warfarin and antiplatelet agents.

4 Results and discussion

Scattering coefficients. Fig. 2 shows the linear S_1 (left) and nonlinear S_2 (right, for $j_1 = 10$) scattering coefficients for patients that did (red crosses) and did not (blue circles) develop ischemic strokes. S_1 is remarkably similar for both classes and thus unsuitable for discrimination. In contrast, S_2 shows significant differences between the classes for several values of j_1 and j_2. Fig. 2 (right) shows the particular case for $j_1 = 10$, where coefficients $S_2(10, j_2)$ are clearly able to discriminate between classes. Notably, patients that developed IS show smaller values for S_2, indicating that their heart rate dynamics are characterized by less nonlinear variability.

It is worth noticing that, interestingly, S_1 reproduces the spectral behavior documented in [2]: the existence of two scaling regimes, for $j \in [2, 8]$ and $j \in [9, 13]$. The cutoff scale is $j_c = 8 \approx 2$ min, also in agreement with findings in [2, 6]. The loss of scaling for $j_1 < 2$ is due to the effects of the interpolation and digitalization, which are limited to fine scales.

Statistical analysis. To assess the ability of scattering coefficients to distinguish between the two classes, we performed individual Wilcoxon ranksum tests on each $\log_2 S_1(j_1)$, for all j_1, and each $\log_2 S_2(j_1, j_2)$, for all j_1 and j_2. Further, we grouped significant neighboring coefficients at contiguous scales j_2 for fixed j_1. The scales j_1 and j_2 involved in these groups are indicated in Table 1. We averaged all (log-transformed) coefficients in such groups to obtain discriminant statistics, and performed Wilcoxon ranksum tests on these groups as well.

Table 1 reports the p-values (for the sake of space, only the significant groups are shown). Further, Fig. 3 shows boxplots for each group and class. It can be seen that statistically significant differences can be found on the second-order coefficients computed from a wide range of time scales 2^{j_1} (ranging from ≈ 2 s for $j_1 = 2$, to ≈ 512 s for $j_1 = 10$).

Note that group SG4 is related to the dynamics of RR intervals in the ultra low frequency range (including time scales larger than 8.5 min). However, groups SG1, SG2 and SG3 indicate that scattering coefficients are also found to be significant *at smaller time scales*, ranging from ≈ 2 s ($j_1 = 2$) to ≈ 2 min. Notably, scattering coefficients are not found to be significant in the very low frequency range, where multiscale entropy was found to be significant in [6].

Table 1: Definition of groups and p-values.

Group	j_1	j_2	p-value
SG1	2 (2 s)	$[5, 7]$ ($[16$ s , 1 min $]$)	0.039
SG2	3 (4 s)	$[5, 8]$ ($[16$ s , 2 min $]$)	0.048
SG3	4 (8 s)	$[5, 8]$ ($[16$ s , 2 min $]$)	0.005
SG4	10 (8.5 m)	$[11, 13]$ ($[17$ min , 1 h $]$)	0.022

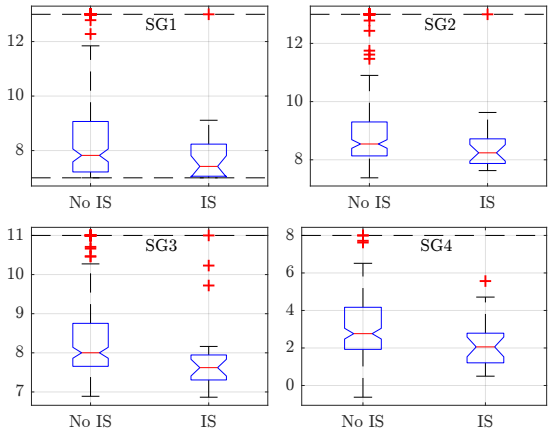

Figure 3: Boxplots of the four groups of scattering coefficients, for patients that did (IS) and did not (no IS) develop an ischemic stroke. Outliers above the dashed line are not displayed.

Correlation. Table 2 shows the Spearman correlation coefficients between each pair of groups. For comparison purposes, multiscale entropy in the very low frequency range ($\text{MeanEn}_{\text{VLF}}$, denoted for brevity as EN), proposed in [6], is also included. It can be seen that all groups show very weak correlations. This suggests that all groups measure different aspects of the RR dynamics and provide complementary information. Further, all groups are uncorrelated with EN, which can be expected from the fact that they are computed at different time scales.

Predictive performance. To assess the power of scattering coefficients to predict the occurrence of ischemic strokes, we performed Receiver Operating Characteristic (ROC) analyses on all groups. For comparison purposes, we also analyzed EN and the CHA_2DS_2-VASc score (CHA), as in [6].

Fig. 4 (top) shows the C-statistics for EN, CHA and the four groups of scattering coefficients. It can be seen that, despite an overall modest performance, groups SG3 and SG4, as well as EN, provide a better predictive power than the standard CHA_2DS_2-VASc score.

If the analysis is restricted to patients not receiving antithrombotic treatment (109 subjects), Fig. 4 (bottom, left), predictive performance increases dramatically, with SG4 reaching almost 80%. In contrast, analysis of pa-

Table 2: Spearman correlation for all scattering group and multiscale entropy (EN).

	SG1	SG2	SG3	SG4	EN
SG1		0.268	0.204	0.053	0.039
SG2			0.188	0.03	0.003
SG3				0.035	0.031
SG4					−0.069

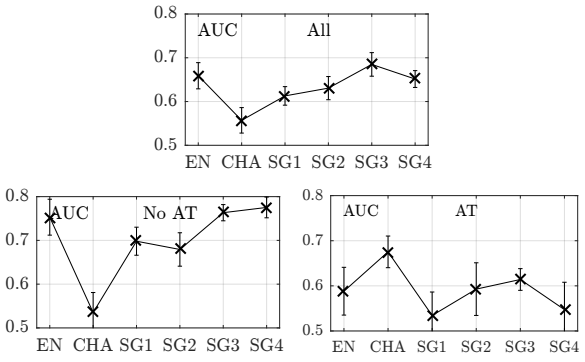

Figure 4: Area under the ROC curve (and 95% confidence intervals computed from 5-fold cross-validation) for multiscale entropy (EN), CHA_2DS_2-VASc score (CHA), and the four groups of scattering coefficients indicated in Table 1. Analysis was performed on all patients (top), and those that did and did not receive antithrombotic treatment (bottom left and right, respectively).

tients under antithrombotic treatment (69 subjects), Fig. 4 (bottom, right), shows that predictive power is poor, and that CHA_2DS_2-VASc is actually the best predictor. This suggests that in these patients the ischemic stroke is actually not associated with AF. Results in this section suggest the promising value of SG3 and SG4, as well as EN, as predictors of ischemic stroke, in particular when patients are not under antithrombotic treatment.

5 Conclusion and future work

In this work, we have made an exploration of the value of scattering coefficients for the prediction of ischemic stroke from patients with atrial fibrillation. Results suggest that scattering coefficients have a good discriminant power, using information from a wide range of time scales and statistical orders. Further, these groups show an acceptable predictive performance, in particular when only patients that are not receiving antithrombotic drugs are considered. Future work will address the improvement of predictive power by the joint use of all the uncorrelated predictors considered here, with an adequate machine learning strategy. Moreover, the exploration of complementary nonlinear features will also be considered.

References

[1] V. Fuster, et al. ACC/AHA/ESC 2006 Guidelines for the Management of Patients With Atrial Fibrillation A Report of the American College of Cardiology/American Heart Association Task Force on Practice Guidelines and the European Society of Cardiology Committee for Practice Guidelines. *Circulation*, 114(7):e257–e354, 2006.

[2] J. Hayano, et al. Spectral characteristics of ventricular response to atrial fibrillation. *Am. J. Physiol. Heart Circ. Physiol.*, 273(6):H2811–H2816, 1997.

[3] J. A. Kirsh, et al. Ventricular response to atrial fibrillation: role of atrioventricular conduction pathways. *J. Am. Coll. Cardiol.*, 12(5):1265–1272, 1988.

[4] G. Y. Lip, et al. Identifying Patients at High Risk for Stroke Despite Anticoagulation A Comparison of Contemporary Stroke Risk Stratification Schemes in an Anticoagulated Atrial Fibrillation Cohort. *Stroke*, 41(12):2731–2738, 2010.

[5] A. Yamada, et al. Reduced ventricular response irregularity is associated with increased mortality in patients with chronic atrial fibrillation. *Circulation*, 102(3):300–306, 2000.

[6] E. Watanabe, et al. Multiscale Entropy of the Heart Rate Variability for the Prediction of an Ischemic Stroke in Patients with Permanent Atrial Fibrillation. *PLOS ONE*, 10(9):e0137144, 2015.

[7] S. Mallat. Group Invariant Scattering. *Comm. Pure Appl. Math.*, 65(10):1331–1398, 2012. arXiv: 1101.2286.

[8] J. Andén and S. Mallat. Deep Scattering Spectrum. *IEEE Trans. Sig. Proc.*, 62(16):4114–4128, 2014.

[9] V. Chudáček, et al. Scattering Transform for Intrapartum Fetal Heart Rate Variability Fractal Analysis: A Case-Control Study. *IEEE Trans. Biomed. Eng.*, 61(4):1100–1108, 2014.

[10] Chudáček, et al. Low dimensional manifold embedding for scattering coefficients of intrapartum fetale heart rate variability. In *Conf Proc IEEE Eng Med Biol Soc*, pages 6373–6376, 2014.

[11] V. Chudáček, et al. Scattering transform for intrapartum fetal heart rate characterization and acidosis detection. In *Conf Proc IEEE Eng Med Biol Soc*, pages 2898–2901, 2013.

[12] B. Mandelbrot and J. Van Ness. Fractional Brownian Motions, Fractional Noises and Applications. *SIAM Review*, 10(4):422–437, 1968.

[13] E. Bacry, J. Delour, and J. F. Muzy. Multifractal random walk. *Phys. Rev. E*, 64(2):026103, 2001.

Address for correspondence:

Patrice Abry
Lab de Physique, ENS de Lyon, Lyon, France
patrice.abry@ens-lyon.fr

Preliminary Investigation of Instantaneous Cardiovascular Dynamics from Contactless video-Photoplethysmography

Gaetano Valenza[1,2], Luca Iozzia[3], Luca Cerina[3], Luca Mainardi[3], and Riccardo Barbieri[2,3]

[1]Research Centre E Piaggio, University of Pisa, Pisa, Italy
[2]Harvard Medical School, Massachusetts General Hospital, Boston, MA, USA
[3]Department of Electronics, Information and Bioengineering, Politecnico di Milano, Milano, Italy

Abstract

There is a fast growing interest in estimating cardiovascular information using contactless video-photoplethysmography (vPPG). Nevertheless, an in-depth validation of time-varying, nonlinear dynamics of the related pulse rate variability is still missing. To this extent, in this study we applied inhomogeneous point-process nonlinear models to assess instantaneous measures defined in the time, frequency, and bispectral domains as estimated through vPPG and standard ECG. Video recordings were processed using our recently proposed method based on zero-phase component analysis. Experimental data were gathered from 60 young healthy subjects (age: 24±3 years) undergoing postural changes (rest-to-stand maneuver).

Results show that, at a group level, there is an overall agreement between linear and nonlinear indices computed from ECG and vPPG during resting state conditions. However, significant differences were found, especially in the bispectral domain, also considering data gathered while standing. Although significant differences exist between cardiovascular estimates from vPPG and ECG, results can be considered very promising as instantaneous sympatho-vagal changes were correctly identified. More research is indeed needed to improve on the precise estimation of nonlinear sympatho-vagal interactions.

Keywords *Contactless video-photoplethysmography, Heart Rate Variability, Point Process, Nonlinear Analysis, Bispectrum, Sympatho-vagal balance, ECG.*

1 Introduction

Contactless video-photoplethysmography (vPPG) refers to a non-invasive, optical technique able to remotely detect blood volume changes in humans using ambient light and a consumer-level digital camera. In the last decade, significant research efforts have been made to effectively derive cardiovascular information from vPPG monitoring [1–5].

Prior studies mainly proposed the estimation of pulse rate and pulse rate variability (PRV) series from video of subject's face [1–5, 5, 6], evaluating the agreement between PRV-derived parameters (defined in the time and frequency domains) obtained from vPPG data as compared to PPG recordings. Conclusions highlighted very promising, statistically comparable results during resting state conditions [1, 2, 6].

Nevertheless, to our knowledge, major shortcomings of previous studies can be listed as follows: 1) a limited number of subjects were involved in the validation process (i.e., $<$20); 2) time-varying, nonlinear dynamics of PRV series from vPPG as compared to standard ECG recordings has not been evaluated yet.

To this extent, we here study instantaneous linear and nonlinear estimates derived from inhomogeneous point-process nonlinear models of heartbeat dynamics in a cohort of 60 young healthy subjects undergoing postural changes. More specifically, we assess the instantaneous features defined in the time domain, as well as measures derived from the dynamic spectrum and bispectrum of series of heartbeat events as estimated through vPPG and standard ECG. In this preliminary evaluation, the comparison of such time-varying measures is performed at a group-wise level considering averaged measures during resting state and upright positions. Of note, video recordings are processed using our recently proposed method based on zero-phase component analysis, in combination with a fully-automatic method for detection and tracking of region of interest located on the forehead, the cheek and the nose [7].

The use of stochastic point-process models for this study is justified by multiple reasons: 1) all point-process linear and nonlinear estimates are defined in the continuous time without the need of interpolation techniques (e.g., linear, spline, etc.) on the original series [8, 9]; 2) the embedded inverse-Gaussian probability structure of the model takes into account underlying physiological dynamics of heartbeat generation [8]; 3) Goodness-of-fit measures are considered to assess the fitting on experimental data [8]; 4) alongside the autoregressive linear combination of the present and past interbeat intervals, nonlinear terms are also included according to a Wiener-Volterra representation [9]; 5) Laguerre filters are used to retain long-term information and lowest number of model parameters [9].

Next, a brief description of the video and standard ECG recordings, along with the experimental procedure including the derivation of vPPG series, the mathematical background of point-process models, and experimental results and conclusions are reported.

2 Materials and Methods

2.1 Experimental Procedure

A homogeneous group of 60 young healthy volunteers (29 woman, age: 24±3 mean±std, range 20-34) was recruited for this study. Each subject signed a comprehensive, written informed consent. Participants had various skin types ranging from type II to type IV. Subjects underwent postural changes to induce sympatho-vagal changes. They were instructed not to move their head in order to reduce movement artifacts. During a 5 minutes resting state session, they were asked to lay on a bed facing the camera while recording standard ECG. The bed was positioned in front of the window to have direct sunlight on subject's face. After the resting state, subjects were asked to stand up while the camera was manually moved to follow their face. During the transition period, both video and ECG recording were suspended. When subjects had reached a stable position and the camera was properly aligned, recordings were restarted for a period of five minutes.

Video recordings were acquired with a frame-rate of 60 frames-per-second and 8-bits resolution, using a GigE Sony XCG-C30C camera whose image sensor was 1/3" color progressive scan with spatial resolution of 659 x 494 pixels. The camera was equipped with 15 mm fixed focal length lenses (Tamron 25 HB), which were used to magnify the region occupied by the participant's face. The camera was fixed on a tripod. The ECG signal was sampled at 256 Hz using a FlexComp Infiniti by Thought Technologies, Inc. device. Electrodes were located on the thorax.

2.2 Derivation of vPPG and related cardiovascular series

Three regions of interests (ROI) were considered: forehead, nose, and cheek. ROI detections were performed through the Viola-Jones face detection algorithm [10], while ROI tracking was obtained by the Lucas-Kanade-Tomasi motion flow tracking algorithm [11]. In each ROI, a spatial average of pixels intensity was calculated for each frame. These time series were firstly detrended using the technique described in [12], setting the smoothness parameter $\lambda = 400$. A hamming bandpass filter with cut-off frequencies of $f_1 = 0.1$Hz, $f_2 = 8$Hz was then applied to remove the high frequencies components, mainly correlated to artificial light, and low frequencies components, associated to slow subject movements. The vPPG signal was extracted using the Zero-phase Component Analysis method [7]. The detection of PRV from vPPG was performed on the first derivative of the signal. Since the detection of the peak was done on the derivative of vPPG signal, the position of each pulse is located on the maximum of first derivative, i.e. along the rising edge of the cardiac pulse (defined as anachrotic phase). The detection of R peaks in the ECG was automatically performed by applying the method described in [13]. The R detections were then visually inspected and the misdetected/erroneous beats were corrected.

2.3 Point-Process Model of Heartbeat Dynamics

In this paragraph, we briefly describe the methodological background of point-process models of heartbeat dynamics, whose details can be found in [8, 9]. Below, we expose the modeling equations referring to standard ECG and related R-waves. The same formulation directly applies for PRV series from vPPG considering the respective fiducial points indentifying heartbeat events. We aim to characterize a family of probability density functions (pdfs) that predict the time of the next heartbeat event, given timing information of the present and past events. As mentioned in the Introduction, such pdfs are known to be physiologically-plausible, continuous Inverse-Gaussian distributions $f(t|\mathcal{H}_t, \xi(t))$ [8,9]:

$$f(t|\mathcal{H}_t, \xi(t)) = \left[\frac{\xi_0(t)}{2\pi(t-u_j)^3}\right]^{\frac{1}{2}} \times \exp\left\{-\frac{1}{2}\frac{\xi_0(t)[t-u_j-\mu_{\mathrm{RR}}(t,\mathcal{H}_t,\xi(t))]^2}{\mu_{\mathrm{RR}}(t,\mathcal{H}_t,\xi(t))^2(t-u_j)}\right\} \quad (1)$$

with $j = \widetilde{N}(t)$ the index of the previous heartbeat event before time t, $\{u_j\}_{j=1}^{J}$ as the ordered set of R-wave events, and $\mathrm{RR}_j = u_j – u_{j-1} > 0$, as the j^{th} R–R interval, $\mathcal{H}_t = (u_j, \mathrm{RR}_j, \mathrm{RR}_{j-1}, ..., \mathrm{RR}_{j-M+1})$, $\xi(t)$ the vector of the time-varying parameters, and $\xi_0(t) > 0$ the shape parameter of the inverse Gaussian distribution. The pdf is parametrized through its first-order moment statistic (mean), $\mu_{\mathrm{RR}}(t, \mathcal{H}_t, \xi(t))$, which is modeled considering the Laguerre expansions of the Wiener-Volterra kernels up to the second order. This choice of expanding the kernels reduces the number of unknown parameters that need be estimated [9]. In addition, the regression is performed on the derivative RR series, in order to improve the achievement of stationarity within the sliding time window $W = 90$ sec [9]. Thus, the obtained Nonlinear Autoregressive with Laguerre expansion model can be written as:

$$\mu_{\mathrm{RR}}(t, \mathcal{H}_t, \xi(t)) = \mathrm{RR}_{\widetilde{N}(t)} + g_0(t) + \sum_{i=0}^{p} g_1(i,t)\, l_i(k) + \sum_{i=0}^{q}\sum_{j=0}^{q} g_2(i,j,t)\, l_i(k)\, l_j(k)\ . \quad (2)$$

where

$$l_i(t) = \sum_{n=1}^{\widetilde{N}(t)} \phi_i(n)(\mathrm{RR}_{\widetilde{N}(t)-n} - \mathrm{RR}_{\widetilde{N}(t)-n-1}) \quad (3)$$

is the output of the Laguerre filters, with $\widetilde{N}(t)$ as a left continuous function of the related counting process, and

$$\phi_i(n) = \alpha^{\frac{n-i}{2}}(1-\alpha)^{\frac{1}{2}} \sum_{j=0}^{i}(-1)^j \binom{k}{j}\binom{i}{j}\alpha^{i-j}(1-\alpha)^j$$

is the i^{th}-order discrete time orthonormal Laguerre function, with ($n \geq 0$) and α the discrete-time Laguerre parameter. Importantly, the instantaneous variance is:

$$\sigma^2_{RR}(t, \mathcal{H}_t, \xi(t)) = \mu^3_{RR}(t)/\xi_0(t). \quad (4)$$

We use the Newton-Raphson procedure to maximize the local log-likelihood defined in [8] in order to estimate the unknown time-varying parameter set $\boldsymbol{\xi}(t) = [\xi_0(t), g_0(t), g_1(0,t), ..., g_1(p,t), g_2(0,0,t), ..., g_2(i,j,t)]$. The optimal order $\{p, q\}$ is estimated by means of the point process model goodness-of-fit applied to a subset of the data [8]. Model goodness-of-fit is based on the Kolmogorov-Smirnov (KS) test and associated KS statistics [8]. Autocorrelation plots are also considered to test the independence of the model-transformed intervals [8]. Once the model's parameters are derived, a few additional steps are required to calculate the quantitative tools, i.e. the instantaneous autospectrum and bispectrum: 1) from the fitted coefficients $g_n(...)$ of eq. (2), use the Laguerre deconvolution to obtain the Wiener-Volterra kernels $\gamma_n(...)$; 2) from $\gamma_n(...)$ compute the Fourier transforms of the symmetric kernels derived from $\gamma_n(...)$; 3) compute the Wiener-Volterra Input-Output kernels [9]; 4) compute the autospectrum $Q(t,f)$ and autobispectrum $Bis(f_1, f_2, t)$. By integrating $Q(t,f)$ in each frequency band, we can compute the instantaneous index within the low frequency (LF = 0.05-0.15 Hz) and high frequency (HF = 0.15-0.5 Hz) ranges, along with their ratio (LF/HF).

Through bispectral analysis it is possible to further evaluate the nonlinerar sympatho-vagal interactions by integrating $|Bis(f_1, f_2, t)|$ in the appropriate frequency bands. Specifically, we evaluate:

$$LL(t) = \int_{f_1=0^+}^{0.15} \int_{f_2=0^+}^{0.15} Bis(f_1, f_2, t) df_1 df_2 \quad (5)$$

$$LH(t) = \int_{f_1=0^+}^{0.15} \int_{f_2=0.15^+}^{0.4} Bis(f_1, f_2, t) df_1 df_2 \quad (6)$$

$$HH(t) = \int_{f_1=0.15^+}^{0.4} \int_{f_2=0.15^+}^{0.4} Bis(f_1, f_2, t) df_1 df_2 \quad (7)$$

3 Statistical Analysis and Results

All features were calculated instantaneously with a 5ms temporal resolution. For each subject and for every feature X, as an exploratory/preliminary step, we condensed the information about the time-varying dynamics of X through its median value. On both resting and stand conditions, we then compared data from vPPG and ECG using non-parametric statistics (Mann-Whitney test) under the null hypothesis that the between-subject medians of the two groups are equal.

In this study, point-process analyses yielded optimal orders of $3 \leq p \leq 5$ and $1 \leq q \leq 2$. KS distances were as low as 0.0434±0.0112 for resting state data, and 0.0419±0.0107, ensuring that our models well-predicted all series of heartbeat events. Visual inspection analysis ensured that more than 98% of autocorrelation plot samples were within 95% boundaries.

Averaged instantaneous series from all subjects are shown in Figs. 1 and 2.

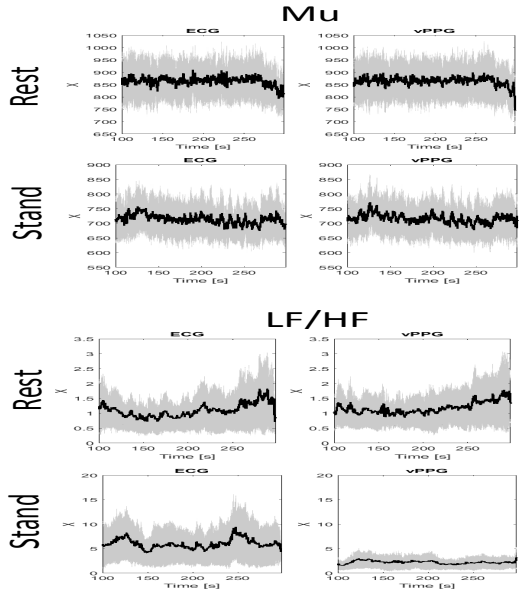

Figure 1: Instantaneous $\mu_{\mathrm{RR}}(t)$ and LF statistics from ECG (left panels) and vPPG (right panels) averaged along all subjects, showing $\mathrm{Median}(X) \pm \mathrm{MAD}(X)$.

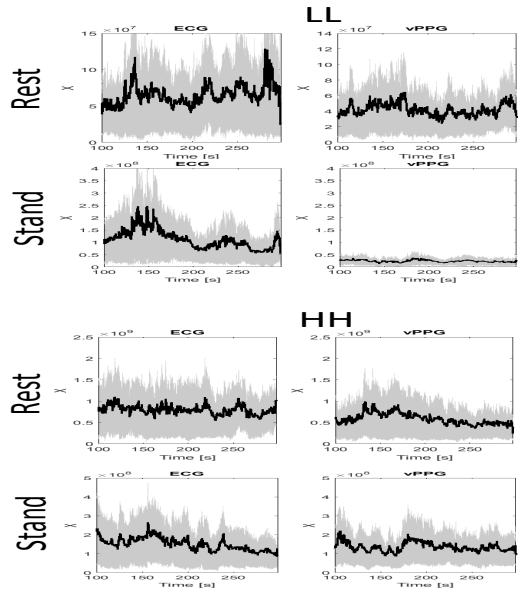

Figure 2: Instantaneous bispectral statistics from ECG (left panels) and vPPG (right panels) averaged along all subjects, showing $\mathrm{Median}(X) \pm \mathrm{MAD}(X)$.

Results of group-wise statistics are shown in Table 1. Considering data from resting state sessions, no significant differences were found between features estimated from ECG and vPPG in all indices but LH ($p < 0.03$). Considering data from standing, significant differences were found between features from ECG and vPPG in σ_{RR} ($p < 0.001$), HF ($p < 0.005$), LF/HF ($p < 0.0001$), LL and LH ($p < 0.003$).

4 Conclusions

Using inhomogeneous point-process nonlinear models, we studied cardiovascular dynamics estimated

Table 1: Results of the comparison between ECG- and vPPG-derived features on the rest-stand data.

Feature	Session	from ECG	from vPPG	p-val
μ_{RR}	Rest	865.74±101.10	864.77±104.38	0.985
	Stand	710.30±77.14	709.41±75.74	0.985
σ_{RR}	Rest	742.57±396.85	931.96±431.81	0.130
	Stand	**346.96±199.65**	**846.15±445.72**	**9.5e-7**
LF	Rest	545.96±299.19	502.82±277.58	0.768
	Stand	576.30±352.77	549.76±336.42	0.444
HF	Rest	456.57±265.84	376.45±184.45	0.780
	Stand	**136.93±95.52**	**217.39±135.11**	**0.004**
LF/HF	Rest	1.01±0.49	1.10±0.51	0.657
	Stand	**6.23±4.44**	**2.00±1.19**	**1.6e-5**
LL	Rest	$(77.25\pm61.13)10^6$	$(46.31\pm30.44)10^6$	0.071
	Stand	$\mathbf{(120.41\pm91.76)}10^6$	$\mathbf{(26.14\pm18.58)}10^6$	**2.5e-8**
LH	**Rest**	$\mathbf{(231.69\pm127.52)}10^6$	$\mathbf{(150.81\pm95.37)}10^6$	**0.024**
	Stand	$\mathbf{(127.98\pm97.37)}10^6$	$\mathbf{(55.72\pm37.89)}10^6$	**0.002**
HH	Rest	$(841.54\pm685.51)10^6$	$(593.94\pm491.44)10^6$	0.093
	Stand	$(176.83\pm132.58)10^6$	$(141.49\pm100.12)10^6$	0.932

Values are expressed as $\mathrm{Median}(X) \pm \mathrm{MAD}(X)$ among subjects.
p-values are from Mann-Whitney tests between vPPG and ECG data.
Lines in bold indicate a significant difference with $p < 0.05$.

from contactless video-photoplethysmography (vPPG) as compared to standard ECG. Specifically, we investigated time-varying, linear and nonlinear dynamics through measures defined in the time (instantaneous mean and standard deviation) and frequency domains (instantaneous power from dynamical spectrum), as well as nonlinear estimates from dynamical bispectra (instantaneous nonlinear sympatho-vagal interactions). The experimental setup foresaw postural changes to induce sympatho-vagal changes. As a preliminary investigation, we condensed the time-varying information of each feature through its median value. Results are very promising. Although during standing conditions the degree of agreement is low, especially considering features defined in the frequency and bispectral domains, at a group-wise level we found an overall agreement between estimates from vPPG and ECG considering linear and nonlinear dynamics during resting state conditions (though with a significant difference in LH). Our results also suggest that our methodology for deriving vPPG from video recording can be considered effective with a wide range of lighting and movement conditions. During resting state, in fact, subjects were lying supine on a bed with minimal movement artifacts. Further research will be focused on improving space and time resolution, inter-subject reliability, and robustness in face tracking under real-world extreme conditions (e.g. low light, high movement). Future validation studies will focus on investigating feature variability of the subject time-varying dynamics, along with the study of further indices of instantaneous cardiovascular dynamics defined within the point-process framework.

References

[1] MZ Poh, DJ McDuff, and RW Picard. Advancements in noncontact, multiparameter physiological measurements using a webcam. *Biomedical Engineering, IEEE Transactions on*, 58(1):7–11, 2011.

[2] Y Sun et al. Noncontact imaging photoplethysmography to effectively access pulse rate variability. *Journal of biomedical optics*, 18(6):061205–061205, 2013.

[3] G de Haan and V Jeanne. Robust pulse rate from chrominance-based rppg. *Biomedical Engineering, IEEE Transactions on*, 60(10):2878–2886, 2013.

[4] L Tarassenko et al. Non-contact video-based vital sign monitoring using ambient light and autoregressive models. *Physiological measurement*, 35(5):807, 2014.

[5] C Takano and Y Ohta. Heart rate measurement based on a time-lapse image. *Medical engineering & physics*, 29(8):853–857, 2007.

[6] J Moreno, J Ramos-Castro, J Movellan, E Parrado, G Rodas, and L Capdevila. Facial video-based photoplethysmography to detect hrv at rest. *Int. J. Sports Med*, 36(6):474–480, 2015.

[7] L Iozzia, L Cerina, and L. Mainardi. Assessment of beat-to-beat heart rate detection method using a camera as contactless sensor. In *Proceedings of IEEE-EMBC*, 2016.

[8] R. Barbieri, E. C. Matten, A. R. A. Alabi, and E. N. Brown. A point-process model of human heartbeat intervals: new definitions of heart rate and heart rate variability. *American Journal of Physiology-Heart and Circulatory Physiology*, 288(1):H424, 2005.

[9] G Valenza, L Citi, EP Scilingo, and R Barbieri. Point-process nonlinear models with laguerre and volterra expansions: Instantaneous assessment of heartbeat dynamics. *Signal Processing, IEEE Transactions On*, 61(11):2914–2926, 2013.

[10] P Viola and M Jones. Rapid object detection using a boosted cascade of simple features. In *Computer Vision and Pattern Recognition, 2001.*, volume 1, pages I–511. IEEE, 2001.

[11] C Tomasi and T Kanade. *Detection and tracking of point features*. School of Computer Science, Carnegie Mellon Univ. Pittsburgh, 1991.

[12] MP Tarvainen, PO Ranta-Aho, and PA Karjalainen. An advanced detrending method with application to hrv analysis. *IEEE Transactions on Biomedical Engineering*, 49(2):172–175, 2002.

[13] V Afonso, WJ Tompkins, TQ Nguyen, and S Luo. ECG beat detection using filter banks. *Biomedical Engineering, IEEE Transactions on*, 46(2):192–202, 1999.

Address for correspondence:

Riccardo Barbieri
Politecnico di Milano, Milano (Italy)
riccardo.barbieri@polimi.it

Savitzky–Golay filter-based detrended fluctuation analysis: Theory and its application to physiological time series

Yutaka Tsujimoto, Yasuyuki Suzuki, Masanori Shimono, Taishin Nomura, Ken Kiyono,

[1]Graduate School of Engineering Science, Osaka University, JAPAN;

Abstract

Detrended fluctuation analysis (DFA) has become a standard technique for quantifying long-range correlation and fractal scaling behavior observed in physiological time series. However, we have recently shown that the DFA detrending procedure using piecewise least-squares fitting results in the nonuniformly weighted estimation of the root-mean-square deviation, and that this property could cause an increase in the estimation error. As a better DFA variant, centered detrending moving average (DMA) analysis has been suggested. Recently, we have shown the equivalence between the detrending operation in the centered DMA and the Savitzky–Golay filter, and developed a fast algorithm for the Savitzky–Golay filter-based scaling analysis. In this paper, we further provide solid mathematical foundations for this methodology. In addition, through the analysis of physiological time series available from PhysioNet, we investigate the performance of the Savitzky–Golay filter-based analysis.

Keywords *Long-range correlation, Fractal scaling, Gait dynamics, Heart rate variability*

1 Introduction

Long-range correlations have been observed in a wide variety of physiological and biomedical time series [1, 2]. The importance of characterizing the long-range correlation in such time series would be underscored by studies demonstrating that its alteration is associated with a disease state and higher mortality risk [3–5]. Thus, reliable characterization of the long-range correlation is an important task.

To achieve reliable detection of long-range correlation, it is important to distinguish deterministic trends from the long-range correlation intrinsic in the stochastic dynamics. To remove or attenuate the adverse effect caused by the deterministic trend, a random-walk analysis method employing detrending techniques, called detrended fluctuation analysis (DFA), was developed by Peng et al. [6, 7], and has since become one of the most widely used methods in physiological and biomedical fields [8–12]. In this method, an *a priori* unknown trend embedded in the time series is eliminated via piecewise least-squares polynomial fitting. However, it is recently shown that the DFA detrending procedure results in the nonuniformly weighted estimation of the root-mean-square deviation, and that this property could cause an increase in the estimation error [13]. In contrast, centered detrending moving average (DMA) analysis using a moving polynomial filter has been recognized as a better DFA variant [13–16]. This method has better estimation properties than DFA, such as uniformity of the root-mean-square deviation estimation and zero phase shift for all frequencies. Recently, we have shown the equivalence between the detrending operation in the centered DMA and the Savitzky–Golay filter, and developed a fast algorithm for the Savitzky–Golay filter-based scaling analysis [14]. Therefore, we refer to centered DMA as Savitzky–Golay filter-based DFA (SG-DFA). In this paper, we further provide solid mathematical foundations for this methodology. In addition, through the analysis of stride interval time series and heart rate variability available from PhysioNet, we investigate the performance of the SG-DFA.

2 Savitzky–Golay filter-based detrended fluctuation analysis

In this section, we briefly review SG-DFA (or equivalently centered DMA) and provide its fundamental properties [14–16]. In SG-DFA, instead of the piecewise least-squares fitting used in the standard DFA, the Savitzky–Golay filter is employed [17]. The procedure of the SG-DFA is the following: 1) To analyze time series $\{x[i]\}_{i=0}^{N-1}$ displaying long-range correlation and non-diffusive behavior, we first integrate the observed time series, $y[i] = \sum_{j=0}^{i-1} (x[j] - \overline{x})$, where $\overline{x}$ is the sample mean of $\{x[i]\}$, and analyze $\{y[i]\}$. 2) The trend component $\{\tilde{y}_n[i]\}$ embedded in the observed time series $\{y[i]\}$ at each scale n is estimated by a Savitzky–Golay filter with length n and polynomial order m, where m is an even number [17]. This filter locally smooths a time series by fitting an mth polynomial of order m to a sliding window. This operation can be effectively achieved by a linear convolution with a set of pre-computed coefficients (see Figure 1). Namely, the detrending operation is described by

$$y[i] - \tilde{y}_n[i] \;=\; y[i] - \sum_{j=-(n-1)/2}^{(n-1)/2} c_j \, y_l[i+j] \qquad (1)$$

In Eq. (1), c_j are given by

$$c_j \;=\; \sum_{k=0}^{m/2} b_{1,2k+1}(n)\, j^{2k}, \qquad (2)$$

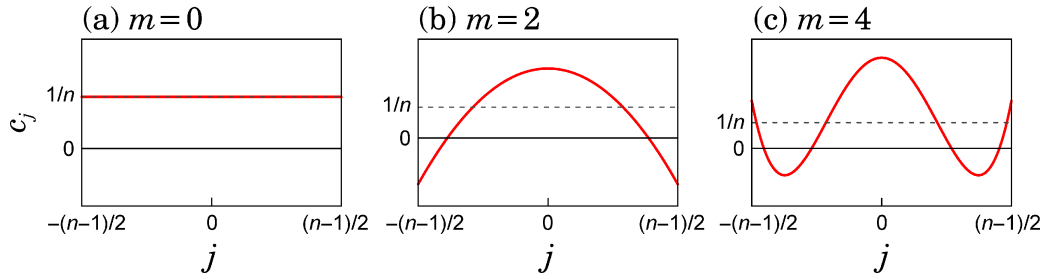

Figure 1: Illustration of coefficients of a Savitzky–Golay (SG) filter. The detrending operation of SG-DFA is described by $y[i] - \sum_j c_j\, y_l[i+j]$. (a) Zeroth order SG filter (centered moving average). (b) Second order SG filter. (c) Fourth order SG filter. The mth order SG filter can remove up to $(m+1)$th order polynomial trend embedded in $\{y[i]\}$.

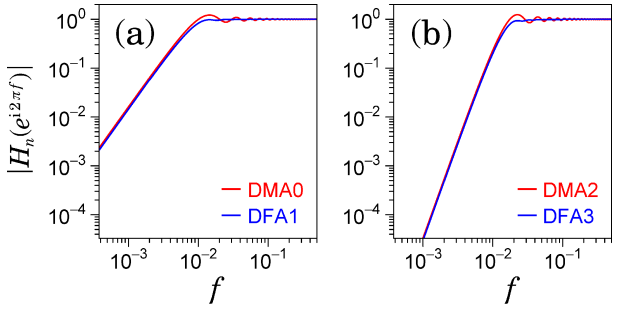

Figure 2: Frequency responses $\left|H_n\left(e^{\mathrm{i}2\pi f}\right)\right|$ of SG-DFA (red) and DFA (blue) when $n = 99$. (a) Comparison between zeroth-order SG-DFA and first-order DFA. (b) Comparison between second-order SG-DFA and third-order DFA.

where $b_{i,j}(n)$ are elements of the $(m+1)\times(m+1)$ matrix $B_m^{-1}(n)$, and $B_m^{-1}(n)$ is the inverse matrix of

$$B_m(n) = \sum_{j=-(n-1)/2}^{(n-1)/2} \begin{bmatrix} 1 & 0 & \cdots & j^m \\ 0 & j^2 & \cdots & 0 \\ \vdots & \vdots & \ddots & \vdots \\ j^m & 0 & \cdots & j^{2m} \end{bmatrix}. \quad (3)$$

3) Using the detrend profiles $\{y[i] - \tilde{y}_n[i]\}$, the estimator of the root-mean-square deviation, called fluctuation function, is defined as

$$F(n) = \left[\frac{1}{N-n+1}\sum_{i=1+(n-1)/2}^{N-(n-1)/2}\left(y[i]-\tilde{y}_n[i]\right)^2\right]^{1/2}, \quad (4)$$

where N is the data length. 4) Steps 2 and 3 are repeated over multiple time scales to characterize the relationship between $F(n)$ and n. A linear relationship on a log-log plot of $F(n)$ as function of n indicates the power-law scaling range, in which the fluctuations can be characterized by a scaling exponent α, the slope of the linear relation between $\log F(n)$ and $\log n$. To carry out the SG-DFA procedure, we have recently developed a fast algorithm [14]. In this paper, we employ this algorithm.

2.1 Fundamental properties of SG-DFA

Based on analytical approaches, we can show the following fundamental properties of SG-DFA (note that here m is an even number) [14, 15]: (1) mth order SG-DFA is equivalent to $(m+1)$th order one; (2) mth order SG-DFA can remove up to mth order polynomial trend in the original time series before integration; and (3) the upper limit of the detectable scaling exponent α by mth order SG-DFA is $m+2$. These facts indicate that the performance of mth order SG-DFA is comparable with that of $(m+1)$th order standard DFA.

In DFA and its variants, the detrending operation generally acts as a high pass filter [16]. In the case of SG-DFA, including higher-order ones, detrending operations are described by a linear convolution. Therefore, its frequency response can be analytically calculated using conventional linear analysis techniques. For instance, frequency response functions of detrending operations in zeroth and second-order SG-DFA are given respectively by

$$H_n(f) = 1 - \frac{\sin(\pi n f)}{n\sin(\pi f)}, \quad (5)$$

and

$$H_n(f) = 1 + \frac{1}{2n^3-8n}\left\{\frac{3\left(n^2+5n+6\right)\sin(\pi n f)}{\sin(\pi f)} + \frac{(15n+30)\cos(\pi(n+1)f)}{\sin^2(\pi f)} - \frac{15\sin(\pi(n+2)f)}{\sin^3(\pi f)}\right\}. \quad (6)$$

These frequency responses (gains) are illustrated in Figure 2, together with the pseudo-frequency responses of DFA [16]. Because $H_n(f)$ of the SG-DFA detrending operation is a real positive function, this filter has zero phase shift for all frequencies. In contrast, the DFA detrending operation generates unnecessary higher frequency components and heterogeneous phase shift of the detrended profile because of nonlinearity of the detrending filter [13]. As will be shown, these properties result in instability of the scaling estimation.

In addition, it should be emphasized that the cutoff frequency of the DFA detrending operation has not been appropriately adjusted from the perspective of filter design. Therefore, a distortion of the relationship between

Table 1: Analytically calculated r_c for DFA and SG-DFA.

order	DFA	SG-DMA
zeroth	$\sqrt{3}$	$\sqrt{6}$
first	$\sqrt{3}\sqrt[4]{5}$	$\sqrt{6}$
second	$\sqrt[6]{7}\sqrt[3]{15}$	$2^{3/4}\sqrt[4]{35}$
third	$\sqrt{3}\sqrt[4]{35}$	$2^{3/4}\sqrt[4]{35}$
fourth	$3^{3/5}\sqrt[10]{11}\sqrt[5]{35}$	$2^{2/3}\sqrt{3}\sqrt[6]{77}$
fifth	$\sqrt{3}\sqrt[12]{13}\sqrt[6]{385}$	$2^{2/3}\sqrt{3}\sqrt[6]{77}$

Table 2: Group means of σ_Δ for SG-DFA and DFA. For stride interval time series, σ_Δ was estimated over $10^1 \le n \le 10^2$, and for HRV, over $10^3 \le n \le 10^4$.

order	stride interval ($n = 10$)	HRV ($n = 54$)
SG-DFA0	0.016	0.004
DFA1	0.044	0.080
SG-DFA2	0.011	0.004
DFA3	0.030	0.032
SG-DFA4	0.015	0.006
DFA5	0.026	0.021

the time and frequency scales is always observed. In standard DFA and SG-DFA, when n is large enough, the cut-off frequency is approximately given by

$$f_c(n) \approx \frac{r_c}{\pi n}, \tag{7}$$

where r_c is a constant. Analytically calculated r_c are summarized in Table 2. To reduce the scale distortion, we define the standardized time scale as $\tilde{n} = n/r_c$ and study the scaling relation between $F(\tilde{n})$ and $\tilde{n}$.

3 Application of SG-DFA

3.1 Methods

To test the performance of SG-DFA, we analyze physiological time series available from PhysioNet using conventional DFA up to the fifth order and SG-DFA up to the fourth order. We study two data sets: (1) Stride interval time series derived from 10 young, healthy men (ages 18-29 yrs); (2) Heart rate variability (RR-interval) time series derived from 54 healthy subjects (ages 28-76 yrs).

As a quantitative parameter to characterize the estimation instability observed in $\log_{10} F(\tilde{n})$, we calculate the standard deviation of the increments of $\log_{10} F(\tilde{n})$ over the range of $N_1 \le n \le N_2$, where N is the data length, and the analyzed scales are integers nearest to the geometric progression with a common ratio of $2^{1/8}$. This parameter is denoted by σ_Δ.

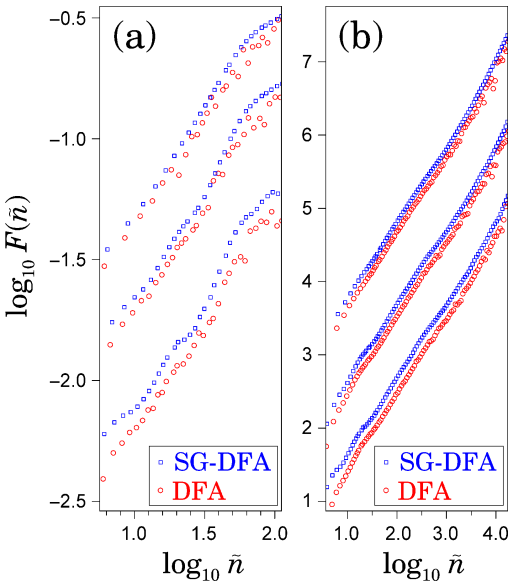

Figure 3: SG-DFA and DFA results using the standardized time scale $\tilde{n}$. (a) Results of stride interval time series. (b) Results of heart rate variability time series. From top to bottom, the SG-DFA orders are 0, 2, and 4; the DFA orders are 1, 3, and 5.

3.2 Results

Figure 3 shows representative results as obtained by DFA and SG-DFA. The DFA results exhibited somewhat irregular behavior in comparison with the corresponding SG-DFA results. Specially, in relatively large scales, irregularity of $F(n)$ estimated by DFA was observed. This irregularity was well characterized by σ_Δ. As shown in Table 2, a better stability was achieved by SG-DFA.

4 Conclusions

We have provided solid mathematical foundations of SG-DFA based on analytical arguments. In addition, through the analysis of physiological time series, we have demonstrated a better stability in the estimated $F(n)$ by SG-DFA than conventional DFA.

To date, the performance of DFA has been systematically studied [18–21], and DFA has become a widely used method. In comparison, studies using SG-DFA are rare. Our results could help further systematic study of the performance of SG-DFA, and facilitate increasingly widespread application of SG-DFA.

Acknowledgements

This work was supported by JSPS KAKENHI, grant numbers 15K01285 and 26461094.

References

[1] M. Kobayashi and T. Musha. *1/f* Fluctuation of heartbeat period. *IEEE Trans. Biomed. Eng.*, BME-29:456–457, 1982.

[2] C-K Peng, J Mietus, JM Hausdorff, S Havlin, H Eugene Stanley, and AL Goldberger. Long-range anticorrelations and non-gaussian behavior of the heartbeat. *Physical review letters*, 70:1343, 1993.

[3] Jeffrey M Hausdorff, Patrick L Purdon, CK Peng, ZVI Ladin, Jeanne Y Wei, and Ary L Goldberger. Fractal dynamics of human gait: stability of long-range correlations in stride interval fluctuations. *Journal of Applied Physiology*, 80:1448–1457, 1996.

[4] Roberto Sassi, Sergio Cerutti, Federico Lombardi *et al.* Advances in heart rate variability signal analysis: joint position statement by the e-cardiology esc working group and the european heart rhythm association co-endorsed by the asia pacific heart rhythm society. *Europace*, 17: 1341-1353, 2015.

[5] Toru Nakamura, Ken Kiyono, Herwig Wendt, Patrice Abry, and Yoshiharu Yamamoto. Multiscale analysis of intensive longitudinal biomedical signals and its clinical applications. *Proc. IEEE*, 104: 242–261, 2016.

[6] C-K Peng, Sergey V Buldyrev, Shlomo Havlin, Michael Simons, H Eugene Stanley, and Ary L Goldberger. Mosaic organization of dna nucleotides. *Physical Review E*, 49:1685, 1994.

[7] C-K Peng, Shlomo Havlin, H Eugene Stanley, and Ary L Goldberger. Quantification of scaling exponents and crossover phenomena in nonstationary heartbeat time series. *Chaos: An Interdisciplinary Journal of Nonlinear Science*, 5:82–87, 1995.

[8] Ronny Bartsch, Thomas Hennig, Arno Heinen, Stefan Heinrichs, and Philipp Maass. Statistical analysis of fluctuations in the ecg morphology. *Physica A: Statistical Mechanics and its Applications*, 354:415–431, 2005.

[9] Plamen Ch Ivanov, Qianli DY Ma, Ronny P Bartsch, Jeffrey M Hausdorff, Luís A Nunes Amaral, Verena Schulte-Frohlinde, H Eugene Stanley, and Mitsuru Yoneyama. Levels of complexity in scale-invariant neural signals. *Physical Review E*, 79:041920, 2009.

[10] Vladimir Matic, Perumpillichira Joseph Cherian, Ninah Koolen, Amir H Ansari, Gunnar Naulaers, Paul Govaert, Sabine Van Huffel, Maarten De Vos, and Sampsa Vanhatalo. Objective differentiation of neonatal eeg background grades using detrended fluctuation analysis. *Frontiers in human neuroscience*, 9:189, 2015.

[11] Jin-Seung Choi, Dong-Won Kang, Jeong-Woo Seo, and Gye-Rae Tack. Reliability of the walking speed and gait dynamics variables while walking on a feedback-controlled treadmill. *Journal of biomechanics*, 48:1336–1339, 2015.

[12] Christopher K Rhea, Adam W Kiefer, W Geoffrey Wright, Louisa D Raisbeck, and F Jay Haran. Interpretation of postural control may change due to data processing techniques. *Gait & posture*, 41:731–735, 2015.

[13] Ken Kiyono and Yutaka Tsujimoto. Nonlinear filtering properties of detrended fluctuation analysis. *Physica A*, in press.

[14] Yutaka Tsujimoto, Yuki Miki, Satoshi Shimatani, and Ken Kiyono. Fast algorithm for scaling analysis with higher-order detrending moving average method. *Phys. Rev. E*, 93:053304, 2016.

[15] Anna Carbone and Ken Kiyono. Detrending moving average algorithm: Frequency response and scaling performances. *Phys. Rev. E*, 93:063309, 2016.

[16] Ken Kiyono and Yutaka Tsujimoto. Time and frequency domain characteristics of detrending-operation-based scaling analysis: Exact dfa and dma frequency responses. *Phys. Rev. E*, in press.

[17] Abraham Savitzky and Marcel JE Golay. Smoothing and differentiation of data by simplified least squares procedures. *Analytical chemistry*, 36:1627–1639, 1964.

[18] Kun Hu, Plamen Ch Ivanov, Zhi Chen, Pedro Carpena, and H Eugene Stanley. Effect of trends on detrended fluctuation analysis. *Physical Review E*, 64:011114, 2001.

[19] Zhi Chen, Plamen Ch Ivanov, Kun Hu, and H Eugene Stanley. Effect of nonstationarities on detrended fluctuation analysis. *Physical Review E*, 65:041107, 2002.

[20] Zhi Chen, Kun Hu, Pedro Carpena, Pedro Bernaola-Galvan, H Eugene Stanley, and Plamen Ch Ivanov. Effect of nonlinear filters on detrended fluctuation analysis. *Physical Review E*, 71:011104, 2005.

[21] Qianli DY Ma, Ronny P Bartsch, Pedro Bernaola-Galván, Mitsuru Yoneyama, and Plamen Ch Ivanov. Effect of extreme data loss on long-range correlated and anticorrelated signals quantified by detrended fluctuation analysis. *Physical Review E*, 81:031101, 2010.

Address for correspondence:

Ken Kiyono
Graduate School of Engineering Science, Osaka University, Japan
kiyono@bpe.es.osaka-u.ac.jp

Conductive Synthetic Fabric Electrodes: Application to ECG Measurement

Yeonsik Noh[1], Sneh K. Sinha[2], Caitlin Eaton-Robb[1], Gregory M. Treich[2], Yang Guo[2], Mengfang Li[2], Xiaozheng Zhang[2], Gregory A. Sotzing[2,3], and Ki H. Chon[1]

[1]Department of Biomedical Engineering, University of Connecticut, USA;
[2]Polymer Program, Institute of Material Science, University of Connecticut, USA
[3]Department of Chemistry, University of Connecticut, USA

Abstract

In this study, an electrically conductive polymer was screen-printed onto a synthetic fabric for ECG measurement. This approach presents an easy fabrication process and produces high-fidelity ECG waveforms. This metal-free approach is superior to Ag/AgCl electrodes which use electrogels that can cause skin irritation. The conductive polymer is safe for prolonged exposure to the body. We found comparable performance of the synthetic fabric electrodes to the Ag/AgCl electrodes in obtaining all morphological features of an ECG waveform. However, the ECG amplitudes were found to be greater with the conducting fabric electrodes. The proposed conductive, dry and flexible textile electrodes can be easily incorporated into garments and have the potential to be used for multimodal bio-signal monitoring applications.

Keywords *PEDOT-PSS, carbon electrodes, electrocardiogram, wearable devices*

1 Introduction

Wearable devices are one of the fastest-emerging areas for unobtrusive continuous monitoring of physiological data. Wearable devices consist of electronic materials that can be easily integrated into textiles and designed in various form factors so that they can be worn comfortably. One of the key applications of such wearables is electrocardiogram (ECG) monitoring. The ECG is an oft-measured vital sign for analyzing physiological conditions of the heart, thus, many wearables incorporate ECG sensors. With the rising global diabetic epidemic and an aging human population, there is a growing need for continuous monitoring of cardiovascular activity especially in patients with high risk of malignant arrhythmia.

Ag/AgCl-based electrodes are the gold standard for measuring ECG. Ag/AgCl electrodes are used with a hydrogel which facilitates better electron charge transfer between skin and electrode. However, hydrogels tend to dry out in a few days and cannot be used for long-term monitoring via a wearable monitoring system. Silver-coated dry (no hydrogel) conductive textile electrodes have been widely used for monitoring ECG signals [1]–[4] and are also incorporated into garments [5], [6] as a wearable system. These dry electrodes have been shown to exhibit low impedance and do not cause skin irritation. However, the silver-based dry conductive textiles are expensive and one of their major limitations is that they need to be wetted prior to use to obtain high fidelity ECG signals. Carbon-based conductive electrodes have emerged in recent years as a more economical alternative to silver electrodes [7]–[11]. These electrodes are easy to construct, reusable, and provide high-fidelity ECG signals in both dry and water immersion conditions. However, the carbon-based electrodes have some rigidity, thus, may not be the best form factor for integration in all wearable devices or garments.

Conductive polymers such as polyaniline, polypyrrole and polythiophenes offer alternative options for incorporation into textiles. Some of these polymers are commercially sold as a colloidal suspension in water with low solid content. These polymers can be cast onto any substrate including textiles, glass, and silicon wafers [12]. Typical coating processes involve spin coating, spray coating, tape casting, brush printing, screen printing and roller printing. Conductive polymers have been reported to be bio-compatible [13] and maintain their conductivity even when stretched (e.g. when incorporated into stretchable fabrics) [14].

ECG monitoring applications using conducting polymer composites have been reported [15], but the fabric is usually soaked in the conducting polymer solution. However, for this study, the conductive polymer is delivered and immobilized onto synthetic fabric using a printing technique. In this study, we introduce screen-printed conductive polymer fabric electrodes and evaluate their performance by comparing ECG signal quality with that of Ag/AgCl electrodes.

2 Methods

A. Materials and Preparation of Samples

An aqueous solution of PEDOT-PSS (1% w/w solution) was used for coating the conducting layer. Dimethyl sulfoxide (DMSO) was obtained from Sigma Aldrich and was used as received. Commercially

available synthetic leather was used as the substrate for printing. The solution for screen printing was prepared by mixing PEDOT-PSS with 5% DMSO followed by concentrating the solution to the appropriate viscosity. This solution was screen printed onto fabrics and dried at 110 °C for 1 hr. The coated fabrics were then used as electrodes for ECG measurement.

B. Experimental Protocol for ECG Measurement

Eight (N = 8) healthy male volunteers of ages ranging from 24 to 41 years (mean ± standard deviation 30.22 ± 5.53), weight 73.44 ± 11.95 kg, height 174.97 ± 4.94 cm, and body mass index (BMI) 24.04 ± 4.06 were enrolled in this study. The study was approved by the Institutional Review Board of the University of Connecticut, CT, USA, and all volunteers consented to be subjects for the experiment.

We designed and fabricated two different ECG monitoring devices, one with the new electrodes and one with conventional Ag/AgCl electrodes, so that we could simultaneously measure single lead ECG signals. Each ECG circuit obtained a Lead I signal from the chest via two electrodes with a virtual right-leg driven circuit. This device provided a 3 dB cutoff from 0.05 to 150 Hz with the use of a second-order band-pass filter, and a sampling rate of 360 Hz. The filtered analog ECG signals were converted to digital data by using a 12-bit analog-to-digital converter (ADC) embedded in a micro-controller (MSP430F2618, Texas Instruments, TX, USA). A 6-point moving average notch filter was applied to the ECG signals for 60 Hz power noise rejection. The ECG signals were transmitted to a personal computer via Bluetooth wireless communication. A LabVIEW software (National Instruments, TX, USA) graphic user interface software was developed for real-time display, and data storage for further off-line data analysis.

The conductive synthetic fabric electrodes are shown in Fig. 1. We used Ag/AgCl snap fasteners to connect leads to the ECG device, and an elastic chest strap was used to immobilize the electrodes onto a subject's chest. For both types of electrodes, we first had the subject rub a small amount of lotion onto the area where the electrodes were going to be placed. This was due to the prevalence of dry skin, to improve conductivity for both electrode types. The chest strap was placed with one electrode on the left and the other electrode on the right side of the rib cage. Each experiment lasted 2 minutes in the sitting position and subjects were instructed to remain relaxed during experiments.

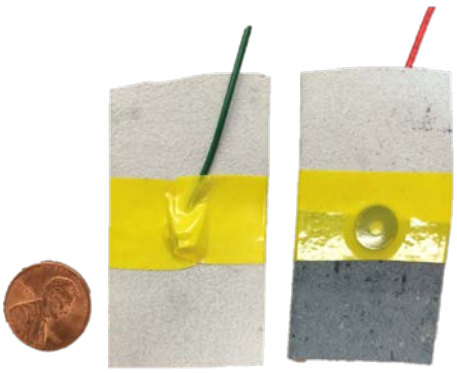

Figure 1. Conducting synthetic fabric electrodes on leather showing the front (right) and back (left) sides of the electrodes.

C. Signal Processing

We chose a 30-second ECG segment, containing stable data. First, the acquired ECG data were filtered with a 4th-order Butterworth bandpass filter with the cutoff bandwidth between 0.1 to 40 Hz. A non-local mean filtering algorithm as a secondary filtering step was applied offline in order to minimize the high frequency noise observed in the collected data [10], [16], [17].

After filtering, R-wave peak detection was performed on the selected ECG segments using a robust QRS complex detection algorithm [18], [19]. ECG templates were computed for each selected ECG segment by creating an ensemble matrix with the corresponding ECG cycles aligned with respect to their R-peak locations, and then averaged at each time instant [10]. We compared ECG amplitude using peak-to-peak value in each ECG template and calculated cross correlation indices of ECG templates between Ag/AgCl and the conducting fabric electrodes.

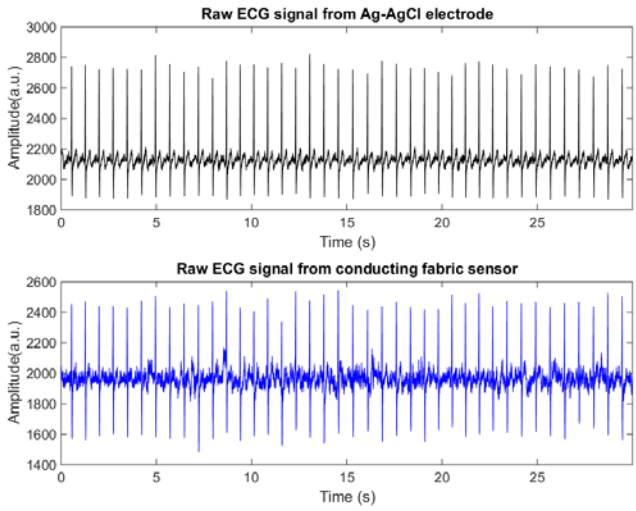

Figure 2. Collected unfiltered ECG signals using Ag/AgCl electrodes (top panel) and conducting fabric electrodes (bottom panel).

3 Results

Comparison of ECG Signal Quality

Fig. 2 and Fig. 3 show representative data from a subject. Amplitude values of the unfiltered ECG signal in Fig. 2 are represented as analog-to-digital conversion values which ranged between 0 and 4096.

TABLE I. EVALUATION OF ECG SIGNAL QUALITY (N = 8); * DENOTES STATISTICAL SIGNIFICANCE

	Ag/AgCl electrode	**PEDOT-PSS based fabric sensor**
Amplitude (a.u.) (mean ± sd)	412.00 ± 192.40	460.68 ± 163.87*
Correlation Coeff. (mean ± sd)	0.99 ± 0.02	

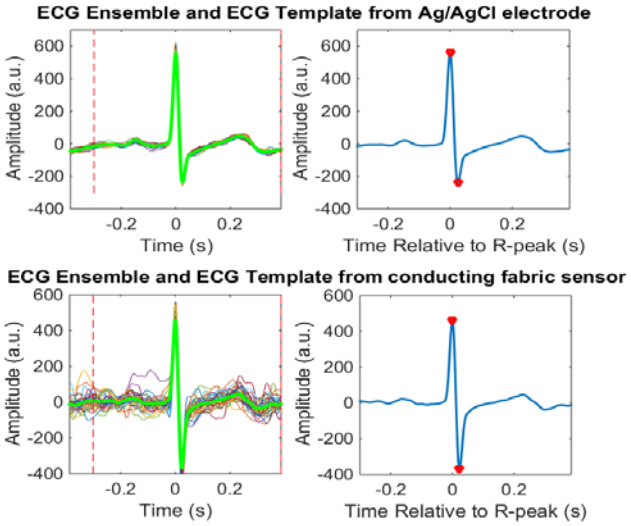

Figure 3. ECG beat ensembles (left panels) and the averaged templates (right panels).

As shown in the right panels of Fig. 3, we observe that the ECG template signal collected using conductive fabric sensors exhibit similar waveform morphologies as those collected by Ag/AgCl electrodes. For ECG amplitude comparison, as shown in Table I, the mean amplitude of ECG signals collected by conducting fabric electrodes was significantly greater than for Ag/AgCl electrodes.

Fig. 3 shows the ECG beat ensembles and the averaged templates computed for both types of electrodes. All ECG morphologies are well captured and delineated for the conducting fabric electrodes. Cross-correlation test results are shown in Table I to quantitatively assess if there were any differences in ECG morphological waveforms between the two types of electrodes. Note the high correlation value between the two types of electrodes.

4 Conclusions

In this study, conductive fabric electrodes were developed using synthetic fabric. A conducting polymer solution of appropriate viscosity was laid onto a fabric using a screen printing coating technique.

As shown in Fig. 3, we confirmed that conducting fabric sensors showed similar performance in capturing all ECG morphologies when compared with Ag/AgCl electrodes. However, we found the signal amplitudes of our conducting fabric sensors to be greater than Ag/AgCl electrodes. This is because the resistance of conducting fabric sensors is smaller than Ag/AgCl electrodes. Note, however, as shown in Fig. 2 and Fig. 3, we found that the ECG signal from our conducting fabric electrodes showed noisier data when compared to Ag/AgCl electrodes. We believe this is not due to the electrode itself but because it was not fully integrated into the wearable chest strap.

Previous works have reported using the screen printing technique with PEDOT for electrode development [20]–[22], but the main advantage of our electrode is that it maintains the conductivity even after more than five washing cycles. To design and fabricate wearable sensors, we need to consider the best approaches for incorporating these sensors into garments, and the connection of these sensors to the input terminals of a biometric device. Conducting polymers can be cast on any substrate including textiles, glass and silicon wafers, and can be shaped in many forms and sizes.

In conclusion, we developed a conductive fabric electrode using a screen printing technique for ECG measurements using wearable devices. The electrodes can potentially also be used to collect other bio-signals such as electromyogram (EMG) and bio-impedance measurements. The screen printing capability of the sensor enables scale-up possibility with possible roll-to-roll manufacturing processes.

Acknowledgements

This work was supported in part by the Office of Naval Research work unit N00014-15-1-2236 and the NSF award #1522087.

References

[1] Y. S. Noh, S. J. Park, S. B. Park, and H. R. Yoon, "A novel approach to classify significant ECG data based on heart instantaneous frequency and ECG-derived respiration using conductive textiles," *Conf. Proc. Annu. Int. Conf. IEEE Eng. Med. Biol. Soc. IEEE Eng. Med. Biol. Soc. Annu. Conf.*, vol. 2007, pp. 1503–1506, 2007.

[2] Y. S. Noh, S. B. Park, K. S. Hong, Y. R. Yoon, and H. R. Yoon, "A Study of Significant data Classification between EDR extracted and frequency analysis of Heart Rate Variability from ECG using Conductive textile," in *World Congress on Medical Physics and Biomedical Engineering 2006*, R. Magjarevic and J. H. Nagel, Eds. Springer Berlin Heidelberg, 2007, pp. 4100–4103.

[3] S.-B. Park, Y.-S. Noh, S.-J. Park, and H.-R. Yoon, "An improved algorithm for respiration signal extraction from electrocardiogram measured by conductive textile electrodes using instantaneous frequency estimation," *Med. Biol. Eng. Comput.*, vol. 46, no. 2, p. 147, Feb. 2008.

[4] R. Gagarin, G. C. Huang, A. Rabbi, and M. F. Iskander, "Textile sensor for monitoring vital signs," in

2014 IEEE Antennas and Propagation Society International Symposium (APSURSI), 2014, pp. 965–966.
[5] M. Pacelli, G. Loriga, N. Taccini, and R. Paradiso, "Sensing Fabrics for Monitoring Physiological and Biomechanical Variables: E-textile solutions," in *3rd IEEE/EMBS International Summer School on Medical Devices and Biosensors, 2006*, 2006, pp. 1–4.
[6] C. R. Merritt, H. T. Nagle, and E. Grant, "Fabric-Based Active Electrode Design and Fabrication for Health Monitoring Clothing," *IEEE Trans. Inf. Technol. Biomed.*, vol. 13, no. 2, pp. 274–280, Mar. 2009.
[7] J. Wang, "Carbon-Nanotube Based Electrochemical Biosensors: A Review," *Electroanalysis*, vol. 17, no. 1, pp. 7–14, Jan. 2005.
[8] J. Wang and M. Musameh, "Carbon Nanotube/Teflon Composite Electrochemical Sensors and Biosensors," *Anal. Chem.*, vol. 75, no. 9, pp. 2075–2079, May 2003.
[9] H. C. Jung, J. H. Moon, D. H. Baek, J. H. Lee, Y. Y. Choi, J. S. Hong, and S. H. Lee, "CNT/PDMS Composite Flexible Dry Electrodesfor Long-Term ECG Monitoring," *IEEE Trans. Biomed. Eng.*, vol. 59, no. 5, pp. 1472–1479, May 2012.
[10] B. A. Reyes, H. F. Posada-Quintero, J. R. Bales, A. L. Clement, G. D. Pins, A. Swiston, J. Riistama, J. P. Florian, B. Shykoff, M. Qin, and K. H. Chon, "Novel electrodes for underwater ECG monitoring," *IEEE Trans. Biomed. Eng.*, vol. 61, no. 6, pp. 1863–1876, Jun. 2014.
[11] Y. Noh, J. R. Bales, B. A. Reyes, J. Molignano, A. L. Clement, G. D. Pins, J. P. Florian, and K. H. Chon, "Novel Conductive Carbon Black and Polydimethlysiloxane ECG Electrode: A Comparison with Commercial Electrodes in Fresh, Chlorinated, and Salt Water," *Ann. Biomed. Eng.*, Jan. 2016.
[12] G. A. Sotzing, S. M. Briglin, R. H. Grubbs, and N. S. Lewis, "Preparation and Properties of Vapor Detector Arrays Formed from Poly(3,4-ethylenedioxy)thiophene−Poly(styrene sulfonate)/Insulating Polymer Composites," *Anal. Chem.*, vol. 72, no. 14, pp. 3181–3190, Jul. 2000.
[13] D. Khodagholy, J. N. Gelinas, T. Thesen, W. Doyle, O. Devinsky, G. G. Malliaras, and G. Buzsáki, "NeuroGrid: recording action potentials from the surface of the brain," *Nat. Neurosci.*, vol. 18, no. 2, pp. 310–315, Feb. 2015.
[14] Y. Ding, M. A. Invernale, and G. A. Sotzing, "Conductivity trends of PEDOT-PSS impregnated fabric and the effect of conductivity on electrochromic textile," *ACS Appl. Mater. Interfaces*, vol. 2, no. 6, pp. 1588–1593, Jun. 2010.
[15] D. Pani, A. Dessì, J. F. Saenz-Cogollo, G. Barabino, B. Fraboni, and A. Bonfiglio, "Fully Textile, PEDOT:PSS Based Electrodes for Wearable ECG Monitoring Systems," *IEEE Trans. Biomed. Eng.*, vol. 63, no. 3, pp. 540–549, Mar. 2016.
[16] B. H. Tracey and E. L. Miller, "Nonlocal means denoising of ECG signals," *IEEE Trans. Biomed. Eng.*, vol. 59, no. 9, pp. 2383–2386, Sep. 2012.
[17] A. Buades, B. Coll, and J.-M. Morel, "A review of image denoising algorithms, with a new one," *SIAM J. Multiscale Model. Simul. SIAM Interdiscip. J.*, vol. 4, no. 2, pp. 490–530, 2005.
[18] V. X. Afonso, W. J. Tompkins, T. Q. Nguyen, and S. Luo, "ECG beat detection using filter banks," *IEEE Trans. Biomed. Eng.*, vol. 46, no. 2, pp. 192–202, Feb. 1999.
[19] A. Schlögl and C. Brunner, "BioSig: A Free and Open Source Software Library for BCI Research," *Computer*, vol. 41, no. 10, pp. 44–50, Oct. 2008.
[20] S. Andreescu and J.-L. Marty, "Twenty years research in cholinesterase biosensors: From basic research to practical applications," *Biomol. Eng.*, vol. 23, no. 1, pp. 1–15, Mar. 2006.
[21] W.-Y. Su and S.-H. Cheng, "Electrocatalysis and sensitive determination of cysteine at

Address for correspondence:

Ki Chon
University of Connecticut
Ki.chon@uconn.edu

R-Wave Magnitude: a Control Input for Ventricular Assist Devices

Seraina Anne Dual[1], Gregor Ochsner[1], Anastasios Petrou[1], Raffael Amacher[2], Markus Wilhelm[3], Mirko Meboldt[1], Marianne Schmid Daners[1]

[1]pd|z Product Development Group Zurich, ETH Zurich, Switzerland;
[2]Wyss Translational Center Zurich, ETH Zurich, Switzerland;
[3]Clinic for Cardiovascular Surgery, University Hospital Zurich, Switzerland;

Abstract

The left ventricular end-diastolic volume (EDV) can be used for physiological control in patients with a ventricular assist device. Such a long-term, real-time, robust signal is not available yet. End-diastolic pressure (EDP) and the R-wave magnitude (RWM) of the electrocardiogram can be acquired in vivo and can relate to the EDV through a power and a linear model, respectively, as proposed in literature. The analysis of in-vivo data acquired in three pigs during volume variations allowed us to quantify the accuracy of estimating EDV from EDP and RWM. The averaged root-mean square error for EDP and RWM derived volumes are 3.22 mL and 4.77 mL, respectively. The order of magnitude is comparable to and lower than the allowable relative sensor error required for control. Furthermore, we observed considerable intra- and inter-animal variability. Therefore, a calibration of the models is necessary for every patient and needs to be repeated over time. We conclude that an equivalent estimate of EDV can be achieved by using either EDP or RWM as a measurement quantity. Thus, to the use of the RWM as an input is a new and promising approach for LVAD control.

Keywords *ECG, end-diastolic volume, left ventricular assist devices, preload, R-wave magnitude*

1 Introduction

Left ventricular assist devices (LVADs) are implanted in patients with end-stage heart failure [1]. LVADs are blood pumps operating in parallel to the diseased heart to ensure a sufficient perfusion of the body. Nowadays, LVADs are passive devices that do not adapt to the physiological requirements of the patient. Physiological adaptation aims to overcome this problem by an automatic adaptation of the pump speed. Our group has developed a robust preload sensitive feedback controller that is to adapt to the physiological requirements by relying on the left ventricular end-diastolic volume (EDV) [2]. However, to date no long-term, real-time, robust left ventricular volume sensor is available.

Requirements for a volume sensor for VAD control are high. From a technical perspective, such a sensor needs to be long-term biocompatible and stable, easy to miniaturize and requiring very little energy. In a previous unpublished study, we could show that from a control perspective the sensor must provide an accurate and robust left ventricular volume (LVV) signal with a relative error of < 20%. The signal must be robustly reliable for LVAD patients with various underlying diseases, with different anatomy and pathophysiology. Lastly, the sensor must be insensitive to a sudden change of hematocrit due to bleeding and arrhythmia or long-term recovery effects like reverse remodeling.

Currently, the measurement of EDV is of interest in the clinic as well as in research to monitor the cardiac performance. In the clinic, the EDV is measured by echocardiography or magnetic resonance imaging systems requiring computationally expensive post processing. In research, admittance catheters are often used for short-term, real-time volume measurements in patients [3], or intensively for pressure-volume loop analysis in animals [4]. Sonomicrometry represents an accurate multidimensional measurement system for volume; however, the invasive nature of the deployment limits the application in humans [5]. In summary, the existing systems are either too large and not real-time capable or too invasive to be used in patients.

Pressure sensors and intracardiac electrocardiogram (ECG) electrodes offer the possibility to acquire long-term, real-time signals of LVAD patients. FDA-approved pressure sensors as well as ECG electrodes in pacemakers have been integrated in commercial systems to be operated in vivo. They are small, biocompatible, easy to integrate and have low power consumption. Models to estimate EDV from these signals have been proposed in literature, but have never been consistently compared.

In this study, we want to investigate and compare how accurately and robustly we can estimate EDV from the end-diastolic pressure (EDV_{EDP}) or from the R-wave magnitude (EDV_{RWM}) of the ECG signal. For this purpose, we acquired left ventricular pressure (LVP), intracardiac ECG and reference volume (EDV_{REF}) data in three pigs.

2 Methods

2.1 End-diastolic Pressure Model

EDP and EDV are related through the end-diastolic pressure-volume relationship (EDPVR). The EDPVR is important to discuss medical conditions of patients in terms of the diastolic function [6]. We modeled the relationship based on a power model investigated by Klotz et al. [7]. The original equation was inverted to compute the EDV_{EDP} as output (1), i.e., our pressure-volume curves are mirrored with respect to the conventional representation.

$$EDV_{EDP} = a_1 \left(\frac{EDP}{A}\right)^{1/B} + b_1 \quad (1)$$

The power model has four parameters, namely A, B, a_1 and b_1. The former parameters were assessed in vivo and were proven to be constant in mice, dogs and humans: A = 22.8 mmHg and B = 2.79 [7]. We successfully applied the same parameters to pigs in this study. The remaining parameters a_1 and b_1 are patient-specific and correspond to a stretching of the power curve and an offset. The parameter a_1 is inversely related to the diastolic myocardial compliance, while the offset b_1 represents the volume at the pressure of 0 mmHg. As the parameters a_1 and b_1 are patient-specific and can change over the long-term, they need to be calibrated.

2.2 ECG R-wave Magnitude Model

R-wave magnitude (RWM) and EDV relate through the so-called Brody effect. An increase of preload, equivalent to EDV, coincides with a decrease of the RWM in the QRS complex of the ECG signal [8]. Recent experiments in pigs have shown a statistically significant correlation of RWM with respiratory pulse pressure, which is a third equivalent measure for preload [9]. Furthermore, LVAD speed changes in ten pigs proved a statistically significant linear correlation of EDV with RWM [10]. The authors propose to use the EDV_{RWM} for monitoring LVAD patient volume status. We use this linear model to represent the relationship between RWM and EDV_{RWM} (2).

$$EDV_{RWM} = a_2\, RWM + b_2 \quad (2)$$

The linear model comprises the two parameters a_2 and b_2. The parameter a_2 represents the sensitivity of the RWM to EDV variations, while the offset b_2 is the theoretical volume at zero RWM. Both parameters a_2 and b_2 of the linear RWM model are patient-specific, i.e., they depend on the heart size, the heart rate and the contractility. As in the previous model, the parameters a_2 and b_2 have to be calibrated.

2.3 Animal Experiment

The animal housing and all procedures and protocols were approved by the Cantonal Veterinary Office (Zurich, Switzerland) under the license number 152/2013. Housing and experimental procedures were in accordance with Swiss animal protection laws. All animals were pre-medicated with ketamine (20 mg/kg), azaperone (1.5 mg/kg) and atropine (0.75 mg). Additionally, they were treated with anti-arrhythmic therapy with amiodarone (2-3 mg/kg bolus iv). During data recording the anesthesia was maintained through co-administration of propofol (5 mg/kg/h) and fentanyl (0.02 mg/kg/h).

In this study we analyze the intracardiac ECG data of three healthy pigs (P1, P2, P3) weighing 89.3 ± 2.6 kg. They were supported by a modified Deltastream DP2 (Medos Medizintechnik AG, Stolberg, Germany) blood pump implanted between the left ventricle and the aorta, simulating an LVAD. The pigs were intubated, assisted by mechanical ventilation, and connected to an extra-corporal heart-lung machine. Fig. 1 shows the positioning of the cannulas and measurement equipment.

The left ventricular loading was altered through variations in pre- and afterload while the LVAD was operated at a constant speed. The speed was set such that the mean residual flow through the aortic valve was approximately 0.5 L/min. For each animal, we conducted four consecutive measurement blocks (A, B, C and D) consisting of several randomized series of preload and afterload variations. Preload variations were induced by the heart-lung machine through infusion or drainage of 500 mL blood volume to or from the animal's circulation. Afterload variations were induced by inflation of a reliant balloon in the descending aorta. Conducting the entire experiment with all four blocks took approximately 3 h.

As EDV_{REF}, we measured long (l_a) and short axes (s_a) of the left ventricle with four ultrasound crystals (UDG, Sonometrics Corp., London, Ont., Canada), three attached intramural and one integrated in the inflow cannula of the LVAD. Based on that data, we calculated the LVV with a hemi-ellipsoid approximation, $LVV = 2/3 \cdot s_a^2 \cdot l_a$ (3). We measured the LVP and intracardiac ECG with a pig-tail conductance catheter (Ventri-Cath 510 / MPVS Ultra, Millar Instruments Inc., Houston, TX, USA). All signals were continuously recorded at 500 Hz. A detailed description and explanation of the in-vivo study was reported in [2].

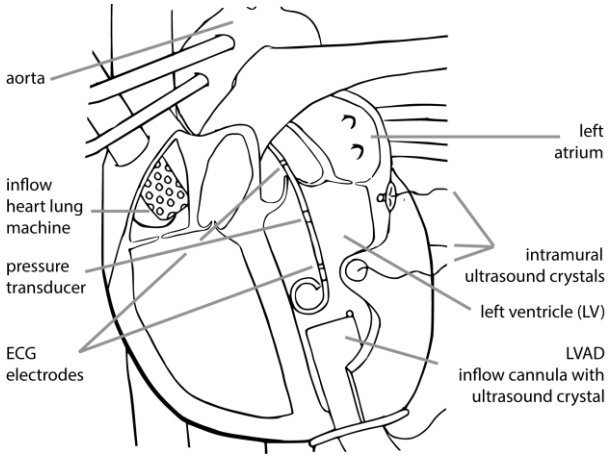

Figure 1: Positioning of the pig-tail catheter, the four ultrasound crystals and the left ventricular assist device

2.4 Data Analysis

The analysis of the data was performed offline on a beat-to-beat basis for LVV, LVP and ECG. The EDV and EDP values were extracted using the R-wave of the ECG signal as a trigger. Fig. 2 shows an example of EDV, EDP and R-wave detection data. Negative EDP values originating from suction events were excluded. The RWM was computed as the difference between the minimum and maximum of the QRS complex of the ECG. We excluded beats with irregular ECG wave forms.

In order to capture intra-animal variability, the calibration and cross-validation of the models described in Equations 1 and 2 was performed block-wise. For each block, we calibrated the parameters a_1, b_1, a_2 and b_2 through a linear least squares fit in MATLAB (R2014b,

The Mathworks Inc., Natick, MA, USA). The calibrated model of each block was cross-validated with the three other blocks of the same animal. For the calibration we report r-squared (r^2) as a quality of fit, while for the cross-validation we report the root mean square error ($RMSE_{EDP,\ RWM}$) between the estimated end-diastolic volumes EDV_{EDP} or EDV_{RWM} and the measured end-diastolic volume EDV_{REF}. Averaged results are always reported as mean ± standard deviation (SD).

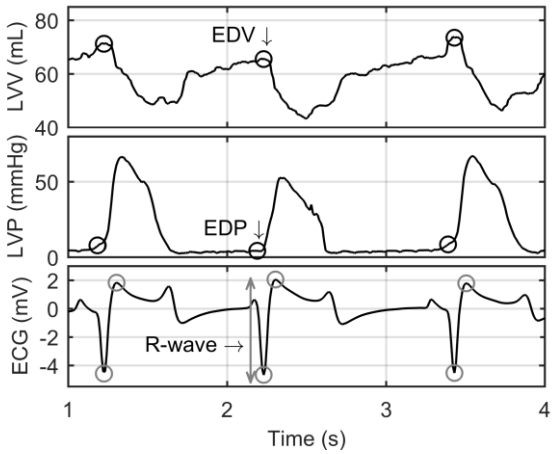

Figure 2: In-vivo data of the left ventricular volume (LVV), the left ventricular pressure (LVP) and the intracardiac ECG. The circles indicate the end-diastolic volume (EDV) and pressure (EDP), and the R-wave.

3 Results

The model parameters were calibrated for each animal (P1, P2, P3) and each block (A, B, C and D). Mean and SD of the measured quantities were EDV (60.13 ± 20.11 mL), EDP (7.04 ± 4.44 mmHg) and RWM (4.60 ± 2.57 mV). Fig. 3 shows the calibration of P1-A with the respective model fit and the 99% confidence interval. The model corresponds well with the data, except for small values of EDP and high values of RWM. The data is not equally distributed across all volumes, but an accumulation occurs around volumes between 64 and 70 mL.

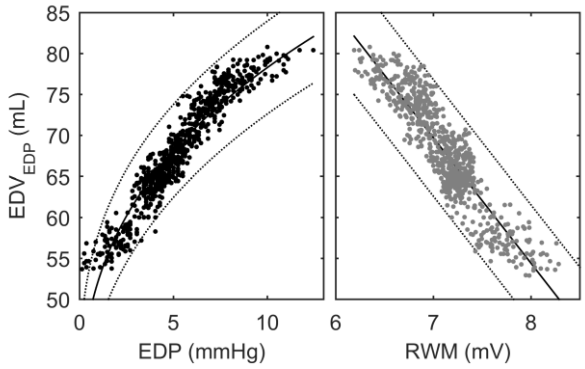

Figure 3: Example data P1-A with model fits and a confidence interval of 99%.

Table 1 lists the calibrated values of the model parameters a_1, b_1, a_2 and b_2 and the resulting r^2 as the average values over the four blocks in each animal. Each parameter is in the same order of magnitude for all animals and all blocks. Intra-animal variations of the parameters are smaller for the EDV_{EDP} compared to the EDV_{RWM}. The quality of fit was found to be marginally higher for EDV_{EDP} than for EDV_{RWM} for all animals.

Parameters estimated per animal				
		a_1 (mL)	**b_1 (mL)**	**r^2**
EDP	P1	54.1±13.9	39.9±9.4	0.92±0.03
	P2	62.2±9.4	23.9±4.9	0.85±0.06
	P3	50.2±6.5	19.1±4.4	0.88±0.04
		a_2 (L/V)	**b_2 (mL)**	**r^2**
RWM	P1	-15.2±2.7	173.9±16.7	0.79±0.03
	P2	-36.6±12.9	145.4±29.2	0.83±0.05
	P3	-11.5±1.1	100.7±2.3	0.85±0.04

a_1, a_2, b_1,b_2: model parameters, r^2: r-square

Table 1: Model parameters and quality of fit with mean ± standard deviation across the four blocks in each animal.

Fig. 4 shows the error between modelled and estimated EDV (ΔEDV) dependent on the reference volume, where the model was calibrated with P1-A and validated against blocks P1-B, P1-C and P1-D. The $RMSE_{EDP}$ and $RMSE_{RWM}$ values are 3.42 mL and 4.21 mL, respectively. A total of twelve such analyses was performed, which are summarized in Fig. 5. The estimation is inferior for extreme volumes, which can be observed for most data sets. Fig. 5 shows the RMSE in the range of 2-8 mL for every block and every animal. In P1, the RMSE for both estimation methods are comparable. In P2 and P3 $RMSE_{EDP}$ is lower and more consistent than $RMSE_{RWM}$. The RMSE varies between the blocks, but not in a consistent way.

Figure 4: Example data of P1-A EDV estimation

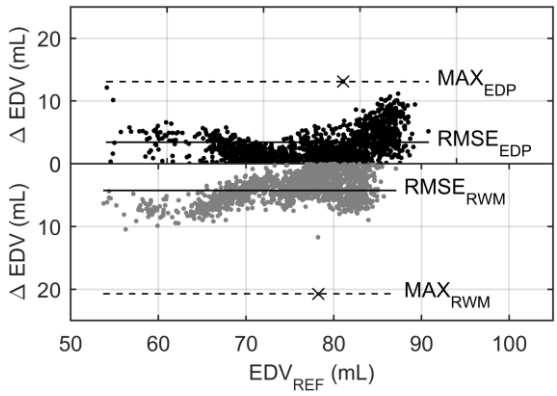

error (ΔEDV) for EDP (b) and RWM (g). Solid line: Root mean square error (RMSE), dashed line: Maximum value (x). The y-axis is mirrored w.r.t zero.

4. Discussion

The models used for the EDV estimation in this study represent the state of the art and convince by their simple structure and their linear dependency on only two parameters. Fitting the model parameters resulted in high-quality fits. In this study, the intracardiac ECG was measured and showed r^2 values similar to those observed by other groups in the external ECG [8,9]. Deviations from the model are observed only at extreme volumes, i.e., more sophisticated models for the estimation of EDV_{RWM} should be developed in the future.

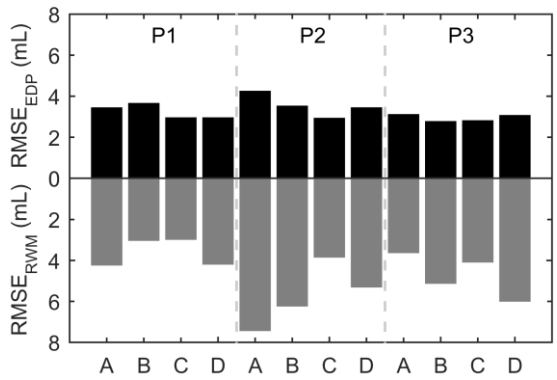

Figure 5: Root mean square estimation error (RMSE) for every block, cross-validated with the three other blocks of the same animal for EDP (b) and RWM (g). The y-axis is mirrored with respect to zero.

Thus far, no study has compared the feasibility of using in-vivo RWM in contrast to EDP as a preload index for the control of LVADs. The $RMSE_{EDP}$ and $RMSE_{RWM}$ provide a first estimate of the uncertainty involved with the usage of EDP or RWM as a control input. Both RMSE values are below the previously defined maximum relative sensor error of 20%, i.e., both signals are potential candidates as control inputs. The inferior results of EDV_{RWM} in the animals P2 and P3 are possibly linked to the high sensitivity of the RWM to the catheter position as well as hematocrit changes in the blood.

In order to use the EDV_{EDP} or EDV_{RWM} as control input the signal needs to be available continuously. A significant number of beats showed irregular wave forms in the ECG. In these beats, no distinct RWM can be detected and they were thus excluded from the analysis. Therefore, when EDV_{RWM} is used as input for physiological control, no EDV signal will be available during these arrhythmic beats. For EDV_{EDP} estimation, the EDP could alternatively be detected directly from the pressure signal without R-wave triggering. However, this detection of EDP is not trivial and therefore is less robust. In summary, discontinuities of EDP and RWM are not directly correlated, thus robust LVAD control method with the EDP, the RWM, or a redundant combination of the two seems feasible.

Inter-animal variability in the parameters and RMSE exists for both estimation methods and is in an acceptable range. The importance of calibration is shown by the inter-animal variation of the offsets b_1 and b_2, which, without calibration, translate directly into an estimation error. It is not possible to use the same parameter set for every animal. The data collected will allow us to further investigate the sensitivity of the output error with more stringent bounds to the calibration effort. For example, one parameter could be kept constant, while only one parameter would be identified, thus requiring fewer calibration data points. Intra-animal variability in the parameters between the timely separated blocks is in the same order of magnitude as between animals. The parameters vary during the course of the experiment for instance, due to sudden bleeding events influencing the hematocrit and therefore, the conductivity of the blood and the RWM. This additional uncertainty implies that if the sensor was implanted in a LVAD patient, the system would most likely have to be recalibrated by using a reference volume measurement such as echocardiography in case of changes in the physiology. Factors influencing the parameters over the long term will have to be thoroughly investigated in human LVAD patients.

The study is limited on the one hand by the use of a healthy porcine model in open chest condition and on the other hand by the reference measurement system. Two-axis ultrasound data combined with the hemi-ellipsoid model to find EDV_{REF} has a limited accuracy and contributes to the error observed. In addition, since no external reference ECG signal was recorded, irregular ECG waveforms may result from arrhythmia or from a contact of the pig-tail electrodes with the myocardium. EDV_{RWM} results are likely to improve with consistent and repeatable positioning.

4 Conclusions

We conclude that the pressure and ECG signals provide an equivalent realistic estimate of EDV. Likely, robust LVAD control is possible with a redundant combination of both signals.

Acknowledgments

This project is part of the Zurich Heart project under the umbrella of "University Medicine Zurich".

References

[1] J. K. Kirklin et al., First annual IMACS report: A global international society for heart and lung transplantation registry et al., for Mechanical Circulatory Support, *J. Hear. Lung Transplant.*, 35-4-407–412, 2016.

[2] G. Ochsner et al., In vivo evaluation of physiological control algorithms for LVADs based on left ventricular volume or pressure, *J Hear. Lung Tranplant.*, 2016.

[3] J. Baan et al., Continuous SV and CO from intra-ventricular dimensions obtained with impedance catheter, *Cardiovasc. Res.*, 15.6-328–334, 1981.

[4] A. E. Wei et al., Use of pressure-volume conductance catheters in real-time cardiovascular experimentation, Hear. Lung Circ., 23-11-1059–1069, 2014.

[5] M. B. Ratcliffe et al., Use of sonomicrometry and multi-dimensional scaling to determine the three-dimensional coordinates of multiple cardiac locations: feasibility and initial implementation., IEEE Trans. Biomed. Eng., 42-6-587–98, Jun. 1995.

[6] D. Abi-Abdallah Rodriguez et al., Simultaneous pressure–volume measurements using optical sensors and MRI for left ventricle function assessment during animal experiment, Med. Eng. Phys., 37-1-100–108, 2015.

[7] S. Klotz et al., Single-beat estimation of end-diastolic pressure-volume relationship: a novel method with potential for noninvasive application., Am. J. Physiol. Heart Circ. Physiol., 291-H403–H412, 2006.

[8] D. A. Brody, A Theoretical analysis of intracavitary blood mass influence on the heart-lead relationship, Circ. Res., IV-731–737, 1956.

[9] R. Giraud et al., Respiratory change in ECG-wave amplitude is a reliable parameter to estimate intravascular volume status, J. Clin. Monit. Comput., 27-2-107–111, 2013.

[10] L. Fresiello et al., The relationship between R-Wave magnitude and ventricular volume during continuous left ventricular assist device assistance: Experimental study, Artif. Organs, 5, 2014.

Address for correspondence:
Dr. Marianne Schmid Daners, Product Development Group Zurich, ETH Zurich, marischm@ethz.ch

A Method of Efficient Cardiac Risk Assessment based on the T-wave Morphology Changes in Holter ECG Recordings

M. Aihara[1], S. Nakamura [1], M. Murakami[1], K. Yana[1]
Takuya Ono[2], Tomohide Ichikawa[3] and Eiichi Watanabe[3]

[1]Graduate school of Science and Engineering, Hosei University, Tokyo Japan;
[2]Department of Cardiology, Nippon Medical School, Tokyo, Japan;
[3]Department of Cardiology, Fujita Health University School of Medicine, Toyoake City Japan

Abstract

This paper proposes a method of efficient assessment of the cardiac risk based on the long term Holter ECG recordings. In order to process a vast amount of clinical data a simplified yet effective method to characterize T-wave morphology changes has been proposed. The method prevents from using procedure with high computational power such as orthogonal signal decomposition or repetitive use of Discrete Fourier Transform. To eliminate artifact, the beat to beat adaptive artifact detection and rectification methods have been introduced. T-wave alternans, T-wave variability and related indices are suggested to be utilized for the integrated cardiac risk assessment. Illustrative examples have been shown to demonstrate the effectiveness of the method.

Keywords *Holter ECG, sudden cardiac arrest, risk assessment, T-wave alternans, biosignal processing*

1 Introduction

The risk assessment of the sudden cardiac arrest (SCA) has been one of the most important issues in the field of health care since SCA is one of the major causes of death worldwide. In the U.S. for example, over 300,000 SCA incidents are reported [1]. Several indices based on ECG recordings for the risk assessment are well known[2]. Recently, indices derived from 24-hour long term Holter ECG recordings attract considerable attention of research community [3]-[5]. Authors have been proposing new indices named T-wave alternans ratio percentile (ARP) and QT-RR co-variability extracted from Holter ECG records[6]. This paper focuses on the use of T-wave morphology changes for the risk assessment and introduces an efficient method to cope with the need to process vast amount of clinical data. An adaptive correlation method is introduced for both artifact rectification and T-wave characterization without using methods with extensive computational power. The paper also briefly discusses the future research direction under the vision of "Computational Electrocardiology (CECG)," where the ECG data were acquired, stored and processed continuously based on wearable sensors and the cloud information processing systems[7].

2 Methods

We briefly review the SCA risk index named alternans ratio percentile (ARP), which we proposed[6], as a mean to detect the presence of alternans in 24 hour Holter ECG recordings. Then a new alternative method for the efficient clinical data analysis will be introduced.

2.1 Alternans Ratio Percentile

T-wave alternans ratio (TWA) has been recognized as an effective measure of SCA risk assessment. The index has been typically measured in the clinical test environment with elevated heart rate[2]. It is desirable if the TWA is evaluated from the Holter ECG recordings in the natural living environment. Although some software has been provided for the Holter ECG evaluation, the large amount of noise contamination makes it difficult to obtain reliable consistent measures.

Instead of performing manual inspection of derived indices, we propose to utilize alternans ratio percentile (ARP) as a measure of SCD risk assessment. The method has been described in [6] in detail. Here is a brief summary of the proposed index. T-wave alternans ratio (AR) has been obtained for all one-minute successive segments of ECG data for 24 hours. T waves have been extracted beat to beat and the singular value decomposition has been applied to extract orthogonal signals behind the T-wave signals. Then, adjacent and one after adjacent vector distances of two orthogonal signals are measured and the distance sequence thus obtained has been analyzed. The T-wave aveform alteration has been detected by the altenans ratio (AR) which is the ratio of the DFT power of the sequence at the Nyquist frequency and the average DFT amplitudes at adjacent frequencies. DFT has been applied to all one-minute segmented data. In such a way we obtain 1,440 AR values for 24 hours. For such large number of segments, there is a good random chance to yield the segment with high AR value. For example, random chance of alternate changes for successive 10 beats is 0.001 which may yield a high AR value. These incidents may happen a few times in average for the normal subjects without any SCD risk. To avoid such random chance cases, θ percentile values of Total ARs in a day is suggested to use for the SCD risk index. We named it the alternans ratio percentile (ARP). The value of θ has to be determined empirically.

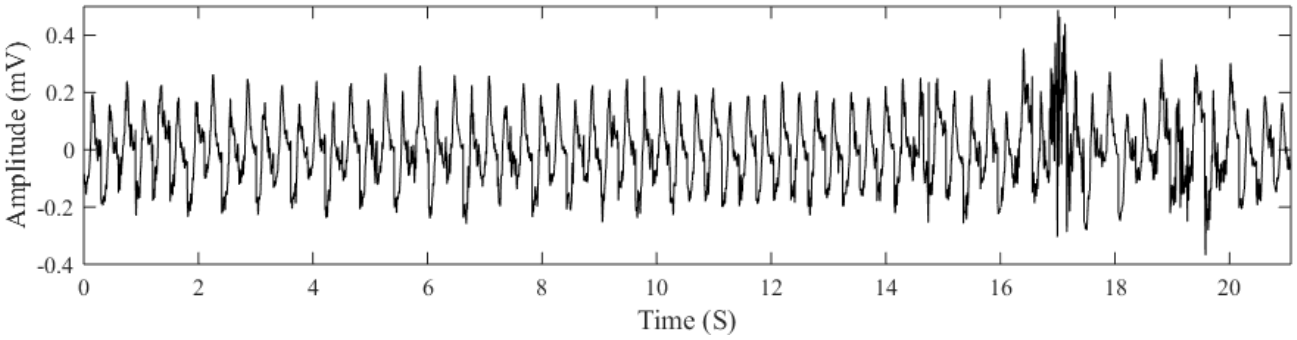

Fig. 1 An example of extracted T-waves for an one-minute segment

2.2 Simplified ARP estimation

In order to estimate the ARP of vast amount of clinical data, the method described in the previous section is too time consuming especially orthogonal signal decomposition takes a lot of time. DFT/FFT calculations for all one-minute data segments are also time consuming. In this section, a simplified method of ARP estimation has been described.

T-wave amplitude estimation

The IIR Bandpass filtering is applied to the original ECG data to reduce the effect of baseline drift. Empirically, we have been adopted 12th order Butterworth band pass filter (0.5-60Hz). The filter removes the drift fairly well, but apparent drift still remains after the filtering. Further increase in the cut off frequency of high pass part of the filter deteriorate the T-wave morphology.

To concur this problem, we introduced the following adaptive method of amplitude estimation with baseband correction. T-wave peak time plus minus 150 *mS* has been extracted for each of successive one-minute ECG segments. Fig. 1 shows a typical example of extracted T-wave's for an one-minute segment. Two types of alternans at the first part of the segment and apparent artifact are visually seen at the end. To perform the reasonable estimate of T-wave amplitude, the average waveform using all T-waves in the segment has been obtained (Fig. 2).

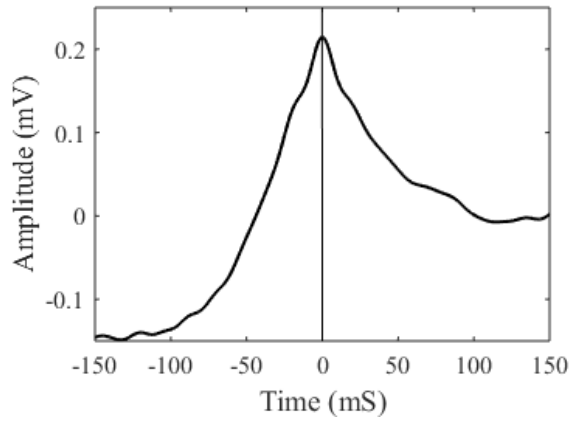

Fig. 2 Averaged T-wave

Now to remove the artifact, correlation coefficients between the averaged T-wave and bias corrected T-wave are estimated. Fig. 3 shows the result for the data shown in Fig. 1. The T-wave with the correlation coefficients less than 80% is assumed to be artifact and if the ratio of artifact is less than 80%, average T-wave is replaced by the artifact. Otherwise the whole segment is excluded from the further analysis. When the artifact is replaced by the average T-wave, the process is repeated until all correlation coefficient values exceed 0.8. The least square curve fit of average T-wave and each T-waves in the segment is utilized to estimate both the drift bias and T-wave amplitude.

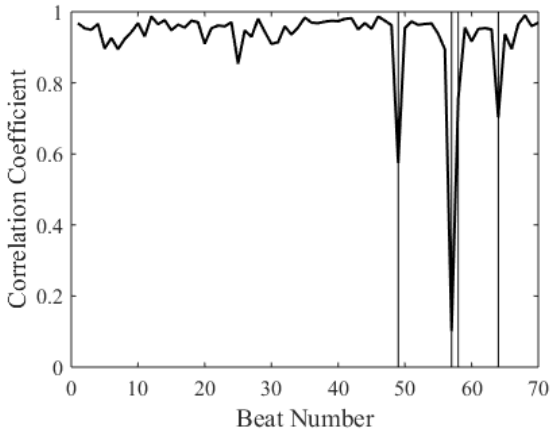

Fig. 3 Correlation coefficients between average and individual T-waves

ARP estimation

Discrete Fourier Transform (DFT) power has been calculated from the T-wave amplitude series thus obtained. Then the alternans ratio, that is the ratio of the power at the Nyquist frequency and the average power at surrounding frequencies, have been estimated for all segments. ARP is finally estimated as the θ percentile values of all ARs. This ARP estimation needs a lot of computational power since it requires the DFT of all segments, *i.e.* DFT calculation of 1,440 times. For simplified measure, the relative amplitude difference between even and odd beats will be utilized. The amplitude sequence can also be used to estimating T-wave amplitude variability (TAV).

3 Results

The ARP is applied to 26 outpatients with SCD risk and 25 control subjects. The outpatients are further divided in to two groups, that is high risk patient group with life threatening incidents or severe arrhythmia and low risk patient group with high blood pressure without arrhythmia or supraventricular tachycardia. The results showed 5 percentile of AR values is most effective to differentiate the high risk group and the rest. *p*-values are less than 0.07×10^{-3} to differentiate high risk from low risk patients. Fig 4 shows the typical examples of ordered ARs for a patient with high SCA risk with the history of severe heart attack (Solid line) and for a control normal subject (dotted line). The differences are apparent and this figure suggests that the ARP can be a stable measure of the presence of T-wave alternans.

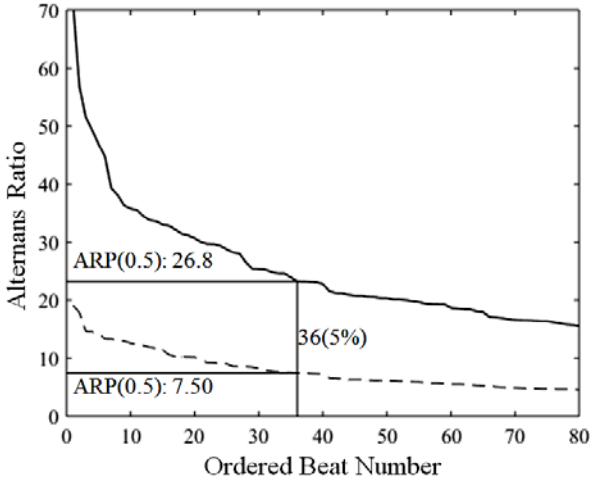

Fig. 4 Ordered Alternans Ratios for 24 hours

The simplified method presented here performs equally well to estimate the alternans ratio. Fig. 5 shows the relative amplitude series obtained by the method described in the previous section for the sample data shown in Fig. 1 where the apparent amplitude alternation is observed. This alteration is also visually seen mainly in the first part of Fig. 1.

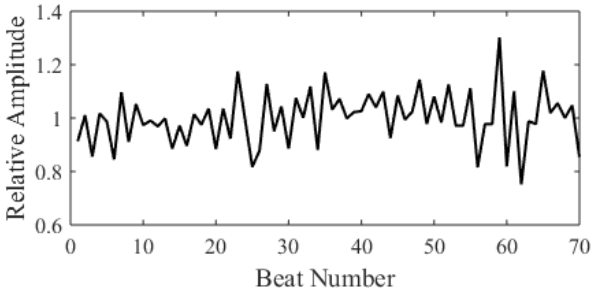

Fig 5. An example of amplitude series with apparent T-wave alternans

DFT power of the amplitude series is calculated and shown in Fig. 6 where excess power at Nyquist frequency is observed.

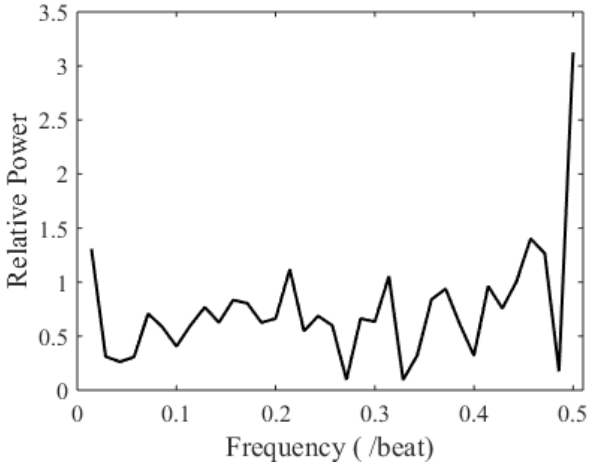

Fig. 6 DFT power of the amplitude sequence with T-wave alternans

As a simplified measure of detecting the presence of T-wave alternans, the *p*-value of statistical test to see the median or mean difference between odd and even T-wave amplitude can be used. Fig. 7 shows the box plot of T-wave amplitude for even and odd beats. The difference in median is significant with *p* value equals to 0.004. Inverted logarithm *p* could be a suitable measure of the presence of T-wave alternans.

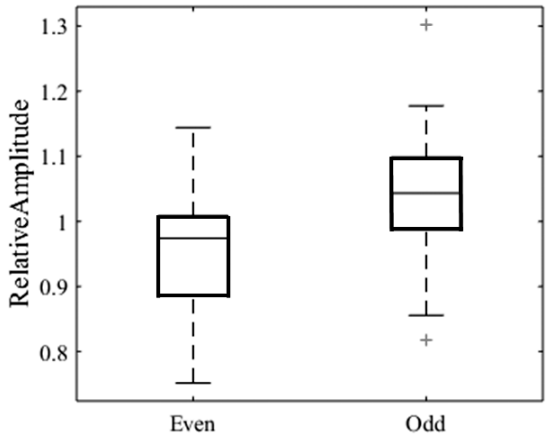

Fig. 7 T-wave amplitude difference between even and odd beats

3 Discussion and Conclusions

An efficient method of SCD risk assessment for processing vast amount of 24 hour Holter clinical data has been proposed. Instead of methods utilizing heavy computational power such as orthogonal signal decomposition or repetitive use of DFT/FFT, the proposed method utilizes fairly simple signal processing methods yet aiming at preserving the accuracy of SCD risk assessment. The comparison of the method with high computational load is shown in Fig 8. Although some commercially available software implements methods to derive the indices for SCD risk assessment, they remain as an experimental stage. Clinicians need to

make considerable amount of eye inspections to eliminate artifacts to get a meaningful result[8]. The automatic artifact detection and processing method proposed in this paper will be utilized for reducing the load of clinicians' eye inspection. This paper focuses on the evaluation of T-wave alternans. However, the method could be applied to derive other indices such as T-wave amplitude variability (TAV). Recently, the heart rate variabilities, short term or long term including the diurnal changes are studied for SCA risk assessment[3]-[6]. Integration of all these measures both derived from ECG waveforms and beat occurrence timing data should be pursued to establish reliable and efficient means to assess the SCA risk assessment. In the latest issue of the journal of methods of information in medicine For-Discussion-Section[7], the future vision of ECG study has been discussed under the symbolic notion of Computational Electrocardiography (CECG). In this vision the continuous multichannel ECG data are acquired by wearable sensors and stored/processed online to make the timely feedback for the health care practice. The SCD risk assessment will be one of the most important development goals for CECG practice. Integration of the risk assessment indices derived from Holter 24 hour or even longer continuous ECG recordings for the timely health care advice is the ultimate goal of the study. To develop such systems, the introduction of a standardized ECG data format will be useful to establish the common foundation of the system development. The integrated file format of ISHINE[9] or MFER[10] and beat annotation format adopted by Rochester University Telemetric and Holter ECG warehouse named THEW file format[11] will be one of promising candidates for such standardization.

References

[1] M. Dariush *et al*., "Heart Disease and Stroke Statistics 2015 Update : A Report From the American Heart Association", *Circulation*, Vol.131, pp.e29-e322, 2014.

[2] J.J. Hein *et al*., "Risk stratification for sudden cardiac death," *Europian Heart Journal*,Vol.35, Issue 25, pp.1642-1651, 2014.

[3] P. Saravanan and N. C. Davidson, "Risk Assessment for Sudden Cardiac Death in Dialysis Patients," *Circ. Arrhythm Electrophysiol.*, Vol. 3, pp. 553-559, 2010.

[4] K. Sakai, T. Ikeda, Y. Miwa, et al., "Time-domain T-wave alternans measured from Holter electrocardiograms predicts cardiac mortality in patients with left ventricular dysfunction," *Heart Rhythm*, Vol. 6, pp. 332-337, 2009.

[5] Kotoko Tanaka, Kenji Yodogawa, Takuya Ono, Kazuo Yana, Masaaki, Miyamoto, Hirotsugu Atarashi, Takao Kato & Kyoichi Mizuno, "Greater insulin resistance indicates decreased diurnal variation in the QT interval in patients with type 2 diabetes," *Heart and Vessels*, Vol. 29, No. 2, pp.256-262, March, 2014

[6] K. Kasahara, M. Shiobara, S. Nakamura, K. Yamashiro, K. Yana and T. Ono, "Sudden cardiac arrest risk stratification based on 24-hour Holter ECG statistics," *Proc. 37th Ann. Int. Conf. IEEE EMBS*, pp. 5817-5820, Aug. 2015.

[7] Kazuo Yana, "Editorial for computational electro cardiography: revisiting Holter ECG monitoring," *Method of Information in Medicine*, Vol. 55, 2016.

[8] Y. Sobue, E. Watanabe, *et at.*, " Beat-to-beat variability of T-wave amplitude for the risk assessment of ventricular tachiyarrhythmia in patients without structural heart diesase, " Europace, Vol. 13, pp. 1612-1618, 2011.

[9] Fabio Badilini, "The ISHNE Holter Standard Output File Format", A.N.E. Vol. 3, No. 3, Part 1. pp.263-266, 1998.

[10]ISO 22077-1:2015 Health informatics -Medical waveform format Part 1: Encoding rules.

[11]Rochester Univ. Telemetric and Holer ECG warehouse data format: http://thew-project.org/ THEWFileFormat.htm

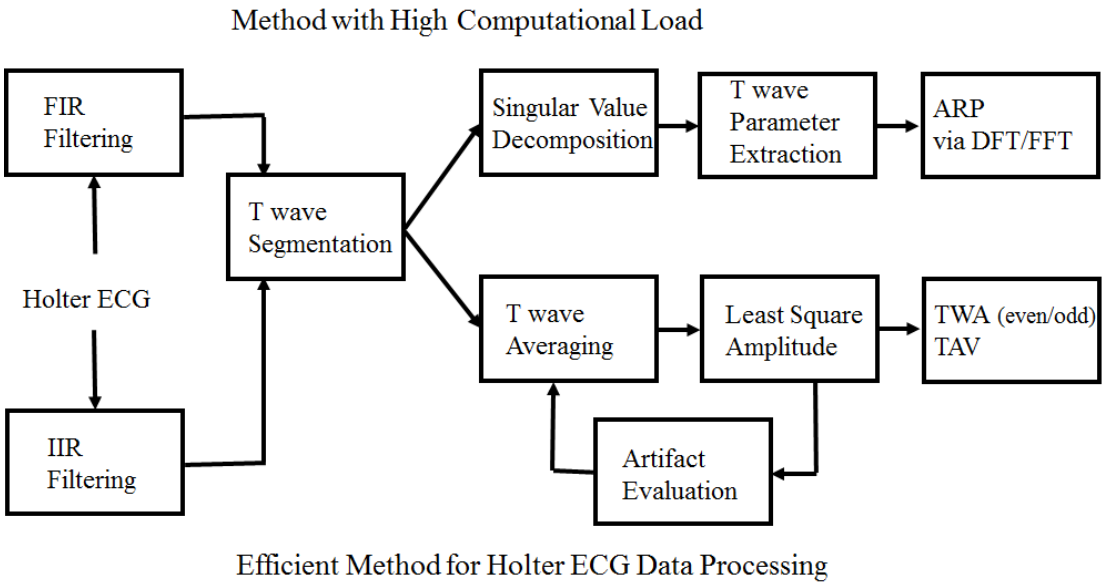

Fig. 8 Schematic Diagram to Extact T-wave Related SCA Risk Indices

Confounding factors in ECG-based detection of sleep-disordered breathing

C Maier[1], H Dickhaus[2]

[1]Medical Informatics, Heilbronn University, Germany;
[2]Institute for Medical Biometry and Informatics, Heidelberg University, Germany;

Abstract

This study investigates the effect of confounding factors - comorbidities, body position, ECG lead, respiratory event type and sleep stage - on recognition of sleep apnea from the ECG. A set of 140 simultaneous recordings of polysomnograms and 8-channel Holter ECGs is stratified for these factors, and minute-by-minute apnea detection performance is assessed using receiver operating characteristics curves. The detection is based on parameters of heart rate, ECG amplitude and respiratory myogram interference. We consider spectral and correlation-based features.

The results show that typical comorbidities and supine body position impede apnea detection from the heart rate. Availability of multiple ECG-leads improves robustness of ECG amplitude based detection with respect to posture influence. But quite robust apnea detection is achievable with a single ECG channel – preferably lead I. Sleep stages and respiratory event type have a significant and quite consistent effect on apnea detection sensitivity with better results for light sleep stages, and worse results for REM sleep. Mixed and obstructive events are better detected than central apneas and hypopneas.

Keywords *Sleep-Disordered Breathing, Confounding Factors, Screening, ECG, Heart Rate*

1 Introduction

Clinically relevant sleep-disordered breathing (SDB) is inherently repetitive and evokes characteristic quasi-periodic modulations in several ECG parameters, which can be quantified to identify SDB from the ECG. Typically, a cyclic variation in heart rate (CVHR) is observed, which is evoked by accelerations due to respiratory arousals, and mediated via the autonomic nervous system (ANS) [1]. Moreover, ECG amplitude [2] and myogram interference in the ECG [3] are modulated in a characteristic fashion.

Most of the published detection algorithms target CHVR or ECG amplitude modulation, or a combination of both. In a previous study we compared the different information sources, and obtained rather unfavorable SDB detection results for features based on heart rate [3]. This motivated us to investigate into potential confounders. The current study stratifies our previous data set with respect to various physiological and technical factors, and assesses their effects on SDB detection performance. The results improve the understanding of current detection limitations and suggest strategies for further development.

2 Methods

The data analyzed in this study consist of 140 parallel recordings of attended overnight polysomnography (PSG) and Holter-ECG (Mortara H12+, 8 channels, 1kHz/ch sample rate). They were registered in 121 different subjects (16 female, 105 male) referred to the Sleep Medicine Center at Thoraxklinik Heidelberg for suspected SDB. The average age was 54.7y±11.4y, and the average AHI was 26.4/h±27.9/h. All ECGs contained less than 5% ectopic beats with one exception (8%). There were no other exclusion criteria.

The PSG annotations served as reference for the ECG based detection of SDB in epochs of one minute duration. Each epoch obtained a binary flag for the presence or absence of respiratory events. We used the same signal processing and classification features as detailed in [3]. The series of RR-intervals was derived, and the series of areas under the QRS complex (QRSA) were extracted as a measure of ECG amplitude in each of the 8 ECG channels. Finally, we assessed the 8 series of respiratory myogram interference (MYO). From each of the series we extracted the following features to assess the SDB modulations:

The magnitude of the maximal FFT spectral coefficient in the frequency range [0.0117Hz, 0.041Hz], corresponding to a period of 25s to 85s, was used as a spectral feature (SMA). Furthermore, the local similarity index (LSI) feature [3] was calculated. It identifies an 'apnea pattern candidate' from the central minute of each 5min segment, and quantifies its local recurrence by means of the correlation function. The sum of all correlation values exceeding a threshold (e.g. 0.9) yield the LSI.

Please note that for the features derived from QRSA and MYO, a maximum value selection was performed over the 8 ECG channels within each 1 min epoch. I.e. only the maximum seen in all channels was used.

To identify the effect of potential influence factors on the features and base data types, we stratified the data set with respect to these factors and assessed minute-by-minute SDB detection accuracy by means of receiver-operating characteristics (ROC) curves. The factors considered are presence of typical comorbidities: diabetes (type II), myocardial infarction (MI) and

periodic limb movements (PLMs), as well as body position, ECG lead, respiratory event type (obstructive, central, mixed or hypopnea) and sleep stage. The latter were scored according to the Rechtschaffen and Kales criteria which were still in place at the time of data collection. We merged sleep stages S3 and S4 into one single stage.

3 Results

Table 1 gives the characteristics of the subgroups with diabetes, MI, PLMs, and of the remaining data, which, however, must not be regarded as free from other diseases or medication. The AHI in the diabetes and in the MI groups tends to be greater than in the control group. The PLM group is the least homogeneous, as indicated by the considerable difference between median and mean AHI.

The effect of comorbidities on apnea detection is shown in Fig. 1A-D. There is one ROC diagram for each of the features LSI(RR), SMA(RR), LSI(QRSA) and LSI(MYO), respectively. The blue curves represent the control group. A fall-off is evident for all comorbidities in the heart rate based features (Fig. 1 A and B) with a smaller effect in the spectral feature SMA (Fig. 1B). In contrast, detection from the QRSA the MYO series is very robust. LSI(QRSA) is negatively affected only by PLMs (Fig. 1C, green curve), and both series show even improved performance in the small MI subgroup (Fig. 1C and D orange curves). In all subgroups, the QRSA- and MYO based features are superior to the RR-based.

Fig. 2A depicts the sleep stage influence on SDB detection sensitivity. The LSI features of all base data types consistently show their best sensitivity for the light sleep stages S1 and S2 (blue bars) in which almost 77% of all events are observed. Sensitivity exceeds 0.8 for QRSA and MYO, but not for RR. In deeper sleep (cyan bars) and REM sleep (yellow bars) the detection is clearly less sensitive (<0.7, and even <0.6 for RR). Remarkably, the spectral heart rate index SMA(RR) provides the best overall sensitivity for REM sleep events (>0.75) despite being the least sensitive feature in all other sleep stages.

The effect of the respiratory event type on apnea detection sensitivity is given in Fig 2B. The highest sensitivity is consistently observed for mixed events (cyan bars) followed by purely obstructive events (blue bars). The sensitivity is reduced for central events (orange bars) and hypopneas. The latter represent more than 50% of all event epochs. The highest sensitivities are found for QRSA and MYO, and exceed 0.9 for mixed and 0.8 for obstructive events. Central events are

Subgroup	N	%SDB	AHI [1/h] mn/med
Diabetes (type II)	17	29.8	31.0 / 25.7
Myocardial Infarction	7	30.9	29.1 / 26.1
PLMs (PLMI > 8)	9	21.7	35.3 / 4.7
Others (“control”)	109	24.3	25.1 / 14.4

Table 1: Subgroup size (column N) and SDB characteristics for the comorbidities under consideration. %SDB: percentage of 1min epochs spent in SDB. AHI mn/med: mean and median AHI.

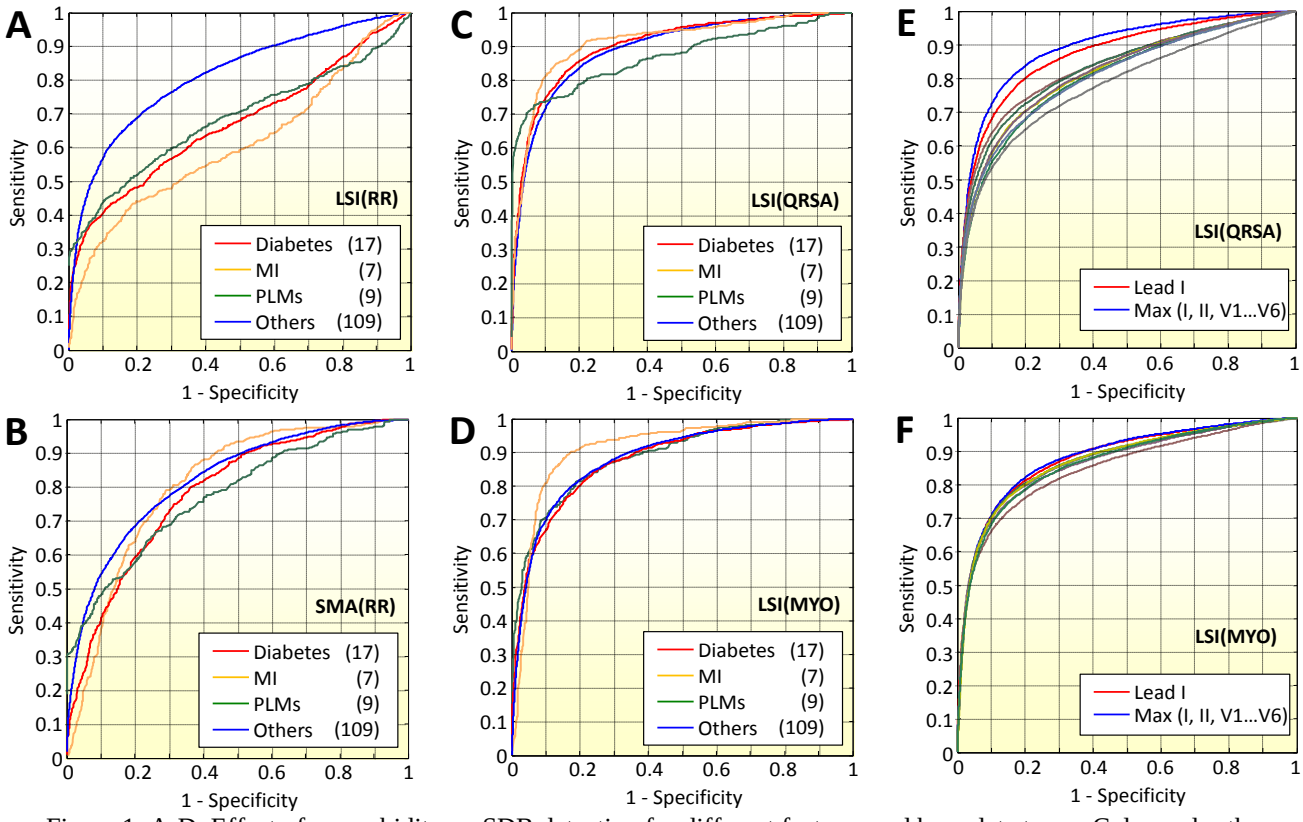

Figure 1: A-D: Effect of comorbidity on SDB detection for different features and base data types. Color codes the presence of comorbidities as indicated in the legends. A: LSI(RR), B: SMA(RR), C: LSI(QRSA), D: LSI(MYO). E, F: Effect of ECG lead on SDB detection based on LSI(QRSA) or LSI(MYO)

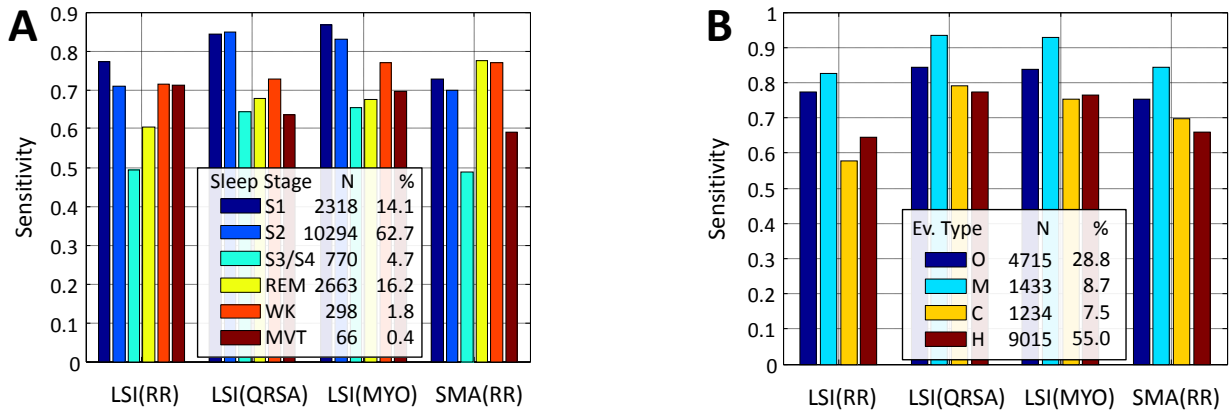

Figure 2: Effect of sleep stages (A) and respiratory event type (B) on the sensitivity of SDB detection. The codes for the event types in B are O-obstructive, M-mixed, C-central and H-hypopnea. N gives the number of minutes spent in a sleep stage (A) or for an event type (B), and % the corresponding percentage.

detected at almost 0.8 sensitivity by QRSA, and for hypopneas the sensitivity exceeds 0.75. The sensitivity for RR-based features is generally reduced

The influence of the body position on the LSI feature of the three base data types is shown in Fig. 3. The most prevalent position is supine (46%) followed by right (17.9%) and left (14.3%) side. The positions prone, prone right and prone left contribute with less than 1% each. For QRSA the performance is quite homogeneous, and largely independent of posture in the prevalent positions (Fig. 3A).

A stronger dependency on position is seen for MYO (Fig. 3B) with slightly better performance for the right side position (red solid line) compared to the left (green solid), and reduced performance for the supine posture (blue solid).

Surprisingly, there is also a clear effect of posture on LSI(RR) with worst performance for the supine position (Fig. 3C, blue solid line) and comparable right and left side results.

There is no dependency of the RR-based features on the ECG lead. Best performance for QRSA is obtained from lead I (Fig. 1E, red curve), and an improvement is observed when the maximum LSI(QRSA) from all available leads is taken (blue curve). MYO is clearly less dependent on the ECG lead (Fig. 1F) with only marginal improvement over lead I (red curve) when all leads are considered (blue curve).

4 Discussion and Conclusions

This study addresses the effect of various factors on the detection of sleep apnea from the ECG. It shows that virtually all investigated factors impact detection performance. Some of the factors – like event type and sleep stage – have a quite universal effect that is similarly observable in each of the base data types heart rate (RR), ECG amplitude (QRSA) and respiratory myogram interference (MYO). With respect to other factors like typical SDB comorbidities or body position, the base data types clearly differ in robustness.

The autonomously mediated modulations in the heart rate are strongly affected by both, comorbidities and body position. This is probably the reason for the unfavorable results we observed previously for features based on heart rate [3], and this may also explain the strong dependence of the results on the sample seen in heart rate based sleep apnea detection [4].

The periodic heart rate accelerations found in PLMs mimic the CVHR modulations and result in a performance loss (Fig. 1A, green line). This effect has also been observed in other studies [5]. But in our data, it is even stronger for diabetes and MI. Interestingly, CVHR does not seem to be abolished in these conditions, since the performance decrease is less pronounced in the absolute spectral magnitude SMA

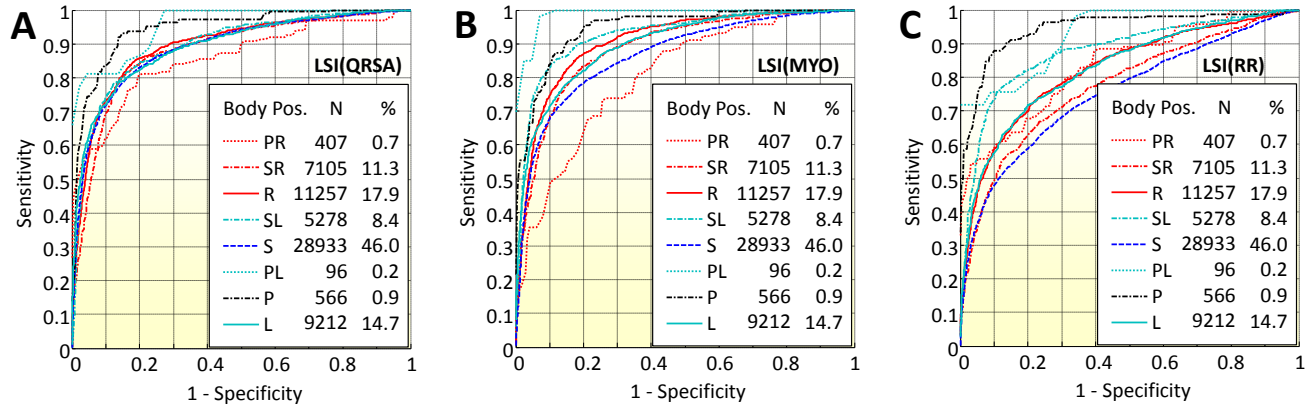

Figure 3: A-C: Effect of body position on SDB detection. Color and line style codes the positions as indicated in the legends. Red lines are associated with right orientations, and green lines with left orientations.
The position labels are: PR: prone, SR: supine right, R: right, SL: supine left, S: supine, PL: prone left, P: prone, L: left.

(Fig. 1B). QRSA and MYO are not mediated via the ANS, and evidently are much more robust against such factors (Fig. 1C and 1D).

We were quite surprised by the strong dependence of LSI(RR) on the body position (Fig. 3C) which indicates a significant postural ANS effect even when lying. The detection accuracy for the very relevant supine position, and also for supine-right, is clearly reduced.

We had expected such dependence rather for QRSA, since the mean value and the magnitude of the respiratory ECG amplitude modulations are heavily affected by posture [3]. However, comparing Fig. 3A to 3B and 3C suggests that QRSA is the most robust data source with respect to body position, with quite consistent performance for all relevant postures. It should be noted that part of this robustness goes back to the availability of multiple ECG leads and that actually the best performing body positions change with the leads for QRSA. The blue curve in Fig. 1E shows that picking the optimal lead in each case clearly improves the performance. But still, lead I alone achieves quite good performance, and is clearly superior to all other leads (Fig. 1E, red curve).

In contrast to QRSA, MYO exhibits a stronger dependence on posture. The max-selection over the leads does not significantly improve LSI(MYO) (Fig. 1F), and the differences between the leads are much smaller. For practical purposes, this means that in a single-lead application, lead I is the lead of choice to capture the ECG amplitude modulation, but the performance will benefit from further leads if available, whereas the benefit from additional leads will be limited for MYO.

There is a remarkable consistency over all features and data types with respect to relative detection sensitivity for the respiratory event types (Fig. 2B). Clearly, the mixed and obstructive apneas are detected best whereas central apneas and hypopneas are more problematic. But the absolute level of sensitivity, in particular for LSI(QRSA), appears still acceptable and sufficient for screening applications.

With respect to sleep-stage dependence, the relative performance is again very consistent for the LSI features (Fig. 2A). Having maximal sensitivity for the light sleep stages S1 and S2 is advantageous since they are prevalent, and daytime sleepiness has been linked to the occurrence of respiratory events in these stages [6]. Subjects with severe sleep apnea rarely reach the deeper sleep stages S3 and S4. Consequently the reduced sensitivity in this stage, which is particularly evident for the RR features, is practically less relevant. However, the reduced sensitivity for REM-events may be of concern. Interestingly, these REM-events appear to be quite pronounced in the spectral domain of HRV, where SMA(RR) clearly stands out. It has been described that nocturnal HRV is mainly governed by sleep stage, and that sleep apnea does not alter the underlying regulatory mechanisms [7]. The similar mechanisms in REM and WK stages are reflected in our data by virtually identical performance for both, LSI(RR) and SMA(RR) (Fig. 2B).

In conclusion, our results show that typical SDB comorbidities adversely affect sleep apnea detection from heart rate modulations. Moreover, its performance is clearly reduced in the supine and supine right body positions. Availability of multiple ECG-leads improves robustness of ECG amplitude assessment with respect to positional influence, but quite robust apnea detection can already be achieved with a single ECG lead – preferably lead I – on basis of the QRSA and MYO series. Sleep stages and respiratory event type have a clear and quite consistent effect on apnea detection sensitivity with better results for light sleep stages, and worse results for REM sleep. Mixed and obstructive events are better detected than central apneas and hypopneas. But future performance improvements appear possible by making clever use of complementary information, e.g. from spectral analysis of heart rate modulations during REM sleep, or by addressing central event detection with separate strategies [8].

References

[1] C. Guilleminault, S. Connolly, R. Winkle, K. Melvin, and A. Tilkian, “Cyclical variation of the heart rate in sleep apnoea syndrome. mechanisms, and usefulness of 24 h electrocardiography as a screening technique.,” *Lancet*, vol. 1, pp. 126–131, Jan 1984.

[2] G. B. Moody, R. G. Mark, A. Zoccola, , and S. Mantero, “Derivation of respiratory signals from multi-lead ecgs,” in *Computers in Cardiology* (A. Murray, ed.), vol. 12, (Washington, DC:), pp. 113–116, IEEE Computer Society Press, 1985.

[3] C. Maier, H. Wenz, and H. Dickhaus, “Steps toward subject-specific classification in ecg-based detection of sleep apnea.,” *Physiol Meas*, vol. 32, pp. 1807–1819, Nov 2011.

[4] M. J. Lado, X. A. Vila, L. Rodríguez-Liñares, A. J. Méndez, D. N. Olivieri, and P. Félix, “Detecting sleep apnea by heart rate variability analysis: Assessing the validity of databases and algorithms.,” *J Med Syst*, Oct 2009.

[5] J. Hayano, E. Watanabe, Y. Saito, F. Sasaki, K. Fujimoto, T. Nomiyama, K. Kawai, I. Kodama, and H. Sakakibara, “Screening for obstructive sleep apnea by cyclic variation of heart rate,” *Circulation: Arrhythmia and Electrophysiology*, vol. 4, no. 1, pp. 64–72, 2011.

[6] N. M. Punjabi, K. Bandeen-Roche, J. J. Marx, D. N. Neubauer, P. L. Smith, and A. R. Schwartz, “The association between daytime sleepiness and sleep-disordered breathing in nrem and rem sleep.,” *Sleep*, vol. 25, pp. 307–314, May 2002.

[7] T. Penzel, J. W. Kantelhardt, C.-C. Lo, K. Voigt, and C. Vogelmeier, “Dynamics of heart rate and sleep stages in normals and patients with sleep apnea.,” *Neuropsychopharmacology*, vol. 28 Suppl 1, pp. S48–S53, Jul 2003.

[8] C. Maier and H. Dickhaus, “Central sleep apnea detection from ecg-derived respiratory signals. application of multivariate recurrence plot analysis.,” *Methods Inf Med*, vol. 49, no. 5, pp. 462–466, 2010.

Address for correspondence:

Christoph Maier
Heilbronn University
E-mail: christoph.maier@hs-heilbronn.de

Reduced cardiac response to sleep apnea and increased risk of mortality

J Hayano[1], E Yuda[1], Y Yoshida[1], H Ogasawara[1], E Watanabe[2]

[1]Department of Medical Education, Nagoya City University Graduate School of Medical Sciences, Japan;
[2]Division of Cardiology, Department of Internal Medicine, Fujita Health University School of Medicine, Japan

Abstract

Studies of heart rate variability indicate that cardiac autonomic dysfunction is an increased risk for mortality in cardiovascular patients and suggest that the development of accurate and effective measures of cardiac autonomic function can improves risk stratification among them. Cyclic variation of heart rate (CVHR) is characteristic heart rate pattern that accompanies apnea-hypopnea episodes in sleep disordered breathing (SDB). CHRV is mediated by the autonomic nervous system and thus, CVHR is less discernible in patients with cardiac autonomic dysfunction. We developed automated algorithm for Holter ECGs that detects nighttime CVHRs and measures their frequency and amplitude (Fcv and Acv). We applied this algorithm to Holter ECG data of prospective cohorts of post-myocardial infarction, end-stage renal disease, and chronic heart failure patients. CVHRs ≥4 episodes per night were detected in most of these patient (>95% for all cohorts) and we found that reduced Acv is powerful independent predictor of mortality risk in all cohorts, while Fcv has no significant mortality predictive power in any of the cohort.

Keywords *Heart rate variability; heart rate response; sleep disorderd breathing; mortality*

1 Introduction

Studies of heart rate variability and heart rate dynamics indicate that cardiac autonomic dysfunction is an independent mortality risk in patients with cardiovascular and renal diseases.[1-5] These studies suggest that more accurate and efficient assessment of cardiac autonomic function could provide better risk-stratifications among these patients. Cyclic variation of heart rate (CVHR) is a characteristic heart rate pattern observed in nighttime ECG in patients with sleep disordered breathing (SDB).[6,7] CVHR is thought to reflect cardiac autonomic responses to cardio-respiratory perturbation caused by apneic/hypoxic episodes. CVHR is thought to be mediated by the cardiac autonomic nervous system and its dysfunction results in less discernible CVHR.[6]

We hypothesized that reduced amplitude of CVHR in nighttime Holter ECG may predicts mortality risk in cardiovascular and renal patients. We developed an automated ECG algorithm that detects nighttime CVHRs.[8,9] Using the algorithm we quantified the hourly frequency (Fcv) and amplitude (Acv) of CVHR and examined their predictive values in prospective cohort data, including two post-myocardial infarction (post-MI) cohorts, an end-stage renal disease on chronic hemodialysis (ESRD) cohort, and a chronic heart failure (CHF) cohort.[10] In this paper, we reviewed these studies and discussed the significance of the analysis of CVHR as an assessment of autonomic function and as the predictor of mortality risk among cardiovascular and renal patents.

2 Assessment of CVHR

We have developed an automated CVHR detection algorithm called autocorrelated wave detection with adaptive threshold (ACAT).[8, 9] ACAT identifies CVHR as cyclic and auto-correlated dips in R-R intervals. In a previous study in 862 patients referred for diagnostic polysomnography, Fcv measured by ACAT correlated with apnea-hypopnea index (AHI) with r = 0.887 (Fig. 1) and patients with AHI >15/h were detected by Fcv with 83% sensitivity and 88% specificity.

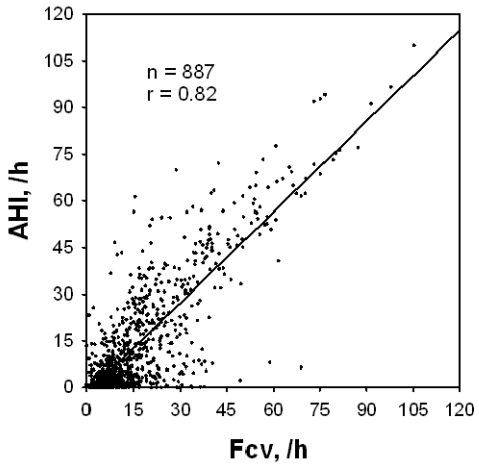

Fig. 1. Frequency of CVHR (Fcv) measured by ACAT algorithm and apnea-hypopnea index (AHI) in patients undergoing polysomnographic study for screening SDB (modified from Figure in reference [8]).

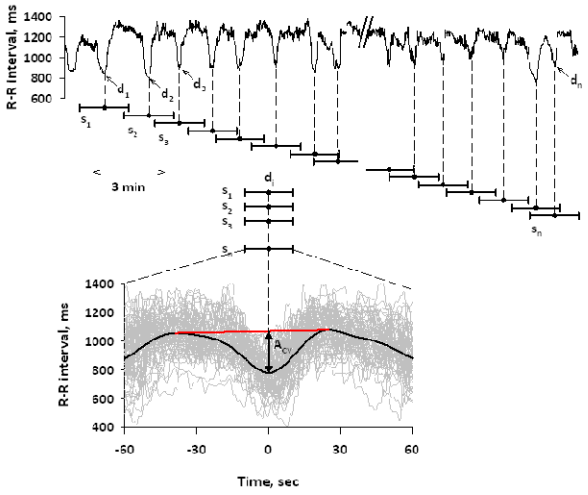

Fig. 1. Measurement of the amplitude of CVHR (Acv) by signal averaging method. Segments of R-R intervals (s_i) around dips attributed to CVHR were alight at their nadir points (d_i) and averaged. Acv was measured as the depth at the center of the averaged curve of R-R intervals (modified from Figure in reference[10]).

Based on ACAT algorithm, we also developed algorithm for measuring Acv by signal-averaging method (Fig. 2), by which all dips in R-R intervals attributed to CVHR were aligned at their nadir points and the depth of averaged curve was measured as Acv.

3 Prognostic value of Acv and Fcv

The algorithm was applied to Holter ECG data in a cohort of 717 post-MI patients who were followed up for a median of 25 months during which 43 patients (6.0%) died. Acv was measured in 688 out of 717 patients (96%). We developed mortality prediction model for Acv and found that Acv was lower in non-survivors than in survivors (median [IQR], 3.4 [2.7-3.9] vs. 5.0 [4.2-5.7] ln[ms], P <0.001). By contrast, Fcv did not differ significantly between non-survivors and survivors (P = 0.6). A survival time analysis for Acv showed two distinct maxima in the log-rank statistics that corresponded to cut-off values of 4.0 and 3.0 ln(ms). Therefore, we adopted a categorical risk stratification scheme for Acv; we classified low-risk patients as category 0 (Acv >4.0), intermediate-risk patients as category 1 (3.0 <Acv ≤4.0), and high-risk patients as category 2 (Acv ≤3.0).

This scheme was applied to another post-MI cohort (n = 220, 56 deaths [25.5%] during 45 months), ESRD patients (n = 299, 84 deaths [28.1%] during 85 months), and CHF patients (n = 100, 35 deaths [35.0%] during 38 months). Acv was able to be measured in >96% of patients. Figure 3 shows the results of survival analyses by Kaplan-Meier method for all cohorts.

Multivariate models showed that the predictive power of Acv and its categories were independent of age, gender, diabetes, β-blocker therapy, left ventricular ejection fraction, mean R-R interval, and Fcv in all cohorts. By contrast, neither Fcv nor its categories showed a significant association with mortality or predictive power in any of the cohorts.

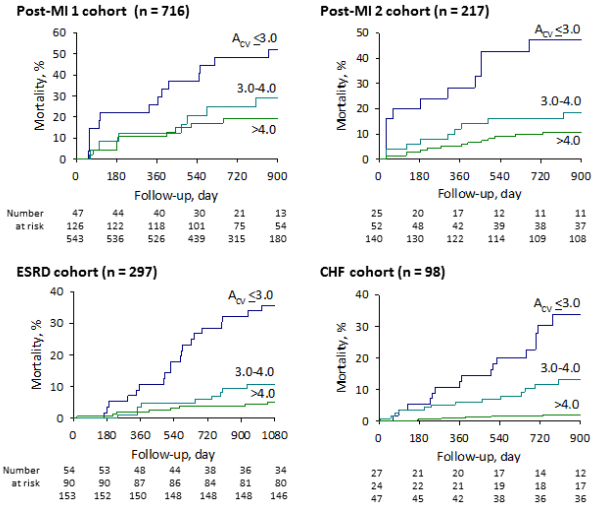

Fig. 3. Kaplan-Meier curves of mortality for patients stratified by the same criteria of Acv cut-off values (4.0 and 3.0) that were optimized for the post-MI 1 cohort: low-risk patients (ACV >4.0), intermediate-risk patients (3.0-4.0), and high-risk patients (≤3.0). The mortality probabilities differed significantly among the post-MI 1 (log-rank chi-square = 105.8, P <0.001); post-MI 2 (38.9, P <0.001); ESRD (28.7, P <0.001); and CHF (9.9, P = 0.007) cohorts (modified from Figure in reference[10]).

Multivariate models showed that the predictive power of Acv and its categories were independent of age, gender, diabetes, β-blocker therapy, left ventricular ejection fraction, mean R-R interval, and Fcv in all cohorts. By contrast, neither Fcv nor its categories showed a significant association with mortality or predictive power in any of the cohorts.

4 Discussion

These studies indicate that blunted CVHR detected by decreased Acv in nighttime Holter ECG monitoring predicts increased mortality risk in post-MI, ESDR, and CHF patients. Because CVHR is thought to reflect cardiac autonomic responses to cardio-respiratory perturbation caused by apneic/hypoxic episodes, blunted CVHR may be a marker of cardiac autonomic dysfunction. Our findings seem consistent with the hypothesis that blunted CVHR predicts mortality risk that is most likely mediated by cardiac autonomic dysfunction.

A variety of autonomic indices of HRV obtained from Holter ECG recordings have been reported as useful markers for risk stratification in various clinical groups including post-MI, ESRD, and CHF patients. Acv seems advantageous over these conventional HRV indices in several points. First, while most of HRV indices reflect nonspecific variation in heart rate, CVHR has its pathophysiologic basis, i.e., heart rate response to apnea/hypopnea during sleep, which would allow us more specific interpretations of findings.

Second, while in case of HRV, different indices have been proposed with respect to each of different clinical conditions, Acv may be used for at least three different diseases (post-MI, ESRD, and CHF) with the same risk stratification criteria. Finally, Acv predicted mortality in CHF patients, in whom most of HRV has no predictive power.[5]

Although Acv assumes the presence of SDB, Acv was able to be measured in 96-98% of post-MI, ESRD, and CHF patients who had no clinical evidence to have SDB. Also, the predictive power of Acv is independent of Fcv that reflects the quantitative severity of SDB and the significant prognostic association of Acv is observed even in patients with a few CVHR. These indicate that for the purpose of risk stratification, Acv may be used practically in most of these patients and that if CVHR occurs, then Acv can predict mortality, irrespective of whether clinical SDB is present or not.

5 Conclusions

Blunted CVHR detected by decreased Acv in nighttime Holter ECG monitoring predicts increased mortality risk in post-MI, ESDR, CHF patients most likely through cardiac autonomic dysfunction in these patients.

References

[1] Kleiger RE, Miller JP, Bigger JT, Jr., Moss AJ, the Multicenter Post-Infarction Research G. Decreased heart rate variability and its association with increased mortality after acute myocardial infarction. Am. J. Cardiol. 1987;59:256-262

[2] Schmidt G, Malik M, Barthel P, Schneider R, Ulm K, Rolnitzky L, Camm AJ, Bigger JT, Jr., Schomig A. Heart-rate turbulence after ventricular premature beats as a predictor of mortality after acute myocardial infarction. Lancet. 1999;353:1390-1396

[3] Bauer A, Kantelhardt JW, Barthel P, Schneider R, Makikallio T, Ulm K, Hnatkova K, Schomig A, Huikuri H, Bunde A, Malik M, Schmidt G. Deceleration capacity of heart rate as a predictor of mortality after myocardial infarction: Cohort study. Lancet. 2006;367:1674-1681

[4] Suzuki M, Hiroshi T, Aoyama T, Tanaka M, Ishii H, Kisohara M, Iizuka N, Murohara T, Hayano J. Nonlinear measures of heart rate variability and mortality risk in hemodialysis patients. Clin J Am Soc Nephrol. 2012;7:1454-1460

[5] Kiyono K, Hayano J, Watanabe E, Struzik ZR, Yamamoto Y. Non-gaussian heart rate as an independent predictor of mortality in patients with chronic heart failure. Heart Rhythm. 2008;5:261-268

[6] Guilleminault C, Connolly S, Winkle R, Melvin K, Tilkian A. Cyclical variation of the heart rate in sleep apnoea syndrome. Mechanisms, and usefulness of 24 h electrocardiography as a screening technique. Lancet. 1984;1:126-131

[7] Zwillich C, Devlin T, White D, Douglas N, Weil J, Martin R. Bradycardia during sleep apnea. Characteristics and mechanism. J. Clin. Invest. 1982;69:1286-1292

[8] Hayano J, Watanabe E, Saito Y, Sasaki F, Fujimoto K, Nomiyama T, Kawai K, Kodama I, Sakakibara H. Screening for obstructive sleep apnea by cyclic variation of heart rate. Circ Arrhythm Electrophysiol. 2011;4:64-72

[9] Hayano J, Tsukahara T, Watanabe E, Sasaki F, Kawai K, Sakakibara H, Kodama I, Nomiyama T, Fujimoto K. Accuracy of ecg-based screening for sleep-disordered breathing: A survey of all male workers in a transport company. Sleep Breath. 2013;17:243-251

[10] Hayano J, Yasuma F, Watanabe E, Carney RM, Stein PK, Blumenthal JA, Arsenos P, Gatzoulis KA, Takahashi H, Ishii H, Kiyono K, Yamamoto Y, Yoshida Y, Yuda E, Kodama I. Blunted cyclic variation of heart rate predicts mortality risk in post-myocardial infarction, end-stage renal disease, and chronic heart failure patients. Europace. 2016; in press

Address for correspondence:

Junichiro Hayano, MD
Department of Medical Education
Nagoya City University Graduate School of Medical Sciences
hayano@med.nagoya-cu.ac.jp

Nonlinearity of heart rate variability induced by respiratory modulation

Yuki Miki[1], Yasuyuki Suzuki[1], Masanori Shimono[1], Eiichi Watanabe[2], Junichiro Hayano[3], Yoshiharu Yamamoto[4], Taishin Nomura[1], Ken Kiyono[1]

[1]Graduate School of Engineering Science, Osaka University, JAPAN;
[2]Department of Cardiology, Fujita Health University School of Medicine, JAPAN;
[3]Department of Medical Education, Nagoya City University Graduate School of Medical Sciences, JAPAN;
[4]Educational Physiology Laboratory, Graduate School of Education, University of Tokyo, JAPAN;

Abstract

Extant studies indicated that healthy human heart rate variability (HRV) exhibits nonlinear properties, such as long-range correlation of HRV amplitude (magnitude), non-Gaussian fluctuation, and multifractality. However, the physiological origin of these nonlinearities was not fully identified. This study investigated nonlinear properties of high-frequency (HF; 0.15 to 0.4 Hz) and low-frequency (LF; 0.04 to 0.15 Hz) components in 122 healthy subjects. An analysis of bandpass-filtered HRV time series data corresponding to HF and LF components revealed that the amplitude variability of HF and LF components displayed long-range correlations. This could not be explained by linear stochastic models. Furthermore, a spectral coherence analysis of HRV HF component and respiration amplitudes was performed. The results demonstrated that long-range correlation observed in HRV HF amplitude was associated with long-range correlated respiratory modulation. This could be a possible physiological mechanism of nonlinear HRV properties.

Keywords *Long-range correlation; nonlinearity; amplitude variability*

1 Introduction

Frequency-domain heart rate variability (HRV) analysis based on power spectral estimation has been used to assess autonomic nervous system function [1]. Experiments conducted by previous studies on healthy subjects under well-controlled conditions indicated that a typical HRV power spectrum displayed two major peaks corresponding to oscillating components in high-frequency (HF; 0.15 to 0.4 Hz) and low-frequency (LF; 0.04 to 0.15 Hz) bands [1]. The HF component reflects synchronization between respiration cycles and HRV, which is also referred to as respiratory sinus arrhythmia (RSA). In contrast, the LF component is associated with Mayer waves (at approximately 0.1 Hz), which are oscillations related to the regulation of blood pressure and vasomotor tone. Typically, HF and LF band powers are used in practical methods of noninvasively assessing the autonomic nervous system activity. Although HF and LF components of HRV are extensively and intensively studied from a linear systems viewpoint, the nonlinear characteristics of these components are not well established. As described by autoregressive models, the power spectrum in the framework of linear stochastic processes provides a complete characterization of the process if the stationary condition is fulfilled [2]. In contrast, nonlinear analysis methods inspired by nonlinear and statistical physics indicate that HRV displays nonlinear properties [3, 4]. These findings suggested that nonlinear HRV properties could provide complementary information on HRV dynamics and physiological functions [3, 4]. However, the physiological origin of this nonlinearity was not fully investigated by extant studies.

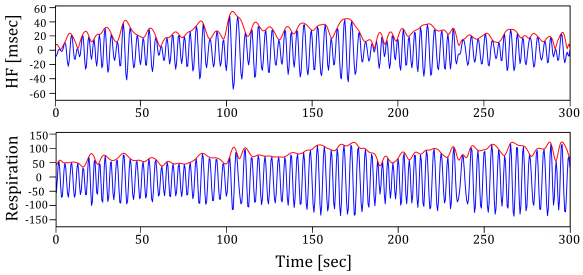

Figure 1: Illustrative examples of HF components of HRV and Respiration signals (blue solid lines). (Red solid lines represent the instantaneous amplitude of each signal.)

The purpose of the present study included investigating as to whether HF and LF components display nonlinear properties. To this effect, a method to characterize the amplitude variation of HF and LF components was proposed. This method was applied to ambulatory HRV in healthy subjects. The results demonstrated that the amplitude variability of HF and LF components displayed long-range correlations involved with nonlinear HRV properties. As previously mentioned, the HRV HF component reflects RSA. Therefore, the long-range correlation of the HF band amplitude variation can be directly associated with the respiration amplitude. This was confirmed by further investigating the relation between the HF component amplitude of HRV and the respiration amplitude.

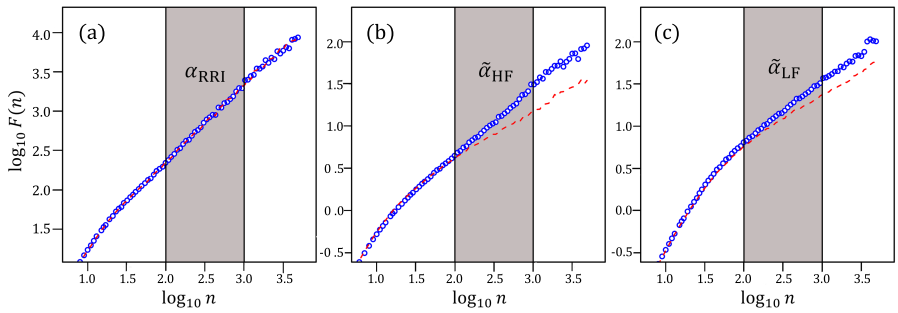

Figure 2: DFA results for RR interval time series (a) and amplitude variability of HF (b) and LF (c) components in a healthy subject. The circles and dashed lines indicate the results of the original time series for the surrogate time series. Scaling exponents, α_{RRI}, $\tilde{\alpha}_{\mathrm{HF}}$ and $\tilde{\alpha}_{\mathrm{LF}}$, were estimated in the range of $2 \leq \log_{10} n \leq 3$ (the shaded area) corresponding to $50 - 500$ s. Differences of $F(n)$ between the original time series (as shown by the circles) and the surrogate (as shown by the dashed lines) indicate nonlinear properties.

2 Method

2.1 Data

The HRV (RR interval) time series derived from 122 healthy subjects (47.4 ± 18.2 y) without any known disease affecting the autonomic control of heart rate (for details, see [5]) was analyzed. For each individual, a 24 h Holter ECG recording was performed, and an RR interval time series was extracted from the ECG recording. Any errors in the R wave classification were manually corrected. The RR interval time series was linearly interpolated and resampled at 2 Hz. Additionally, this study analyzed the daytime (12:00 - 18:00) data. In order to remove nonstationary trends embedded in the RR interval time series, the resampled time series was high-pass filtered with a cut-off at $1/3600$ Hz after removing the mean value.
Furthermore, ECG and respiration signals were recorded simultaneously in a single subject (23 years old male) to confirm the relation between HF band amplitude variability and respiration. The subject was seated in a resting position during the measurement (three recordings of 30 min each). PowerLab and LabChart Pro softwares (AD Instruments) were used to record the ECG and respiration signals at a sampling frequency of 1000 Hz. Respiratory airflow was recorded with a thermistor flow sensor placed in front of the nose and the mouth of the subject. In the analysis, RR interval time series derived from the ECG recording was linearly interpolated and resampled at 2 Hz. Moreover, the respiration airflow signal was also resampled at 2 Hz.

2.2 Amplitude variability of HRV and respiration

In order to extract the amplitude variability of HF and LF components in RR interval time series (Fig. 1), the following procedure was employed: 1) Fourth-order bandpass Butterworth filters that pass frequencies from 0.15 Hz to 0.4 Hz and from 0.04 Hz to 0.15 Hz were used to extract HF and LF components, respectively. 2) The Hilbert transform was used as shown below:

$$x_i(t) = \frac{1}{\pi} PV \int_{-\infty}^{+\infty} \frac{x_r(t)}{t-\tau} d\tau, \tag{1}$$

where $x_r(t)$ denotes the analyzed time series, and PV denotes the Cauchy principal value. The HF and LF component time series were converted to analytic signals $x(t)$: $x(t) = x_r(t) + i x_i(t)$, where i denotes the imaginary unit, and $x_i(t)$ denotes the imaginary part of the analytic signal. 3) The instantaneous amplitude $A(t)$ of the analytic signal was calculated as follows: $A(t) = \sqrt{x_r^2 + x_i^2}$. Log-transformed time series of $A(t)$ were used for further analysis because the distribution of $A(t)$ was skewed.
Similarly, the HF component (0.15 Hz - 0.4 Hz) of the respiratory airflow signal was extracted using fourth-order bandpass Butterworth filters. This was followed by calculating the instantaneous amplitude through the Hilbert transform.

2.3 Detrended fluctuation analysis

Detrended fluctuation analysis (DFA) was used to characterize long-range correlations [6–9]. The DFA procedure included the following steps: 1) The analyzed time series were integrated. 2) The integrated time series were divided into window size n, and in each segment the regression line was fitted. 3) The root-mean-square deviation $F(n)$ from the regression line was estimated. 4) Steps 2) and 3) were repeated over multiple time scales (window sizes) to characterize the relationship between $F(n)$ and n. A linear relationship on a log-log plot of $F(n)$ as function of n indicated the power-law scaling range in which the long-range correlation of the analyzed time series could be characterized by a scaling exponent α. This corresponded to the slope of the linear relation between $\log F(n)$ and $\log n$. The study of long-term HRV involved using linear regression to estimate the slope in the range of $100 \leq n \leq 1000$ (points) corresponding to $50 - 500$ s. The scaling exponents of the original time series and amplitude variability of HF and LF components were denoted as α_{RRI}, $\tilde{\alpha}_{\mathrm{HF}}$ and $\tilde{\alpha}_{\mathrm{LF}}$, respectively.

2.4 Spectral coherence analysis

The coherence was calculated using all segments to evaluate the correlation between HRV and respiration. The coherence function of the two time series $x_i^{(1)}$ and $x_i^{(2)}$ is defined as follows:

$$\gamma_{1,2}^2 = \frac{\langle |S_{12}(f)|^2 \rangle}{\langle S_{11}(f) \rangle \langle S_{22}(f) \rangle} \quad (2)$$

where $S_{12}(f)$ denotes the cross-spectrum between $x_i^{(1)}$ and $x_i^{(2)}$, $S_{11}(f)$ and $S_{22}(f)$ denote the auto-spectra of $x_i^{(1)}$ and $x_i^{(2)}$, respectively. Additionally, $\langle \cdot \rangle$ denotes the mean of all the segments. If $\gamma_{1,2}^2$ equals zero, it indicates that $x_i^{(1)}$ and $x_i^{(2)}$ are completely uncorrelated. In the calculation of $\gamma_{1,2}^2$, the 30 min recordings of the RR interval and respiration time series were segmented into a sliding windows of 5 min with an overlap of 50 %.

2.5 Surrogate data analysis

Surrogate data analysis was performed as a validity check of the nonlinear properties of HF and LF components [10, 11]. In order to generate surrogate time series, an iterative amplitude adjusted Fourier transform algorithm that preserved the temporal correlation of original time series, was used [11]. Thus, the linear properties, such as HF and LF band powers and the scaling exponent α_{RRI}, were also preserved in the surrogate time series. In contrast, the nonlinear properties of HF and LF components were not preserved in the surrogate time series. Therefore, the differences in the statistical properties between original and surrogate time series indicated the nonlinear properties of the analyzed time series.

2.6 Statistical analysis

In the study, data were reported as mean $\pm$ SD for continuous variables. The differences between the groups were compared using unpaired Student's t-test. A P value of less than 0.05 was set as the significance level.

3 Results and Discussions

3.1 Nonlinear properties of HF and LF components in healthy subjects

The DFA results for RR interval time series and amplitude variability of HF and LF components in a healthy subject are shown in Fig. 2(a), 2(b) and 2(c), respectively, as illustrative examples. Power-law scaling behavior was observed in the original RR interval time series (Fig. 2(a)). This corresponded to the results of previous studies [7]. As shown in Fig. 2(a), it is important to note that the scale dependence of $F(n)$ (circles) is preserved in the surrogate time series (dashed lines). In contrast, as shown in Figs. 2(b) and 2(c), with respect to the amplitude variability of both HF and LF components, the scale dependence of $F(n)$ between the original time series (represented by circles) and surrogate time series (represented by dashed lines) showed clear differences in the range of $\log_{10} n > 2$. This indicated the presence of nonlinear properties. A power-law scaling behavior was also observed in this range, and the slope of the original time series was found to be steeper than that of the surrogate time series.

Table 1: Heart rate variability indices in healthy subjects

	original	**surrogate**	P value
TP (ms^2)	4422 $\pm$2519	4421 $\pm$ 2524	
ln	8.22 $\pm$ 0.63	8.22 $\pm$ 0.63	NS
HF (ms^2)	166 $\pm$ 188	166 $\pm$188	
ln	4.63$\pm$1.05	4.62 $\pm$ 1.05	NS
LF (ms^2)	609 $\pm$ 482	608 $\pm$480	
ln	6.05 $\pm$ 0.98	6.05 $\pm$ 0.98	NS
VLF(ms^2)	1624 $\pm$1055	1617 $\pm$1050	
ln	7.16 $\pm$ 0.74	7.16 $\pm$ 0.74	NS
α_{RRI}	1.10 $\pm$ 0.12	1.10 $\pm$ 0.12	NS
$\tilde{\alpha}_{\mathrm{HF}}$	0.81$\pm$0.08	0.64$\pm$0.07	< 0.0001
$\tilde{\alpha}_{\mathrm{LF}}$	0.73$\pm$0.05	0.66$\pm$0.06	< 0.0001

TP: total power spectral density; HF: power spectral density of the high frequency components; LF: power spectral density of the low frequency components; α_{RRI}: DFA scaling exponent of RR interval time series; $\tilde{\alpha}_{\mathrm{HF}}$: DFA scaling exponent of amplitude variability of HF component; $\tilde{\alpha}_{\mathrm{LF}}$: DFA scaling exponent of amplitude variability of LF component. Values indicated means $\pm$ SD.

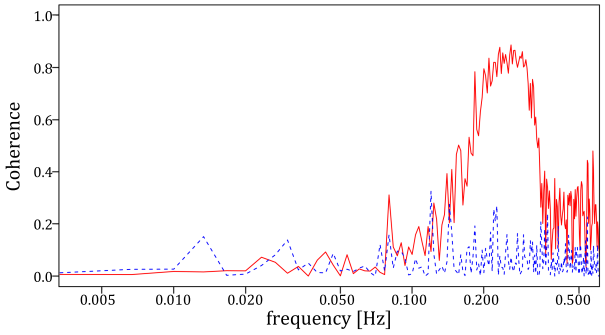

Figure 3: Coherence between the RR interval time series and respiration airflow signal (solid lines). Dashed lines show coherence with surrogate data.

Table I presents the HRV indices in healthy subjects and their comparison with surrogate data. Given that the surrogate time series preserved the linear properties of the HRV, all linear indices, such as HF and LF powers and α_{RRI}, did not show significant differences between the original and surrogate time series. In contrast, the scaling exponents of amplitude variability for the HF and LF components, namely $\tilde{\alpha}_{\mathrm{HF}}$ and $\tilde{\alpha}_{\mathrm{LF}}$, showed significant differences between the original and surrogate time series. This finding indicated the presence of nonlinear properties of HF and LF components.

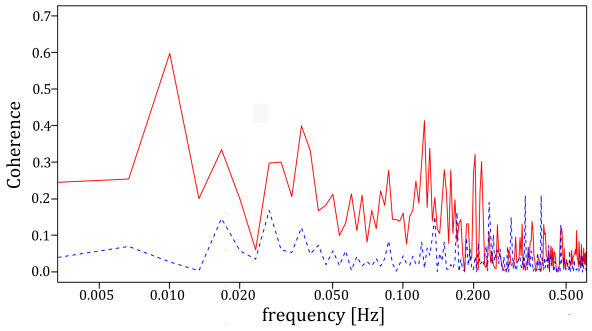

Figure 4: Coherence between the HRV HF amplitude and respiration amplitude (solid lines). The dashed lines represent the coherence with surrogate data.

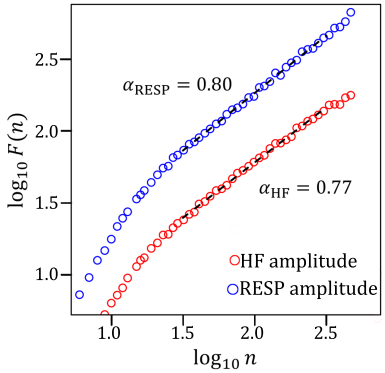

Figure 5: DFA results for HRV HF component amplitude (red) and respiration airflow amplitude (blue).

3.2 Relation between HRV amplitude and respiration amplitude

As shown in Fig. 3, the observations revealed strongly correlated behavior between RR interval time series and respiration airflow at approximately 0.25 Hz. This behavior was noted by previous studies as RSA. However, as shown in Fig. 4, the amplitude variations of these two time series showed higher coherence at very low frequencies (< 0.04 Hz) and LF ranges. As shown in Fig. 5, both HRV HF amplitude and respiration airflow amplitude displayed long-range correlations. Therefore, the coherence analysis suggested that long-range correlations in these amplitude variations had the same physiological origin.

4 Conclusions

This study investigated the properties of amplitude variability of HF and LF components of HRV in healthy subjects. The findings revealed that the HF and LF component amplitude variability displayed long-range correlations. A comparison between the original HRV time series and the corresponding surrogate time series demonstrated that the long-range correlations of HF and LF amplitude variability reflected HRV nonlinear dynamics. Furthermore, the results indicated that the long-range correlation observed in the amplitude variability of the HRV HF component was associated with the amplitude variability of respiration.

Acknowledgements

This work was supported by JSPS KAKENHI, grant numbers 15K01285 and 26461094.

References

[1] Task Force of the European Society of Cardiology, the North American Society of Pacing, and Electrophysiology. Heart rate variability: standards of measurement, physiological interpretation and clinical use. *Circulation*, 93:1043–1065, 1996.

[2] J.D. Hamilton. *Time series analysis*, Princeton, N.J. Princeton University Press, 1994.

[3] R. Sassi, S. Cerutti, and F. Lombardi et al. Advances in heart rate variability signal analysis: joint position statement by the e-cardiology esc working group and the european heart rhythm association co-endorsed by the asia pacific heart rhythm society. *Europace*, 17:1341–1353, 2015.

[4] T. Nakamura, K. Kiyono, H. Wendt, P. Abry, and Y. Yamamoto. Multiscale analysis of intensive longitudinal biomedical signals and its clinical applications. *Proc. IEEE*, 104:242–261, 2016.

[5] S. Sakata, J. Hayano, S. Mukai, A. Okada, and T. Fujinami. Aging and spectral characteristics of the nonharmonic component of 24-h heart rate variability. *Am. J. Physiol*, 276:1724–1731, 1999.

[6] C.K. Peng, S.V. Buldyrev, S. Havlin, M. Simons, H. E. Stanley, and A. L. Goldberger. Mosaic organization of dna nucleotides. *Phys. Rev. E*, 49(2):1685–1689, 1994.

[7] C.K. Peng, S. Havlin, H.E. Stanley, and A. L. Goldberger. Quantification of scaling exponents and crossover phenomena in nonstationary heartbeat time series. *Chaos*, 5:82–87, 1995.

[8] K. Kiyono. Establishing a direct connection between detrended fluctuation analysis and fourier analysis. *Phys. Rev. E*, 92:042925, 2015.

[9] K. Kiyono and Y. Tsujimoto. Time and frequency domain characteristics of detrending-operation-based scaling analysis: Exact DFA and DMA frequency responses. *Phys. Rev. E*, 94:012111, 2016.

[10] T. Schreiber and A. Schmitz. Improved surrogate data for nonlinearity tests. *Phys. Rev. Lett*, 77:635–638, 1996.

[11] T. Schreiber and A. Schmitz. Surrogate time series. *Physica D: Nonlinear Phenomena,*, 142:346–382, 2000.

Address for correspondence:

Ken Kiyono
Graduate School of Engineering Science, Osaka University, Japan
kiyono@bpe.es.osaka-u.ac.jp

Linear and nonlinear functional connectivity methods to predict brain maturation in preterm babies

M Lavanga[1,2], O De Wel[1,2], A Caicedo[1,2],K Jansen[3,4], A Dereymaeker[3],G Naulaers[3], S Van Huffel[1,2],

[1]Department of Electrical Engineering (ESAT), STADIUS Center for Dynamical Systems, Signal Processing and Data Analytics, KU Leuven, Belgium;
[2]iMinds Medical IT, KU Leuven, Belgium;
[3]Department of Development and Regeneration, Neonatal Intensive Care Unit, UZ Leuven, Belgium;
[4]Department of Development and Regeneration, Child Neurology, UZ Leuven, Belgium

Abstract

In this paper we investigate the relationship between functional connectivity (FC) and early brain maturation. On one hand, the objective was to provide a model able to predict age in premature babies, on the other hand to shed light on the maturation mechanism of brain interdependencies in first stages of life. The study was a follow-up considering the data in [1]. FC was assessed through the means of mean squared coherence *(MSC),* phase locking value *(PLV) and* activity synchrony index *(ASI). A feature selection indicated that coherence in β bands and ASI were the best predictors of the postmenstrual age (PMA), so they were combined in a single multivariate linear regression model. The prediction performance showed* the root mean square error *($\sqrt{MSE}$) equal to 2.05 $weeks$. Further, the results indicated a decrease/increase in coherence/ASI with age. This can be due to the shift from the thalamo-cortical connections to cortico-cortical connections, leading to more localized and task dedicated networks. Finally, a larger correlation of ASI and coherence was found in the left hemisphere compared to the right hemisphere.*

Keywords *Preterm infants, Early brain maturation, Coherence, ASI, Functional connectivity*

1 Introduction

The need for maturation charts of pediatric brain development in order to detect neural disorders has been widely discussed in literature [2]. Franke [2] has assessed the brain maturation through the study of functional connectivity (FC) using fMRI. In particular, the author focused on the prediction of the chronological age until adolescence using a support vector regression (SVR) in two cohorts of children, one born full-term and the other born prematurely. In the early newborns, as their brain matures, the EEG waveforms change their characteristics [3]. Therefore, the EEG can be a valuable, non-invasive and much easier recording procedure, than fMRI [4], to describe the wiring evolution of the neuron pools in the cerebral cortex. Gonzalez [4] argued the necessity to use new approaches to describe brain maturation beyond linear tools, such as the EEG spectrum. In particular, Gonzalez [4] applied linear and nonlinear methods to describe the functional EEG interdependencies. Among the linear methods, the *mean squared coherence* (MSC) has already been used in literature to evaluate maturation in children as function of age [5], and in preterm infants as function of gestational age or postmenstrual age (PMA) [6]. In addition, phase synchronization methods like *phase locking value* (PLV) have also been applied in brain maturation studies [4]. The goal of this study is twofold: on one hand, it aims to provide a simple model for the estimation of maturational age in these infants (as discussed by [7]), on the other hand it evaluates the brain connectivity in preterm neonates as function of the PMA, using linear and nonlinear methods to estimate FC, such as the *activity synchrony index* (ASI).

2 Methods

2.1 Dataset

This study was carried out using EEG recordings from 48 preterm neonates. 20 of these recordings have been used in a previous study [1]. The additional 28 subjects were recruited at the same neonatal intensive care unit (NICU), in the University Hospitals Leuven. The patients included in this study had a PMA ranging from 27 to 42 weeks. EEG measurements for each patient were recorded at least once during their stay at the unit and lasted at least 2 hours. The total number of recordings was 104. Labels for quiet sleep (QS) and active sleep/awake (AS) were provided. The EEG was recorded using a sampling frequency of 256 or 500 Hz. The measuring electrodes were located according to the 10-20 system. The monopolar electrodes (F_1,F_2,C_3,C_4,T_3,T_4,O_1,O_2) were chosen as first step to study FC among brain regions. Each channel was bandpass filtered between 1-20 Hz and downsampled to 100 Hz. Only the quiet sleep epochs were considered for this study, since the co-occurrence of activity bursts during quiet sleep has been considered as a key component in assessing background activity [8].

2.2 Functional connectivity measures

In order to quantify the FC among the different EEG channels, three methods were applied. Since each method is applied on channels in a pairwise fashion and there are 8 monopolar electrodes, each FC index provides a matrix 8×8, where each row and each column represents a specific channel. The obtained matrix is symmetric because the coupling direction was not investigated. The first method was the cross-coherence, a linear method defined between signal x and y at frequency f as

$$k^2_{xy}(f) = \frac{|P_{xy}(f)|^2}{P_{xx}(f)P_{yy}(f)} \quad (1)$$

where $P_{xy}(f)$ is the cross-spectrum between the two times-series and $P_{yy}(f)$, $P_{xx}(f)$ are the autospectra of the signals. k^2_{xy} was computed for each channel pair in 30s epochs without overlapping and the spectra were computed using the Welch method with 5 s windows and 50% overlapping, as suggested by [5]. For each pair, the MSC was computed in the frequency bands: δ (1-4 Hz), θ (4-8Hz), α (8-13 Hz), β (13-21 Hz) [4]. The second method used is PLV, which is defined as

$$PLV_{xy} = \frac{1}{N}\left|\sum_{t=0}^{N} e^{j\varphi_{xy}(t)}\right| \quad (2)$$

where $\varphi_{xy}(t) = \varphi_x(t) - \varphi_y(t)$. $\varphi_x(t)$ and $\varphi_y(t)$ represent the phases of the time series x and y and are derived from the analytical signal $\tilde{x}(t) = x(t) + jx_H(t)$ (or $\tilde{y}(t)$), where $x_H(t)$ is the Hilbert transform of $x(t)$. The complete signal, with a frequency band between 1-20 Hz, is used in this method. The last one is the nonlinear method ASI, which is computed by Räsänen [8] using the *energy weighted temporal dependency function* (ETDF):

$$ETDF_{xy}(\tau) = \sum_{ij} A(a_i)A(b_j)\frac{p^2(a_i, b_j)}{p(a_i)p(b_j)} \quad (3)$$

where a_i and b_j are downsampled and requantized versions of the channels $x(t)$ and $y(t)$, with $y(t)$ delayed by a lag τ. $A(a_i)$, $A(b_j)$ are the amplitudes respectively for the sample a_i and b_j. $p(*,*)$ and $p(*)$ are the joint and marginal probability distributions respectively. The ASI is defined as follows

$$ASI_{xy} = \frac{ETDF_{norm}(\tau = 0)}{(\frac{1}{101}\sum_{\tau=-50}^{\tau=50} ETDF_{norm}(\tau))} \quad (4)$$

where $ETDF_{norm}(\tau) = ETDF_{xy}(\tau) - \min\{ETDF_{xy}(k), k \in [-50, 50]\}$. $ETDF$ is derived from the definition of mutual information for different time lags between the signals [8]. Both PLV_{xy} and ASI_{xy} were computed on 5 min epochs without overlapping. These three indices provide 6 matrices 8×8 for each considered epoch (2 matrices for the the nonlinear methods, 4 matrices for the coherence). The matrices belonging to QS periods are subsequently averaged for each EEG measurement. In order to have a more general overview of neonatal brain connectivity, the average matrix can be used to derive indices of general synchrony, intra and interhemispheric connectivity, as well as anterior and posterior connectivity as shown in [1]. In particular, the last two are obtained as average values of matrix entries associated respectively to anterior electrodes and posterior electrodes. In a similar way, the intrahemispheric connectivity is measured as the average of the entries associated to the left or to the right electrodes. The interhemispheric connectivity is just the average of the symmetric channel combinations between hemispheres. In addition to the connectivity measures, the evolution and the loss of a discontinuity pattern in the brain electrical activity with maturation can be easily monitored by means of the *suppression curve* (SC), as thoroughly reported in [3]. This index was computed in 5 min epochs of EEG channels and was then averaged over all QS epochs.

2.3 Linear Regression and statistical analysis

One of the main objectives of this study is to develop a model for the prediction of PMA. On one hand we evaluated the performance of a model containing information coming from the different features extracted from the EEG signals. On the other hand, in order to evaluate whether the use of different features improves the prediction capabilities of the model, we also study the performance of different regression models using features from ASI, PLV or coherence analysis solely. In both cases a linear multi-variable model was chosen. A total of 229 features were extracted from each recording. For the PLV and coherence matrices, only the off-diagonal upper triangular elements were considered as input for the model. For the ASI matrix also the diagonal elements were included. Due to the reduced amount of training points, 104, we performed a feature selection procedure prior the training of the multivariate models. First, the predictive power of each feature, individually, was assessed by means of the *root mean squared error* ($\sqrt{MSE}$), which was computed from results of a linear regression between each feature and the PMA. For this phase the data was split in training set and a test set (2/3-1/3) 100 times. After the estimation of the model on the training set, the performance as $\sqrt{MSE}$ and Pearson's correlation (ρ) between the prediction and the response variable in the *test set* were reported as median with *interquartile range*, i.e. q_{50}(IQR) for each variable. In the first case, the model considering all the extracted attributes, eleven features with lowest $\sqrt{MSE}$ were selected for the final model. Afterwards, we applied least absolute shrinkage and selection operator (LASSO) regression from the obtained features set to reduce even more the number of input regressors and the amount of redundant information. For the models using ASI, PLV and coherence as input only the LASSO procedure was used in order to reduce the dimensionality of the input space. Once the features were

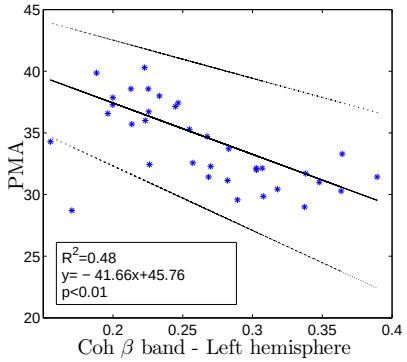

Figure 1: Regression plot of PMA as function of $k^2_{LEFT}(\beta)$ on the *test set*.

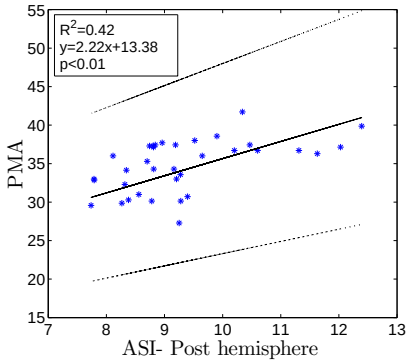

Figure 2: Regression plot of PMA as function of ASI_{POST} on the *test set*.

selected, the dataset was divided once again in training set and a test set (2/3-1/3) in order to train the different multivariate models. For both cases, the data splitting and the LASSO were performed 100 times. The performance of the different models were measured using fraction of explained variance R^2 and the $\sqrt{MSE}$ on the *test set*, presented as q_{50}(IQR).

3 Results

Table 1 shows the features with lowest MSE on the test set as individual predictors of PMA, the Pearson's correlation (ρ) and the number of times when the correlation is significant. For each iteration or re-estimation of the model, the correlation was always significant for most of the twelve features. Among the top eleven features, the SC was the best to describe brain maturation using neonatal EEG. SC shows a negative correlation with PMA, as shown in [3]. Looking at linear methods, the coherence in β band is the attribute that mostly reflects the cerebral evolution of the infants, with the lowest $\sqrt{MSE}$, compared to the coherence in other bands (Table 1). The remaining features belong to the different ASI indexes (Table 1). As shown in [6], $MSC(\beta)$ presents a negative correlation with age. An example of linear regression between MSC in the left brain hemisphere ($k^2_{LEFT}(\beta)$) and PMA is reported in Figure 1. Table 1 also shows that ASI is the nonlinear connectivity index that describes the

Features	$\sqrt{MSE}$ $(weeks)$	ρ (%)
SC	2.23(0.37)	-78.28(8.16) §
$k^2_{LEFT}(\beta)$	2.62(0.43)	-69.40(11.66) §
ASI_{C_4,C_4}	2.73(0.33)	66.14(7.31) §
ASI_{POST}	2.79(0.41)	59.91(10.36) §
ASI_{C_3,C_3}	2.80(0.30)	62.43(9.80) §
$k^2_{C_4,O_2}(\beta)$	2.81(0.38)	-62.54(11.79) #
ASI_{O_1,O_1}	2.82(0.40)	61.03(13.15) §
ASI_{LEFT}	2.83(0.34)	62.66(9.69) §
ASI_{C_3,C_4}	2.90(0.39)	57.54(11.06) §
ASI_{O_2,O_2}	2.91(0.45)	59.63(14.29) §
ASI_{ANT}	2.92(0.42)	58.27(12.64) §

Table 1: The best eleven predictors of PMA with the lowest MSE using a linear regression model. MSE and Pearson's ρ are reported as q_{50}(IQR). § means $p \leq 0.05$ for each iteration, # means $p \leq 0.05$ for more than 90 iterations.

Features	$\sqrt{MSE}$ $(weeks)$	R^2
Best eleven	2.05(0.44)	.64(.14) §
PLV matrix	2.72(0.66)	.37(.26) §
ASI matrix	2.80(0.57)	.37(.25) §
$k^2_{xy}(\delta)$ matrix	3.19(0.91)	.16(.51) §
$k^2_{xy}(\theta)$ matrix	2.63(0.43)	.40(.30) §
$k^2_{xy}(\alpha)$ matrix	2.85(0.58)	.35(.23) §
$k^2_{xy}(\beta)$ matrix	2.63(0.43)	.42(.20) §

Table 2: Comparison between the different multivariate regression models to predict PMA. MSE and R^2 are reported as q_{50}(IQR). § means $p \leq 0.01$ for each iteration.

evolution of the brain with lowest $\sqrt{MSE}$. The selected ASI indexes cover most of the brain region: posterior, anterior and left (ASI_{POST}, ASI_{LEFT}, ASI_{ANT}). It can also be noticed that auto-ASI (the ASI computed between a channel and itself) of channels C_4, C_3, O_1 and O_2 are listed in the top eleven. Figure 2 shows the linear regression between ASI_{POST} and PMA, where a positive correlation can be seen, as reported in Table 1 and in [1]. Table 2 shows the performance of the regression models using a multivariate approach. The combination of best features in a linear multivariate regression increases the prediction performance, i.e. the total $\sqrt{MSE}$ is reduced to 2.05 $weeks$, as shown by Table 2. The median fraction of explained variance is $R^2 = .64$ ($p \leq 0.01$). Table 2 compares the performance also with the other models where the features come from the 6 FC connectivity matrices, as described above. However, the model in which best features are selected outperforms the other ones. One can also observe that matrices of coherence in β and θ bands have better performances in terms of MSE and R^2 compared to the nonlinear index matrices, whose prediction power is comparable with the best individual features in Table 1. All the regression models were statistically significant in all 100 iterations.

4 Discussions

As discussed by [3], the brain maturation is reflected by the progressive disappearance of bursts in the EEG, leading to a more continuous waveform. Indeed, the maturation modifies the amplitude distribution in the signal, making the SC a good predictor of PMA [3]. By combining different FC measures a better model for the prediction of PMA was obtained. Further, these results are comparable with the ones obtained by [7], whose slightly lower MSE can be explained by the usage of a smaller cohort of babies and a more complex regression model. Besides the methodological aspects, interesting neurophysiological aspects emerge. The coherence decreases with the postnatal maturation, as shown by Table 1 and Figure 1. Meijer [6] highlighted that this reduction is on one hand a consequence of the EEG waves evolution (reduction of bursts, that are also called δ bursts or brushes), on the other hand of the development of more localized and decentral connections for specific tasks. In the early development, the infant brain is moving from thalamocortical connections to cortico-cortical connections, which tend to separate the brain region from a functional point of view. This is also reflected by the relative increase of EEG power in β band, as shown in [7] and [4]. An important aspect of this study is that the decrease of coherence was accompanied by an increase of ASI, i.e. an increase of synchrony of neonates' cerebral activity [1]. It is interesting to notice that some of the best individual features to predict age are the auto-ASI, as symptom of more localized connections. For sake of completeness, the increase in auto-ASI values can be due to the reduction of the discontinuity pattern in the infant EEG with maturation. Moreover, both ASI and coherence in β bands are showing left spatial indices more correlated with PMA, probably due tot the left asymmetry shown by [1].

5 Conclusion

The study showed that FC connectivity measures can improve the PMA prediction performance compared to EEG features, like SC, by means of multivariate linear regression. In addition, FC connectivity changes with the postnatal maturation. In particular, the EEG coherence in β band and ASI show specific trends with PMA: the first one decreases and the latter one increases with increasing age. This might be a consequence of the shift from thalamocortical to cortical-cortical connections in the neonates cerebral networks.

6 Acknowledgements

This research is supported by Bijzonder Onderzoeksfonds KU Leuven (BOF): The effect of perinatal stress on the later outcome in preterm babies (# C24/15/036); iMinds Medical Information Technologies (SBO- 2016); Belgian Federal Science Policy Office, IUAP # P7/19/ (DYSCO, 'Dynamical systems, control and optimization', 2012-2017); Belgian Foreign Affairs-Development Cooperation (VLIR UOS programs (2013-2019)); ERC Advanced Grant: BIOTENSORS (n° 339804). A.C. is a post-doc fellow of Fonds voor Wetenschappelijk Onderzoek-Vlaanderen (FWO), supported by Flemish government.

References

[1] N. Koolen, A. Dereymaeker, O. Räsänen, K. Jansen, J. Vervisch, V. Matic, G. Naulaers, M. De Vos, S. Van Huffel, and S. Vanhatalo. Early development of synchrony in cortical activations in the human. *Neuroscience*, 322:298–307, 2016.

[2] K Franke, E Luders, A May, M Wilke, and C Gaser. Brain maturation: predicting individual BrainAGE in children and adolescents using structural MRI. *Neuroimage*, 63(3):1305–1312, 2012.

[3] N. Koolen, A. Dereymaeker, K. Jansen, J. Vervisch, V. Matic, M. De Vos, G. Naulaers, and S. Van Huffel. The suppression curve as a new representation of the premature EEG maturation. *BMC Neuroscience*, 16(Suppl 1):P216, 2015.

[4] J. J. González, S. Mañas, L. De Vera, L. D. Méndez, S. López, J. M. Garrido, and E. Pereda. Assessment of electroencephalographic functional connectivity in term and preterm neonates. *Clinical Neurophysiology*, 122(4):696–702, 2011.

[5] L. Tarokh, M. A. Carskadon, and P. Achermann. Developmental changes in brain connectivity assessed using the sleep EEG. *Neuroscience*, 171(2):622–634, 2010.

[6] E.J. Meijer, K. H. M. Hermans, A. Zwanenburg, W. Jennekens, H. J. Niemarkt, P. J. M. Cluitmans, C. Van Pul, P. F. F. Wijn, and P. Andriessen. Functional connectivity in preterm infants derived from EEG coherence analysis. *European journal of paediatric neurology*, 18(6):780–9, 2014.

[7] J. M. O'Toole, G. B. Boylan, S. Vanhatalo, and N. J. Stevenson. Estimating functional brain maturity in very and extremely preterm neonates using automated analysis of the electroencephalogram. *Clinical Neurophysiology*, 2016.

[8] O. Räsänen, M. Metsäranta, and S. Vanhatalo. Development of a novel robust measure for interhemispheric synchrony in the neonatal EEG: Activation Synchrony Index (ASI). *NeuroImage*, 69:256–266, 2013.

Address for correspondence:

Mario Lavanga
Department of Electrical Engineering (ESAT), STADIUS Center for Dynamical Systems, Signal Processing and Data Analytics, KU Leuven, Belgium
mlavanga@esat.kuleuven.be

Quantification of the central-autonomic-network applying normalized short-time partial directed coherence approach

Steffen Schulz[1], Mathias Bolz[2], Karl-Jürgen Bär[3], Andreas Voss[1],

1Institute of Innovative Health Technologies IGHT, Ernst-Abbe-Hochschule Jena, Germany;
2Department of Child and Adolescent Psychiatry, University Hospital Jena, Germany;
3Department of Psychiatry and Psychotherapy, Pain and Autonomics-Integrative Research, University Hospital Jena, Germany;

Abstract

The central control of autonomic nervous system (ANS) and the complex interplay of its components can be described by a functional integrated mode - the central-autonomic-network (CAN). CAN represents the integrated function and interaction between, the central nervous system (CNS) and ANS (parasympathetic and sympathetic activity). This study investigates the CAN analyzing heart rate (HR), blood pressure and frontal EEG in 17 healthy subjects (CON). The objective of this study is to determine how these couplings (central-autonomic) are composed by the different regulatory aspects of the CNS-ANS. We found that CAN were of bidirectional character, and that the causal influences of central activity towards HR was stronger than those towards systolic blood pressure (SYS). This suggests that the central-cardiac regulation process (closed-loop) in CON is mainly focusing on changing/ adapting the heart rate via the sinoatrial node than focusing on SYS. The CNS-ANS coupling directions with respect to central spectral power bands were mostly characterized as bidirectional where HR and SYS acting as the driver in nearly each frequency band (unidirectional for α, α1 and α2). This study provides a more in-depth understanding of the interplay of neuronal and autonomic regulatory processes in CON and a most likely greater insight into the complex CAN.

Keywords *autonomous nervous system, causal coupling analysis, central-autonomic-network, partial directed coherence*

1 Introduction

The neurovisceral integration model suggests that neural networks implicated in emotional and cognitive self-regulation are involved in the control of cardiac autonomic activity. Frontal, cingulate and subcortical brain regions have been hypothesized to play a critical role in such self-regulatory functions through top-down control from the frontal cortex over subcortical regions involved in reward and emotion, such as the amygdala [1]. A recent meta-analysis [2] revealed that resting heart rate variability (HRV) is tied to the functioning of frontal-subcortical circuits. Higher resting HRV is associated with the effective functioning of frontal-top-down control over subcortical brain regions that support flexible and adaptive responses to environmental demands [3]. Cardiovascular adjustments due to a shift in central autonomic control and remodeling of the heart are most prominent features of exercising [4]. It has been suggested that a reduced sympathetic modulation and an increased parasympathetic dominance may be caused by adaptations of peripheral and central regulatory systems [5]. Cardiovascular centers in the brainstem work through various cardiovascular reflex mechanisms such as the baroreflex, the chemoreflex and the cardiopulmonary reflex [6]. It has been assumed that various autonomic function processes are generated by a network of interaction showing specificity for task and autonomic division. For healthy ones, Beissner et al. suggested that asymmetric frontal EEG responses to emotional arousal in the form of positive and negative emotions may elicit different patterns of cardiovascular reactivity [7].

The aim of this study was to investigate the central-autonomic-network (CAN) by determining the causal coupling (strength and direction) in healthy subjects applying the normalized short-time partial directed coherence (NSTPDC). Investigating healthy subjects, we determine whether significantly different correlations existed between changes in EEG activity at the frontal lobe and changes in heart rate, as well as in systolic blood pressure.

2 Methods

2.1 Subjects

In this study, 17 healthy subjects (CON; 4 females, mean age 37.7±13.1 years) were enrolled. Interviews and clinical investigations were performed for CON to exclude any potential psychiatric or other diseases, as well as to double-check for any interfering medication. The structured clinical interview and a personality inventory (Freiburger Persönlichkeitsinventar) were also applied to the subjects to detect personality traits and any disorders which might influence autonomic function. All participants provided their written informed consent to a protocol approved by the local ethics committee of the Jena University Hospital. This study complies with the Declaration of Helsinki.

2.2 Data recordings and pre-processing

From all healthy subjects, a 3-channel short-term ECG (500 Hz), a non-invasive continuous blood pressure (200 Hz) and a 64-channel EEG were recorded synchronously for 15 minutes. The EEG was acquired using 64 active Ag/AgCl electrodes, and transmitted via a BrainAmp Amplifier (Brain Products, Germany, sampling rate 500 Hz, AFZ: ground, FCZ: reference). The electrodes were positioned according to the extended 10-20-system using an electrode cap. The impedance levels (<25 KΩ) for all electrodes were checked following attachment of the electrode cap to each participant's scalp. The arterial blood pressure was recorded using the volume-clamp photoplethysmographical blood pressure device Portapres Model-2 (TNO Biomedical Instrumentation, Netherlands). All subjects' recordings were started after a supine resting period of 10 minutes. Subjects were asked to close their eyes, relax and breathe normally to avoid hyperventilation.

The following time series with respect to autonomous regulation were automatically extracted from the raw data records:

- Heart rate (lead I) consisting of successive beat-to-beat intervals (BBI, [ms]),
- Maximum successive systolic blood pressure amplitude values in relation to the previous R-peak (SYS, [mmHg]),
- Mean power P_{EEG} from the EEG (in relation to each RR-interval).

EEG recordings (without any stimulation) were band-pass filtered (0.05Hz-60 Hz, Butterworth filter, order=3) in order to remove slow drifts resulting from slow body movements or sweating, and to prevent higher frequency content from additional noise.

For EEG analyses, artefact-free time series from the frontal area (the frontal area (Fp1, Fp2, AF3, AF4, AF7, AF8, Fz, F1, F2, F3, F4, F5, F6, F7, F8, FC1, FC2, FC3, FC4, FC5, FC6, FT7, FT8, FT9, FT10) were used. Based on the P_{EEG}, new time series consisting of the EEG spectral band components as delta (0.5-3.5 Hz), theta (3.5-7.5 Hz), alpha (7.5-12.5 Hz), alpha1 (7.5-9.5 Hz), alpha2 (9.5-12.5 Hz), beta (12.5-25 Hz), beta1 (12.5-17.5 Hz), beta2 (17.5-25 Hz) and gamma (>25-60 Hz) activity were derived (Butterworth filter, order=3). The resulting filtered time series (P_{EEG}, $P_{EEG\delta}$, $P_{EEG\theta}$, $P_{EEG\alpha}$, $P_{EEG\alpha1}$, $P_{EEG\alpha2}$, $P_{EEG\beta}$, $P_{EEG\beta1}$, $P_{EEG\beta2}$ and $P_{EEG\gamma}$, [μV^2]) were used for further analyses.

All extracted time series (autonomous, central) were filtered by applying an adaptive variance estimation algorithm to remove and interpolate seldom occurring ventricular premature beats and artefacts (e.g., movement, electrode noise and extraordinary peaks) to obtain normal-to-normal beat time series (NN). To obtain synchronized time series, BBI, SYS, P_{EEG} and $P_{EEGbands}$ were resampled using a linear interpolation method (2 Hz).

2.3 Normalized short-time partial directed coherence

To quantify the central-autonomic-network related to the causal coupling between the CNS- and ANS time series, the NSTPDC approach was applied [8]. It is based on a multivariate autoregressive model with model order p to determine linear Granger causality in the frequency domain basing on the time-variant partial directed coherence approach (tvPDC). For the selection of the optimal order p of the AR(p) model the stepwise least squares algorithm and the Schwarz's Bayesian Criterion (SBC) were used. With the view to determine the coupling strength and direction between two time series, e.g. BBI and P_{EEG}, a coupling factor (CF) was proposed. CF was obtained by dividing the mean value of P_{EEG} coupled with BBI by the mean value of BBI coupled with P_{EEG}. Afterwards, the results were normalized to a specific set of values leading to the normalized factor (NF). The normalization factor NF determines the strength and the direction of all causal links between a set of multivariate time series as a function of frequency f.

The NF can take the following values:

NF = {−2, −1, 0, 1, 2}.

Strong unidirectional coupling is indicated if NF is equal −2 or 2, bidirectional coupling with the determination of the driver-responder relationship exists if NF is equal−1 or 1, and a similar influence in both directions and no coupling is present if NF is equal to 0. Here, NSTPDC indices were calculated by applying a window (the Hamming window) of lengths l, with l=80 samples and a shift of 20 samples (60 samples overlap between each window).

In addition to NF, the areas ($A_{BBI\rightarrow PEEG}$, $A_{PEEG\rightarrow BBI}$, [a.u.]) were determined for identifying the coupling strength using a trapezoidal numerical integration function to approximate the areas generated in space by CF values (one CF in each window). $A_{BBI\rightarrow PEEG}$ and $A_{PEEG\rightarrow BBI}$ take values from the range of [0,1]. $A_{PEEG\rightarrow BBI}$=1 indicates that all causal influences originating from central part are directed toward BBI, $A_{PEEG\rightarrow BBI}$=0 indicates that the central part does not influence BBI. Thereby, arrows (→) indicating the causal coupling direction from one time series to the other one, e.g., BBI←P_{EEG}, indicates the causal link from P_{EEG} to BBI. Thus, $A_{BBI\rightarrow PEEG}$ represents the causal coupling strength for the causal link from BBI to the central part (P_{EEG}) and $A_{PEEG\rightarrow BBI}$ represents the causal coupling strength for the causal link from P_{EEG} to BBI.

All results were presented as mean ± standard deviation.

3 Results

Concerning the coupling of the ANS (BBI, SYS) with CNS (P_{EEG}), we found for the entire frontal area that the coupling strength from CNS to ANS ($A_{PEEG\rightarrow BBI}$=0.23) were increased compared to the direction from ANS to CNS ($A_{BBI\rightarrow PEEG}$=0.10) (table 1, figure 1). Furthermore, the coupling strength from ANS to CNS ($A_{SYS\rightarrow PEEG}$) and

from CNS to ANS ($A_{PEEG→SYS}$) revealed a similar behavior (0.13 vs. 0.14) in both directions (table 2, figure 1). For the coupling between BBI and P_{EEG} it was shown that mean NF was −0.64 pointing to a bidirectional coupling from P_{EEG}→BBI, with the driver being P_{EEG}, and BBI the target variable. For the coupling between the systolic blood pressure (SYS) and P_{EEG} we revealed mean NF values of nearly 0, indicating an equal coupling influence in both directions.

Table 1: Results (NSTPDC) of the causal central-autonomic coupling analysis of BBI (beat-to-beat intervals) with P_{EEG} (the mean power in BBI-related EEG intervals) for healthy subjects for the frontal area.

		frontal	α	α1	α2	β
		mean ± std	mean ± std	mean ± std	mean ± std	mean ± std
BBI/P_{EEG}	NF	-0.64 ± 0.86	1.31 ± 0.65	1.28 ± 0.69	1.32 ± 0.62	0.84 ± 0.90
	$A_{BBI→PEEG}$	0.10 ± 0.05	0.25 ± 0.06	0.24 ± 0.07	0.25 ± 0.06	0.23 ± 0.07
	$A_{PEEG→BBI}$	0.23 ± 0.16	0.08 ± 0.06	0.08 ± 0.09	0.08 ± 0.07	0.12 ± 0.09
		β1	β2	δ	γ	θ
		mean ± std	mean ± std	mean ± std	mean ± std	mean ± std
	NF	1.07 ± 0.79	0.82 ± 0.97	0.26 ± 0.96	-0.34 ± 1.00	0.85 ± 0.93
	$A_{BBI→PEEG}$	0.24 ± 0.07	0.23 ± 0.07	0.18 ± 0.06	0.17 ± 0.08	0.20 ± 0.07
	$A_{PEEG→BBI}$	0.10 ± 0.08	0.12 ± 0.10	0.16 ± 0.11	0.28 ± 0.18	0.11 ± 0.09

Table 2: Results (NSTPDC) of the causal central-autonomic coupling analysis of SYS (maximum systolic blood pressure amplitude values over time) with PEEG (the mean power in BBI-related EEG intervals) for healthy subjects for the frontal area.

		frontal	α	α1	α2	β
		mean ± std	mean ± std	mean ± std	mean ± std	mean ± std
SYS/P_{EEG}	NF	0.00 ± 1.07	1.71 ± 0.49	1.66 ± 0.59	1.70 ± 0.52	1.36 ± 0.81
	$A_{SYS→PEEG}$	0.13 ± 0.07	0.32 ± 0.09	0.31 ± 0.09	0.31 ± 0.08	0.29 ± 0.09
	$A_{PEEG→SYS}$	0.14 ± 0.10	0.04 ± 0.03	0.05 ± 0.05	0.04 ± 0.04	0.07 ± 0.06
		β1	β2	δ	γ	θ
		mean ± std	mean ± std	mean ± std	mean ± std	mean ± std
	NF	1.51 ± 0.69	1.32 ± 0.87	0.84 ± 0.91	0.12 ± 1.11	1.33 ± 0.79
	$A_{SYS→PEEG}$	0.31 ± 0.09	0.29 ± 0.10	0.22 ± 0.08	0.20 ± 0.10	0.26 ± 0.09
	$A_{PEEG→SYS}$	0.06 ± 0.05	0.07 ± 0.06	0.09 ± 0.06	0.16 ± 0.10	0.06 ± 0.05

Table 3: Coupling directions (NF: normalization factor) of healthy subjects for the frontal area. (↔ indicates bidirectional coupling, → indicates unidirectional coupling, − indicates equal influence in directions or no coupling, d: denotes the driver variable, BBI: beat-to-beat intervals, SYS: maximum systolic blood pressure amplitude values over time, $P_{EEGband}$: the mean power in the BBI related EEG-spectral band intervals).

	NF	↔	d		NF	↔	d
BBI/$P_{EEGband}$	$P_{EEGδ}$	−	−	SYS/$P_{EEGband}$	$P_{EEGδ}$	↔	SYS
	$P_{EEGθ}$	↔	BBI		$P_{EEGθ}$	↔	SYS
	$P_{EEGα}$	↔	BBI		$P_{EEGα}$	→	SYS
	$P_{EEGα1}$	↔	BBI		$P_{EEGα1}$	→	SYS
	$P_{EEGα2}$	↔	BBI		$P_{EEGα2}$	→	SYS
	$P_{EEGβ}$	↔	BBI		$P_{EEGβ}$	↔	SYS
	$P_{EEGβ1}$	↔	BBI		$P_{EEGβ1}$	↔	SYS
	$P_{EEGβ2}$	↔	BBI		$P_{EEGβ2}$	↔	SYS
	$P_{EEGγ}$	−	−		$P_{EEGγ}$	−	−

Considering the spectral bands (e.g. $P_{EEGδ}$), CAN (BBI−$P_{EEGbands}$) revealed that for nearly all spectral band components with the exception of $P_{EEGδ}$ and $P_{EEGγ}$ (− equal influence) BBI was the driver (table 3, figure 2). Furthermore, we found for nearly all the spectral bands that the coupling strengths from ANS to CNS ($A_{BBI→PEEGbands}$) were increased compared to the opposite direction ($A_{PEEGbands→BBI}$) with the exception of the γ band ($A_{BBI→PEEGγ}$) where the strongest influence of central activity towards BBI was found (figure 2). The fact that BBI influences the central spectral components stronger is the opposite of that was found for the central-autonomic coupling ($A_{PEEG→BBI}$) where P_{EEG} had a stronger influence on BBI (table 1).

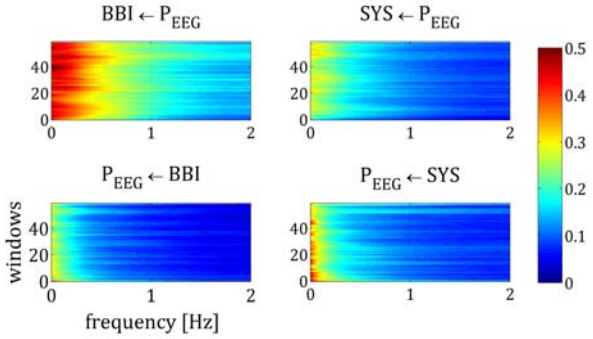

Figure 1: Averaged NSTPDC plots for the central-autonomic-network analyses for healthy subjects. Arrows indicating the causal coupling direction from one time series to the other one (e.g., BBI←P_{EEG}: causal link from P_{EEG} to BBI). Coupling strength ranges from blue (no coupling) to red (maximum coupling). With BBI - beat-to-beat intervals, SYS - successive systolic blood pressure values over time, and P_{EEG} - mean power in BBI-related EEG intervals.

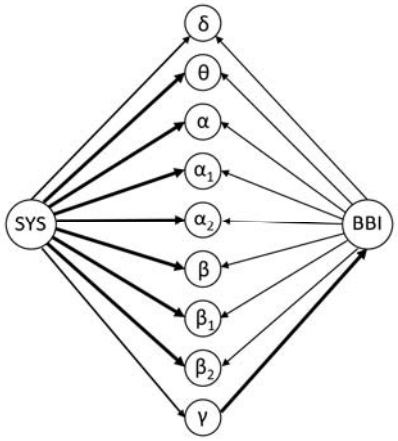

Figure 2: Visualization of coupling strength between autonomic activity (BBI, SYS) and central spectral activity ($P_{EEGband}$: δ, θ, α, α1, α2, β, β1, β2, γ) for healthy subjects. Arrows indicate the coupling direction, where black solid lines indicate the direction from driver variable towards the target variable (line width represents the coupling strength).

The results of causal coupling between SYS and PEEGbands revealed comparable results. The autonomic part (SYS) stronger influences the central spectral components (PEEGbands) as it was also shown for BBI. In detail, PEEGβ, PEEGβ1, PEEGβ2, PEEGδ and PEEGθ revealed bidirectional coupling (mean NF~1.3)

with the driver SYS. SYS was also the driver towards α central activity (PEEGα, PEEGα1, PEEGα2) but here the mean NF≥1.7 points to an unidirectional coupling. The causal connection between SYS and the γ activity (PEEGγ) indicated to an equal influence in both directions (mean NF~0.1) as already shown for BBI (table 3, figure 2).

4 Discussion and conclusions

In this very extensive study we found that the central-cardiac coupling in healthy subjects is a bidirectional one, with central driving mechanisms (P_{EEG}→BBI) towards autonomic system (BBI) in CON. This suggests that the central-cardiac regulation process (closed-loop) in CON is mainly focusing on changing/ adapting the heart rate via the sinoatrial node than focusing on SYS.

The central-vascular coupling analysis demonstrated that the coupling strength is equal in both directions (P_{EEG}↔SYS). This closed-loop in CON indicates a balanced relation ($A_{PEEG→SYS}$ corresponding to $A_{SYS→PEEG}$, NF~0) between central and vascular regulation processes. The lower influence of central activity towards the vascular system might be due to that blood pressure is mainly regulated by the ANS via the baroreflex control loop. The central-cardiac and central-vascular coupling directions with respect to central spectral power bands were mostly characterized as bidirectional with BBI and SYS acting as the driver in nearly each frequency band (unidirectional for α, α1 and α2). This may suggest that the autonomous system provides feedback information towards the different central oscillatory components (with the exception of γ and δ). All these components together might be considered as the whole central activity provide, in turn, feedforward information to the ANS. Different studies were published concerning cognitive processes of healthy subjects. These studies are related to oddball paradigms with results on target and standard stimuli, working paradigm and simple auditory and visual-evoked potentials. The enhancement of delta and theta responses, prolongation of alpha oscillations, and the appearance of a second theta response window are some of the relevant features of the target response [9]. In this study, however, we investigated for the first time the CAN under resting conditions.

The output of the CAN is directly linked to HRV. In addition, sensory information from peripheral end organs such as the heart and the immune system are feedback to the CAN, one important example of which is the baroreceptor reflex. As such, HRV is an indicator of central-peripheral neural feedback and CNS-ANS integration [10].

In this regard, it must be considered that the interactions between the CNS and ANS can be assumed to be a feedback-feedforward system which supports flexible and adaptive responses to environmental demands. This study improves the understanding of physiological processes of the central-autonomic network in healthy subjects without any stimulation.

Acknowledgements

This work was partly supported by grants from the Federal Ministry for Economic Affairs and Energy (BMWI) KF 2447308KJ4 and KF 2447309KJ4.

References

[1] T. F. Heatherton, and D. D. Wagner, "Cognitive neuroscience of self-regulation failure," *Trends Cogn Sci,* vol. 15, no. 3, pp. 132-9, Mar, 2011.

[2] J. F. Thayer, F. Ahs, M. Fredrikson, J. J. Sollers, 3rd, and T. D. Wager, "A meta-analysis of heart rate variability and neuroimaging studies: implications for heart rate variability as a marker of stress and health," *Neurosci Biobehav Rev,* vol. 36, no. 2, pp. 747-56, Feb, 2012.

[3] J. F. Thayer, and R. D. Lane, "A model of neurovisceral integration in emotion regulation and dysregulation," *J Affect Disord,* vol. 61, no. 3, pp. 201-16, Dec, 2000.

[4] P. C. Brum, G. J. Da Silva, E. D. Moreira, F. Ida, C. E. Negrao, and E. M. Krieger, "Exercise training increases baroreceptor gain sensitivity in normal and hypertensive rats," *Hypertension,* vol. 36, no. 6, pp. 1018-22, Dec, 2000.

[5] J. Sugawara, H. Murakami, S. Maeda, S. Kuno, and M. Matsuda, "Change in post-exercise vagal reactivation with exercise training and detraining in young men," *Eur J Appl Physiol,* vol. 85, no. 3-4, pp. 259-63, Aug, 2001.

[6] R. A. Dampney, "Functional organization of central pathways regulating the cardiovascular system," *Physiol Rev,* vol. 74, no. 2, pp. 323-64, Apr, 1994.

[7] S. R. Waldstein, W. J. Kop, L. A. Schmidt, A. J. Haufler, D. S. Krantz, and N. A. Fox, "Frontal electrocortical and cardiovascular reactivity during happiness and anger," *Biol Psychol,* vol. 55, no. 1, pp. 3-23, Nov, 2000.

[8] S. Schulz, K. J. Bär, and A. Voss, "Analyses of Heart Rate, Respiration and Cardiorespiratory Coupling in Patients with Schizophrenia," *Entropy,* vol. 17, no. 2, pp. 483-501, 2015.

[9] E. Basar, and B. Guntekin, "A review of brain oscillations in cognitive disorders and the role of neurotransmitters," *Brain Res,* vol. 1235, pp. 172-93, Oct 15, 2008.

[10] J. F. Thayer, "What the Heart Says to the Brain (and vice versa) and Why We Should Listen," *Psychological Topics,* vol. 16, no. 2, pp. 241-250, 2007.

Address for correspondence:

Prof. Dr. Andreas Voss
Ernst-Abbe-Hochschule Jena, Institute of Innovative Health Technologies IGHT, Carl-Zeiss-Promenade 2; 07745 Jena, Germany
E-mail: andreas.voss@eah-jena.de

Transfer Entropy Analysis of Linear Model Residuals

F El-Hamad[1], M Baumert[1]

[1]School of Electrical and Electronic Engineering, University of Adelaide, Australia.

Abstract

Several cardiovascular mechanisms exhibit both linear and nonlinear interactions. A linear approximation of these interactions cannot capture the nonlinear dynamics rendering results incomplete, while nonlinear methods generally do not distinguish between linear and nonlinear relationships. In this study, we investigated whether nonlinear analysis (transfer entropy analysis) of a linear model's residuals can provide this distinction. The linear dynamics in the data were captured using a linear autoregressive model. Transfer entropy analysis was applied to the model residuals to investigate whether they hold information regarding nonlinear dynamics. This procedure was tested on simulated data and then applied to real data to study the relationship between muscle sympathetic nerve activity (MSNA) and repolarization variability (QT). Results from simulated data show that the procedure was able to separate linear and nonlinear dynamics. While analysis of real data showed that a linear model was adequate for quantifying QT-MSNA relationship since no information transfer was detected in the residuals.

Keywords *linear, nonlinear, cardiovascular, transfer entropy.*

1 Introduction

The cardiovascular system exhibits complex interactions between cardiac, vascular and neural mechanisms, which can be represented by a class of linear parametric multivariate models [1]. The residuals of these models are usually attributed to noise, nonlinearities or other mechanisms unaccounted for by the model [2, 3]. While the linear approximation of these mechanisms is widely accepted and used by many researchers in the field, this notion has not been investigated thoroughly against the null hypothesis of a nonlinear relationship [1]. This might render results related to the variability unexplained by the model inconclusive. Indeed, employing linear models in the presence of both linear and nonlinear system characteristics means that any nonlinear interactions are overlooked and remain confined in the model residuals [4]. Nonlinear methods have also been employed for the analysis of cardiovascular variability [1, 5-7]. However these methods generally cannot separate linear and nonlinear interactions. It has been suggested that analysis of a linear model's residuals might be fruitful for exploring nonlinear aspects of the system under investigation [4]. We hypothesize that, using a nonlinear method, the analysis of a linear model's residuals can separate nonlinear from linear interactions in systems where both type of interactions are present. In this paper, the proposed analysis was restricted to an open-loop autoregressive model with two external drivers (ARXX). Analysis was carried out on both, simulated and real data comprising beat-to-beat values of heart period (RR), muscle sympathetic nerve activity (MSNA) and ventricular repolarization duration of the heart (QT). Changes in beat-to-beat QT have been suggested to reflect changes in the level of sympathetic outflow to the heart [8, 9]. MSNA is an invasive measure of postganglionic sympathetic nerve activity measured in the peroneal nerve [10]. To investigate the extent to which repolarization variability can be used as a noninvasive measure of sympathetic activity, we studied the relationship between beat-to-beat changes in QT and MSNA. Sympathetic activity and RR are thought to exhibit influences on QT in a feed forward fashion, hence an open-loop ARXX model was selected for this specific study.

2 Materials and Methods

To test our hypothesis, a linear autoregressive model with two external inputs (ARXX) [11] combined with standard system identification procedures was employed to quantify linear relationships within bivariate data. Subsequently, information domain analysis based on transfer entropy [5] was used to investigate the presence of any remaining, nonlinear relationships in the model residuals.

Linear model residuals

A parametric linear autoregressive model with two external inputs defined as

$$A_Y(z)\,Y(n) = B_1(z)\,X(n) + B_2(z)\,Z(n) + w_Y(n), \quad (1)$$

was used to represent the data. In Eq. 1, Y is the target variable, and X and Z are external input variables which are not modulated by Y. Also, A_Y, B_1, and B_2 are polynomials of the model parameters in the z-domain, w_Y is a white Gaussian noise source, and n is the sample number. X and Z were modeled as independent autoregressive processes. Details of the model structure are described in [11], while details of the adopted model

estimation and validation procedures are described in [2]. After model estimation and validation, the estimated model parameters were used to filter out the variance of the target variable Y which is not explained by the model; i.e. model residuals [3].

Nonlinear analysis of the residuals

To test whether the residuals hold any information regarding nonlinear dynamics from the inputs to the output, a binning estimator with non-uniform embedding was used to estimate the information transfer from X to the residuals of Y ($TE_{X->Y}$) in the case of simulated data, and the conditional information transfer from Z to the residuals of Y given X ($TE_{Z->Y|X}$) for both simulated and real data [5]. The same analysis was carried out on the original data to compare the detection of information transfer with and without the linear component.

Simulated data

In order to test the ability of the proposed procedure to distinguish linear from nonlinear interactions, we used simulated data generated from a non-linear autoregressive model with two external inputs defined as in Eq. 2-4. The simulation model was adapted from [12].

$$Y(n) = 0.707\,Y(n-1) - 0.5\,X^2(n-2) + 0.3536\,Z(n-1) + w_Y(n), \quad (2)$$

$$X(n) = 0.3536\,X(n-1) - 0.2025\,X(n-2) + w_X(n), \quad (3)$$

$$Z(n) = 0.707\,Z(n-1) - 0.707\,Z(n-2) + w_Z(n). \quad (4)$$

Eq. 2 shows that Y is a combination of a linear function of its own past and Z, and a nonlinear function of X. On the other hand, X and Z are represented by two independent linear autoregressive models. Also, $w_Y, w_X, and\ w_Z$ are uncorrelated Gaussian white noises with zero mean and unit variance.

Real data

We studied 10 healthy subjects selected from a previously published study [13]. Continuous signals of lead III ECG, arterial blood pressure and muscle sympathetic nerve activity (MSNA) were recorded simultaneously for 10 minutes in supine and 40 degrees tilt in each subject with a sampling frequency of 1600 Hz. Beat-to-beat series of the heart period (RR) and repolarization duration series, measured as the temporal distance between the onset of the Q-wave and the end of the T-wave (QT) were obtained using an algorithm recently proposed in [14]. MSNA was used as a surrogate for sympathetic activity. Beat-to-beat MSNA series were obtained by calculating the time average of the integrated MSNA signal between two consecutive diastolic points to compute the average MSNA per beat. For each subject, data segments of around 200 beats were selected for the analysis. Data were detrended using the smoothness priors method described in [15], then normalized to zero mean and unit standard deviation.

Statistics

Paired t-test was used to test whether the estimated transfer entropies computed from simulated data were different to those computed from their residuals. Wilcoxon sign rank test was used to test for differences in the transfer entropy estimated in supine and tilt conditions, using both real data and its residuals. Values of $p < 0.05$ were considered statistically significant.

3 Results

Simulated data

The linear model fit to the simulated data was 58% ± 4.0% (mean ± SD). Table 1 shows that the estimates of the parameters related to the linear components (A_Y and B_2) were acceptably close to their simulated values, while the parameter related to the nonlinear component (B_1) were poorly estimated.

Parameter	Simulated	Estimated (mean)
$A_Y(z)$	$0.707z^{-1}$	$0.719\ z^{-1}$
$B_1(z)$	$-0.5z^{-2}$	$-0.015\ z^{-2}$
$B_2(z)$	$0.3536z^{-1}$	$0.285\ z^{-1}$

Table 1: ARXX model simualted and estimated parameters.

Fig. 1 shows the results of the transfer entropy estimated using both; simulated data and the residuals resulting from fitting the simulate data to the linear ARXX model. $TE_{Z->Y|X}$ was significantly reduced in the residuals compared to the data ($p < 0.0001$), while the estimated $TE_{X->Y}$ remained unchanged ($p > 0.3$).

Cardiovascular data

The linear model fit to the cardiovascular data was on average 51% in supine and 41% following tilt. Fig. 2 shows the transfer entropy from MSNA to QT given RR ($TE_{MSNA->QT|RR}$) estimated using both; real data and the residuals resulting from fitting the real data to the linear ARXX model. $TE_{MSNA->QT|RR}$ demostrated a slight insignificant increase using real data ($p > 0.5$), while the information transfer was negligible (median = 0.027) in the residuals in the supine position, and not detected (median = 0) following tilt. $TE_{MSNA->QT|RR}$ computed from the residuals was decreased compared to real data in both supine and tilt. However this decrease was not statisticall significant ($p > 0.1$ for both supine and tilt conditions).

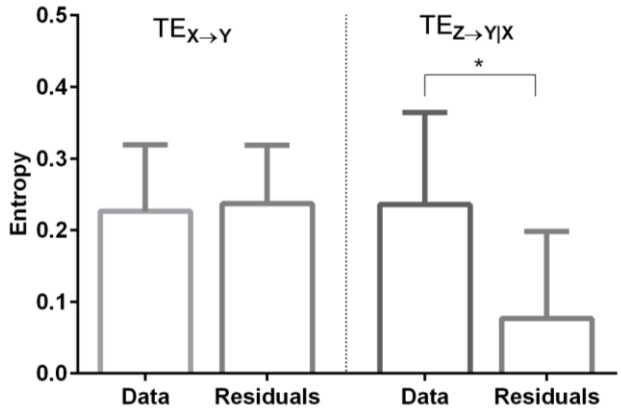

Figure 1: Information transfer from the inputs to Y estimated from simulated data and residuals. (A) information trasfer from X to Y ($TE_{X->Y}$), and (B) conditional information transfer from Z to Y given X ($TE_{Z->Y|X}$). Values shown are mean ± std. * indicates a signifcant difference.

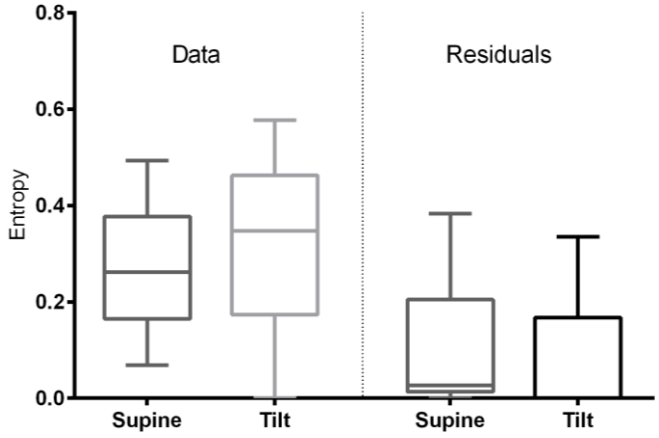

Figure 2: Conditional information transfer from MSNA to QT give RR ($TE_{MSNA->QT|RR}$) estimated from real data and residuals. Values shown are median (25th – 75th percentiles).

4 Conclusions

The cardiovascular system consists of complex interactions between different subsystems involving both linear and nonlinear dynamics. Linear estimations of these interactions render result inconclusive as nonlinearities are confined in the residuals [4], while nonlinear estimations do not distinguish linear from nonlinear dynamics.

Simulated data

In this paper we used simulated data to demonstrate that analysis of a linear model's residuals can distinguish linear from nonlinear dynamics driving the system. The simulated model involves both linear and nonlinear dynamics. The good model fit and the estimation of the linear parameters show that the linear model was able to capture the linear dynamics adequately rendering the model residuals a reliable estimation of the true variance which cannot be explained by a linear model. Then, the transfer entropy was computed using both simulated data and residuals. $TE_{X->Y}$ was detected in both data and residuals, while $TE_{Z->Y|X}$ was only detected in the data. This shows that the procedure was able to separate and identify both; the linear component from Z to Y was filtered and captured by linear model, while the nonlinear component from X to Y remained in the residuals and was clearly identifiable using the transfer entropy method.

Real data

The proposed procedure was applied to real data consisting of QT, RR and MSNA. In a previous study [2], we used the same linear model to study the relationship between MSNA and QT variability in an attempt to investigate the extent to which QT variability can be used as a measure of sympathetic activity. Power contribution analysis showed that MSNA contribution to QT was small but not negligible. We concluded that MSNA might not exhibit influences on QT variability, or that these influences might be complex and not quantifiable using a linear model. To test whether MSNA exhibits nonlinear influences which might have been confined in the model residuals, we computed $TE_{MSNA->QT|RR}$ from both real data and the residual s (Fig. 2). $TE_{MSNA->QT|RR}$ was detected in the data but not the residuals, which supports the notion that MSNA does not exhibit nonlinear influences on QT variability at moderate levels of sympathetic activation. Furthermore, the reduction in the transfer entropies estimated from the residuals compared to real data, despite being statistically insignificant, support the notion that the model in our previous study has captured the MSNA-QT dynamics adequately.

In conclusion, we have displayed how analysis of a linear model's residuals (using an ARXX model as an example) can distinguish linear from nonlinear dynamics. However, the clinical merit of this separation is yet to be established with further testing on larger datasets investigating cardiovascular mechanisms which are known to exhibit nonlinear dynamics; such as baroreflex [16, 17], and cardiac repolarization lability [18-20].

Acknowledgements

We would like to acknowledge Luca Faes for providing the toolbox for the information transfer estimation.

References

[1] J. Batzel, G. Baselli, et al. Modelling and disentangling physiological mechanisms: linear and nonlinear identification techniques for analysis of cardiovascular regulation. *Philosophical Transactions*

of the Royal Society A: Mathematical, Physical and Engineering Sciences, 367: 1377-1391, 2009.
[2] F. El-Hamad, E. Lambert, et al. Relation between QT interval variability and muscle sympathetic nerve activity in normal subjects. *Am J Physiol Heart Circ Physiol*, 309: H1218-1224, 2015.
[3] A. Porta, E. Tobaldini, et al. RT variability unrelated to heart period and respiration progressively increases during graded head-up tilt. *American Journal of Physiology- Heart Circulation Physiology*, 298: 1406–1414, 2010.
[4] A. Porta, G. Baselli, et al. Implicit and explicit model-based signal processing for the analysis of short-term cardiovascular interactions. *Proceedings of the IEEE*, 94: 805-818, 2006.
[5] L. Faes, G. Nollo, et al. Non-uniform multivariate embedding to assess the information transfer in cardiovascular and cardiorespiratory variability series. *Computers in biology and medicine*, 42: 290-297, 2012.
[6] M. Baumert, M. Javorka, et al. Joint symbolic dynamics for the assessment of cardiovascular and cardiorespiratory interactions. *Philosophical Transactions of the Royal Society of London A: Mathematical, Physical and Engineering Sciences*, 373, 2015.
[7] A. Porta, M. Baumert, et al. Enhancing dynamical signatures of complex systems through symbolic computation. *Philosophical Transactions of the Royal Society of London A: Mathematical, Physical and Engineering Sciences*, 373, 2015.
[8] M. Baumert, A. Porta, et al. QT interval variability in body surface ECG: measurement, physiological basis, and clinical value: position statement and consensus guidance endorsed by the European Heart Rhythm Association jointly with the ESC Working Group on Cardiac Cellular Electrophysiology. *Europace*, 18: 925-944, 2016.
[9] M. Baumert, M. P. Schlaich, et al. Relation between QT interval variability and cardiac sympathetic activity in hypertension. *American Journal of Physiology—Heart and Circulatory Physiology*, 300: 1412–1417, 2011.
[10] B. A. Kingwell, J. M. Thompson, et al. Heart rate spectral analysis, cardiac norepinephrine spillover, and muscle sympathetic nerve activity during human sympathetic nervous activation and failure. *Circulation*, 90: 234–240, 1994.
[11] G. Baselli, A. Porta, et al. Spectral decomposition in multichannel recordings based on multivariate parametric identification. *IEEE Transactions on Biomedical Engineering*, 44: 1092–1101, 1997.
[12] A. Montalto, L. Faes, et al. MuTE: a MATLAB toolbox to compare established and novel estimators of the multivariate transfer entropy. 2014.
[13] E. Lambert, N. Eikelis, et al. Altered sympathetic nervous reactivity and norepinephrine transporter expression in patients with postural tachycardia syndrome. *Circulation Arrhythmia and Electrophysiology*, 1: 103–109, 2008.
[14] M. Schmidt, M. Baumert, et al. Two-Dimensional Warping for One-Dimensional Signals: Conceptual Framework and Application to ECG Processing. *IEEE Transactions on Signal Processing*, 62: 5577-5588, 2014.
[15] M. P. Tarvainen, P. O. Ranta-aho, et al. An advanced detrending method with application to HRV analysis. *IEEE Transactions on Biomedical Engineering*, 49: 172–175, 2002.
[16] N. Wessel, A. Voss, et al. Nonlinear analysis of complex phenomena in cardiological data. *Herzschrittmachertherapie und Elektrophysiologie*, 11: 159-173, 2000.
[17] M. Riedl, A. Suhrbier, et al. Modeling the cardiovascular system using a nonlinear additive autoregressive model with exogenous input. *Physical Review E*, 78: 011919, 2008.
[18] M. Baumert, B. Czippelova, et al. Decoupling of QT interval variability from heart rate variability with ageing. *Physiological Measurement*, 34: 1435, 2013.
[19] M. Baumert, B. Czippelova, et al. Entropy Analysis of RR and QT Interval Variability during Orthostatic and Mental Stress in Healthy Subjects. *Entropy*, 16: 6384, 2014.
[20] M. Baumert**.** Measurement of T wave variability in body surface ECG. *Journal of Electrocardiology*, 2016.

Connectivity of Epileptiform Discharges during Epileptic Seizure in Temporal Lobe

H. Yoshida[1], Y Yoshioka[2], M. Miyauchi[3], N. Nakano[3], A. Kato[3]

[1]Department of Computational Systems Biology, Kindai University, Japan;
[2]LSI Development Headquarters, ROHM semiconductor, Japan;
[3]Department of Neurosurgery, Kindai University, Japan;

Abstract

Surgery is an effective treatment for intractable epilepsy where the seizure cannot be controlled by medication. Intractable epilepsy is generally treated by removing epileptic foci and propagation paths. It is, therefore, important to determine epileptic foci and propagation paths in surgery. Surgical site is determined by visual inspection using magnetoencephalogram(MEG), MRI, electroencephalogram(EEG) and, electrocorticogram(ECoG). However, diagnosis by visual inspection of a doctor is fraught with problems which depends on the experience. We aim for establishment of diagnostic indicator which can show quantitative and objective evidence. In this paper, we propose a new connectivity analysis. In the connectivity analysis, we calculate the maximum correlation value and the delay time for each channel-to-channel using correlation function from ECoG which is recorded at preoperative evaluation. Next, we define connectivity strength using linear combination of the maximum correlation value and its delay time between channels of ECoG. Finally, the propagation structure[1] of patients with intractable epilepsy is estimated by using minimum spanning tree whose edge length is connectivity strength. We estimated the propagation structure of epileptiform discharges from two ECoG who patients of intractable epilepsy using connectivity analysis. As a result, each patient's epileptiform discharges propagated from the temporal lobe where epileptic foci were located to the frontal lobe. We compared the estimated results and results of MEG that showed commonresults. Therefore, the connectivity analysis we proposed here is considered an effective analysis. We believe that the connectivity analysis can become an effective diagnostic indicator of quantitative and objective evidence not use MEG of large system.

Keywords *Biosignal and Image Interpretations, Conference Paper, Instructions*

[1]In this paper, we discriminate the term "propagation paths" and "propagation structure." The "propagation paths" means "propagation structure" with direction of information flow.

1 Introduction

Epilepsy is a common cranial nerve disease that affects up to 1% of the population. Seizure is caused by epileptiform discharges propagating throughout the brain leading to loss of normal brain function. Epileptic seizures have a lot of symptoms as they propagate throughout the brain. About 75% of these patients can control seizures by medication, but 25% of them cannot be cured by medication, which is known as intractable epilepsy[1]. Intractable epilepsy can be treated by surgery[2]. Patients are cured by removing epileptic foci and propagation structure. In order to further improve the surgical outcome and avoid any neurological deficits from the removal of the lesion, the precise origin of the seizure activity must be accurately localized[3]. Epileptic foci and propagation paths are diagnosed by visual inspection of doctor using ECoG, which is recorded for inspection before operation[4], MRI and, MEG. Visual inspection depends on the experience of the doctor to diagnose epileptic foci and propagation path of epileptiform discharges from ECoG, less experienced doctors cannot accurately diagnose the surgical site.

Connectivity analsysis has been a wide area in the brain research these days. In particular, functional brain network analysis of fMRI data is conducted by many researchers. However, there are few research on connectivity analysis of patients with epilepsy. Mizuno, et.al. proposed a method estimating epileptic foci and connectivity of epileptiform discharges, which was observed from ECoG, using cross correlation map[5]. The method, however, indicates only a cross-correlation map of the channels in order to express the connectivities between the channls. After estimating the quantitative propagation structure of epileptiform discharges using cross-correlation function, visualization using a graph theory has not been reported.

In this paper, we developed a new method of estimation and visualization of epileptic foci and propagation structure of epileptiform discharges. We used cross-correlation function and the minimum spanning tree of graph theory. We estimated propagation structure of epileptiform discharges from ECoG which were two patients ' data at seizure onset using connectivity analysis. We consider the effectiveness of our method by comparing two estimated results and the results of MEG.

2 Methods

2.1 Data acquisition

We used the ECoG which was recorded on subdural for inspection before operation[2]. Placement of intracranial Electrodes of patient A are shown in Fig.1. Channel zero to channel 15 were located at the left frontal lobe, channel 16 to channel 23, channel 40 to channel 44 were located at the interior left temporal lobe and, channel 24 to channel 39 were located at the left temporal lobe. Placement of intracranial electrodes of patient B are shown in Fig.2. Channel zero to channel seven were located at the right temporal lobe, channel eight to channel 15 were located at the interior right frontal lobe and, channel 16 to channel 23 were located at the right interior temporal lobe.The ECoG of patient A and patient B were shown in Fig.3 and Fig.4, respectively. The ECoG shown in green is the frontal lobe, blue is the interior temporal lobe and, red is the temporal lobe. Both patients lost their normal brain function after the propagation of epileptiform discharges throughout the brain which was at around 35 seconds in patient A and around 25 seconds in patient B. After that, the amplitude of epileptiform discharges decreased. Epileptiform discharges of patient A terminated around 140 seconds. Epileptiform discharges of patient B terminated around 130 seconds. After the termination of epileptiform discharges, flat ECoG are observed for a while.

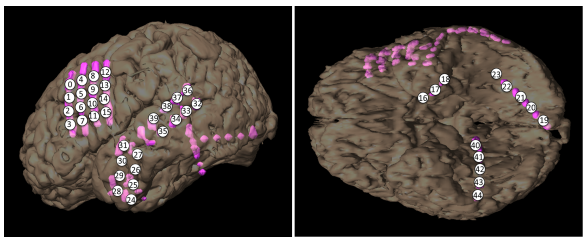

Figure 1: Electrode layout of patient A

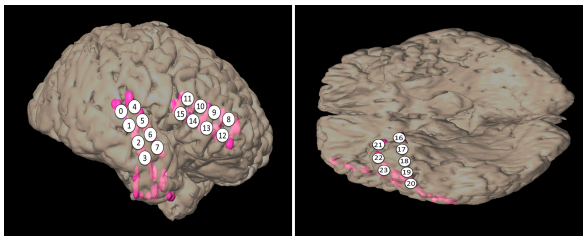

Figure 2: Electrode layout of patient B

[2]This study has been reviewed/approbed by Ethics Review Committe of Kindai University, Faculty of Medicine(21-135) and Faculty of Biology-Oriented Science and Techonology(H26-1-008).

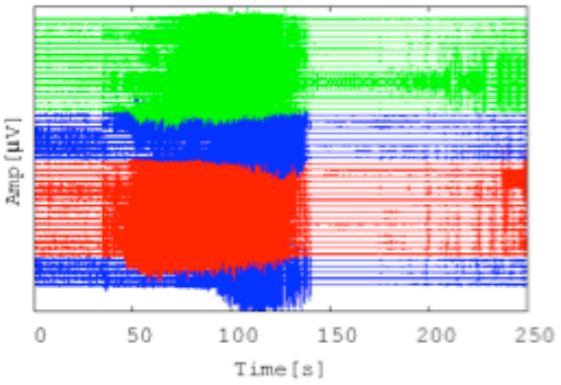

Figure 3: Electrocorticography: patient A

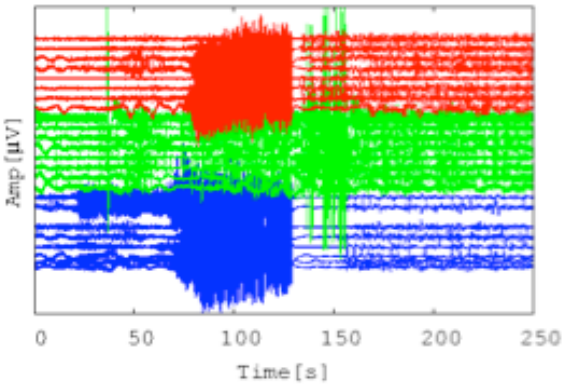

Figure 4: Electrocorticography: patient B

2.2 Connectivity analysis

First, we calculated cross-correlation function from ECoG every channel-to-channel as follows:

$$\rho_{ij}(\tau) = \frac{E[(x_i(t) - \mu_i)(x_j(t-\tau) - \mu_j)]}{\sqrt{E[(x_i(t) - \mu_i)^2]E[(x_j(t-\tau) - \mu_j)^2]}}, \tag{1}$$

where x_i and x_j are ECoG of channel i and j, and μ_i and μ_j are averages of x_i and x_j, respectively. $E[\cdot]$ shows expected value and τ is the delay time. In this report, the range of τ was from -0.1 seconds to 0.1 seconds. Time averaging window for calculating correlation function was set to 1 second. Next, we searched the maximum correlation value $\max_\tau\{|\rho_{ij}|\}$ and the delay time from cross-correlation function ρ_{ij}. Here, in order to eliminate the influence of small value of the maximum correlation $\max_\tau\{|\rho_{ij}|\}$ which is to be statistically uncorrelated, namely null hypothesis fails to reject with 99.9% confidence interval using the z-test, was assinged as 0. In the case of the maximum correlation value was 0, a delay time τ was set to 0.1 second, which is the longest delay time in this study. The correlation maps between channel to channel is shown in Fig.5. Then we defined connectiv-

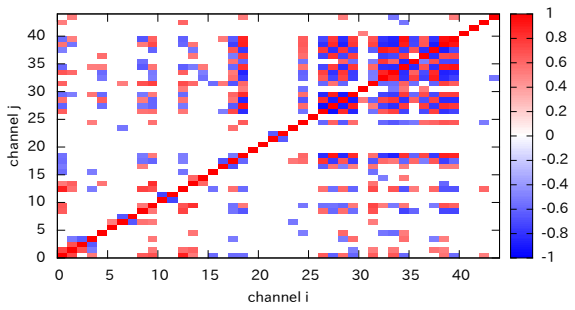

Figure 5: Correlation map

ity strength as follows:

$$d_{ij} = \alpha(1 - \max_{\tau}\{|\rho_{ij}(\tau_{ij})|\}) + (1-\alpha)\frac{|\tau_{ij}|}{\max_{ij}\{\tau_{ij}\}}, \quad (2)$$

where $\max\{\rho_{ij}(\tau)\}$ is maximum correlation values of each channel-to-channel with respect to τ_{ij}. The delay time is used which has been normalized by dividing by the longest delay time $\max_{ij}\{\tau_{ij}\}$ in this study. α is an arbitrary constant which determines the weights of both the maximum correlation term and the deley term. In this study, α is set to 0.5, which is the weight of the maximum correlation value and the delay time is equal. In order to use the connectivity strength d_{ij} as edge length in configure the minimum spanning tree, the lower values the higher connectivity strength.

Finally, we configured minimum spanning tree using connectivity strength to edges. We estimated and visualized the propagation structure of epileptiform discharges. The minimum tree is a undirected graph which does not have closed path together with the minimal total weighting for its edges. In other words, the estimated propagation structure results of epileptiform discharges formed in this report assumes there is no ECoG loop between channels.

3 Results

The estimated minimal spanning tree of seizure onset of patient A is shown in Fig.6. In the estimation results, circles indicate nodes and the number represents the channel number. The colors of the circle indicate the position of the channel. Light gray, gray and dark gray present frontal robe, interior temporal robe and exterior temporal robe, respectively. Also, the lines indicate that the stronger the connectivity thicker the line. In this study, a root node of the minimum spanning tree configured the node which has the highest connectivity strength.

In the estimated results of propagation structure which is the seizure onset of patient A, the channels located in the left temporal lobe is first connected and then they are connected to the interior left temporal lobe then the connections are made to the left frontal lobe. Fig.7 shows the estimated minimal spanning tree of seizure onset of patient B. In the result of patient B, the channels located in the right interior temporal lobe is first connected and then they are connected to the right temporal lobe then the connections are made to the right frontal lobe.

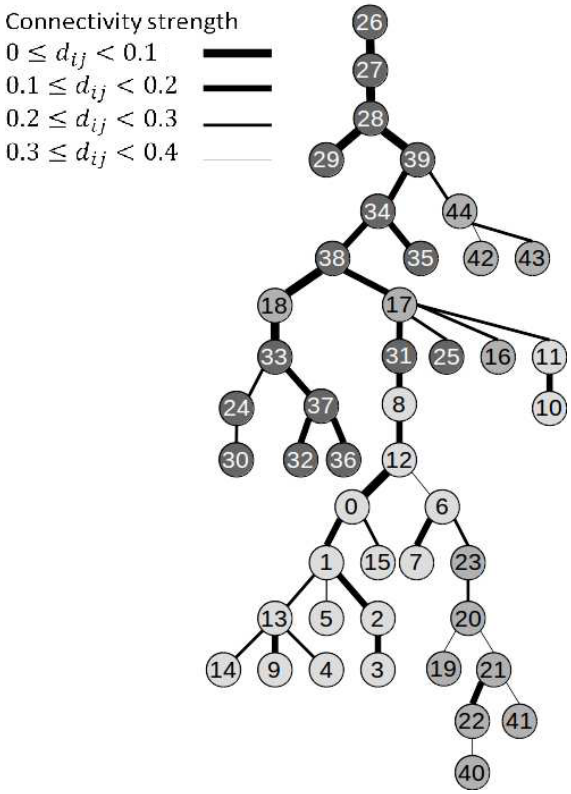

Figure 6: Estimated Spanning Tree: patient A

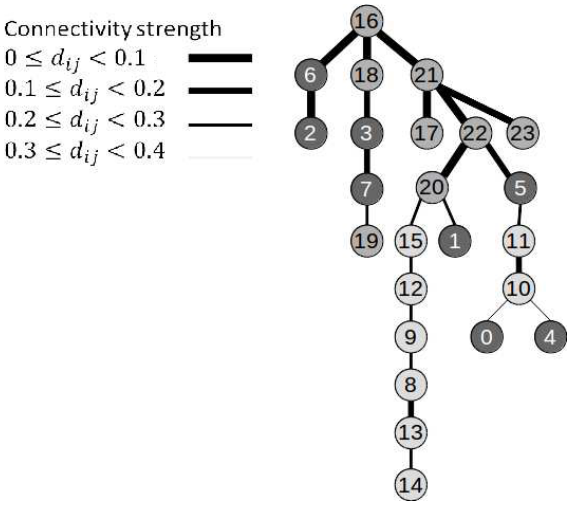

Figure 7: Estimated Spanning Tree: patient B

4 Discussion

Fig.8 shows the results of MEG of a sporadic epileptiform discharge of patient A. The results indicate the epileptiform spikes in red moving from the left temporal lobe to the interior left temporal lobe then finally to

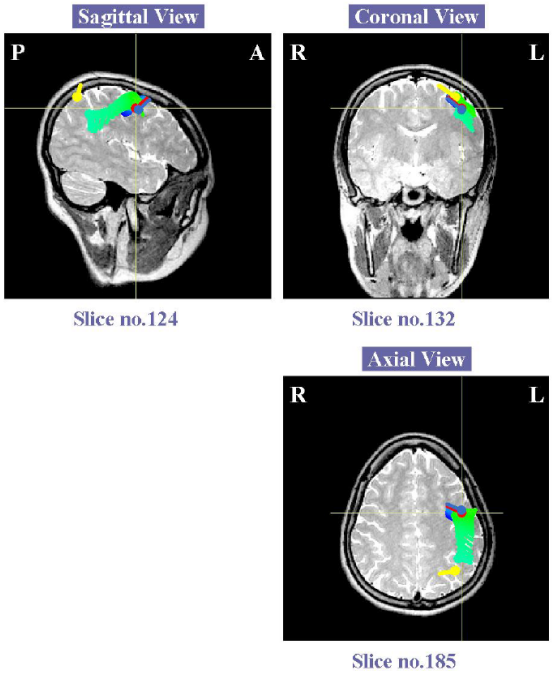

Figure 8: Result of MEG Analysis: patient A

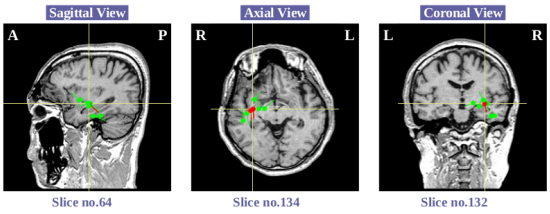

Figure 9: Result of MEG Analysis: patient B

the left frontal lobe. As we mentioned earlier, the estimated propagation structure of epileptiform discharges of patient A begin at the left temporal lobe where the epileptic foci were located. Then epileptiform discharge propagates to the interior left temporal lobe, then finally to the left frontal lobe. Both results show the same appearance of propagation structure.

The results of MEG analysis of a sporadic epileptiform discharge of patient B is shown in Fig.9. The reslts show the epileptiform spikes in red moving from the right interior temporal robe, then spread out around them. Also, the propagation structure of epileptiform discharges of patient of B propagated from the interior right temporal lobe where the epileptic foci were located to the right temporal lobe to the right frontal lobe. The results also show similar appearance of propagation structure.

Since both results indicate a similar propagation structure, that our method used in this study is considered to be effective in demonstrating the sporadic epileptiform discharges and the onset of the epileptic seizure is similar.

5 Conclusion

We developed a new analysis method of connectivity analysis using cross-correlation function and minimum spanning tree based on the graph theory. Estimated propagation structures of seizure onset obtained by proposed method were similar to the results of the MEG analysis. These results show the effectiveness of the method. The connectivity analysis using ECoG for the propagation structure of epileptiform discharges enables quantitative estimation without using a large-scale system like MEG.

Acknowledgements

This research was supported in part by Strategic Research Foundation Grant-aided Project for Private Universities (S1311045) from the Ministry of Education, Culture, Sports, Science and Technology.

References

[1] G. D. Cascino. Commentary: How has neuroimaging improved patient care? *Epilepsia*, 35:S103–S107, 1994.

[2] S. Wiebe, W. T. Blume, J. P. Girvin, and M. Eliasziw. A Randomized, Controlled Trial of Surgery for Temporal Lobe Epilepsy. *N.Engl. J. Med*, 345(5):311–318, 2001.

[3] E. Niedermeyer and F. Lopes da Silva. *Electroencephalograph*. Lippincott Williams & Wilkins, 1993.

[4] S. Jenssen, CM. Roberts, EJ. Gracely, DJ Dlugos, and MR. Sperling. Focal seizure propagation in the intracranial EEG. *Epilepy Research*, 93:25–32, 2011.

[5] Y. Mizuno-Matsumoto, K. Okazaki, A. Kato, T. Yoshimine, Y. Sato, S. Tamura, and T. Hayakawa. Visualization of Epileptogenic Phenomena Using Cross-Correlation Analysis: Localization of Epileptic Foci and Propagation of Epileptiform Discharges. *IEEE Transactions on Biomedical Engineering*, 46(3):271–279, 1999.

Address for correspondence:

Hisashi Yoshida
Department of Computational Systems Biology, Kindai University
yoshida@waka.kindai.ac.jp

Partial correlation-based functional connectivity analysis of the optical intrinsic signals of the mouse neocortex during resting state

Yuto Yoshida[1], Mitsuyuki Nakao[1], Norihiro Katayama[1],

[1]Biomodeling Laboratory, Graduate School of Information Sciences, Tohoku University, Japan.

Abstract

Spontaneous hemodynamic signals of the brain express cooperativity between functional regions in the brain. To examine the functional connectivity between the regions, marginal correlation analysis is widely performed. However, many fMRI studies of human brain function have suggested that partial correlation analysis is more suitable to detect effective connectivity. In this study, we compared the functional connectivity networks estimated by the marginal and partial correlation analyses of optically measured hemodynamic signals of the mouse neocortex. It was confirmed that the functional network estimated by partial correlation analysis was sparser than that estimated by marginal correlation analysis. Correspondence of the former functional connectivity seemed more consistent with the physiological and the anatomical findings. Hence, it is suggested that the partial correlation analysis would be more suitable for detecting skeleton network of the mouse brain.

Keywords *Optical Intrinsic Signal (OIS) Imaging, Partial Correlation Analysis, Functional Connectivity, Resting-State Network (RSN)*

1 Introduction

Recent studies suggest that the resting-state network (RSN) of the human brain has a close relationship with psychiatric and neurological disorders [1][2]. Therefore, RSN analysis is expected to be a next-generation diagnostic method for these disorders. However, basic studies have been performed to reveal the mechanism and treatment of these disorders using mice because of applicability of various experimental methods including genetic engineering techniques [3]. Due to the small size of the mouse brain, optically measured hemodynamic signals are adopted for functional brain imaging and connectivity analysis instead of fMRI used in studies of human brain functions [4].

To examine the functional connectivity in the acting brain, marginal correlation analysis is performed widely. It has been demonstrated that the analysis is useful for extracting subnetwork structures including default-mode network [4]. Although functional connectivity between the brain regions tends to be interpreted as an implication of direct linkage between brain regions, it is inappropriate because marginal correlation does not imply actual connectivity between them. If two independent components were activated by a common driver, they would show strongly correlated activities. To examine “effective” connectivity in the brain, partial correlation analysis has been proved to be useful in the field of fMRI studies of human brain function [5][6]. However, so far, there is no report that partial correlation analysis was applied to hemodynamic signals that were optically measured from the mouse brain.

In this study, we compared marginal and partial correlation analysis of the hemodynamic signals that were measured from the mouse neocortex. Based on the results and the previous findings obtained by the fMRI, anatomical and physiological studies, usability and plausibility of the partial correlation for the functional connection analysis of the cortical hemodynamic signals will be discussed.

2 Materials and Methods

2.1 Measurement

All experimental procedures were approved by the Institutional Animal Care and Use Committee of Tohoku University and were performed according to the Japanese Government Animal Protection and Management Law (No. 105). All efforts were made to minimize animal suffering.

Six male mice (C57BL/6, 23-25 g) were used for this study. Experimental methods were described previously [7][8]. Briefly, to monitor local blood-volume change in the neocortex, optical intrinsic signals (green reflectance, 530 nm) were transcranially imaged with a cooled CCD camera (C9100-13, Hamamatsu Photonics, Japan) at 28 fps. Neocortical electroencephalograms (EEGs) and neck muscle electromyograms (EMGs) were also amplified and sampled at 1 kHz along with CCD exposure timings. During measurements, mice were maintained in a dark shielded cage. The sleep/wake stages of the animal were detected on the basis of the EEG and EMG signals according to the method by Veasey *et al.* [9]. Only the optical intrinsic signals (OIS) during quiet wakefulness were used in the present study.

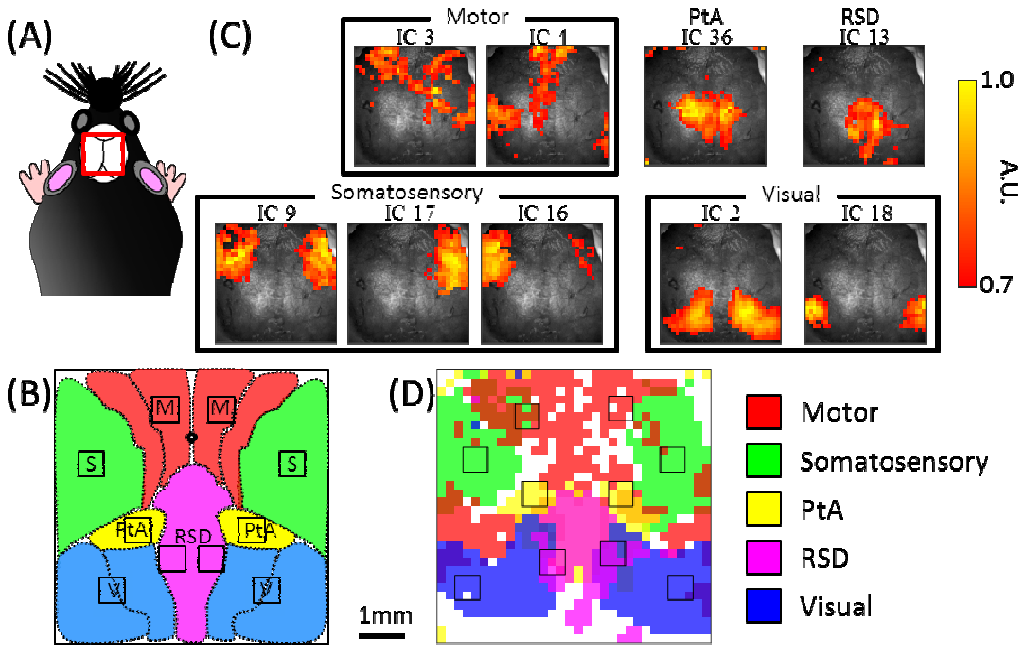

Figure 1: Functional brain mapping of the mouse neocortex by the combination of OIS imaging and ICA (A) The field of view of the OIS imaging (red square). (B) A typical spatial arrangement of functional regions of the mouse neocortex. The drawing was made according to ref. [10]. The circle indicates the position of bregma. (C) Color-coded spatial-intensity maps of ICs superposed on the monochrome image of the skull. Intensity is normalized from 0 to 1 and only the pixels of which normalized intensity >0.7 are depicted. (D) Overlaid functional maps estimated by the ICA. See text for abbreviations for the name of cortical regions.

2.2 Functional brain mapping

The size of field of view of OIS image was 6×6 mm (Fig. 1A), which almost covered bilateral motor cortexes (M), somatosensory cortexes (S), parietal association cortexes (PtA), retrosplenial dysgranular cortexes (RSD), and visual cortexes (V). The OIS data $I(t,\mathbf{x})$ was given as functions of time t and space $\mathbf{x}$.

Spatial arrangement of the functional regions of the neocortex were identified by the independent component analysis (ICA)-based method [8] with reference to the mouse brain atlas (Fig. 1B) [10]. Briefly, the OIS data were decomposed into statistically independent components (ICs) by the fast ICA algorithm as follows:

$$I(t,\mathbf{x}) = \sum_{i=1}^{N} A_i(\mathbf{x}) IC_i(t), \qquad (1)$$

where $IC_i(t)$ is the i-th ICs, $A_i(\mathbf{x})$ is the spatial intensity map of the contribution of the i-th IC, and N is the number of ICs. In this study, we set N = 40. This formula is called spatial ICA and was introduced by McKeown *et al*. for fMRI data analysis [11]. Functional brain regions were estimated according to the spatial distribution of the spatial-intensity maps (Fig. 1C) with reference to the mouse brain atlas [10]. An example of the brain map of a mouse estimated by the method is shown in Fig. 1D.

2.3 Functional connectivity analysis

Before correlation analyses, the change of OIS intensity to the baseline intensity was calculated, band-pass filtered in 0.008-0.09 Hz, and normalized [4][12]. For marginal correlation analysis, Pearson's correlation ($R_{i,j}$) was calculated for the pair of OIS data $I_i(t)$ and $I_j(t)$, where $I_i(t)$ is the green reflectance intensity in the i-th region of interest (ROI) at time t (Fig. 1D). Marginal correlation matrix was given by $\mathbf{R} = (R_{i,j})$. Partial correlation matrix $\mathbf{\Pi} = (\Pi_{i,j})$ was calculated according to the following definition [13]:

$$\Pi_{i,j} = (-1)^{i+j} \frac{C_{i,j}}{\sqrt{C_{i,i} C_{j,j}}}, \qquad (2)$$

where, $C_{i,j}$ represents the (i,j)-th cofactor of the marginal correlation matrix $\mathbf{R}$.

3 Results and Discussion

Figure 2A shows an averaged marginal correlation matrix obtained from the neocortical OIS of resting-state mice (n = 6). It was found that the observed area can be divided into 3 regions (subnetworks) according

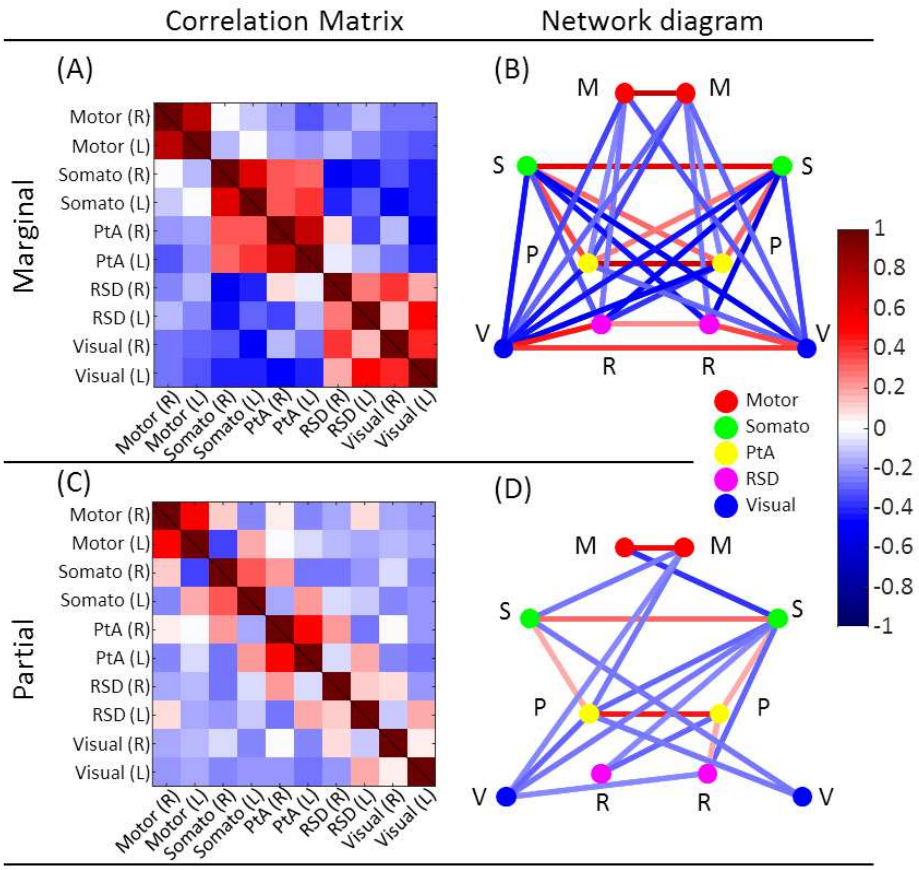

Figure 2: Marginal (A, B) and partial (C, D) correlation analyses for resting-state activities of the mouse neocortex. Magnitude of the correlation coefficient (r) is color-coded. In the correlation network diagrams (B and D), the neocortical regions are represented as nodes (circles) and correlation coefficients between the regions are depicted as color-coded edges. Only the edges with $|r| > 0.2$ are drawn.

to the positive correlation: (a) bilateral motor cortexes, (b) bilateral somatosensory cortexes and PtA, and (c) bilateral RSD and visual cortexes. In addition, these subnetworks were negatively correlated with each other except the motor and somatosensory networks (Fig. 2B). Most of strong negative correlations were found between the regions in the contralateral hemispheres.

The positive correlation network was almost consistent with the previous fMRI studies of human [5][6] and mouse brain [3], except the RSD and the visual cortexes. It was reported that when the cerebral blood-flow signals were used, positive correlation between the RSD and visual cortexes was stronger than the value calculated using the oxygenated hemoglobin signals [14]. In the present study, single-wavelength OIS was used for the analysis, which is strongly affected by the blood flow. Since thick superior veins are located near the RSD and the visual cortexes [15], they would cause correlated changes of the blood flow/volume in those regions. Overall, the negative correlations were stronger than those in previous reports. This could be caused by the blood-volume conservation property in the brain.

Next, partial correlation analysis was performed using the same OIS data to examine effective connectivity. As shown in Figs. 2C and 2D, the overall functional connectivity network was sparser than the network estimated by the marginal correlation analysis.

Interhemispheric positive correlations were also detected in the motor, the somatosensory and the PtA cortices as well as the marginal correlation analysis. In contrast, correlation between the RSD and the visual cortex was not evident. Thus, these results were more consistent with the previous studies. Correlation between the left and right visual cortices was weak. Since the experiments were performed in the dark cage in this study, activities in the visual cortexes would be uncorrelated.

Negative correlations between the regions in the same hemisphere were significantly fewer than the marginal correlation analysis. However, many interhemispheric negative connections were also found by the partial correlation analysis. So far, many physiological and anatomical studies have proved existence and functional significance of interhemispheric inhibitory connections

[16][17]. Thus, it is suggested that these synaptic connections would underlie the negative correlations detected by the partial correlation analysis.

4 Conclusions

In this study, we compared functional connectivity networks estimated by marginal and partial correlation analyses of the transcranially imaged optical intrinsic signals of the mouse neocortex. It was found that the partial correlation estimates sparser functional connectivity network than marginal correlation. Furthermore, interhemispheric inhibitory connections remain even in the sparse partial correlation network. Correspondence of the functional connectivity estimated by partial correlation analysis seemed more straightforward to the physiological and anatomical connections. Thus, it is suggested that the partial correlation analysis would also be more suitable for detecting skeleton of the network underlying correlated activities of the mouse brain.

Acknowledgements

This study is partly supported by JSPS KAKENHI Grant Numbers 15K01276, 16H05485 and a Grant-in-Aid for Scientific Research on Innovative Areas “Platform of Advanced Animal Model Support” from the Ministry of Education, Science, Sports, and Culture of Japan.

References

[1] M.D. Greicius, G. Srivastava, A.L. Reiss, and V. Menon. Default-mode network activity distinguishes Alzheimer’s disease from healthy aging: Evidence from functional MRI. *Proc Natl Acad Sci., U. S. A.* 101(13):4637–4642, 2004.

[2] M.P. van den Heuvel and H.E. Hulshoff Pol. Exploring the brain network: A review on resting-state fMRI functional connectivity. *Eur Neuropsychopharmacol,* 20(8):519–534, 2010.

[3] A.W. Bero, A.Q. Bauer, F.R. Steward, B.R. White, JR. Cirrito, M.E. Raichle, J.P. Culver, and D.M. Holtzman. Bidirectional relationship between functional connectivity and amyloid-β deposition in mouse brain. *J Neurosci*, 32(13):4334–4340, 2012.

[4] B.R. White, A.Q. Bauer, A.Z. Snyder, B.L. Schlaggar, J.M. Lee, and J.P. Culver. Imaging of functional connectivity in the mouse brain. *PLoS One*, 6(1):e16322, 2011.

[5] G. Marrelec, A. Krainik, H. Duffau, M. Pelegrini-Issac, S. Lehericy, J. Doyon, and H. Benali. Partial correlation for functional brain interactivity investigation in functional MRI. *Neuroimage*, 32(1):228–237, 2006.

[6] P. Fransson and G. Marrelec. The precuneus/posterior cingulate cortex plays a pivotal role in the default mode network: Evidence from a partial correlation network analysis. *Neuroimage*, 42(3):1178–1184, 2008.

[7] Y. Yoshida, D. Nakagawa, A. Karashima, M. Nakao, and N. Katayama. Reduction of light source noise from optical intrinsic signals of mouse neocortex by using independent component analysis. *Conf Proc IEEE Eng Med Biol Soc*, 6277–6280, 2015.

[8] Y. Yoshida, N. Katayama, D. Nakagawa, and M. Nakao. Estimation of functional brain map of mice based on optical intrinsic imaging and independent component analysis. *Conf Proc SICE Life Engineering Symp, 2015*. 205–210, 2015.

[9] S.C. Veasey, O. Valladares, P. Fenik, D. Kapfhamer, L. Sanford, J. Benington, and M. Bucan. An automated system for recording and analysis of sleep in mice. *Sleep*, 23(8):1025–1040, 2000.

[10] B.J. Keith, G.P. Franklin, G. Paxinos. *The mouse brain in stereotaxic coordinates*. Academic Press. 2008.

[11] M.J. McKeown, L.K. Hansen, and T.J. Sejnowsk. Independent component analysis of functional MRI: What is signal and what is noise? *Curr Opin Neurobiol,* 13(5):620–629, 2003.

[12] M.D. Fox, A.Z. Snyder, J.L. Vincent, M. Corbetta, D.C. Van Essen, and M.E. Raichle. The human brain is intrinsically organized into dynamic, anticorrelated functional networks. *Proc Natl Acad Sci USA,* 102(27):9673–9678, 2005.

[13] L. Guttman. Multiple rectilinear prediction and the resolution into components. *Psychometrika*, 5(2):75–99, 1940.

[14] K.M. Bergonzi, A.Q. Bauer, P.W. Wright, and J.P. Culver. Mapping functional connectivity using cerebral blood flow in the mouse brain. *J Cereb Blood Flow Metab,* 35(3):367–370, 2015.

[15] Margaret J. Cook. The Anatomy of the Laboratory Mouse. Academic Press, 1965. [Online]. Available: http://www.informatics.jax.org/cookbook/.

[16] V.A. Fedan and V.A. Shepelev. Interhemispheric transmission of visual information to the cat somatosensory cortex: Role of subcortical commissures. *Bull Exp Biol Med.*, 97(1):5–7, 1984.

[17] L.M. Palmer, J.M. Schulz, S.C. Murphy, D. Ledergerber, M. Murayama, and M.E. Larkum. The cellular basis of GABA(B)-mediated interhemispheric inhibition. *Science,* 335(6071):989–993, 2012.

Address for correspondence:

Norihiro Katayama, Ph. D.
Biomodeling Laboratory, Graduate School of Information Sciences, Tohoku University
6-6-05, Aramaki Aza-Aoba, Sendai 980-8579, Japan.
katayama@ecei.tohoku.ac.jp

From Information Flow to Microconnectomics

Masanori Shimono[1]

[1] Department of Mechanical Science and Bioengineering, Osaka University, Japan

Abstract

Brain is one of the most complex systems, made up of many components. In order to understand the system of the brain, we will need to extract information regarding how the many components, neurons, interact each other. This report and presentation will review how we could extract interactions among more than several hundred neurons meaningfully, and by this could reach new findings presented as a unified network system consisting of mutually connected neurons. The new picture will provide us more accurate and comprehensive understandings of the intertwined complex interactions among neurons (Microconnectome).

Keywords *Network, Information, Microconnectome, Neuroscience*

1 Introduction

Brain holds network organizations at both of macroscopic and microscopic scales. At the same time, nervous systems are organisms, which have been designed for processing information to survive in the evolutional process [1]. Although it is obvious that the microscopic neurons show network organizations by connecting each other through axons and dendrites, the quantitative evaluations of the network organization of many neurons, Microconnectome, is still almost completely unknown. Furthermore, if we want to understand how there emerge various functions from the network organization, we need to quantify the information flow, effective networks, coming from electrical activities between neurons beyond observation of only the underlying structural networks. This presentation will demonstrate the design of the Microconnectome, and will discuss how we can effectively connect findings in Microconnectome with other findings in Meso- or Macro-scopic Connectomics [2, 3].

2 Methods

2-1. Experiment

All *in vitro* data was acquired according to guidelines form the National Institutes of Health, and all animals were prepared after approval by the Animal Care and Use Committee in Indiana University and University of California, Santa Cruz. Cultured slices were selected from somatosensory cortex of P6 to P7 black mice as $5mm^3$ sections, and slices into 400μm thickness, and the neuronal spikes were recorded for ~1hour with a 512 ch. Multi-electrode array system, and the effective connectivity was analyzed after performing a spike sorting. The performance of the spike-sorting algorithm was evaluated in retina because we can estimate the positions of neurons and stimulated timing by knowing the positions and timings of photo-stimulations on retina [4].

The *in vivo* data was also used to characterize the topology which was used to compare with *in vitro* data later. The experimental procedure was approved by the University of California, Los Angeles, Chancellor's Animal Research Committess. All surgeries were performed under anesthetized conditions with isoflurane in a stereotaxic apparatus constraint to the animal's head. The microprobes held five prongs spacing 0.3-0.4 mm, and, on each prong contained ~51 recording sites, and was placed at orbitofrontal cortex. After extracting the resting period from sorted spikes, we performed the subsequent effective network analyses. Refer [5,6] to understand more details in experimental procedures and preprocessing of recorded spikes.

2-2. Data analysis

This subsection focuses on effective network analyses. The essential issue in effective network analysis is *Causality*. Causality is the relationships from cause to effect. However, because in biological systems, many components co-exist, the causal interactions are intertwined. Therefore, once we have obtained the complex networks, then we need to intertwine them.

To reconstruct the causal interaction among neurons, we needed to select some quantities, which measure the intensity of each connection. In order to select the best quantity, we evaluated the prediction performance of structural networks based on effective networks reconstructed from recorded data in sufficiently long time length (~1hours). When observing long-term activities of neurons, electrical currents naturally run through underling structural networks in high percentages. Therefore, if we were succeeded to select the most optimal measure, it may become closer to the ground truth topology of the structural networks after long-term observation [5]. This property provides a critical criterion to select and to design physiologically reliable computational measures.

In mathematical model studies, Garofalo et al. and our collaboration team had predicted that Transfer Entropy (TE) has the best detectability of causal interaction relating to the structural network among Cross-Correlation (CC) and several information measures [7, 8].

With preparing a new evaluation scheme purely from experimental data [5], we selected time-delayed TE and relating optimal parameters. The selection naturally satisfied good similarities of topologies between effective networks and structural networks.

The equation (1) expresses the definition of TE [9]:

$$\mathrm{TE}_{J\to I}(d) = \sum p(i_t, i_{t-1}, j_{t-d}) \log_2 \frac{p(i_t|i_{t-1}, i_{t-d})}{p(i_t|i_{t-1})}. \quad (1)$$

i_t and j_t indicate the states of neuron I or neuron J at time t. When the neuron I or J fires, the value is 1, and otherwise the value is 0. This equation measures the incorrectness of the assumption that the status of neuron J at time t has no influence on the transition of status of neuron I from past two time points t and t-d to time t+1. Beyond just calculating TE, we prepared the optimal filter to select sharp and strong peaks on the time axis. The filtering process avoided that we select confounding connections caused by common drivers or indirect connections. The preprocessing is critically important to extract truly physiologically reliable effective connections (Refer to the supplemental material in Reference [5] about the detailed analysis procedure.).

Now, we could reconstruct causal information flow in the neuronal system. From the distribution of the information flows, we could ask questions about basic statistical properties, such as if they hold long-tails or not, and if they distribute log-normally or normally.

These questions are important to characterize designs of neuronal network. However, simple forms of distributions are not sufficient to understand detailed designs of the information processing in a group of neurons as one unified and organized system. In order to achieve such understanding, we need to untangle the intertwined complex information flows. Graph theory provides a very useful and effective basis to tackle the complex non-uniformity [10]. We call this approach Microconnectome. This report and presentation will demonstrate several network measures, such as Hub, Cluster, Community, Rich-Club, Diversity, and Dynamic Importance. Hubs were defined as well-connected and highly central nodes. Clusters are group of several nodes holding specific connectivity patterns in the groups. Community is a group of many nodes having more connectivity density within same groups than between different groups.

3 Results

3-1. Information flows

The histogram of intensities of information flow was log-normally distributed [fig.1-(a)]. At same time, if we observe the binary connections while ignoring the weights or strengths of connections, we can observe the degree-histograms, and also could find out that the degree-histogram also decayed exponentially. Furthermore, from the accumulated functions produced by accumulating the weights from stronger ones to weaker ones from the original lognormal distribution, we could estimate only 20% of the neurons store 70% of the information in the network organization [fig.1-(b)]. These findings are consistent with properties of synaptic connections (structural connections), and these results mean that the distribution also held a long-tailed network, so the distributions of the systems are very non-equal [11,12].

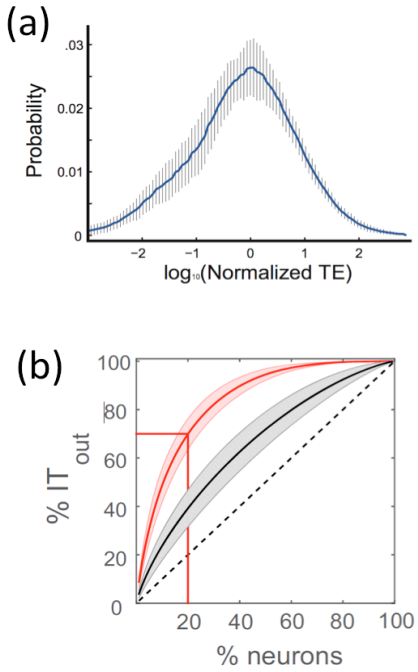

Figure 1. The normalized histogram of intensities of information flow (IT) quantified by Transfer Entropy (TE). (a) Log-normal form of the histogram. (b) The accumulated value of intensities of the information flow. They are re-plotted from the reference [5] and [6]

3-2. Microconnectome

As mentioned in the previous section, the effective networks of neurons showed a long-tailed distribution. Therefore, we could say that the network organization includes some special neurons which are connecting with more other neurons, Hubs [Fig.2].

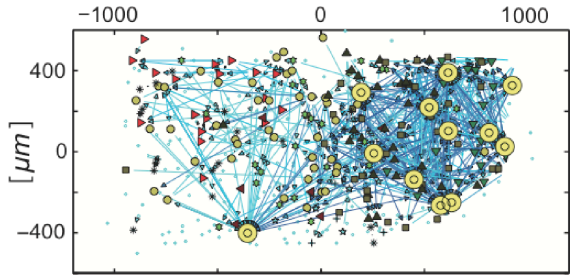

Figure 2. A spatial map of effective networks of neurons. Yellow circles show hubs in the microconnectome. This

figure was re-plotted from the reference [5] (you can see stained images at the front page of Indiana University, Network Science Institute: http://iuni.iu.edu/).

From further analyses of the multi-scale organization, we observed groups of 5-10 neurons and of 50-100 neurons. In our data, these groups nicely corresponded with Clusters and Communities in terms of Graph Theory, and we checked their fragility based on dependency on hubs. From the results, we could find, although clusters seem to be supported by only 1% hubs, communities are supported by ~7% hubs. Therefore, we could find the two different kind non-uniformities, Clusters and Communities, should be different architectures, and can say that the hubs were surrounded by hierarchical or multi-scale organizations (Refer [5] in detail).

Besides, the following studies showed an important role of non-hub neurons, which receiving inputs from more than one of the out-degree hubs. Such non-hub neurons could gain information when combining the receiving information [13]. Furthermore, we could find hubs produced a Rich Club (RC) organization by directly connecting to each other, and such hubs participating in RC organization also has specific roles, for example, highly active, and shows high Dynamic Importance in the system etc. [6].

4 Conclusions

The non-randomness of information flow up to 700 neurons showed a complex but highly organized design holding hierarchical groupings, and specific connectivity patterns for gaining information and for efficient propagation of information among many segmented groups of the neurons. The non-randomness seems to reflect the mechanism for efficient segregation, process, and integration of information under realistic spatial constraints.

In the future studies, with extending the past findings, much progress can be made, not only for deeper understanding of the Microconnectome but also for producing connections of Microconnectome with Meso-/Macro-scale networks [3], for evaluations in various species and various disease states are expected outcomes.

Acknowledgements

M.S. would like to appreciate J. M. Beggs for his longstanding supports, and A. Litlke, O. Sporns for many supports and discussions to achieve these studies.

References

[1] van den Heuvel M.P., Bullmore E.T., Sporns O., Comparative Connectomics, *Trends in Cognitive Neurosciences*, 20(5), 345-361, 2016.

[2] Fulcher B.D., Fornito A. A transcriptional signature of hub connectivity in the mouse connectome. *Proceedings of the National Academy of Sciences*, 201513302, 2016.

[3] Shimono, M. Non-uniformity of cell density and networks in the monkey brain. *Scientific reports*, *3*, 2013.

[4] Litke A.M., Bezayiff N., Chichilnisky E.J., Cunningham W., Dabrowski W., Grillo A.A., Grivich M., Grybos P., Hottowy P., Kachiguine S., Kalmar R.S., Mathieson K., Petrusca D., Rahman M., Sher A. What does the eye tell the brain?: Developent of a system for the large-scale recording of retinal output activity. *IEEE Trans. Nucle. Sci.*, 51(4), 1434-1440, 2004.

[5] Shimono M., Beggs J.M., Functional clusters and communities in the microconnectome. *Cerebral Cortex,* bhu252, 2014.

[6] Nigam S., Shimono M., Ito S., Yeh F-.C., Timme N., Myroshnychenko M., Lapish C.C., Tosi Z., Hottowy P., Smith W.C., Masmanidis S.C., Litke A.M., Sporns O., Beggs J.M., Rich-club Organization in Effective Connectivity among Cortical Neurons. *The Journal of Neuroscience* (2015) 36 (3): 670-684.

[7] Garofalo M., Nieus T., Massobrio P., Martinoia, S. Evaluation of the performance of information theory-based methods and cross-correlation to estimate the functional connectivity in cortical networks. *PloS one*, *4*(8), e6482, 2009.

[8] Ito S., Hansen M., Heiland R., Lumsdine A., Litke A.M. Beggs J.M., Extending Transfer Entropy Improves Identification of Effective Connectivity in a Spike Cortical Network Model. *PLOS One*, 6(11), e27431, 2011.

[9] Schreiber T., Measuring Information Transfer. *Phys. Rev. Lett*., 85, 2, 461-464, 2000.

[10] Newman, M., Barabasi, A.-L. & Watts, D. J. The Structure and Dynamics of Networks (Princeton Univ. Press, 2006).

[11] Song S., Sjöström P.J., Reigl M., Nelson S., Chklovskii D.B. Highly nonrandom features of synaptic connectivity in local cortical circuits. *PLoS Biol*, *3*(3), e68, 2005.

[12] Perin R., Berger T.K., Markram H., A synaptic organizing principle for cortical neuronal groups. *Proc Natl Acad Sci USA* 108(13): 5419-5424, 2011.

[13] Timme, N. Ito S., Myroshnychenko M., Nigam S., Shimono M., Yeh F-C., Hottowy P., Litke A.M., Beggs J.M., High-degree neurons feed cortical computations. *PLOS Computational Biology*, 12(5):e1004858, 2015.

Address for correspondence:

Masanori Shimono
Osaka University
E-mail: smn@bpe.es.osaka-u.ac.jp
nori417@gmail.com

Analysis of facial expression recognition by event-related potentials

Taichi Hayasaka and Ayumi Miyachi

Department of Information and Computer Engineering,
National Institute of Technology, Toyota College, Japan

Abstract

Recognition of facial expression is an important ability in human life, and it is related with emotion closely. In this article, we performed the psychophysical experiments for the purpose of clarifying the process of facial expression recognition by analyzing event-related potentials (ERP). We examined the difference of ERP between smile and anger faces, and classified the results of smiling faces with the mouth opened or closed. From a viewpoint of the late positive ERP components, experimental results suggest that (i) an anger face is handled than smile earlier, (ii) the smile with the mouth closed is processed similar to an anger face, in comparison with a grinning face, and (iii) P500 response is related to the final categorization of emotions. Moreover, differences of ERP in the prefrontal cortex were obtained between participants, in which it is argued by the difference in scheme that they took for expression discrimination. Based on the hypotheses, we proposed an information processing model to recognize smiling and anger faces.

Keywords *Event-related potential (ERP), Facial expression recognition, Emotion, Psychophysical experiment, Information processing model*

1 Introduction

In the human communication, facial expression becomes the important clue to guess the feelings of the partner. If the information processing about emotion becomes clear, it is expected to help the development of technologies for smooth communication, such as the robot which can understand human feelings better.

Event-related potentials (ERP) is one of the useful measures to study the mechanism of information processing in the human brain, and several studies detected the components of ERP specific for face recognition[1]. Since ERP is superior in temporal resolution, it is thought that applying it is suitable to analyze the information processing of facial expression.

In this article, we perform psychophysical experiments for the purpose of clarifying the process of the facial expression recognition. By analyzing measured ERP, we identify the characteristics of electric potentials related to the facial information processing.

2 Psychophysical Experiment

Stimulus: We used 10 Japanese female portraits in JAFFE database[2]. Based on the attached evaluations, 10 images were chosen for each expression, *e.g.*, smiling (*happy*), anger (*angry*), sad, and surprised faces. The stimuli were displayed in random order, at the area of an angular size 7.9 x 8.8 degrees in the LCD monitor (Samsung SyncMaster 2233RZ). PST E-Prime 2.0, which is a suite of applications for psychological experiments, was used for control of the stimulus presentation.

Procedure: The experiment was conducted in a darkroom. The participant attached the electroencephalograph Emotiv EPOC during the experiment.

We instructed to the participants that they replied by pushing the button of PST Serial Response Box whether a displayed face image was an appointed expression, *happy* or *angry*. Only in the case of the appointed expression, the participants were directed to react.

After showing a fixation point during 500 milliseconds, a face stimulus was displayed in 100 milliseconds. Then a random-dot image was presented for masking. The screen which forces a participant to answer was displayed for up to 2,000 milliseconds. This trial was repeated 320 times (40 stimuli presentation a set). Between the sets when an intermission screen was displayed, the participants could take a rest in the darkroom.

Participant: 8 males and 3 females (for *happy* condition, 6 males and 2 females for *angry* condition) from 20 to 22 years old with (corrected) normal vision were participated as volunteers.

3 Results

The average rate of incorrect answers was 7.5%. The analysis was carried out along the answers of the participants, not expressions connected with face images. We employed EEGLAB[3], which is a MATLAB toolbox for processing EEG.

3.1 Comparison between smiling and anger faces

Figure 1 and 2 show the event-related potential (ERP) of the right hemisphere for *happy* and *angry* conditions, which is obtained by the average of 11 participants (for *happy* condition, 8 participants for *angry* condition). The averaged ERP are derived from the trials when the participants pushed the button.

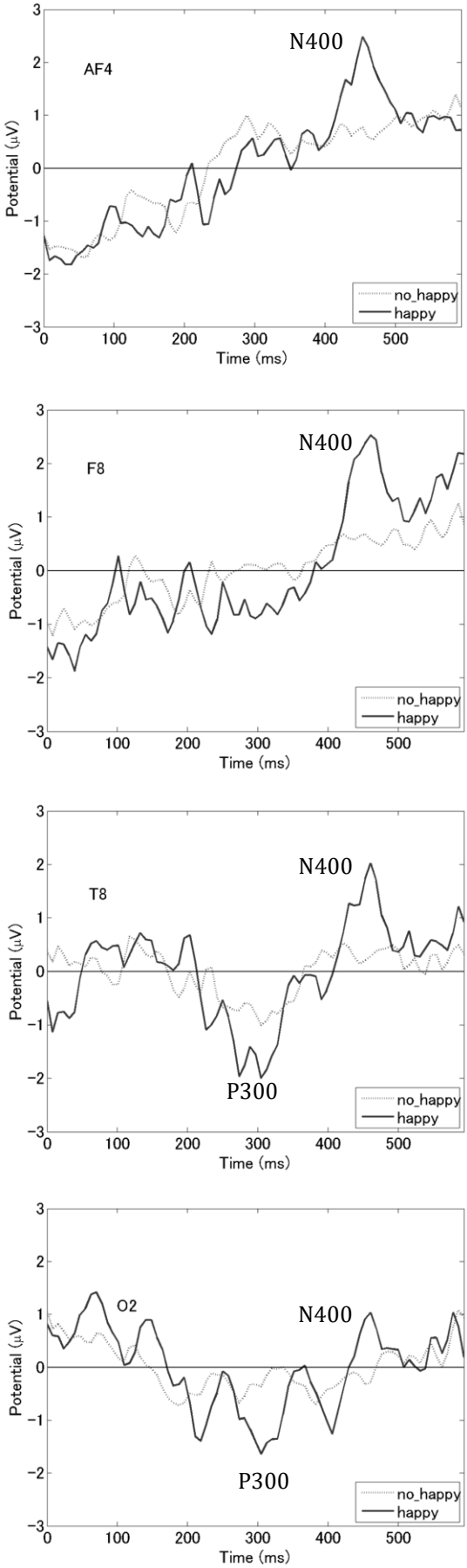

Figure 1: ERP for *happy* condition.

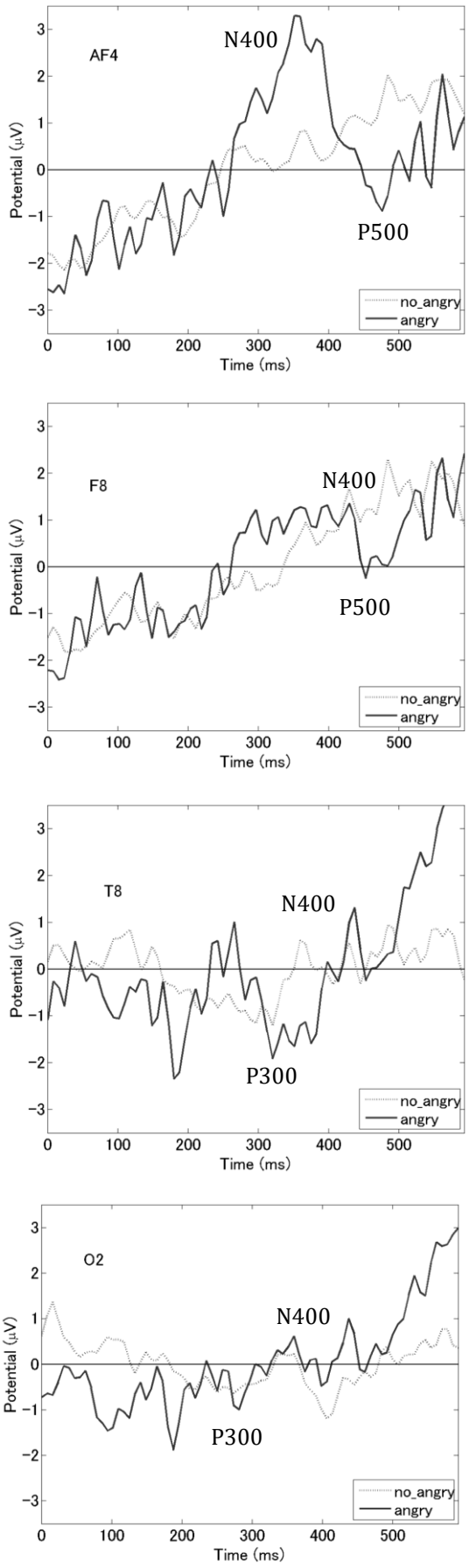

Figure 2: ERP for *angry* condition.

P300 are observed with the electrodes at middle temporal gyrus for both *happy* and *angry* conditions. It is thought that the attention of the participants is surely turned to the face images, because P300 is an endogenous potential to reflect processes involved in stimulus discrimination.

In the *angry* condition, the individual differences are occurred for the latency of P300. Since each participant's latency of P300 is about 200 milliseconds, 400 milliseconds, or nothing, the averaged ERP include two positive components dispersively. As an overall tendency, the positive components are distinctly visible in the ERP in the right hemisphere, but not clearly in the left because of the differences between the participants.

Although the P500 component is commonly appeared for most participants, the latency or existence of N400 is highly individual. Compared between Figure 1 and Figure 2, the latency of P500 for the *angry* condition is earlier, in which it is about 450 milliseconds in Figure 2. The difference suggests that processing of anger faces in brain is performed earlier than smiling.

Focusing the ERP components observed with the electrodes at the occipital lobes for both *happy* and *angry* conditions, participants were divided into two types: N400 clearly appeared, or fibrillation of potentials were recorded. Basically, individual differences emerged more greatly than the expression differences. That tendency might be dispersed by the scheme that participants took for the tasks.

3.2 Comparison between smiling with the mouth closed and grinning faces

A human face may be an expression with different characteristics even if it expresses the same emotion. We divided 10 images of the *happy* condition into 2 groups; 4 smiling faces with the mouth closed (*smile*) and 6 grinning faces (*laugh*). Figure 3 shows ERP for both stimuli which is obtained by the average of 11 participants. The averaged ERP are derived from the trials when the participants pushed the button.

Although presence or latency of P300 and N400 is inconsistent by the participants, the late positive ERP components P500 is commonly observed in the frontal lobes. The amplitude for the *smile* stimuli appears more definitely and is larger than the *laugh* stimuli. The latency of P500 for *smile* stimuli is later than *angry* condition. For the participants who P300 and N400 appear for both stimuli, the latency of the *angry* condition tends to be the shortest, and the *laugh* stimuli is the second in order. As a result of individual participant, the electric potential of the late ERP shows a tendency to raise. The positive component VPP around 170 milliseconds is recorded as for almost all participants for the *smile* stimuli, but not for the *laugh* stimuli.

In the temporal lobes, P300 and N400 are observed for both *smile* and *laugh* stimuli. The difference of the latency is not consistent, but the amplitude of P500 component for the *smile* stimuli is larger than the *laugh* stimuli.

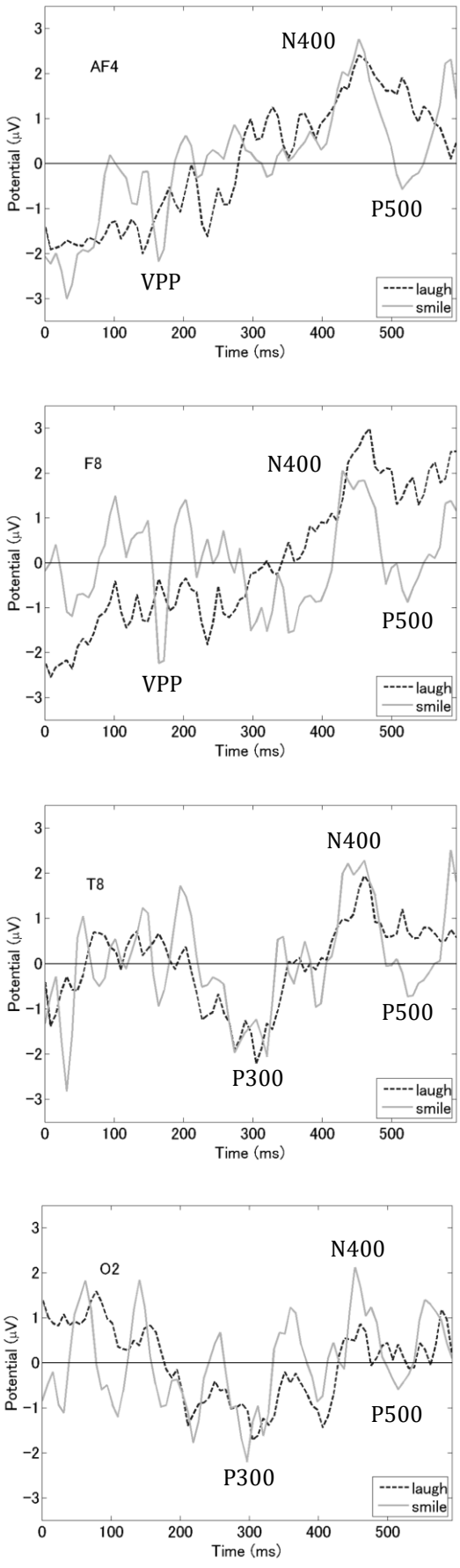

Figure 3: Difference of ERP between smiling (*smile*) and grinning (*laugh*) faces for the *happy* condition.

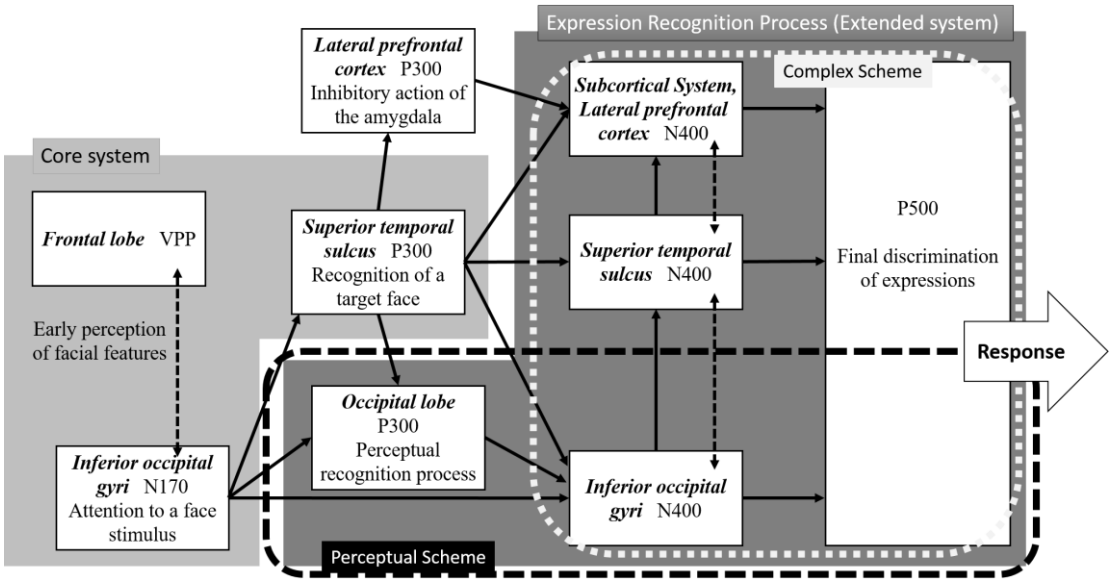

Figure 4: Information processing model to recognize smile and anger faces.

In the occipital lobe, multiple positive components arise from 200 to 400 milliseconds. Similar to the other electrodes, the amplitude of P500 for the *smile* stimuli is larger as for several participants.

4 Discussions

Based on the features of ERP components, we propose an information processing model to recognize smiling and anger faces, as shown in Figure 4.

When an anger face was displayed, unconscious processing to detect the menace might occur, mainly in the amygdala. However, since the activation of the amygdala was not observed under our experiment that imposed the emotional category discrimination for the expression, it is suggested that activation of the right lateral prefrontal cortex affects inhibitory action of the amygdala[4]. Results of independent component analysis, in which the estimated sources would be around AF3 and AF4, argue that P300 recorded in the electrodes of frontal lobe may be the component related to the inhibition.

We consider that it is branching after the recognition of a target face, in which it seems to be represented by P300 components at the temporal lobes and the source may be the superior temporal sulcus, by the difference in scheme which the participants took. The process from the early perception represented by VPP and N170 components to the face recognition in the superior temporal sulcus corresponds to the *Core system*[5] by Haxby, *et al.* We hypothesize that the features of ERP are caused by the difference in scheme in the following *Extended system*[5].

If a participant takes a simple perceptual scheme for a clear expression of the emotional category such as grinning, the prefrontal cortex may not be activated so much but the recognition process in the temporal and occipital lobes may be carried out based on the rough morphological characteristics of a face. In the case where the complex scheme is taken for the expression stimulus hard to discriminate its emotion perceptually, it is supposed that the wide area of subcortical system cooperates on the process. Although we could not estimate the sources of N400 or P500 which arise from the latter process, such components were observed at the broad field, similar to the process when an emotionless or an ambiguous face is displayed.

Patient-based evidence[6] suggests that the expression processing is atypical and independent to the facial identity. We suppose that P500 components observed at most electrodes involve final discrimination process of expressions. Since the latency of P300 or N400 was highly individual, however, further experiments would be necessary.

References

[1] E. I. Olivares, J. Iglesias, C. Saavedra, N. J. Trujillo-Barreto, and M. Valdés-Sosa, *Behavioural Neurology*, 2015, doi: 10.1155/2015/ 514361.

[2] M. J. Lyons, S. Akamatsu, M. Kamachi, and J. Gyoba, *Proceedings of 3rd IEEE International Conference on Automatic Face and Gesture Recognition*, 200-205, 1998

[3] A. Delorme and S. Makeig, *Journal of Neuroscience Methods*, 134:9-21, 2004

[4] M. Nomura, H. Ohira, K. Haneda, T. Iidaka, N. Sadato, T. Okada, Y. Yonekura, *Neuroimage*, 21(1): 352-363, 2004

[5] J. V. Haxby, E.A. Hoffman, and M.I. Gobbini, *Trends in Cognitive Sciences*., **4**(6):223-233, 2000

[6] S. Bate and R. Bennetts, *Frontiers in Psychology*, 2015, doi: 10.3389/2015/00770

Address for correspondence:

Taichi Hayasaka
Department of Information and Computer Engineering, National Institute of Technology, Toyota College, 2-1 Eisei, Toyota-shi, Aichi, 471-8525 Japan
hayasaka@toyota-ct.ac.jp

To assess mental stability using electroencephalography

Yuko Mizuno-Matsumoto[1]

[1] Graduate School of Applied Informatics, University of Hyogo, Japan

Abstract

The objective of this research was to assess brain function by electroencephalography (EEG) and autonomic nervous function by photoplethysmography (PS) during emotional stimuli. The psychological status of healthy young adults was also evaluated using several questionnaires. EEG and PS were measured during emotional audio-visual stimuli. We abstracted how the neurophysiological responses under the emotional situations varied according to the subjects' mental stability. The results show that an EEG activity on the temporal area and a sympathetic nervous response were high when the subject's mental status was unstable. These results show that brain information processing and autonomic nervous system for an emotional situation of the mentally unstable people are different from those of the mentally stable people.

Keywords *Electroencephalography, Emotion, Photoplethysmography*

1 Introduction

The number of young adults who easily go ballistic over the slightest things has increased [1]. Mental and behavioral disturbances in young adults who have been labeled social misfits in their youth is a serious social issue. These phenomena are related to the growing number of people who suffer from mental disorder.

Although morphological examinations such as magnetic resonance imaging (MRI) can detect steady-going changes in the brain, functional examinations such as electroencephalography (EEG) can find brain changes in the earliest stage of progress to diseases [2].

Photoplethysmography (PS), which detects changes in the autonomic nervous system, is useful in evaluating psychosomatic states [3]. The advantages of PS are that it is a sensitive measure of reactions to stressful stimuli and that habituation of stimuli tends not to occur [4].

The aim of this research was to evaluate the brain function and autonomic nervous responses to emotional stimuli. Moreover, these reactions were assessed in groups of subjects with different mental stabilities.

2 Methods

The subjects were thirty healthy young adults, and EEG and PS of the subjects were measured under and after emotional audio-visual stimuli. Emotional stimuli consisted of relaxed stimuli, pleasant stimuli, and unpleasant stimuli. EEG was analyzed using wavelet-crosscorrelation analysis to obtain the wavelet-crosscorrelation coefficient (WCC) [5], and independent component analysis (ICA) to obtain the occurrence rate of the independent component [2]. PS was analyzed with wave form analysis [6]. The low amplitude of PS means that the activity of sympathetic nerve of the autonomic nervous system is high.

Personality Inventory (PI) and Cornell Medical Index (CMI) were used as the questionnaires to evaluate mental and physical aspects of the subjects. The subjects were categorized into stable and unstable mentality groups according to the scores of the questionnaires. We compared the features of EEG and PS changes by emotional stimuli between the subjects with stable mentality and unstable mentality.

3 Results

The results from WCC indicated that EEG changes of the subjects with stable mentality were different between the pleasant stimuli and the unpleasant stimuli.

The results from ICA showed that the high EEG activity on the temporal area under the unpleasant stimuli was provoked if the mentality of the subject was unstable, and the high EEG activity on the occipital area under the pleasant stimuli was provoked if the mentality of the subject was stable.

The results also showed the amplitude of PS under the unpleasant stimuli was low, and the amplitude under the pleasant stimuli was high. The amplitudes after the stimuli were higher than the amplitudes during the stimuli. All the amplitudes of the subjects with unstable mentality were lower than those with stable mentality.

4 Discussion

We found that the brain function and the autonomic nervous system of people with unstable mentality differently responded under the emotional stimuli from those with stable mentality. We could comprehend the relationship between the brain function and the autonomic nerve to reveal the whole mental and psychosomatic symptoms of the psychiatric patients.

Acknowledgements

This work is partially supported by JSPS KAKENHI

Grant Number JP (16K01367).

The author would like to thank the members of Mizuno-Lab for analysis.

References

[1] Hofmann S.G. Trait affect moderates cortical activation in response to state affect. Intern. J. Psychophysiolo. 63, 258-264, 2007.

[2] Mizuno-Matstumoto Y., Hayashi T., et al., Measurement of Personality Stability in Infants and Young Adults Under Emotional Stimuli Using a Brain Functional Reaction Method. IC-MED, 4 (1,2), 39-64, 2011.

[3] Ahlund C., Petterssion K., et al., Pulse wave analysis on fingertip arterial pressure effects of age, gender and stressors on reflected waves and their relation to brachial and femoral artery blood flow, Clin Physiol Fuct Imaging, 28, 86-95, 2007.

[4] Yoshida N., Mizuno-Matsumoto Y., et al., Evaluation of the autonomic nervous function with plethysmography under the emotional stress stimuli, Trans Jap Society Med Biol Eng, 49, 91-99, 2011. (in Japanese)

[5] Mizuno-Matsumoto Y., Webber W.R.S., Lesser R.P., et al., Wavelet-crosscorrelation analysis can help predict whether bursts of pulse stimulation will terminate afterdischarges. Clinical Neurophysiology, 113(1), 33-42, 2002.

[6] Miyagawa D., Mizuno-Matsumoto Y., et al., Evaluation of autonomic nervous function using photoplethysmography under emotional stress stimulation a cellular phone," Jap J Clin Neurophysiol, 40, 540-546, 2012. (in Japanese)

Address for correspondence:

Yuko Mizuno-Matsumoto, M.D., Ph.D.
Graduate School of Applied Informatics, University of Hyogo
7-1-28, Minatojima-minamimachi, Chuo-ku, Kobe, Hyogo
650-0047, Japan
yuko@ai.u-hyogo.ac.jp

Wavelet-crosscorrelation analysis of abnormal EEG in patients with mental disorders

Kozue Yamaguchi[1], Yuko Mizuno-Matsumoto[1],

1 Graduate School of Applied Informatics, University of Hyogo;

Abstract

The electroencephalography (EEG) can be used for the diagnosis of mental disorders. Abnormal EEG sometimes appears in patients with mental disorders. We quantitatively investigated the abnormal EEG. The subjects were 8 patients suffering from mental illness. We analyzed EEG using wavelet-crosscorrelation. We compared 3 epochs: before the appearance of the abnormal EEG (2 segments), during the abnormal EEG (1 segment), and after the abnormal EEG (2 segments). We calculated wavelet-crosscorrelation coefficients (WCC) for frequencies in the theta band for each segments in all the patients. We found that the values of WCC were higher during abnormal EEG than the values in the other epochs. This result on the theta activity suggests that there is not only functional minute disorders but abnormalities in connectivity in the brain of patients with mental illness.

Keywords *Coherence, Electroencephalography, Mental disorde, Theta activity, Wavelet-crosscorrelation*

1 Introduction

In recent years, the number of people with mental disorders consulting a medical doctor has increased. Mental illnesses have become the predominant chronic diseases of the 21st century society. In September 2009, the Ministry of Health, Labor and Welfare in Japan reported that about 25 % people suffered from a mental disorder [1]. The cause of the mental disease varies, but there is not a clear answer yet. Epilepsy and brain function of disorders are also considered to be causing mental disorders.

The electroencephalography (EEG) can be used for the diagnosis of diseases. In order to judge EEGs, it is important to determine what is normal and what is abnormal. If theta waves are clearly visible in the entire region of the the brain during a state of rest, it can be said that the EEG is abnormal [2].

An abnormal EEG sometimes appears in some patients with mental disorders. Although research related to abnormal EEG has already been conducted, the correlation between the sites during an abnormal EEG has not yet been elucidated. Therefore, a quantitative evaluation of the brain function related to abnormal EEG is necessary.

In this paper, we analyzed abnormal EEGs appearing in patients with mental disorders using wavelet-crosscorrelation analysis, and quantitatively investigated the abnormal EEGs.

2 Methods

We recorded electroencephalography (EEG) from 8 patients. The patients have a state of depression, and they were diagnosed to have mental disorders which could be partially caused by abnormal EEG. The WEG was measured during a state of relaxation while the eyes were closed. The study protocol was approved by the Ethics Committee of the Matsumoto clinic.

The EEGs were recorded 12 channels using the international 10–20 electrode positions with 500 samples per second (NIHON KODEN, JAPAN). Low-pass filter was set to 60 Hz and high-pass to 0.5 Hz.

We assessed 3 epochs: before the appearance of the abnormal EEG, during the abnormal EEG, and after the abnormal EEG. We evaluated all pairs within the group of 12 channels using wavelet-crosscorrelation analysis to get wavelet-crosscorrelation coefficients (WCC) [3].

Wavelet-crosscorrelation analysis is a method that can decompose signals that have rapidly changing components. This analysis can reveal the characteristics of transient changes, various frequency components, and coherence between sites. When we represent the wavelet transform of the two signals by $Wf_x(b,a)$ and $Wf_y(b,a)$, the wavelet cross-correlation function $WC_{xy}(a,\tau)$ is defined by Equation 1.

$$\mathrm{W}C_{x,y}(a,\tau) = \lim_{T\to\infty} \frac{1}{2T} \int_{-T}^{T} \overline{Wf_x(b,a)} Wf_y(b+\tau)\, db, \quad (1)$$

τ indicates a time delay of the wavelet coefficients in the wavelet space, and $\overline{Wf_x(b,a)}$ represents a complex conjugate. The WCC $WR_{xy}(a,\tau)$ from the real part of the wavelet-crosscorrelation function $RWC_{x,y}(a,\tau)$ is defined by Equation 2.

$$\mathrm{W}R_{x,y}(a,\tau) = \frac{RWC_{x,y}(a,\tau)}{\sqrt{RWC_x(a,0)RWC_y(a,0)}}, \quad (2)$$

By calculating the WCC, $WR_{xy}(a,\tau)$ between any of the electrodes, relevant to the strength of the coherence for each frequency band between the sites in the brain can be abstracted [4]. The closer WCC is to 1, the higher and more significant the coherence is; the closer WCC is to 0, the lower and less significant the

coherence is.

In this research, the window length was set at 2 seconds, the number of channel pairs was 66, and a threshold of 0.3 was adopted in order to enable the coherence of WCC values. In other words, WCC values below 0.3 were left out of the analysis because it is less meaningful.

We calculate WCC for 2 seconds in the 4–7 Hz frequency range (theta band) and analyzed 5 segments in 3 epochs (Fig. 1). The 3 epochs were "BEFORE" (for 4 seconds before the abnormal EEG appears: A, B), "ABN" (for 2 seconds during the appearance of the abnormal EEG: C) and "AFTER" (for 4 seconds after the disappearance of the abnormal EEG: D, E).

We compared WCC in the 5 segments using one-way analysis of variance (one-way ANOVA) with Bonferroni corrections, since all the date were independent.

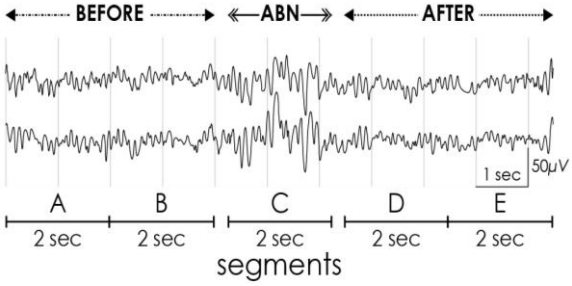

Figure 1: An example of an abnormal EEG. We divided EEG into 2 seconds to calculate WCC and analyzed 5 segments in 3 epochs.

3 Results

Table 1 shows the 8 patients' information (age range: 33–61 years; 2 males, 6 females). They were medicated with anti-epileptic and psychoactive drugs.

Table 1: Patient profile. (mean age = 46.88 years, SD = 9.78 years) F = Female, M = Male.

Patient number	Age [years old]	sex	disorder	Number of segments
#1	61	F	Epilepsy	25
#2	52	F	Schizophrenia	25
#3	57	F	Depression	20
#4	45	M	Depression	15
#5	35	M	Neurosis	15
#6	39	F	Depression	25
#7	53	F	Depression	10
#8	33	F	Schizophrenia	10

Figure 2 shows a typical example of frequency–segments of the wavelet scalogram in the right central channel (C4). In the map, red color shows a high spectrum value and blue color shows a low spectrum value. The spectrum value of ABN were higher than the values of other epochs. The dominant frequency is about 5–7 Hz.

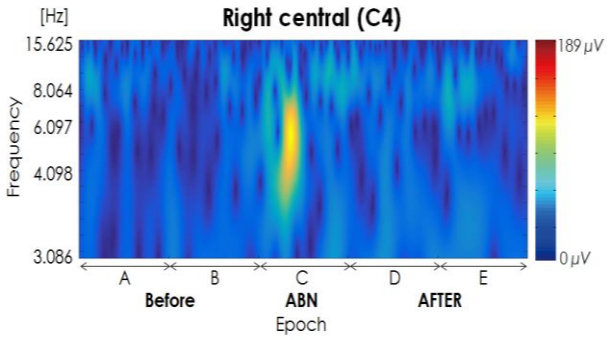

Figure 2: The frequency segments of the wavelet scalogram in the right central channel. The abscissa show the segments and the ordinates show the frequency.

Figure 3 shows a typical example of mean WCC values between the 12-channel sets in 5 Hz in 5 segments (Patient #2). In C (during the appearance of the abnormal EEG segment), the high coherence values are shown not only in the intrahemispheric pairs but in the interhemispheric pairs.

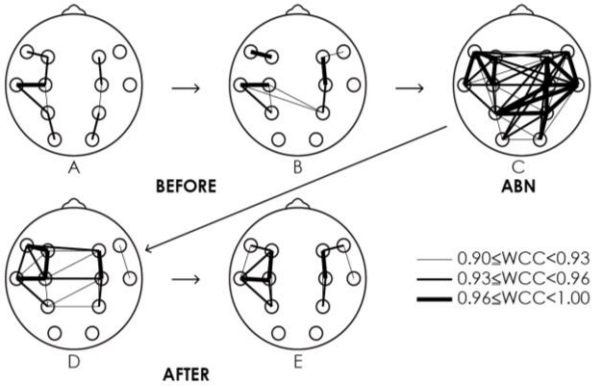

Figure 3: Representative maps showing WCC values between all channel sets for 5 Hz in patient #2. The WCC value is portrayed by the thickness: 0.90 ≤ WCC < 0.93, thin; 0.93 ≤ WCC < 0.96, medium; 0.96 ≤ WCC < 1.00, thick.

Figure 4 shows mean WCC values of all channel pairs in the theta band in all the segments of all the patients. The WCC values of C were significantly larger than the values of A, B, D, and E.

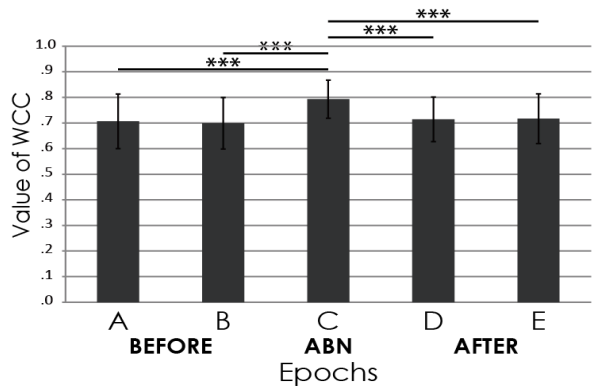

Figure 4: The mean WCC values in 3 epochs. Differences among the 5 segments were assessed by the one-way ANOVA and Bonferroni corrections: N = 66, *** P < 0.001.

4 Discussion

We found that the values of WCC were higher during the abnormal EEG than the other epochs. The theta wave activity of about 5–7 Hz has been reported to show a very small disorder in brain function [2]. The coherence between sites reflects the interaction of neural cellular population and shows the connections between the sites of the brain [5]. These results on the theta activity suggest that there is not only functional minute disorders but abnormalities in connectivity in the brain of patients with mental illness. In the next step, we are planning to analyze the EEG from healthy subjects to abstract the feature of the EEG from the patients.

Acknowledgements

This work is partially supported by JSPS KAKENHI Grant Number JP (16K01367).

References

[1] Ministry of Health, Labor and Welfare. Report on Mental Health and Medical Welfare Measures. *http://www.mhlw.go.jp/shingi/2009/09/dl/s0924-2a.pdf,* 2009.

[2] T. Okuma. Clinical Electroencephalography. *Igaku–Shoin Ltd*, 1999.

[3] Y. Mizuno-Matsumoto, G.K. Motamedi, W.R.S. Webber, R.P. Lesser. Wavelet-crosscorrelation analysis can help predict whether bursts of pulse stimulation will terminate afterdischarges. *Clinical Neurophysiology*, 113(1):33-42, 2002.

[4] Y. Mizuno-Matsumoto, S. Ukai, R. Ishii, S. Date, T. Kaishima, K. Shinosaki, S. Shimojo, M. Takeda, S. Tamura, T. Inouye. Wavelet-crosscorrelation analysis: Non-Stationary Analysis of Neurophysiological Signals. *Brain Topography*, 17(4):237-52, 2005.

[5] S. Weiss, P. Rappelsberger. Long-range EEG synchronization during word encoding correlates with successful memory performance. *Cognitive brain research*, 6; 9(3):299-312, 2000.

Address for correspondence:

Kozue Yamaguchi
Graduate School of Applied Informatics, University of Hyogo
7-1-28, Minatojimaminami-machi, Chuo-ku, Kobe, Hyogo
650-0047, Japan
kozue.y1@gmail.com

Features of diffuse alpha pattern in electroencephalography

Steven M. A. Carpels[1], Kozue Yamaguchi[1], Yuko Mizuno-Matsumoto[1],

[1]Graduate School of Applied Informatics, University of Hyogo, Japan;

Abstract

On electroencephalography (EEG), alpha waves are usually visible in the occipital region of the brain during the closing of the eyes. In some individuals suffering from brain illnesses, alpha waves can be seen in many regions of the brain and this is considered to be an abnormal EEG (known as diffuse alpha pattern). We quantitatively investigated normal and abnormal EEGs. The subjects were 5 healthy individuals and 4 patients suffering from brain diseases. We used wavelet-crosscorrelation analysis to compare diffuse alpha patterns with normal EEGs. We calculated wavelet-crosscorrelation coefficients (WCC) for frequencies in the alpha band for all epochs in each of the patients and healthy persons. We found that the values of WCC were higher in the abnormal EEG with the diffuse alpha pattern than in the normal EEG.

Keywords *Alpha band, Diffuse alpha pattern, Electro-encephalography, Wavelet-crosscorrelation analysis*

1 Introduction

The clinical application of electroencephalography (EEG) is being carried out in many hospitals and is being used for the assessment of neurophysiological pathologies [1]. For the clinical study of EEG, frequency analysis is one of the most important methodologies [2].

Alpha waves have a frequency ranging from 8 to 13.9 Hz and can be seen the most clearly in healthy individuals in the occipital region of the brain during the closing of the eyes. There are cases where alpha waves do not only appear in the occipital region but can also continuously appear in all regions in the cranium. This phenomenon is called “diffuse alpha pattern”, and is regarded as a type of abnormal EEG [1].

This research aims to compare the EEG of patients suffering from brain diseases with the EEG of healthy individuals, and, using wavelet-crosscorrelation analysis, to calculate wavelet-crosscorrelation coefficients (WCC). We compared the appearance of the diffuse alpha pattern with the appearance of the normal alpha pattern and investigated whether or not the coherence between the different parts inside the brain changes according to these 2 patterns.

By calculating WCC, we can obtain coherence values which provide information about the correlation between the sites of the brain, as well as the patterns in connectivity inside the brain. We can hypothesize that not only the WCC values, but also the connectivity pattern between the parts in the brain will differ between healthy individuals and mental disorder patients.

2 Methods

We recorded electroencephalography (EEG) from 5 healthy individuals and 7 patients. The patients were diagnosed with mental disorders, and abnormalities can be observed in the EEG. The EEG was measured during a state of relaxation while the eyes were closed. There was no sound at the time of recording. To obtain the EEG recordings, the electrodes were placed according to the International 10–20 electrode positions. The sampling frequency was 500 Hz. The study protocol was approved by the Ethics Committee of the Matsumoto Clinic.

The analyzing method used was wavelet-crosscorrelation analysis [3]. It is a combination of wavelet analysis and crosscorrelation analysis. By using wavelet analysis, a wavelet spectrum can be obtained that displays the activity of the various frequency bands. Crosscorrelation analysis enables the degree of waveform similarity between 2 different time series to be determined. Wavelet-crosscorrelation analysis is a new method that, while storing time information, makes it possible to investigate the coherence between the parts inside the brain. As opposed to crosscorrelation analysis, it can also be used for non-stationary data [4]. It displays that the closer the value of the obtained wavelet-crosscorrelation coefficients (WCC or in other words the coherence) is to 1, the more the waves are the same in terms of shape and nature (a value of 1 means exactly the same). The closer the value of WCC is to 0, the more different the waves are in shape and nature (0 means the waves are completely different). The EEGs recorded 19 electrode channels. Therefore 171 channel pair combinations are possible and each of these pair combinations has a coherence (WCC) value.

We used the software Vital Tracer, developed by Kissei Comtec Company, to abstract the EEG. There were 1000 analysis points, and the analyzing time was 2 seconds. The Frequency bandwidth is between 8 and 13.9 Hz (alpha bandwidth). The programming software MATLAB R2015b was used to obtain WCC values. We used SPSS Statistics 18 to do the statistical analysis. The method for statistical analysis was the Student’s T-

test for comparing 2 averages, and analysis of variance (ANOVA) with Bonferroni corrections for comparing more than 2 averages.

3 Results

Table 1 shows the healthy subjects' information (mean age = 24.00 ± 2.00 years). Table 2 shows the patients' information (mean age = 54.71 ± 8.33 years). The patients were medicated with psychoactive drugs.

Patient number	Age [years]	Gender	Number of epochs
1	21	Female	5
2	27	Female	5
3	23	Male	5
4	24	Female	5
5	25	Male	5

Table 1: Healthy subject profile.

Patient number	Age [years]	Gen-der	Disorder	Number of epochs
1	58	F	Schizophrenia	5
2	40	F	Low IQ and Depression	5
3	55	M	Neurosis	5
4	50	M	Depression	5
5	56	F	Insomnia	5
6	70	M	Dementia	5
7	54	M	Depression	5

Table 2: Patient profile; F = Female, M = Male.

The obtained wavelet spectra can be seen in Figs. 1 and 2. The abscissa show the time and the ordinates show the frequency. In the map, red color signifies a high spectrum value and purple color signifies a low spectrum value. In the healthy individuals, much less alpha activity is visible in C4 (Fig. 1). More alpha wave activity is visible in O2 during eyes closed, which is the normal state.

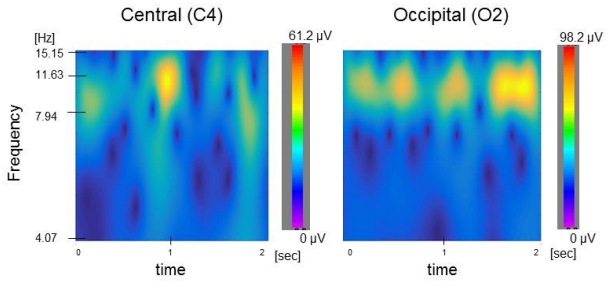

Figure 1: Wavelet spectra of the normal alpha pattern.

Figure 2 shows that both the C4 and O2 electrodes of the patients have more alpha wave activity compared to the healthy persons.

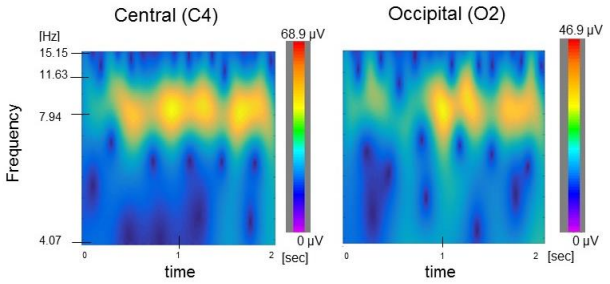

Figure 2: Wavelet spectra of the diffuse alpha pattern.

Figure 3 shows the WCC values between all electrodes on a map using Tcl/TK according to the International 10–20 electrode positions (Fig. 3). In an individual who has normal alpha wave activity, the WCC values are less high. We can observe high coherence values in the post-temporal and occipital areas (Fig. 3A). In the brain of a patient, high WCC values can be observed between all electrodes, especially in the frontal area (Fig. 3B).

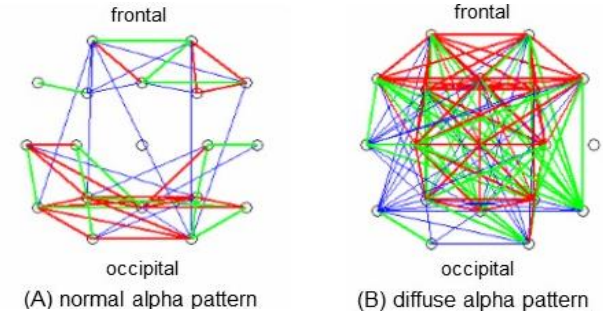

Figure 3: Display of WCC in a map using Tcl/TK. The left figure shows the WCC values between electrodes at a frequency of 11.1 Hz, the right figure shows WCC at a frequency of 8.48 Hz. The colors represent thresholds for WCC values. For the left figure blue represents $0.8 \leqq WCC < 0.85$, green $0.85 \leqq WCC < 0.9$, and red $0.9 \leqq WCC \leqq 1$. For the right figure blue represents $0.9 \leqq WCC < 0.94$, green $0.94 \leqq WCC < 0.97$, and red $0.9 \leqq WCC \leqq 1$.

Figure 4 shows the comparison of the average of the 171 WCC values in each epoch of all 7 patients with the average of the WCC values in each epoch of all 5 healthy persons using a Student's T–test. A significantly higher average value of coherence between all electrodes can be observed in the patients compared to the healthy individuals (Fig. 4).

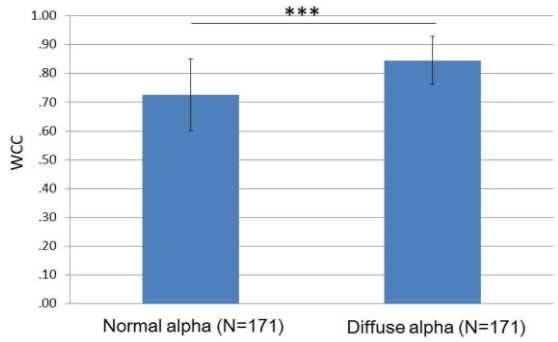

Figure 4: comparison of averages of WCC using a Student's T–test (*** P<0.001).

4 Discussion

The connectivity inside the brain can be abstracted using WCC. The results confirm that the WCC values and the connectivity pattern between the sites in the brain of patients suffering from mental disorders differs from the brain of healthy individuals.

It has already been reported that in healthy persons the alpha activity is at a higher frequency and patients have alpha activity at a lower frequency [1]. The obtained wavelet spectra confirm a lower frequency in the alpha band of patients. It is also known that the diffuse alpha pattern is visible in people with a small brain disorder and low brain function [1].

Interpreting these results, we can consider that the diffuse alpha pattern not only reflects low brain function, but also that there is an abnormality in the connectivity of the sites in the brain. It could be the case that healthy people do not use a lot of neurons in an idling state. In this state, it could be sufficient to use only the neurons of the occipital area of the brain [5]. We can consider that patients or some elderly individuals, even in an idling state, might use the whole area of the brain, rather than a small area.

In the future, we will investigate the EEGs of older healthy individuals and younger patients with mental disorders in order to be able to compare the normal and diffuse alpha patterns between subjects of the same age.

Acknowledgements

This work is partially supported by JSPS KAKENHI Grant number JP 16K01367.

References

[1] T. Okuma. Clinical Electroencephalography. *Igaku-Shoin Ltd*, 1999.

[2] E. Niedermeyer, and F. Lopes da Silva. Electroencephalography. Basic principles, clinical applications, and related fields. Fourth edition. *Baltimore: Lippincott, Williams and Wilkins,* 1999.

[3] Y. Mizuno-Matsumoto, S. Ukai, R. Ishii, S. Date, T. Kaishima, K. Shinosaki, S. Shimojo, M. Takeda, S. Tamura, and T. Inouye. Wavelet-crosscorrelation analysis: Non-stationary analysis of neurophysiological signals. *Brain Topography*, 17(4):237-52, 2005.

[4] Y. Mizuno-Matsumoto, G.K. Motamedi, W.R.S. Webber, R.P. Lesser. Wavelet-crosscorrelation analysis can help predict whether bursts of pulse stimulation will terminate afterdischarges. *Clinical Neurophysiology*, 113(1):33-42, 2002.

[5] T. Asakawa, T. Hayashi, and Y. Mizuno-Matsumoto. Coherence analysis of EEG under emotional stimuli related to mental states. *Electronics and communications in Japan,* 97(8):14-23, 2014.

Address for correspondence:

Carpels Steven
Graduate School of Applied Informatics, University of Hyogo
7-1-28, Minatojimaminami-machi, Chuo-ku, Kobe, Hyogo
650-0047, Japan
stevencarpels@hotmail.com

Convolutional neural networks using supervised pre-training for EEG-based emotion recognition

Miku Yanagimoto [1], Chika Sugimoto [2]

[1]Graduate School of Engineering, Yokohama National University, Japan;
[2]Center for Future Medical Social Infrastructure Based on Information Communication Technology, Yokohama National University, Japan;

Abstract

EEG-based emotion recognition (EEG-ER), which is one of the utilization of Brain Computer Interaction (BCI) to recognize human emotions, has recently drawn a great deal of attention. The authors developed EEG-ER models using the deep neural network (DNN) which can learn a superior internal representation in order to make accuracy higher than models using shallow classifiers. The models were evaluated by having them to classify and recognize EEG signals according to the emotional states "positive" or "negative" which were caused by watching music videos. One kind of DNNs, convolutional neural network (CNN), was employed as the model. Supervised pre-training was also adapted to the CNN to increase the accuracy. The CNNs had greater accuracy using smaller training data than conventional models even though CNNs are not good at learning on small datasets. The result implies CNNs can extract features from raw EEG data as good as other modalities.

Keywords *BCI, EEG, Emotion recognition, CNN, Deep learning, Feature*

1 Introduction

Due to extension of machines' ability, people is just beginning to have more opportunities to work with machines familiarly. In addition, there has been much interest in studies of unconscious mental states which are hard to verbalize recently. The affective models which can link recorded data with mental states and recognize emotions based on data should be useful in such studies.

Emotion recognition (ER) technique is indispensable to realize these systems. Physiological signals, images of expression, and speech signals are inputted into the ER model and apposite emotional labels of the data are outputted. Especially, when EEG signals are used as input, ER technique is called EEG-based Emotion Recognition (EEG-ER). In EEG-ER, the models have been conventionally implemented using statistic values in time or frequency domains for the features; Support Vector Machines (SVMs), Decision Trees, Linear Discriminant Analysis (LDA) are used for the classifiers. However, these models using "shallow" classifiers demand that features are distributed to be classified into correct classes as easily as possible.

Deep Neural Networks (DNNs) have received considerable attention in recent years because of their high accuracies and versatility by learning excellent internal representation based on raw data. The methods using deep learning have broken records in various tasks and data modalities. In EEG-ER, Deep Belief Networks (DBNs)[1] and Stacked Autoencoders (SAEs)[2] both of which perform unsupervised pre-training are used. These studies indicate that DNNs perform more accurately than conventional models. However, raw data of EEG recordings, in other words multichannel time sequential signals are not used as DNNs' input in these works to report on the ability of feature extraction.

In this paper, we propose the models using CNNs, which are not pre-trained in unsupervised way and have been used as EEG-ER models in a few cases so far. The CNN using multichannel time sequential signals gotten from 16 electrodes as input data is able to more accurately recognize emotions than conventional models are. Moreover, the CNN added pre-training technique outperforms the basic CNN.

2 Method

We implemented EEG-ER models which estimate classes of emotional states using EEG data as input. The models consisting of feature extractors and shallow classifiers are also implemented for comparison. Hereafter they are referred to as "shallow models".

2.1 Emotion recognition models

2.1.1 CNN

CNNs are one kind of feedforward DNNs and mainly used in image processing. Convolutional layers and pooling layers which are special layers with local connections characterize CNNs' architectures. Normally, convolutional and pooling layers are alternated several times, then fully-connected layers are arranged.

In terms of the l-th convolutional layer, its input is a 3D array with K 2D feature maps of size $W_1 \times W_2$. Each component is denoted by $z_{ijk}^{l-1}(i = 0, \cdots, W_1 - 1, j = 0, \cdots, W_2 - 1, k = 0, \cdots, K - 1)$. A filter bank consists of M kinds of kernels and each component is denoted by $h_{pqkm}(p = 0, \cdots, H_1 - 1, q = 0, \cdots, H_2 - 1, k = 0, \cdots, K - 1, m = 0, \cdots, M - 1)$. Each kernel as well as input has K channels, so the size

is $H_1 \times H_2 \times K$. Parallel calculation with respect to each kernel($m = 0, \cdots, M-1$) is made to output u_{ijm}. Then an activation function $f(\cdot)$ is applied to u_{ijm} to get the output of the l-th convolutional layer z^l_{ijk}. The operations as stated above are written as

$$u_{ijm} = \sum_{k=0}^{K-1} \sum_{p=0}^{H_1-1} \sum_{q=0}^{H_2-1} z^{l-1}_{i+p,j+q,k} h_{pqkm} + b_{ijm} \quad (1)$$

$$z^l_{ijm} = f(u_{ijm}) \quad (2)$$

where b_{ijm} is the bias and generally $b_{ijm} = b_m$ is used. If input data are multichannel time sequential signals, unlike images, we can consider $W_2 = H_2 = 1$.

There are some ways to pooling, especially max pooling is the function which is often used and written as

$$u_{ijk} = \max_{(p,q) \in P_{ij}} z_{pqk} \quad (3)$$

where P_{ij} is the area applied to the function on the input feature maps.

2.1.2 Features of shallow models

a) FD: It is known that EEG signals have the fractal property[3], therefore the fractal dimensions of EEG signals are available to evaluate brain activities objectively. Assuring the stationarity of signals by the short-time observation, secondary moment $\sigma_2(\tau)$ of a time sequential signal $f(t)$ whose fractal dimension is D is written as

$$\sigma_2(\tau) = \left\langle |f(t+\tau) - f(t)|^2 \right\rangle \approx |\tau|^{2H}. \quad (4)$$

Hurst exponent H and the estimated value of fractal dimension $\hat{D}$ are given by

$$H = \frac{1}{2} \frac{\delta \log \sigma_2(\tau)}{\delta \log |\tau|} \quad (5)$$

$$\hat{D} = 2 - H. \quad (6)$$

We cut out a time sequential signal $f_k(t)$ ($t = 0, \cdots, W-1$) from each EEG channel ($k = 1, \cdots, K$) using rectangular window (its size and stride are denoted by W and W_S, respectively). Substituting $f_k(t)$ into Eq. (4)–(6), we obtain $\hat{D}_k$. The K-dimensional vector consisting of the same time $\hat{D}_k$ is defined as the feature FD of the time.

b) ES: The energy spectral densities (ESD) or the power spectral densities (PSD) of EEG signals as well as the values transformed from them are often used as the features of emotions or intentions of human in BCI (Brain Computer Interaction). They have measurable results[1][2]. A time sequential signal which is cut out using rectangular window (size W, stride W_S) is denoted by $f(t)$ ($t = 0, \cdots, W-1$). ESD is given as

$$ESD(\omega) = \frac{1}{2\pi} \left| \int_{-\infty}^{\infty} f(t) e^{-i\omega t} dt \right| \quad (7)$$

We use $ESD(\omega)$ as explanatory variables composing the feature vector ES. When frequency band f_{min}–f_{max}[Hz] ($0 \leq f_{min}, f_{max} \leq f_S/2, f_S$ denotes the sampling rate) is assigned, an ES consists of $ESD(\omega)$ ($\omega = f_{min}, \cdots, f_{max}$). For instance, the ES is a (ceil$(W/2) \times K$)-dimensional vector consisting of $ESD(\omega)$ when the frequency band is assigned as 0–$f_S/2$[Hz].

2.2 Experiment and evaluation method

2.2.1 Conditions of EEG data

a) Database: We got EEG data ($f_S = 512$ [Hz]) to train and test the models from DEAP dataset[4]. In this database, each subject watched 40 one-minute highlight music videos in randomized order and performed a self-assessment of their levels of a certain kind of emotion at the end of each video. EEG signals were recorded when subjects were watching videos, and emotional information includes the values of emotional levels 1–9. Hereafter we refer to the one-minute multichannel EEG signal which was recorded when a subject was watching a video as "one epoch signal". The dataset of each subject consists of 40 pairs of an epoch signal and its emotional levels.

b) Dataset: We used EEG signals which were gotten from 16-channel electrodes (Fp1, Fp2, F3, F4, F7, F8, C3, C4, T7, T8, P3, P4, P7, P8, O1, O2) and values of valence levels in the analysis. The datasets of 10 subjects (s01–10) were used for pre-training of CNNs, the datasets of 3 subjects (s01–03) were used for evaluation of the models. The basic idea of the classification task set in this experiment is to recognize whether the emotion of each subject is "positive" or "negative" from EEG data. Eleven epochs were taken out in descending order from the highest level of valence and 11 epoch signals in ascending order from the lowest level of valence with respect to each subject[1]. The dataset of one subject consists of 22 epoch signals whose labels were "positive" or "negative".

c) Electrodes and channels: We prepare 2 ways of making channels of data. One way is to set the number of channels ($= K$) to the number of used electrodes ($= 16$) in this study. The other way is to set K to 120 ($= {}_{16}\mathrm{C}_2$) by making differential signals of combinations of 16 electrodes.

d) Size of data: The purpose of the present work is to construct EEG-ER models which can recognize human emotions at high time resolution in order to follow the change of his or her emotional state. When we cut out signals and make the minimal amount of data by rectangular window, therefore, its size and stride should be set as small as possible. The size and the stride of the window are set $W = 512$ [point] ($= 1$ [sec]$\times f_s$[Hz]) and $W_S = 64$ [point] ($= 0.125$ [sec]$\times f_s$[Hz]), respectively. The size of the minimal amount of data is denoted by $512 \times 1 \times K$ according to Sec.2.1.1. The number of the minimal amount of data in a dataset of a subject is equal to 10,406 ($= 22 \times \{(60-1)/0.125 + 1\}$).

e) Preprocesses of EEG signals: As the preprocess of EEG analysis, the average of 5 [sec] potentials before each epoch was subtracted from the epoch potentials. We optimized the filter for preprocess based on the tendency chart of feature appearance (Fig. 1) gotten in the analysis using a feature ES, a classifier random forest (RF), and the univariate feature selection. Selected explanatory variables are concentrated on the placement T7 and the high frequency band about 50–175[Hz], so we employed 50–175 [Hz] bandpass filter when FDs or CNNs were used for models. We confirmed that the filter is reason-

[1]Eleven is the maximum number which makes no duplication of valence values between the classes even if 2 values taken from 2 classes one by one were evaluated by different subjects.

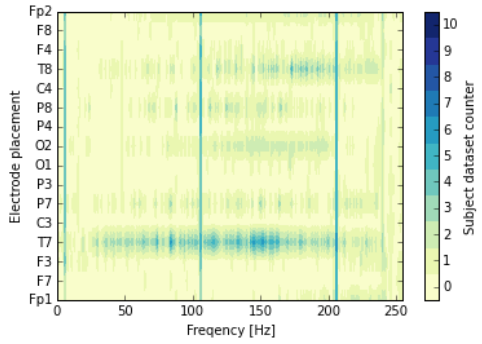

Figure 1: The tendency chart of feature appearance of s01–s10 on electrode placements and energy spectra.

able because the accuracies on filtered data was equally higher than the accuracies on not-filtered data.

2.2.2 Evaluation method

We took out epoch signals from each class one by one and made 11 pairs randomly on each subject dataset. Eleven-fold cross validation was performed on each subject dataset by using 10 pairs as training and validation data and 1 pair as test data. The seed of random function employed to make random pairs was fixed so that epoch signals of pairs were same at any time the cross validation was performed. In terms of shallow models, parameters were set in the ways mentioned in Sec.2.2.3 or optimized in experiments according to their accuracies. Therefore, we did not set validation data and used 10 pairs as test data. In terms of CNNs, there is no guarantee that the larger the maximum number of training epochs[2] ($= Epoch$) is, the higher the accuracies of the CNN are. Because of this, the set of parameters $(h(epoch), b(epoch))$ $(epoch = 0, \cdots, Epoch - 1)$ needs to be determined by choosing the optimum number of $epoch$ as $epoch^{opt}$. Validation data were employed to determine $epoch^{opt}$ as the value whose accuracy on validation data is the highest in all training epochs. We used 2 pairs selected from 10 pairs randomly as validation data and 8 pairs as training data. The amount of training data used by CNNs is smaller than that of shallow models.

2.2.3 Conditions of models

a) CNN: In image processing, the method of pre-training a CNN on other dataset in the supervised way and initializing its set of parameters (h, b) is often employed[5] and works well. To apply this to our work, when training and test are performed on a dataset of one of ten subjects(s01–10), the set of parameters (h, b) is initialized by supervised pre-training using the other datasets of 9 subjects. We used $18.2\%(= (36/198) \times 100)$ epoch signals in 9 subjects' datasets for validation data and $81.8\%(= (162/198) \times 100)$ epoch signals for training data.

The preliminary experiment was performed to decide the hyper parameters (including the setting of architecture) of NN. The maximum number of training epochs[3] and learning rate are set to 100 and 0.01, respectively. The architecture is finally determined to be a 10-layer CNN shown in Table 1. An increasing trend in accuracy with the number of layers was observed when we obtained accuracies of CNNs which have 1–7 layers in the first convolutional section. Here we set it to 6 because that difference was not so big. We also obtained the accuracies using some sets of hyper parameters with $K = 16, 120$. Since the accuracies of $K = 120$ tended to be higher than those of $K = 16$, K was set to 120 for CNNs.

Table 1: Settings of hyper parameters of CNNs.

Order of layers	6C→2CP→2FC
Convolutional layers (C)	
Sizes of kernels	5, 5, 5, 5, 5, 5
Numbers of kernels	200, 200, 200, 200, 200, 200
Convolutional pooling layers (CP)	
Sizes of kernels	5, 5
Numbers of kernels	200, 200
Sizes of pooling	2,2
Fully-connected layers (FC)	
Numbers of units	256, 2
Non-linearities	ReLU, softmax
Rates of dropout	0.5, 0.5

b) FD: FDs have a parameter "number of channels" K. The value of K was selected properly based on the evaluation. Hereafter feature FD with number of channels K is denoted by FD(K).

c) ES: ESs have a fixed parameter "number of channels" of 16 because of its much explanatory variables. The varying parameter "frequency components" $f_b(= [f_{min}, f_{max}], 0 \leq f_{min}, f_{max} \leq f_S/2)$ was properly selected based on the evaluation. Hereafter the feature ES with frequency components f_b is denoted by ES(f_b).

d) SVM: Cubic polynomial function $k(x) = (\gamma \langle x, x' \rangle + r)^3$ where $\gamma = 1/\sqrt{n\_feature}, r = 0$, and $n\_feature$ denotes the number of feature dimensions was used as the kernel. The penalty parameter and the tolerance are set to 1 and 10^{-3}, respectively.

e) RF: In terms of trees, the number of features to consider looking for the best split, the function to measure the quality of a split, the maximum depth and number of nodes, the minimum number of samples required to split an internal node, and the minimum number of samples in newly created leaves were set to $\sqrt{n\_feature}$, Gini impurity, unlimited, 2, 1, respectively. In terms of forests, the number of trees and whether to use out-of-bag samples were set to 500 and False, respectively.

3 Results

Table 2 shows the accuracies of the shallow model (ES(ω)+RF) and the CNNs. In the table, "no." represents the number of the test following 11-fold cross validation scheme. "ave" represents the average of accuracies and standard errors of 11 tests. The shallow model compared with CNNs is decided as ES(ω)+RF in the tests which are also following same 11-fold cross validation scheme. Table 3 shows the averaged accuracies of the shallow models on each subject's dataset.

[2]This "epoch" has different meaning from what was defined in Sec.2.2.1.

[3]Actual number of training epochs is smaller than 100 because of using early stopping.

Even though raw EEG data are inputted and smaller training dataset are used for CNNs, the averaged accuracies of CNNs are higher than that of the shallow model. From the result of CNN and CNN$_{PT}$, the accuracy of pre-training is higher than that of no pre-training. While there are substantial differences between datasets of different subjects, there are also commonality. The commonality in pre-training can be taken advantage.

Table 2: The accuracies of the shallow model and the CNNs. CNN$_{PT}$ denotes the CNN with pre-training.

subject	no.	shallow	CNN	CNN$_{PT}$	no.	shallow	CNN	CNN$_{PT}$
s01	1	35.4	34.0	49.8	2	43.4	38.8	50.1
	3	40.1	37.9	31.2	4	83.3	87.6	86.4
	5	91.9	92.2	57.0	6	72.6	85.6	84.3
	7	96.4	99.5	99.2	8	73.4	72.9	92.7
	9	98.8	100.0	99.8	10	99.5	100.0	93.0
	11	82.1	97.1	93.0	ave	74.3±6.9	76.5±7.6	75.8±7.1
s02	1	50.0	51.2	50.1	2	50.0	50.1	50.1
	3	93.1	55.4	88.1	4	83.3	87.6	86.4
	5	99.3	100.0	99.9	6	97.3	100.0	100.0
	7	70.1	49.9	49.9	8	49.2	49.9	49.9
	9	90.3	58.4	98.6	10	87.7	100.0	93.0
	11	1.6	0.0	0.0	ave	71.5±8.9	59.9±8.1	70.9±3.8
s03	1	51.5	64.1	62.9	2	54.3	56.6	66.5
	3	46.7	50.6	94.5	4	82.0	74.6	71.0
	5	22.1	47.4	58.1	6	76.2	52.3	85.6
	7	61.0	92.6	91.3	8	70.8	94.9	65.0
	9	47.4	52.3	62.5	10	58.7	83.6	84.5
	11	75.1	91.3	85.0	ave	58.7±4.9	69.1±5.4	75.2±3.8
5 subjects					ave	68.1±4.3	68.5±4.3	73.9±4.2

Table 3: The averaged accuracies of shallow models. The standard errors are omitted. In our notation, $\theta, \alpha, \beta, \gamma, \omega, \rho$, and all denote frequency bands 4–8, 8–13, 13–30, 30–64, 64–128, 128–256, and 0–256 [Hz], respectively.

model		s01	s02	s03	ave	model		s01	s02	s03	ave
FD(16)	+SVM	58.7	67.1	66.2	64.0	ES(θ)	+RF	55.4	65.1	50.9	57.1
FD(120)	〃	70.1	59.2	68.4	65.9	ES(α)	〃	63.0	66.0	55.9	61.6
FD(16)	+RF	69.2	60.2	64.2	64.5	ES(β)	〃	66.1	68.1	58.0	64.1
FD(120)	〃	70.3	62.8	69.1	67.4	ES(γ)	〃	70.8	70.3	62.3	67.8
						ES(ω)	〃	74.3	71.5	58.7	68.1
						ES(ρ)	〃	71.0	70.7	62.0	67.9
						ES(all)	〃	72.1	71.3	59.4	67.5

4 Discussion

Fundamentally, massive data are needed for supervised DNNs like CNNs to learn good features from raw data. CNNs in general cannot recognize test data correctly with high accuracy on relatively small datasets because of overfitting. However, the result shows the possibility that the basic CNN is comparable to shallow models in terms of averaged accuracy of EEG-ER. Indeed, the result does not necessarily ensure the availability of CNNs as EEG-ER models because the amount of test data is small in this study. Considering this absence of persuasiveness, we experimented with more test data of subjects in the next study[6]. It verifies that the CNN is more suitable for processing of massive data and also illustrates that there is the interpersonal commonality of EEG properties.

From the accuracies of ES+RF in Table 3, it is surmised that there is interpersonal difference of the frequency bands where features appear. This difference exists not only in methods of inducing emotions or persons but also recording trials. Therefore, optimizing the frequency filter in learning of NN is more desirable than separating the processing of the NN and the frequency filter.

Emotions can be classified as longer ones or shorter ones in terms of the duration. The purpose of this work is to recognize emotions of longer duration. Recognizing emotions of shorter duration can be done by using the methodology of ERP (Event Related Potential). It is better for the system to have higher resolution. However, we should give priority to suitability of the system's output over high resolution. It is desirable to decide the minimal window's size which makes the accuracy higher in experiments.

5 Conclusion

The EEG-ER models using CNNs were developed in order to make the accuracy higher than that of the shallow models. Even the basic CNN had high accuracy using slight smaller training data than the conventional models. Moreover, we showed that supervised pre-training helps CNNs to increase their accuracies not only in image processing but also in EEG-ER.

Acknowledgements

This work was supported by Japan Society for Promotion of Science KAKENHI 26330189.

References

[1] W.-L. Zheng, J.-Y. Zhu, Y. Peng, and B.-L. Lu, "EEG-based emotion classification using deep belief networks," 2014 IEEE International Conference on Multimedia and Expo (ICME), pp.1–6, Chengdu, China, 2014.

[2] S. Jirayucharoensak, S. Pan-Ngum, and P. Israsena, "EEG-based emotion recognition using deep learning network with principal component based covariate shift adaptation," The Scientific World Journal, vol.2014, 2014.

[3] K. Ogo, and M. Nakagawa, "On the caos and fractal properties in EEG data," Electronics and Communications in Japan Part III Fandamentals, vol.78, no.10, pp.27–36, 1995.

[4] S. Koelstra, C. Muehl, M, Soleymani, J.-S. Lee, A. Yazdani, T. Ebrahimi, T. Pun, A. Nijholt, and I. Patras, "DEAP: a database for emotion analysis using physiological signals," IEEE Trans. Affective Computing, vol.3, no.1, pp.18–31, 2012.

[5] A. Krizhevsky, I. Sutskever, and G.E. Hinton, "ImageNet classification with deep convolutional neural networks," In Proc. Advances in Neural Information Processing System 25, pp.1090–1098, 2012.

[6] M. Yanagimoto, and C. Sugimoto, "Recognition of persisting emotional valence from EEG using convolutional neural networks," 2016 IEEE 9th International Workshop on Computational Intelligence and Applications, Hiroshima, 2016.

Address for correspondence:
Miku Yanagimoto
Graduate School of Engineering, Yokohama National University,
79-5 Tokiwadai, Hodogaya-ku, Yokohama 240-8501 JAPAN
yanagimoto-miku-hb@ynu.jp

An EEG-based Communication Aid that Uses the Robot Avatar.

RP Hasegawa[1], Y Nakamura[1]

[1]Human Informatics Research Institute, AIST, Japan

Abstract

We have been developing a cognitive BCI/BMI system, "Neurocommunicator" to support communication of people with severe motor disabilities. The original system can predict a user's decision about a message to be expressed by his/her CG avatar, which is based on a real-time analysis of EEG data, especially event-related potentials (ERPs). In this study we attempted to use the robot avatar to facilitate the communication with its dynamic gestures. Most of the subjects (normal volunteers) were able to use this system with the high-accuracy decoding techniques.

Keywords *Brain-Computer Interface, Brain-Machine Interface, EEG, Robot, Avatar*

1 Introduction

Brain-computer/machine interfaces (BCI/BMI) to provide a direct link between the brain and external devices [1-4]. As one of those systems, we have been developing the "Neurocommunicator" [5], an EEG-based communication aid for people with severe motor disabilities. This system uses a compact headgear with wireless EEG recorder to analyze an event-related potential (ERP) to the sequentially flashed pictograms to indicate a desired message, and predicts the user's choice in the brain in a short time (3-5 sec). The message is expressed by the animation talk of the CG avatar.

In this study, we have extended the system so that the robot avatar (small but humanoid type) expressed the message by its dynamic gesture as well as its artificial voice (Fig. 1). We examined the accuracy of the neural decoding of the target pictograms, each of which was linked to the specific gesture of the robot.

2 Methods

We collected EEG data from 8 normal adult subjects under the protocol approved by the guideline and the committee of our institutes. All subjects were tested in two sessions ('training' and 'test') each. Each session consisted of 8 'games'. In each game, the subject focused attention on one of 8 pictograms ('target') in the matrix, which was prescribed by the investigator. During each game, each pictogram was flashed at 8Hz, displaying 4 Japanese characters (e.g. "Ko-Re-Ka-Na") with green color (Fig. 1①). In a brock of 8 flashes, all 8 pictograms were selected in a pseudorandom fashion. A block of 8 flashes were consecutively repeated 15 times for 'training' session and 5 times for 'test' session. Eight channels of EEG data were obtained by a custom-made recording system, in which a wireless EEG recorder was attached on a plastic headgear that localized the electrode positions around the top of the head (Fig. 1②). In the PC, the original 8 channels of continuous EEG data were downsampled to 21.3Hz after additional software bandpass filter (1-30Hz). Then the data were aligned to extract the event-related potential (ERP) associated with the onset of the single flash of each pictogram.

We performed linear discriminant analysis (LDA) to generate a pattern recognition model after the training session. The accuracy (success rate of target prediction) in the test session was examined using the single model generated by all data of the training session of each subject. The optimized LDA model was designated to produce a high score for the target and a low score for the non-target. The pictogram with the highest total (accumulative) discriminant score was regarded as the target (Fig. 1③). In the test session real-time feedback was given to the subject about the prediction of the target on the final (5th) block after each game. The message linked to the selected pictogram was expressed by the voice and the related gesture of humanoid robot (modified by the Kondo-Kagaku, KHR ver.2.0) (Fig. 1 ④).

After the 8 games of a session, the success rate was computed by dividing the number of the successfully predicted games (0 to 8) by the number of total games (8) in each subject. We mainly focused on the success rate on the final (5th) block of the test session as the index of the accuracy of our system.

3 Results

In this study, it was expected for the flash of the target pictogram to extract the P300, which should be strong enough for the real-time prediction. We first made sure whether the P300 was included, at least, in the average ERP. We compared average ERPs between the target and non-target conditions in the training session. The response to the target was typically stronger than that to the non-target, showing a positive peak around 200-400ms, to some extent, at all electrode positions. Although the waveform of the P300 was similar, within the subject, between the training and the test session, we observed a variety of individual differences among

subjects about temporal patterns of waveforms at each electrode location. Instead of the waveform of P300 itself, the converted LDA scores made it possible to predict the target in single games. We compared the accumulative LDA scores among pictograms. While the target pictogram generally produced the positive LDA score, the non-target pictograms generally produced the negative LDA scores. Although the non-target pictograms sometimes showed the positive score too, the pictogram with the highest scores tended to be the correct target (if not such prediction were considered to be unsuccessful). We compared the accumulative LDA scores among pictograms and found that most of the pictogram with the highest LDA score was the correct target, in which the related message was extracted by the avatar. Average success rate of all 8 subjects was 96% at the 5th block in the test session.

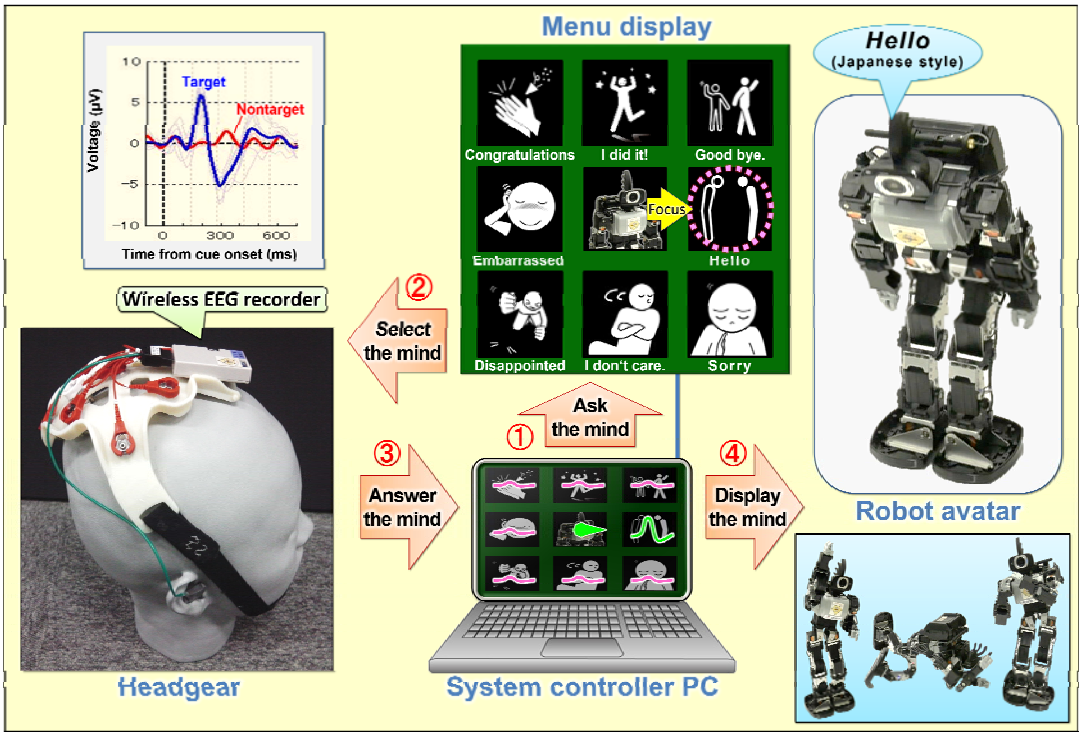

Figure 1 Schematic drowing of the control of the robot avatar by the EEG decoding.

4 Conclusions

We have succeeded in the development of the practical EEG-based robot control system as an extension of the Neurocommunicator. The robot avatar efficiently conveys affective information with its dynamic gesture, one of the representative nonverbal behavior which is important for communicating feelings and attitude in any face-to-face communication [6].

The result about accuracy of decoding (96% of success rate at the final/5 block in the test session) corresponded to 5 seconds, which made the subjects surprised. It is, however, important to speed-up the system for smooth communication in daily life of patients. Therefore, we are currently working on the speed-up of the decoding.

It is also important to increase the candidate of messages/gestures of the robot avatars. In addition to the 8 default candidates that are linked to the generation of emotional gestures of the robot avatar, we also hope to have candidates of the commands to the robot such as moving directions as well as actions to help the patients. We have already modified the system, in which the repetition of the choices by the brain (Fig. 1①-③) gives the users more possibilities to control the robot.

Acknowledgements

This work was supported by NEDO (15102349-0).

References

[1] L.A. Farwell and E. Donchin. Talking off the top of your head: toward a mental prosthesis utilizing event-related brain potentials. *Electroencephalogr. Clinical Neurophysiol.*, 70:510-523, 1988.

[2] M.A. Lebedev and M.A. Nicolelis. Brain-machine interfaces: past, present and future. *Trends Neurosci* 29: 536-546, 2006.

[3] C. J. Bell, P. Shenoy, R. Chalodhorn and R. P. Rao. Control of a humanoid robot by a noninvasive brain-computer interface in humans. *J Neural Eng.* 5:214-220, 2008.

[4] J.R. Wolpaw, N. Birbaumer, D. J. McFarland, G. Pfurtscheller and T. M. Vaughan. Brain–computer interfaces for communication and control. *Clinical Neurophysiol.*, 113:767–791, 2002.

[5] R.P. Hasegawa. Development of a cognitive BMI neurocommunicator as a communication aid of patients with severe motor deficits. *Rinsho Shinkeigaku* (*Clinical Neurol.*), 53:1402-4, 2013.

[6] A. Mehrabian. *Silent Messages: Implicit Communication of Emotions and Attitudes (2nd ed.).* Belmont, CA: Wadsworth. 1981.

Address for correspondence:

Ryohei P. Hasegawa, PhD.
Human Informatics Research Institute, AIST
r-hasegawa@aist.go.jp

Driver Fatigue Analysis Based on Binary Brain Networks

Chi Zhang[1], Fengyu Cong[1], Hong Wang[2]

1Department of Biomedical Engineering, Dalian University of Technology, China;
2Department of Mechanical Engineering and Automation, Northeastern University, China;

Abstract

Driving mental fatigue is a contributing factor that causes thousands of traffic accidents. Functional brain networks are supposed to reflect the interaction dynamics between brain regions. To investigate the interactions among distributed brain regions of drivers, we constructed binary brain networks from EEG data of the mental fatigue induced by the simulated driving task. Clustering coefficient, characteristic path length and global efficiency served as statistical network characteristics. The results showed that the number of the brain network links decreases with the accumulation of the fatigue. The statistical characteristics of functional brain networks embodied the risk of driving fatigue.

Keywords *Driver fatigue, EEG, Brain networks*

1 Introduction

In transportation system, fatigue is one of the major factors that cause thousands of automobile crashes all over the world [1]. The death toll in traffic accidents caused by fatigue makes up 57% of that in all traffic accidents every year [2]. Fatigue is a feeling of extreme physical or mental tiredness [3]. Hence how to measure the physiological dynamics during driving fatigue draws wide concern.

Numerous physiological indicators are available to quantify and assess the fatigue. The electroencephalographic (EEG) signal may be one of the most significant and reliable measurements since it reflects directly human brain activity [4]. Therefore, the following computerized analysis is implemented by processing the EEG recordings. Many studies have shown that fatigue will bring the changes of EEG rhythms (i. e. delta, theta, alpha, and beta) [5]–[7]. For example, theta rhythms increase and beta waves reduce. The papers in [6] and [7] show that α, α/β, θ/β, $(\alpha+\beta)/\theta$, and $(\theta+\alpha)/(\alpha+\beta)$ can be used as the effective indicators of driver fatigue. However, these studies use the same preselected frequency bands for all subjects, resulting in estimators that are partly insensitive to individual frequency-band differences. The paper in [8] assesses the information on alertness available in each operator's full EEG spectrum, which shows better performance for error rate estimation. Since the recorded EEG signals are nonlinear, time-varying, space-varying, and nonstationary, more and more studies focus on nonlinear dynamical analysis. Nonlinear dynamical analysis can provide complementary information about the dynamics under physiological or psychological states compared with classical linear time series analysis methods such as Fourier or spectral analysis [9]. For example, in [10] , [11] and [12], the nonlinear entropy-based methods were used to characterize irregularity and complexity of EEG data. The results show that the complexity parameters are significantly decreased with the fatigue level increasing.

Nevertheless, the analyzed EEG signals in the literatures above are just from the specified electrodes. The interactive dynamic information between different electrodes has not been considered. This is the novelty that this paper brings.

The neuronal elements of the brain constitute a formidably complicated structural network and it has also been widely recognized that this anatomical substrate supports the dynamic emergence of coherent physiological activity in different brain regions to make up a functional network [13]. Functional brain networks are supposed to reflect the interaction dynamics between brain regions [14]. A variety of network measures is now available that allow one to characterize constructed brain networks. Among these measures clustering coefficient, characteristic path length, and global efficiency are important statistical characteristics of network structure [15].

In this paper, we present a binary brain network method based on the recorded EEG signals of human subjects for driving fatigue analysis. The wavelet-based method was used to isolate and remove a wide variety of artifacts to obtain corrected EEG. Then the cross-correlation function of the corrected EEG was calculated to construct the binary brain networks of different subjects. At last, the clustering coefficient, the characteristic path length, and the global efficiency were used to measure the characteristics of the functional brain networks.

2 Methods

2.1 Experiments and data

The experiments were conducted on 10 healthy male subjects between age of 20 and 35. All the subjects are with normal intelligence and without mental disorders. During the experiments, they must avoid taking any type of medicine and stimulus such as irritant alcohol, tea or coffee. Each subject was asked to drive for 2

hours to collect the EEG signals in simulated driving situation. Standard scalp electrodes were placed in accordance with the International 10-20 System: Fp1, Fp2, F7, F3, Fz, F4, F8, T3, C3, Cz, C4, T4, T5, P3, Pz, P4, T6, O1, and O2. The EEG's sampling frequency is 1000Hz.

2.2 Experimental data preprocessing

The raw EEG signals are disturbed by numerous high frequency and low frequency noise known as artifacts. Wavelet transform is an effective tool for time frequency signal analysis and processing [16].

The wavelet transform decomposes a signal into a set of basic functions called wavelets. These basic functions are obtained by dilations, contractions and shifts of a unique function called wavelet prototype [17]. The wavelet transform is divided into the continuous wavelet transform (CWT) and the discrete wavelet transform (DWT).

DWT analyses the signal at different frequency bands with different resolutions by decomposing the signal into a coarse approximation and detailed information. DWT employs the sets of scaling functions and wavelet functions, which are associated with lowpass filters and highpass filters, respectively [18]. The original signal is first passed through a pair of high pass and low pass filters. After filtering, half of the samples will be cleared according to the Nyquist' rule, and the coarse approximation and detailed information can be distinguished. At successive levels the approximate component is further decomposed. We use wavelet decomposition with 4 levels to obtain the EEG range we care about (0–30 Hz). Then the wavelet enhanced independent component analysis in [19] was used to isolate and remove ocular artifacts and body movement artifacts to obtain corrected EEG.

2.3 Construction of brain networks

Representing the complex system brain as a network requires identification of nodes and edges [14]. Here, we assign EEG electrodes to the nodes of the brain networks. The adjacency relations among the nodes in the networks can be described by the adjacency matrix $\boldsymbol{A}$ whose element $\boldsymbol{A}(i, j)$ shows the measured edge between electrodes (nodes) i and j. A simple and most commonly used measure of the edges is the cross-correlation function [15]. The correlation between EEG signals s_i and s_j can be calculated by the following equations.

$$\gamma_{ij} = \left| \frac{CC(s_i, s_j)(\tau)}{\sqrt{CC(s_i, s_i)(0)CC(s_j, s_j)(0)}} \right|, \qquad (1)$$

$$CC(s_i, s_j)(\tau) = \begin{cases} \sum_{t=1}^{N-\tau} s_i(t+\tau)s_j(t), & \tau \geq 0 \\ CC(s_j, s_i)(-\tau), & \tau < 0 \end{cases}, \qquad (2)$$

We here consider the equal-time cross-correlation function, i. e. τ=0. γ_{ij} is corresponding to the element of the cross correlation matrix $\boldsymbol{R}$, which presents in ith row and jth column.

The adjacency matrix $\boldsymbol{A}$ can be obtained by the correlation matrix $\boldsymbol{R}$. First, define the adjacency matrix $\boldsymbol{A}$=$\boldsymbol{R}$. To exclude self-connections of nodes, the elements on the main diagonal of $\boldsymbol{A}$ were set to zero. The other elements of $\boldsymbol{A}$ reflect the correlation among the EEG signals in different channels. Here we construct binary brain networks using a thresholding approach. If the non-diagonal elements of the adjacency matrix $\boldsymbol{A}$ exceed a threshold value T, they will be set to 1 (i. e. a_{ij}=1, $i \neq j$) and to 0 (i. e. a_{ij}=0, $i \neq j$) otherwise. In order to determine the threshold T, we use the connectedness-based method in [20] to make sure the constructed networks belong to connected graphs. If any two nodes in a graph can be connected by a path along edges, the graph is said to be connected. In fact, when our brains deal with problems, the nervous systems in different functional brain areas need to work synergistically. Information can be automatically delivered to all the needed nodes (brain regions). That means there must be signal transmission pathways. Therefore, the model of the connected graph is reasonable and the connectedness-based method is applicable to healthy EEG.

2.4 Computation of network characteristics

There are two analytic approaches to functional brain architecture: namely, functional segregation and functional integration [21]. Based on the basic principles of functional segregation and functional integration, we used the clustering coefficient C, the characteristic path length L, and the global efficiency E_{global} to measure the characteristics of the functional brain networks.

If there is a link between two nodes, they can be called neighbor nodes and they are the nearest to each other. If the nearest neighbors of a node are also directly connected to each other, they form a cluster [22]. The clustering coefficient of a node is the ratio of the number of links that exist between the nearest neighbors of the chosen node and the number of possible links between them. The clustering coefficient of a network, $C(G)$, is the average over the clustering coefficient of all nodes.

$$C(G) = \frac{1}{N} \sum_{(i,j,h) \in G} \frac{2a(i, j)a(i, h)a(j, h)}{k_i(k_i - 1)}, \qquad (3)$$

where G represents the set of a network. N is the total number of nodes. k_i denotes the detgree, i.e., the number of the links of channel i. $a(i, j)$, $a(i, h)$, and $a(j, h)$ are the elements of adjacency matrix $\boldsymbol{A}$.

The shortest path length $d(i, j)$ is defined as the minimum number of links that must be traversed to go from node i to node j [22]. According to the definition,

$d(i, j) \geq 1$. The average of the shortest path length between all pairs of the nodes of a network is called the characteristic path length.

$$L = \frac{1}{N(N-1)} \sum_{i,j \in G, i \neq j} d(i,j), \qquad (4)$$

where $d(i, j)$ is the shortest path length between nodes i and j.

In a network, the efficiency of information exchange between two nodes is defined to be inversely proportional to the shortest path length. The global efficiency of a network is the sum of the efficiencies of all node pairs, normalized by maximal number of links $N(N-1)/2$.

$$E_{\text{global}}(G) = \frac{1}{N(N-1)} \sum_{i,j \in G, i \neq j} \frac{1}{d(i,j)}, \qquad (5)$$

where $d(i, j)$ is the shortest path length between nodes i and j.

3 Results and discussion

Figure 1 shows the binary functional brain networks during the experiment of driver fatigue. Considering the speed of calculation, we used a sliding window with the length of 180 times sampling length to obtain the structure change of the brain networks. The window moves forward along the experimental data. The three graphs are corresponding to the brain networks when the window moved to 0h, 1h, and 2h, respectively. As showed in Fig. 1, with the accumulation of the fatigue, the number of the network links decreases. The link number at the end of the experiment is significantly less than the link number of the initial state. This indicates the interactions among different brain regions are weakened during driving fatigue, which may affect the brain processing for traffic information.

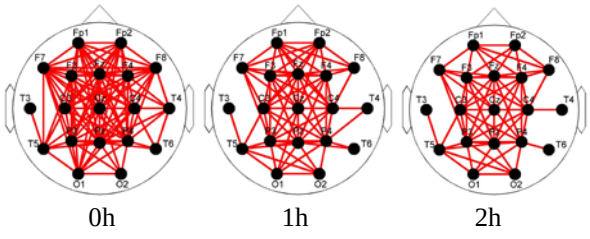

Figure 1: Brain networks during driving fatigue.

Figures 2-4 shows the statistical characteristics of functional brain networks (clustering coefficients, characteristic path length, and global efficiency respectively). As showed in Fig. 2, the averaged clustering coefficients of all the subjects are gradually reduced. Densely interconnected neighbors yield high clustering coefficients, while sparsely interconnected neighbors return low coefficients [15]. Networks with low clustering coefficient have smaller resilience, which indicates the ability to maintain the normal operation of the network is gradually reduced with the increase of driver fatigue level.

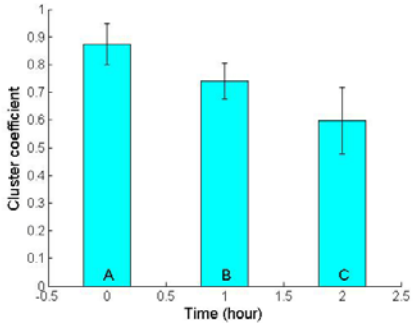

Figure 2: Clustering coefficient.

As showed in Fig. 3, the averaged characteristic path length of all the subjects gradually increases. It illustrates that the integration potential of the brain networks is reduced and the information in the brain networks flows with difficulty, when the drivers are fatigued.

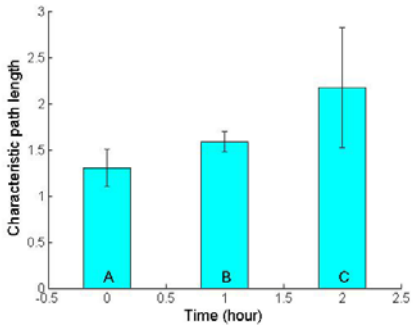

Figure 3: Characteristic path length.

As showed in Fig. 4, the averaged global efficiency of all the subjects gradually decreases. The global efficiency reflects the efficiency of communication among all the nodes. Therefore, the efficiency of information communication and processing is reduced.

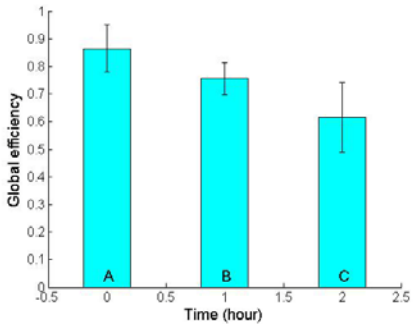

Figure 4: Global efficiency.

Overall, the decreasing clustering coefficients and the increasing characteristic path length reflected the fact that the small-world property of the networks became weak, when the drivers were fatigued. In this case, the systems may not maintain the normal operation, because the links which can support each other in a subset became fewer (see Fig. 2). In addition, the speed of information transmission was slower, because the probability of the "shortcut" emergence became lower

(see Fig. 3). Of course, the global efficiency is reduced (see Fig. 4), because it is inversely proportional to the characteristic path length (see Eq.4 and Eq.5). In the process of the experiments, driver fatigue affected normal brain activity, which is quite dangerous in the traffic system. Correspondingly the statistical characteristics of functional brain networks embodied the risk of driver fatigue.

Acknowledgements

This work was supported by "the Fundamental Research Funds for the Central Universities" (1306/852012) and National Natural Science Foundation of China (Grant No. 51505069).

References

[1] A. Williamson, D. A. Lombardi, S. Folkard, J. Stutts, T. K. Courtney, and J. L. Connor. The link between fatigue and safety, *J. Sci. Commun*, 43(2):498-515, 2011.

[2] W. Sun, W. Zhang, X. Zhang, C. Lü, and G. Chen. Development of Fatigue Driving Detection Method Research, *Automobile Technology*, 2:1-5, 2009.

[3] M. Chipman and Y. L. Jin, Drowsy drivers: The effect of light and circadian rhythm on crash occurrence, *Safety Science*, 47(10):1364-1370, 2009.

[4] A. Yildiz, M. Akin, M. Poyraz, and G. Kirbas. Application of adaptive neuro-fuzzy inference system for vigilance level estimation by using wavelet-entropy feature extraction, *Expert Systems with Applications*, 36:7390-7399, 2009.

[5] S. K. L. Lal and A. Craig. A critical review of the psychophysiology of driver fatigue, *Biological Psychology*, 55(3): 173-194, 2001.

[6] H. J. Eoh, M. K. Chung, and S. H. Kim. Electroencephalographic study of drowsiness in simulated driving with sleep deprivation, *International Journal of Industrial Ergonomics*, 35(4): 307-320, 2005.

[7] B. T. Jap, S. Lal, P. Fischer, and E. Bekiaris. Using EEG spectral components to assess algorithms for detecting fatigue, *Expert Systems with Applications*, 36(2, Part 1): 2352-2359, 2009.

[8] T. P. Jung, S. Makeig, M. Stensmo, and T. J. Sejnowski, Estimating alertness from the EEG power spectrum, *IEEE Transactions on Biomedical Engineering*, 44(1): 60-69, 1997.

[9] E. Bullmore and O. Sporns. Complex brain networks: graph theoretical analysis of structural and functional systems, *Nature reviews Neuroscience*, 10(3):186-198, 2009. S. Janjarasjitt, M. S. Scher, and K. A. Loparo, Nonlinear dynamical analysis of the neonatal EEG time series: The relationship between sleep state and complexity, *Clinical Neurophysiology*, 119(8): 1812-1823, 2008.

[10] E. Bullmore and O. Sporns. Complex brain networks: graph theoretical analysis of structural and functional systems, *Nature reviews Neuroscience*, 10(3):186-198, 2009. Y. Xiong, J. Gao, Y. Yang, X. Yu, and W. Huang. Classifying driving fatigue based on combined entropy measure using EEG signals. *International Journal of Control and Automation*, 9(3): 329-338, 2016.

[11] S. Kar, M. Bhagat, and A. Routray, EEG signal analysis for the assessment and quantification of driver's fatigue, *Transportation Research Part F*, 13: 297-306, 2010.

[12] C. Zhang, H. Wnag and R. Fu. Automated detection of driver fatigue based on entropy and complexity measures, *IEEE Transactions on Intelligent Transportation Systems*, 15(1): 168-177, 2014.

[13] E. Bullmore and O. Sporns. Complex brain networks: graph theoretical analysis of structural and functional systems, *Nature reviews Neuroscience*, 10(3):186-198, 2009.

[14] K. Lehnertz, G. Ansmann, S. Bialonski, H. Dickten, C. Geier, and S. Porz. Evolving networks in the human epileptic brain, *Physica D: Nonlinear Phenomena*, 267:7-15, 2014.

[15] M. T. Horstmann, S. Bialonski, N. Noennig, H. Mai, J. Prusseit, J. Wellmer, H. Hinrichs, and K. Lehnertz. State dependent properties of epileptic brain networks: Comparative graph–theoretical analyses of simultaneously recorded EEG and MEG, *Clinical Neurophysiology*, 121(2):172-185, 2010.

[16] H. Wang, C. Zhang, T. Shi, F. Wang, and S. Ma. Real-Time EEG-Based Detection of Fatigue Driving Danger for Accident Prediction, *International journal of neural systems*, 25(2):1-14, 2015.

[17] M. Kurt, N. Sezgin, M. Akin, G. Kirbas, and M. Bayram. The ANN-based computing of drowsy level, *Expert Systems with Applications*, 36(2):2534-2542, 2009.

[18] A. Yildiz, M. Akin, M. Poyraz, and G. Kirbas. Application of adaptive neuro-fuzzy inference system for vigilance level estimation by using wavelet-entropy feature extraction, *Expert Systems with Applications*, 36(4):7390-7399, 2009.

[19] N. P. Castellanos and V. A. Makarov. Recovering EEG brain signals: Artifact suppression with wavelet enhanced independent component analysis, *Journal of Neuroscience Methods*, 158(2):300-312, 2006.

[20] K. A. Schindler, S. Bialonski, M. T. Horstmann, C. E. Elger, and K. Lehnertz. Evolving functional network properties and synchronizability during human epileptic seizures, *Chaos*, 18(3):1-6, 2008.

[21] P. van Mierlo, M. Papadopoulou, E. Carrette, P. Boon, S. Vandenberghe, K. Vonck, and D. Marinazzo. Functional brain connectivity from EEG in epilepsy: Seizure prediction and epileptogenic focus localization, *Progress in Neurobiology*, 121(2014):19-35, 2014.

[22] H. Onias, A. Viol, F. Palhano-Fontes, K. C. Andrade, M. Sturzbecher, G. Viswanathan, and B. de Araujo. Brain complex network analysis by means of resting state fMRI and graph analysis: Will it be helpful in clinical epilepsy?, *Epilepsy & Behavior*, 38:71-80, 2014.

Address for correspondence: Chuang Xin Yuan Da Sha, Linggong Road #2, Ganjingzi District, Dalian City, Liaoning Province, 116024, P.R. China

Chi Zhang
Dalian University of Technology
Department of Biomedical Engineering
Email: chizhang@dlut.edu.cn

Cortical Dipole Imaging of Visual Evoked Potential Using Sigmoid Function-Based Filtering Property

J Hori[1], S Takasawa[1,2],

[1]Graduate School of Science and Technology, Niigata University, Japan;
[2]Terumo Corporation, Japan

Abstract

The aim of this study is to improve the accuracy of the cortical dipole imaging by focusing on the filtering property when solving the cortical inverse problem. We proposed a spatial inverse filter that optimizes the filtering property using a sigmoid function. The proposed inverse filter was applied to human experimental data of visual evoked potentials. As a result, the estimation accuracy was improved as compared with the traditional inverse techniques.

Keywords *EEG, Cortical Dipole Imaging, Inverse Problem, Filtering Property, Visual Evoked Potential*

1 Introduction

The spatial resolution of electroencephalogram (EEG) data is limited because of the low conductivity of the skull. Cortical dipole imaging that estimates the equivalent dipole distribution on a virtual layer within a brain from the scalp potential has been proposed to solve this problem [1]. The cortical dipole distribution is estimated from the scalp potentials by solving an inverse problem of the transfer matrix from the dipole layer to the scalp surface based on a head model. In the present study, we paid attention to filtering property when solving the cortical inverse problem in order to improve the accuracy of cortical dipole imaging.

2 Methods

According to the filtering property, the terms easily influenced by noise are reduced when singular value decomposition is applied to the inverse solution [2]. Figure 1 shows examples of the filter factors of Tikhonov regularization, truncated singular value decomposition (TSVD), and truncated total least squares (TTLS) against the singular values. The terms for large singular values were passed while the terms for small singular values were attenuated in all filter factors. We estimated optimum filtering property using the least squares method in the simulation of several signal source configurations. A filtering property model was constructed by approximating with a sigmoid function. Estimated optimal filtering property was intermediate between the property of Tikhonov regularization and the property of TSVD as shown in Fig.1.

3 Results

The proposed method was compared with traditional inverse techniques in computer simulations. The localization with less noise was accomplished by sigmoid function. The relative error of the sigmoid function is significantly smaller than that of the other methods.

The proposed method was applied to human experimental data of visual evoked potential. The EEG data were measured from healthy subject after obtaining informed consent. The signal was localized at the primary visual field in dipole distributions estimated by our method. It was possible to represent the process of signal propagation through ventral pathway using the sigmoid function. In conclusion, the sigmoid function was widely applicable in various situations and it would be effective for human experimental data.

This work was supported in part by a Grant-In-Aid for Scientific Research (C) 26350496 from the Japanese Society for the Promotion of Science.

References

[1] Y. Wang and B. He. A computer simulation study of cortical imaging from scalp potential. *IEEE Trans. Biomed. Eng.*, 45(6): 724-735, 1998.

[2] D.R. Fierro, H.G. Golub, C.P. Hansen, and P.D. O'leary. Regularization by truncated total least squares. *SIAM J. Sci. Comput.*, 18(4): 1223-1241, 1997.

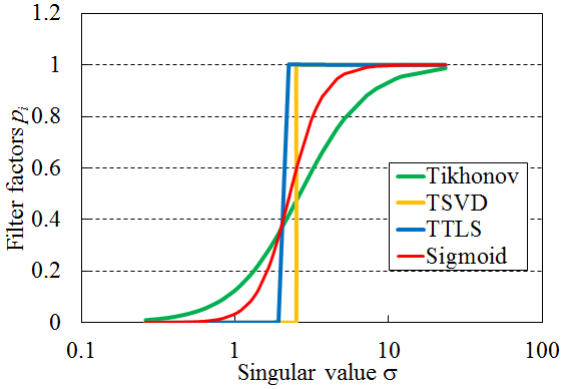

Figure 1: Filter factors of various inverse techniques against the singular value.

Address for correspondence:

Junichi Hori
Niigata University
hori@eng.niigata-u.ac.jp

Motion Aftereffect Direction-Specific Responses in the Steady-State Visual Evoked Potentials

S Arimitsu[1], K Momose[2]

1 Graduate School of Human Sciences, Waseda University, Japan;
2 Faculty of Human Sciences, Waseda University, Japan;

Abstract

Topography of direction specific response in steady-state visual evoked potential (SSVEP) was investigated. 64-channel SSVEPs were recorded during test stimulus of oscillating vertical sinusoidal grating (0.5 or 2 c/deg, 4 or 9 Hz) with/without motion adaptation. Phase of 1F component under right-adaptation in occipital and occipito-temporal area was shifted from that under left-adaptation, agreeing with the previous studies. The phase-shift topography revealed that the MAE direction-specific responses are appeared in occipital and occipito-temporal area, and spatial and temporal frequency selective, indicating that there are several different motion detectors with different sensitivity.

Keywords *Motion aftereffect, Motion direction-specific response, Perception of movement, SSVEP*

1 Introduction

Noninvasive methods for probing direction-selective neuronal activity are of significant value for understanding human motion perception. Motion aftereffects (MAE) has been used to investigate the human motion detection and processing system, because MAE isolate neural activity related to the processing of motion perception in human. It has been reported that direction-specific activity can be detected as phase of the steady-state visual evoked potential (SSVEP) [1][2]. Phase shift of 180 degrees were obtained from fundamental frequency (1F) components of SSVEPs with conditions of left and right adaptation. In this study, the effect of spatial and temporal frequency on direction specific response topography was investigated.

2 Methods

Nine healthy university students (males, 23.5±1.3 years old) with normal vision participated in this experiment. Test stimulus was 12 sec oscillating vertical sinusoidal grating (0.5 or 2 c/deg, 4 or 9 Hz) that presented immediately after the adaptor of 20 sec drifting grating (2 or 4.5 deg/s) presenting. EEG was recorded during the stimulus using a 64-channel Geodesic Sensor Net with 0.1-50Hz filtering. Participants' perceived direction of MAE was behaviorally recorded using 2-buttons (left and right) during the adaptor and test stimuli presenting. Fundamental frequency (1F) component was extracted from the EEG during the participants perceived MAE by using Fourier analysis.

3 Results

As previously presented [3], for all stimuli (0.5 or 2 c/deg, 4 or 9 Hz), all participants' perceived MAE under motion adaptation conditions. In this report, 1F phase of SSVEP during participants' perceived MAE was extracted. The phase under right-adaptation in over occipital (O1, Oz and O2) and temporal (T2 and T6) cortex area was shifted from that under left-adaptation. The phase shift magnitudes were dependent on spatial and temporal frequency of stimuli and the electrode positions. For 9 Hz, the phase shift magnitude for 0.5 c/deg was maximum at Oz, but not for 2 c/deg (Fig. 1). These spatial and temporal frequency selectivity may indicate that there are several different motion detectors with different sensitivity.

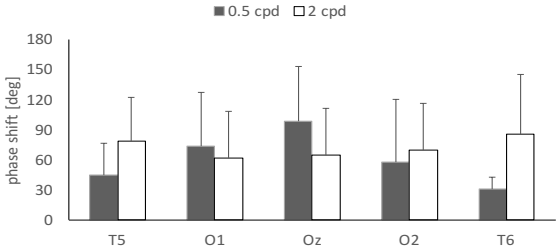

Figure 1: Magnitudes of phase shift between left and right motion adapted SSVEP for 9 Hz

References

[1] J. M. Ales, A. M. Norcia, *JOV*, 9(7):8, pp. 1–13, 2009.

[2] K. Momose, A. Yakovleva, and A. M. Norcia, *14th Annual Meeting of the Vision Sciences Society (VSS2014)*, 2014.5.

[3] S. Arimitsu, K. Momose, *38th Annual International Conference of the IEEE EMBS (EMBC16)*, 2016.8.

Address for correspondence:

Keiko Momose
Faculty of Human Sciences, Waseda University
momose@waseda.jp

Multifractal characteristics of external anal sphincter based on sEMG signals

Paulina Trybek[1,2], Michal Nowakowski[3], Lukasz Machura[1,2]

[1]Silesian Center for Education and Interdisciplinary Research, Chorzow, PL
[2]Department of Theoretical Physics, Institute of Physics, University of Silesia, Katowice, PL
[3]Department of Medical Education, Faculty of Medicine, Jagiellonian University Medical College, Krakow, PL

Abstract

This paper presents the application of Empirical Mode Decomposition based Multifractal Detrended Fluctuation Analysis to the surface electromyography signals obtained from the patients suffering from rectal cancer. The electrical activity of external anal sphincter at different level of treatment is considered. Two different range of scales are determined for the calculation of the multifractal spectra. In addition the results from standard MFDFA and the EMD–based MFDFA method are compared.

Keywords *electromyography, multifractal analysis, empirical mode decomposition*

1 Introduction

Over the last few decades the surface electromyography (sEMG) has become a promising apparatus for the non-invasive analysis of muscles. This work is focused on quite a unique application of the sEMG concerning the diagnosis of anal sphincter function during the treatment process of rectal cancer [1, 2]. Surface EMG is a very promising method of testing of innervation of muscles. Since innervation deficits are one of suggested mechanisms for severe treatment related complications in up to 40% of rectal cancer patients development of proper innervation assessment methodology is crucial. Proper evaluation of sEMG signals remains to be a significant problem inhibiting diagnostic potential of this methodology. Regardless of applications, sEMG always represents highly complex signal with many difficulties in interpretation [3]. Traditional analysis, mainly based on the conventional statistical tests of mean or median brings only limited knowledge on the actual process hidden behind the acquired data.

In the context of biosignal interpretation the Multifractal Detrended Fluctuation Analysis (MFDFA) developed by Kantelhardt et al. [4] became a popular method for the study nonlinear phenomena for all types of data. The MFDFA has been used in many disciplines and still attracts considerable attention in the field of physiology, economy, climatology, to name but a few. In relation to the electrophysiological signals, MFDFA brought a significant contribution to the analysis of heart rate variability [5, 6]. For the Empirical Mode Decomposition (EMD) the equally wide range of applications can be find, including the removal of artifacts and noise reduction from the signal, also in relation to the surface electromyography [7]. An advantage for this method is the lack of requirements for the use of pre testing process. The EMD also exhibits better results in the process of the detrending [8] in comparison for example with the typically used least square method. Here an approach combining EMD and MFDFA named EMD based MFDFA is addressed. This approach outperforms standard MFDFA for large fluctuations [9]. The paper is organized as follows: Section 2 discuss the experimental data. In Section 3, the EMD and MFDFA methods for data analysis are introduced and illustrated with the data under consideration. The results are presented in Section 4. The last section summarizes the results and draws the conclusions.

2 sEMG signal source

Our analysis is focused on the sEMG signals recorded for the external anal sphincter. The electrical activity of this specific muscle group is frequently investigated in the context of the patients with defecation disorders [10]. The sEMG is a non-invasive technique for monitoring of the anal sphincter function [11, 12, 13]. In this work the signals of patients suffering from rectal cancer are considered. The analyzed time series were recorded at four stages: before the treatment (D_1) and one month (D_2), six months (D_3) and one year (D_4) after the surgical procedure. The detailed information about the surgery of the rectal cancer and the role of sEMG for the patient diagnosis can be found in [14]. Rectal cancer remains to be one of the most frequent cancers in humans. It requires complex multimodal treatment composed of surgery, irradiation and chemotherapy. All those methods of treatment can cause significant stool continence related problems hence proper assessment of anorecatal innervation before and after the treatment can be crucial for prevention and treatment of complications. Signals were obtained from 16 pairs of electrodes arranged concentrically at three levels (5cm, 3cm, 1cm) of rectal canal depth. The sampling frequency was 2048 Hz, which for the 10 seconds of the measurement gave 20480 data points. For our calculations signal recorded during voluntary contraction at the depth of 1 cm was used. This specific choice of depth was dictated by the maximal amplitude of EMG signal resulting from the most superficial localisation of external anal sphincter muscle and the biggest bulk of the

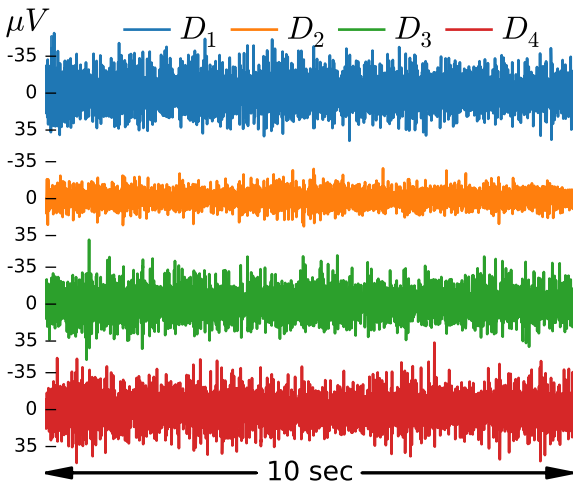

Figure 1: The raw signals at four stages of rectal cancer treatment: D_1 is assigned to the state before surgery, D_2 – D_4 correspond to one month, six months and one year after the surgery, respectively.

muscle at this depth. The signal presented on fig. 1 is in fact the averaged signal from the first 3 channels which corresponds to the first three pairs of the electrodes. The nearest neighbours average was performed due to the fact that the placement of the probe in consecutive measurements could be inaccurate. In other words the specific electrodes may not represent exactly the same placement at the consecutive measurements after the surgery.

3 Fluctuation Analysis

In the following two methods EMD and MFDFA are incorporated in order to characterise sEMG signals presented above. Both techniques can be used to trace out the features of non–linear and non–stationary signals. The EMD is an iterative technique which decomposes the signal into finite number of Intrinsig Mode Functions (IMFs) $c_i(t)$ (1). The final residual $r_n(t)$ stands for the actual trend.

$$x(t) = \sum_{i=1}^{n} c_i(t) + r_n(t) \tag{1}$$

The calculated signal must satisfied two conditions in order to be IMFs: (i) the number of extrema and the number of zero crossing must be equal or differ at most by one; and (ii) the mean value of the upper and lower envelope defined by local maxima and minima must be zero. The standard EMD method often faces some difficulties, which are recurrently the consequence of signal intermittency referred to as Mode Mixing problem [15]. Ensemble Empirical Mode Decomposition (EEMD, 2009) [15] and later Complete Ensemble Empirical Mode Decomposition (CEEMD, 2011) [16] have been proposed in order to overcome this complication. Both methods are based on the averaging over several realisations of Gaussian noise artificially added to the original signal. For this publication, however, we use only standard EMD due to the fact that only residual r_n, i.e. the data trend, is needed for further calculations and none of the individual IMFs are considered here explicitly.

MFDFA is based on the scaling properties of the fluctuations. The brief description of the method is presented below, however, for the detailed description we suggest works by Kantelhardt et al. [4, 17], Ihlen [18] or Salat et al. [19]. The procedure starts with calculation of the profile y_i as the cumulative sum of the data x_i with the subtracted mean $\langle x \rangle$: $y_i = \sum_{k=1}^{i} [x_i - \langle x \rangle]$. Next, the cumulative signal y_i is split into N_s equal non-overlapping segments of size s. Here for the length of the segments we use powers of two, $s = 2^r, r = 4 \ldots 11$. For all segments $v = 1, \ldots, N_s$ the local trend $y^m_{v,i}$ is calculated. At this point our analysis was branched into standard method based on DFA algorithm and non-standard one based on EMD. The former method is based on the least–square fit of the order m. In this work $m = 2$ was chosen. The latter utilizes the fact that the residual r_n represents the local trend, thus the standard polynomial fitting (DFA) can be replaced by a residuum based trend for each segment [8, 20]. An example of local trends calculated with both methods is presented on fig. 2 for the segment size $s = 64$. The slight differences between solid black and red lines, which represent DFA and EMD method, respectively, have strong influence on the resulting fractal spectrum.

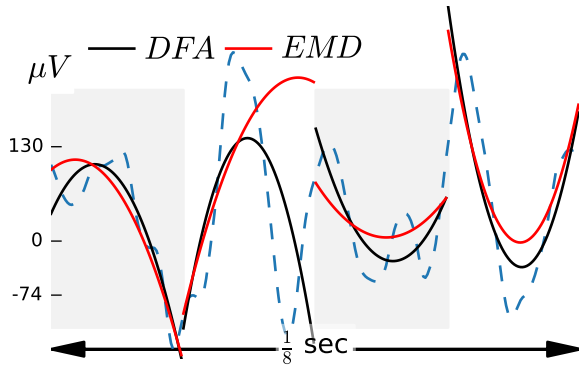

Figure 2: Two detrending methods: DFA (solid black) and EMD (solid red) are presented for the profile y_i of the sEMG data at a stage D_1 (dashed blue). The visible differences result in shifted fractal spectrum.

Next the variance F^2 as a function of the segment size s is calculated for each segment v separately

$$F^2(s,v) \equiv \frac{1}{s} \sum_{i=1}^{s} \left(y^m_{v,i} - y_{v,i} \right)^2 . \tag{2}$$

As the next step the fluctuation function being the q^{th} statistical moment of the calculated variance is determined

$$F_q(s) = \begin{cases} \left(\frac{1}{2N_s} \sum_{v=1}^{2N_s} [F^2(s,v)]^{\frac{q}{2}} \right)^{\frac{1}{q}} & q \neq 0 \\ \exp\left\{ \frac{1}{4N_s} \sum_{v=1}^{2N_s} \ln \left[F^2(s,v) \right] \right\} & q = 0 \end{cases} \tag{3}$$

In the last step the determination of the scaling law $F_q(s) \sim s^{h(q)}$ of the fluctuation function (3) is performed with the use of the log–log plots of $F_q(s)$ versus segment sizes s for all values of q Clearly, MFDFA is not

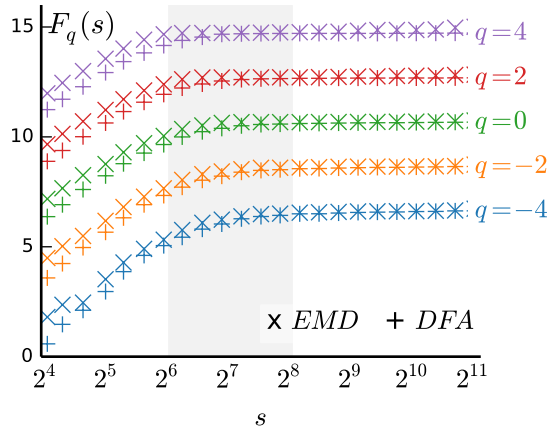

Figure 3: q-th order fluctuation function (3) with both DFA(2) and EMD detrending methods presented for data before the surgery D_1 for selected values of q. Characteristics were artificially shifted for better visibility.

a black–box method and always requires some individual decisions. First of all, the choice of the scaling range can have significant impact on the appropriate estimation of the fluctuation function (F_q) and consequently the final results [6, 18]. The length of the analyzed time series N consists of 20480 data points. For the calculations presented in this work, the considered range of scales are between $s \in [2^4, 2^{11}]$. The q-order parameter should consist of positive and negative values in order to detect periods with small and large fluctuations [18]. In our case $q \in [-5, 5]$ were chosen. The set of q-order fluctuation functions F_q *vs* segment size s is presented in Fig. 3. The two different scale ranges are clearly visible for all $F_q(s)$ characteristics. This bisection into two distinct scaling regimes plays a crucial role for determination the q-order Hurst exponent $h(q)$ and wherefore on the further analysis. The Fig. 3 presents results for DFA and EMD based detrending method. Two separate scaling domains was accepted, namely $s \in [2^4, 2^6]$ and $s \in [2^8, 2^{10}]$. Further analysis have been performed for both of this regions. The middle values $s \in (2^6, 2^8)$ are omitted, as there is no clear linear scaling present.

4 Multifractal spectra

The q-order Hurst exponent $h(q)$ is required in order to calculate the further dependencies. First quantity is the mass exponent obtained from $\tau(q) = qh(q) - 1$. It is than used to calculate a q–order singularity exponent $\alpha = \tau'(q)$ where the prime means differentiation with the respect to the argument. This quantity is also known as a Hölder exponent. From the above the q–order singularity dimension

$$f(\alpha) = q\alpha - \tau(q) = q[\alpha - h(q)] + 1. \qquad (4)$$

can be constructed. The singularity dimension $f(\alpha)$ is related to the mass exponent $\tau(q)$ by Legendre transform. The multifractal spectrum, i.e. the dependence $f(\alpha)$ vs α is the final result of MFDFA method.

For all of the examined cases and for all four levels of treatment process D_1 – D_4 the wide spectra for the short scales $s < 2^6$ can be observed. For the large scales $s > 2^8$ the small sets of points located around $\{0, 1\}$ is visible, c.f. Fig. 4. This indicates the multifractal character of the sEMG signal for the short scales $s < 2^6$ and rather monofractal character for large scales $s > 2^8$. On the comparison of the spectra obtained by the two methods a shift towards the smaller values of α (left) side of the spectrum for the small scales $s < 2^6$ is visible for all sEMG signals in the case of the EMD–based–MFDFA.

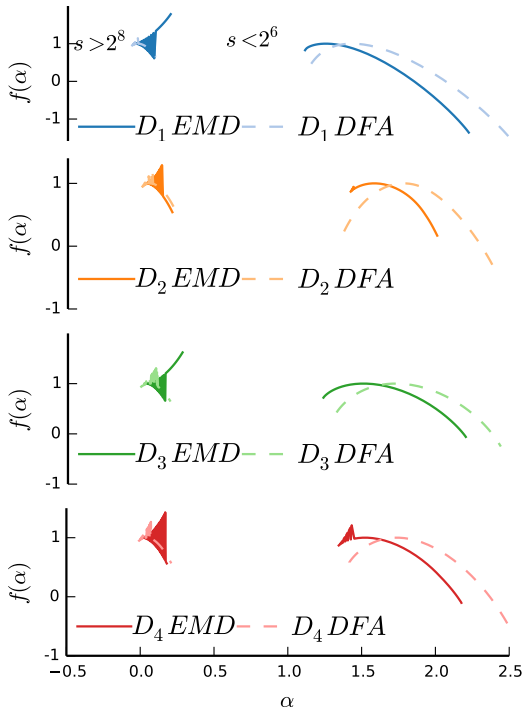

Figure 4: Multifractal spectrum calculated at the four stages of rectal cancer treatment D_1 – D_4. At each panel two sets of distinct spectra can be found: right which corresponds to the scaling region $s < 2^6$ and left for $s > 2^8$. For each scaling regions two spectra are presented – for the EMD-based MFDFA (dark solid lines) and standard DFA-based MFDFA (light dashed lines). One can notice the generally found degeneracy of the spectra for $s > 2^8$ and the shift towards the smaller values of α for the EMD-based detrending.

5 Conclusions

The paper tests the multifractal character of the surface electromyography signal recorded at the external anal sphincter. The multifractal spectra calculated with the standard Multifractal Detrended Fluctuation Analysis is compared with Empirical Mode Decomposition based MFDFA. Table 1 presents the average values of

the spectrum width $\langle\Delta\rangle$ and the specific singularity exponent $f(\alpha_{max}) = 1$ which corresponds to the maximum of the spectrum calculated for all of the 16 electrodes at each treatment state. For all the analyzed time series, two distinct scaling regions were identified. The spectra calculated for both regions exhibit the shift in the case of short scales.he non-standard EMD-based-MFDFA shifts the spectrum towards the lower values of singularity exponent α – c.f. Fig. 4 and table 1. For the large scales $s > 2^8$ both multifractal methods suggests only monofractal properties of the sEMD signal.

Table 1: Average values of the spectrum width $\langle\Delta\rangle$ and maximum of spectrum α_{max} together with the standard deviations presented for all channels at each state of the treatment D_1 – D_4. Results are presented for MFDFA and EMD based MFDFA method.

Average spectrum width $\langle\Delta\rangle$ for s $< 2^6$				
	D_1	D_2	D_3	D_4
DFA	1.381 $\pm$ 0.348	1.364 $\pm$ 0.320	1.427 $\pm$ 0.243	1.401 $\pm$ 0.264
EMD	1.096 $\pm$ 0.176	1.086 $\pm$ 0.264	1.254 $\pm$ 0.254	1.124 $\pm$ 0.276
Average spectrum width $\langle\Delta\rangle$ for s $> 2^8$				
DFA	0.076 $\pm$ 0.017	0.085 $\pm$ 0.019	0.08 $\pm$ 0.02	0.099 $\pm$ 0.019
EMD	0.049 $\pm$ 0.014	0.059 $\pm$ 0.20	0.049 $\pm$ 0.017	0.071 $\pm$ 0.021
Maximum of the spectrum α_{max} for s $< 2^6$				
DFA	1.596 $\pm$ 0.055	1.583 $\pm$ 0.103	1.620 $\pm$ 0.071	1.608 $\pm$ 0.101
EMD	1.390 $\pm$ 0.053	1.390 $\pm$ 0.91	1.410 $\pm$ 0.066	1.404 $\pm$ 0.087
Maximum of the spectrum α_{max} for s $> 2^8$				
DFA	0.019 $\pm$ 0.003	0.022 $\pm$ 0.002	0.019 $\pm$ 0.003	0.021 $\pm$ 0.003
EMD	0.011 $\pm$ 0.003	0.012 $\pm$ 0.004	0.010 $\pm$ 0.004	0.010 $\pm$ 0.002

Acknowledgements

This work was partially supported by the JUMC research grant: K/ZDS/006369.

References

[1] M. Nowakowski, K. A. Tomaszewski, R. M. Herman, J. Sałówka, M. Romaniszyn, M. Rubinkiewicz, and J. A. Walocha, International journal of colorectal disease **29**, 747 (2014).

[2] R. Merletti, A. Bottin, C. Cescon, D. Farina, M. Gazzoni, S. Martina, L. Mesin, M. Pozzo, A. Rainoldi, and P. Enck, Digestion **69**, 112 (2004).

[3] E. Clancy, E. L. Morin, and R. Merletti, Journal of Electromyography and Kinesiology **12**, 1 (2002).

[4] J. W. Kantelhardt, S. A. Zschiegner, E. Koscielny-Bunde, S. Havlin, A. Bunde, and H. E. Stanley, Physica A: Statistical Mechanics and its Applications **316**, 87 (2002).

[5] D. Makowiec, A. Rynkiewicz, R. Gałaska, J. Wdowczyk-Szulc, and M. Żarczyńska-Buchowiecka, EPL (Europhysics Letters) **94**, 68005 (2011).

[6] J. Gierałtowski, J. Żebrowski, and R. Baranowski, Physical Review E **85**, 021915 (2012).

[7] A. O. Andrade, S. Nasuto, P. Kyberd, C. M. Sweeney-Reed, and F. Van Kanijn, Biomedical Signal Processing and Control **1**, 44 (2006).

[8] D. Liu, M. Luo, Q. Fu, Y. Zhang, K. M. Imran, D. Zhao, T. Li, and F. M. Abrar, Water Resources Management pp. 1–18 (2015).

[9] X.-Y. Qian, G.-F. Gu, and W.-X. Zhou, Physica A: Statistical Mechanics and its Applications **390**, 4388 (2011).

[10] A. López, B. Y. Nilsson, A. Mellgren, J. Zetterström, and B. Holmström, Diseases of the colon & rectum **42**, 482 (1999).

[11] P. Enck, H. Hinninghofen, R. Merletti, and F. Azpiroz, Neurogastroenterology & Motility **17**, 60 (2005).

[12] D. W. Kauff, N. Wachter, A. Heimann, T. B. Kruger, K. P. Hoffmann, H. Lang, and W. Kneist, Eur Surg Res **57**, 81 (2016).

[13] C. Cescon, L. Mesin, M. Nowakowski, and R. Merletti, J Electromyogr Kinesiol **21**, 394 (2011).

[14] G. G. Delaini, M. Scaglia, G. Colucci, and L. Hultén, in *Rectal Cancer* (Springer, 2005), pp. 147–155.

[15] Z. Wu and N. E. Huang, Advances in adaptive data analysis **1**, 1 (2009).

[16] M. Torres et al, IEEE Int. Conf. on Acoust., Speech and Signal Proc. ICASSP **11**, 4144 (2011).

[17] J. W. Kantelhardt, in *Mathematics of complexity and dynamical systems* (Springer, 2012), pp. 463–487.

[18] E. A. Ihlen, Fractal Analyses: Statistical And Methodological Innovations And Best Practices p. 97 (2012).

[19] H. Salat, R. Murcio, and E. Arcaute, arXiv preprint arXiv:1606.02957 (2016).

[20] P. Caraiani, PloS one **7**, e40693 (2012).

Address for correspondence:

Paulina Trybek
University of Silesia, Institute of Physics
ul. Uniwersytecka 4, 40 - 007 Katowice, Poland
paulina.trybek@smcebi.edu.pl

Random point process modeling of the spike trains in response to sinusoidally modulated pulsatile electric stimuli in auditory nerve fiber models

Hiroyuki Mino[1]

[1]Department of Electrical Engineering, Kanto Gakuin University, Japan;

Abstract

This paper presents modeling of the spike trains of auditory nerve fiber (ANF) models stimulated by sinusoidally modulated pulsatile electric stimuli with inhomogeneous Poisson processes. It was investigated whether or not the intensity function of inhomogeneous Poisson process was represented by a periodic function of von Mises distribution. The results of computer simulations show that the intensity function estimated from the parameters of von Mises distribution is agreed well with the post-stimulus time histogram at a smaller modulation depth by performing the goodness-of-fit hypothesis test, Kuiper's test. These findings may play a key role in determining optimal parameters of pulsatile electric stimuli, and further in the design of better auditory neural prostheses.

Keywords *Random Point Process, Electrical Stimulation, Auditory Neural Prostheses*

1 Introduction

Periodic or cyclic phenomena have been quantitatively analyzed by directional statistics, like von Mises distribution, [1]. The auditory nerve spikes in response to natural sound pressure have also been expressed as directional statistics with random point processes [2], [3],[4].

However, it is yet unclear whether or not the electrically stimulated auditory nerves could be represented by inhomogeneous Poisson process [5] with the intensity function specified by a periodic function of von Mises distribution, although some research regarding a point process framework has been reported [6].

The objective of this article was to investigate whether or not the spike trains in response to sinusoidally modulated pulsatile electric stimuli could be modeled by inhomogeneous Poisson process whose intensity function was represented by a periodic function of von Mises distribution through computer simulations.

The intensity function of inhomogeneous Poisson process, $\lambda(t)$, can be expressed as a periodic function of von Mises distribution:

$$\begin{aligned} \lambda(t) &= \lim_{\Delta \to 0} \frac{Pr[N[t, t+\Delta) = 1]}{\Delta} \\ &= X exp(\kappa cos(2\pi f t + \mu)) \end{aligned} \quad (1)$$

where $N(t)$ denotes the counting process, f denotes sinusoidal frequency, and κ, and μ denote the parameters of von Mises distribution. X stands for the parameter relating to the firing rate.

In this study, the validity of modeling is assessed by performing the single sample goodness-of-fit hypothesis test, Kuiper's test [9], as the modulation depth of sinusoidally modulated pulsatile electric stimuli is varied.

2 Methods

The ANFs were represented by a multi-compartment cable model with a spiral ganglion with a diameter of 27 μm, and 40 nodes of Ranvier. The parameters of the ANF model are described in [7]. The 40 nodes of Ranvier consisted of stochastic ion channels, 180 sodium channels, and 100 potassium channels, in order to generate plausible neural responses, like those observed in cat single-fiber experiments. The stochastic ion channels were implemented by the computationally efficient channel-number-tracking algorithm [8].

The transmembrane potentials of 200 ms in time length were generated for each simulation in which sampling steps were set at 2 μs. The stimulating electrode was located at a distance of 1 mm above the 2nd node of Ranvier. The stimulating current, $I_{stim}(t)$, was expressed as:

$$I_{stim}(t) = I_{pulse}(t)\{1 + \frac{m}{100} sin(2\pi f t + \Phi)\} \quad (2)$$

where f stands for the sinusoidal frequency set at 20 Hz, Φ denotes a randomized initial phase taking a value between 0 and 2π, m designates a modulation depth, set at 5, 8, 10, 12, 15, 17, or 20 $\%$ and where $I_{pulse}(t)$ denotes the unmodulated biphasic, periodic pulsatile waveform at a pulse amplitude of 0.275 mA, a pulse frequency of 250 Hz, and a pulse duration of 40 μs.

The spike firing time was detected by determining when the transmembrane potential took the peak amplitude and was greater than 50% of the peak amplitude of typical action potentials. The post-stimulus time (PST) histogram and period histogram were generated from the spike trains in response to the stimulating current presented repeatedly 150 times.

The parameters of von Mises distribution were estimated from sample realizations of the spike trains of the ANF models in response to sinusoidally modulated low-rate pulsatile electric stimuli by maximizing the log like-

lihood function of inhomogeneous Poisson process:

$$\begin{aligned} L(N(t)|\theta) &= -\int_0^T \lambda(\sigma)d\sigma + \int_0^T ln[\lambda(\sigma)]dN(\sigma) \\ &= X\int_0^T e^{\kappa cos(2\pi f\sigma+\mu)}d\sigma + N(T)ln(X) \\ &+ \kappa\int_0^T cos(2\pi f\sigma+\mu)dN(\sigma) \end{aligned} \quad (3)$$

where $\theta = [X\ \kappa\ \mu]^T$ denotes the parameters of von Mises distribution.

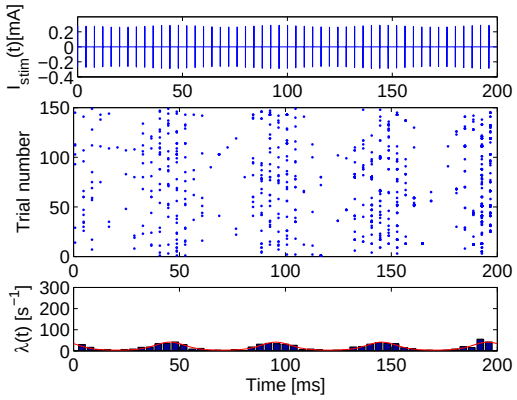

Figure 1: The stimulating current waveform (top), the dot raster plot (middle), and PST histogram (bottom) with the intensity function estimated from the parameters of von Mises distribution (thick red line) at $\hat{X}$=11.67, $\hat{\kappa}$=1.26, and $\hat{\mu}$=0.56, those corresponding to a firing rate of 16.77, and a vector strength of 0.53 at f =20 Hz and m= 5 %.

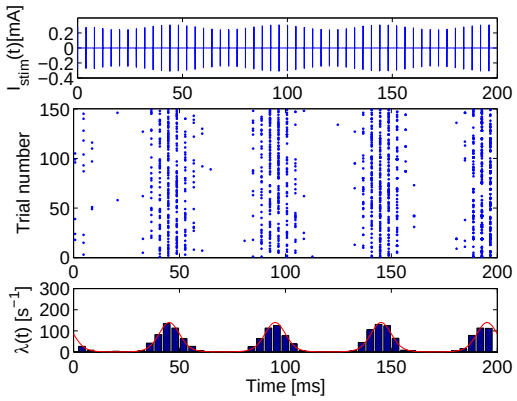

Figure 2: The stimulating current waveform (top), the dot raster plot (middle), and PST histogram (bottom) with the intensity function estimated from the parameters of von Mises distribution (thick red line) at $\hat{X}$=8.91, $\hat{\kappa}$=2.74, and $\hat{\mu}$=0.60, those corresponding to a firing rate of 35.57, and a vector strength of 0.78 at f =20 Hz and m= 12 %.

The single sample goodness-of-fit hypothesis test, Kuiper's test, was performed to determine if the random sample data could have the hypothesized continuous cumulative distribution function. The null hypothesis in this study is as follows: "The periodic spike timing data are sampled from a population of von Mises distribution". The significance level was set at 5 %. Kuiper's test is utilized for directional or circular data, instead of Kolmogorov-Smirnov (K-S) test, since the K-S test tends to be sensitive around median value of the distribution and less sensitive at the distribution tails.

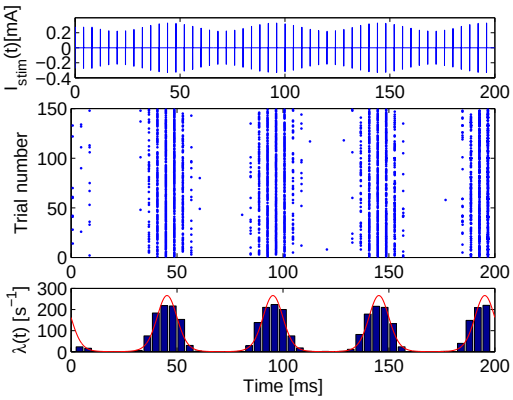

Figure 3: The stimulating current waveform (top), the dot raster plot (middle), and PST histogram (bottom) with the intensity function estimated from the parameters of von Mises distribution (thick red line) at $\hat{X}$=14.70, $\hat{\kappa}$=2.90, and $\hat{\mu}$=0.59, those corresponding to a firing rate of 65.97, and a vector strength of 0.79 at f =20 Hz and m= 20 %.

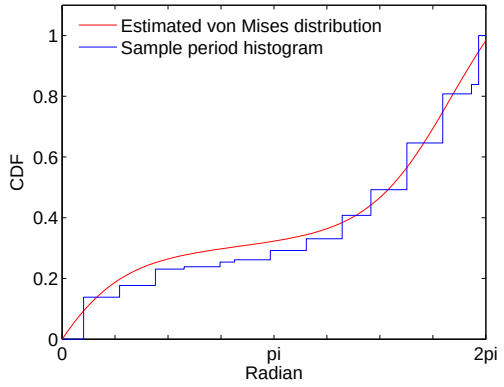

Figure 4: The cumulative distribution function (CDF) of von Mises distribution as a function of angle [0, 2π) and the sample cumulative distribution function calculated from the period histogram at f =20 Hz and m= 5 %. The null hypothesis that the sample was taken from a population with cumulative distribution function was not rejected at a significance level of 5 % according to single sample goodness-of-fit hypothesis test for directional statistics, Kuiper's test.

3 Results

The sinusoidally modulated pulsatile electric stimuli as a function of time for 200 ms at f= 20 Hz and m= 5, 12,

and 20 % are depicted in the top row of Figs. 1, 2, and 3. The dot raster plots of 150 spike trains are shown in the middle row of figures. The post-stimulus time (PST) histogram is drawn with a bin width of 4 ms in the bottom row of figures, and the intensity function calculated from the estimated parameters is superimposed as well.

The parameters of von Mises distribution were estimated with the maximum likelihood method from 150 sample realizations of the spike trains: $\hat{X}$=11.67, $\hat{\kappa}$=1.26, and $\hat{\mu}$=0.56 at m= 5 %, $\hat{X}$=8.91, $\hat{\kappa}$=2.74, and $\hat{\mu}$=0.60 at m= 12 %, and $\hat{X}$=14.70, $\hat{\kappa}$=2.90, and $\hat{\mu}$=0.59 at m= 20 %.

At m= 5 %, the intensity function estimated from the parameters described above looks similar to PST histogram, as shown in Fig.1, but the vector strength (VS = 0.53) calculated from κ is not good enough, since an optimal value of VS is found to be about 0.7-0.8 in a single auditory nerve fiber [10]. The estimated intensity function shows a good agreement with the PST histogram, and the VS is estimated to be 0.78, at m= 12 %, as shown in Fig. 2. At m= 20 %, the estimated intensity function would look a little bit different than PST histogram, as shown in Fig.3. The intensity function estimated from the parameters of von Mises distribution is shown to be a good agreement qualitatively with the PST histogram obtained from the spike trains in response to the electric stimuli repeatedly presented 150 times, as shown in the bottom row of Figs 1-3.

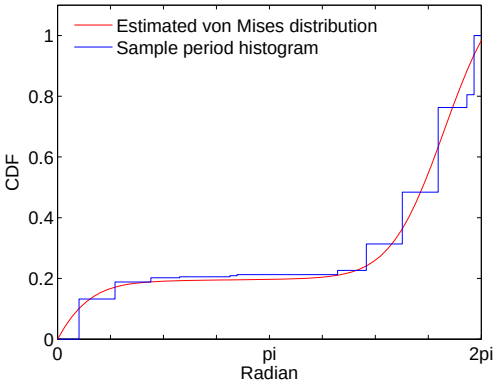

Figure 5: The cumulative distribution function (CDF) of von Mises distribution as a function of angle [0, 2π) and the sample cumulative distribution function calculated from the period histogram at f =20 Hz and m= 12 %. The null hypothesis that the sample was taken from a population with cumulative distribution function was not rejected at a significance level of 5 % according to single sample goodness-of-fit hypothesis test for directional statistics, Kuiper's test.

To quantitatively assess the goodness-of-fit of von Mises distributions, Kuiper's test [9] was performed for period histogram at a significance level of 5 %, while the modulation depth m was varied as 5, 8, 10, 12, 15, 17, and 20 %.

Fig.4 shows the cumulative distribution function

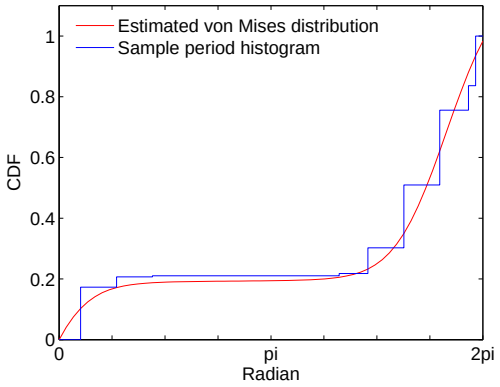

Figure 6: The cumulative distribution function (CDF) of von Mises distribution as a function of angle [0, 2π) and the sample cumulative distribution function calculated from the period histogram at f =20 Hz and m= 20 %. The null hypothesis that the sample was taken from a population with cumulative distribution function was rejected at a significance level of 5 % according to single sample goodness-of-fit hypothesis test for directional statistics, Kuiper's test.

(CDF) of von Mises distribution as a function of angle [0, 2π) and the sample cumulative distribution function calculated from the period histogram at f =20 Hz and m= 5 % (See the bottom row of Fig. 1). The null hypothesis that the sample data were taken from a population of von Mises distribution was not rejected at a significance level of 5 % and at m= 5 %.

Fig.5 also shows the CDF of von Mises distribution and the sample cumulative distribution function calculated from the period histogram at f =20 Hz and m= 12 % (See the bottom row of Fig. 2). The null hypothesis was not rejected at a significance level of 5 % and at m= 12 %.

At m= 20 %, the null hypothesis was rejected at a significance level of 5 %, due to the difference between two curves in Fig. 6, like the curve of the intensity function looks different from that of the PST histogram in the bottom of Fig.3.

It is summarized that the null hypothesis was not rejected at m = 5, 8, 10, and 12 %, whereas the null hypothesis was rejected at m = 15, 17, and 20 %. It follows that the goodness-of-fit tended to disappear as the modulation depth m was increased greater than about 15 %, since the shape of period histogram tended to be close to uniform distribution.

4 Concluding remarks

It has been shown that the spike trains of ANF models in response to sinusoidally modulated pulsatile electric stimuli can be modeled by inhomogeneous Poisson process whose intensity function is represented by a periodic function of von Mises distribution, when the modulation depth m is set at or below 12 %. At a modulation depth

greater than 12 %, the goodness-of-fit hypothesis was rejected by Kuiper's test with a significance level of 5 % due to a saturation of spike firing rates.

It follows from the above that the modulation depth is related to the parameters of von Mises distribution, and likewise that the stimulating waveforms can be expected to be determined on the basis of the parameters of von Mises distribution, X, and κ, under the situation where the spike firing rate is not saturated.

However, the modeling of inhomogeneous Poisson process without temporal history in the present study would not be good enough, because the neural spike trains are usually considered a random point process with spike timing history due to neural refractoriness. It would be worthwhile to incorporate the spike firing history into random point processes, when the vibration of sinusoidal modulation waveform could not be fast enough compared to neural refractory periods. Likewise, in the present study, statistical analyses were performed for only three cases, and the modulation frequency was set just for one case. Therefore, it would be necessary to access the validity of the proposed model as the parameters are widely varied in future investigations.

In conclusion, these findings may play a key role in determining optimal parameters of pulsatile electric stimuli, and further in the design of better auditory neural prostheses.

Acknowledgements

This work was supported by JSPS KAKENHI Grant Number JP15K01397.

References

[1] K. V. Mardia, and P. E. Jupp, ***Directional Statistics***, John Wiley and Sons, Chichester, 1999.

[2] G. Ashida, H. Wagner, and C. E. Carr, Processing of Phase-Locked Spikes and Periodic Signals, in ***Analysis of Parallel Spike Trains*** . Sonja Grun, and Stefan Rotter, Editors, New York, Springer, pp.59-74, 2010.

[3] J. L. van Hemmen, A. Longtin, A. N. Vollmayr AN, Testing resonating vector strength: auditory system, electric fish, and noise, Chaos, 21, 047508, 2011.

[4] J. L. van Hemmen, Vector strength after Goldberg, Brown, and von Mises: biological and mathematical perspectives, Biol Cybern., 107, pp.385396, 2013.

[5] D. L. Snyder and M. I. Miller, ***Random Point Processes in Time and Space***, Second Edition, Springer-Verlag, New York, 1991.

[6] J. H. Goldwyn, E. Shea-Brown, J. T. Rubinstein, Encoding and decoding amplitude-modulated cochlear implant stimuli – a point process analysis, J. Comput. Neurosci., 28, pp.405424, 2010.

[7] H. Mino, Encoding of Information Into Neural Spike Trains in an Auditory Nerve Fiber Model with Electric Stimuli in the Presence of a Pseudospontaneous Activity IEEE Trans. on Biomed. Eng., 54, pp.360-369, 2007.

[8] H. Mino, J. T. Rubinstein, J. A. White, Comparison of Computational Algorithms for the Simulation of Action Potentials with Stochastic Sodium Channels. Ann. Biomed. Eng. 30, 578-587, 2002.

[9] M. A. Stephens, The goodness-of-fit statistic Vn. distribution and significance points, Biometrika, 52, No. 3-4, pp.309-321, 1965.

[10] P. X. Joris, D. H. Louage, L. Cardoen, and M. van der Heijden, Correlation Index: A new metric to quantify temporal coding Hearing Research, 216217, pp.1930, 2006.

Address for correspondence:

Hiroyuki Mino
Kanto Gakuin University
mino@ieee.org

Activity Analysis of Neuronal Networks with Altered Excitatory/Inhibitory Balance

S Iida[1], K Shimba[1,2,3], K Kotani[4,5], Y Jimbo[1],

1School of Engineering, The University of Tokyo, Japan;
2School of Engineering, Tokyo Institute of Technology, Japan;
3Japan Society for the Promotion of Science, Japan;
4Research Center for Advanced Science and Technology, The University of Tokyo, Japan;
5JST PRESTO, Japan;

Abstract

Cerebral cortex contains two types of neurons, excitatory (glutamatergic) and inhibitory (GABAergic) neurons. The ratio of both neurons is important to maintain cortical function. In order to elucidate the contribution of GABA-mediated inhibition to cortical function, it is important to know how spontaneous activity patterns of neuronal network are modulated by alteration in excitation/inhibition balance. We aimed to construct neuronal networks with various excitatory/inhibitory conditions in vitro using induced pluripotent stem (iPS) cells, and to analyze activity patterns of the iPS cell-derived neuronal networks using a microelectrode array.

Keywords *Induced pluripotent stem cell-derived neurons, Excitation/inhibition balance, Cortical neuronal network, Network burst*

1 Introduction

Cerebral cortex contains two types of neurons, excitatory and inhibitory neurons. The excitation/ inhibition balance is important to maintain cortical function. Excessive excitation can cause neurological disorders such as autism, schizophrenia and epilepsy [1][2]. In order to elucidate the contribution of GABA-mediated inhibition to maintenance of cortical function, it is important to know how spontaneous activity patterns of neuronal network are modulated by alteration in excitation/inhibition balance. However, it is difficult to alter neuronal network structure or ratio of excitatory/inhibitory neurons *in vivo*.

Here, we aimed to construct neuronal networks with various excitatory/inhibitory conditions *in vitro* using induced pluripotent stem (iPS) cells, and to record and analyze activity patterns of the neuronal networks using a microelectrode array (MEA) [3].

2 Methods

2.1 Neural Induction of iPS Cells

Mouse iPS cells were induced to differentiate into cortical excitatory/inhibitory neurons selectively. The mouse iPS cell line (iPS-Stm-FB/gfp-99-1) [4][5] was provided by RIKEN Bio Resource Center through the Project for Realization of Regenerative Medicine and the National Bio-Resource Project of the MEXT, Japan.

We constructed three types of neuronal populations from iPS cells with morphogen-based induction methods: (1) excitatory-rich population (Exc), in which cyclopamine was supplemented to medium; (2) inhibitory-rich population (Inh), in which smoothened agonist was supplemented; (3) morphogen-free control population (Cont), in which no morphogen was supplemented and mixture of excitatory/inhibitory neurons was expected to be formed. Cyclopamine and smoothened agonist induces the dorsal and ventral part of the forebrain, where excitatory and inhibitory neurons are derived *in vivo*, respectively [6]. Neural induction was initiated 6 days before seeding on MEAs.

2.2 Activity Recording and Analysis

Activity patterns of iPS cell-derived neurons were recorded and analyzed. Three types of neuronal populations induced with the morphogen-based methods were passaged onto MEAs separately (day 0). From day 5, spontaneous activity was recorded for 20 min once a week.

Relationships between neuronal activity patterns and neuronal network conditions were analyzed. Synchronized network bursts between multiple electrodes were detected with a method reported in a previous study [7]. For evaluation of burst dominance level in neuronal activity, an index named Burstiness was used. Burstiness indicates a ratio of the number of spikes included in network bursts to all detected spikes.

3 Results and Discussion

3.1 Neural Differentiation

Fig. 1 (*upper*) shows an immunofluorescent image of the differentiated cells on day 3. Nestin$^+$ fibers (red) and microtubule- associated protein 2 (MAP2)$^+$ cells (green) were observed. Nuclei were stained with DAPI (blue). In Fig. 1 (*lower*), on day 9, β3-tubulin$^+$ processes (blue) are shown. Some of those processes co-localized GABA (red) in all three iPS cell-derived cell

populations induced with the morphogen-based methods. The results of the immunocytochemistry indicate that iPS cells differentiated to Nestin^{+} neural stem cells and finally to neurons including GABAergic neurons. Thus, we successfully induced neural differentiation of mouse iPS cells.

3.2 Maturation and Bursts of Neurons

As a result of MEA recording, in all iPS cell-derived cell populations, spontaneous activities were observed at a multiple electrodes on day 12, although there were few activities on day 5. Spike frequency increased gradually until about 1 month and became stable. From day 12, network burst activities among several electrodes were observed, especially strongly in Exc, although there were few bursts in Inh. About 1 month after seeding, burst rate, inter-burst interval (IBI), burst duration, and Burstiness reached steady state in all three populations. In addition, Burstiness level in each of three populations was different, namely, high, middle and low level in Exc, Cont and Inh, respectively.

According to the results of MEA recording, it is suggested that iPS cell-derived neurons acquired a neuronal property between day 5 and 12 and that excitatory synapses were formed by day 12. Developmental changes in the indices, such as spike rate, burst rate, IBI, burst duration and Burstiness, show that it took about 1 month for iPS cell-derived neurons to mature. Moreover, the level of Burstiness was the highest in Exc and the lowest Inh. This difference might be because of the network condition. In other words, in Exc and Inh, more glutamatergic and GABAergic neurons were formed, and glutamate-mediated excitation and GABA-mediated inhibition might be dominant, respectively.

Taken together, our results indicate that neurons differentiated from iPS cells with selective induction methods can be a suitable tool for studying the contribution of GABA-mediated inhibition to neuronal network activity.

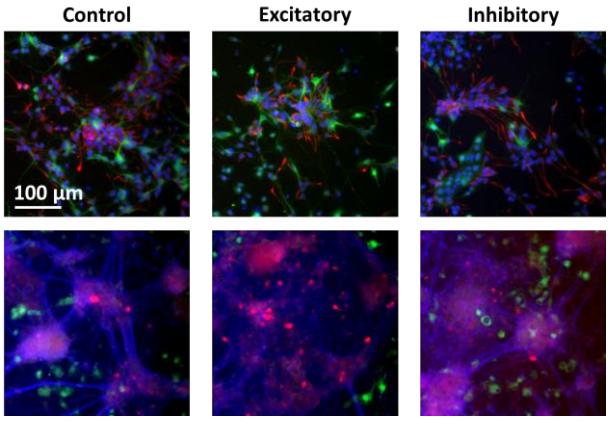

Figure 1: Mouse iPS cell-derived neural cells.

4 Conclusion

In this study, mouse iPS cells were differentiated into neurons including GABAergic neurons with morphogen-based selective induction methods. Spontaneous activities and synchronized firing of iPS cell-derived neuronal populations were observed by MEA recording, suggesting that they functionally matured and formed synaptic connections. Therefore, our culture system combining iPS cell-derived neurons with MEA can be of use in elucidating the role of GABAergic neurons in cortical network. In the future, we plan to confirm and control excitatory/inhibitory ratio in mouse iPS cell-derived neuronal networks induced with selective induction methods.

Acknowledgements

This work is partially supported by KAKENHI (16H03162, 16K12870).

References

[1] J. F. Cryan and K. Kaupmann. Don't worry 'B' happy!: a role for $GABA_B$ receptors in anxiety and depression. *Trends Pharmacol. Sci.*, 26:36–43, 2005.

[2] P. Levitt, K. L. Eagleson, and E. M. Powell. Regulation of neocortical interneuron development and the implications for neurodevelopmental disorders. *Trends Neurosci.*, 27:400–406, 2004.

[3] Y. Jimbo, N. Kasai, K. Torimitsu, T. Tateno, and H. P. C. Robinson. A system for MEA-based multisite stimulation. *IEEE Trans. Biomed. Eng.*, 50:241–248, 2003.

[4] K. Okita, M. Nakagawa, H. Hyenjong, T. Ichisaka, and S. Yamanaka. Generation of mouse induced pluripotent stem cells without viral vectors. *Science*, 322:949–953, 2008.

[5] T. Aoi, K. Yae, M. Nakagawa, T. Ichisaka, K. Okita, K. Takahashi, T. Chiba, and S. Yamanaka. Generation of pluripotent stem cells from adult mouse liver and stomach Cells. *Science*, 321:699–702, 2008.

[6] T. Danjo, M. Eiraku, K. Muguruma, K. Watanabe, M. Kawada, Y. Yanagawa, J. L. R. Rubenstein, and Y. Sasai. Subregional specification of embryonic stem cell-derived ventral telencephalic tissues by timed and combinatory treatment with extrinsic signals. *J. Neurosci.*, 31:1919–1933, 2011.

[7] J. van Pelt, P. S. Wolters, M. A. Corner, W. L. C. Rutten, and G. J. A. Ramakers. Long-term characterization of firing dynamics of spontaneous bursts in cultured neural networks. *IEEE Trans. Biomed. Eng.*, 51:2051–2062, 2004.

Address for correspondence:

Shoko Iida
School of Engineering, The University of Tokyo, Japan
iida@neuron.t.u-tokyo.ac.jp

sEMG power spectrum after rectal cancer surgery

Lukasz Machura[1,2], Paulina Trybek[1,2], Michal Nowakowski[3]

[1]Silesian Center for Education and Interdisciplinary Research, Chorzow, Poland;
[2]Department of Theoretical Physics, Insitute of Physics, University of Silesia, Katowice, Poland;
[3]Department of Medical Education, Jagiellonian University Medical College, Krakow, Poland

Abstract

The power spectral density analysis of the medical signals obtained from the patients suffering from rectal cancer is presented. The exponential and stretched–exponential behaviour of the electrical activity of external anus sphincter are found and presented for all stages of medical treatment.

Keywords *electromyography, spectral density, stretched exponential*

1 Introduction

Around 14 million of new cases and 8 million of cancer related deaths are recorded each year [1]. There are more than 100 types of cancers. In fact any part of the body can be affected. Colorectal cancer can be found among 5 most common types of cancer that kill both men and women. Cancers of major public health relevance such as breast, cervical and colorectal cancer can be cured if detected early and treated adequately. Here we focuse on quite a unique application of the sEMG concerning the diagnosis of anal sphincter function during the treatment process of rectal cancer [2, 3].

2 sEMG power spectral density

Any time series $x_n, n = 1, \ldots, N$ possesses a corresponding frequency spectrum. For a discrete time variable x_n one can define a power spectral density (PSD), which describes the distribution of power of a signal over frequency. It is given by a truncated Fourier transform of a signal

$$PSD = \tilde{S}_{xx}(\omega) = \frac{(\Delta t)^2}{T}\left|\sum_{n=1}^{N} x_n e^{-i\omega n}\right|^2 .$$

The analyzed time series were recorded for 10 seconds at four stages: before the treatment (D_1) and one month (D_2), six months (D_3) and one year (D_4) after the surgical procedure [4]. The signals were obtained from 16 pairs of the electrodes arranged concentrically at the three levels (5cm, 3cm, 1cm) of rectal canal depth. The sampling frequency was 2048 Hz.

The detailed description of the PDS calculated by means of direct Fourier transform and the Welch method will be presented in details for all stages and for all 16 channels at three depths. Fig. 1 presents the PSD and three fits of the stretched–exponential function $S(f) = A\exp[-(f/\lambda)^{\beta}]$ for the averaged signal from the first 3 channels which corresponds to the first three pairs of the electrodes 1 month after the surgery. This particular characteristics seem to be the general case for the sEMG signals acquired from anal sphincter.

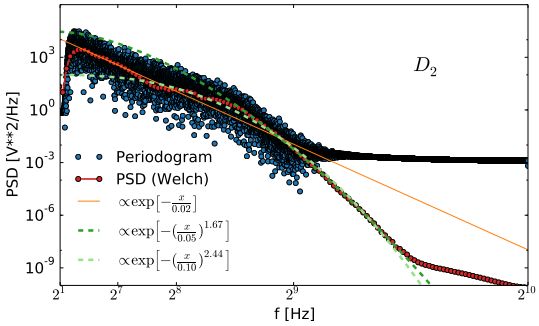

Figure 1: Power spectral density of the sEMG signals acquired from the anal sphincter 1 month after the surgery D_2.

Acknowledgements

This work was partially supported by the JUMC research grant: K/ZDS/006369.

References

[1] B Stewart, et al., World cancer report 2014, WHO.

[2] M Nowakowski, et al. *Int J Colorectal Dis* **29** 747 (2014).

[3] R Merletti, et al. *Digestion* **69** 112 (2004).

[4] GG Delaini, et al. in *Rectal Cancer*, p147–155. Springer (2005).

Address for correspondence:

Lukasz Machura
Department of Theoretical Physics, Insitute of Physics, University of Silesia, Katowice, Poland
lukasz.machura@smcebi.edu.pl

The relationship between recovery from muscle fatigue of the skeletal muscle and magnetic stimulation

Yuya Yokota1, Atsuo Nuruki1

1Depertment of Information Science and Biomedical Engineering Faculty of Engineering, Kagoshima University, Japan;

Abstract

Muscle fatigue is common in everyday life and sports. Magnetic stimulation therapy is known to be effective for early recovery from muscle fatigue. However, the mechanism is still unknown. In order to clarify the mechanism of magnetic stimulation effect on muscle fatigue, we performed magnetic stimulation on the muscle during isometric contraction for fourteen normal adult males. The load strength of the exercise assumed 30% and 60% maximum voluntarily contraction MVC. Moreover, exercise performance was evaluated using an electromyography analysis technique under two conditions: use and non-use of magnetism stimulation. No significant difference was observed between the two conditions regardless of load strength. In a previous study, an improvement in exercise performance was observed when magnetic stimulation was applied to a resting muscle after an exercise with 60% MVC. Careful assessment of the physiological difference between resting and exercising reveals possible differences in energy consumption. In order to this difference, it might occur for the recovery effect difference by the magnetic stimulation.

Keywords Muscle fatigue, Magnetic stimulation, Recovery, Electromyogram

1 Introduction

Muscle fatigue is common in everyday life and sports. Muscle fatigue is defined as “an inability of the muscle to generate force “or “decrease in muscle performance "[1]. And it is demanded to immediately recover from muscle fatigue.

Electromyography (EMG) has been widely used to quantitatively evaluate muscle fatigue as a physiological index. Because electromyography adds up and records action potentials that occur in muscle fiber, the state of activity of the whole muscle can be read. In addition, measurement may be simple because placing an electrode on the skin is the only requirement.

Electrical stimulation therapy is known to be an effective technique for reducing muscle fatigue and causes pain and discomfort [2][3][4][7]. Moreover, it is difficult to stimulate deep areas of muscle. Therefore, we focused on magnetic stimulation therapy, which is less invasive than the electrical stimulation technique. In a previous study [5] that applied magnetic stimulation with a coil to a muscle resting after exercise with 60% maximum voluntarily contraction (MVC), it was reported that recovery was promoted. However, the mechanism of the recovery process is still unknown. In this study, to elucidate the mechanism behind the effect of magnetic stimulation on muscle fatigue, we performed magnetic stimulation during muscle exercise with two types of load strength (30% of MVC, 60% of MVC) and examined fatigue reduction.

2 Methods

2.1 Subjects

We enrolled 14 normal adult males (average age 21.75±0.957 years) and the target muscle was the right biceps brachii muscle. All subjects were right-handed.

Written informed consent was obtained from each subjects prior to experiments. The study was approved by the local Ethical Committee.

2.2 Experiment System

The system that was used for the experiment is shown in Fig 1.

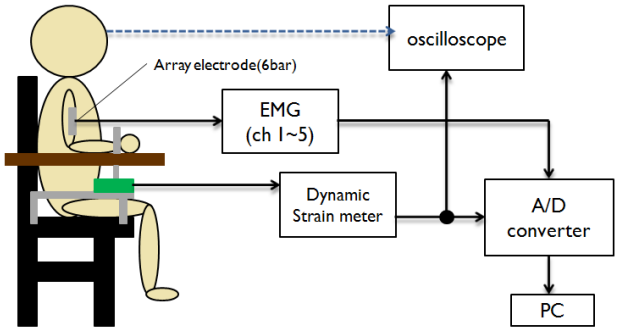

Figure 1: Experiments System Constitution.

A subject sat down on a chair that was constructed for this experiment in our labolatry. This experimentation system can measure an electromyogram (EMG) and also the force that is produced from the subject’s biceps brachii during isometric contraction. And a subject can receive display muscle strength of his muscle from oscilloscope in front.

First, the subject shows three times the MVC value. A load strength of this subject was defined using the biggest MVC value. After we allowed the subject

enough rest, the subject maintained a load that was equivalent to 60% of MVC until the muscle was fatigued and the subject could not maintain the load. Subjects received visual feedback of their muscle strength with an oscilloscope in front of them to help them adjust muscle strength. Magnetic stimulation was administered to the biceps brachii muscle using a double coil at every 5 second during this exercise. The apparatus used for magnetic stimulation was Magstim 200 (Magstim Corp., UK) and the stimulation strength was at 10% of maximum power (approximately 0.22 T). Fig 2 shows a magnetism stimulation device and the coil that was used for this stimulation.

Figure 2 left:Magstim200, Right: double coile.

In addition, this technique needs to only placed so that the center of the stimulation coil was located on the motor point of the biceps brachii muscle, and the direction of the coil aligned with the upper arm. Whilst the subjects exercised and received magnetic stimulations, subjects listened to “white noise” to not hear anysound for example magnetism stimulation device’s one.

The load equivalent to 30% MVC was tested like the 60% MVC load. In addition, a one-week interval was existed between the application and non-application of magnetic stimulation.

2.2 EMG analysis

EMG was simultaneously recorded with the muscle strength display. Skin resistance was lower than 5 kΩ and EMG had a band pass filter of 10-490 Hz. The EMG was divided into a section every 1.024 seconds (defined as 1 segment) and we computed the integral calculus EMG (integrated EMG: iEMG) and mean power frequency (MPF) of all segments. In addition, to obtain MPF, EMG was converted into a frequency domain using Fourier transformation. After conversion, the following expression (1) was used to calculate the MPF of each segment.

$$MPF = \frac{\int_{x1}^{x2} f * P(f)\,df}{\int_{x1}^{x2} P(f)\,df} \qquad \begin{matrix} P\cdots power \\ f\cdots frequency \end{matrix} \qquad (1)$$

Because the change of the index expresses the degree of leaning of the approximately straight line, this unit[%/seg] was used.

MPF is known to become a slow wave with accumulation of muscle fatigue in isometric contraction. By, as for the factor to shift to a low frequency, Type II fiber getting fatigue. From this, it is thought that "a firing rate decreasing" or "ignition synchronizes to maintain muscular strength"[1]. However, iEMG increases with the accumulation of muscle fatigue. It is thought that a new motor unit is mobilized to supplement it, when muscle is getting fatigue and can't display required force [6]. An example of the progression of typical fatigue observed in this study can be seen in Fig 3.

The change of these indexes between the group that received magnetic stimulation and the group that did not receive magnetic stimulation was compared.

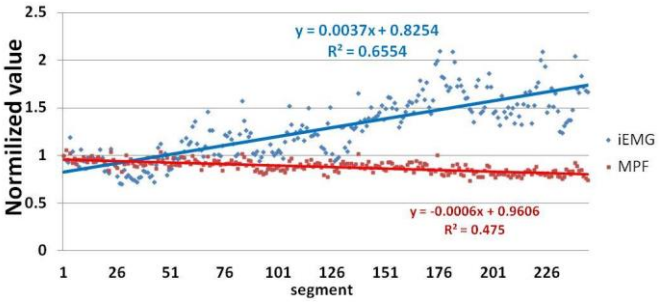

Figure3 typical progression of muscle fatigue

3 Results

3.1 Results of 60%MVC task

In 60% MVC, Figure 4 compares the endurance time between the group that received (defined as “exposure group”) and the group that did not receive magnetic stimulation (defined as “control group”). Comparison of the two indexes was conducted using the t-test with correspondence, but a significant difference was not observed ($p < 0.05$).

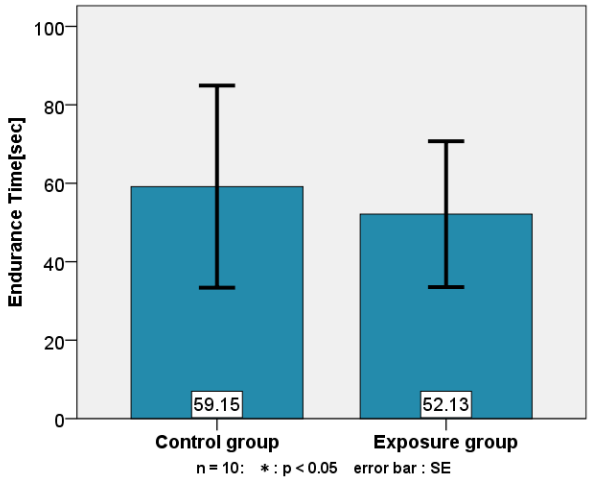

Figure 4 endurance time when load is 60%MVC

Similarly, changes in iEMG and MPF were compared. The rate of iEMG change in the control group was +1.699 %/seg and that in the exposure group was +2.342 %/seg. A statistically significant difference was not observed between these two indexes ($p < 0.05$).

Similarly, the rate of MPF change of the control group was -0.712 %/seg, and that in the exposure, was -0.758 %/seg. A statistically significant difference was also not seen between these two indexes ($p < 0.05$).

3.2 Results of 30%MVC task

Figure 5 compares the endurance time of the control group and the exposure group for the 30% MVC load.The two endurance times using the t-test with correspondence were compared, but a statistically significant difference was not observed ($p < 0.05$). The rate of iEMG change in the control group was +0.250 %/seg and that in the exposure group was +0.898 %/seg. A statistically significant difference was not observed between the two indexes ($p < 0.05$). Similarly, the rate of MPF change in the control group was -0.700 %/seg, and that in the exposure group, was -0.825%/seg. A significant difference was not observed between the two indexes ($p < 0.05$).

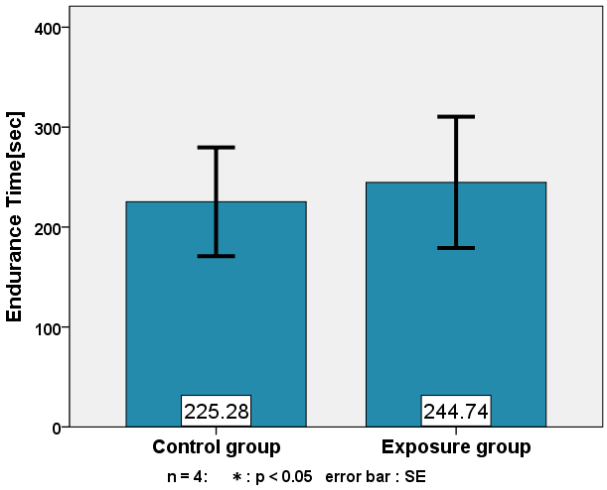

Figure 5 endurance time when load is 30%MVC

3.3 Discussion

No performance gain was observed when magnetic stimulation was used in both 60% MVC and 30% MVC. In a previous study conducted in our laboratory, the subject performed 60% MVC for 30 seconds and was allowed 120 seconds of rest. The experimenter administered magnetic stimulation to the subject during this rest period except 20seconds (first 10seconds of rest and last 10seconds of rest). The subject performed this exercise and rested repeatedly as one cycle, until the muscle was fatigued. Fig 6 shows the time schedule used in this previous study.

The stimulation frequency and the stimulation strength of the magnetic stimulation were same condition as in our present study (at every 5 second, 10% strength, double coil). In this previous study, magnetic stimulation and no magnetic stimulation were compared by the researchers. During magnetic stimulation, the number of cycles that subjects were able to perform was significantly increased. The rate of MPF change was also significantly improved. Thus, there was an improvement in exercise performance. However, there was no improvement in exercise performance at our experiment. The timing for magnetic stimulation differed between this previous study and our present study. In the previous study, magnetism stimulation was only conducted during the rest period. However, in the present study, magnetism stimulation was applied when subjects were undergoing contraction.

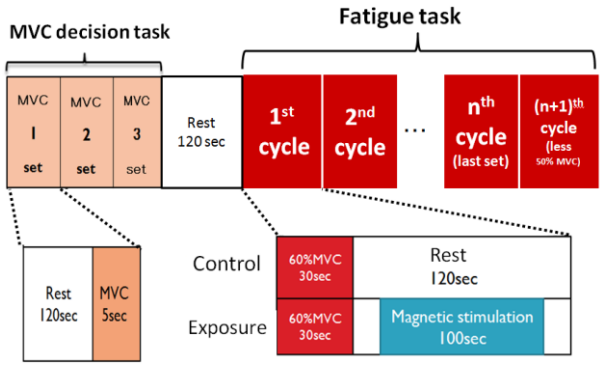

Figure 6 time schedule used by the previous study

The effects of magnetic stimulation may differ based on the difference of physiological phenomenon during rest and exercising.

In addition, the number of times of magnetic stimulation are depended on endurance time. For example, the subject who has 100seconds of endurance time is given 20 times of magnetic stimulation. However the subject who has 50seconds of endurance time is given only 10 times of magneticstimulation. These factor might change perfomances.

4 Conclusions

To elucidate the mechanism of action of magnetic stimulation on muscle fatigue, magnetic stimulation was administered to exercising biceps brachii muscles and an attempt was made to reduce muscle fatigue. However, regardless of load strength (30% of MVC, 60% of MVC), fatigue reduction due to the magnetic stimulation was not observed. In a previous study, magnetic stimulation was applied during rest using the same conditions as this study. In that study, a reduction in muscle fatigue was observed. Consequently, it may be suggested that the conditions for effective magnetism stimulation are different during rest and exercise.

Acknowledgements

On the occasion of this study, I would like to express gratitude to Mr.Yunokuchi who had various instructions. In addition, I thank colleagues and younger students of our laboratory. I also thank the people who took care of a subject willingly in the experiment.

References

[1] Komiyama T, Kawai T, Furubayashi T: Neurophysiological basis of muscle fatigue, Chiba University,42:(2),

[2] Yona M, Muro M, Sunamoto H: Electromyographical Analysis on Effects of Two Different Electric Stimulation Patterns durinng Muscle Fatigue in Triceps Surae, The Japanese society of physical fitness and sport medicine, 40:848, 1991

[3] Miyazaki S, Sato N, Hashimoto T, Tamashita Y: Clinical Effect of the Microcurrent Electrical Neuromuscular Stimulation, Tokai University,37:91-95, 2007

[4] Okabe T, Takuma Y, Miyamoto S, Inoue Y, Miyamoto K, Takebayashi H: Changes in Blood Volume and Muscle Oxygenation in The Tibialis Anterior Muscle During Low-Frequency Electrical Stimulation -Examination Different The Stimulation Frequencies-, Tosa rehabilitation jarnal(1):19-25, 2002

[5] Oda T, Nuruki A, Yunokuchi K: Recovery Effect of the muscle fatigue by the Pulse Magnetic Stimulation, The institute of electrical engineers of japan-Study Group document, Vol.MAG-13, No.1-4.6-14, pp.27-31, (2013)

[6] Yamada H, Kizuka T, Masuda T, Kaneko K, Yokoi T, Kaneko F, Okada M: Noninvasive Evaluation of Neuromuscular Function Using Electromyography during fatiguing Contracction, Biomechanism,Vol.16:47-59, 2002

[7] Kuno S, Regulating ATP Metabolism in Skeletal Muscle During High Intensity Exercise, Tukuba University, 20:19-27, 2007

Address for correspondence:

1-21-24 Korimoto Kagoshima-city Kagosima-Pref

890-0085 Japan

nuruki@ibe.kagoshima-u.ac.jp

Atsuo Nuruki

A microsaccade detection method by using an order-statistic time-window analysis

Shohei OHTANI[1], Takeshi KOHAMA[2], Sho KIKKAWA[2], and Hisashi YOSHIDA[2]

[1]Graduate School of Biology-Oriented Science and Technology, Kindai University, Japan;
[2]Faculty of Biology-Oriented Science and Technology, Kindai University, Japan;

Abstract

Recent studies have shown that microsaccades, which are small involuntary shifts in fixation eye movements, are modulated by the visual attention system. Microsaccades are generally detected by thresholding differentiation of eye movement signals. However, there is no formula to determine appropriate threshold values for precise detection of microsaccades. In this study, we propose a new microsaccade detection method based on an order-statistic time-window analysis with simple differentiation around the center of each window. Since the time-window which contains a microsaccade shows a large slope around its median value, the averaged differentiation value of microsaccade periods is significantly different from the total average. The results indicate that the proposed method is able to extract microsaccades of various amplitudes by setting the α level systematically. Moreover, the main sequence analyses also suggest that the proposed method detects microsaccades precisely, at any level of amplitude.

Keywords *Fixation eye movements, Microsaccades, Order-statistic time-window, Main sequence.*

1 Introduction

Involuntary miniature ocular movements which occur when eyes are fixated at a visual target are called "fixation eye movements." Fixation eye movements are traditionally classified in three components: drift, tremor, and microsaccades[1][2]. Recent studies have shown that microsaccades are modulated by the visual attention system. These studies point out that microsaccade rates increase simultaneously with the shift of focal attention[3][4][5]. On the other hand, some of the studies show that microsaccade rates and amplitudes are modulated by the shapes of fixation targets[6].

Since microsaccades are rapid and involuntary fixation eye movements, the detection methods of microsaccades are generally based on thresholding differentiation of eye movement signals. However, repeated trial and error by the visual observation is required to determine the threshold values, because there is no definition of appropriate threshold values for precise detection of microsaccades. Furthermore, a false detection of small-amplitude microsaccades would often be drawn by using these conventional methods.

In this study, we proposed a new microsaccades detection method based on order-statistic time-window analysis with simple differentiation around the center of each window. We evaluated the efficacy of the proposed method by applying it to fixation eye movement data.

2 Microsaccade detection algorithm

Fig.1 indicates an example of fixation eye movement data smoothed by a five-point moving average. Since microsaccades are ballistic movements, the segment which contains a microsaccade will monotonically increase or decrease for tens of milliseconds. Therefore, rank-ordered time series data of these periods have a relatively large slope around the median value (Fig.2a). On the other hand, rank-ordered data which does not contain any microsaccades shows a gradual increase and they have a smaller slope around the median value (Fig.2b).

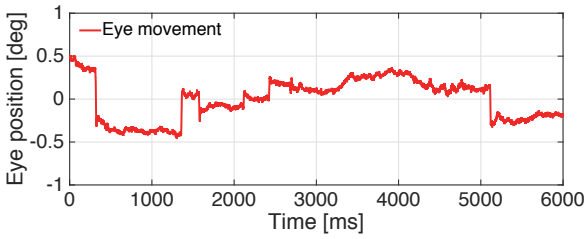

Figure 1: An example of fixation eye movement data containing six microsaccades.

Fig.3 indicates our proposed algorithm. Fixation eye movements were measured by EyeLink 1000 (SR Research Ltd.) with a sampling frequency of 2000 Hz. First of all, raw eye movement data was smoothed by a five-point moving average to remove high-frequency quantization noises (Fig.3a).

We defined an order-statistic time-window as $f(i;t) = x(i;t)\,(i = 1, \cdots, 2N+1)$ where $x(i;t)$ are order-statistics of observed data $x(t)$. The differentiation between pre- and post-N_1 points of the median of $f(i;t)$ was calculated by following Eq.1.

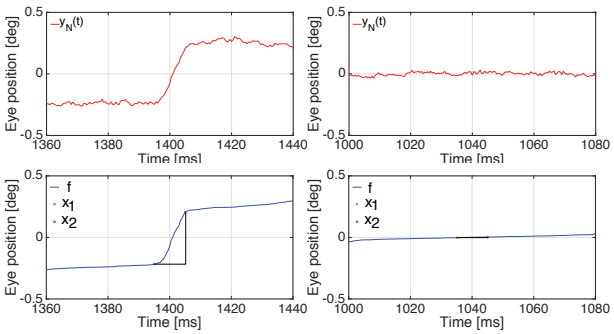

(a) microsaccade section (b) drift section

Figure 2: Fixation eye movement and its rank-ordered data. (a) The time period which contains a microsaccade shows a large slope around its median value. (b) The rank-ordered data of drift period does not have such a slope.

$$\begin{aligned} \Delta x(t) &= x_2(t) - x_1(t), \\ where,\ x_1(t) &= f(N+1-N_1;t), \\ x_2(t) &= f(N+1+N_1;t) \end{aligned} \tag{1}$$

A large value of $\Delta x(t)$ means a microsaccade-like rapid shift was contained in the window (Fig.3b)).

A set of $\Delta x(t)$:$\Delta M = \{\Delta x(t)\}$ was obtained as much as possible from measured fixation eye movements avoiding the periods with eye blinks (Fig.3c). Then we obtained $\Delta N_1(t) = \{\Delta x(t_j)\}$ from $2N_1$-point windows, where $t_j = t + j\,(j = -N_1, ..., -1, 0, 1, .., N_1)$. The differences between averaged ΔM ($\overline{\Delta M}$) and $\Delta N_1(t)$ ($\overline{\Delta N_1(t)}$) were tested by two-sample Student's t-test. When the average values were significantly different at certain α level, it was judged that there might be a microsaccade in the closed interval $[t-N_1, t+N_1]$ (Fig.3d).

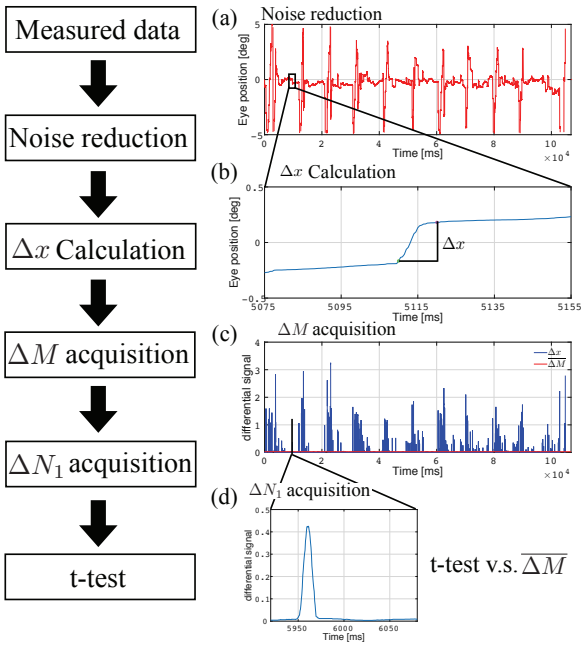

Figure 3: Procedure flow of the proposed algorithm.

3 Results

Fig.4 shows examples of horizontal fixation eye movements with detected microsaccades by the proposed method. Each vertical color bar indicates the period in which $\overline{\Delta M}$ and $\overline{\Delta N_1(t)}$ were significantly different at certain α level. In this figure, color bars show $1-\alpha$ values, the reason of which will be described later. The α level was systematically changed from 0.01 to 0.4. The sizes of the moving-windows were determined as $N = 80$ and $N_1 = 10$ to detect microsaccade as precisely as possible.

The proposed method is able to detect microsaccades of various amplitudes by setting the α level as indicated in Fig.4a. The duration of each colored period corresponds to the duration of each microsaccade. This indicates that the proposed method is also applicable to determine start-and-end-point of a microsaccade.

The segment which has the position shift of larger amplitude and longer duration indicates that it is a very typical microsaccade. Since this property of microsaccades corresponds to the value of $(1-\alpha)$, we applied it as an index of "potential microsaccades."

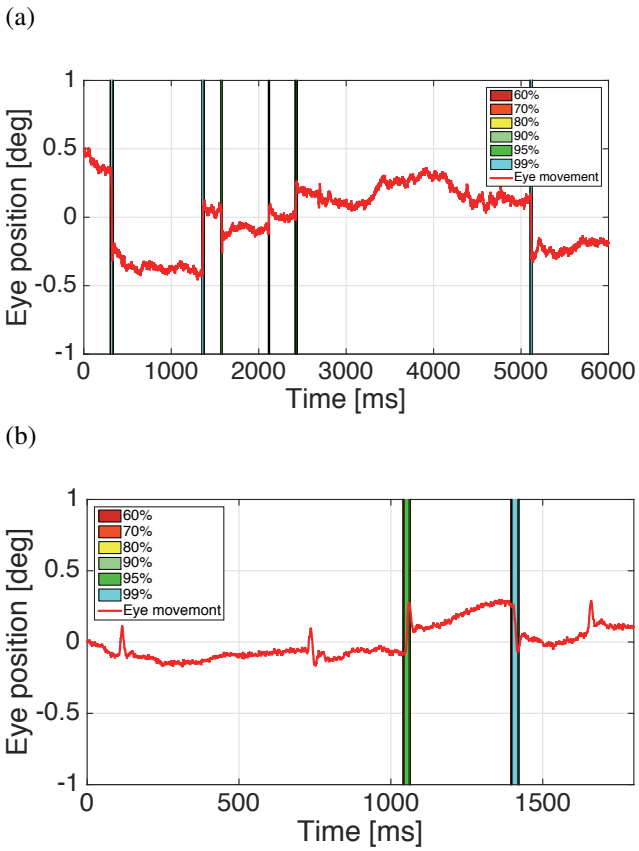

Figure 4: Examples of horizontal fixation eye movements with detected microsaccades by proposed method. The α level was systematically changed from 0.01 to 0.4. (a) Microsaccades of various sizes of were detected by changing the value of α level. (b) The proposed method does not detect spiny movements.

Table 1 indicates the detection rates and the number of false detection of microsaccades of each $(1-\alpha)$ value. The detection rate was defined by a ratio of the total number of detected microsaccades to the gold-standard of microsaccades. The gold-standard of microsaccades was determined by three referees who are currently working on eye movement studies.

Sometimes the referees judged spiny movements shown in Fig.4b as microsaccades. However, these spiny movements do not show positional shift which is a property of an ordinary microsaccade, indicating that it is doubtful whether they are microsaccades. Fig.5 show the enlarged version of the horizontal component and vertical component of a spiny motion. As it is thought that these spiny motions were the crosstalks of vertical microsaccades, we decided not to regard the spiny motions as microsaccades. The number of spiny motions is only seven, and the total number of gold-standard microsaccades without spiny motions is 134.

As indicated by Table 1, the detection rate becomes higher and the number of false detections increases when potential microsaccade becomes lower. We could not compare with conventional methods, because detected microsaccades would change according to the threshold value by these methods.

Table 1: Detection rate and the number of false detection of microsaccades. When potential microsaccade becomes lower, the detection rate becomes higher, but the number of false detections increases.

Potential MS	Correct detection	False detection
60%	126 (94.0%)	8
70%	123 (91.8%)	6
80%	120 (89.6%)	6
90%	115 (85.8%)	6
95%	112 (83.6%)	5
99%	105 (78.4%)	5

3.1 Evaluation experiment

We carried out an experiment to evaluate the effectiveness of the proposed method. Fig.6a shows the experimental procedure. It has been shown that the shapes of fixation target affect frequencies or amplitudes of microsaccades[6]. We used seven targets, which are composed of a dot, a circle, and a cross, according to Thaler et al.'s experimental procedure (Fig.6b). The viewing angle of the dot was 0.4[deg], and the sizes of the cross and the circle were both defined as 3.0[deg]. The experiments were carried out in a simple dark room in order to avoid the influence of indoor lighting devices. The subjects were instructed to maintain fixation on the center of a target, which was selected at random, during a trial. Stimuli were controlled by using Psychtoolbox on Matlab. The subjects were two college students (a male and a female) in their twenties.

We calculated the main sequence of microsaccades, which refers to the relation between the microsaccade's

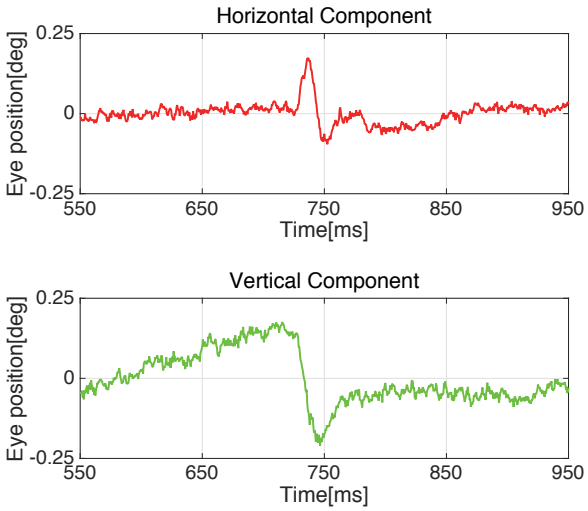

Figure 5: Horizontal and vertical components of a spiny motion. These spiny motions were regarded as the crosstalks of vertical microsaccades.

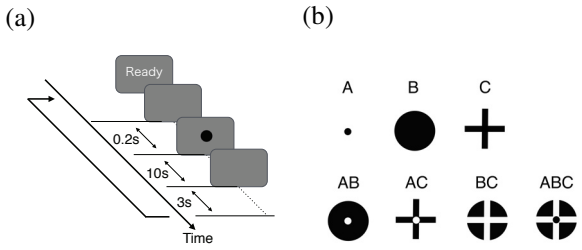

Figure 6: Overview of the evaluation experiment. (a) Experimental protocol. Subjects were instructed to maintain fixation on the center of the targets. (b) Visual targets used in the experiment. The size of the dot was 0.4[deg], and the sizes of cross and circle were 3.0[deg].

peak-velocity and amplitude, to evaluate detection precision of small-amplitude microsaccades, and also confirmed whether dynamics of microsaccades were affected by target patterns. The value of potential microsaccade 90% was used to determine the start-and-end-point of each microsaccade (Fig.7). The detection precision of microsaccades at this value was more than 80%. Peak-velocity of a microsaccade was determined from the low-pass differentiation signal of the microsaccade period. The low-pass differentiation is defined as following Eq.2. Where SR is the sampling rate $SR = 2000$, and $N = 15$ is the window size.

$$x_{vel}(t) = \frac{SR}{N(N+1)} \sum_{n=1}^{N} \{x(t+n) - x(t-n)\} \quad (2)$$

Fig.8 shows the main sequence curves fitted to the scatter plots of peak-velocity versus amplitude of microsaccades. Since the relation between peak velocity and amplitude of saccades can be characterized by non-linear function, the regression function Eq.3 was fitted to the scatter plots [7].

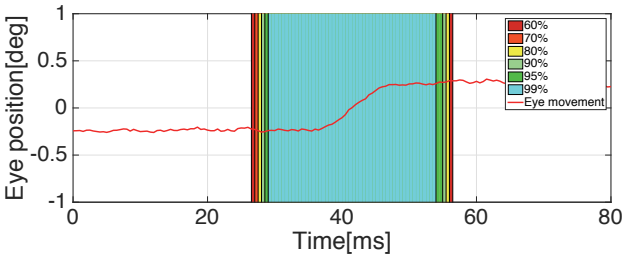

Figure 7: Detected microsaccade periods. The start-and-end-point of a microsaccade systematically change as a function of $1-\alpha$ value.

$$PV = PV_C(1-\exp(-A/A_C)) \quad (3)$$

where PV is the peak velocity of microsaccades, A is the amplitude of microsaccade. PV_C and A_C are constant values.

Fig.8 shows that peak velocity and amplitude property of microsaccades is well-fit by regression function, even for tiny amplitude microsaccades. This indicates that the proposed method can detect microsaccades of various amplitude with high accuracy. Even though a target shape which is composed of the dot and the cross resulted in combined low dispersion and microsaccade rate[6], we found that the difference of fixation target pattern has no effect on the dynamics of microsaccades.

(a)

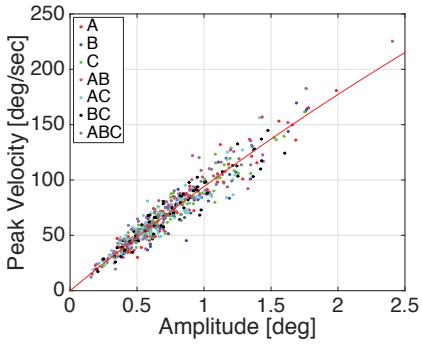

(b)

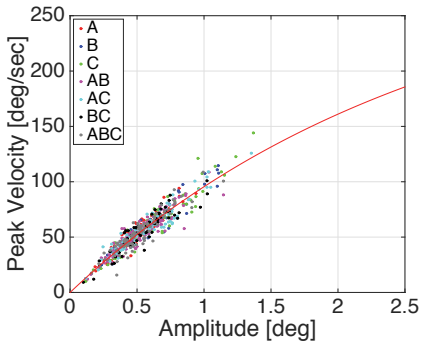

Figure 8: Peak velocity versus amplitude of detected microsaccades ("main squence") for each subject. The proposed method is able to detect microsaccades precisely, even tiny amplitude microsaccades.

4 Conclusions

In this study, we proposed a detection method of microsaccades based on an order-statistic time-window analysis with simple differentiation around the center of each window. Since the segment which contains a microsaccade shows a large slope around its median value, while the drift-only period does not have such a slope, the averaged differentiation values of microsaccade periods in most cases were significantly different from the total average. As a result, the proposed method is able to detect microsaccades of various amplitudes by setting the α level systematically. Moreover, the value of $1-\alpha$ was shown to become the index of "potential microsaccades." By comparison between the detected microsaccades and the gold-standard of microsaccades, it was shown that the detection rate becomes higher and the number of false detections increases when the potential microsaccade index $1-\alpha$ becomes lower. Furthermore, we carried out an experiment to evaluate the effectiveness of the proposed method. The subjects were instructed to maintain fixation on one of the seven target patterns. Furthermore, the results of the main sequence analyses indicate that the proposed method detects microsaccades precisely, at any level of amplitude.

References

[1] S. Martinez-Conde, J. Otero-Millan, and S.L. Macknik. The impact of microsaccades on vision: towards a unified theory of saccadic function. *Nature Rev.Neurosci.*, 14:83–96, 2013.

[2] M. Rolfs. Microsaccades: small steps on a long way. *Vision Res.*, 49:2415–2441, 2009.

[3] T. Kohama and S. Usui. Attentional effects on microsaccadic eye movements. *Current Psycholgy of Cognition,*, 21:377–395, 2002.

[4] R. Engbert and R. Kliegl. Microsaccade uncover the orientation of covert attention. *Vision Res.*, 43:1035–1045, 2003.

[5] J. Laubrock, R. Engbert, and R. Kliegl. Microsaccade dynamics during covert attention. *Vision Res.*, 45:721–730, 2005.

[6] L. Thaler. What is the best fixation target? The effect of target shape on stability of fixational eye movements. *Vision Res.*, 76:31–42, 2013.

[7] R. W. Baloh, A. W. Sills, W. E. Kumley, and V. Honrubia V. Quantitative measurement of saccade amplitude, duration, and velocity. *Neurology*, 25:1065–1070, 1975.

Address for correspondence:

Takeshi KOHAMA
Faculty of Biology-Oriented Science and Technology, Kindai University, Japan
kohama@waka.kindai.ac.jp

Simulation of spike propagation in neural network

Shun Sakuma[1], Yuko Mizuno-Matsumoto[1], Yoshi Nishitani[2], Shinichi Tamura[3],

1 Graduate School of Applied Informatics, University of Hyogo, Japan;
2 Graduate School of Medicine, Osaka University, Japan;
3 NBL Technovator Co., Ltd., Japan;

Abstract

It is well known that there is intercommunication among the different areas of the brain. However, the rules of communication in the brain have not been successfully revealed. In this paper, we carried out neural network simulation in 25×25 2D array to analyze behavior of spikes. We considered that the change in the propagation path of the firing of neurons needs a little variance of the synaptic propagation delay and refractory period.

Keywords *Dynamic Time Warping, Refractory Period, Spike Wave, Synaptic Delay*

1 Introduction

The brain forms a huge network, and information is transmitted by spikes. The action potential is transmitted to the behind neurons from the previous neuron with delay. Until the potential change occurs, it takes more time than 0.5 msec. This is referred to as "synaptic propagation delay"[1]. When neuron fires once, it can't fire for a certain time. This is referred to as "refractory period"[2]. Each neuron has variances of the synaptic propagation delay and refractory period. They fluctuate time to time and can be regarded as a kind of noise. Intellectual brain activity such as memory processing could be conducted with spike propagation. However, information processing in brain is rather stable in spite of such variabilities. It is an important target to analyze the spike propagation and information transmission mechanism. To essentially understand information processing in the brain, we simulated assuming the interaction of the firing activity of a large number of neural network [3]. In this paper, we simulated the spike responses for stimulations under various synaptic propagation delays and refractory periods. From a view point of communication, we analyze information-flow of the network.

2 Methods

Twenty-five × twenty-five 2D neural network was implemented (Figure 1). We used integrate-and-fire model without leak as a neuron model [4, 5]. Each neuron had connection weights to and from eight neighboring neurons.

Three neurons were stimulated simultaneously at time 0.1 msec as shown in Figure 1. We defined such three neurons "neuron group." Spike-waves propagated from the stimulated neuron group to the other neuron groups, which we defined "transmitting neuron group." Instantaneous variances of synaptic propagation delay and the refractory period were set to between 0.000 and 2.000. In our previous wet-lab experiments, we applied time sampling rate of 0.1 msec, which was called as "bin." So, we also use time unit of "bin = 0.1 msec." Bin^2 were set in 0.167, 0.333, 0.500, 0.667, 1.000 and 2.000 (bin = 0.1 msec) [4].

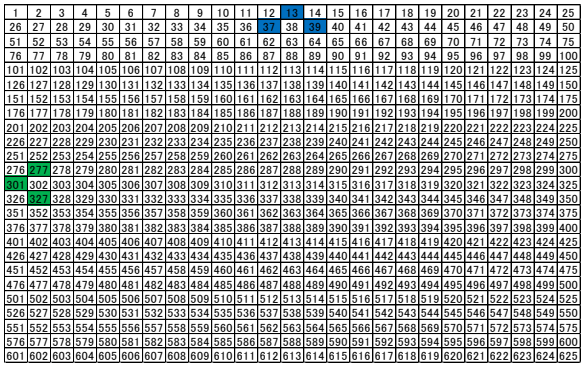

Figure 1 : 25×25 2D neural network and the stimulation neuron groups.
Group number 1: blue
Group number 2: green

We obtained the spike-interval sequences for 625 cells (total 6250 sequences) as stimulation group number 1 (Figure 2).

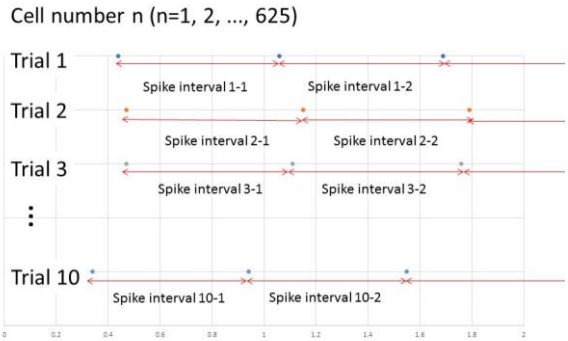

Figure 2 : the n-th (n = 1, 2, ..., 625) spike interval of the neuron

We also obtained the spike-interval sequences for 625 cells (total 6250 sequences) with stimulation group number 2. And we conducted “Dynamic Time Warping：DTW” in combination of 10 trials (total 45 sets) to calculate the spike-interval time differences between the trial sets of stimulation group number 1 (figure 3). We also conducted DTW in combination of 10 trials (total 45 sets) to calculate the spike-interval time differences between the trial sets of stimulation group number 2.

DTW is an algorithm for measuring the degree of difference between the two signals sequences having different time or fast. When the degree of difference is higher, the value approaches 1 while the value approaches 0 when the degree of difference is lower.

We measured DTW values in combination of 10 trials with same stimulated groups（1 or 2）and calculate the average of such 90 sets（= 45 × 2 sets）. We define such calculations “Local DTW” (See Figure 3).

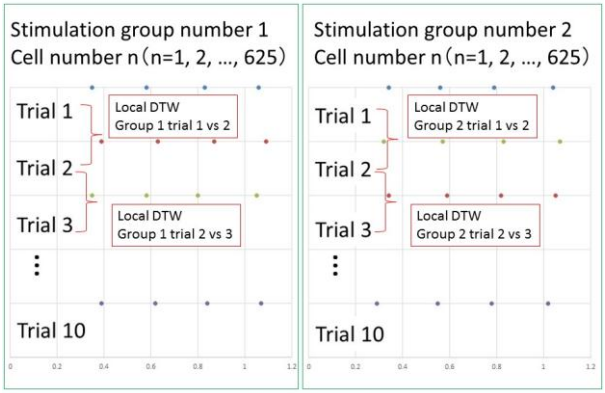

Figure 3：Illustration of Local DTW distance.

We calculated DTW in combination of both stimulation group number 1 and 2’s 10 trials (total 100 sets) to calculate the spike-interval time differences between the trial sets (Figure 4). We calculated the average of 100sets. We define such calculations “Inter DTW.”

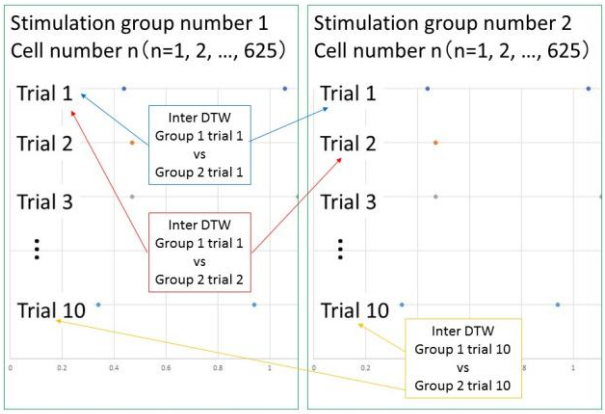

Figure 4：Illustration of Inter DTW distance.

We applied T-test between “Local DTW” and “Inter DTW.” We counted the number of such neurons whose “Inter DTW” was significantly higher than “Local DTW.” We calculated the t-test of the both-sided at the 5% significance level between “Local DTW” and “Inter DTW.” We thought that neurons with significantly higher test statistic were able to identify the stimulation group number 1 and 2.

3 Results

3.1 Difference of propagation speed

Figure 5 shows the two results of positions of the firing neurons from the different variances. The variances of the synaptic delay and refractory period were 0.167 (yellow in Figure 5) and 2.000 (red in Figure 5). Blue in Figure 2 shows the results from both 0.167 and 2.000 variances. Figure 5 shows the scene when 5.6 - 6.0 msec has passed after the stimulation. We could see that the propagation speed with 2.000 variance value (red) is faster than the propagation speed with 0.167 variance value (yellow). As a result, when changing the fluctuation of the synaptic delay and refractory period, the larger the variance value is, the faster the propagation speed is.

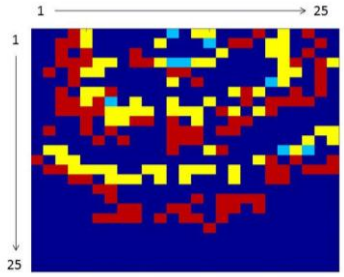

Figure 5: When stimulated the group 1, comparison between variances 0.167 and 2.000.
Red: variance 2.000
Yellow: variance 0.167
Blue: variances 2.000 and 0.167

3.2 Classification of stimulated sites

Figure 6 shows the number of the firing neurons which caused the different firing time calculated by DTW. A vertical line shows the number of neurons. A horizontal line shows bin^2 for the variances of the synaptic delay and refractory period. When the variance value of the synaptic delay and refractory period from increased 0.167 to 0.667, the number of the firing neurons which caused the different firing time increased. However, when the variance is more than 0.667, the number of neurons that could identify the stimulated neurons decreased.

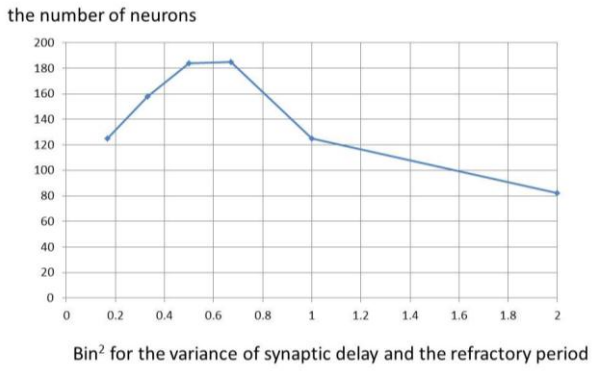

Figure 6: The number of neurons which could communicate.

4 Dictation and Consideration

The results showed that the propagation path and the propagation velocity changed by putting the variance of synaptic propagation delay and refractory period. The reason may be that the larger the variances of the synaptic delay and the refractory period, the more quickly the spike propagated. As a result, the stimulus arrives early. From the results of DTW, there are many signaling pathways spatially different from transmitting neuron groups to receiving neuron. They are transmitted in parallel.

However, a spike which has reached to a neuron first, makes the neuron firing. We can see the approximate flow of information if we discuss only spatially representative pathway. At that time, when there is no variation in the synaptic propagation delay and refractory period, it will always pass through the same typical route in each trial. At that time, the route to each transmission neuron from the receiving neuron might overlap from half-way. In that case, receiving-neuron will be hard to identify information from transmission neurons. If there is instantaneous variation in the synaptic propagation delay and refractory period, it is considered to be passing through the temporally various representative routes. In general, two paths from two transmitting neurons to a receiving neuron would exist, the variances of the synaptic delay and refractory period could be large [5]. Thus, if there would be variations in the synaptic propagation delay and refractory period, spike-wave could pass through the various representative routes. Then, it increases the possibility of the identification. When the variance is too large with large bin^2, the firing neuron could receive noise. Then identification of spike wave itself could be difficult. We considered that the change in the propagation path of the firing of neurons needs a little variance of the synaptic propagation delay and refractory period.

Acknowledgements

This study was supported in part by the Grant-in-Aid for Scientific Research of Exploratory Research 21656100, 25630176, 16K12524 and Scientific Research (A) 22246054 of Japan Society for the Promotion of Science.

References

[1] Eugene M. Izhikevich, Polychronization: Computation with spikes. *Neural Computation*, vol.18, pp.245-282, 2006.

[2] Hiroyoshi Miyakawa, Masashi Inoue, Biophysics of neurons. *Maruzen Publishing*, 2013.

[3] Shinichi Tamura, Yoshi Nishitani, Yakuya Kamimura, Yasushi Yasushi, Chie Hosokawa, Tomomitsu Miyoshi, Hajime Sawai, Yuko Mizuno-Matsumoto, Chen Yen-Wei. Multiplexed spatiotemporal communication model in artificial neural networks. *Automation, Control and Intelligent Systems*, 2013

[4] Wulfram Gerstner, Werner Kistler, Spiking Neuron Models. Single Neurons, Populations, Plasticity, Cambridge *University Press*, 2002.

[5] Shinichi Tamura, Yoshi Nishitani, Chie Hosokawa, Tomomitsu Miyoshi, Hajime Sawai. Simulation of code spectrum and code flow of cultured neuronal networks. *Computational Intelligence and Neuroscience*, 2016.

Address for correspondence:

Shun Sakuma
Graduate School of Applied Informatics, University of Hyogo
7-1-28, Minatojimaminami-machi, Chuo-ku, Kobe, Hyogo
650-0047, Japan
y09024@gmail.com

Invited lecture

Signal recording and non-linear processing in sleep research

Thomas Penzel

Charite-Universitatsmedizin Berlin, Germany

Abstract

Sleep disorders are found to be more prevalent than previously realized. This may be a consequence of a modern society which optimizes work and social activities up to the edge. In order to investigate normal and disturbed sleep, we record biosignals both in the sleep laboratory and at home. Signals may be recorded directly, such as EEG, EOG, EMG from the head of the sleeping person, or indirectly, such as ECG, heart rate, respiration, pulse wave. Signals may be recorded with little contact or no contact systems such as actigraphy, body movement, bed sensors or bedside radiofrequency sensors. Some signals are new in sleep research and require new technology and analysis concepts. Always biosignals were recorded with an appropriate time and amplitude resolution, and then we derive physiological functions. We can identify wakefulness and sleep, we can derive details about sleep, such as light sleep, deep sleep, and REM sleep, arousals and sleep fragmentation. Not only classical methods in the time and frequency domain are used, but also more recent methods using statistical approaches are applied. This allows recognizing normal and restorative sleep and identifying sleep disorders as well. Some sleep disorders imply cardiovascular consequences and require treatment. Sleep disordered breathing is the disorder with most cardiovascular consequences. Many diagnostic tools focus on this group of disorders [1]. Diagnostic methods and perspectives are presented in this communication.

[1] IEEE Engineering in Biology and Medicine Society: ``The Science of Sleep''. Pulse Magazine. Sept./Oct. issue 2014.

Markov Modeling of Sleep Stage Transitions and Ultradian REM Sleep Rhythm: A Simulation Study

Akifumi Kishi, Ikuhiro Yamaguchi, Fumiharu Togo, Yoshiharu Yamamoto

Educational Physiology Laboratory, Graduate School of Education, The University of Tokyo, Japan

Abstract

The cyclic sequence of non-rapid eye movement (NREM) and REM sleep, or the so-called ultradian rhythm of sleep, is a highly characteristic feature of sleep. Although over a half a century has passed since the discovery of REM sleep, surprisingly, the mechanism responsible for the ultradian REM sleep rhythm has not to date been fully elucidated. In the present study, we aim to provide a mechanistic insight into the generation of the ultradian REM sleep rhythm. By simulating hypnograms with dynamic feature of sleep stage transitions, i.e., stage transition probabilities and stage-specific survival time functions, we show that the second-order Markov transition probabilities and the stage-specific survival time functions can reproduce the central position (∼90 min) of the REM-onset intervals (ROI), but with larger variance of the distribution. We also demonstrate the direct effect of increased probability of transitions from light to deep sleep within NREM sleep on the prolongation of the ROI in a dose-response manner. These results suggest that dynamic sleep stage transitions constitute the basis of the formation of ultradian rhythm of sleep, yet further elaboration of the model would be required to reduce the variability of the rhythmicity.

Keywords *Markov Chain Modeling, Sleep Stage Transitions, Survival Time Function, Ultradian Rhythm*

1 Introduction

Sleep is, by nature, not a static but a dynamic phenomenon, resulting from complex interactions of the behavior of central neurons, mainly in the hypothalamus and brainstem [1, 2]. Above all, the cyclic sequence of non-rapid eye movement (NREM) and REM sleep, or the so-called ultradian rhythm, is a highly characteristic feature of sleep [3]. While there exists the well-known reciprocal interaction model describing ultradian periodicity, in which NREM–REM cycles are controlled by both cholinergic and monoaminergic neuronal systems [2, 4], the mechanism generating the ultradian REM sleep rhythm, particularly in humans, has not to date been fully elucidated.

Recently, analysis of dynamic aspects of sleep, probabilities of sequential transitions of sleep stages (wake [W], stage 1 [S1], stage 2 [S2], slow-wave sleep [SS] and REM [R]) and statistical distributions of duration of each stage, has been shown to be useful since it can shed light on new properties of sleep regulation [5, 6]. A recent study has shown that the second-order or higher Markov chain model contains valuable information compared to the simple first-degree Markov transitions, and thus the second-order Markov chain model might be suitable for sleep stage transition analysis [7]. We have shown that the probability of transitions from S2 to SS was increased when the REM-onset intervals (ROI) was prolonged by administrating monoaminergic antagonist in humans [8].

In the present study, we hypothesized that the stage transition mechanism underlies the generation of the ultradian REM sleep rhythm. Specifically, we ran simulations to see if minimal rules of stage transition dynamics could reproduce which aspects of ultradian rhythm of sleep. To this end, first, we re-analyze the available data of human sleep hypnograms [9] to extract parameters characterizing the dynamic aspects of sleep, i.e., the first-order and the second-order transition probabilities between sleep stages and the equations of the survival time function of the continuous runs for each sleep stage. Second, we model sleep stage dynamics and run simulations to generate hypothetical human hypnograms. We show that the second-order Markov transition probabilities and the stage-specific survival time functions can reproduce the central position (approximately 90 min) of the ROI. We also demonstrate by simulation that the increased probability of transitions from S2 to SS leads to the prolongation of the ultradian REM sleep rhythm.

2 Methods

2.1 Dataset

The subjects were 26 healthy women (age: 38 ± 8 years; mean $\pm$ SD) [9]. None of these subjects had clinically evident sleep disorders nor major depressive disorder. To reduce variability, menstruating subjects were all studied in the follicular phase of their menstrual cycles. All the subjects gave their informed consent, approved by the New Jersey Medical School's Institutional Review Board, to participate in this research. Following instructions to refrain from alcohol and caffeine ingestion and avoid engaging in prolonged and/or strenuous exercise in the daytime before study nights, the subjects underwent one night of polysomnographic recording in a

quiet, shaded hospital room. The subjects went to bed at their usual bedtime and awoke the next morning between 7:15 and 8:00 A.M.

The subjects underwent full nocturnal polysomnography consisting of electroencephalogram (C3/A2, O1/A2 and FZ/A2), electrooculogram, submental electromyogram (EMG), anterior tibialis EMG, a lead II electrocardiogram, thoracic and abdominal motion, airflow using a nasal cannula/pressure transducer and an oral thermistor, and pulse oximetry. Sleep was scored every 30 sec by a single scorer according to standard criteria of Rechtschaffen and Kales [10]. To approximate the modified American Academy of Sleep Medicine standard guidelines for sleep stage scoring [11], stages 3 and 4 were combined into SS. More details of the polysomnographic recordings, including the scoring of the arousals and respiratory events, have been described elsewhere [9].

2.2 Data Analysis

According to the definition of the first-order Markov chain process, the first-order transition probabilities were calculated as $Pr_{X\to Y} = (n_{X\to Y}/\sum_A n_{X\to A}) \times 100$, where {*A, X, Y*} are derived from {W, R, S1, S2 and SS} and $n_{X\to Y}$ is the number of transitions from sleep stages *X* to *Y* (*X* $\neq$ *Y*) during the whole night's sleep. The second-order transition probabilities were calculated as $Pr_{X\to Y\to Z} = (n_{X\to Y\to Z}/\sum_A n_{X\to Y\to A}) \times 100$, where {*A, X, Y, Z*} are derived from {W, R, S1, S2 and SS} and $n_{X\to Y\to Z}$ is the number of transitions from sleep stages *X* to *Y* to *Z* (*X* $\neq$ *Y* and *Y* $\neq$ *Z*) during the whole night's sleep. Mean $\pm$ SD of the number of continuous runs of each sleep stage (i.e., periods of consecutive epochs of the same stage bounded by one of the other stages) analyzed per subject for this healthy group have been presented elsewhere [9]. Mean $\pm$ SD of the total number of continuous runs for all stages during whole night's sleep were 147.7 $\pm$ 41.8.

As we have previously reported [6, 9], survival time function (as well as duration distributions of continuous runs) takes a different form for each sleep stage: survival time function $P(t)$ of continuous runs (duration t) for S1 and REM sleep follow an exponential function $exp(-t/\tau)$, where the τ is a constant, $P(t)$ for S2 sleep follow a stretched exponential function $exp(-t/\tau)^\beta$, where the β and the τ are constants, and $P(t)$ for wake and SS follow a power-law $At^{-\alpha}$, where the α and the A are constants. The survival curves for durations of continuous runs for each sleep stage were generated by pooling those of all the individuals. The constant parameters were estimated by the least squares fitting technique.

The intervals between the onset of one REM period and the beginning of the next (REM-onset intervals; ROI) were calculated according to criteria derived from Feinberg [12]. In keeping with these criteria, a REM period was accepted as complete if it was $\geq$5 min in duration (except for the first REM period, which has no minimum length). REM periods of duration $<$5 min were conjoined with the succeeding REM period. REM periods interrupted by NREM sleep $\leq$15 min were treated as single periods; if $>$15 min of NREM sleep intervened, they were scored as two separate REM periods. For the treatment of the waking time, we subtracted the waking time when calculating the intervals, because a previous study has shown that the REM sleep cycle is sleep dependent [13]. Distributions of ROI were analyzed by pooling those of all of the individuals or the simulations.

S2→	**W**	**S1**	**SS**	**R**
Normal	23.5	30.0	36.7	9.7
Moderate	13.5	20.0	56.7	9.7
Substantial	3.5	10.0	76.7	9.7

Table 1: Probability parameters for the first-order simulation.

W→S2→	**W**	**S1**	**SS**	**R**
Normal	42.5	35.8	17.3	4.5
Moderate	32.5	25.8	37.3	4.5
Substantial	22.5	15.8	57.3	4.5
S1→S2→	**W**	**S1**	**SS**	**R**
Normal	28.6	45.2	13.9	12.3
Moderate	18.6	35.2	33.9	12.3
Substantial	8.6	25.2	53.9	12.3

Table 2: Probability parameters for the second-order simulation.

2.3 Simulation

Simulated hypnograms were generated by the following 2 steps: 1) determining a stage sequence based on the transition probabilities and 2) determining the stage run durations based on the survival time functions for each sleep stage. Uniform random numbers (ranging from 1 to 10,000) were generated and the first number was used to determine the destination of transitions and durations of the stage runs. For the first step, the number of sequence (runs) was set to 150 based on the actual data, and either the first-order or the second-order transition probabilities was used in each simulation.

In addition, based on our previous experimental observation [8], direct effect of increased probability of transitions from S2 to SS on ROI was examined on the simulation. To investigate the dose-response relationship, probability parameters ("moderate" and "substantial" increase of S2 to SS transition probability) were set as shown in Table 1 for the first-order simulations and Table 2 for the second-order simulations. The moderate increase of S2 to SS transition probability corresponds to the actual increase by the monoaminergic antagonist [8]. None of the probabilities of transitions related to REM were altered since it might affect the ROI directly.

Simulation was repeated 1,000 times for each pattern of simulations and all of the 1,000 simulated hypnograms were used to estimate the distribution of the ROI.

from W						**from S1**						**from S2**					
(%)	W	S1	S2	SS	R	(%)	W	S1	S2	SS	R	(%)	W	S1	S2	SS	R
						S1→W		94.9	5.1	0.0	0.0	S2→W		88.0	11.5	0.0	0.5
W→S1	25.0		70.1	0.0	5.0							S2→S1	9.0		87.3	0.0	3.7
W→S2	42.5	35.8		17.3	4.5	S1→S2	28.6	45.2		13.9	12.3						
W→SS	0.0	0.0	0.0		0.0	S1→SS	0.0	0.0	0.0		0.0	S2→SS	3.1	0.6	96.2		0.0
W→R	20.0	65.9	14.1	0.0		S1→R	20.2	74.6	5.2	0.0		S2→R	21.5	61.1	17.4	0.0	

from SS						**from R**					
(%)	W	S1	S2	SS	R	(%)	W	S1	S2	SS	R
SS→W		50.5	49.5	0.0	0.0	R→W		85.9	2.7	0.0	11.4
SS→S1	0.0		100.0	0.0	0.0	R→S1	8.4		15.5	0.0	76.1
SS→S2	11.6	6.7		77.8	4.0	R→S2	33.2	13.0		5.5	48.3
						R→SS	0.0	0.0	0.0		0.0
SS→R	0.0	0.0	0.0	0.0							

Table 3: Second-order transition probabilities between sleep stages in healthy subjects.
The labels in the rows denote the two preceding stages, and those in the columns denote the subsequent stages of transitions.

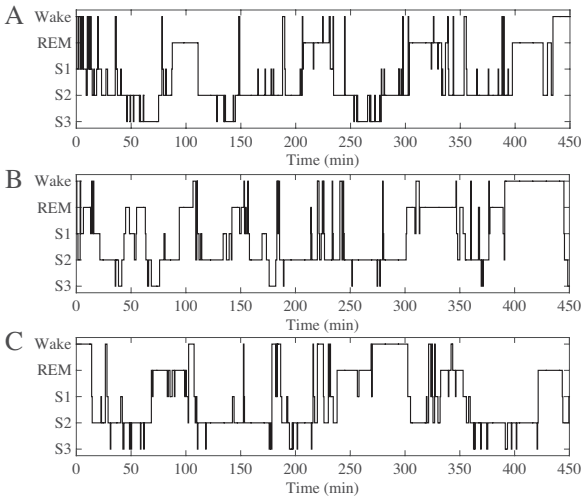

Figure 1: A typical example of the hypnograms.
(A) Actual hypnogram of a healthy subject, (B) simulated hypnogram using the first-order transitions and (C) simulated hypnogram using the second-order transitions.

3 Results

3.1 Experimental Results

A typical example of the hypnogram of a healthy subject was shown in Fig.1A.

The first-order transition probabilities between sleep stages in our sample of healthy subjects have been reported elsewhere [9]. The second-order transition probabilities between sleep stages were shown in Table 3.

The survival time distributions (i.e., cumulative probability distributions) of continuous runs for each sleep stage of our sample of healthy subjects have been presented elsewhere [9]. The parameters for the survival time functions of continuous runs for each sleep stage were now estimated by the least squares fitting technique and summarized in Table 4.

The distribution of the ROI for our sample of the healthy subjects was shown in Table 5. The median ROI was 89.5 min (73.9 min and 103.8 min; the first and the third quartiles, respectively) for the healthy controls.

Stage	**Fitted Model**	**Parameters**
wake	power-law	$\alpha = 1.05$, $A = 0.46$
S1	exponential	$\tau = 0.92$
S2	stretched exponential	$\beta = 0.78$, $\tau = 4.6$
SS	power-law	$\alpha = 1.35$, $A = 0.38$
REM	exponential	$\tau = 6.40$

Table 4: Parameters for the survival time function of continuous runs for each sleep stage.

3.2 Simulation Results

Typical examples of the hypnograms generated by the normal first-order and the normal second-order simulations were shown in Fig.1B and C, respectively.

Reliable estimations of the quartile statistics of the ROI distribution for the hypnograms generated by the normal first-order and the normal second-order simulations were summarized in Table 5. The median ROI estimated by the normal second-order simulation was 89.0 min, which was almost same as that of the actual hypnograms (89.5 min). On the other hand, the median ROI estimated by the normal first-order simulation was 67.0 min, which was about 20 min shorter than that of the actual hypnograms. Interquartile range (IQR) of the ROI estimated by the normal first-order and the normal second-order simulations were relatively larger (27.0 min for the normal first-order and 38.7 min for the normal second-order simulations) than that of the actual hypnograms (14.9 min).

The median ROI estimated by the second-order simulation with moderately and substantially increased S2-to-SS transition probability was prolonged to 98.0 min and 108.5 min, respectively, compared to that of the normal second-order simulation (89.0 min). The median ROI estimated by the first-order simulation with moderately and substantially increased S2-to-SS was also prolonged to 73.0 min and 79.0 min, respectively, compared to that of the normal first-order simulation (67.0 min). For any of these cases, estimated IQRs were larger than the simulation with normal transition probabilities.

ROI	25%	Median	75%	IQR
Actual data				
Healthy subjects	73.9	89.5	103.8	14.9
Simulation with normal transition probability				
First-order	45.0	67.0	99.0	27.0
Second-order	57.1	89.0	134.5	38.7
Simulation with moderately increased S2-to-SS				
First-order	47.5	73.0	111.5	32.0
Second-order	61.0	98.0	154.0	46.5
Simulation with substantially increased S2-to-SS				
First-order	51.5	79.0	124.5	36.5
Second-order	65.0	108.5	163.6	49.3

Table 5: Quartiles and interquartile range (IQR) of the REM-onset intervals (ROI) for the actual data and the simulated hypnograms.

4 Conclusions

We demonstrated that simulated hypnograms generated by 1) second-order Markov transition probabilities between stages and 2) stage-specific survival time functions of stage runs durations could reproduce the central position of the distribution of the ROI, while the width of the distribution (i.e., variance or IQR) was greater compared to the actual distribution. We have also shown the *direct* effect of increased probability of transitions from S2 to SS on the prolongation of the ROI in a dose-response manner. These findings suggest that the mechanism governing sleep stage transitions underlies the generation of the ultradian rhythm of sleep. Further elaboration of the model, such as incorporation of the homeostatic regulation of slow-wave sleep as well as the circadian regulation of REM sleep [14], could greatly reduce the variability without altering the 90 min ultradian rhythm.

Acknowledgements

The authors thank Dr. Benjamin H. Natelson for his cooperation in this study. This work was partly supported by JSPS KAKENHI Grant Number 15K16416 to AK.

References

[1] C. B. Saper, T. C. Chou, and T. E. Scammell. The sleep switch: hypothalamic control of sleep and wakefulness. *Trends Neurosci*, 24:726–731, 2001.

[2] E. F. Pace-Schott and J. A. Hobson. The neurobiology of sleep: genetics, cellular physiology and subcortical networks. *Nat Rev Neurosci*, 3:591–605, 2002.

[3] J. A. Hobson, R. Lydic, and H. A. Baghdoyan. Evolving concepts of sleep cycle generation: from brain centers to neuronal populations. *Behav Brain Sci*, 9:371–448, 1986.

[4] R. W. McCarley and J. A. Hobson. Neuronal excitability modulation over the sleep cycle: a structural and mathematical model. *Science*, 189:58–60, 1975.

[5] C.-C. Lo, L. A. Nunes Amaral, S. Havlin, P. Ch. Ivanov, T. Penzel, J.-H. Peter, and H. E. Stanley. Dynamics of sleep-wake transitions during sleep. *Europhys Lett*, 57:625–631, 2002.

[6] A. Kishi, Z. R. Struzik, B. H. Natelson, F. Togo, and Y. Yamamoto. Dynamics of sleep stage transitions in healthy humans and patients with chronic fatigue syndrome. *Am J Physiol Regul Integr Comp Physiol*, 294:R1980–1987, 2008.

[7] A. Schlemmer, U. Parlitz, S. Luther, N. Wessel, and T. Penzel. Changes of sleep-stage transitions due to ageing and sleep disorder. *Phil Trans R Soc A*, 373:20140093, 2015.

[8] A. Kishi, H. Yasuda, T. Matsumoto, Y. Inami, J. Horiguchi, M. Tamaki, Z. R. Struzik, and Y. Yamamoto. NREM sleep stage transitions control ultradian REM sleep rhythm. *Sleep*, 34:1423–1432, 2011.

[9] A. Kishi, B. H. Natelson, F. Togo, Z. R. Struzik, D. M. Rapoport, and Y. Yamamoto. Sleep-stage dynamics in patients with chronic fatigue syndrome with or without fibromyalgia. *Sleep*, 34:1551–1560, 2011.

[10] A. Rechtschaffen and A. Kales. *A manual of standardized terminology, techniques and scoring system for sleep states of human subjects*. US Government Printing Office, Washington, DC, 1968.

[11] C. Iber, S. Ancoli-Israel, A. Chesson, and S. F. Quan. *The AASM manual for the scoring of sleep and associated events: rules, terminology, and technical specifications.* American Academy of Sleep Medicine, Westchester, IL, 1st edition, 2007.

[12] I. Feinberg. Changes in sleep cycle patterns with age. *J Psychiat Res*, 10:283–306, 1974.

[13] J. Moses, A. Lubin, L. C. Johnson, and P. Naitoh. Rapid eye movement cycle is a sleep-dependent rhythm. *Nature*, 265:360–361, 1977.

[14] A. J. K. Phillips, P. A. Robinson, and E. B. Klerman. Arousal state feedback as a potential physiological generator of the ultradian REM/NREM sleep cycle. *J Theor Biol*, 319:75–87, 2013.

Address for correspondence:

Akifumi Kishi, Ph.D.
Graduate School of Education, The University of Tokyo
kishi@p.u-tokyo.ac.jp

Wake-Sleep Transition from the Perspective of Cortico-Thalamo-Cortical Loop: Electroencephalogram Data Analysis and Simulation

Ikuhiro Yamaguchi[1], Akifumi Kishi[1], Fumiharu Togo[1], Toru Nakamura[1], Yoshiharu Yamamoto[1]

[1]Department of Physical and Health Education, The University of Tokyo, Japan;

Abstract

The thalamus has been recognized to play an important role in sleep. Although the direct detection of functional changes of the thalamus is not possible using scalp electroencephalogram (EEG), some inferences may be possible by this method because functional change of the thalamus is thought to affect EEG signals and these effects can be mathematically modelled by the thalamocortical model (TC model). In this paper, we propose a novel method to estimate the Cortico-Thalamo-Cortical (CTC) loop strength. By identifying the transfer function of the Autoregressive (AR) model with the transfer function of the TC model, we derived a direct expression of CTC loop strength using AR coefficients. Sleep-EEG data analysis using this method clearly tracked the wake-sleep transition; consistent with previous studies, the estimated cortico-thalamo-cortical loop strength decreases to almost zero during the wake-sleep transition. Furthermore, we propose a stochastic process model for Waking during Nocturnal Sleep (WS) based on this method. The model simulates the experimental observation well, suggesting usefulness and validity of the method from the perspective of CTC loop.

Keywords *Autoregressive Model, Cortico-Thalamo-Cortical Loop, Electroenchephalogram, Transfer Function, Wake-Sleep Transition*

1 Introduction

The thalamus has been recognized to play an important role in sleep onset [1, 2]. Although the direct detection of functional changes of the thalamus is not possible using scalp EEG (electroencephalogram), some inferences may be possible by this method because functional change of the thalamus is thought to affect EEG signals and these effects can be mathematically modelled by the thalamocortical model (TC model) [3, 4]. While some studies have shown the validity and effectiveness of TC models [3-6], further technical investigation is needed towards practical and clinical applications. One issue which needs to be dealt with is time resolution. In most cases, a power spectrum is used for model-fitting [5, 6] but this process causes time resolution deterioration because long-time data are required to extract reliable power spectrums from noisy (stochastic) EEG data. A second issue is the so-called "local minimum" or non-uniqueness in the fitting (optimizing) procedure, arising from having a large number of fitting parameters and nonlinear contributions of parameters to the power spectrum.

In this paper, we propose a novel method to deal with the abovementioned issues. The basic idea is parallel use of an auto-regressive (AR) model with the TC model in data processing. The AR model is a "stochastic" model that shortens the time to extract power spectrums and is also a "linear" model that is free from the local-minimum problem. By identifying the transfer function of the AR model with the transfer function of the TC model, we derived a direct expression of CTC loop strength using AR coefficients. Sleep-EEG data analysis using this method clearly tracked the wake-sleep transition; the estimated CTC loop strength (c_2) decreases to almost zero during the wake-sleep transition as is consistent with previous studies [1-3].

We also found that the c_2 –distribution during nocturnal sleep exhibits a clear bimodal nature, which can be well approximated by superposition of two Gaussian distributions corresponding to sleep (Non-REM 1-4 and REM) and wake states, respectively. We show that this finding naturally leads a stochastic process model of waking during nocturnal sleep (WS) and that the model simulates the experimental observation well. We believe that the method from the perspective of CTC loop provides new insight into Wake-Sleep Transition.

2 Methods

2.1 Analytical Method to Estimate Cortico-Thalamo-Cortical Loop Strength

We use the compact model proposed by Kim and Robinson [4, 5]. The frequency transfer function of the model is derived as

$$H^{-1} = (-t_e^2\omega^2 - c_1 - c_2\cos\omega t_0) + j(2t_e\omega + c_2\sin\omega t_0) \quad . \qquad (1)$$

Here c_2 denotes cortico-thalamo-cortical (CTC) loop strength which is focused on in this study. t_0 denotes loop delay. c_1 and t_e are related to cortical activity.

To extract c_2 from EEG data with the least interference of the other parameters, we deform (1) to the next equation.

$$c_2 = \frac{1}{\pi}\int_0^{\frac{2\pi}{t_0}} \frac{d\,\mathrm{Im}[H^{-1}]}{d\omega}\cos\omega t_0 d\omega \qquad (2)$$

On the other hand, we are also able to derive the frequency transfer function with the help of Auto Regressive (AR) model as

$$H_{AR}^{-1} = \sum_{m=0}^{M} a_m e^{-jm\omega T_s} . \qquad (3)$$

Replacing H_{AR} with H in (2) derives the next equation giving a direct estimation of c_2 from AR coefficients as

$$c_2 = -\frac{T_s}{t_0}\sum_{m=1}^{M} a_m m\left\{\mathrm{sinc}[(mT_s + t_0)\frac{2\pi}{t_0}] + \mathrm{sinc}[(mT_s - t_0)\frac{2\pi}{t_0}]\right\} \qquad (4)$$

So if t_0 is known, we can extract c_2 from EEG data.

We adopt two ways for t_0 treatment; assuming a nominal constant value (t_0 = 80msec) [3, 4], and "variable t_0" (computing c_2 - t_0 curve). The constant assumption makes the analysis simple and is suited to the first step to further analysis. Using a variable t_0 is somewhat complicated and time-consuming, but expected to extract richer information from EEG.

We can draw a theoretical c_2 - t_0 curve using (1) and (2). Assuming $t_{0=}$ t_0 (forward) in (1) and $t_{0=}$ t_0(inverse) in (2), the ratio r = c_2 (inverse simulated) / c_2 (used in forward simulation) can be obtained as

$$r = y[\mathrm{sinc}2\pi(y+1) + \mathrm{sinc}2\pi(y-1)] \qquad (5)$$

Here, y= t_0 (forward) / t_0 (inverse). Fig.1 shows the t_0 - r curve obtained by (5), assuming t_0=90ms.

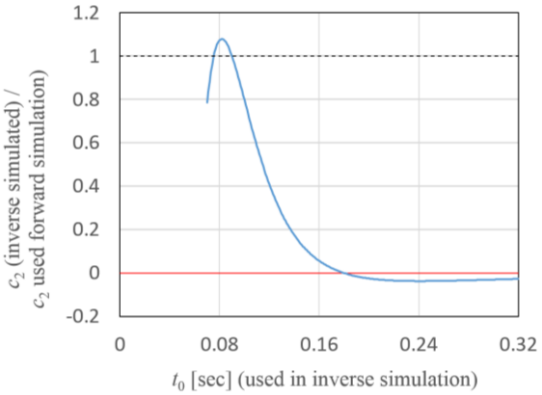

Fig. 1: Theoretical r - t_0 curve.

2.2 Data Acquisition

To evaluate the validity of the theory described above and elucidate the dynamical change of c_2 during nocturnal sleep, a dataset used in previous work [7] (but only from healthy subjects) was analyzed. The subjects, 26 healthy women (age: 38 ± 8 years; mean ± SD) underwent full nocturnal polysomnography. Measurements included EEG (electrode C3/A2, sampling period Ts =1/128Hz), electrooculogram, submental electromyogram, anterior tibialis electromyography, a lead II electrocardiogram, thoracic and abdominal motion, airflow using a nasal cannula/pressure transducer and an oral thermistor, and pulse oximetry. Sleep was scored every 30 seconds by a single scorer according to standard criteria of Rechtschaffen and Kales. See [7] for more details.

3 Results

3.1 Wake to Sleep Transition

Fig.2 shows an example for one subject of c_2 time series during the Wake-Sleep transition estimated by (4) every 15 seconds, with sleep stage time series determined by polysomnography. C3 electrode (international 10-20 system), T_s=1/128Hz, t_0=80ms and M=10 ($T_s \times M \fallingdotseq t_0$) are used. We can see that c_2 tracks the Wake-Sleep transition well, i.e. c_2 decreases from a positive value just before falling sleep, and after falling sleep c_2 is almost constant nearly equal to zero. The same dynamical change was observed also in the other subjects. Fig.3 shows averaged time course over 26 subjects. We defined the sleep onset of each subject as "the first N2" and designated that timing as t = 0.

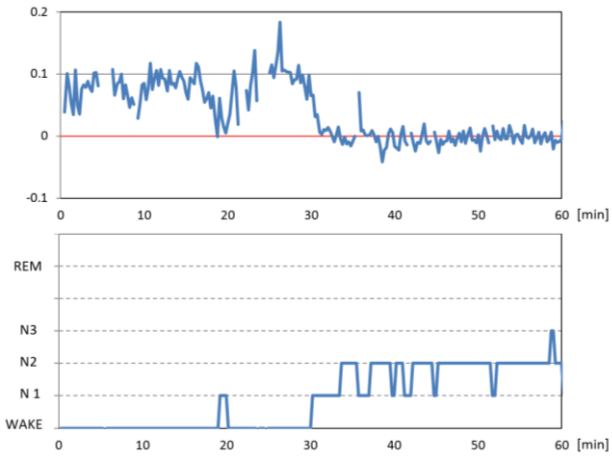

Figure 2: Estimated c_2 time series during Wake-Sleep transition.

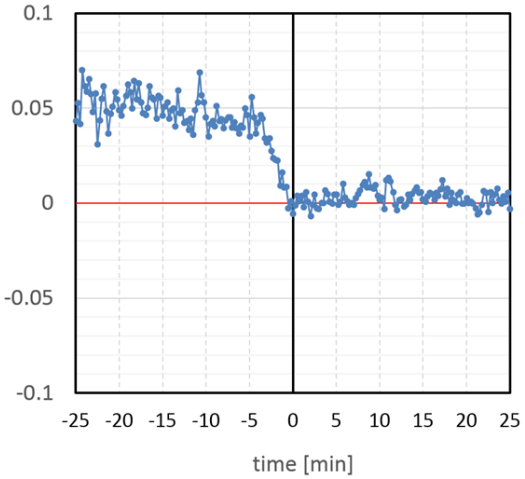

Figure 3: Estimated c_2 time series during Wake-Sleep transition (averaged over 26 subjects).

3.2 During Nocturnal Sleep

Fig.4 shows the c_2 - t_0 curve averaged in each sleep stage and averaged over 26 subjects. In this estimation, we use "variable t_0" to investigate the loop resonance effect further. A short t_0 region corresponding to high frequency oscillations (higher than about 15Hz) is omitted because Kim and Robinson's compact model and therefore the analyzing method based on it loses validity in such a high frequency region [1,2]. In Wake, the c_2-t_0 curve shows a predominant peak around t_0=80msec which is naturally interpreted as CTC resonance. Note that the curve in Fig.1 imitates the curve of Wake in Fig. 4. On the other hand, in N2-4, curves are rather flat near the horizontal axis (Fig.4). Most importantly, these curves do not resemble the curve in Fig.1, even if flipped upside down. Slight peaks observed in N2-3 may originate from sources other than the CTC loop, i.e. the intra-thalamus loop. As for N1 and REM sleep, they can be understood as transient or intermediate states between Wake and Non-REM sleep.

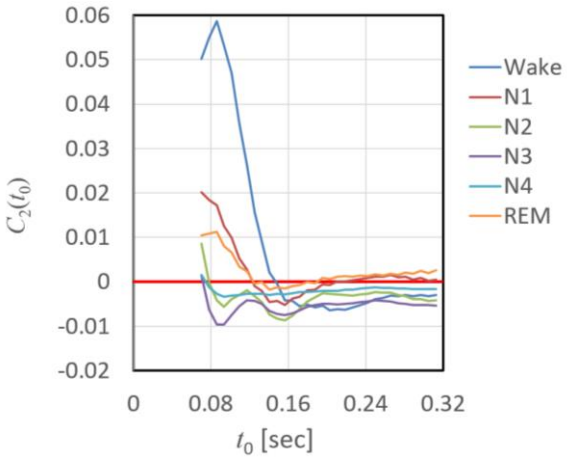

Figure 4: c_2 - t_0 curves in each sleep stage.

3.3 Waking During Nocturnal Sleep

Fig.5 shows the c_2-distribution (heathy subjects, n = 26) during nocturnal sleep. The distribution exhibits a clear bimodal, which can be well approximated by superposition of two Gaussian distributions corresponding to sleep (Non-REM 1-4 and REM) and wake states, respectively. This observation suggests that the dynamical change of c_2 obeys the Ornstein–Uhlenbeck process in each state. Based on these findings, we propose a stochastic process model of Waking during Nocturnal Sleep as below.

$$c_2(t+\Delta t)-\overline{c_2}[i(t)]=\left\{c_2(t)-\overline{c_2}[i(t)]\right\}\exp\left(-\frac{\Delta t}{\tau[i(t)]}\right)+\sigma[i(t)]\bullet n(t) \quad (6)$$

$$P_r(i(t+\Delta t\neq i(t))=\frac{1}{1+\alpha H[i(t),c_2(t)]} \quad (7)$$

$$H[i,c_2]=\frac{A[i]}{\sqrt{\pi(\sigma[i])^2\tau[i]}}\exp\left(-\frac{\{c_2-\overline{c_2}[i(t)]\}^2}{(\sigma[i])^2\tau[i(t)]}\right) \quad (8)$$

Here, i denotes a stochastic state variable (0: sleep, 1:wake); τ, σ and overbar denote time constant, noise strength, and equilibrium value of Ornstein–Uhlenbeck process in each state, respectively. $A[0]$ and $A[1]$ ($A[0]$ + $A[1]$=1) are the ratio of sleep and wake during nocturnal sleep, respectively. α is a parameter controlling the frequency of wake-sleep transitions. Eq.6 describes stochastic time evolution of c_2 as discrete time Ornstein–Uhlenbeck process in each state (sleep/wake), while Eq.7 with Eq.8 describes transition between sleep and wake.

Figure 6 shows the simulated c_2-distribution during nocturnal sleep. $\overline{c_2[0]}=0.00$, $\overline{c_2[1]}=0.08$, $\tau[0]$=1.0min, $\tau[1]$=1.8min, $\sigma[0]$=0.02min$^{-1/2}$, $\sigma[1]$=0.04min$^{-1/2}$, $A[0]$=0.95, $A[1]$=0.05, α =6.685 are used.

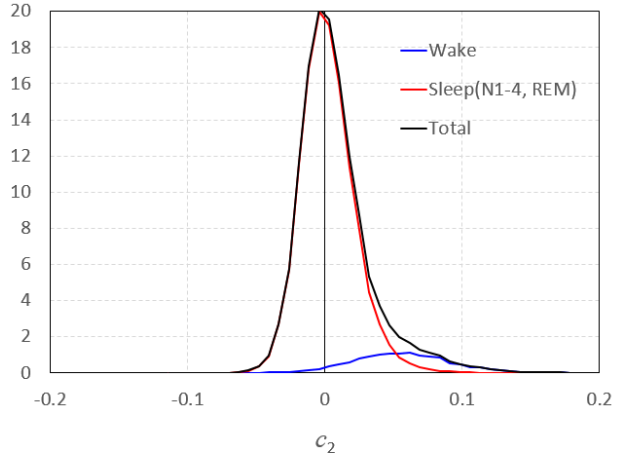

Figure 5: c_2-distribution during nocturnal sleep

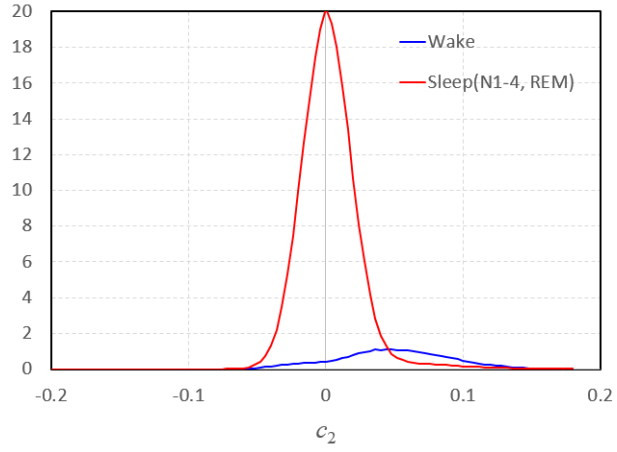

Figure 6: c_2-distribution during nocturnal sleep (simulated).

The simulated distribution corresponds to the experimental one very well, including slight distortion from Gaussian distribution.

Fig.7 shows an example for experimental and simulated patterns of transitions between Wake and Sleep during nocturnal sleep. The simulated pattern resembles the experimental one very well.

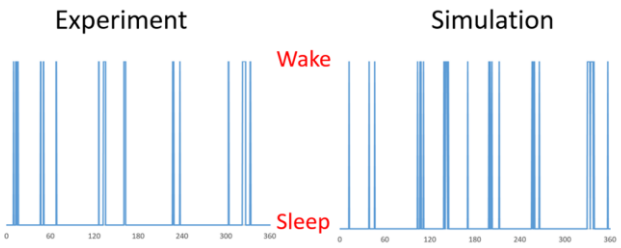

Figure 7: Wake-Sleep Transition Pattern during Nocturnal Sleep.

Fig.8 shows the probability density of Wake Duration (WD) during nocturnal sleep. In the range below several minutes, the simulated distribution of WD agrees with the experimental distribution, obeying a power law [7, 8].

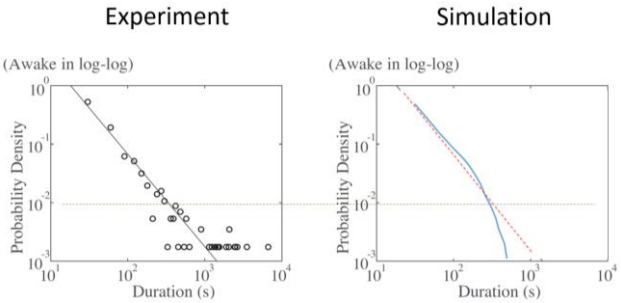

Figure 8: probability density of Wake Duration during nocturnal sleep.

4 Conclusions

In this work, we proposed a novel data processing method to analyze the Wake-Sleep transition based on a cortico-thalamic neural mass model. We confirmed that the parameter c_2 decreases at the sleep onset and is almost zero in deep sleep (N2-N4). As c_2 represents the effective strength of the CTC loop, this finding suggests that the Wake-Sleep transition can be understood as an "opening" of the CTC loop, which might be related to losing consciousness during sleep. Furthermore, we proposed a stochastic process model for waking during nocturnal sleep based on the analysis. We believe that these findings provide new insight into the Wake-Sleep transition with a new method of scalp EEG analysis.

Acknowledgements

The authors thank Professor Benjamin H. Natelson at Albert Einstein College of Medicine for his providing data and useful discussion. This work was supported by JSPS KAKENHI Grant Number 15K01499.

References

[1] D. Picchioni, ML. Pixa, M. Fukunaga, WS. Carr, SG. Horovitz, AR. Braun, JH. Duyn, Decreased connectivity between the thalamus and the neocortex during human non-rapid eye movement sleep, *Sleep*, 37(2), 2014

[2] GR. Poudel, CRH. Innes,PJ. Bone, R. Green and RD. Jones, Losing the Struggle to Stay Awake: Divergent Thalamic and Cortical Activity During Micro sleeps, *Human Brain Mapping* 35:257–269, 2014

[3] RG. Abeysuriya and PA. Robinson, Real-time automated EEG tracking of brain states using neural field theory, *Journal of neuroscience methods*, 258, 28-45, 2016

[4] JW. Kim and PA. Robinson, Compact dynamical model of brain activity, *Physical Review E*, 75, 3, 031907, 2007

[5] I. Yamaguchi, Y. Ogawa, H. Nakao, Y. Jimbo, K. Kotani, Linear Analysis of the Corticothalamic Model with Time Delay, *Electronics and Communications in Japan*, 97(8), 32-44, 2014

[6] M. Saggar, AP. Zanesco, BG. King, DA. Bridwell, KA. MacLean, SR. Aichele, TL. Jacobs, BA. Wallace, CD. Sarond, R. Miikkulainen, Mean-field thalamocortical modeling of longitudinal EEG acquired during intensive meditation training, *NeuroImage*, 114, 88-104, 2015

[7] A. Kishi, BH. Natelson, F. Togo, ZR. Struzik, DM. Rapoport and Y. Yamamoto, Sleep-stage dynamics in patients with chronic fatigue syndrome with or without fibromyalgia, *Sleep*, 34(11), 1551, 2011.

[8] C.-C. Lo, L. A. Nunes Amaral1, S. Havlin, P. Ch. Ivanov, T. Penzel, J.-H. Peter and H. E. Stanley, Dynamics of sleep-wake transitions during sleep, *Europhysics Letters*, 57(5), 625, 2002

Address for correspondence:

Ikuhiro Yamaguchi
The University of Tokyo
ikuhiro@p.u-tokyo.ac.jp

Time delay between beta EEG and heart rate variability during sleep transitions: Comparison of insomnia patients and normal controls

H. B. Kwon[1], J. W. Choi[2], Y. J. Lee[2], D. -U. Jeong[2] and K. S. Park[3]

[1]Interdisciplinary Program of Bioengineering, Seoul National University, Korea
[2]Department of Neuropsychiatry and the Center for Sleep and Chronobiology, Seoul National University Hospital, Korea
[3]Department of Biomedical Engineering, the College of Medicine, Seoul National University, Korea

Abstract

Previous studies have described the presence of unsynchronized changes of the autonomic nerve system (ANS) and brain activity in time. The studies revealed that cardiac changes interact with EEG changes by a few minutes time delay in healthy subjects. Insomnia is known as a risk factor for psychiatric disorders, chronic medical disorders and cardiovascular disease. However, how the insomnia alters the interaction between cardiac autonomic system and EEG during sleep has yet been established. In this study, the time delay between HRV parameters which can access the ANS and beta EEG frequency band at the sleep transition moment was calculated with cross-correlation function in insomnia patients was compared with those in normal controls. As a result, at the sleep transition from light sleep to REM sleep, the time delay between frequency HRV parameters and beta EEG frequency band in insomnia were shorter than those in normal controls. The results suggest that the interaction between autonomic cardiac activity and sleep EEG decrease in insomnia patients.

Keywords *Beta EEG, Heart rate variability, Sleep transition, Insomnia, and Autonomic nervous system*

1 Introduction

Heart rate variability (HRV) analysis is one of the simplest non-invasive methods to easily measure changes in autonomic activity which reflects the relationship between the parasympathetic and the sympathetic nervous system [1,2]. HRV analysis can be conducted using time or frequency domain analysis in R-R intervals which is the time between consecutive R-peak of the QRS complex on the electrocardiogram (ECG) [3].

In the past decade, changes in HRV in accordance to changes in sleep architecture as seen on the electroencephalogram (EEG) within the sleep-wake cycle have been studied. These studies have described the presence of unsynchronized changes of the autonomic nerve system (ANS) and brain activity in time [4-8]. The previous studies reported that cardiac changes preceded EEG changes by a few minutes in healthy subjects [3,6,8]. The results suggested that the relation between cardiovascular control and sleep regulation structure, such as thalamus and cortex, could be a system of two phase coupled oscillators. It can be noted that the time delay between EEG and cardiac activity indicates the interaction.

Insomnia is defined as a feeling difficulty falling asleep or maintaining sleep, which results in decline in the quality of sleep. Insomnia may cause the development of psychiatric disorders such as depression, anxiety and other chronic medical disorders such as diabetes and arthritis [9]. And insomnia is reported as an independent risk factor for cardiovascular disease such as coronary heart disease and myocardial infraction [10-12]. However, how the insomnia alters the interaction between cardiac autonomic system and EEG during sleep has yet been established.

Jurysta et al., 2009 studied the interaction between a HRV parameter and sleep EEG power with coherency analysis and demonstrated that primary insomnia showed a less coherence between HRV and delta sleep EEG power than normal controls. But the primary insomnia has no significant difference in the time delay between two time series in comparison with normal controls. However, the methodology under the study did not take into account the possible impact of non-stationarity of the signals [7]. Moreover, the study considered only one HRV parameter (normalized high frequency).

We, therefore, hypothesize that the interaction between autonomic cardiac activity and sleep EEG is altered in insomnia patients. To test the hypothesis, the time delay between six HRV parameters and beta EEG frequency band at the sleep transition moment was calculated with cross-correlation function in insomnia patients was compared with those in normal controls.

2 Methods

2.1 Subjects

In the current study, 20 patients with primary insomnia according to DSM-IV criteria (American Psychiatric Association, 1994) and 20 healthy controls who had undergone diagnostic overnight PSG at the Center for Sleep and Chronobiology of Seoul National University Hospital were included The nocturnal polysomnographic

recordings were conducted based on the standard PSG manual and scored by certified sleep technologists and verified by sleep physicians in accordance with the 2007 AASM manual [13]. All subjects were free of any cardiovascular disorders; neurological disorder; sleep-related movement disorder; psychiatric pathologies. Anthropometric and sleep parameters of the subjects are summarized in table 1. The gender ratio, age, and body mass index (BMI) were matched between the two groups. The apnea-hypopnea index (AHI) and periodic limb movement index were lower than 10 events/h.

Characteristic	Normal	Insomnia
N	20	20
Sex, M/F	6/14	6/14
Age, y	45.8 ± 15.3	47.5 ± 10.2
BMI, kg/m^2	23.7 ± 1.8	22.7 ± 2.4
AHI, /h	5.5 ± 3.2	6.3 ± 2.0
PLMI, /h	5.3 ± 4.1	6.8 ± 3.8
Total Sleep Time, min	427.9 ± 54.1	329.1 ± 56.4
Sleep latency, min	16.1 ± 6.6	38.6 ± 15.4*
Sleep Efficiency, %	91.5 ± 6.7	77.8 ± 7.0**
% Wake	7.23 ± 5.11	11.61 ± 8.07
% Light sleep	62.40 ± 6.61	63.03 ± 7.65
% Deep sleep	6.49 ± 7.20	5.35 ± 4.18
% REM sleep	23.67 ± 4.97	19.81 ± 5.81**

Table 1. Comparisons of insomniac patients and healthy controls with Mann-Whitney U test. Means ± Standard Deviation. BMI, body mass index; AHI, apnea-hypopnea index; PLMI, periodic limb movement index; $^*p < 0.05$. $^{**}p < 0.01$. $^{***}p < 0.001$.

2.2 Experimental Design

The EEG activity was quantified by beta spectral power band, 16.0–25 Hz. The EEG power band was obtained by a fast Fourier transformation of EEG recordings during each non-overlapping 5-s data window. The spectral power was averaged over 30-s epochs. The HRV parameters were derived from the ECG signals over a 9-epoch window centered on each 30-s epochs to include reliable heartbeats for reduction of signal noise. HR, SDNN, LF, HF, VLF and LF/HF were included for HRV parameters. Afterwards, all parameters were normalized to zero mean and unit variance (Z-score) for each recording.

To calculate time delay between the changes of HRV and EEG activity, we considered the periods with 10 epochs (5 min) before and after each sleep transition moment to obtain sufficient data for cross-correlation analysis. The sleep transitions which have under 5% were excluded considering relying data for analysis (Table 2).

Moreover, the periods where the only one sleep transition occurred in each period were included for analysis to avoid other transition effects [8] and the periods where any respiratory or sleep movement event occurred were excluded [14, 15]. In totally, 212 periods and 193 periods were selected from all recordings (Table 3).

State		The next state			
		Deep sleep	Light sleep	Wake	REM sleep
The previous state	Deep sleep		11.9	0	0
	Light sleep	10.8		22.7	10.8
	Wake	1.1	30.8		1.1
	REM sleep	0.07	4.7	1.6	

(a)

State		The next state			
		Deep sleep	Light sleep	Wake	REM sleep
The previous state	Deep sleep		15.4	0	0
	Light sleep	7.6		27.1	11.5
	Wake	0.04	27.7		3.8
	REM sleep	0.1	4.4	2.3	

(b)

Table 2. (a) Mean percentages of sleep transitions in normal controls (b) Mean percentages of sleep transitions in insomnia patients. Gray: excluded transitions.

Transition	Number of transitions, n	
	Normal	Insomnia
W → LS	46	41
LS → W	38	35
LS → RS	62	59
LS → DS	35	31
DS → LS	31	27
In total	212	193

Table 3. Number of transitions in normal controls and insomnia patients

To study the time delay between HRV parameters and beta EEG frequency band at sleep transition, cross-correlation function was applied [16]. The cross-correlations are often used to quantify temporal delay between two sets of time-series data. For a pair of sequences x_i and y_i of size N with same sampling rate, the cross-correlation function is given by

$$r_{xy}(k) = \frac{\sum_{i=1}^{k}(x_i - \bar{x})(y_{i+N-k} - \bar{y}) + \sum_{i=k+1}^{N}(x_i - \bar{x})(y_{i-k} - \bar{y})}{\sqrt{\sum_{i=1}^{N}(x_i - \bar{x})^2}\sqrt{\sum_{i=1}^{N}(y_i - \bar{y})^2}} \quad (1)$$

Where k refers a time shift of one signal(y) relative to the other signal (x) and r_{xy} vary from -1 to 1 representing the similarity between the two signals with k time shift. Also, $\bar{x}$ and $\bar{y}$ are the sample mean of signal x and y, respectively. The delayed time $\Delta\tau$ was calculated by the time shift with maximum absolute correlation coefficient as following:

$$\Delta\tau = \underset{k}{argmax}\left|r_{xy}(k)\right|, \quad k = 1,2,\cdots,N \quad (2)$$

A positive $\Delta\tau$ value indicates that EEG frequency band change precedes HRV parameters time lag $\Delta\tau$ (30-s epochs). Conversely, a negative value means that EEG

frequency band changes later than HRV parameters on average.

2.3 Statistical analysis

To detect differences between insomnia patients and healthy controls, the comparison of time delay between HRV parameter changes and EEG changes in insomnia patients and healthy controls were performed with nonparametric test (i.e., the Mann–Whitney U test) because that the distribution was not normal. The significance level was set at $p < 0.05$.

3 Results

The calculated time delay and the correlation coefficient at sleep transitions are written in Table 4. The significant difference between normal controls and insomnia patients appeared only in the sleep transition from light sleep to REM sleep.

In sleep transition light sleep to REM sleep, HR and SDNN in insomnia did not differ from those in normal, but LF, HF, VLF and LF/HF were shown as shorter time delay in insomnia with 1-1.5 min than normal with 2.5 min-4.5min.

HRV parameter		W → LS	LS → W	LS → RS	LS → DS	DS → LS
HR	Δτ	-1	0	-1	-1	0
	r	0.88	0.80	0.85	-0.70	-0.81
SDNN	Δτ	-2	-4	-2	-3	-4
	r	0.82	0.68	0.53	0.66	0.70
LF	Δτ	-4	-2	-5	-3	-3
	r	0.76	0.77	0.63	0.74	0.87
HF	Δτ	-4	-3	-8	-4	-4
	r	-0.76	-0.65	-0.64	-0.76	-0.78
VLF	Δτ	-5	-3	-9	-4	-5
	r	0.81	0.67	0.49	0.64	0.77
LF/HF	Δτ	-5	-6	-7	-6	-6
	r	0.70	0.68	0.65	0.80	0.76

(a)

HRV parameter		W → LS	LS → W	LS → RS	LS → DS	DS → LS
HR	Δτ	-1	0	-1	-1	-1
	r	0.68	0.74	0.81	-0.88	-0.71
SDNN	Δτ	-3	-4	-1	-3	-3
	r	0.86	0.56	0.65	0.48	0.68
LF	Δτ	-5	-2	-2*	-3	-4
	r	0.84	0.81	0.65	0.71	0.69
HF	Δτ	-4	-5	-3**	-5	-5
	r	-0.62	-0.63	-0.71	-0.73	-0.70
VLF	Δτ	-5	-3	-2**	-4	-4
	r	0.76	0.77	0.84	0.78	0.80
LF/HF	Δτ	-5	-7	-2**	-6	-5
	r	0.77	0.68	0.65	0.70	0.71

(b)

Table 4. Results of time delay Δτ [30-s] and the maximum correlations coefficients *r* between beta EEG frequency band and six HRV parameters for sleep transition from light sleep to REM sleep. (a) Normal controls (b) Insomnia patients. *$p < 0.05$. **$p < 0.01$.

4 Conclusions

In current study, we investigated the time delay between cardiac and brain activity for different sleep transitions in sleep of normal and insomnia patients. We demonstrated that patients suffering from chronic primary insomnia showed a decreased amount of interaction between beta EEG band and HRV frequency domain parameters in sleep transitions from light sleep to REM sleep. Patient with insomnia exhibit the increased beta EEG activity during sleep in comparison with normal controls [17, 18].

According to the neuronal transitias probability (NTP) model [19], the rate of decline in beta activity over the NREM sleep cycle is slower and thus may represent phase shifted waveform. The phase-shifted beta EEG wave affects the time delay between beta EEG and HRV at the transition moment.

The results suggest that the interaction between autonomic cardiac activity and sleep EEG decrease in insomnia patients.

Previous research on the coupling between EEG and cardiac autonomic activity has focused mainly on the interactions between sleep delta activity and normalized high frequency cardiac activity [9], while our study extended this analysis to beta EEG frequency band. Also, the signals considered in this study were time series at the transition moments which were not have any impact of respiratory or sleep movement event and non-stationary signal.

These investigations helped provide better insight into the complex relation between sleep and autonomic system, and led also to promising indications about the diagnosis and treatment of insomnia.

Acknowledgements

This research was supported by Coway Co., Ltd..

References

[1] Acharya, U. Rajendra, et al. Heart rate variability: a review. *Medical and biological engineering and computing*, 44.12: 1031-1051, 2006.

[2] Palma, J. A., Alegre, M., Valencia, M., Artieda, J., Iriarte, J., & Urrestarazu, E. Basal cardiac autonomic tone is normal in patients with periodic leg movements during sleep. *Journal of Neural Transmission,* 121(4), 385-390, 2014.

[3] Jurysta, F., Lanquart, J. P., Van De Borne, P., Migeotte, P. F., Dumont, M., Degaute, J. P., & Linkowski, P. The link between cardiac autonomic activity and sleep delta power is altered in men with sleep apnea-hypopnea syndrome. American Journal of Physiology-Regulatory, *Integrative and Comparative Physiology*, 291(4), R1165-R1171, 2006.

[4] Brandenberger, G., Ehrhart, J., Piquard, F., & Simon, C. Inverse coupling between ultradian oscillations in delta wave activity and heart rate variability during sleep. *Clinical*

neurophysiology, 112(6), 992-996, 2001.

[5] Ako, M., Kawara, T., Uchida, S., Miyazaki, S., Nishihara, K., Mukai, J. & Okubo, Y. Correlation between electroencephalography and heart rate variability during sleep. *Psychiatry and clinical neurosciences*, 57(1), 59-65, 2003.

[6] Jurysta, F., Van De Borne, P., Migeotte, P. F., Dumont, M., Lanquart, J. P., Degaute, J. P., & Linkowski, P. A study of the dynamic interactions between sleep EEG and heart rate variability in healthy young men. *Clinical neurophysiology*, 114(11), 2146-2155, 2003.

[7] Dumont, M., Jurysta, F., Lanquart, J. P., Migeotte, P. F., Van De Borne, P., & Linkowski, P. Interdependency between heart rate variability and sleep EEG: linear/non-linear?. *Clinical neurophysiology*, 115(9), 2031-2040, 2004.

[8] Long, X., Arends, J. B., Aarts, R. M., Haakma, R., Fonseca, P., & Rolink, J. Time delay between cardiac and brain activity during sleep transitions. *Applied Physics Letters*, 106(14), 143702, 2015.

[9] Jurysta, F., Lanquart, J. P., Sputaels, V., Dumont, M., Migeotte, P. F., Leistedt, S. & Van De Borne, P. The impact of chronic primary insomnia on the heart rate–EEG variability link. *Clinical neurophysiology*, 120(6), 1054-1060, 2009.

[10] Schwartz, S. W., Cornoni-Huntley, J., Cole, S. R., Hays, J. C., Blazer, D. G., & Schocken, D. D. Are sleep complaints an independent risk factor for myocardial infarction? *Annals of epidemiology*, 8(6), 384-392, 1998.

[11] Schwartz, S., Anderson, W. M., Cole, S. R., Cornoni-Huntley, J., Hays, J. C., & Blazer, D. Insomnia and heart disease: a review of epidemiologic studies. *Journal of psychosomatic research*, 47(4), 313-333, 1999.

[12] Sofi, F., Cesari, F., Casini, A., Macchi, C., Abbate, R., & Gensini, G. F. Insomnia and risk of cardiovascular disease: a meta-analysis. *European journal of preventive cardiology*, 21(1), 57-64, 2014.

[13] C. Iber and American Academy of Sleep Medicine. The AASM manual for the scoring of sleep and associated events: rules, terminology and technical specifications. Westchester, IL: American Academy of Sleep Medicine, 2012.

[14] Sasai, T., Matsuura, M., & Inoue, Y. Change in heart rate variability precedes the occurrence of periodic leg movements during sleep: an observational study. *BMC neurology*, 13(1), 139, 2013.

[15] Varon, C., Caicedo, A., Testelmans, D., Buyse, B., & Van Huffel, S. A novel algorithm for the automatic detection of sleep apnea from single-lead ECG. *IEEE Transactions on Biomedical Engineering*, 62(9), 2269-2278, 2015.

[16] Abdullah, H., Maddage, N. C., Cosic, I., & Cvetkovic, D. Cross-correlation of EEG frequency bands and heart rate variability for sleep apnoea classification. *Medical & biological engineering & computing,* 48(12), 1261-1269, 2010.

[17] Lamarche, C., Ogilvie, R. Electrophysiological changes during the sleep onset period of psychophysiological insomniacs, psychiatric insomniacs, and normal sleepers. *Sleep*. 20:724-7331 1997.

[18] Perlis, M. L., Merica, H., Smith, M. T., & Giles, D. E. Beta EEG activity and insomnia. *Sleep medicine reviews*, 5(5), 365-376, 2001.

[19] Merica, H., & Fortune, R. D. A neuronal transition probability model for the evolution of power in the sigma and delta frequency bands of sleep EEG. *Physiology & behavior*, 62(3), 585-589, 1997.

Address for correspondence:

Hyunbin Kwon
Interdisciplinary Program of Bioengineering, Seoul National University
chaskwon@bmsil.snu.ac.kr

Heart Rate and Heart Rate Variability Monitoring during Sleep using 24-GHz Microwave Radars Located beneath the Mattress on the Bed

M Kagawa[1], K Suzumura[2], A Hashizume[2], T Matsui[2],

[1]Faculty of System Design, Tokyo Metropolitan University, Japan;
[2]Graduate School of System Design, Tokyo Metropolitan University, Japan;

Abstract

Here, we describe a microwave radar system and analysis method for non-contact monitoring of heart rate (HR) and heart rate variability (HRV). Microwave radar parameters were compared with those obtained with a reference polysomnography measurement. The proposed system can measure pulse waves of a sleeping patient using two 24-GHz microwave radars placed under the mattress. We developed a method that dynamically selected the window width of the moving average filter to extract the pulse waves from the radar output signals. Test measurements were performed in 10 healthy male subjects. The mean Pearson correlation coefficients for the two overnight HR and HRV measurements derived from the microwave radars versus those from the reference polysomnography were 0.89 and 0.69, respectively. The accuracy of sleep stage classification using the radar system ranged from 0.59 to 0.79. These data suggest that our dual microwave radar system can accurately measure high sensitivity pulse waves. Measurement of HR and HRV derived from microwave radar may be useful in assessment of sleep quality and other health-related parameters at nursing care facilities.

Keywords *Physiological monitoring, Heart rate, Heart Rate Variability, Non-Contact Measurement, Radar*

1 Introduction

There is increasing interest in use of non-contact measurement techniques for health assessment, including cardiac activity for elderly people in nursing homes [1], drivers in a car [2], and athletes during exercise [3]. Electrocardiogram (ECG) measurements, particularly heart rate (HR) and heart rate variability (HRV), provide important data on autonomic nervous system (ANS) activity and various health-related indicators. Further, by analyzing ANS activity, it is possible to classify sleep stages and diagnose the severity of obstructive sleep apnea. The Holter-type measurement device is the traditional method for long-term ECG recording, although it requires obtrusive wired electrodes. Thus, techniques for non-contact monitoring of nighttime cardiac activity in unaware patients have been developed, using direct or indirect measurement of the small skin displacements caused by arterial blood pulse waves, as well as electromagnetic energy generated in the heart [4]. These non-contact methods include microwave and ultrasound (40 kHz) radars (termed direct mechanical methods) [5, 6], ballistocardiograms (pressure sensitive sensors; termed indirect mechanical methods) [1, 7, 8], and capacitive type electrodes (textile electrodes; termed electromagnetic methods) [9, 10]. However, these systems have a number of limitations, including relatively small distances between the measuring sensor and the human body, and susceptibility to environmental disturbances and movement artifacts. These limitations are method dependent. For example, ballistocardiograms and capacitive type electrodes are more dependent on the distance (<5 cm) between the sensor and the subject than microwave radars. By contrast, microwave and ultrasound radar techniques are capable of extracting HR information over large distances [4]. However, they exhibit a susceptibility to human posture and position in bed. Successful detection of respiratory rate and HR based on frequency analysis using microwave radar from four sides of the human body was also reported [5], although accurate detection of the overnight RR intervals is required for calculation of HRV.

In the present study, we propose a novel HR and HRV monitoring system using microwave radars and dynamic selection of the window width of the moving average filter, which allows robust and reliable long-term overnight measurement. This method can overcome the movement artifacts commonly associated with microwave radars, and can accurately classify sleep stages in test subjects.

2 Methods

2.1 Measuring system and data collection

The non-contact HR and HRV monitoring system is shown in Fig. 1. Two microwave radar sensors (24 GHz, NJR4262J; New Japan Radio, Tokyo, Japan) were installed beneath the mattress of each subject's bed, located at their home or nursing care facility. The output of the radar was 40 mW equivalent isotropically radiated power, and the incident power density on the body surface was 1.5×10^{-2} mW/cm^2, which is much lower than the Japanese safety guidelines for protection from harmful electromagnetic waves (1 mW/cm^2). Sample output signals are shown in Fig. 1. Radar output signals

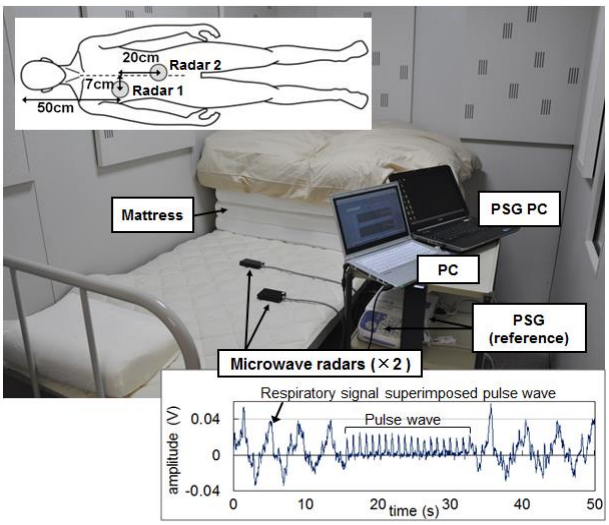

Figure 1: Setup of the HR and HRV monitoring system and representative microwave radar signals.

are composed of respiratory movements, pulse waves, and body movements. A representative example of the appearance of the pulse waves without breathing artifact is shown in Fig. 1. The microwave radar provides two orthonormal baseband signals (in-phase and quadrature baseband outputs). We used the dynamic channel selection (DCS) technique to select the optimal radar channel with the least number of irregular RR intervals from four radar output signals.

Ten healthy male volunteers from Tokyo Metropolitan University (age 22.7 ± 0.9 y) participated in this study. Recordings were performed for one night for each individual. Polysomnography (PSG) recordings (PSG1100; Nihon Kohden, Tokyo, Japan) were performed for every subject. After PSG measurement, expert personnel evaluated the subject's sleep, and stages (wake, REM, N1, N2, N3, and N4) were classified in 30 s epochs according to the American Academy of Sleep Medicine rules. All recording durations were 8 h, lasting from 22:00 to 06:00 the next morning. The research protocol was approved by The Tokyo Metropolitan University Ethics Committee, and all subjects gave written informed consent.

2.2 Detection of pulse waves from radar output signals

It is difficult to detect pulse waves from radar output signals, as this requires extraction of a small signal (pulse waves) in a large amount of background noise (respiratory and body movements). We used a moving-average filter and a background-subtraction technique to detect the pulse waves from the radar output signals (Fig. 2). For the radar-output data series, with S sampled at 100 Hz, $\mathrm{S}(n)$ can be expressed as in Eq.1.

$$\mathrm{S}(n) = \mathrm{H}(n) + \mathrm{R}(n) + \mathrm{B}(n) + \mathrm{W}(n), \qquad (1)$$

where $\mathrm{H}(n)$ are the pulse waves, $\mathrm{R}(n)$ are the respiratory movements, $\mathrm{B}(n)$ are the body movements, and $\mathrm{W}(n)$ is the white noise, at the estimated point n. Despite its simplicity, the moving-average filter is optimal for this task, as the low-pass filter removes the high-frequency components while retaining a sharp step response. The output of the symmetric moving-average filter with the input of $\mathrm{S}(n)$ is given by Eq.2.

$$\mathrm{MA}(i) = \frac{1}{N}\sum_{j=-m}^{j=m} \mathrm{S}(i+j),\ N = 2m+1, \qquad (2)$$

where N is the number of points in the average, denoted as a window width, given i as a measuring-point index. The cutoff frequency of this filter decreases with the width of the window N. For example, for a frequency cutoff of 0.55, N should be 81 (810 ms). Similarly, the window width is 41, 21, or 11 at a cutoff frequency of 1.1 Hz, 2.2 Hz, or 4.4 Hz, respectively. If the window width N is an appropriate value (e.g., 81, 41, 21, or 11), the moving-average filter provides an excellent low-pass filter, and eliminates the high-frequency movements $\mathrm{H}(i)$ and $\mathrm{W}(i)$. Thus, the filter output signal $\mathrm{MA}(i)$ can be approximated as in Eq.(3).

$$\mathrm{MA}(i) \cong \mathrm{R}(i) + \mathrm{B}(i). \qquad (3)$$

We subtracted the filter output $\mathrm{MA}(i)$ from the radar output $\mathrm{S}(i)$ to extract the pulse waves, as in Eq. (4).

$$\mathrm{S}(i) - \mathrm{MA}(i) \cong \mathrm{H}(i) + \mathrm{W}(i) \cong \mathrm{H}(i). \qquad (4)$$

The conditions required to collect pulse waves by radar can change according to body position and posture in the bed. Thus, every minute, we dynamically selected the window width (DSWW) from four values (81, 41, 21, or 11) to provide the least number of irregular periods in the detected RR intervals (Fig. 2). Posture-dependent small-amplitude R-peaks and a lower signal-to-noise ratio were observed with this method (Fig. 2b). Next, we averaged the ten newest RR intervals and defined irregular intervals as those <83% or >166% of this average [11]. R-peaks were detected using an adaptive-threshold algorithm. HR was calculated from the average of the ten newest RR intervals.

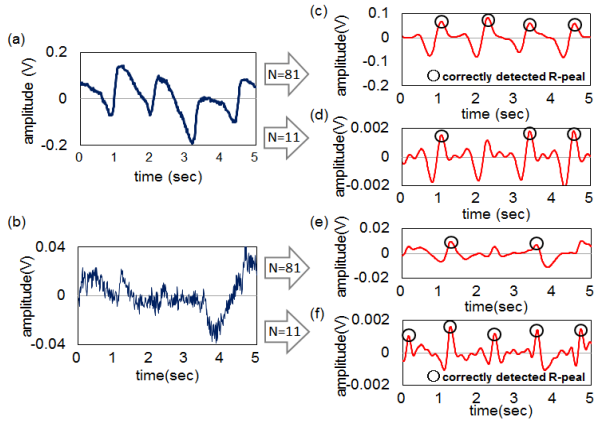

Figure 2: Dynamic selection of the most suitable window width. (a, b) Radar output signals and (c–f) extracted pulse waves. (c) and (f) are examples of the optimal choice for the window width N.

2.3 Compensation for respiratory-related noise

In our test measurements, the noise amplitude of the respiratory-related signal peak was occasionally higher

than the actual R-peak amplitude (Fig. 3). Thus, in cases where the pulse waves were contaminated by respiratory movement components, we selected the R-peak that corresponded to the position of intermediate time between two surrounding R-peaks, rather than the peak with the highest amplitude.

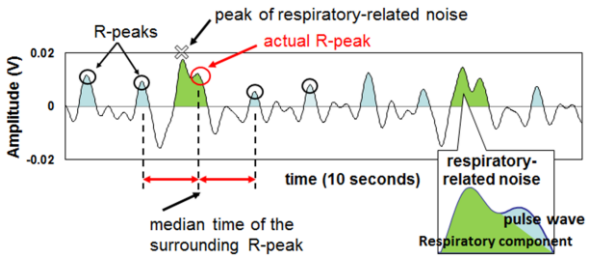

Figure 3: Compensation for respiratory-related noise. The amplitude of the pulse wave can occasionally overlap with background respiratory-related noise. In such cases, the peak corresponding to the median time of the surrounding R-peak, rather than the biggest peak, is selected as the R-peak.

2.4 HRV calculation

HRV spectral analysis was applied using the autoregressive method on a series of 120 RR intervals obtained from radar pulse waves. We determined the low-frequency (LF) components (0.04–0.15 Hz), which largely reflect sympathetic modulation with some parasympathetic influence, and the high-frequency (HF) components (0.15–0.4 Hz), which reflect parasympathetic activity. HRV is highly sensitive to artifact and errors. Thus, we used the DSWW method to remove artifacts and RR interval errors prior to spectral analysis.

3 Results and Discussion

3.1 HR and HRV measurement

Overnight time series data for HR, LF, and HF derived from the microwave radars (solid line) and by ECG (dashed line) from subject t3 are shown in Fig. 4. The Pearson correlation coefficients of the HR, LF, and HF values derived from the microwave radar with DSWW were higher than those from the microwave radar without DSWW. There was a strong correlation ($r=0.91$, $p<0.001$) of radar measurement with ECG, with an average difference of 2.5% (Fig. 4d). However, the algorithm for detecting the R-peak by microwave radar was not suitable when the RR interval rapidly decreased. The performance of this system compared with ECG is shown in Table 1. Although the average correlation coefficient of HRs derived from overnight microwave radar with the reference ECG was 88.5% (n=10), the average correlation coefficients for LF and HF parameters were lower at 73.3% and 64.5%, respectively. Although a direct comparison between our findings and previous studies is difficult because of differences in error estimators, or as reported results are for shorter, non-overnight measurements, our findings showed high HR coverages and were equivalent to capacitive type electrodes attached to the human body [9, 10].

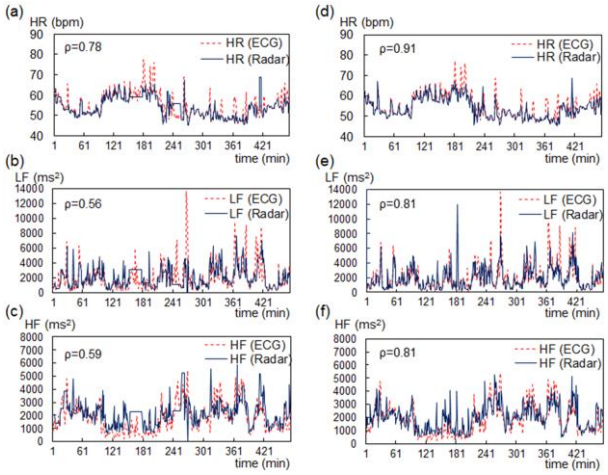

Figure 4: HR and HRV values derived from overnight microwave radars (solid line) or ECG (dashed line) from subject t3. (a) HR, (b) LF, and (c) HF without DSWW. (d) HR, (e) LF, and (f) HF with DSWW.

Table 1: Performance of the microwave radar system compared with ECG.

Subject	Pearson correlation coefficients		
	Heart rate	LF	HF
t1	0.93	0.75	0.52
t2	0.93	0.77	0.58
t3	0.91	0.81	0.81
t4	0.94	0.86	0.84
t5	0.67	0.61	0.68
t6	0.97	0.73	0.69
t7	0.90	0.71	0.57
t8	0.96	0.79	0.73
t9	0.86	0.69	0.52
t10	0.78	0.61	0.51
mean	0.885	0.733	0.645

3.2 Sleep stage classification

By applying a decision tree analysis (Weka v.3.8: The Waikato Environment for Knowledge Analysis, University of Waikato, New Zealand) that builds a predictive model using entropy to calculate the homogeneity of the data set, we classified sleep stages according to the LF/HF ratio, HF, HR, mean respiratory rate (MR), standard deviation of respiratory intervals (SDR) and the body movement index (BI) [12] derived from microwave radar data. The decision tree generated by Weka is shown in Fig. 5. BI, SDR, and LF/HF ratio were strong indices for classification of sleep stage. The performance of the classification was evaluated in each leave-one-out (LOO) cross-validation loop. The accuracy of this method compared with PSG is shown in Table 2. The accuracy of identifying two stages (wake and sleep) was 78.9%, of classifying three stages (wake, REM, and NREM) was 72.4%, and of classifying four stages (wake, REM, LIGHT, and DEEP) was 58.9%.

This was higher than that derived from canonical discriminant analysis using the same input data. The accuracy of the two-stage classification of the subject (t5) was <50%, which is why the BI indices while asleep were stronger than for other subjects.

The performance of our system was equivalent to that of recent studies using bed-sensor or decision-tree support-vector machines [7, 13]. Thus, our non-contact radar system may be useful for assessment of sleep stages classification at nursing care facilities as well as the general public.

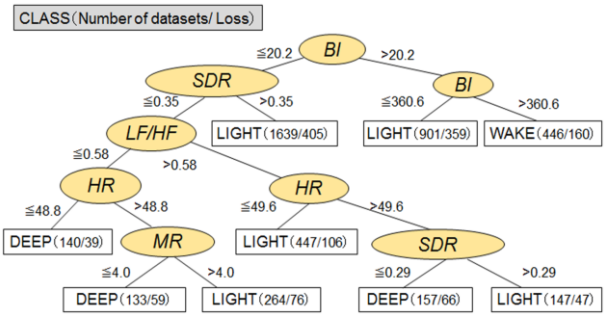

Figure 5: Decision tree generated by machine learning.

Table 2: Performance of sleep stage classification using microwave radars.

Subject	Accuracy (%)		
	2 stages	3 stages	4 stages
t1	94	80.2	65.3
t2	83.4	79.1	53.4
t3	74.8	71.7	60.1
t4	88.1	75.8	64.8
t5	43.9	26.5	26.9
t6	74.3	72.2	58.7
t7	85.3	84.5	63.3
t8	84.4	80.2	67.4
t9	79.2	75.8	71.9
t10	81.6	77.7	57.6
mean	78.9	72.4	58.9

4 Conclusions

We developed a novel non-contact overnight cardiac monitoring system that uses two microwave radars, and applied a number of signal processing techniques to assess HR and HRV in unaware subjects. This system exhibited high sensitivity, without the need for body contact, and may be useful in many health-related fields. Further studies are required to fully develop this system, including an algorithm to account for rapidly changing heartbeat intervals.

Acknowledgements

The authors thank Dr. H. Tojima at Tokyo Rosai Hospital for generous support of this research and clinical advice. This research was supported in part by the Japan Society for the Promotion of Science KAKENHI (Grant Number 26350507).

References

[1] D.W. Jung, S.H. Hwang, H.N. Yoon, Y.-J.G. Lee, D.-U. Jeong and K.S. Park. Nocturnal awakening and sleep efficiency estimation using unobtrusively measured ballistocardiogram. *IEEE Trans Biomed Eng*, 61:131-138, 2014.

[2] L. Leicht, E. Skobel, M. Mathissen, S. Leonhardt, S. Weyer, T. Wartzek, S. Reith, W. Mohler and D. Teichmann. Capacitive ECG recording and beat-to-beat interval estimation after major cardiac event. *Conf Proc IEEE Eng Med Biol Soc,* 1:7614-7, 2015.

[3] Y. Sun, S. Hu, V. Azorin-Peris, S. Greenwald, J. Chambers and Y. Zhu. Motion-compensated noncontact imaging photoplethysmography to monitor cardiorespiratory status during exercise. *J Biomed Opt*, 16:077010-1–077010-9, 2011.

[4] J. Kranjec, S. Beguš, J. Drnovšek and G. Geršak. Novel Methods for Noncontact Heart Rate Measurement: A Feasibility Study. *IEEE Trans Instrum Meas*, 63:838-847, 2013.

[5] C. Li, J. Lin and Y. Xiao. Robust overnight monitoring of human vital signs by a non-contact respiration and heartbeat detector. *Conf Proc IEEE Eng Med Biol Soc*, 1:2235-8, 2006.

[6] M. Kagawa, Y. Yoshida, M. Kubota, A. Kurita and T. Matsui. Non-contact heart rate monitoring method for elderly people in bed with random body motions using 24 GHz dual radars located beneath the mattress in clinical settings. *J Med Eng Technol*, 36:344-350, 2012.

[7] J. M. Kortelainen, M. O. Mendez, A. M. Bianchi, M. Matteucci and S. Cerutti. Sleep staging based on signals acquired through bed sensor. *IEEE Trans Inf Technol Biomed*, 14:776-785, 2010.

[8] J. Paalasmaa. A respiratory latent variable model for mechanically measured heartbeats. *Physiol Meas*, 31:1331-1344, 2010.

[9] S.B. Park, Y.S. Noh, S.J. Park and H.R. Yoon. An improved algorithm for respiration signal extraction from electrocardiogram measured by conductive textile electrodes using instantaneous frequency estimation. *Med Biol Eng Comput*, 46:147-158, 2008.

[10] M. Peltokangas, J. Verho and A. Vehkaoja. Night-time EKG and HRV monitoring with bed sheet integrated textile electrodes. *IEEE Trans. Inf Technol Biomed*, 16:935–942, 2012.

[11] J. Pan and WJ. Tompkins. A Real-Time QRS Detection Algorithm. *IEEE Trans Biomed Eng*, 32:230-236, 1985.

[12] M. Kagawa, N. Sasaki, K. Suzumura and T. Matsui. Sleep stage classification by body movement index and respiratory interval indices using multiple radar sensors. *Conf Proc IEEE Eng Med Biol Soc*, 1:7606-9, 2015.

[13] T. Lajnefa, S. Chaibia, P. Ruby, PE. Aguera, JB. Eichenlaub, M. Sameta, A. Kachouri and K. Jerbi. Learning machines and sleeping brains: Automatic sleep stage classification using decision-tree multi-class support vector machines. *J Neurosci Methods*, 250:94-105, 2015.

Address for correspondence:

Masayuki Kagawa
Faculty of System Design, Tokyo Metropolitan University, 6-6 Asahigaoka, Hino, Tokyo 191-0065, Japan
kagawa.masa2@key.ocn.ne.jp

Automatic Two-Channel Sleep-Staging Using A Predictor-Corrector Method

S. Riazy[1], T. Wendler[1], J. Pilz[2],

[1]HTW Berlin, Germany;
[2]Alpen-Adria university Klagenfurt, Austria;

Abstract

We implemented a predictor-corrector method for the classification of two-channel EEG data into sleep stages. The predictor step is realized by a Markov Chain producing an informative prior distribution via a transition matrix. The correction step is realized by applying a Bayes Classifier using the (preprocessed) data and this prior. The preprocessing step consists of a frequency analysis, a log transformation and a dimensionality reduction via Principle Component Analysis. The software automatically generates sleep profiles in which it detects wakeful phases as well as the different sleep stages with error rates of 20%-34%, where we compared our results to ones of a certified polysomnographic technologists, who used a full polysomnography and rated according to the Rechtschaffen and Kales criterion.

Keywords *Automatic sleep-staging, predictor-corrector method, Markov Chain, Bayesian statistics, EEG*

1 Introduction

Electroencephalography, a method for measuring potential differences on the head surface, is a vital instrument for the diagnosis of illnesses of the central nervous system. Ever since the 1960ies, EEGs have also been used for the examination of sleep processes. With their help, one can classify different stages of sleep as well as diagnose forms of insomnia, dysfunctions of the circadian rhythm and other pathological states of dormancy. So far, the evaluation of EEGs is done by hand with the help of a polysomnography software, which still requires time and effort. To reduce the strain of sleep-staging, it is our goal to implement an automatic sleep-staging software. Further, we are using only two-channel measurements (A_1 and A_2) in constrast to a full polysomnography, proving that machine learning algorithms require only very reduced measurement data.

1.1 Automatic Sleep-Staging

The automatic staging of sleep phases has been attempted with various different methods ([1, 2, 3, 4]). Among these methods, there are different Machine Learning algorithms, such as the classification using support vector machines (SVM) as in [2], rule-based algorithms such as in [4] or even hidden Markov models (as in [5]), the success of these algorithms varies, as the method of measurement and the data sets also greatly vary.

1.2 Two-Channel Staging

The automatic sleep-staging of single-channel or two-channel EEGs has been used in different contexts so far. In [6], ear EEGs have been proven to record signals that represent alpha activity, K complexes and other significant EEG structures and further, mastoid signals have been used for sleep-staging in [7] and [8]. This leads us to believe that ear measurements contain sufficient information for the classification of sleep stages. In our case, we will also consider the two-channel measurement of the nodes A_1 and A_2, which are measured at the ears and are typically used as reference electrodes. We used three sets of two-channel measurements.

1.3 Overview and Notation

Our data set consists of A_1- and A_2- measurements over 8 hours of sleep of several persons with a sampling rate of 256Hz. This data is divided into blocks of 30 seconds that contain 256*30=7680 measurements each for A_1 and A_2, resulting in so-called epochs

$$E_1^{A_k}, \ldots, E_T^{A_k} \in \mathbb{R}^{7680}, \;\; k = 1, 2.$$

We divide the set of epochs into a training set and a test set

$$\mathcal{E}^k_{\text{train}} = (E_1^{A_k}, \ldots, E_{T_{\text{train}}}^{A_k}), \quad \mathcal{E}^k_{\text{test}} = (\tilde{E}_1^{A_k}, \ldots, \tilde{E}_{T_{\text{test}}}^{A_k}),$$

for $k = 1, 2$. In our case, we divided the 8-hour-measurement into two halves and used the first half as the training set and the second half as the test set. This choice shall be improved in the next stages of this project, as it is known that REM sleep typically occurs more often in the second half of the night. The sleep stages corresponding to these epochs will be denoted by random variables

$$X_1, \ldots, X_{T_{\text{train}}}, \quad Y_1, \ldots, Y_{T_{\text{test}}} \in \mathcal{S}, \text{ where}$$
$$\mathcal{S} = \{\text{'Awake', 'Stage 1', 'Stage 2', 'Stage 3', 'REM'}\}$$

The epochs were classified by a professional scorer,

$$X_\tau = x_\tau, \; \tau = 1, \ldots, T_{\text{train}}, \quad Y_t = y_t, \; t = 1, \ldots, T_{\text{test}}$$

which we will assume to be the "true" classification.

Our aim is to train our algorithm using only the mapping

$$\Psi_{\text{prof}}\colon (E_\tau^{A_1}, E_\tau^{A_2}) \mapsto x_\tau,\ \ \tau = 1, \dots, T_{\text{train}},$$

of the training set to classify the test set

$$\Psi_{\text{est}}\colon (E_t^{A_1}, E_t^{A_2}) \mapsto y_t^{\text{est}},\ \ t = 1, \dots, T_{\text{test}},$$

where est stands for estimate, such that $y_t^{\text{est}} = y_t$ with high probability.

2 Methods

2.1 Preprocessing

For the classification of EEG data, the frequencies of the current epoch are a much more significant indicator for the sleep stage than the measurement vectors $E_i^{A_k} \in \mathbb{R}^{7680}$ (which are difficult to compare due to e.g. shifts in time). Therefore it is meaningful to take the Fourier transform of each measurement:

$$E_t^{A_k} \in \mathbb{R}^{7680} \ \mapsto\ F_t^{A_k} = |\text{FFT}(E_t^{A_k})| \in \mathbb{R}^{7680}.$$

In addition, switching to the frequency domain provides the possibility to get rid of confounding measurements, also called *artifacts*, which is a common problem when dealing with EEG data arising from movements of the patient or sweat on his skin. This is realized by *low pass filtering*, i.e. ignoring all frequencies above a certain threshold (85 Hertz):

$$F_t^{A_k} \ \mapsto\ \tilde{F}_t^{A_k} = \text{proj}(F_t^{A_k}) \in \mathbb{R}^{2560},$$

where $\text{proj}(v)$ is just the projection of a vector $v \in \mathbb{R}^{7680}$ onto its first 2560 coordinates. This does not lead to a loss of relevant data, since the frequencies used for professional scoring are below this threshold.

It turned out that the resulting 2560-dimensional vector space is too huge to classify upon, making a further dimension reduction step necessary. This was realized using a Principle Component Analysis (PCA), projecting onto the 20 dominant Eigenspaces of the covariance matrix of the data. The number of optimal Eigenspaces was determined via a scree plot.

Since higher frequencies tend to have smaller amplitudes, in fact, the coefficients in the Fourier transforms we considered decay exponentially, the data was logarithmized prior to the PCA. This way, an a-priori bias towards the lower frequencies is avoided.

$$\tilde{F}_t^{A_k} \ \mapsto\ \log(\tilde{F}_t^{A_k}) \in \mathbb{R}^{2560} \ \xmapsto{\text{PCA}}\ m_t^{A_k} \in \mathbb{R}^{20},.$$

where m_t is the result of the PCA. As an alternative to taking the logarithm, a scaling of each Fourier coefficient (the amplitude of each frequency) with the inverse of its mean can be performed.

Overall, the preprocessing consists of the following steps:

$$\begin{array}{ccccccc} \mathbb{R}^{7680} & \to & \mathbb{R}^{2560} & \to & \mathbb{R}^{2560} & \to & \mathbb{R}^{20} \\ E_t^{A_k} & \xmapsto[\text{proj}]{\text{FFT}} & \tilde{F}_t^{A_k} & \mapsto & \log \tilde{F}_t^{A_k} & \xmapsto{\text{PCA}} & m_t^{A_k} \end{array}$$

So, from now on, we are going to work with vectors $m_t = (m_t^{A_1}, m_t^{A_2}) \in \mathbb{R}^{40}$.

2.2 Bayes Classifier

Important elements of Bayesian inference are the *prior*, the distribution of a random variable before measurements and the *posterior*, which can be viewed as the distribution of the same random variable given (or conditioned on) a measurement. Generally speaking, for random variables A, B, with density functions ρ_A, ρ_B and realizations a of A and b of B, Bayes' theorem states:

$$\rho_A(a|B=b) = \frac{\rho_A(a)\rho_B(b|A=a)}{\rho_B(b)},$$

where each of the terms has the following name,

$$\text{posterior} = \frac{\text{prior} \times \text{likelihood}}{\text{evidence}}.$$

For a given measurement $B = b$ and an unknown random variable A, the Bayes Classifier assigns the maximum-a-posteriori (MAP) estimate:

$$a_{\text{MAP}} = \arg\max_a \rho_A(a|B=b).$$

2.3 Predictor-Corrector Method

In an attempt to improve the result of the Bayes Classifier proper prior distributions π_t are chosen for each time step. The posterior distributions p_t resulting from the application of Bayes classifier to the measurements m_t are computed and the final classification is chosen as the MAP-estimator of these distributions.

$$y_t^{\text{est}} = \arg\max_{s \in \mathcal{S}} p_t(s)$$

More specifically, the prior distribution π_1 for the initial stage Y_1 is chosen using the relative frequencies of the single stages in the training set:

$$\pi_1(s) = \frac{\#\{x_\tau = s \mid \tau = 1, \dots, T_{\text{train}}\}}{T_{\text{train}}}, \quad s \in \mathcal{S}$$

This prior distribution is updated using the (preprocessed) measurement $m_t \in \mathbb{R}^{40}$ (here for $t = 1$) and its likelihoods $L_{s,t} = \rho_{M_t}(m_t|S_t = s),\ s \in \mathcal{S},\ t = 1, \dots, T_{\text{test}}$, given the respective stages (here we denoted the random variable of preprocessed data by M_t and its realization by m_t). The posterior distribution p_t in each time step is computed via Bayes' rule:

$$p_t(s) = \frac{\pi_t(s)\, L_{s,t}}{\sum_{s' \in \mathcal{S}} \pi_1(s')\, L_{s',t}}, \quad s \in \mathcal{S}.$$

The prior π_{t+1} for the next stage Y_{t+1} can include more information than the initial stage, since we already have knowledge on the previous stage Y_t and it is e.g. more likely to transition from 'Stage 1' to 'Stage 2' than from 'Stage 1' to 'Stage 3' (in fact, it is most probable to

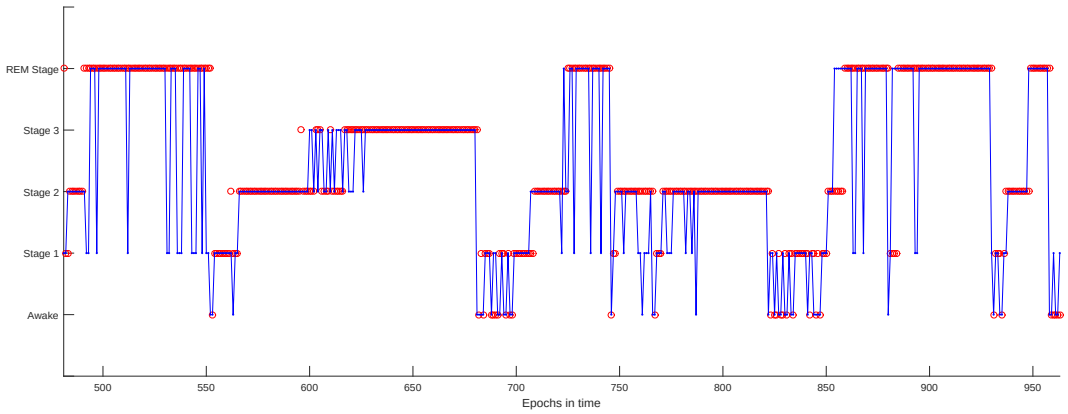

Figure 1: Classification using the predictor-corrector-based software in blue. In comparison, the classification of a professional scorer, who used the measurements of a polysomnography, is plotted in red.

stay in each stage). In accordance with the Chapman-Kolmogorov equation for discrete Markov Chains, we choose

$$\pi_{t+1} = P p_t,$$

where $P \in \mathbb{R}^{5\times 5}$ is the transition matrix computed form the relative frequencies of the transitions between each pair of stages:

$$P_{s,s'} = \frac{\#\{x_{\tau+1} = s,\ x_\tau = s' \mid \tau = 1, \ldots, T_{\text{train}} - 1\}}{\#\{x_\tau = s' \mid \tau = 1, \ldots, T_{\text{train}} - 1\}}.$$

This way, a predictor-corrector method (or discrete-time-discrete-state Kalman filter) is implemented using the information from the previous posterior for the construction of the current prior and the measurements and Bayes' rule for the update to the current posterior.

3 Results

As it can be seen in Figure 1, the overall structure of the automatic classification comes close to the scoring of a professional, who used a polysomnography. The total error rates for three patients in comparison to professionals were 20%, 24% and 34% for three patients. The detailed error rates for the three patients are given in the following table:

Stage	Awake	Stage 1	Stage 2	Stage 3	REM
Patient 1	0.21	0.34	0.19	0.10	0.21
Patient 2	0.35	0.38	0.13	0.15	0.44
Patient 3	0.36	0.33	0.19	0.17	1

Table 1: Percentage of False Classification For Each Stage

Further, the confusion matrices show that there is fairly certain classification for stages 1,3 and 4. However, stage 2 seems to be difficult to classify and the REM stage is often falsely classified as stage 1.

		Classification				
		Awake	Stage 1	Stage 2	Stage 3	REM
Stages	Awake	23	6	0	0	0
	Stage 1	14	41	4	0	3
	Stage 2	4	15	130	7	4
	Stage 3	1	0	6	63	0
	REM	4	24	6	0	128

Table 2: Confusion matrix of patient 3, where the classifications of a professional scorer are compared to the output of the algorithm.

4 Discussion

In conclusion, we can see as a proof of concept that a considerable amount of information can be extracted from the two channels A_1 and A_2 that are usually only used as reference electrodes. Also, the predictor-corrector method offers relatively few errors, even beyond the recognition of wakefulness and sleep.

Limitations of the method include the loss of information when only using two-channel sleep-staging. Certain frequencies that can mostly be measured in certain areas of the scalp, which are lost when the measurements are reduced to A_1 and A_2. Also, a better subdivision of a test and training set would have been favorable, as there is significantly more REM sleep in the second portion of the night. The classification of the measurements of Patient 3 has a very large error, as there is no REM sleep in the training set. Therefore it is impossible to be recognized in the second half of the night.

Future work will include different divisions of training and test set. Possibly, one could record two seperate measurements for the same patient, so as to use one of the measurements as training and the second one as a test set. Also, we will further use better dimension reduction and feature selection methods. Lastly, we are planning an improved adaptation of the classifier to the problem at hand, meaning that we will implement a new Bayes Classifier using an adjusted likelihood.

References

[1] Tagliazucchi, Enzo, et al. "Automatic sleep staging using fMRI functional connectivity data." Neuroimage 63.1 (2012): 63-72.

[2] Gudmundsson, Steinn, Thomas Philip Runarsson, and Sven Sigurdsson. "Automatic sleep staging using support vector machines with posterior probability estimates." Computational Intelligence for Modelling, Control and Automation, 2005 and International Conference on Intelligent Agents, Web Technologies and Internet Commerce, International Conference on. Vol. 2. IEEE, 2005.

[3] Redmond, S., and C. Heneghan. "Electrocardiogram-based automatic sleep staging in sleep disordered breathing." Computers in Cardiology, 2003. IEEE, 2003.

[4] Liang, Sheng-Fu, et al. "A rule-based automatic sleep staging method." Journal of neuroscience methods 205.1 (2012): 169-176.

[5] Pan, Shing-Tai, et al. "A transition-constrained discrete hidden Markov model for automatic sleep staging." Biomed. Eng. Online 11 (2012): 52.

[6] Zibrandtsen, I., et al. "Case comparison of sleep features from ear-EEG and scalp-EEG." Sleep Science (2016).

[7] Wang, Ying, et al. "Evaluation of an automated single-channel sleep staging algorithm." Nature and science of sleep 7 (2015): 101. APA

[8] Koley, B., and D. Dey. "An ensemble system for automatic sleep stage classification using single channel EEG signal." Computers in biology and medicine 42.12 (2012): 1186-1195.

Address for correspondence:

Shirin Riazy
HTW Berlin
riazy@HTW-berlin.de

Activation pattern of Extensor digitorum brevis muscle during child walking

A Strazza[1], M S Palmieri[2], A Mengarelli[1], S Fioretti[1], L Burattini[1], O Orsini[2], A Bortone[2], F Di Nardo[1],

1 Department of Information Engineering, Università Politecnica delle Marche, 60131 Ancona, Italy;
2 Centro ambulatoriale di Riabilitazione Santo Stefano, 62018 Porto Potenza Picena, Italy;

Abstract

The purpose of the study was the assessment of the activation pattern of Extensor digitorum brevis (EDB) muscle in healthy children, during walking at self-selected speed and cadence. To this aim, the Statistical Gait Analysis was performed on surface electromyographic (sEMG) signals, in a large number (hundreds) of strides per subject. Results from eight healthy children showed a large variability in number of muscle activations, occurrence frequency, and onset-offset instants across strides analyzed. The assessment of the different modalities of activation allowed identifying a single activity pattern, common for all the modalities and able to characterize the behavior of EDB during normal gait. The pattern of muscle activity centered in two main regions of the gait cycle: the second half of the stance phase (detected in 100% of the subjects) and in final swing phase (50%). This "normality" pattern represents the first attempt to develop a reference for dynamic sEMG of EDB in healthy children that is able to include the physiological variability of the phenomenon. The present results could be useful for discriminating physiological and pathological behavior in children and for deepening the maturation of gait.

Keywords: s*EMG, Extensor digitorum brevis, Statistical Gait analysis*

1 Introduction

The assessment of muscles activity plays a relevant role in evaluation of children disorders during gait. In order to correctly interpret surface electromyography (sEMG) in pathological conditions, reliable normative data in non-pathological children are required for direct comparison. To this aim, many studies focused on assessing the variability of muscles activity during normal gait [1-4]. In particular, the analysis of ankle muscles is fundamental in the characterization in children of pathologies such as spastic cerebral palsy.

During normal walking in adults such as in children, the main role of the ankle dorsi-flexors is to prevent slapping of the foot on the ground in initial stance, to permit the forefoot to clear the ground in initial swing, and to hold the ankle in position for initial contact [5]. Instead, ankle plantar flexors act to restrain the forward rotation of the tibia on the talus during stance phase, provide ankle stability, contribute to knee stability, and conserve energy by minimizing vertical oscillation of the whole-body center of mass [5]. Moreover, there is a relationship between ankle and foot muscle. The foot is a complex structure, functionally important in static posture and dynamic activities. The movement and stability of the foot is controlled by intrinsic and extrinsic muscles [5]. So, human foot muscles provide to stabilize the foot during propulsion, to improve pressure distribution on the plantar surface, adapting to dynamic or postural load changes during normal gait [6-8].

One of the main foot intrinsic muscles carrying out these tasks is Extensor digitorum brevis muscle (EDB). EDB is a relatively flat muscle which occupies an exposed position on the dorsum of the foot. This muscle arises from the forepart of the upper and lateral surfaces of the calcaneus and passes to the dorsum of the foot to insert on the dorsal aponeurosis of the 2nd to 4th toes (Fig.1). EDB controls the movements of the foot toes, assisting with extension of the second, third and fourth toes at the metatarsophalangeal joints [9]. The role of EDB, during gait, is only partially understood and little work has been done to investigate the activation pattern of EDB activity [5, 10, 11]. To our knowledge, no data were reported in children population. Thus, the aim of the present study was to quantify the variability of the activity of Extensor digitorum brevis in healthy children, during gait at self-selected speed and cadence. sEMG signals were acquired in numerous strides per subject (hundreds), to consider the expected large variability of the muscular activity.

Figure .1 EDB anatomy

2 Methods

2.1 Subjects

Data from eight healthy children were analyzed. Mean (±SD) characteristics are: age 8.3 ± 1.7 years; height 136± 8 cm; mass 30.9 ± 6.2 kg. Participants with a previous medical history involving foot or ankle surgery, inflammatory arthritis, neuromuscular disease, balance disorders, an inability to walk unaided were excluded from the study. Parental consent and child assent were obtained.

2.2 Signal Acquisition and Processing

Signals were acquired (sampling rate: 2 kHz; resolution: 12 bit) and processed by the multichannel recording system, Step32, Medical Technology, Italy. For each subject, three foot-switches (size: 10 × 10 × 0.5 mm; activation force: 3 N) were attached beneath heel, first and fifth metatarsal head of each foot. Two electro-goniometers were attached to the lateral side of each lower limb for measuring knee-joint angles and ankle-joint angles in the sagittal plane. sEMG signals were detected with single-differential sEMG probes with fixed geometry constituted by Ag/Ag-Cl disks (size: 7 × 27 × 19 mm; inter-electrode distance: 12 mm, gain: 1000, high-pass filter: 10 Hz, input impedance > 1.5 GΩ, CMRR > 126 dB, input referred noise ≤ 1 μVrms). sEMG signals were further amplified and low-pass filtered (450 Hz) by the recording system. An overall gain, ranging from 1000 to 50,000, could be chosen to suit the need of the specific muscle observed [9]. Before positioning the electrodes, the skin was shaved, cleansed with abrasive paste and wet with a soaked cloth. To assure proper electrode-skin contact, electrodes were dressed with highly-conductive gel. Electrodes were applied over EDB for each foot by a licensed physical therapist, following the SENIAM recommendations for electrode location and orientation [12]. Participant set-up is shown in Fig. 2. Then, subjects were asked to walk barefoot overground for 4 min at natural speed and cadence, back and forth over a 12-m hallway. Natural pace was chosen because walking at a comfortable speed improves the repeatability of EMG data, while variability increases when subjects are asked to walk abnormally.

Goniometric signals were low-pass filtered (FIR filter, 100 taps, cut-off frequency 15 Hz) [2]. Knee and ankle angles in the sagittal plane along with sequences and durations of gait phases derived by basographic signal, were used by a multivariate statistical filter, to detect outlier cycles like those relative to deceleration, reversing, and acceleration. Footswitch signals were debounced, converted to four levels, heel contact (H), flat foot contact (F), push-off (P), swing (S), and processed to segment and classify the different gait cycles. Cycles with improper sequences of gait phases (i.e. different from H–F–P–S sequence), not corresponding to straight walking and with abnormal timing and knee angles, with respect to a mean value computed on each single subject, were discarded [13]. sEMG signals were high-pass filtered (FIR filter, 100 taps, cut-off frequency of 20 Hz) and processed by a double-threshold statistical detector for the assessment of muscle activation intervals [14].

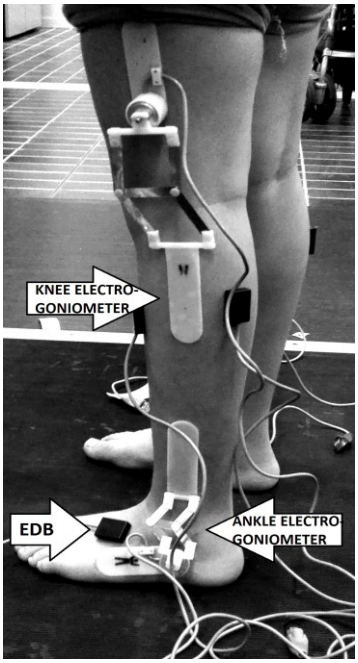

Figure 2. Participant set-up

2.3 Statistical Gait Analysis

Statistical gait analysis (SGA) [13] is a recent methodology, which performs a statistical characterization of gait by averaging spatial-temporal and sEMG-based parameters over a high number (hundreds) of strides, during the same walking trial. SGA relies on the fact that the number of muscle activations is cycle dependent, so that averaging should be performed only over onset/offset instants of cycles including the same number of activations, i.e. belonging to the same activation modality. Activation modality is defined as the number of times a muscle activates during a single gait cycle (*n*-activation modality consists of *n* activation intervals for the considered muscle, during a single gait cycle).

Mean activation intervals (normalized with respect to gait cycle) for each activation modality are achieved, according to the following steps. First, muscle activation intervals relative to each gait cycle are identified, computing muscle onset/offset instants in temporal space [14]. Then, muscle activations are grouped according to their modality. Eventually, the onset/offset time instants of each activation modality are averaged over the eight subjects. Averaged onset/offset percentage time instants are normalized with respect to gait cycle to provide mean activation intervals in percentage of gait cycle. SGA was performed by the Step32 system.

3 Results

For each subject, a mean (± standard deviation, SD) of 265.11 ± 30.4 strides has been considered. From the total of 3712 strides considered, 339 strides (9.1% of total strides) have been removed from the analysis because they did not follow the H-F-P-S foot-switch pattern and/or were outlier cycles relative to deceleration, reversing, and acceleration. The mean results are reported with data from right and left lower limbs considered together.

The SGA of myoelectric signals indicated that muscles show different numbers of activation intervals in different strides of the same walking session. A graphic representation of the patterns of the three main EDB activation modalities is showed in Fig. 3. The most recurrent modality of activation for EDB (Fig. 3) consists of two activations (2-activation modality, EBD2), observed in 42.6±12.4% of total strides; the first occurs in early mid-stance (from 8.25±7.0 to 50.3±15.0 % of gait cycle), and the second activation in swing phase, from 73.8±13.8% to 91.5±7.1% of GC. Instead, in 30.8±19.6% of total strides a 1-activation modality was detected (EDB1); this activation modality was observed from 17.5±14.7% to 79.0±15.3% of GC. In a further 20.3±12.9% of total strides, three activations were detected for EDB (EDB3): from 4±3.6 to 36.6±18.8% of GC, from 52.0±13.6 to 66.4±8.7% of GC and during swing phase from 83.8±8.3 to 95.0±4.7 % of GC. The 4 and 5 activation modality for EDB showed a large variability and a not significant percentage; thus, they are not considered in the present analysis. Considering the three main modalities of activation all together, a graphic representation of a single pattern for sEMG activity of the EDB muscle is reported in Fig. 4.

4 Discussion and Conclusions

The present study was designed to quantitatively assess the recruitment of EDB in healthy children, during walking at self-selected speed and cadence. The analysis showed that EDB muscle adopts different modalities in number of activations, in occurrence frequency [15], and in timing of signal onset/offset, in different strides of the same walking trial. Similar findings on muscle-activity variability were reported also for further ankle muscles in school-aged children [1-4] and in adults [16-18].

Results showed that EDB activity pattern was observed mainly during the second half of the stance phase. In this phase, the EDB activity was detected in 100% of the considered subjects (black area in Fig. 4). The activity in this percentage of the gait cycle (around 30-55%) is recognized as the typical activation for EDB during normal walking [5]. In adult, the EDB recruitment during early mid-stance phase has been interpreted as the active participation of this intrinsic dorsal muscle of the foot in controlling midtarsal dorsiflexion to regulate shock absorbing mechanism [3]. Moreover, advancing the body, the action of EDB is suggested to be present to control mid foot stability developing muscle tension for weight-bearing [5]. Considering that the recruitment of EDB reported by the present study is comparable with what reported in adults, the previous physiological considerations could be reasonably extended to children.

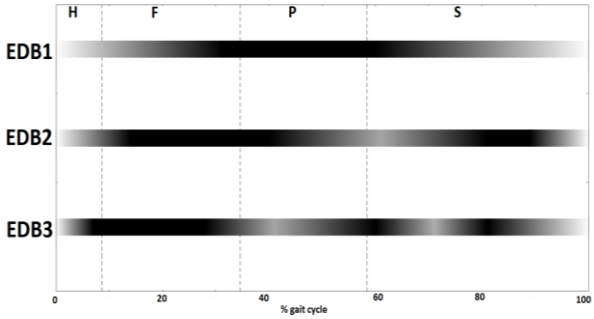

Figure 3. Mean values of EDB activation intervals vs. percentage of gait cycle. EDB activation intervals are reported separately for the modalities with 1, 2 and 3 activations. Horizontal bars are gray-level coded, according to the number of subjects where a certain condition is observed. Black: condition observed for all subjects. White: condition never met. H, F, P and S phases are delimited by dashed grey vertical lines.

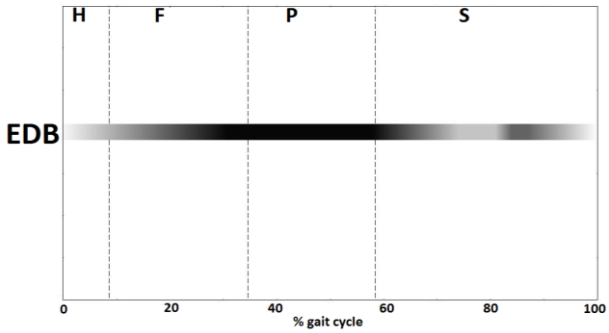

Figure 4. EDB activations over the population, as percentage of gait cycle, considering the three main modalities of activation all together. Horizontal bars are gray-level coded, according to the number of subjects where a certain condition is observed. Black: condition observed for all subjects in every activation modality. White: condition never met. H, F, P S phases are delimited by dashed light-gray vertical lines.

A further region of EDB activity was detected in swing phase. This activity occurs in a minor number of subjects (50%) as depicted by the grey area reported in Fig. 4, around the 85% of gait cycle. To our knowledge, this activity has never been reported neither in children nor in adults. An explanation of the recruitment of EDB in this phase of gait cycle could be related to the activity of muscle for the correct positioning of the foot,

in preparation of the following heel strike. However, further studies are evoked to deepen the physiological interpretation of the EDB recruitment in swing.

In conclusion, the ‘‘normality’’ pattern, identified in the present study, represents the first attempt for the development of a reference frame for dynamic sEMG activity of EDB in healthy children. Although further investigations are needed, these findings have the merit to provide novel data on the variability of the role of EDB during child walking, allowing a deeper insight in the physiological mechanisms that regulate ankle-foot stability. Thus, it can be useful for comparison between normal and pathological walking in the clinical context for designing future gait studies and could be valuable in order to give a further insight in the process of maturation of gait.

References

[1] F. Di Nardo, A. Mengarelli, L. Burattini, E. Maranesi, V. Agostini, A. Nascimbeni, M. Knaflitz, S. Fioretti. Normative EMG patterns of ankle muscle co-contractions in school-age children during gait. *Gait Posture*, 46: 161-166, 2016.

[2] V. Agostini, A. Nascimbeni, A. Gaffuri, P. Imazio, M. G. Benedetti and M. Knaflitz. Normative EMG activation patterns of school-age children during gait. *Gait Posture,* 32: 285–289, 2010.

[3] A. Mengarelli, S. Fioretti, E. Maranesi, L. Burattini, F. Di Nardo, V. Agostini, M. Knaflitz. A. Nascimbeni. Comparison of ankle-muscles activity between school-aged children and young adults during gait: An electromyographic analysis. 12th International Workshop on Intelligent Solutions in Embedded Systems, WISES, 7357001, 167-170, 2015.

[4] F. Di Nardo; A. Mengarelli; E. Maranesi; L. Burattini; S. Fioretti; V.Agostini; M. Knaflitz; A. Nascimbeni. Myoelectric activity of antagonist ankle-muscles in 6-to-8-year-old children during walking. 2015 12th International Workshop on Intelligent Solutions in Embedded Systems, WISES, 7357000, 163-166, 2015

[5] J. Perry. Gait Analysis – Normal and Pathological Function. Thorofare, USA: Slack Inc., 1992.

[6] D.H. Sutherland, R. Olshen, L. Cooper, S.L. Woo. The development of mature gait. *J Bone Joint Surg Am.* 62: 336–53, 1980.

[7] E.P. Mulligan, P.G. Cook. Effect of plantar intrinsic muscle training on medial longitudinal arch morphology and dynamic function. *Manual Therapy*, 2013.

[8] W. G. Wright, Y. P. Ivanenko, V. S. Gurfinkel. Foot anatomy specialization for postural sensation and control. *Journal of Neurophysiology*, 107: 1513-1521, 2012.

[9] P.O. McKeon, J. Hertel, D. Bramble, I. Davis. The foot core system: a new paradigm for understanding intrinsic foot muscle function. *J Sports Med*, 2013.

[10] P.L. Williams, L.H. Bannister, M.M. Berry, M. Dyson, J.E. Dussek, M.W.J. Ferguson. Gray’s anatomy. 38th ed. Edinburgh: Churchill Livingstone; 1995.

[11] L.A. Reeser, R.L. Susman, J.T. Stern. Electromyographic Studies of the Human Foot: Experimental Approaches to Hominid Evolution. *Foot and ankle*, 3: 391-407, 1983.

[12] B. Freriks, H.J. Hermens, C. Disselhorst-Klug, G. Rau. The recommendations for sensors and sensor placement procedures for surface electromyography. *J Electromyogr Kinesiol*, 10: 361–374, 2000.

[13] V. Agostini and M. Knaflitz. Statistical Gait Analysis. Distributed Diagnosis and Home Healtcare, R. U. Acharya, F. Molinari, T. Tamura, D. S. Naidu, J. S. Suri, Eds. Stevenson Ranch: American Scientific Publishers, 2: 99–121, 2012.

[14] P. Bonato , T. D’Alessio, and M. Knaflitz. A statistical method for the measurement of muscle activation intervals from surface myoelectric signal during gait. *IEEE Trans. Biomed. Eng*., 45: 287–99, 1998.

[15] F. Di Nardo, V. Agostini, M. Knaflitz, A. Mengarelli, E. Maranesi, L. Burattini, S. Fioretti. The occurrence frequency: A suitable parameter for the evaluation of the myoelectric activity during walking. Conf Proc IEEE Eng Med Biol Soc. 6070-3, 2015.

[16] F. Di Nardo, G. Ghetti, S. Fioretti. Assessment of the activation modalities of gastrocnemius lateralis and tibialis anterior during gait: a statistical analysis. *J Electromyogr Kinesiol*, 23: 1428–33, 2013.

[17] F. Di Nardo, A. Mengarelli, G. Ghetti, S. Fioretti. Statistical Analysis of EMG Signal Acquired from Tibialis Anterior during Gait. IFMBE Proceedings 41: 619-622, 2014.

[18] F. Di Nardo, S. Fioretti. Emg-based analysis of treadmill and ground walking in distal leg muscles. IFMBE Proceedings 41: 611-614, 2014.

Address for correspondence:

Francesco Di Nardo
Department of Information Engineering,
Università Politecnica delle Marche, 60131 Ancona, Italy.
f.dinardo@univpm.it

Intermittent Control Properties of Car Following: Driving Simulator Experiment

Ihor Lubashevsky, Hiromasa Ando

Computer Science Division, University of Aizu, Japan

Abstract

Characteristic features of human actions in car driving within the car-following setup are studied using TORCS car-driving simulator. Eight subjects participated in these experiments were instructed to drive a virtual car without overtaking and not losing sight of the lead car in any convenient style. The lead car was driven by computer at a fixed speed. As a main result, we draw a conclusion that human behavior in car driving should be categorized as a generalized intermittent control with noise-driven activation. Besides, we hypothesize that the extended phase space required for modeling human actions in car driving has to comprise four phase variables: the headway distance, the velocity of car, its acceleration, and the car jerk.

Keywords *Human control, Intermittency, Car-driving*

1 Introduction

According to modern point of view, human actions in governing unstable mechanical systems should be categorized as discontinuous (intermittent) control which repeatedly switches off and on (for a review see, e.g., [1]). As a result, the control process takes the form of a sequence of alternate phases of passive and active behavior with the event-driven transitions between them.

Previously, based on the experimental data on the balancing of overdamped stick we proposed a novel mechanism of noise-driven control activation which argues for substantially probabilistic scenario of these phase transitions [2]. As its characteristic features, the distribution function of the main control variable has to possess a sharp peak at the origin and this variable itself has to be an essential component of the extended phase describing human control.

Based on preliminary experiments, we suppose that in car-driving the intermittency of human control should be pronounced and affect the motion dynamics substantially. The purpose of the present work is to elucidate how the basic properties of human intermittent control manifest themselves in the characteristics of car-driving.

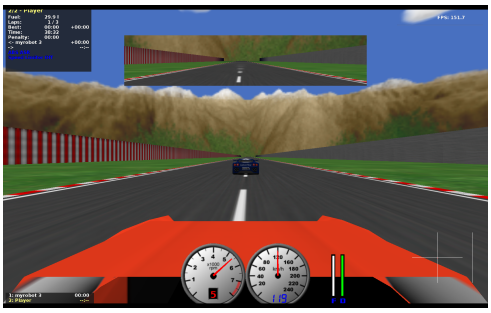

Figure 1: Screenshot of car-following experiments. The car ahead (in blue) is driven by computer at a fixed speed.

2 Car Driving Simulator

In the conducted experiments we explored a car-driving simulator created based on the open source engine TORCS [3]. The used track has a rectangular form (with smoothed corners) whose longest straight parts are of length about 70 km. One trial of experiments is implemented via driving along one of the longest parts. The width of the track road is 15 meters. The roadside of the track includes a special pattern of stripes enabling a subject to get feeling of the current speed (Fig. 1).

The set of experiments consisted of trials where the lead car speed was set equal to $V = 60$ km/h, 80 km/h, 100 km/h, and 120 km/h. Each of these trials was continued for 60 minutes totally with possible breaks caused, e.g., by the necessity to move from one long-distant track to the other. Eight male students of age around 22-25 were involved in these experiments.

3 Results and Discussion

In the car-following, drivers can control the car dynamics only via changing the position of the accelerator or brake pedals. Time variations in the headway distance, velocity, acceleration, etc. are determined by the car mechanics and the pedal position. Therefore, at the first step, we analyzed the corresponding time patterns of (*i*) the pedal positions and (*ii*) their time derivatives. There are at least two reasons for including the pedal position time derivative into the list of the main characteristics of driver actions. First, turning to our causal experience it is clear that drivers focus their attention on the car arrangement in traffic flow, the current velocity and acceleration rather

than on the particular position of the pressed pedal. So the pedal position on its own cannot be the main control parameter. However, after making decision on correcting the current state of car motion a driver consciously (or automatically based on the gained experience) slow or fast pushes or releases the corresponding pedal. In other words, the rate of pedal movement can be a quantity controlled by the driver's active behavior. Second, the main parameter that is controlled directly by a human operator and, in its turn, quantifies the operative actions has to exhibit a special characteristic property. Namely its distribution function has to possess a sharp peak at the origin [2]. It means that during the passive phase where the operator control is suspended this quantity does not change. In accordance with the obtained results, the pedal position time derivative is this type variable.

Figure 2 (upper row) shows typical forms of the pedal position time patterns found in the conducted experiments. The time pattern classified as style 1 demonstrates the strategy of car driving when a driver pushes the accelerator pedal for a relatively short time then release it also for a short time and so on. This style enables a driver to keep up the desired velocity and headway without the precise control over the pedal position just changing the duration of pressing or releasing the pedal. The time pattern classified as style 2 demonstrates the opposite strategy of car-driving, when a driver is able to keep up the required pedal position for a relatively long time interval. The found third style may be classified as a certain mixture of styles 1 and 2. The mixed style is worthy of individual investigation and is not discussed here.

Figure 2 (lower two rows) shows the typical form of the distribution of the pedal position and its time derivative for styles 1 and 2. As seen, the distribution of the pedal position, the p-distribution, are completely different, as should be expected. For style 1 the p-values are scattered rather widely in the possible acceleration interval (0,1) with a non-pronounced maximum at the required value p_V for the steady-state motion. For style 2 the p-distribution is located near the corresponding value p_V and has the form of the Laplace distribution. The distributions of the pedal position time derivatives, the dp/dt-distributions, differ for styles 1 and 2 in the form and scales. Nevertheless, all the found dp/dt-distributions possess a common feature, it is a sharp peak at the origin. We relate the appearance of this peak to the basic properties of human intermittent control.

The statistical properties of the other characteristics of the car dynamics, namely, the headway distance between the cars, their relative velocity, the following car acceleration, and the jerk, i.e., the time derivative of the car acceleration are shown in Fig. 3 for styles 1 and 2. The headway distribution and the relative velocity distribution are similar in form with each other as well as the corresponding distributions obtained for the real traffic, see, e.g., [4, 5, 6, 7].

For style 2 the difference between the distribution of the car acceleration and jerk is not so clear because the peak of acceleration distribution and that of the jerk distribution look rather similar; both of them are approximately of the same thickness and located at the origin. So, appealing to these plots it is difficult to recognized which variable—the acceleration or the jerk—causes the appearance of the peak of the other variable. However, additional analysis demonstrated that the jerk distributions peak is closer to the power law in form whereas that of the acceleration distribution is not so pronounced. It allows us to attribute the leading role the car jerk and regard it as the phase variable of the car dynamics.

The drawn conclusion about the leading role of the car jerk is also justified by time patterns of the car acceleration and jerk shown in Fig. 3 (right column). As seen, only the jerk demonstrates the time pattern typical for the human intermittent control; they are a sequence of alternate phases of subject's passive and active behavior, where the passive phase corresponds to a certain fixed parameter and the active phase fragments show dynamic variation of this parameter.

Besides, studying the distributions in the phase planes "acceleration–pedal position" and "jerk–pedal position derivative" we demonstrates the relationship between the variables of the car dynamics and human actions. Namely based on the data for both the styles 1 and 2 we can write the relationship between the pedal position p, the car acceleration a and the jerk

$$j = \frac{da}{dt}$$

in the form

$$\tau_c j = \kappa p - a\,, \tag{1}$$

where the time scale τ_c and the coefficient κ should characterize the mechanical characteristics of car. The existence of the transient term—the right hand side of equation (1)—is found in the data for some subjects. Nevertheless, it should be a minor effect and the steady-state approximation of relationship (1)

$$a = \kappa p \tag{2}$$

can be used in modeling the car-following.

In this way we get the relationship between the pedal position time derivative and the jerk

$$j = \kappa \frac{dp}{dt}\,, \tag{3}$$

which explains why the car jerk can be treated as the main control parameter.

In conclusion, the obtained results for the car-following enable us to state that:

- The car-driving exhibits characteristic features of human intermittent control. Namely, the subject actions in controlling the car motion form a sequence of alternate phases when the subjects kept the accelerator pedal fixed (passive phase) or changed it position to correct the current state of motion (active phase).

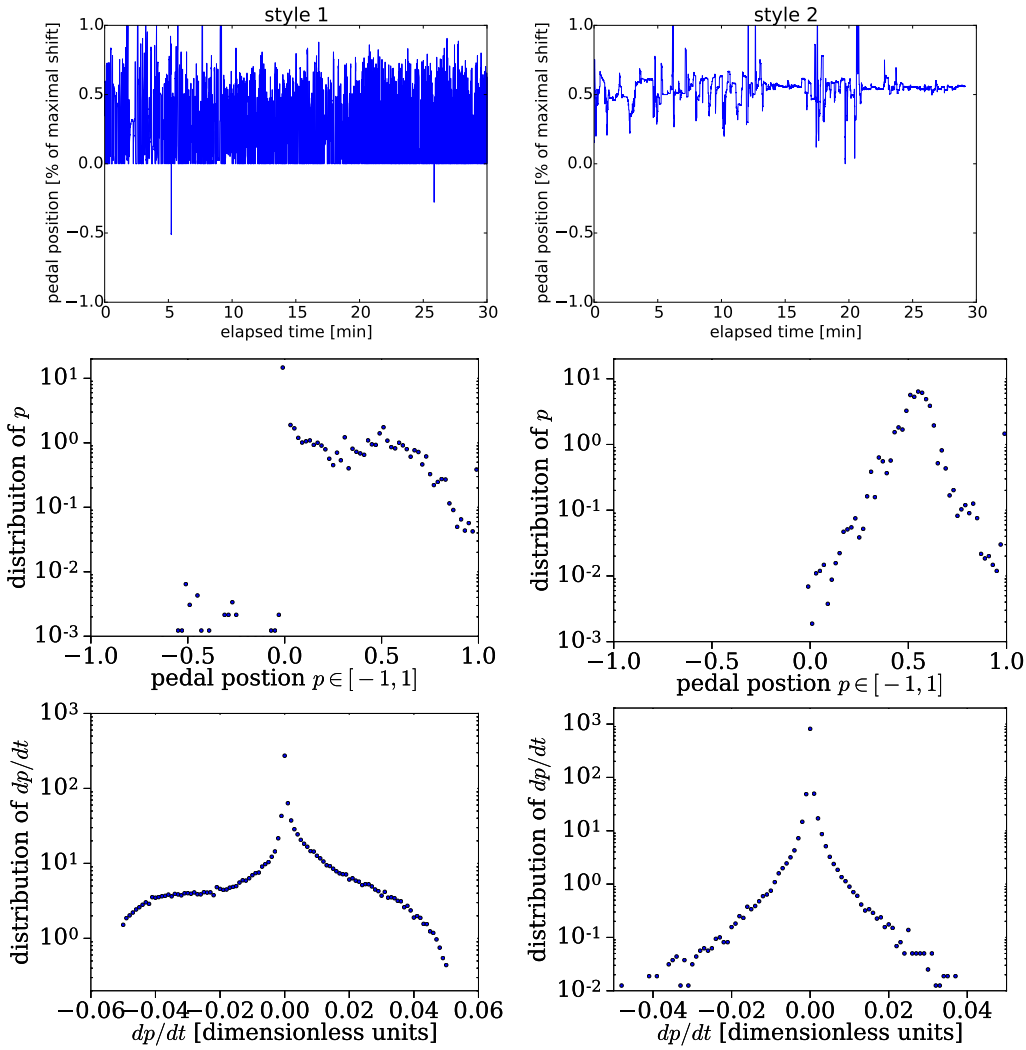

Figure 2: Characteristic forms of the pedal position time patterns and the distributions of the pedal position and its time derivative for styles 1 and 2.

- The distribution of the car jerk (directly related to the pedal position time derivative) exhibits sharp peak at the origin, which is a typical property of the main control parameter in human intermittent control.

- By virtue of the previous statement, we come to the conclusion that the four-dimensional phase space—comprising the headway distance, the car velocity, its acceleration and jerk—is required to describe the car dynamics governed by a human driver. In this collection of phase variable the jerk can be replaced by the time derivative pedal position which explicitly reflects the driver actions.

References

[1] Ian D. Loram, Henrik Gollee, Martin Lakie, and Peter J. Gawthrop. Human control of an inverted pendulum: is continuous control necessary? Is intermittent control effective? Is intermittent control physiological? *The Journal of Physiology*, 589(2):307–324, 2011.

[2] Arkady Zgonnikov, Ihor Lubashevsky, Shigeru Kanemoto, Toru Miyazawa, and Takashi Suzuki. To react or not to react? Intrinsic stochasticity of human control in virtual stick balancing. *Journal of The Royal Society Interface*, 11:20140636, 2014.

[3] The official site of TORCS. `http://torcs.sourceforge.net/index.php`.

[4] Peter Wagner and Ihor Lubashevsky. Empirical basis for car-following theory development. *arXiv preprint cond-mat/0311192*, 2003.

[5] Peter Wagner. How human drivers control their vehicle. *The European Physical Journal B-Condensed Matter and Complex Systems*, 52(3):427–431, 2006.

[6] Peter Wagner. A time-discrete harmonic oscillator model of human car-following. *The European Physical Journal B*, 84(4):713–718, 2011.

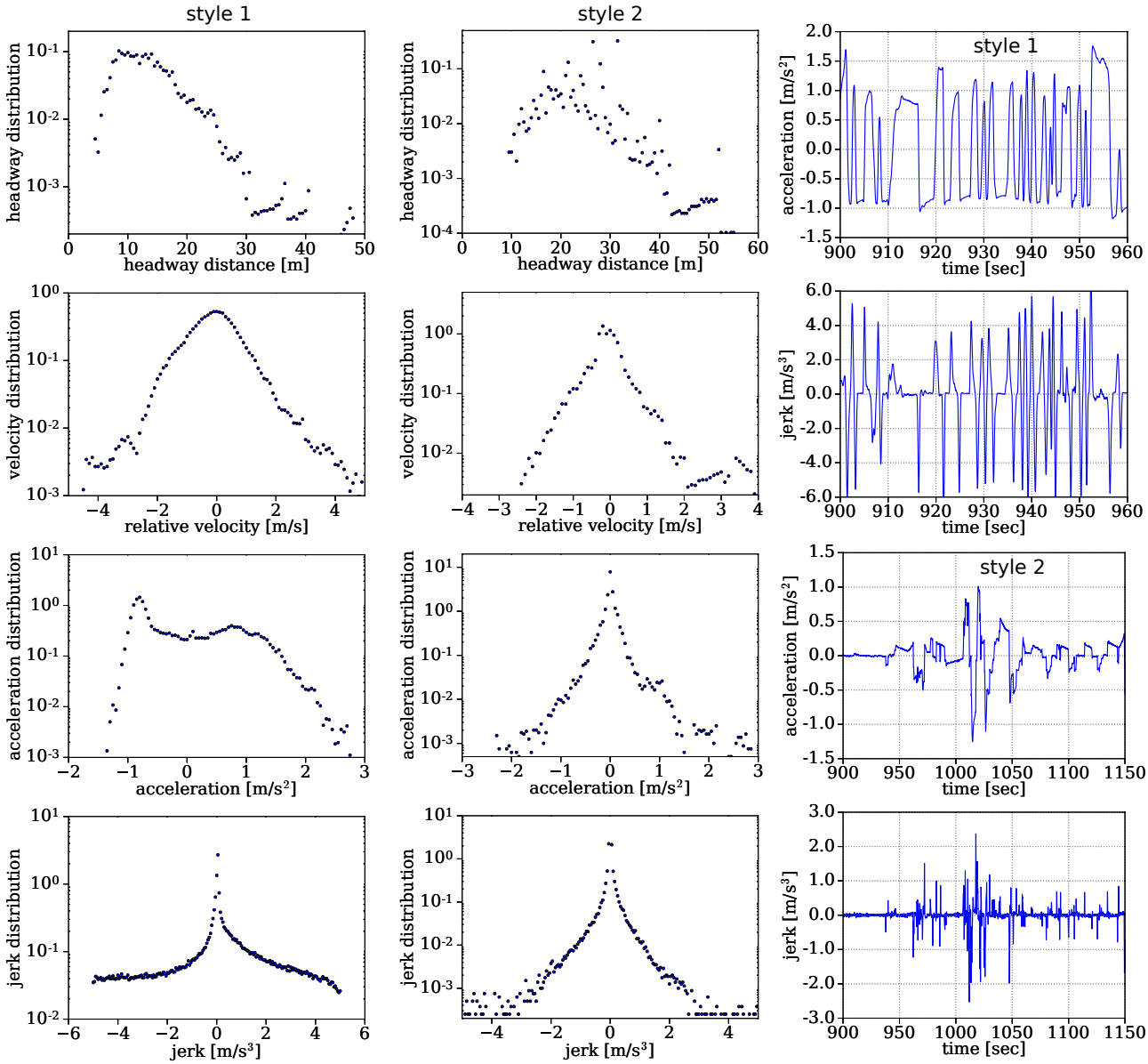

Figure 3: Characteristic forms of the distributions of the headway distance, the relative velocity, the car acceleration and jerk as well as the time patterns of the car acceleration and jerk.

[7] Peter Wagner. Analyzing fluctuations in car-following. *Transportation Research Part B: Methodological*, 46(10):1384–1392, 2012.

Address for correspondence:

Ihor Lubashevsky
University of Aizu
i-lubash@u-aizu.ac.jp

Application of Empirical Mode Decomposition to Mother and Infant Physical Activity: Synchronization of Circadian Rhythms is Associated with Maternal Mental Health Symptoms

Etsuko Shimizu[1], Toru Nakamura[1, 2], Jinhyuk Kim[3], Kazuhiro Yoshiuchi[4], Yoshiharu Yamamoto[1],

1 Graduate School of Education, The University of Tokyo, Japan;
2 JST, PRESTO, Japan;
3 Department of Psychosomatic Medicine, National Institute of Mental Health, National Center of Neurology and Psychiatry, Japan;
4 Graduate School of Medicine, The University of Tokyo, Japan;

Abstract

Disturbances in maternal circadian rhythms are indicated as substantial risk factors for maternal depression. Such disturbances are thought to be attributed not only to intrinsic maternal factors but also to interacting factors with her baby's rhythms. Therefore, to study the relationships between maternal circadian rhythms and subjective symptoms (e.g. depressive mood), the influences from infants should be considered. In this study, we conducted longitudinal recordings of maternal symptoms of fatigue, stress and mood states by ecological momentary assessment, together with simultaneous measurements of mother and infant physical activity data in daily life (N = 20; >1 week). The mother and infant circadian components in the physical activity data were extracted by ensemble bi-variate empirical mode decomposition, and their instantaneous phases then were obtained by the Hilbert transformation. The relationships between diurnal maternal mental health symptoms and phase differences of mother-infant circadian rhythms (a synchronization index) were evaluated using multilevel models. Fatigue and depressive mood scores showed positive and significant correlation ($p < 0.05$) with the increase of phase differences. These findings suggest the possibility that modifications of maternal and/or infant circadian rhythms might alleviate fatigue and improve mood states during the childrearing period.

Keywords *circadian rhythm, ecological momentary assessment, subjective symptoms, physical activity, emprical mode decomposition*

1 Introduction

Disturbances in maternal circadian rhythms, especially sleep-wake patterns, are known to be harmful for maternal mental health [1]. Thus, the management of maternal rhythms is of great importance for the prevention of mental disorders during the postpartum period.

A variety of studies on maternal rhythms, including research about sleep-wake patterns or sleep disturbances, have demonstrated their considerable relations with maternal mental health, together with their associations with the development of postpartum depression [2, 3]. However, these studies only focused on maternal rhythms and did not pay attention to infant rhythms, which might be an important determinant of maternal rhythms. On the other hand, infant rhythms are also influenced by maternal rhythms though parenting behaviors and other social activities. Therefore, to study the relationships between maternal rhythms and maternal symptoms of fatigue, stress and mood states (hereafter referred to as maternal mental health symptoms), mother-infant interactions should be considered.

In this study, we hypothesized that decreased synchronization of maternal-infant circadian rhythms, specifically the increase of their phase differences, is associated with the worsening of maternal mental health symptoms. To test this, we conducted longitudinal recordings of maternal mental health symptoms by Ecological Momentary Assessment (EMA) [4-6], together with simultaneous measurements of mother and infant physical activity data in daily life.

Historically, cosinor-based or periodgram techniques have been widely applied to physical activity data as a tool to investigate circadian rhythms [7, 8]. However, these methods cannot fully deal with mother-infant interactions (e.g. carrying, or hugging behaviors), affecting the amount and/or patterns of their physical activity. Therefore, we adopted bi-variate empirical mode decomposition (EMD), which can decompose a bi-variate signal into oscillatory components at multiple timescales considering their mutual dependences.

We show that bi-variate EMD can successfully extract mother and infant circadian components from the physical activity data, and further demonstrate that the increase of phase differences between mother and infant circadian components has a significant

relationship with the worsening of maternal mental health symptoms.

2 Methods

Twenty healthy mother-infant pairs [mothers: 33.4 ± 4.4 (mean ± SD) years; infants: 12 males/8 females, 7.0 ± 2.3 months] participated in this study. All mothers were requested to record their subjective mental health symptoms during the study period (> one week). Physical activity was also measured from mothers and their infants. The procedures are summarized in the following sub-sections.

2.1 Assessment of subjective symptoms

Ecological momentary assessment (EMA) [4, 5] was adopted to examine momentary mental health symptoms in mothers. This approach allows researchers to address subjects' behavior, psychological states, and physiological reactions at multiple time points as they are experienced in daily life. In this study, a custom-made EMA Android smartphone application was used to record momentary symptoms (Fig. 1(a)).

Mothers were instructed to complete EMA questionnaires at randomly selected times within ± 10 min of pre-scheduled times (10:00, 14:00, and 18:00) during the study period. They were also asked to record the EMA questionnaires when they woke up and before they went to bed.

The EMA questionnaires rated maternal fatigue intensities, stress levels and mood states by using a visual analog scale from 0 to 100 displayed on the smartphone screen (Fig. 1(a)). Mood states, specifically depressive mood and anxiety (total depression and total anxiety, respectively), were scored using the Depression and Anxiety Mood Scale (DAMS) [6, 9, 10] (Fig. 1(c)).

2.2 Assessment of physical activity

A watch-type activity monitor (Actigraph; Ambulatory Monitors Inc., Ardsley, NY, USA) was used for continuous and simultaneous recordings of maternal and infant physical activity. This device is equipped with a uni-axial piezo-electric accelerometer capable of detecting small changes in bodily acceleration (≥0.01 G/rad/s), which makes it possible to register even slight movements in daily life. Throughout the study period, all the mothers wore the device on the wrist of their respective non-dominant hand, and the infants wore it on their left ankle (Fig.1(b)). Zero-crossing acceleration counts were accumulated for every minute.

2.3 Data analysis

2.3.1 Empirical mode decomposition

EMD is a data-driven multiscale time-frequency analysis that adaptively decomposes a non-stationary signal into oscillatory modes modulated in both amplitude and frequency [11]. The oscillatory modes embedded in a given signal are named intrinsic mode functions (IMF) and satisfy the following two conditions: (a) the number of extrema and the number of zero crossings in the signal must either equal or differ at most by one; and (2) the mean value of the envelopes defined by the local maxima and minima of the signal are equal to zero at any time. With these definitions, in practice, the extracted IMFs are supposed to be narrow band signals without complex riding waves, and also symmetric around zero.

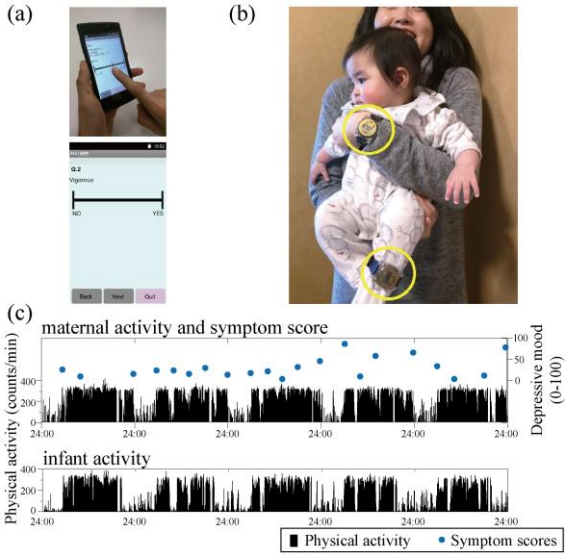

Figure 1: (a) Smartphon EMA system and (b) activity monitors. (c) An example of the data.

2.3.2 Bi-variate empirical mode decomposition

Bi-variate EMD [12, 13] is a natural extension of the basic EMD making it possible to conduct a joint analysis of bi-variate oscillatory components included in bi-variate signals (Fig. 2). In this extension, the bi-variate signal is dealt with as a complex-valued signal in which one signal is the real part and another is the imaginary part, respectively. Then, decomposition is conducted on both parts simultaneously considering their mutual dependencies [14]. Intuitively, basic EMD separates faster oscillations from slower oscillations, while bi-variate EMD separates rapid rotations from slower ones embedded in the trajectory on a complex plane[12]. In this study, we considered the mother and infant physical activity data as bi-variate signals.

2.3.3 Extraction of circadian component

In order to identify the circadian component from the extracted IMFs, the mean instantaneous frequency (i.e. period) was calculated by using the Hilbert transformation. In this study, the IMF corresponding to the circadian component was identified by searching for the IMF whose period is closest to 24 hours (red curves

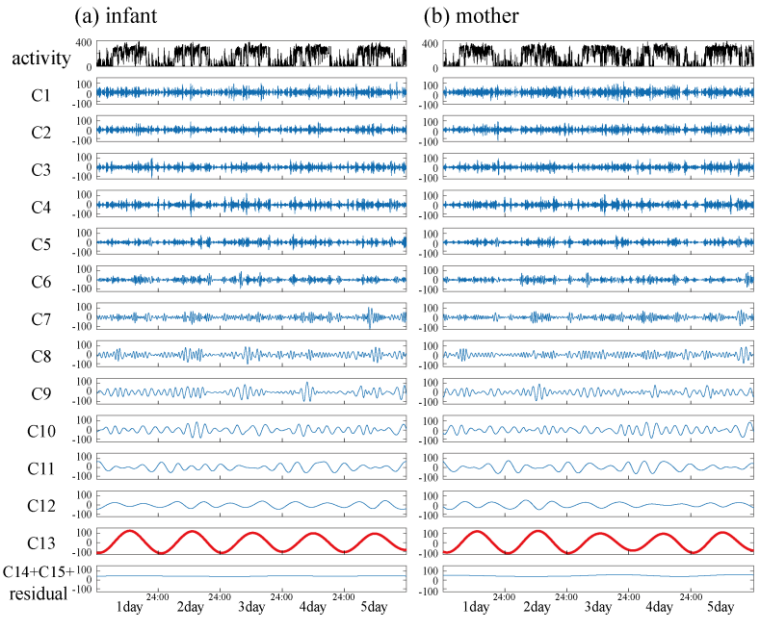

Figure 2: IMFs derived by the bi-variate EMD from (a) maternal and (b) infant physical activity data.

in Fig. 2).

The mode mixing problem, the dispersion of very similar oscillations into different modes, is one of the major drawbacks of EMD [15, 16]. To overcome this problem, a noise assisted technique, named ensemble EMD, has been proposed [15, 16]. The idea of ensemble EMD relies on averaging the modes obtained by EMD applied to several realizations of Gaussian white noise added to the original signal. The addition of the noise can well solve the problem by populating the whole time-frequency space uniformly with the constituting components of different scales separated by the filter bank properties of EMD.

In this study, we generated 100 samples for each mother-infant dataset by adding independent noise series with zero mean and a variance of 0.2 times that of the data, and then calculated the ensemble average of the identified circadian components for mother and infant data. The instantaneous phases were evaluated from the averaged circadian components using the Hilbert transformation. The absolute values of mother-infant phase differences $|\triangle P_{(t)}|$ were calculated as follows;

$$|\triangle P_{(t)}| = |\triangle P_{mother(t)} - \triangle P_{infant(t)}|, \quad (1)$$

where $\triangle P_{mother(t)}$ and $\triangle P_{infant(t)}$ is mother and infant instantaneous phases, respectively (Fig. 3).

2.4 Statistics

EMA recordings were conducted at multiple times during the study period, leading to a hierarchical structure of the data set. Therefore, multilevel modeling [17-19], which is an extension of traditional regression models making it possible to deal with within- and between-individual variances and also both random and fixed effects together in the same model, was used.

To test the relationships between momentary symptoms and corresponding mother-infant phase differences, the following multilevel model was evaluated;

$$symptom_{ij} = \gamma_{00} + \gamma_{10}|\triangle P_{ij}| + \zeta_{0i} + \varepsilon_{ij}, \quad (2)$$

where $|\triangle P_{ij}|$ is the absolute value of the phase difference of j-th recording for the i-th subject.

SAS Proc Mixed (SAS 9.2, SAS Institute Inc., Cary, NC) was used for all statistical tests. A p- value of less than 0.05 was considered significant.

3 Results

Figure 3(a) shows an example of circadian components extracted by ensemble bi-variate EMD. The method successful identified circadian components from all maternal and infant physical activity data (the mean periods of extracted circadian components were 23.97±1.10 hrs for mothers, and 23.94 ± 0.86 hrs for infants). Furthermore, the dynamical changes of mother-infant phase differences, which cannot be adequately accessed by the traditional cosinor method, were also evaluated (Fig. 3(b)).

Table 1 summarizes the results of diurnal associations between the corresponding instantaneous phase differences and maternal mental health symptoms. Fatigue levels and depressive mood scores were concurrently associated with the phase differences, while stress levels tended to increase with the widening of phase differences (γ_{10} = 8.4 ± 4.2, p = 0.05). These results indicate the presence of the covariations between maternal mental health symptoms and phase differences in their diurnal variations. For anxiety, we did not find any significant associations.

4 Conclusions

This study has the following methodological advantages: 1) the first use of the EMA approach to assess the diurnal changes in maternal mental health

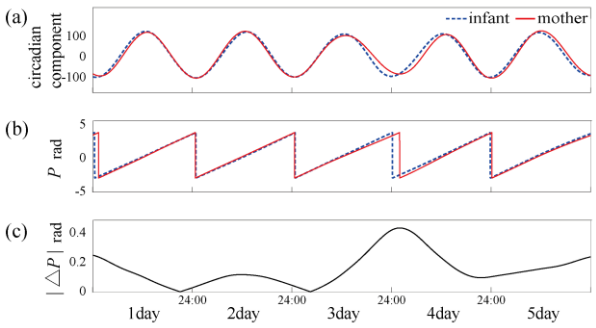

Figure 3: (a) The circadian components extracted from mother and infant physical activity (a). The corresponding instantaneous phases (b) and their absolute differences (c).

symptoms during the childrearing period, 2) an application of the ensemble bi-variate EMD to derive circadian rhythms from physical activity data by taking mother-infant interactions into consideration.

In this study, we demonstrated that the synchronization of the mother-infant circadian rhythms is associated with diurnal maternal symptoms of fatigue and depression. This suggests that appropriate modifications of mother and/or infant rhythms may lead to the improvement of maternal mental health symptoms.

Acknowledgements

The authors would like to thank Dr. Jerome Foo for editing the manuscript. This study was partly supported by Grants-in-Aid for Exploratory Research [15K12679] (to T. N.) from the Ministry of Education, Culture, Sports, Science and Technology. This study also supported by funds for SEEDS research project from the Center for Early Childhood Development, Education, and Policy Research, the University of Tokyo (to Y.Y.).

References

[1] S. Bhati and K. Richards, A systematic review of the relationship between postpartum sleep disturbance and postpartum depression, *J Obstet Gynecol Neonatal Nurs,* 44: 350-7, 2015.
[2] S. K. Dorheim, G. T. Bondevik, M. Eberhard-Gran*, et al.*, Sleep and depression in postpartum women: a population-based study, *Sleep,*32:847-55, 2009.
[3] D. Goyal, C. Gay, and K. Lee, Patterns of sleep disruption and depressive symptoms in new mothers, *J Perinat Neonatal Nurs,* 21:123-129, 2007.
[4] S. Shiffman, A. A. Stone, and M. R. Hufford, Ecological momentary assessment, *Annu Rev Clin Psychol,*4:1-32, 2008.
[5] A. A. Stone and S. Shiffman, Ecological momentary assessment (EMA) in behavioral medicine, *Ann Behav Med,* 16:199-202, 1994.
[6] J. Kim, T. Nakamura, H. Kikuchi*, et al.*, Covariation of Depressive Mood and Spontaneous Physical Activity in Major Depressive Disorder: Toward Continuous Monitoring of Depressive Mood, *IEEE J Biomed Helth Inform,*19:1347-1355, 2015.

	diurnal associations		
	mean (SE)	*t*-value	*p*-value
fatigue			
intercept: γ_{00}	39.7(3.8)	10.5	< 0.0001
coefficient: γ_{10}	17.9(5.3)	3.4	<0.01
stress			
intercept: γ_{00}	18.6(2.9)	6.3	< 0.0001
coefficient: γ_{10}	8.4(4.2)	2.0	0.05
total anxiety			
intercept: γ_{00}	11.9(1.9)	6.3	< 0.0001
coefficient: γ_{10}	-0.8(1.8)	-0.4	0.66
total depression			
intercept: γ_{00}	30.9(1.7)	18.3	< 0.0001
coefficient: γ_{10}	6.5(2.6)	2.5	0.01

Table 1: Diurnal associations between self-reported symptoms and phase differences.

[7] S. Y. Tsai, K. A. Thomas, M. J. Lentz*, et al.*, Light is beneficial for infant circadian entrainment: an actigraphic study, *J Adv Nurs,*68:1738-1747, 2012.
[8] B. Gnidovec, D. Neubauer, and J. Zidar, Actigraphic assessment of sleep-wake rhythm during the first 6 months of life, *Clin Neurophysiol,* 113:1815-21, 2002.
[9] I. Fukui, The depression and anxiety mood scale (DAMS): scale development and validation, *Jpn J Behav Ther,* 23:83-93, 1997.
[10] J. Kim, T. Nakamura, H. Kikuchi*, et al.*, Co-variation of depressive mood and locomotor dynamics evaluated by ecological momentary assessment in healthy humans, *PLoS One,* 8:e74979, 2013.
[11] N. E. Huang, Z. Shen, S. R. Long*, et al.*, The empirical mode decomposition and the Hilbert spectrum for nonlinear and non-stationary time series analysis, *Proc R Soc Math Phys Eng Sci,* 454:903-995, 1998.
[12] A. Ahrabian, N. U. Rehman, and D. Mandic, Bivariate Empirical Mode Decomposition for Unbalanced Real-World Signals, *IEEE Sign Proc Lett,* 20:245-248, 2013.
[13] G. Rilling, P. Flandrin, P. Goncalves*, et al.*, Bivariate empirical mode decomposition, *IEEE Sign Proc Lett,* 14:936-939, 2007.
[14] C. Park, D. Looney, P. Kidmose*, et al.*, Time-Frequency Analysis of EEG Asymmetry Using Bivariate Empirical Mode Decomposition, *IEEE Trans Neural Syst Rehabil Eng,* 19:366-373, 2011.
[15] Z. Wu and N. E. Huang, Ensemble empirical mode decomposition: a noise-assisted data analysis method, *Adv Adapt Data Anal ,* 01:1-41, 2009.
[16] M. E. Torres, M. A. Colominas, G. Schlotthauer*, et al.*, A complete ensemble empirical mode decomposition with adaptive noise, *ICASSP*, 4144-4147, 2011.
[17] J. E. Schwartz and A. A. Stone, Strategies for analyzing ecological momentary assessment data, *Health Psychol,* 17:6-16, 1998.
[18] A. S. Bryk and S. W. Raudenbush, *Hierarchical linear models : applications and data analysis methods*. Newbury Park: Sage Publications, 1992.
[19] J. D. Singer and J. B. Willett, *Applied longitudinal data analysis : modeling change and event occurrence*. New York: Oxford University Press, 2003.

Address for correspondence:

Toru Nakamura
Graduate School of Education, The University of Tokyo, Japan
nakamura@p.u-tokyo.ac.jp

Preceding Psychological Factors and Calorie Intake in Patients with Type 2 Diabetes: Investigation by Ecological Momentary Assessment

Shuji Inada[1], Yoko Iizuka[2], Ken Ohashi[3], Hiroe Kikuchi[4], Yoshiharu Yamamoto[5], Takashi Kadowaki[2], Kazuhiro Yoshiuchi[1],

1 Department of Stress Sciences and Psychosomatic Medicine, Graduate School of Medicine, The University of Tokyo, Japan;
2 Department of Diabetes and Metabolic Diseases, Graduate School of Medicine, The University of Tokyo, Japan;
3 Department of Internal Medicine, National Cancer Center Hospital;
4 Department of Psychosomatic Medicine, National Institute of Mental Health, National Center of Neurology and Psychiatry, Japan;
5 Educational Physiology Laboratory, Graduate School of Education, The University of Tokyo;

Abstract

Psychological factors have been reported to have influence on eating habits in patients with diabetes. However, previous studies used a questionnaire to investigate the association, which suffers from recall bias. To overcome the disadvantage, ecological momentary assessment (EMA) has been used to record subjective symptoms and behavior in subjects' daily lives. Therefore, the aim of the present study was to investigate the influence of preceding psychological factors on calorie intake using computerized EMA for six months. The participants were nine outpatients with type 2 diabetes, aged 34-72. They were instructed to use the personal digital assistance as an electronic diary for six months to record subjective symptoms such as psychological stress, anxiety, and depressive mood, and food and drink that they had. The association between preceding psychological factors and calorie intake within 5 hours was investigated using multilevel modeling. With regard to snacks, preceding psychological stress was positively associated with calorie intake while preceding psychological stress, anxiety, and depressive mood were negatively associated with calorie intakes regarding regular meals. In conclusion, preceding psychological factors could influence calorie intake in patients with type 2 diabetes, which may lead to developing psychological intervention to prevent overeating.

Keywords *Ecological momentary assessment, type 2 diabetes, electronic food diary, psychological factors, multilevel modeling*

1 Introduction

Psychological factors such as anxiety and depressive mood has been reported to have influence on eating habits in patients with life-style diseases such as diabetes, which could raise risks of cardiovascular diseases [1]. Many studies on the influence of psychological factors on eating habits used a questionnaire, which could suffer from recall bias [2]. To overcome the disadvantage, ecological momentary assessment (EMA), which avoids recall bias, has been used in the area of behavioral medicine to record subjective symptoms and behavior in subjects' daily lives.

There have been some previous studies to investigate the association between psychosocial factors and food intake using EMA [3] [4] [5] [6]. However, there were methodological problems in the previous studies due to using paper-and-pencil diaries [7] or only two-day duration. Stone et al. revealed that patients completed only 11% of their symptom records on the scheduled time [7].

Therefore, the aim of the present study was to investigate the influence of preceding psychological factors on calorie intake quantitatively using computerized EMA for six months.

2 Methods

2.1 Participants and Procedure

The study protocol was approved by the ethical committee of Graduate School of Medicine, The University of Tokyo. The participants in this study were part of another study [8], and nine outpatients with type 2 diabetes diagnosed according to the current criteria of the Japan Diabetes Society [9] (three men; median age = 49 years, range = 34 to 72). Inclusion criteria were age ≥20 and outpatients with type 2 diabetes at the University of Tokyo Hospital. Participants were excluded if they had HbA1c≥8.4%, had any active mental disorder, followed a restrictive diet with protein ≤0.5 g/kg/day or salt ≤5 g/day due to another disease,

had cognitive impairment, or had severe complications that interfered with self-care activities. After providing written informed consent, participants were instructed to record daily dietary intake using the PDA-based food diary, SELFOOD [10] and to record mood states such as anxiety and depression to a personal digital assistant (PDA) (WS020SH, Sharp Corp, Osaka, Japan, 135g, 50x116x17.9 mm, Windows Mobile 6.1), which was equipped with a 3.0-in color liquid crystal display and a touch panel manipulated by a finger. They were asked to record as soon as possible after eating for 6 consecutive months.

2.2 Dietary Intake

We developed an electronic food diary, "SELFOOD", implemented into PDA), and the accuracy of it has been confirmed [10]. SELFOOD was equipped with a reference database with 423 color photographs of food and drink items, and also allowed patients to add their own meals and recipes to the database if their nutrient information was given.

2.3 Momentary Psychological Stress and Mood State

To record psychological stress, anxiety, and depressive mood, the PDAs were used as electronic diaries [11]. The subjects were instructed on the use of the device and given manuals before the beginning of the study period.

The subjects hold the PDAs for six consecutive months. Signal-contingent recordings were defined as recordings that were prompted with a beep as a signal [2], and they were programmed to occur randomly within an interval of 30 min around 10:00, and 15:00. If the subjects did not enter a recording when the computer beeped, they were allowed to postpone input for 30 min. Recordings not made within 30 min were cancelled. The subjects were also asked to record their psychological stress, anxiety, and depressive mood when they woke up and when they went to bed by choosing "waking up" or "going to bed" from the menu. After selecting a "going to bed" recording, the computers suspended the signal-contingent recordings until a "waking up" recording was selected to avoid sleep disturbance. Signal-contingent recordings and recordings when waking up and going to bed were treated as scheduled recordings. Momentary psychological stress, anxiety, and depressive mood were rated with a visual analog scale (VAS) that ranged from 0 to 100, which was displayed on the screen.

2.4 Statistical Analysis

Multilevel modeling was used to investigate preceding psychological factors on dietary intake for statistical analyses because the dataset in this study had a nested structure in which a number of recordings belonged to each participant. Pairs of preceding psychological factors and dietary intake were lagged in the ranges of −5 to 0 h [12]. The level of significance was set at 0.05. SAS Proc Mixed (SAS 9.3, SAS Institute Inc., Cary, NC, USA) were used. Each dietary intake recordings were paired with preceding momentary recordings of psychological stress and the mood states for each patient. Dietary intake was treated as the dependent variable. Momentary psychological stress, anxiety, and depressive mood were separately modeled as the independent variable either as a fixed or random effect. Goodness of fit was compared to determine the best-fit model with a −2 log likelihood function and χ^2 test when one model was nested in the other; otherwise, AIC was used. The level-1 (within-individual level) intercept was modeled as a random effect. In all analyses, the variance–covariance matrix (G matrix) was modeled as unstructured.

3 Results

3.1 Recording Profiles

For all of nine subjects, there were 1353 days of recordings. The compliance rate for regular dietary intake was 77.2%, while the compliance rate of signal-contingent recordings of psychological factors was 42.8%. With regard to pairing dietary intake and preceding psychological factors, 1517 of 3667 dietary intakes could be paired with preceding psychological factors.

3.2 Preceding Psychological Stress and Dietary calorie Intake

Preceding psychological stress was significantly positively associated with dietary intake for lunch and dinner, but negatively associated for snacks (Tab 1). The final model is as follows:

Level 1 equation:

$$Y_{ij} = \pi_{0i} + \pi_{1i}\text{Company}_{ij} + \pi_{2i}\text{Place}_{ij} + \pi_{3i}\text{Stress}_{ij} + \varepsilon_{ij}. \quad (1)$$

Level 2 equations:

$$\pi_{0i} = \gamma_{00} + \zeta_{0i} (\pi_{0i} = \gamma_{00} + +\gamma_{01}\text{TargetCal}_i + \zeta_{0i} \text{ for dinner}). \quad (2)$$

$$\pi_{1i} = \gamma_{10}. \quad (3)$$

$$\pi_{2i} = \gamma_{20}. \quad (4)$$

$$\pi_{3i} = \gamma_{30}. \quad (5)$$

where Y_{ij} is each momentary calorie intake for the ith patient; Company_{ij} is the corresponding accompanying person, which is alone or somebody; Place_{ij} is the corresponding eating place, which is home, office/school, dining out, or other; Stress_{ij} is the corresponding preceding psychological stress; TargetCal_i is the target calorie for ith patient. γ_{00} is the average true value of mean calorie intake when all predictors are zero. π_{1i}, π_{2i}, and π_{3i} is the individual i's slopes representing the effects of accompanying person(s), eating place(s), and preceding psychological stress on momentary calorie intake respectively, and γ_{10}, γ_{20}, and γ_{30} are the average slopes. ε_{ij} and ζ_{0i} are

Lunch	Coefficient (standard error)	F value	P value
Intercept: γ_{00}	565.7(47.3)		< .0001
Accompanying person: γ_{10}		F(1,7) =19.0	.0033
Alone	446.8(35.6)		
Somebody	525.9(36.0)		
Place: γ_{20}		F(3,10) =11.4	.0015
Home	489.2(34.6)*		
Office/school	410.2(41.9)*		
Dining out	565.6(35.4)		
Other	480.5(45.1)		
Stress: γ_{30}	-1.73(.44)	F(1,467) =15.6	< .0001
Dinner			
Intercept: γ_{00}	-256.2(297.6)		.4179
Accompanying person: γ_{10}		F(1,6) =5.6	.0562
Alone	484.6(40.4)		
Somebody	548.5(37.5)		
Place: γ_{20}		F(3,4) =12.3	.0174
Home	577.6(30.4)		
Office/school	366.4(57.0)*#		
Dining out	684.2(44.5)		
Other	438.3(60.7)*		
Stress: γ_{30}	-1.22(.51)	F(1,385) =12.3	.0175
Snacks			
Intercept: γ_{00}	93.5(48.7)		.0961
Accompanying person: γ_{10}		F(1,5) =7.36	.0422
Alone	100.3(41.8)		
Somebody	154.9(42.0)		
Place: γ_{20}		F(3,7) =6.62	.0188
Home	158.1(41.1)		
Office/school	69.2(43.6)*#		
Dining out	189.2(49.6)		
Other	93.9(44.1)#		
Stress: γ_{30}	1.25(.54)	F(1,186) =5.36	.0216

*: significant difference with "dining out"
#: significant difference with "home"
($p<0.05$ for all using Tukey-Kramer's correction).

Table 1: Effect of preceding psychological stress on calorie intake for lunch, dinner and snacks

residuals at each level. Including ζ_{0i} in the equation means that the intercept was modeled as random, which suggested that intercept could vary across individuals. The second level 2 equation include no residual, which means that the effects of accompanying person(s), eating place(s), and preceding psychological stress on momentary calorie intake were modeled as fixed effects.

3.3 Preceding Anxiety and Dietary calorie Intake

Breakfast	Coefficient (standard error)	F value	P value
Intercept: γ_{00}	596.2(50.6)		< .0001
Accompanying person: γ_{10}		F(1,4) =7.7	.0502
Alone	419.0(35.8)		
Somebody	489.7(37.2)		
Place: γ_{20}		F(3,5) =4.5	.0708
Home	413.8(29.7)		
Office/school	375.9(66.2)		
Dining out	516.5(49.7)		
Other	511.3(51.5)		
Anxiety: γ_{30}	-1.80(.76)	F(1,395) =5.6	.0185

Table 2: Effect of preceding anxiety on calorie intake for breakfast

Preceding anxiety was significantly negatively associated with dietary intake only for breakfast (Table 2). The final model is as follows:

Level 1 equation:

$$Y_{ij} = \pi_{0i} + \pi_{1i}Company_{ij} + \pi_{2i}Place_{ij} + \pi_{3i}Anxiety_{ij} + \varepsilon_{ij}. \quad (6)$$

Level 2 equations:

$$\pi_{0i} = \gamma_{00} + \zeta_{0i}. \quad (7)$$

$$\pi_{1i} = \gamma_{10}. \quad (8)$$

$$\pi_{2i} = \gamma_{20}. \quad (9)$$

$$\pi_{3i} = \gamma_{30}. \quad (10)$$

where Y_{ij} is each momentary calorie intake for the ith patient; $Company_{ij}$ is the corresponding accompanying person, which is alone or somebody; $Place_{ij}$ is the corresponding eating place, which is home, office/school, dining out, or other; $Anxiety_{ij}$ is the corresponding preceding anxiety.

3.4 Preceding Depression and Dietary calorie Intake

Preceding depressive mood was significantly negatively associated with dietary intake only for lunch (Tab 3). The final model is the same as the model for anxiety, in which $Anxiety_{ij}$ is replaced with $Depression_{ij}$.

4 Conclusions

Using computerized EMA for six months, significant within-individual relationships between preceding psychological factors and calorie intake within five hours were shown in patients with type 2 diabetes. Although a causal relationship could not be established, it supports the possibility that psychological factors can influence calorie intake in patients with type 2 diabetes, which has not been investigated previously in the daily lives of the patients.

In the present study, the results showed that there were differences in the association between preceding

Lunch	Coefficient (standard error)	F value	P value
Intercept: γ_{00}	564.6(43.3)		< .0001
Accompanying person: γ_{10}		F(1,7) =22.3	.0022
Alone	442.8(29.9)		
Somebody	528.2(30.6)		
Place: γ_{20}		F(3,10) =11.7	.0013
Home	491.4(28.8)*		
Office/school	414.1(37.2)*		
Dining out	569.2(29.9)		
Other	467.2(40.7)		
Depression: γ_{30}	-3.64(.98)	F(1,467) =13.7	.0002

*: significant difference with "dining out" ($p<0.05$ for all using Tukey-Kramer's correction).

Table 3: Effect of preceding depressive mood on calorie intake for lunch

psychological factors and calorie intake among the types of food. With regard to snacks, the present study showed that preceding psychological stress was positively associated with calorie intake. This result was consistent with the results of previous studies [3] [5] [6] although they had methodological problems as mentioned above. Because results in studies using different methods were consistent, psychological stress might increase calorie intake of snacks. Eating snacks may be used as a coping strategy for reducing psychological stress [13].

With regard to regular meals, preceding psychological stress, anxiety, and depressive mood were negatively associated with calorie intakes. The results in previous studies were not consistent regarding the association between psychological factors and calorie intake [3] [4]. Because all of the subjects were women in the two previous studies, it would be difficult to compare the results of the present study with those of the two previous studies. Therefore, future studies were necessary to confirm the association between preceding psychological factors and regular meals.

Calorie intake was generally greater with person(s) than without anyone, and when eating out than when eating at home, controlling for psychological factors. Therefore, this result might confirm the results shown in a previous study that calorie intake increased in social situations [4].

There were some limitations in the present study. First, the sample size was small. Second, most of the patients in the present study were men. Therefore, future studies with more patients including men and women were necessary. In addition, there was not a control group of healthy people. Therefore, it is not possible to expand the results in the present study to healthy people.

In conclusion, preceding psychological factors could influence calorie intake in patients with type 2 diabetes, which may lead to developing psychological intervention to prevent overeating, such as noticing not to overeat the snack when recorded stress was high or display the list of coping strategies substituted for snack.

Acknowledgements

The authors thank all of the study participants. The University of Tokyo (person in charge: Dr. Yoshiuchi) conducted cooperative research with Sharp Cooperation.

References

[1] F. Bonnet, K. Irving, J.L. Terra, P. Nony, F. Berthezene, and P. Moulin. Anxiety and depression are associated with unhealthy lifestyle in patients at risk of diovascular disease. *Atherosclerosis*, 178: 339-44, 2005.
[2] A.A. Stone and S. Shiffman. Ecological momentary assessment (EMA) in behavioral medicine. *Ann Behav Med*, 16; 199-202, 1994.
[3] M.R. Lowe and E.B. Fisher, Jr. Emotional reactivity, emotional eating, and obesity: a naturalistic study. *J Behav Med*, 6: 135-49, 1983.
[4] K.A. Patel and D.G. Schlundt. Impact of moods and social context on eating behavior. *Appetite*, 36: 111-8, 2001.
[5] D.B. O'Connor, F. Jones, M. Conner, B. McMillan, and E. Ferguson. Effects of daily hassles and eating style on eating behavior. *Health Psychol*, 27:S20-31, 2008.
[6] A.J. Tomiyama, T. Mann, and L. Comer. Triggers of eating in everyday life. *Appetite*, 52: 72-82, 2009.
[7] A.A. Stone, S. Shiffman, J.E. Schwartz, J.E. Broderick, and M.R. Hufford. Patient non-compliance with paper diaries. *BMJ*, 324: 1193-1194, 2002.
[8] S. Inada, K. Yoshiuchi, Y. Iizuka, K. Ohashi, H. Kikuchi, Y. Yamamoto, T. Kadowaki, and A. Akabayashi. Pilot Study for the Development of a Self-Care System for Type 2 Diabetes Patients Using a Personal Digital Assistant (PDA). *Int J Behav Med*, 2016.
[9] Y. Seino, K. Nanjo, N. Tajima, T. Kadowaki, A. Kashiwagi, E. Araki, C. Ito, N. Inagaki, Y. Iwamoto, M. Kasuga, T. Hanafusa, M. Haneda, and K. Ueki. Report of the committee on the classification and diagnostic criteria of diabetes mellitus. *Diabetol Int*, 1: 2-20, 2010.
[10] W. Fukuo, K. Yoshiuchi, K. Ohashi, H. Togashi, R. Sekine, H. Kikuchi, N. Sakamoto, S. Inada, F. Sato, T. Kadowaki, and A. Akabayashi. Development of a hand-held personal digital assistant-based food diary with food photographs for Japanese subjects. *J Am Diet Assoc*. 109: 1232-6, 2009.
[11] H. Kikuchi, K. Yoshiuchi, N. Miyasaka, K. Ohashi, Y. Yamamoto, H. Kumano, T. Kuboki, and A. Akabayashi. Reliability of recalled self-report on headache intensity: investigation using ecological momentary assessment technique. *Cephalalgia*, 26: 1335-43, 2006.
[12] H. Kikuchi, K. Yoshiuchi, T. Ando, and Y. Yamamoto. Influence of psychological factors on acute exacerbation of tension-type headache: Investigation by ecological momentary assessment. *J Psychosom Res*. 79: 239-42, 2015.
[13] M. Macht. How emotions affect eating: a five-way model. *Appetite*, 50: 1-11, 2008.

Address for correspondence:
Kazuhiro Yoshiuchi
Department of Stress Sciences and Psychosomatic Medicine, Graduate School of Medicine, The University of Tokyo, Japan
kyoshiuc@umin.ac.jp

Atomic Force Microscopy for Bladder Cancer Detection

Eugene Demidenko, Igor Sokolov, John Seigne

Abstract – Cystoscopy is the traditional but unpleasant and fairly expensive gold standard method for bladder cancer detection. Although several less expensive and repetitive cytology methods have been considered to analyze urine sample for bladder cancer they all suffer from low sensitivity. We propose a novel technique to analyze cells in urine using Atomic Force Microscopy on the nanoscale. Results of statistical cell discrimination based on 83 AFM cell images from urine samples of 20 individuals are promising: we are able to discriminate cells with 100% sensitivity and 100% specificity using two characteristics of the AFM surface cell images.

***Index Terms*—Cell imaging, nanoscale, hierarchical data, statistical discrimination**

I. Introduction

Bladder cancer is the fourth most common cancer in men and the ninth most common cancer in women [15]. The current gold standard for evaluating patients with suspected cancer, such as individuals with hematuria or back pain, is white light cystoscopy (WLC) of bladder with or without random biopsies. WLC illuminates the area within the bladder, allowing evaluation of gross morphologic changes and the extent of tumor mass. Subsequent biopsy analysis by histopathologists grades and stages tumors according to location, tissue stratification, nucleation, and assays for tumor-specific antigens. Cystoscopy is not always accurate, with a sensitivity in the range from 73% to 90% [16] and specificity as low as 37% [22]. Most importantly, cystoscopy is invasive and unpleasant procedure: no wander patients try to avoid repetitive cystoscopy for bladder cancer monitoring to detect early recurrence, typical for this kind of cancer. Much efforts has been put into development of urine cytology test and respective urine biomarkers [21], [1]. These tests typically have high specificity but low sensitivity, as low as 50% [20], [23], [3]. Although some biomarker tests, such as based on hyaluronic acid and hyaluronidase [17] have high sensitivity for high grade cancers they fail to detect low-grade cancers [18]. Some urine exams are based on technologic methods, such as photonics, □uorescence [13], [19] or more recent RAMAN molecular imaging [10] to improve sensitivity but fail in specificity. Current cytology tests have low sensitivity. We suggest to improve the urine analysis by using the AFM cell imaging that is noninvasive and repetitive, and may work in conjunction with existing diagnostic techniques. In our previous very preliminary work we were able to discriminate cancer and normal bladder epithelial cells using topography and adhesion AFM maps. The goal of this proposal is to collect sufficient preliminary data to demonstrate that AFM is capable of discriminating between low and high grade tumors. We believe that atomic force microscopy (AFM) may become a clinically important technological modality for noninvasive repetitive bladder cancer detection and monitoring because it relies on the investigation of one cell at a time and therefore one urine cell will be enough to identify the likelihood of cancer.

Eugene Demidenko is with Geisel School of Medcine at Dartmouth at the Department of Biomedical Data Science and Mathematics, (eugened@dartmouth.edu). Igor Sokolov is with Tufts University, Boston. John Seigne is with Dartmouth Hitchcock Medical Center, USA.

II. Methods

Urine samples have been collected at the Urology Department, DHMC, Lebanon, New Hampshire, USA. Three cohorts of patients have been targeted: (1) normals: patients with bladder cancer symptoms, such as hematuria or frequent and painful urination, but not confirmed bladder cancer, (2) new bladder cancer: patients with symptoms and pathology-confirmed cancer, (3) previously detected bladder cancer: treated and follow up patients. Subjects will be identified in the Urology clinic of DHMC who have undergone cystoscopy and found to have a bladder tumor (any stage and grade). The study was explained and those willing to participate have been given an informative consent letter and a urine sample was collected. The final pathological diagnosis (tumor histology, stage and grade) as well as the results of urine cytology and urinalysis were collected as well. No personal identity information have been collected or linked to urine specimen. Specifically, the collection protocol was as follows: (a) 50 mL of voided urine will be collected and transported to the cytology laboratory within 15 minutes of collection, (b) The urine will be divided into two 25 mL aliquots; one aliquot will be fixed with alcohol, per standard DHMC procedure. The 2nd aliquot will be fixed with Karnovsky fixative, (c) The fixed cells from the 2nd aliquot will be shipped to Tufts University for the AFM imaging and preprocessing; (d) The digital images will be uploaded to the server at Tufts for further data download and statistical analysis at Dartmouth for cancer cell discrimination.

III. Atomic Force Microscopy

A recently introduced AFM modality is a new cell imaging technology that allows not only imaging the cell surface with substantially higher resolution than optical and even electron microscopy, but provides a unique mapping of various physical

properties of the cell surface (force, like rigidity, adhesion, energy dissipation, deformability, etc.) at the nanoscale; see Fig. 1. AFM enables obtaining both lateral and vertical resolutions which can be attained on fixed cells are ~1-5 nm and 0.01 nm, respectively, which is ~40-200x (for lateral resolution) and >10000x (for vertical resolution) better than the resolution attained with optical microscopy, and even higher than that typically obtained with electron microscopy [11]. These new AFM modalities allow obtaining of up to eight novel images/maps of cell surface, more than 150 new parameters that have not yet been studied for cell characterization. Previously we had success in virtually ambiguous discriminating cancer from normal cervical cells using this AFM imaging method. It was discovered that the fractal dimension of the adhesion AFM images allows unambiguously segregate normal cells from a mix of precancerous and cancerous cells [14], [9]. There are already fully automated AFMs (currently used in semiconductor industry, for example, Bruker Dimension AFP, https://www.bruker.com). Such microscopes can readily be used to image dried fixed cells in air as proposed without the need in trained technician.

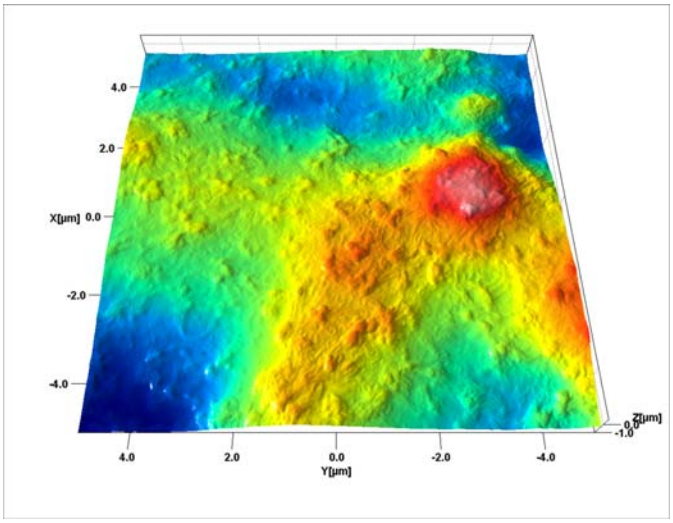

Fig. 1. Typical AFM *force* image of a cell surface.

IV. Statistical Methods of Classification

According to general classification [7], AFM images belong to the family of content independent images. In the past, we have been successful in applying cumulative distribution function and implied ordered statistics, empowered by classical nonparametric tests such as Kolmogorov-Smirnov [4], [5], [6] for classification of content independent, and particularly cancer cell images. Fig. 2 depicts three typical AFM height images of urine cells with three pseudo coloring at quantiles 33% and 66%. Unlike traditional image recognition techniques [2], [12], [24] that deal with one image at a time we will be using statistical analysis of ensemble of images and compute the p-value for image comparison and classification and implied sensitivity, specificity, and the ROC curve [8].

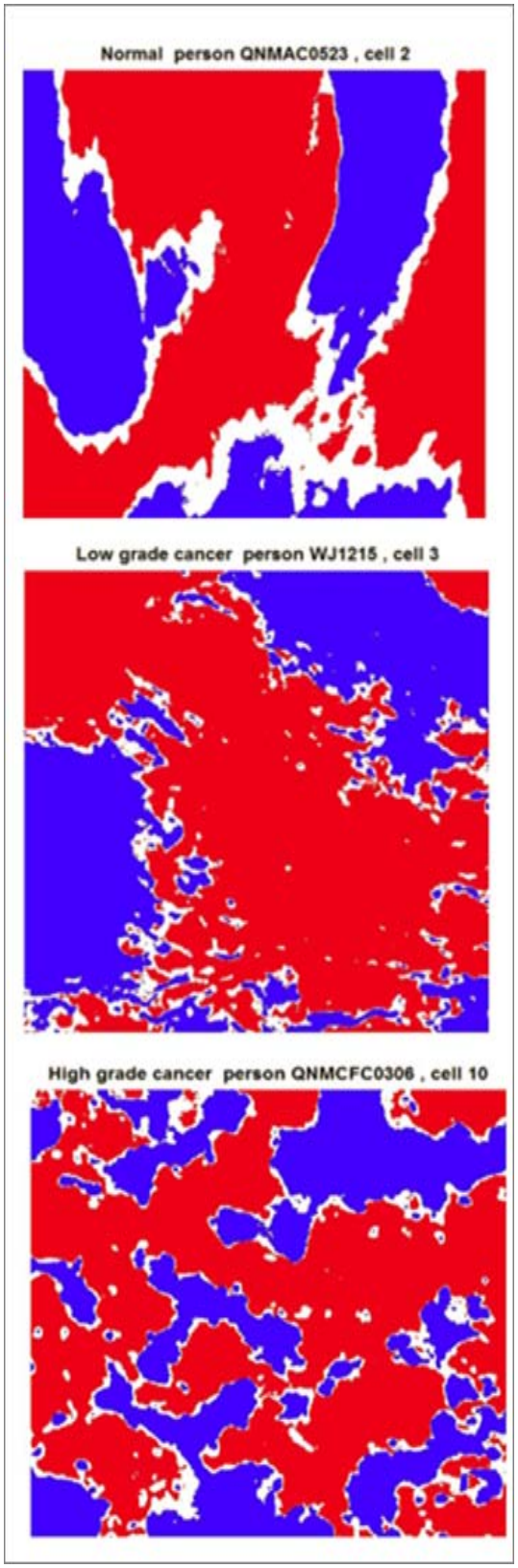

Fig.2. Pseudo-color AFM images of bladder cells.

V. Results

The classification of 83 AFM cell images in 20 urine samples derived under previous protocol is depicted in Fig. 3. Two image topography/height parameters, Sdr=Surface Area Ratio (the roughness of the surface) and Sds=Surface density

(the number of maxima of surface density per unit square) perfectly discriminate cancer cells from controls. Empty circle represents the cell and solid circle represents the median across cells found in the urine sample (about 4 cells per urine sample).

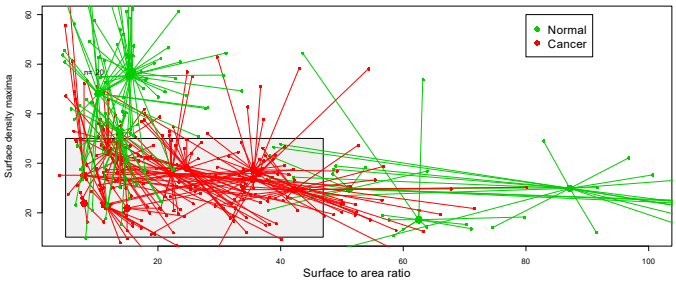

Fig.3. 83 AFM cell images from 20 individuals.

We can perfectly separate controls and cancers using the rule area < 47 and density maxima < 35. An important observation is that the variation of the AFM image parameters is smaller within the sample compared to the variation across samples/patients. Although some cells may be misclassified (green points within the grey rectangular) combined together they uniquely classify individuals into normal and cancer groups. Our very preliminary data has encouraging 100% sensitivity and 100% specificity of cancer detection using just two AFM image parameters but we need to collect more urine data to demonstrate the feasibility of detection of low-grade cancers.

REFERENCES

[1] Bangma CG, Loeb S, Busstra M, et al. Outcomes of a bladder cancer screening program using home hematuria testing and molecular markers, European Urology 64, 41-47, 2013.
[2] Barrett HH, Myers KJ. Foundations of Image Science, Wiley, 2004.
[3] Cheng L, Davison DD, Adams J, Lopez-Beltran A Wang L, Montironi R, Zhang S. Biomarkers in bladder cancer: Translational and clinical implications, Oncology Hematology 89, 89, 73-11, 2014.
[4] Demidenko E. Kolmogorov-Smirnov test for image comparison. Lecture Notes in Computer Science, 3046: 933–939, 2004.
[5] Demidenko E. Statistical comparison of color cancer cell images. Oncology Reports, 15:1077–1079, 2006.
[6] Demidenko E. Statistical hypothesis testing for postreconstructed and postregistered medical images. SIAM Journal on Imaging Sciences, 2: 1049–1067, 2009.
[7] Demidenko E. Mixed Models: Theory and Applications with R. New York: Wiley, 2013.
[8] Demidenko E. The p-value you can't buy. American Statistician 70(1):33–38, 2016.
[9] Dokukin ME, Guz NV, Woodworth CD, Sokolov I. Emergence of fractal geometry on the surface of human cervical epithelial cells during progression towards cancer, New Journal of Physics 17, March 2015 doi:10.1088/1367-2630/17/3/033019
[10] Draga RO, Grimbergen MC, Vijverberg PL, van Swol CF, Jonges TG, Kummer JA, Ruud Bosch JL. In vivo bladder cancer diagnosis by high-volume Raman spectroscopy. Analytical Chemistry 82:5993-5999, 2010.
[11] Gaikwad RM, Vasilyev SI, Datta S, Sokolov I. Atomic force microscopy characterization of corneocytes: effect of moisturizer on their topology, rigidity, and friction. Skin Res Technol, 2010. 16(3): p. 275-82.
[12] Gonzalez RG, Woods RE. Digital Image Processing, Prentice Hall, 2002.
[13] Fu CY, Ng BK, Razul SG, Chin WW, Tan PH, Lau WK, Olivo M. Fluorescence detection of bladder cancer using urine cytology, International Lournal of Oncology 31: 525-530, 2007.
[14] Iyer KS, Gaikwad RM, Woodworth CD, Volkov DO, Sokolov I. Physical labeling of papillomavirus-infected, immortal, and cancerous cervical epithelial cells reveal surface changes at immortal stage. Cell Biochemistry and Biophysics 63, 109-116, 2012. DOI: 10.1007/s12013-012-9345-2
[15] Konety BR, Molecular markers in bladder cancer: A critical appraisal. Urologic Oncology: Seminars and Original Investigations 24:326-337, 2006.
[16] Kriegmair M, Baumgartner R, Knuchel R, et al. Detection of early bladder cancer by 5-aminolevulinic acid induced porphyrin □uorescence. J Urol, 155:105-110, 1996.
[17] Hautmann SH, Schroeder GL, Civantos F, et al. Hyaluronic acid and hyaluronidase. 2 new bladder carcinoma markers. Urologe A 2001;40:121-126.
[18] Lokeshwar VB, Schroeder GL, Selzer MG, et al. Bladder tumor markers for monitoring recurrence and screening comparison of hyaluronic acid-hyaluronidase and BTA-Stat tests. Cancer 2002;95: 61-72.
[19] Palmer S, Sokolovski SG, Rafailov E, Nabi G. Technologic developments in the field of photonics for the detection of urinary bladder cancer. Clinical Genitourinary Cancer, Vol. 11, No. 4, 390-396, 2013.
[20] Rhijn BWG, Poel H, Kwast TH. Cytology and urinary markers for the diagnosis of bladder cancer. European Urology Supplements 47, 736-748, 2005.
[21] Rosser CJ, Urquidi V, Goodison S. Urinary biomarkers of bladder cancer: an update and future perspectives. Biomarkers Med 7: 779-790, 2013.
[22] Sarosdy MF, Schellhammer P, Bokinsky G, et al. Clinical evaluation of a multi-target □uorescent in situ hybridization assay for detection of bladder cancer. J Urol, 168:1950-1954, 2002.
[23] Tilki D, Burger M, Dalbagni G, Grossman HB, Hakenberg OW, Palou J, Reich O, Roupre M, Shariat SG, Zlotta AR. Urine markers for detection and surveillance of non–muscle-invasive bladder cancer, European Urology 60, 484-492, 2011.
[24] Tosteson T, Pogue BW, Demidenko E, McBride TO, and Paulsen KD. (1999). Confidence maps and confidence intervals for near infrared images in breast cancer, IEEE Transactions on Medical Imaging, 18:1188-1193, 1999.

A normalized non-stationary wavelet based analysis approach for computer assisted classification of laryngoscopic high-speed video recordings

Mona K. Fehling[1,3], Jakob Unger[2], Dietmar J. Hecker[3], Bernhard Schick[3], Jörg Lohscheller[1],

[1]Department of Computer Science, Trier University of Applied Sciences, Trier, Germany;
[2]Department of Biomedical Engineering, University of California, Davis, USA;
[3]Department of Otorhinolaryngology, Saarland University Hospital, Homburg/Saar, Germany;

Abstract

Voice disorders originate from disturbances of the two vocal folds' (VF) vibration patterns. Laryngeal high-speed videoendoscopy (HSV) is the state-of-the-art technique to examine and analyze objectively the 2D VF vibration pattern.
We present an approach allowing a fully automated analysis of the HS video data based on wavelet analysis of so-called phonovibrograms (PVG), which are extracted from the high-speed videos. Using a principal component analysis (PCA), a low-dimensional feature set is derived from each PVG. These clinically relevant features are suitable to automatically classify healthy and pathological voices using a support vector machine (SVM) as a machine learning approach. In addition a registration of PCA spaces is presented, allowing for a normalization of the derived measures.

Keywords *Wavelet-based analysis, Multiscale product, normalization, computer assisted classification, high-speed laryngoscopy, vocal fold analysis, phonovibrogram.*

1 Introduction

Voice production is a highly complex process, initiated by VF vibrations, which modulate the airstream from the lungs [1]. Voice disorders have been causally related to irregularities in these vibrations. The VF movements can be assesed using HSV endoscopy, which allows new insights into physiologic and pathologic mechanisms of VF vibrations. The Laryngeal images are captured in real-time using samplingrates of 2,000 - 20,000 fps and are therefore also capable for examination of dynamic phonations [2].

In clinical routine, the VF vibrational behavior is assessed by a time consuming and subjective visual inspection, rating asymmetry, asynchrony, irregularity and stability of the vibration pattern. The PVG is an approach for an objective analysis to quantify vibration characteristics from the HSV. It provides a compact description and visualization of the entire vibration pattern [4]. Fig. 1 shows the PVG construction process and further analysis. Different approaches for assessing quantitative features from the PVG has been shown, having two main limitations: (a) extremly high number of extracted features and (b) the features are not understandable within a clinical context [5]. We present an approach to overcome these limitations by a wavelet-based procedure in combination with a PCA to analyze the PVGs geometric structure. On basis of the three dominant eigenvalues λ_1, λ_2 and λ_3, the most significant properties of the VF vibration patterns are extracted by quantifying the main characteristics of the PVG geometry. The eigenvalues provide a compact representation of the complex VF vibration patterns along the entire glottal axis. Furthermore they are clinically interpretable as they correlate with a rating scheme elaborated by the European Laryngological Society (ELS) [6]. A correlation between $\lambda_{1,2,3}$ and the glottal closing characteristics has successfully been shown. But subjects projected into different PCA spaces cannot be compared directly, due to their dependency on the dataset used to span the respective PCA space. This impeeds significantly the application in clinical context.
To overcome this limitation we propose a normalization of the PCA space, employing an affine registration approach using synthetic PVG contours. Further, an automated classification for pathologic and physiologic vibrations is presented based on the temporal variation of the eigenvalues using a support vector machine (SVM).

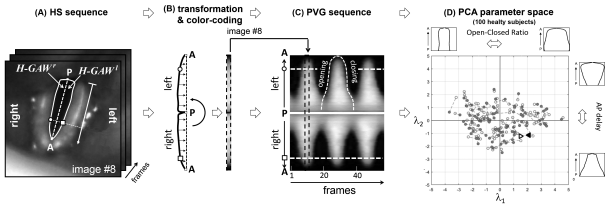

Figure 1: Wavelet based PVG analysis [3]. (A) Segmentation of VF edges in each frame. (B) Rotation of the left VF edge and color-coding distances. (C) PVG construction. (D) Result obtained by stationary wavelet-based analysis projected into a PCA space.

2 Methods

The proposed method was developed and verified based on clinical laryngeal HSV. Endoscopic imaging during phonation was performed using the Endocam

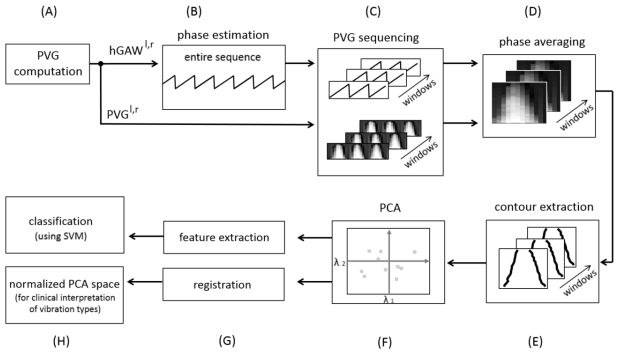

Figure 2: Steps of a non-stationary PVG analysis. (A)-(E) show the non-stationary PVG analysis approach: PVG computation, phase estimation, PVG sequencing, phase averaging and contour extraction. (F) illustrates a PCA space spanned by λ_1 and λ_2. (G) and (H) show the classification, based on feature extraction, as well as the normalization of the PCA space using a registration approach.

5526 high-speed camera system (Richard Wolf GmbH), which provides a resolution of 256 $\times$ 256 pixels at 4,000 fps. For the analysis 500 frames were evaluated.
PCA spaces used for the normalization approach were spanned from 100 healthy subjects (females: 63, age 41.27 $\pm$ 15.84 yr; males: 37, age 49.05 $\pm$ 15.33 yr). As a testset, 20 subjects were used, containing 10 healthy (10 females, age 20.1 $\pm$ 1.9 yr) and 10 pathologic subjects (unilateral VF paresis: 5 females, age 43.8 $\pm$ 13.2 yr & muscle tension dysphonia: 5 females, age 48.6 $\pm$ 11.4 yr). Fig. 2 visualizes a non-stationary PVG analysis (n.stat.anal.).
Subsequent steps and used parameters are shortly summarized in the following, details can be found in [2]. For automated classification, additional to the set of 100 healthy subjects, 50 subjects (females: 28, age 48.80 $\pm$ 18.43 yr, males: 22, age 56.40 $\pm$ 12.81 yr) diagnosed with unilateral vocal fold paresis, were used. All subjects[1] were collected in a previous study [3] and examined during sustained phonation of the vowel /ae/ at a comfortable pitch and loudness for at least 1s using rigid endoscopy.

2.1 Non-stationary PVG analysis

Different vibration types of the VF occure in a PVG as characteristic geometric pattern [3], providing a basis for pattern recognition. During sustained phonation, only a slight change of the geometric PVG pattern throughout an entire HSV sequence can be noticed. In contrast, a dynamic phonation leads to considerable changes, implicating a n.stat.anal. which extracts the PVG contours as a function of time. First, the vibrating VF edges in the HSV are segmented using a region-growing algorithm. The distances of the VF edges relative to the glottal axis are color-coded and construct the 3D PVG-matrix (Fig. 1). To describe spatiotemporal properties, the PVG is split into subsequent cycles. Therefore the complex wavelet phase of the hemi-glottal area function $hGAW^{l,r}$, as well as an analytic Morlet wavelet, and a continuose wavelet transform, is used to derive required phase information. Based on these cycles, for a n.stat.anal., the PVG is divided into a series of equally sized windows $w = [1, ..., W]$ (see Fig. 2(C)), such that short time stationarity can be assumed. Afterwards an average cycle geometry is estimated. A windowsize of 62.5 ms equal to $M = 250$ images per window, with an overlap of 25 frames, is used to track temporal changes with a high degree of precision. The following steps are applied on each window individually. After identification and normalization of the cycles, the VF deflections are averaged over the extracted cycles of the corresponding window w. This mean pattern reflects the mean vibration type of the windows average PVG cycle. Using a Mexican hat wavelet and a multiscale product approach for computation of the distances between the opening and the closing instants alongside the anterior-posterior axis, the characterization of the VF vibration mode is finally performed for each window and each VF [3]. A compact representation of the mean geometry is achieved by projecting corresponding distance vectors into a parameter space. This parameter space is spanned by the first three eigenvalues $\lambda_{1,2,3}$, which are obtained by a PCA (Fig.1(D) & Fig.2(F)). λ_1 encodes the open-closed ratio, λ_2 discriminates between zipper-like openings and λ_3 discriminates between oval and hour-glass vibration type [3]. For a n.stat.anal. of so far unknown HSV, the distance vectors of each VF and window are projected individually into the spanned PCA space. This results into a pair of trajectories $(\lambda_1^{l,r}(w), \lambda_2^{l,r}(w), \lambda_3^{l,r}(w))$, allowing an easily interpretable representation of PVG contours in clinical practice and a powerful data reduction [3, 2].

2.2 Feature extraction

A short overview on parameters rating asymmetry, asynchronity, irregularity and stability of the vibration is given, detailed information can be found in [3].
The lateral vibratory asymmetry $F_{asym}(w)$ is defined by the L^2 distance of the projection of the left and the right VF into the PCA subspace:

$$F_{asym}(w) = \sqrt{\sum_{i=1}^{3} \left(\lambda_i^l(w) - \lambda_i^r(w)\right)^2}.$$

The irregularity of the vibration pattern $F_{irr}^{l,r}(w)$ is defined as absolute sum off all eigenvalues order ≥ 4

$$F_{irr}^{l,r}(w) = \sum_{i \geq 4} \left|\lambda_i^{l,r}(w)\right|.$$

The average phase delay $F_{async}(w)$ between the left and the right VF is defined by

$$F_{async}(w) = \frac{1}{M} \sum |\arg\left(e^{i(\phi_w^l(a_0(b),b) - \phi_w^r(a_0(b),b))}\right)|$$

and using the wavelet phases of the left and the right hemi-glottal area waveform functions $\phi_w^{l,r}(a_0(b), b)$.
The stability of the vibration is expressed by the standard deviation $\|std(\lambda_{1,2,3}^{l,r})\|_2$ of the eigenvalues, a higher irregularity leading to higher values.
For a healthy voice during a sustained phonation, the VF vibration pattern can be assumed to be time-invariant,

[1] Note that a part of the here shown HSV including the PVGs are provided in the "medDB" open access research database (http://lea.hochschule-trier.de).

indicated by stable projection within the PCA space. For pathologic voice however, due to the unstable VF vibration, a shift in the PCA space is expected. Symmetry and temporal stability of the dominant vibration pattern of left and right VF during a sustained phonation are described by the twenty-dimensional feature vector F_S, which assembles the mean values and standard deviations for the parameters $F_{asym}(w)$, $F_{irr}^{l,r}(w)$, $F_{async}(w)$ and $\lambda_{1,2,3}^{l,r}$ for a single subject.

2.3 Classification: paretic vs. healthy

Since a stat.anal. might not be sufficient for a reliable diagnosis on the vibration asymmetry, the benefit of the generalized n.stat.anal., leading to a twenty dimensional feature vector F_S, is demonstrated, using HSV from 20 subjects. A recent approach [3], resulting in a ten-dimensional feature vector F_{Ref} and serving as benchmark, was applied using the same group of subjects. The investigated group consists of 100 healthy subjects and 50 subjects diagnosed with unilateral VF paresis.
Due to the small group size of paretic subjects, the maximum number of selectable features was set to five. [7, 8] A supervised machine learning approach is used to classify an unseen feature vector to the class 'healthy' or to the class 'paresis'. A Support Vector Machine (SVM) with polynomial kernel was applied to build a predictive model for classification, using the identified features as well as the reference feature set F_{Ref} as input.

2.4 Normalization of PCA-spaces

In general, subjects in different PCA spaces cannot be compared directly, because their eigenvalues depend on the dataset used to span the respective PCA space (Fig. 3(A)). We propose a normalization, allowing comparability between subjects in different PCA spaces by using a registration approach transforming subjects from different PCA spaces on a corresponding point in a normalized PCA space.
First, a stationary PCA space is spanned by healthy subjects in which a set of synthetic distance vectors (visualized by '+' in Fig. 3), is projected. These distance vectors describe vibration patterns, each characterized by only one of the three eigenvalues, according to the definition of the ELS. They lead to a set of reference points for each PCA space dimension, which is slightly distorted relative to the PCA space axis. By applying a registration approach according to [9], the coordinates of the synthetic contours are transformed such that $\lambda_{1,2,3}^{T} \in [-1, 1]$ in the new PCA^T space (3(B)). This allows direct comparability between different normalized PCA spaces originally spanned by different healthy subjects and is furthermore suitable for fast and reliable voice assesment in clinical practice.
To verify the proposed normalization, different PCA spaces were calculated. After normalization, a testset of 20 subjects was projected into the PCA space. Hereby the spreading of the dominant eigenvalues relative to the respective eigenvalues in a reference PCA space (spanned by 100 healthy subjects) is determined and used as a measurement for reliability of the normalization. Also the relative error of the projection in the normalized PCA space spanned by varying number of subjects was investigated.

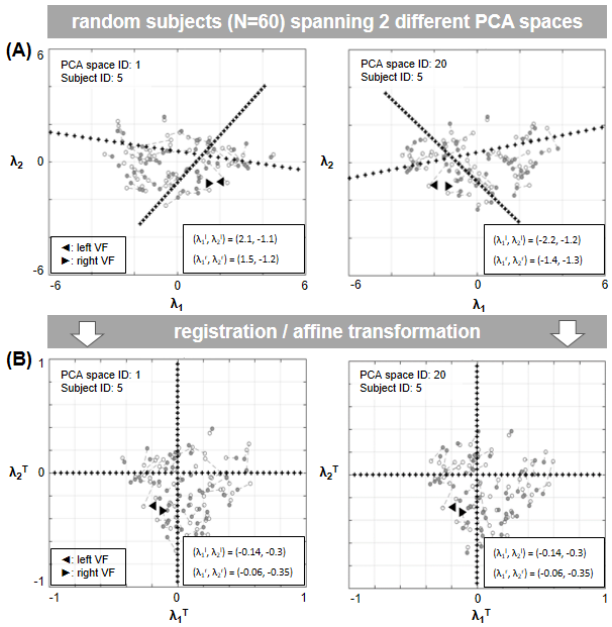

Figure 3: PCA space normalization using a registration approach. (A) An exemplary subject, indicated by one triangle for each VF, projected into different PCA spaces (each spanned by 60 randomly chosen healthy subjects) before normalization. (B) PCA spaces after normalization demonstrating the power of the presented normalization approach, illustrated by the subjects identical localization.

3 Results

3.1 Classification

Based on feature selection, a machine learning approach using a SVM was applied for discrimination between physiologic and pathologic vibrations. A stat.anal. approach, resulting into a single data point for each VF, is used as benchmark.
The F_{asym} measures of the healthy subject (stat.anal.: $F_{asym} = 1.11$, n.stat.anal.: $\bar{F}_{asym} = 1.16$, $\|std(\lambda_{1,2,3}^{l})\|_2 = 0.177, \|std(\lambda_{1,2,3}^{r})\|_2 = 0.083$), show only a slight change of the vibration pattern over the time. For the VF paralysis subject, a distinct change of both VF eigenvalue distributions can be seen (stat.anal.: $F_{asym} = 1.02$, n.stat.anal.: $\bar{F}_{asym} = 1.28$, $\|std(\lambda_{1,2,3}^{l})\|_2 = 0.746, \|std(\lambda_{1,2,3}^{r})\|_2 = 0.638$). Since this change in vibration symmetry cannot be observed using a stat.anal., a n.stat.anal. is necessary to investigate features describing the temporal stability that seem to be sufficient for distinction between physiologic and pathologic vibrations. For reduction of the feature space dimension, the described feature selection approach was applied to the non-

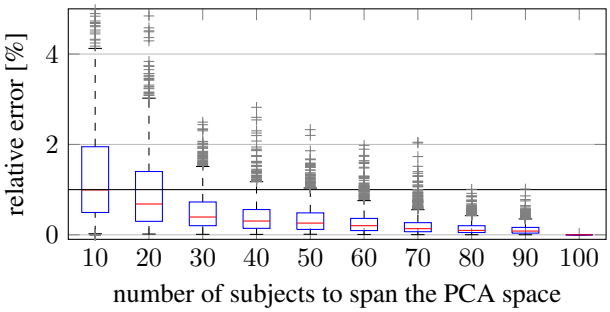

Figure 4: Relative Error decreasing significantly with higher numbers of subjects used to span the PCA space. Reliable results with a relative error of $<1\%$ can be recieved by spanning the PCA space with more than 60 subjects.

stationary feature vector, resulting in five appropriate features $\bar{F}_{asym}$, $\bar{F}_{async}$, $std(F_{async}(w))$, $\bar{F}_{irr}$, $\bar{\lambda}_2^r$, which were fed into the SVM for automatic classification. A classification accuracy of 91.3% (sensitivity: 80%, specificity: 97%) was achieved for the five selected features based on a leave-one-out validation scheme, and a classification accuracy of 89.3% (sensitivity: 76.0%, specificity: 96.0%) for the benchmark feature set F_{Ref}.

3.2 Normalization

The presented classification approach is eligible to discriminate between physiologic and pathologic vibrations, but for direct comparability of the subjects a normalization is required. For better visualization only PCA subspaces spanned by $\lambda_1^{l,r}$ and $\lambda_2^{l,r}$ are displayed. The light grey data points in the background represent the eigenvalue distribution of the subjects used span the PCA space. Exemplarily, one analyzed subject is projected into different PCA spaces and visualized by dark data triangles. Fig. 3 shows the projection before (A) and after (B), demonstrating a successful normalization by same localization in the PCA^T spaces. The normalization is reliable for healthy as well as for pathologic subjects (results not shown) and the spreading in constant PCA space size is independent from the vibration pattern. Also the influence of the number of subjects used to span the respective PCA space was investigated (Fig. 4), showing a significant decrease of the relative error with higher number of subjects. For reliable results with a relative error of less than 1% a minimum of 60 healthy subjects is recommended to spann the PCA space.

4 Conclusion

The temporal stability of the VF vibration was found to be useful for an automatic identification of voice disorders. We presented an automated classification approach, which is able to to discriminate between a physiological and a pathological vibration pattern based on the temporal variation of the eigenvalues using a SVM. But for a reliable diagnosis based on the temporal stability of the VF vibration pattern, a sustained phonation that satisfy the steady-state criterion is necessary to avoid wrong diagnosis.
Further a normalization of PCA spaces spanned by different subjects, as well as for the projection of the subjects to be investigated, has been demonstrated. It provides reliable and comparable results for PCA spaces spanned by at least 60 subjects and allow for a better interpretation of the VF vibration characteristics in clinical practice.

Acknowledgment

This work was supported by the German Research Foundation (DFG), LO-1413/2-2.

References

[1] J.G. Švec and H.K. Schutte. Videokymography: High-speed line scanning of vocal fold vibration. *Journal of Voice*, 10(2):201–205, 1996.

[2] J. Unger, M. Schuster, D.J. Hecker, B. Schick, and J. Lohscheller. A generalized procedure for analyzing sustained and dynamic vocal fold vibrations from laryngeal high-speed videos using phonovibrograms. *Artificial Intelligence in Medicine*, 66:15–28, 2016.

[3] J. Unger, D.J. Hecker, M. Kunduk, M. Schuster, B. Schick, and J. Lohscheller. Quantifying spatiotemporal properties of vocal fold dynamics based on a multiscale analysis of phonovibrograms. *IEEE Transactions on Biomedical Engineering*, 61(9):2422–2433, 2014.

[4] J. Lohscheller, U. Eysholdt, H. Toy, and M. Doellinger. Phonovibrography: Mapping high-speed movies of vf vibrations into 2-d diagrams for visualizing and analyzing the underlying laryngeal dynamics. *IEEE Trans. Med. Imag.*, 27(3):300–309, 2008.

[5] G. Hughes. On the mean accuracy of statistical pattern recognizers. *IEEE Trans. Inform. Theory*, 14(1):55–63, 1968.

[6] P.H. Dejonckere, P. Bradley, P. Clemente, G. Cornut, L. Crevier-Buchman, G. Friedrich, P. Van De Heyning, M. Remacle, and V. Woisard. A basic protocol for functional assessment of voice pathology, especially for investigating the efficacy of (phonosurgical) treatments and evaluating new assessment techniques. *Eur. Arch. Otorhinolaryngol.*, 258(2):77–82, 2001.

[7] M. Katz. Fractals and the analysis of waveforms. *Comput. Biol. Med.*, 18(3):145–156, 1988.

[8] H. Peng, F. Long, and C. Ding. Feature selection based on mutual information: Criteria of max-dependency, max-relevance, and min-redundancy. *IEEE Trans Pattern Anal Mach Intell.*, 27(8):1226–1238, 2005.

[9] A. Myronenko and X. Song. Point set registration: Coherent point drift. *IEEE Transactions on Pattern Analysis and Machine Intelligence*, 32(12):2262–2275, 2010.

Address for correspondence:

Mona K. Fehling
Trier University of Applied Sciences, Germany
m.fehling@hochschule-trier.de

Fetal Heart Rate Classification: First vs. Second Stage of Labor

J Spilka[1], R Leonarduzzi[2], V Chudáček[1], P Abry[2], M Doret[3]

[1]CIIRC, Czech Technical University in Prague, Czech Republic;
[2]Univ Lyon, Ens de Lyon, Univ Claude Bernard, CNRS, Laboratoire de Physique, F-69342 Lyon, France;
[3]Femme-Mère-Enfant Hospital, Bron, France;

Abstract

Fetal Heart Rate (FHR) is clinically used for early detection of fetal acidosis. Despite a marked interest in automatic detection procedures, FHR analysis remains a challenging signal processing task, receiving considerable research attention. Among other difficulties, the two stages of labor (dilation and active pushing) produce very different FHR dynamics. Most research efforts, however, have either ignored these differences or analyzed only one of the two stages of labor. In this work, we propose to assess the impact of labor stages on acidosis detection performance. A state-of-the-art sparse support vector machine classifier that performs simultaneously feature selection and classification is applied to a large-size and well documented FHR database. It shows that the selected set of features differs for each stage and that detection performance improves when the difference between labor stages is considered.

Keywords *Fetal Heart Rate, Acidosis detection labor stages, scale-free features, Sparse SVM,*

1 Introduction

Intrapartum Fetal Monitoring. Fetal heart rate (FHR) provides major information about fetal health and is thus routinely monitored in clinical practice. It is mainly used to assess well-being of the fetus, and to decide on an operative delivery. In daily clinical routine, FHR is examined by visual inspection following clinical guidelines issued by the International Federation of Gynecology and Obstetrics (FIGO) [1]. However, the intrinsic complexity of FHR makes its visual interpretation difficult and the sole use of FIGO guidelines leads to a substantial inter and intra observer variability [2], which is in part responsible for a growing number of unnecessary Caesarean sections [3]. There are hence numerous research efforts devoted to automated fetal acidosis early detection.

Automatic FHR processing. Automatic acidosis detection relies on the use of supervised machine learning, based on features aiming to capture the relevant characteristics of FHR temporal dynamics. A wide range of signal processing techniques have been explored to devise such features, ranging from computerized FIGO guidelines [1] to multifractal analysis [4]; cf. [5] for review.

Labor stages. Automatic FHR analysis is further complicated by the existence of two distinct labor stages. The first stage (dilatation), is characterized by progressive cervical dilatation and regular contractions. The second stage (active pushing), is characterized by a fully dilated cervix and expulsive contractions. Both stages are characterized by largely different temporal dynamics.

State-of-the-art approach is to study either single labor stage alone, cf. e.g. [6,7] or not to distinguish between the stages at all [8,9]. While the former approach is methodologically correct, it discards data that might be useful for detection improvement. The latter approach is impaired by the potential different FHR dynamics: relevant features might thus change drastically from one stage to the other, and negatively impact classifier generalization ability.

Related works. There have been only few attempts to study the impact of the transition between stages in FHR detection. Nevertheless, some preliminary analyses have been performed to assess how each stage impacts the Hurst exponent [10] and entropy rates [11]. However there is no systematic reports on how such stage differences impact supervised classification.

Goals, contributions and outline. The present contribution aims to investigate the impact of labor stages in supervised classification. Both the selection of relevant features and classification performance are compared between the two stages, with emphasis on the existence of features that are discriminative in both stages. To achieve these goals, Sparse-Support Vector Machine (S-SVM), for joint classification and feature selection, is applied to a comprehensive set of FHR features, computed from a large FHR database (cf. Section 2). Classification performance and feature selection are compared, jointly for both stages and independently for each one, cf. Section 3.

2 Methods

Database. FHR data were collected at Femme-Mère-Enfant hospital, in Lyon, France, during daily routine monitoring from 2000 to 2010. Recording were performed using STAN S21 or S31 devices with internal scalp electrodes. Clinical information was provided by the obstetrician in charge, notably the umbilical artery

Work supported by Czech Science Foundation Agency project No. 14-28462, ANR AMATIS grant, and Hospices Civil de Lyon, Hôpital Femme Mere Enfant, Project Hospitalier de Recherche Clinique.

Table 1: **Clinical data for both stages (acidotic *vs.* normal group)**, reported as mean (standard deviation). Statistical differences between acidotic and normal subjects($p < 0.05$) are indicated with †.

	S_I		S_{II}	
	Acidotic n=27	Normal n=1015	Acidotic n=28	Normal n=734
Birth-weight (g)	3383 (446)	3329 (472)	3452 (400)	3366 (444)
Operative delivery for fetal distress (n)	12 (44%)	213 (21%)†	13 (46%)	151 (21%)†
Umbilical cord arterial pH	7.01 (0.03)	7.24 (0.07)†	7.01 (0.04)	7.22 (0.06)†
Apgar score at 5 minutes	9.37 (0.93)	9.89 (0.53)	9.57 (0.79)	9.90 (0.43)
Length of second stage (min)	8.67 (5.02)	6.82 (5.09)	27.86 (9.67)	27.64 (9.85)
Time from end of rec. and birth (min)	1.61 (2.72)	0.81 (1.87)†	1.93 (3.36)	0.96 (2.08)

pH after delivery and the decision for intervention due to suspected acidosis [12]. Subject inclusion criteria were detailed in [7, 12], leading to a set, S, of $N = 1804$ recordings, gathering: *acidotic* subjects, $N_+ = 55$, with pH ≤ 7.05 and *normal* cases, $N_- = 1749$, with pH > 7.05 [13]. For the purpose of first *vs.* second stage comparison, subjects were further split into two groups based on the second stage duration (t_{II}): set S_I with $t_{II} \leq 15$ min and set S_{II} with $t_{II} > 15$ min. Relevant clinical data are reported in Table 1. FHR analysis was systematically conducted on the last 20 minutes of FHR recordings, as illustrated in Fig. 1.

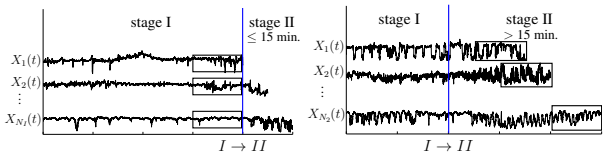

Figure 1: **Analyzed regions.** Rectangles indicate the last 20 min under analysis S_I (left) and S_{II} (right).

Features. The set of 20 features as described in [7] is used. They are organized in three groups labeled *automated FIGO*, *spectral* and *scale-free dynamics*.

FIGO enhanced and automated FIGO features. They are based on FIGO guidelines, used by obstetricians to evaluate FHR: baseline evolution, variability and characterisation of accelerations/decelerations [1]. Baseline evolution is modeled by a linear regression: $B(t) = \beta_0 + \beta_1 t$. Long and short term variability (LTV and STV, respectively) are computed with the standard procedures detailed in [1]. The number of accelerations and decelerations ($\#acc$ and $\#dec$) are counted using the definitions in [1]. Finally, decelerations are further quantified by their average depth MAD_{dtrd}, average duration T_{stress} and average area A_{dec}.

Spectral features. Spectral behavior of FHR is quantified by computing the energy in predefined frequency bands. Since no consensus has been reached on the definition of such bands for fetuses (cf. [14, 15] for discussions), the definitions for adults [15] are used: very low frequency E_{VLF} ($[0.003, 0.04]$ Hz), low frequency E_{LF} ($[0.04, 0.15]$ Hz), and high frequency E_{HF} ($[0.04, 0.15]$ Hz). Finally, the ratio of E_{LF} and E_{HF}, denoted as LF/HF, and the spectral index α [15], estimated over both LF and HF bands, are computed. All spectral estimates are computed using the Welch periodogram.

Scale-free dynamics features. Following [4, 7, 15], scale-invariance/multifractal features are computed to quantify the multiscale and complex FHR temporal dynamics. All these features are estimated using linear regressions based on relevant multiresolution quantities. Features H and h_{min} are computed from the moments of wavelet coefficients. Features c_1, c_2, c_3 and c_4 are computed from the cumulants of wavelet leaders [16]. Features H and c_1 are related to the correlation structure of FHR, while h_{min}, c_2, c_3 and c_4 measure information contained in its higher-order statistics. see also e.g. [4, 15].

Feature preprocessing. Outliers were removed by Winsorization in the interval $[Q_1 - 3IQR, Q_3 + 3IQR]$, where Q_i is the i-th quartile and $IQR = Q_3 - Q_1$ is the interquartile range. All features were standardized.

Sparse Support Vector Machine. S-SVM is a machine-learning tool that performs jointly classification and feature selection [17]. Like traditional SVM, S-SVM computes an optimal hyperplane that separates normal and acidotic cases. In addition, S-SVM performs feature selection by imposing an ℓ_1-norm regularization that leads to a decision rule that effectively involves only a limited subsets of features regarded as relevant. S-SVM thus outputs a feature-weight vector $\mathbf{w} = (w_i)$ that quantifies the importance granted to each feature: $w_i = 0$ indicates features that are poorly discriminant and thus not used in classification, whereas larger w_i indicates a large discriminative power of feature i. Training of S-SVM depends on a regularization parameter C that controls the trade-off between decision rule (or feature) sparsity and misclassification rate (with higher values of C decreasing sparsity). For further details on S-SVM, see [7, 17] and references therein.

Performance assessment. Performance is quantified by the specificity (SP), sensitivity (SE) and balanced error rate: $BER = (SP + SE)/2$. Selection of C, computation of weights w_i and performance assessment are performed using double-loop stratified k-fold cross validation (CV), where k is chosen as the number of acidotic cases (see [7] for details).

3 Comparisons between the labor stages

Pairwise correlation. Fig. 3 displays the pairwise correlations of all features, for each stage, and reveals several interesting characteristics. First, the correlation structure

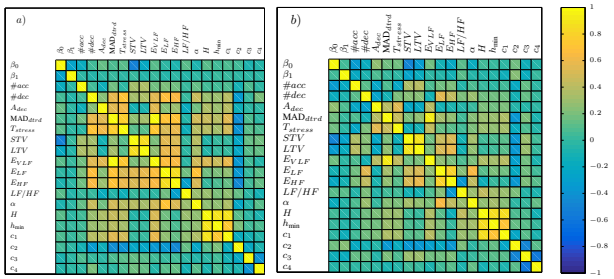

Figure 3: **Correlation.** Pairwise correlation matrix of all the features for the two labor stages: *a)* S_I, *b)* S_{II}.

Table 2: **Selected features and weights.**

S	w	S_I	w	S_{II}	w
c_1	.68	MAD_{dtrd}	.82	c_1	.89
T_{stress}	.43	β_0	.50	c_2	.45
MAD_{dtrd}	.41	c_1	.24		
c_2	.29	T_{stress}	.16		
E_{HF}	.18				
STV	.17				
β_0	.16				

is similar for both stages, but overall correlation is higher during S_I than during S_{II}. Second, several features (e.g. $\beta_0, \beta_1,, c_2$) are uncorrelated to all others, irrespective of the stage. Third, features H, c_1, and $\text{h}_{\min}$ have very high correlations [7] in both stages. Due to proximity of H, $\text{h}_{\min}$ and c_1 in nature, H and $\text{h}_{\min}$ are considered redundant to c_1 and are removed from further analysis to ease interpretation of results. Other highly-correlated features are kept since they are of different natures.

Feature selection and classification. Fig. 2 displays the weights produced for each feature (top panels) and classification performance (bottom panels), as functions of the sparsity parameter C. First, it illustrates that low values of C promote sparsity with less features involved in classification. Second, it shows that optimal performance is obtained for a level of sparsity referred to as C_{opt} that never corresponds to the use of all available features. This highlights the need to perform feature selection to prevent unnecessary over-complicated and over-fitted models.

Optimal feature set. Table 2 shows selected features and their corresponding weights, at the optimal level $C = C_{opt}$ (only those with nonzero weights are displayed). It can be seen that classification in S_I requires only four features: MAD_{dtrd} and T_{stress} (decelerations' amplitude and frequency), β_0 (baseline level), and c_1 (scale-free *linear* variability). For S_{II} the feature vector is even more sparse and contains only two features: c_1 and c_2 (scale-free *nonlinear* variability). In contrast, for S, not only the features that are significant for S_I and S_{II}, but also extra features such as measures of short term variability like STV and E_{HF} are included. These additional features are likely needed to account for the additional inter-stage variability, which leads to an overall decrease in detection performance compared to what can be achieved using the knowledge about the stage of the delivery. Finally, Table 2 highlights that c_1 is the only feature used in all groups. Interestingly, it consists of robust quantification of FHR variability (cf. e.g., [7, 15]).

First *versus* second stage. S-SVM selects for S_I features classically rooted in clinical practice, such as MAD_{dtrd}, T_{stress} (both quantifying the impact of decelerations), and β_0 (average level of baseline). Interestingly, these features are no longer used for S_{II}. Since the second stage is associated with active maternal pushing, large and frequent decelerations are present in most records, irrespective of acidosis. In light of the loss of discriminative power from MAD_{dtrd}, T_{stress}, S-SVM conveniently replaces them with c_2 (which is associated with changes in local regularity and burstiness of data), as a companion to the already selected c_1.

Optimal classification performance. Classification performance for $C = C_{opt}$ is presented in Table 3. It indicates that that independent evaluation of S_I and S_{II}

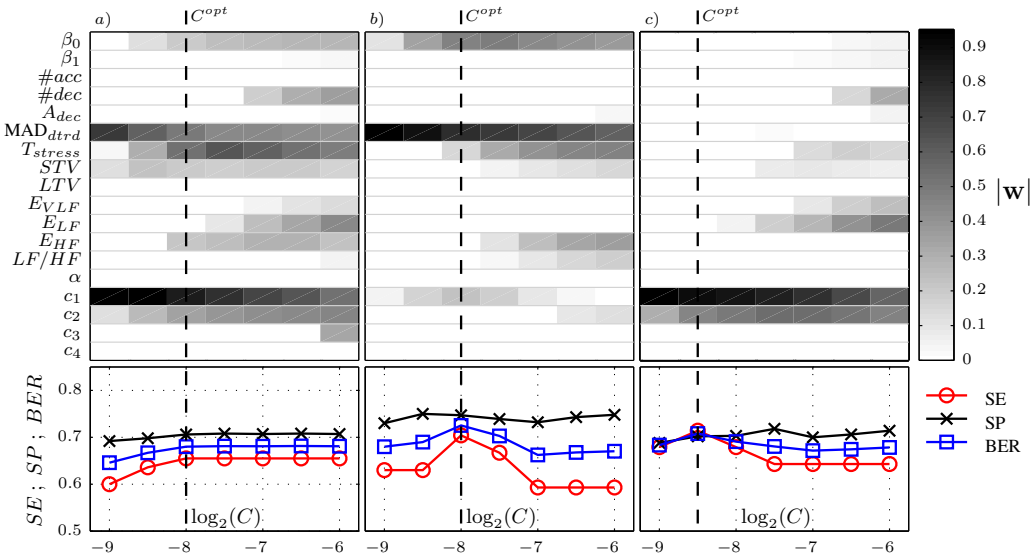

Figure 2: **S-SVM performance.** Feature selection (top row) and classification performance (bottom row) as function of the regularization parameter C. Results for different sets: *a)* S, *b)* S_I, and *c)* S_{II}.

Table 3: **Optimal classification performance** for different combinations of training / testing sets.

Tr / Te	SE	SP	BER	#TP	#FN	#TN	#FP
S/S	.62	.71	.66	34	21	1241	508
S_I/S_I	.67	.74	.70	18	9	752	263
S_{II}/S_{II}	.68	.70	.69	19	9	515	219
S/S_I	.56	.80	.68	15	12	807	208
S/S_{II}	.68	.59	.64	19	9	434	300

results in better classification performance, since simple models with only the relevant features for each stage are used. Interestingly, if the classifier trained from S is tested only with samples from S_I and S_{II}, dramatic loses of either sensitivity or specificity are observed; this indicates that the loss of performance is due to a suboptimal training of the classifier that fails to fully account for the characteristics of each stage.

4 Conclusions

This contribution explores the influence of the two stages of labor on feature selection and classification performance in a supervised classification task. To that end, it uses a comprehensive set of FHR features and a Sparse-SVM framework on three scenarios: i) naive classification without recognizing labor stages ; ii) separate classification of records in the first stage ; iii) separate classification of the records in the second stage. It was shown that failure to recognize the stages leads to a complex model, involving a large number of features, with inferior performance. In contrast, results indicate that an independent evaluation of both stages provides simpler models (less features) with better performance. Further, selected features for the first stage confirm the predominance of decelerations and variability for acidosis detection while, for the second stage, decelerations are no longer informative and other measures of variability, namely c_1 and c_2, are preferred.

References

[1] D. Ayres-de Campos, et al. Figo consensus guidelines on intrapartum fetal monitoring: Cardiotocography. *Int J Gynaecol Obstet*, 131(1):13–24, Oct 2015.

[2] L. Hruban, et al. Agreement on intrapartum cardiotocogram recordings between expert obstetricians. *Journal of Evaluation in Clinical Practice*, 21(4):694–702, 2015.

[3] Z. Alfirevic, D. Devane, and G. Gyte. Continuous cardiotocography (CTG) as a form of electronic fetal monitoring (EFM) for fetal assessment during labour. *Cochrane Database Syst Rev*, 3(3):CD006066, 2006.

[4] M. Doret, et al. Multifractal analysis of fetal heart rate variability in fetuses with and without severe acidosis during labor. *Am J Perinatol*, 28(4):259, 2011.

[5] J. Spilka, et al. Using nonlinear features for fetal heart rate classification. *Biomed Signal Process Control*, 7(4):350–357, 2012.

[6] A. Georgieva, et al. Phase-rectified signal averaging for intrapartum electronic fetal heart rate monitoring is related to acidaemia at birth. *BJOG*, 121(7):889–894, Jun 2014.

[7] J. Spilka, et al. Sparse support vector machine for intrapartum fetal heart rate classification. *IEEE J Biomed and Health Inform*, PP(99):1–1, 2016.

[8] A. Costa, et al. Prediction of neonatal acidemia by computer analysis of fetal heart rate and st event signals. *Am J Obstet Gynecol*, 201(5):464.e1–464.e6, Nov 2009.

[9] P.A. Warrick, et al. Classification of normal and hypoxic fetuses from systems modeling of intrapartum cardiotocography. *IEEE Trans Biomed Eng*, 57(4):771–779, 2010.

[10] J. Spilka, et al. Impacts of first and second labour stages on hurst parameter based intrapartum fetal heart rate analysis. In *Computing in Cardiology Conference (CinC), 2014*, pages 777–780, 2014.

[11] Jongil Lim, et al. Quantitative comparison of entropy analysis of fetal heart rate variability related to the different stages of labor. *Early Hum Dev*, 90(2):81–85, Feb 2014.

[12] M. Doret, et al. Use of peripartum st analysis of fetal electrocardiogram without blood sampling: a large prospective cohort study. *Eur J Obstet Gynecol Reprod Biol*, 156(1):35–40, May 2011.

[13] I. Amer-Wåhlin, et al. Cardiotocography only versus cardiotocography plus ST analysis of fetal electrocardiogram for intrapartum fetal monitoring: a Swedish randomised controlled trial. *Lancet*, 358(9281):534–538, Aug 2001.

[14] S. Siira, et al. Do spectral bands of fetal heart rate variability associate with concomitant fetal scalp pH? *Early Hum Dev*, 89(9):739–742, Sep 2013.

[15] M. Doret, et al. Fractal Analysis and Hurst Parameter for intrapartum fetal heart rate variability analysis: A versatile alternative to Frequency bands and LF/HF ratio. *PLoS ONE*, 10(8):e0136661, 08 2015.

[16] H. Wendt, P. Abry, and S. Jaffard. Bootstrap for Empirical Multifractal Analysis. *IEEE Signal Proc. Mag.*, 24(4):38–48, 2007.

[17] L. Laporte, et al. Nonconvex Regularizations for Feature Selection in Ranking With Sparse SVM. *IEEE Trans Neural Netw Learn Syst*, 25(6):1118–1130, 2014.

Address for correspondence:

Jiří Spilka, jiri.spilka@ciirc.cvut.cz
CIIRC, Czech Technical University in Prague

Assessment of cardiovascular oscillations in amnestic Mild Cognitive Impairment

N Toschi[1,2#], G Valenza[1,3#], L Citi[4], M Guerrisi[1], S Orsolini[5], C Tessa[6], S Diciotti[5], R Barbieri[2,7]

1 Massachusetts General Hospital-Harvard Medical School, Boston, USA;
2 Department of Biomedicine and Prevention, University of Rome "Tor Vergata", Rome, Italy
3 Department of Information Engineering, and Research Centre "E. Piaggio", University of Pisa, Pisa, Italy.
4 School of Computer Science and Electronic Engineering, University of Essex, Colchester, UK.
5 Department of Electrical, Electronic, and Information Engineering "Guglielmo Marconi", University of Bologna, Cesena, Italy
6 Versilia Hospital, Viareggio, Italy.
7 Department of Electronics, Informatics and Bioengineering, Politecnico di Milano, Milano. Italy.
#These authors contributed equally to this publication

Abstract

Amnestic mild cognitive Impairment (aMCI) is a frequent form of cognitive dysfunction which increases the risk of culminating in Alzheimer's disease (AD)-related dementia. Previous studies have demonstrated that AD is accompanied by alterations in autonomic function, which in turn have been linked to cognitive performance in non-demented subjects. In this study, we employ a probabilistic model of linear and nonlinear heartbeat dynamics to investigate the possibility of detecting subtle autonomic alterations in aMCI, using heartbeat information alone. To this end, we compared age- and gender-matched 13 healthy controls to 13 MCI patients without ouvert dysautonomia by feeding an autonomic nervous system related feature set computed from a probabilistic heartbeat model into a classification framework. We obtained a satisfactory classification performance (73% balanced accuracy), which dropped to 65% when excluding cardiovascular nonlinear/complex features. Our results point toward the presence of subtle autonomic dysfunction even in aMCI (a possible prodromal condition to AD), which can only be detected using comprehensive time-varying, nonlinear/complex estimates of heartbeat dynamics.

Keywords *Heart Rate Variability, Autonomic Nervous System, Support Vector Machine, Autonomic dysfunction, Mild Cognitive Impairment*

1 Introduction

Amnestic mild cognitive Impairment (aMCI) is a frequent form of cognitive dysfunction which increases the risk of culminating in Alzheimer's disease (AD)-related dementia. AD is a progressive disease and, along with neurological alterations and cognitive degeneration, it can involve autonomic dysregulation [1-3], most probably due to the involvement of central nervous system structures known to participate both in autonomic modulation and in cognitive processing, such as part of the telencephalon (e.g. anterior cingulate cortex, insula, amygdala [4]), the hypothalamus as well as brainstem structures. More in detail, it is known that the insula, a structure which has been seen to be associated with cardiac autonomic dysfunction [5], is affected even in the preclinical stages of AD. Accordingly, a number of previous studies have investigated the cardiac branch of the autonomic nervous system in AD using techniques like orthostatic reflexes, modulation by breathing and Valsalva's maneuver, mostly reporting alterations of sympathovagal balance in AD [6]. Additionally, a number of studies have investigated possible relationships between heart rate variability (HRV) - related estimates of autonomic nervous system (ANS) outflow and cognition in non-demented subjects. Most of these studies show an association between varying degrees of cognitive impairment and cardiac autonomic dysfunction [7-10].

The aim of this study is therefore to investigate for the first time if, using only cardiac signals, autonomic alterations can be detected in patients suffering from aMCI, a condition which causes a slight but noticeable decline in cognitive abilities, and which represents an increased risk of developing AD or other dementias.

2 Methods

2.1 Experimental Procedures

Plethysmographic (PPG) signals were recorded with a sample frequency of 50 Hz from 13 healthy controls (HC, 9 males, 4 females, age 64.60 ± 6.84 years, median ± MAD, where MAD(X)=Median(|X-Median(X)|)) and 13 aMCI patients (8 males, 5 females, age 72.80 ± 2.72 years, median ± MAD). No significant group difference was found in age (p=0.065, Mann-Whitney test, null-hypothesis of equal medians) and gender (p=0.680, Chi Square test, null-hypothesis of no gender-group interaction). Subjects were placed horizontally in a supine position and remained at rest during the whole recording (600s). During the

acquisition, all subjects were instructed not to talk and maintained relaxed spontaneous breathing. All participants gave written informed consent to participating in the study, which was approved by the local ethics committee.

2.2. Patient Evaluation

Clinical assessment included history of disease-related symptoms and signs, and full neurological examination. All patients were screened for cardiovascular autonomic dysfunction, which was considered as exclusion criterion. Additionally, cognitive functions were assessed among our patients through a pool of standardized neuropsychological tests, hence classifying them into either the HC o the aMCI group. MCI patients suffering from Parkinson's Disease (which is known to involve ANS dysfunction) were excluded from this study.

2.3 Point process modeling of heartbeat dynamics

In order to accurately model heartbeat dynamics and simultaneously extract dynamic estimates of linear and nonlinear features of autonomic nervous system, we employed a probabilistic point process model. Assuming history dependence, the probability distribution of the waiting time $t-u_j$ until the next R-wave event u_{i-1} follows an inverse Gaussian model [11]:

$$f(t \mid \mathrm{H}_t, \xi(t)) = \left[\frac{\xi_0(t)}{2\pi (t-u_{\tilde{N}(t)})^3} \right]^{\frac{1}{2}} \times \exp\left\{ -\frac{1}{2} \frac{\xi_0(t)[t-u_{N(t)} - \mu_{RR}(t, \mathrm{H}_t, \xi(t))]^2}{\mu_{RR}(t, \mathrm{H}_t, \xi(t))^2 (t-u_{\tilde{N}(t)})} \right\}$$

with the instantaneous mean RR defined as:

$$\mu_{\mathrm{RR}}(t, \mathrm{H}_t, \xi(t)) = \mathrm{RR}_{\tilde{N}(t)-1} + \gamma_0(t) + \sum_{i=1}^{p} \gamma_1(i,t) \Delta \mathrm{RR}_i + \sum_{i=1}^{q} \sum_{j=1}^{q} \gamma_2(i,j,t) \Delta \mathrm{RR}_i \, \Delta \mathrm{RR}_j + \sum_{i=1}^{r} \sum_{j=1}^{r} \sum_{k=1}^{r} \gamma_3(i,j,k,t) \Delta \mathrm{RR}_i \, \Delta \mathrm{RR}_j \Delta \mathrm{RR}_k + \dot{o}(t)$$

where $\tilde{N}(t) = \max\{k : u_k < t\}$ is a left continuous function denoting the index of the previous R-wave event occurred before time t, $\mathrm{H}_t = (u_j, RR_j, RR_{j-1}, \ldots)$ is the history of events, $\Delta RR_i = (RR_{\tilde{N}(t)-i} - RR_{\tilde{N}(t)-i-1})$, $\xi(t) = [\xi_0(t), \gamma_0(t), \ldots, \gamma_3(r,r,r,t)]$ is the parameter vector, and $\dot{o}(t)$ are independent, identically distributed Gaussian random variables. The choice of a third order nonlinear autoregressive (NAR) system retains an important part of the non-linearity of the system and provides robustness against the presence of measurement noise in the data [11]. For parameter estimation, a local maximum likelihood method [12] using a sliding window of duration W is used to estimate the unknown time-varying parameter set. After parameter vector estimation, conventional HRV features defined in the time domain (the mean, μ_{RR}, and variance, σ_{RR}, of the RR interval series, the variance of the probabilistic heart rate, σ_{HR}) and defined in the frequency domain (spectral power in the low frequency, 0.04-0.15 Hz, LF, high frequency power, 0.15 – 0.45 Hz, HF, along with their ratio, LF/HF) can be estimated in an instantaneous manner from the first order regression terms [12, 13].

2.4. Bispectral Measures

The higher-order spectral representation allows for the estimation of statistics beyond the second order, as well as phase relations between frequency components which would otherwise be suppressed. A detailed description of the instantaneous bispectrum derivation from point-process nonlinear models can be found in [13]. The second order structure allows us to evaluate the instantaneous presence of nonlinearity in heartbeat series by calculating nonlinear sympatho-vagal interactions in the low frequency (LL), low and high frequency (LH), and high frequency (HH).

2.5 Instantaneous Lyapunov Exponents

The Lyapunov exponents can be derived by estimating the Jacobian over the corresponding time-varying vector of parameters defined by the point process model. The estimation is performed at each time *t*, yielding instantaneous measures of complexity. In this study, we employed the Instantaneous Dominant Lyapunov Exponent (IDLE) [14].

2.6. Inhomogeneous Point-Process Entropy Measures

While traditional algorithms estimating measures of entropy provide a single value (or a set of values) within a predetermined time window, in this study we use the recently introduced definition of *instantaneous* approximate and sample entropy (ipApEn and ipSampEn, respectively) [15]. In the mathematical formulation, *m* and *r(t)* are the embedding dimension and time delay of the phase space, respectively, that are chosed as as $r(t)=0.2\sigma_{RR}(t)$ and $m=2$ [15]. As the definition of the proposed entropy measure is fully embedded into the inhomogeneous point-process nonlinear framework, it is possible to obtain an instantaneous tracking of the system's complexity as defined by *ipApEn*.

2.7. Construction of feature vectors and statistical analysis

All features were calculated instantaneously with a Δ=5 ms temporal resolution. In order to build subject-specific feature vectors, for every subject and for every feature X, we condensed the information about the time-varying dynamics of X through its median (X^m) and its respective absolute deviation (X^{mad}) over time.

As an exploratory/preliminary step, for each feature, we evaluated between-group differences in median and MAD for every feature using non parametric statistics (Mann-Whitney test) under the null hypothesis that the between-subject medians of the two groups are equal.

2.8. Classification

In order to investigate whether the possibility of efficient single-subject discrimination by using heartbeat dynamics alone, we employed a well-known SVM-based classification method. In this context, data gathered from each subject constitutes one multidimensional point in the feature space along with its label (HC/aMCI), and each feature constitutes a single dimension of this feature space. A multidimensional point was considered an outlier if z-scores associated to its dimensions were greater than 3. To assess the out-of-sample predictive accuracy of the system, we adopted a Leave-One-Out (LOO) procedure based on a Support Vector Machine (SVM)-based classifier. Specifically, we employed a nu-SVM (nu = 0.5) with a radial basis kernel function with $\gamma = n^{-1}$, where n is equal to the number of features. Within the LOO scheme, the training set was normalized by subtracting the median value and dividing by the MAD over each dimension. These values were then used to normalize the example belonging to the test set. During the LOO procedure, this normalization step was performed on each fold. Additionally, we applied a support vector machine recursive feature elimination (SVM-RFE) procedure in a wrapper approach (RFE was performed on the training set of each fold) and we computed the median rank for each feature over all folds. We specifically chose a recently developed nonlinear SVM-RFE which employs a radial basis function kernel and includes a correlation bias reduction strategy into the feature elimination procedure [16].

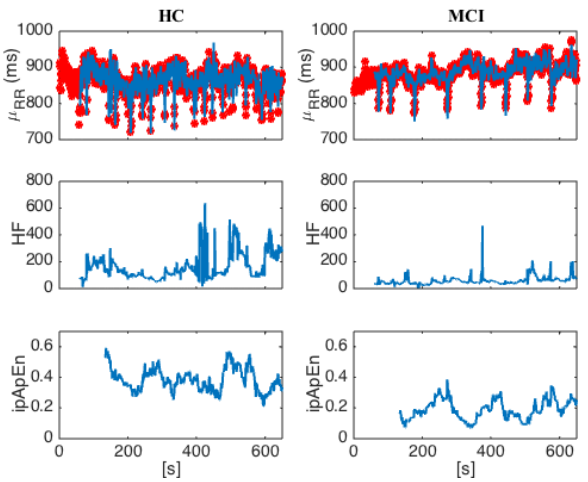

Figure 1: Representative analysis results for one HC (left) and one aMCI patient (right).

3 Results

Exemplary signals and analysis results from two representative subjects are shown in Figure 1. When employing univariate nonparametric statistics we were not able to detect any differences in autonomic function between HC and MCI populations (Table 1). However, employing a high dimensional nonlinear classifier resulted in a satisfactory performance with approximately 61% sensitivity, 84% specificity and 73% balanced accuracy (see Table 2). Moreover, when repeating the classification task employing linear features exclusively, the performance dropped to 69% specificity and 65% balanced accuracy (Table 3). Of note, 5 out of the first 8 most informative features were derived from cardiovascular nonlinear/complex dynamics (mainly instantaneous bispectral and entropy measures - Table 1).

Feature	HC	MCI	p-val	Rank
LL^{m}	8.15E+07	7.24E+07	0.837	24
LL^{mad}	3.66E+07	3.66E+07	0.538	23
LH^{m}	2.69E+08	2.49E+08	1.000	3
LH^{mad}	8.25E+07	8.07E+07	1.000	13
HH^{m}	4.77E+08	6.29E+08	0.798	9
HH^{mad}	1.74E+08	2.32E+08	0.959	7
$IDLE^{m}$	-3.4E-03	-1.8E-02	0.758	18
$IDLE^{mad}$	7.32E-02	8.07E-02	0.837	22
$ipApEn^{m}$	2.76E-01	2.49E-01	0.918	14
$ipApEn^{mad}$	4.63E-02	5.41E-02	0.608	8
$ipSampEn^{m}$	2.47E-01	2.27E-01	0.739	17
$ipSampEn^{mad}$	5.81E-02	6.51E-02	0.573	2
μ_{RR}^{m}	9.18E-01	9.38E-01	0.682	10
μ_{RR}^{mad}	1.49E-02	1.97E-02	0.124	6
σ_{RR}^{m}	2.50E+02	2.27E+02	0.442	12
σ_{RR}^{mad}	6.70E+01	6.20E+01	0.720	4
σ_{HR}^{m}	2.50E+02	2.27E+02	0.442	11
σ_{HR}^{mad}	6.70E+01	6.20E+01	0.720	1
LF^{m}	1.80E+02	2.63E+02	0.137	19
LF^{mad}	7.70E+01	1.96E+02	0.091	5
HF^{m}	1.14E+02	1.83E+02	0.383	20
HF^{mad}	4.52E+01	4.37E+01	0.644	15
LF/HF^{m}	1.26E+00	1.91E+00	0.238	21
LF/HF^{mad}	5.98E-01	1.29E+00	0.218	16

Table 1: Univariate statistical comparison in feature values (Mann Whitney U-test) between healthy controls (HC) and aMCI patients, as well as median rank of each feature in feature selection

	HC	aMCI
HC	61.54	38.46
aMCI	15.38	84.62

Table 2: Confusion matrix (values in %, true class in columns, predicted class in rows) for classification between healthy controls (HC) and aMCI patients obtained when using the full feature set. Balanced Accuracy = 73.08%.

	HC	aMCI
HC	61.54	38.46
aMCI	30.77	69.23

Table 3: Confusion matrix (values in %, true class in columns, predicted class in rows) for classification between healthy controls (HC) and aMCI patients obtained when using linear features only. Balanced Accuracy = 65.38%.

4 Conclusions

In this paper we employed a probabilistic heartbeat model based on point-process theory to extract several linear and nonlinear features from PPG recordings alone, hypothesizing that this augmented feature set may be sensitive to subclinical disease-related alterations in aMCI. Given our previous findings [13-15], we also hypothesized that nonlinear/complex heartbeat dynamics would play a crucial role in this assessment. Accordingly, we have shown that our nonlinear framework provides measures that can be used to discern aMCI patients from healthy subjects with good accuracy using heartbeat features alone, pointing toward the presence of a subtle autonomic dysfunction in patients suffering from cerebral pathology which could in turn increase the risk of developing AD. Importantly, removing linear features from the feature set resulted in a drop of about 8% in classification performance, demonstrating the central value of our framework in characterizing aMCI patients in a personalized fashion. While in this pilot study on a relatively small cohort we cannot exclude some amount of overfitting, since univariate analysis did not show significant differences between patients, our feature set further represents a multivariate autonomic patient profiling tool to be employed as a whole. In the future, comprehensive HRV-based autonomic screening may become useful as a quick and inexpensive patient characterization and stratification tool. Also, future work will focus on the validation of these preliminary results in larger datasets with longitudinal information about conversion to AD of aMCI patients.

References

[1] M. A. Toledo and L. F. Junqueira, Jr., "Cardiac autonomic modulation and cognitive status in Alzheimer's disease," *Clin Auton Res,* vol. 20, pp. 11-7, Feb 2010.

[2] R. Zulli, F. Nicosia, B. Borroni, C. Agosti, P. Prometti, P. Donati*, et al.*, "QT dispersion and heart rate variability abnormalities in Alzheimer's disease and in mild cognitive impairment," *J Am Geriatr Soc,* vol. 53, pp. 2135-9, Dec 2005.

[3] A. Algotsson, M. Viitanen, B. Winblad, and G. Solders, "Autonomic dysfunction in Alzheimer's disease," *Acta Neurologica Scandinavica,* vol. 91, pp. 14-18, 1995.

[4] Z. Nonogaki, H. Umegaki, T. Makino, Y. Suzuki, and M. Kuzuya, "Relationship between cardiac autonomic function and cognitive function in Alzheimer's disease," *Geriatr Gerontol Int,* Dec 8 2015.

[5] D. R. Royall, J. H. Gao, and D. L. Kellogg Jr, "Insular Alzheimer's disease pathology as a cause of "age-related" autonomic dysfunction and mortality in the non-demented elderly," *Medical Hypotheses,* vol. 67, pp. 747-758, 2006.

[6] G. D. Femminella, G. Rengo, K. Komici, P. Iacotucci, L. Petraglia, G. Pagano*, et al.*, "Autonomic dysfunction in Alzheimer's disease: tools for assessment and review of the literature," *J Alzheimers Dis,* vol. 42, pp. 369-77, 2014.

[7] D. H. Kim, L. A. Lipsitz, L. Ferrucci, R. Varadhan, J. M. Guralnik, M. C. Carlson*, et al.*, "Association between reduced heart rate variability and cognitive impairment in older disabled women in the community: Women's Health and Aging Study I," *Journal of the American Geriatrics Society,* vol. 54, pp. 1751-1757, 2006.

[8] J. Frewen, C. Finucane, G. M. Savva, G. Boyle, R. F. Coen, and R. A. Kenny, "Cognitive function is associated with impaired heart rate variability in ageing adults: the Irish longitudinal study on ageing wave one results," *Clin Auton Res,* vol. 23, pp. 313-23, Dec 2013.

[9] A. J. Shah, S. Su, E. Veledar, J. D. Bremner, F. C. Goldstein, R. Lampert*, et al.*, "Is heart rate variability related to memory performance in middle-aged men?," *Psychosom Med,* vol. 73, pp. 475-82, Jul-Aug 2011.

[10] A. L. Hansen, B. H. Johnsen, J. J. Sollers, 3rd, K. Stenvik, and J. F. Thayer, "Heart rate variability and its relation to prefrontal cognitive function: the effects of training and detraining," *Eur J Appl Physiol,* vol. 93, pp. 263-72, Dec 2004.

[11] K. H. Chon, J. K. Kanters, R. J. Cohen, and N. H. Holstein-Rathlou, "Detection of chaotic determinism in time series from randomly forced maps," *Physica D,* vol. 99, pp. 471-86, Jan 1 1997.

[12] R. Barbieri, E. C. Matten, A. A. Alabi, and E. N. Brown, "A point-process model of human heartbeat intervals: new definitions of heart rate and heart rate variability," *Am J Physiol Heart Circ Physiol,* vol. 288, pp. H424-35, Jan 2005.

[13] G. Valenza, L. Citi, E. P. Scilingo, and R. Barbieri, "Point-Process Nonlinear Models With Laguerre and Volterra Expansions: Instantaneous Assessment of Heartbeat Dynamics," *IEEE Transactions on Signal Processing,* vol. 61, pp. 2914-2926, Jun 2013.

[14] Valenza, G., Citi, L., & Barbieri, R. (2014). Estimation of instantaneous complex dynamics through lyapunov exponents: a study on heartbeat dynamics. PloS one, 9(8), e105622..

[15] G. Valenza, L. Citi, E. P. Scilingo, and R. Barbieri, "Inhomogeneous point-process entropy: an instantaneous measure of complexity in discrete systems," *Phys Rev E Stat Nonlin Soft Matter Phys,* vol. 89, p. 052803, May 2014.

[16] K. Yan, D. Zhang, Feature selection and analysis on correlated gas sensor data with recursive feature elimination, Sens. Actuators B: Chem. 212 (2015) 353–363.

Address for correspondence:

Nicola Toschi
Department of Biomedicine and Prevention
University of Rome "Tor Vergata"
Via Montpellier 1, 00133 Rome, IT
toschi@med.uniroma2

A study of an evaluation method for analgesic level using fuzzy inference based on multiple analgesia indices during general anesthesia

S. Taniguchi[1], Y. Cao[1], E. Furutani[1], T. Takeda[2], G. Shirakami[2]

[1]Department of Electrical Engineering, Kyoto University, Japan;
[2]Department of Anesthesia, Kagawa University, Japan;

Abstract

It is essential to evaluate the analgesia-nociception balance for maintaining sufficient analgesia during general anesthesia. Various analgesia indices have been proposed over the last few decades. However, there is no sufficiently reliable one when solely used. In this paper, we have developed an evaluation method of analgesic level during general anesthesia based on multiple analgesia indices using fuzzy inference. We choose Surgical Pleth Index, Entropy Difference and Analgesia/Nociception Index as our multiple analgesia indices based on a comparison result of areas under the receiver operating characteristic curves, and determine their membership functions and fuzzy rules according to literature and clinical data. The results show that the developed method gives a higher areas under the receiver operating characteristic curve than the existing indices and may reflect patients' state more precisely.

Keywords *analgesia index, fuzzy inference, receiver operating characteristic curves*

1 Introduction

During surgery, anesthetics must be provided for patients to achieve desirable states, that is, hypnosis, analgesia, muscle relaxation, and suppression of harmful reflexes. If the anesthesiologist gives the patient too few anaesthetics, it is likely to cause intraoperative arousal and body movement which are harmful for patients. On the other hand, an overdose of anesthetics not only causes harmful side effects such as bradycardia and respiratory depression, but also delays postoperative recovery. Therefore, inadequate anesthetic administration should be avoided as much as possible.

To this end, the anesthesiologist has to administrate anesthetics at a suitable rate according to their own experiences and knowledge for maintaining patients' state at all times during surgery, which is a heavy burden to anesthesiologists. For reducing troubles and risks of insufficient anesthesia or anesthetic overdose, various automatic control systems have been studied [1]. To realize such systems, reliable indices of anesthetic states are necessary. Regarding hypnosis index, Bispectral index (BIS) [2] is fairly reliable to be used in anesthesia automatic control systems; regarding analgesia index, various indices such as Surgical Pleth Index (SPI) [3] based on finger photoplethysmograph, Entropy Difference (ED) [4] based on electroencephalogram and facial electromyogram, LF/HF [5] and Analgesia/Nociception Index (ANI) [6] based on heart rate variabiliry (HRV) have been developed, however, it is difficult to evaluate analgesic level due to influence of respiratory rate change and the noise of electric knife. Thus, there is no analgesia control systems that obtains satisfactory results although various analgesia control systems not only using the single analgesia index [7] but also using multiple analgesia indices [1] have been developed.

In this paper, we develop an assessment method of analgesic level based on multiple analgesia indices SPI, ED, ANI using fuzzy inference. Firstly, we determine its membership functions and fuzzy rules according to literature and clinical data, then verify its performance by comparing the areas under the receiver operating characteristic (ROC) curves.

2 The existing analgesia indices

The literature [8] compared areas under the ROC curves of SPI, ED, LF/HF and ANI. ROC curve is obtained by plotting sensitivity and specificity of the index on the horizontal and vertical axes respectively for different thresholds. Comparing the area under the curve (AUC) of ROC curve is one of the quantitative measures to assess the performance of diagnostic tests. With the value of AUC getting close to 1, the diagnostic test will have better performance. From the result of literature [8], we know that the AUC of ANI based on HRV is significantly larger than LF/HF also based on HRV, and there are no significant difference among ANI, SPI and ED based on the clinical data from 14 patients. Therefore, in this paper, we utilize SPI, ED and ANI as our multiple analgesia indices to develop an assessment method of analgesic level under general anesthesia. In the following subsections, SPI, ED and ANI will be explained.

2.1 Surgical Pleth Index (SPI)

SPI is calculated by linear combination of normalized pulse amplitude and pulse interval from photoplethysmograph [3]. During general anesthesia, both pulse ampli-

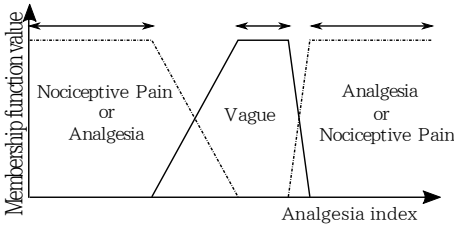

Figure 1: Shape of the membership functions

tude and pulse interval will decrease with pain stimulation. Therefore, SPI have been developed to quantify the level of surgical stress or nociception during anesthesia.

2.2 Entropy Difference (ED)

ED could reflect noxious stimulation and evaluate the depth of analgesia during general anesthesia by getting response entropy (RE) and state entropy (SE) from the signals of electroencephalogram (EEG) and facial electromyogram (FEMG) [4]. ED is the difference between RE and SE, which represents activity from 32 Hz to 47 Hz. During general anesthesia, ED=0 means no painful stimulation and the increase of ED is associated with the facial muscle activity due to painful stimulation, that is, the more stress the patients suffer, the greater the ED value becomes.

2.3 Analgesia/Nociception index (ANI)

ANI based on heart rate variability (HRV) of electrocardiogram (ECG) has been developed to evaluate analgesia/nociception balance during general anesthesia [6]. ANI is derived from frequency component between 0.15 Hz and 0.5 Hz of R-R interval (RRI) of ECG, which is related to the high frequency component of HRV. For the patient in the stabilized anaesthetic state during general anesthesia, parasympathetic tone is dominant and the magnitude of RR series is high. It leads to relatively high value of ANI. On the contrary, when painful events happen, sympathetic activity increases and parasympathetic activity decreases, which makes the magnitude of RR series small, and thus the value of ANI becomes lower.

3 An evaluation method for analgesic level based on multiple analgesia indices using fuzzy inference

In this section, we propose an assessment method of analgesic level by combining analgesia indices SPI, ED and ANI. In the following, we determine the membership functions of each analgesia index and fuzzy rules based on the relevant literatures [4, 9-14].

3.1 Membership functions of each analgesia index

We consider three states “Nociceptive pain”, “Vague” and “Analgesia” to represent patients’ analgesic state.

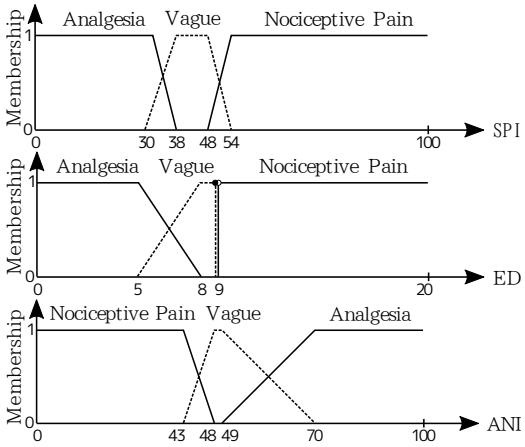

Figure 2: The membership functions of each analgesia index

The membership functions for each analgesia index are represented as a trapezoid function shown in Fig.1. In this case, the membership functions of each analgesia index can be defined by determining the range corresponding to 1 for each state. According to literatures [4, 9-14], we determine the ranges of each state as follows.

Nociceptive pain： The intersection of the nociception range of all of the literatures.

Analgesia：The intersection of the analgesia range of all of the literatures.

Vague：The ranges cannot surely be confirmed as nociception or analgesia from the literatures.

The obtained membership functions are shown in Fig.2.

3.2 Membership functions of analgesic level

We represent the analgesic level between 0 and 100; 0 and 100 means complete absence of pain, and the most painful state respectively. By dividing analgesic state into nine levels, the membership functions of analgesic level are given as nine triangular functions with the peak value of 0, 12.5, ..., 50, 62.5, ..., 100, which are corresponding to A4, A3, ..., NA, N1, ..., N4, as shown in Fig.3. Here, NA is the level that belongs neither to analgesic state nor to nociceptive state; A stands for “analgesia” state and N stands for “nociceptive” state, and the number is the degree of the state, i.e., the larger number means the greater degree.

3.3 Fuzzy rules

Dealing with all the analgesia indices equivalently, we set fuzzy rules as Table 1. Here, Index 1, Index 2, and Index 3 correspond to any one of SPI, ED, and ANI; Noc, Vag, and Ana correspond to nociceptive pain, vague, and analgesia states of the indices respectively. For example, when all of Index 1, 2, 3 are Ana, the analgesic level is A4, the most steady state. When all of Index 1, 2, 3 are Vag or the Index 1 is Noc, the Index 2 is Ana, and Index

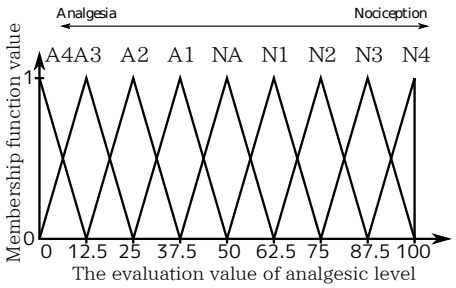

Figure 3: The membership functions of analgesic level

Table 1: Fuzzy rules

Index1=Noc

Index2 \ Index3	Noc	Vag	Ana
Noc	N4	N3	N2
Vag	N3	N1	NA
Ana	N2	NA	A2

Index1=Vag

Index2 \ Index3	Noc	Vag	Ana
Noc	N3	N1	NA
Vag	N1	NA	A1
Ana	NA	A1	A3

Index1=Ana

Index2 \ Index3	Noc	Vag	Ana
Noc	N2	NA	A2
Vag	NA	A1	A3
Ana	A2	A3	A4

3 is Vag, the analgesic level is NA.

3.4 Analgesic level evaluation

The analgesic evaluation value is calculated by the min-max inference method and center of gravity defuzzification, which is one of the widely used techniques in the fuzzy inference [15]. An example of the obtained evaluation values on the SPI-ANI plane for ED=8 is shown in Fig.4.

4 Comparison the performance of the proposed method and the existing indices

In this section, we retrospectively compare the proposed method and the existing indices SPI, ED and ANI utilizing the AUC of ROC curve. We use clinical data of 11 patients from 14 patients in [8] who underwent general anesthesia for orthopedic surgery in the Kyoto University Hospital because not all analgesia indices of 3 patients are available. For calculating the AUC of ROC curve, it is necessary to define the analgesia and nociceptive pain period during surgery. We define nociceptive pain period as the period of 60 seconds after intubation and extubation, 30 seconds before and after body movement, and both systolic blood pressure and heart rate exceeding 15% than baseline; analgesia period is the period between analgesic infusion and skin incision except for nociceptive period

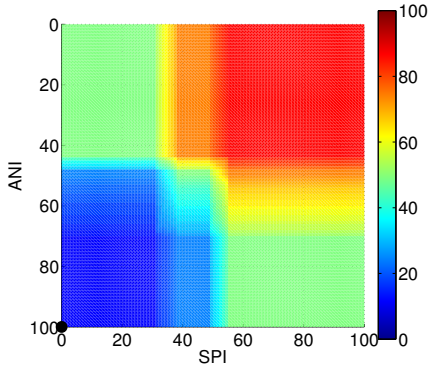

Figure 4: An example of the proposed analgesic level obtained from the existing analgesic indices (SPI, ED and ANI) for ED=8 (the obtained level is shown by color)

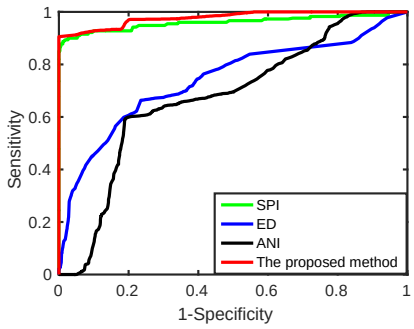

Figure 5: ROC curves of the proposed method and the existing analgesic indices for a patient

as described above.

Fig.5. shows the ROC curves of the proposed method and the existing analgesic indices for a patient. In addition, the results of comparing the median of the AUC of ROC curve using the proposed method and the existing indices are shown in Table 2. They show that the proposed method gives a higher AUC than the existing indices. However, there are no significant difference among the proposed method and the existing analgesia indices by the Wilcoxon signed-rank test.

5 Discussion

In this paper, we propose an evaluation method of analgesic state combining the existing analgesia indices SPI, ED, and ANI. Since these existing indices include pulse amplitude and interval, EEG, FEMG and HRV, the proposed method could be a unified evaluation based on them. From the comparison results, the proposed method may reflect patients' state more appropriately than the ex-

Table 2: The median of the AUC of ROC curve using the proposed method and conventional indices

The proposed method	SPI	ED	ANI
0.9093	0.8778	0.7073	0.7323

isting indices.

In our analgesic level evaluation method, we deal with all the analgesic indices equivalently. However, from Table 2, we observe that the reliability of each index may be different. Therefore, an evaluation method considering its difference should be studied. Moreover, we defined the period of analgesia and nociceptive pain only from the measured data and the time of stimulation. The periods should be defined from real-time judgement of anesthesiologists during operation. In addition, during surgery, all of the analgesia indices cannot be obtained due to contact failure of electrodes, noise from electric knife, compression of the arm for non-invasive blood pressure measurement, etc. Therefore, in the future research, we will construct an evaluation method in the case of lack of one of the analgesia indices.

6 Conclusion

In this paper, we develop an assessment method of analgesic level under general anesthesia based on multiple analgesia indices using fuzzy inference. The result of comparing the AUC of ROC curve suggests that the proposed method reflects patients' state more appropriately than the existing indices.

Acknowledgements

We thank Professor K. Fukuda and Professor K. Hirota (now in the Kansai Medical University) of Department of Anesthesia, Kyoto University Hospital who provided the clinical data in this paper.

References

[1] E. Furutani, K. Tsuruoka, et al.: A hypnosis and analgesia control system using a model predictive controller in total intravenous anesthesia during day-case surgery, SICE Annual Conference 2010, pp. 223-226 (2010)

[2] J.C. Sigl, N.G. Chamoun: An introduction to bispectral analysis for the electroencephalogram; *J. Clin. Monit.*, Vol. 10, pp. 392-400 (1994)

[3] M. Huiku, K. Uutela, et al.: Assessment of surgical stress during general anaesthesia; *Br. J. Anaesth.*, Vol. 98, No. 4, pp. 447-455 (2007)

[4] H. Viertio-Oja, V. Maja, et al.: Description of the entropy algorithm as applied in the Datex-Ohmeda S/5 entropy module; *Acta. Anaesthesiol. Scand.*, Vol. 48, No. 2, pp. 154-161 (2004)

[5] M. Jeanne, R. Logier, et al.: Heart rate variability during total intravenous anesthesia: Effects of nociception and analgesia; *Auton. Neurosci. Basic. Clin.*, Vol. 147, No. 1-2, pp. 91-96 (2009)

[6] M. Jeanne, R. Logier, et al.: Validation of a graphic measurement of heart rate variability to assess analgesia/nociception balance during general anesthesia; *31th Annual International Conference of the IEEE EMBS*, pp. 1840-1843 (2009)

[7] S. Taniguchi, T. Ota, et al.: A study on analgesia control based on Analgesia/Nociception Index(in Japanese); The 58th Annual Conference of the Institute of Systems, Control and Information Engineers, 4 pages (2014)

[8] S. Taniguchi, T. Ota, et al.: Comparison of analgesia/nociception index with other analgesia indices in terms of sensitivity and specificity; SICE Life Engineering Symposium 2014, 4 pages (2014)

[9] G. Weil, S. Passot: Does spectral entropy reflect the response to intubation or incision during propofol-remifentanil anesthesia?; *Anesth. Analg.*, Vol. 106, No. 1, pp. 152-159 (2008)

[10] E. Boselli, M. Daniela-Ionescu, et al.: Prospective observational study of the non-invasive assessment of immediate postoperative pain using the analgesia/nociception index; *Br. J. Anaesth.*, Vol. 111, No. 3, pp. 453-459 (2013)

[11] M. Le Guen, M. Jeanne, et al.: The analgesia/nociception index: a pilot study to evaluation of a new pain parameter during labor; *Int. J. Obstet. Anesth.*, Vol. 21, No. 2, pp.146-151 (2012)

[12] M. Gruenewald, C. Ilies, et al.: Influence of nociceptive stimulation on analgesia nociception index (ANI) during propofol-remifentanil anaesthesia; *Br. J. Anaesth.*, Vol. 110, No. 6, pp. 1024-1030 (2013)

[13] M. Jeanne, C. Clment, et al.: Variations of the analgesia nociception index during general anaesthesia for laparoscopic abdominal surgery; *J. Clin. Monit.*, Vol. 26, No. 4, pp. 289-294 (2012)

[14] S. Mustola, T. Parkkari, et al.: Performance of surgical stress index during sevoflurane-fentanyl and isoflurane-fentanyl anesthesia; *Anesthesiol. Res. Pract.*, Vol. 2010, Article ID. 810721(2010)

[15] E.H. Mamdani, S. Assilian: An experiment in linguistic synthesis with a fuzzy logic controller; *Int. J. Man-Mach. Stud.*, Vol. 7, No. 1, pp. 1-13 (1975)

Address for correspondence:

Kyoto University, Katsura, Nishikyo-ku, Kyoto, Japan
Yujing Cao
Department of Electrical Engineering, Graduate School of Engineering, Kyoto University
caoyujing@rotary.kuee.kyoto-u.ac.jp

An Adaptive and Automatic Parameter Selection Method based on Rational Dilation Wavelet Transform for Wheeze Type Classification

Sezer Ulukaya[1], Gorkem Serbes[2], Yasemin P. Kahya[3],

[1]Electrical and Electronics Engineering, Bogazici and Trakya University, Turkey;
[2]Biomedical Engineering, Yildiz Technical University, Turkey;
[3]Electrical and Electronics Engineering, Bogazici University, Turkey;

Abstract

In this study, a Rational Dilation Wavelet Transform based adaptive and automatic decomposition algorithm is proposed with the aim of obtaining a peak energy ratio metric which is used for discriminating monophonic and polyphonic wheezes. Wheeze signals are analysed by employing various set of parameters which control the Q-factor of wavelets. The peak energy ratio is calculated for each parameter set from the decomposed subbands and the best representation is chosen. It is shown that a specific parameter set can not be achieved to represent monophonic and polyphonic wheezes. This highlights the importance of an adaptive method. Support Vector Machine classifier is employed to quantify the performance of peak energy ratio metric in classification of wheezes. The peak energy ratios of best time frequency representations are used as features and 81.4 % accuracy is achieved.

Keywords *Monophonic Wheeze, Polyphonic Wheeze, Peak Energy Ratio*

1 Introduction

The classical stethoscope has some limitation such as attenuating frequencies above 120 Hz [1] and is unable to record lung sounds for remote analysis. The need for an automatic and cheap analysis tool has become vital during recent years in the diagnosis of lung diseases. The cooperation between engineering and medicine produces electronic stethoscope products [2] which benefit medical doctors by providing objective measurements.

Lung sounds may be categorized into two basic groups depending on the condition of the pulmonary system: vesicular for healthy and adventitious for pathological subjects. Adventitious sounds which are indicators of various lung diseases are either discontinuous , i.e. crackles, or continuous, i.e. wheezes. Unlike crackles, wheezes are musical and continuous in nature and have narrow representations in frequency domain.

A lung sound segment is accepted as wheeze according to American Thoracic Society (ATS) if its main frequency is higher than 400 Hz and its duration is longer than 250 ms [3] while according to Computerized Respiratory Sound Analysis (CORSA), the main frequency needs to be higher than 100 Hz and the duration needs to be longer than 100 ms [4]. On the other hand, in the study [5], the summarized frequency range for wheezes is between 100 to 1000 Hz while the minimum duration is 80 ms.

Wheezes are closely related with diseases such as asthma and chronic obstructive pulmonary disease (COPD) [6]. The degree and severity of the disease is related with wheeze duration in the flow cycle and wheeze characteristics such as mean frequency, number of wheezes [6, 7]. Monophonic (MP) wheezes comprised of either single pitch frequency or multiple pitch frequencies starting and ending at different times stem from single bronchial narrowing and may related with asthma [8, 9]. Polyphonic (PP) wheezes composed of harmonically unrelated multiple pitch frequencies starting and/or ending simultaneously originate from multiple central bronchial compression and are commonly related with COPD [8, 9]. A MP and a PP wheeze sample in time and time-frequency (TF) domain may be depicted in Fig. 1. Despite advances made in the analysis of lung sounds, differentiation of multiple MP and PP wheezes is still an open problem [10].

In [8], it is reported that there is statistically significant differences between MP and PP wheezes of the same pathology (asthma or COPD) using wavelet based bispectrum and bicoherence features, paving the way for classification studies. In literature very few studies can be found in MP-PP classification. In [11], nine monophonic-polyphonic wheezes are detected using spectrogram based peak continuity resulting in 89 % accuracy. In [12], 92 % F_1 score is reached using dominance spectrogram based on instantaneous frequency on normal, monophonic, polyphonic and stridor classes although 72 % using the classical spectrogram. A recent work [13] using time domain based higher order statistics reached 91.1 % classification accuracy using 102 wheezing sounds.

Our previous study [5] on this classification problem suggests to explore robust and discriminative features for PP wheezes. In this work, unlike previous studies which uses fixed TF resolution based on Fourier transform, we propose to determine an optimal (better TF resolution) and adaptive (automatic and tunable) wavelet based tech-

nique to discriminate MP and PP wheezes in a more robust and objective manner. Properties of the database is described in Section 2.1, while Section 2.2 gives details of the wavelet based method and Section 2.3 introduces the proposed method, respectively. In Section 3, experimental results and conclusion are interpreted.

2 Methods

2.1 Data Acquisition and Database

The 14-channel data acquisition system [14] designed in Boğaziçi University Lung Acoustics Laboratory (BULAL) is utilized to record wheeze sounds. 9600 samples per second sampling rate is employed and each data recording session lasts 15 seconds. Each patient has a nose clip and a flow-meter is employed to measure airflow. An informed consent is taken from all the patients before data acquisition. Wheeze sound is collected from asthma and COPD patients who are under treatment in the Istanbul Yedikule Teaching Hospital for Chest Diseases and Thoracic Surgery. Database is comprised of four male and three female subjects at the age of 50 ∓ 17. Wheeze sounds are labeled by visual verification of time expanded waveforms and auditory inspection by an expert. The database consists of 121 MP and 110 PP wheezes, where the duration of each segment is at least 80 ms being coherent with literature.

2.2 Rational Dilation Wavelet Transform

According to the definition, wheezes that occur with a single peak or with the harmonics of a single basal peak are called MP wheezes, while those with variable peaks that differ in harmonics are called PP wheezes [10]. Due to the similarities between MP and PP wheezes, differentiating multiple MP wheezes from PP wheezes is still an open and important task. In MP wheezes when the severity of pathology is very strong, a fundamental (basal peak with high energy) signal can occur with accompanying harmonics (peaks with lower energy). This MP pattern may be confused with PP wheezes in which various peaks with relatively close energies show up. In order to discriminate the MP and PP wheezes in time-scale domain, a wavelet transform, in which the frequency selectivity of the sub-bands can be adjusted, is needed. Therefore in this study, the RADWT [15], which has finer and adjustable frequency resolution with acceptable redundancy, is proposed as a suitable feature extractor for processing lung sounds.

The RADWT [15] is a frequency-domain (FFT based) design transform which does not employ rational transfer functions and offers greater design flexibility. Moreover, the RADWT is a rational (based on non-dyadic dilations), fully discrete, approximately shift-invariant and easily invertible transform. The non-dyadic (rational) behaviour of the RADWT yields to attain a range of Q-factors and redundancy factors. In the RADWT, the Q-factor of wavelets, which controls the frequency resolution of transform, is built upon three positive integers p, q and s satisfying $1 \leq p < q$ and $p/q + 1/s \geq 1$, where p and q are co-prime.

In RADWT, the relation between the scaling ($\phi(t)$)/wavelet ($\psi(t)$) functions and the low ($h_0(n)$)/high ($g_0(n)$) pass filters can be given as,

$$\phi(t) = (q/p)^{1/2} \sum_{n\in\mathbb{Z}} h_0(n)\phi\left(\frac{q}{p}t - n\right) \tag{1}$$

$$\psi(t) = (q/p)^{1/2} \sum_{n\in\mathbb{Z}} g_0(n)\phi\left(\frac{q}{p}t - n\right) \tag{2}$$

Mathematically, the frequency responses of $h_0(n)$ ($H_0(\omega)$) and $g_0(n)$ ($G_0(\omega)$) are given as,

$$H_0(\omega) = \begin{cases} \sqrt{pq} & \omega \in [0, (1-\frac{1}{s})\frac{\pi}{q}], \\ \sqrt{pq}\theta(\frac{\omega-a}{b}) & \omega \in [(1-\frac{1}{s})\frac{\pi}{q}, \frac{\pi}{q}], \\ 0 & \omega \in [\frac{\pi}{q}, \pi], \end{cases} \tag{3}$$

$$G_0(\omega) = \begin{cases} 0 & \omega \in [0, (1-\frac{1}{s})\pi], \\ \sqrt{s}\theta_c(\frac{\omega-pa}{pb}) & \omega \in [(1-\frac{1}{s})\frac{\pi}{q}, \frac{p}{q}\pi], \\ \sqrt{s} & \omega \in [\frac{p}{q}\pi, \pi], \end{cases} \tag{4}$$

where

$$a = \left(1-\frac{1}{s}\right)\frac{\pi}{p}, b = \frac{1}{q} - \left(1-\frac{1}{s}\right)\frac{1}{p} \tag{5}$$

the transition function $\theta(\omega)$ is,

$$\theta(\omega) = \frac{1}{2}(1+cos(\omega))\sqrt{2-cos(\omega)} \quad \text{for} \quad \omega \in [0,\pi] \tag{6}$$

and $\theta_c(\omega)$ is

$$\theta_c(\omega) := \sqrt{1-\theta^2(\omega)} \tag{7}$$

The transition function, $\theta(\omega)$, which is used to construct the transition bands of $G_0(\omega)$ and $H_0(\omega)$, originates from Daubechies orthonormal wavelet filters with two vanishing moments. As it can be seen from above equations, the bandwidth, center frequency and transition bands of high-pass and low-pass filters are determined by using p, q and s values. As the q/p ratio approaches one, higher number of decomposition levels are needed. Therefore, the number of subbands (J) must also be considered as an important parameter in analysis.

2.3 Proposed Adaptive Energy-Ratio Parameter Selection Method

A single peak and at least two peaks must be obtained when the time-scale representations of MP and PP wheezes are investigated respectively. However, the location, amplitude and bandwidth of these peaks differ for each sample due to the physiological properties of the lung and the mechanism of the pathology. This results in a need for an adaptive and automatic algorithm that can locate peaks in TF domain for processing MP and PP wheezes. In the proposed algorithm, the RADWT is applied to MP and PP wheezes by using a set of various

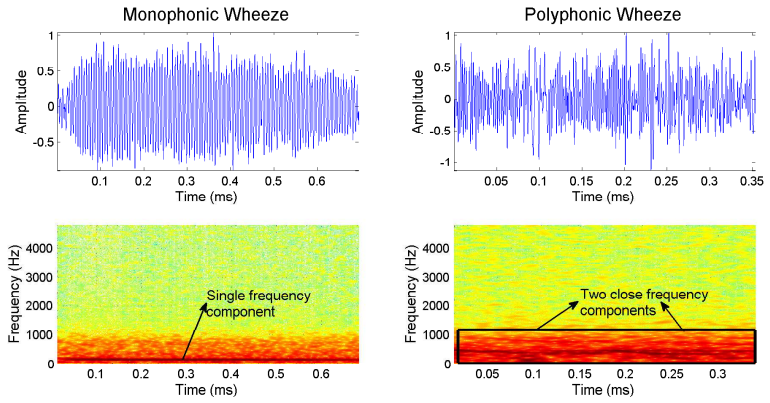

Figure 1: Time domain and time-frequency domain representation of MP (left) and PP (right) wheezes

p, q, s and J values, which are given in Table 1 with an aim to achieve an optimum representation. In this sense optimum representation is defined as two distinct peaks, where one belongs to basal peak in MP wheezes or first peak in PP wheezes and the other belongs to weak harmonics in MP wheezes or second peak in PP wheezes. Then a metric named as the peak-energy-ratio (PER) is defined as,

$$\text{PER} = \frac{\text{Energy of first peak}}{\text{Energy of second peak}} \quad (8)$$

The RADWT is applied to a wheeze with one of 22 various p, q, s and J combinations as given in Table 1. For each set, two distinct peaks are found and the PER is calculated. As a result, for one signal, 22 different PER values are obtained. The minimum PER value is accepted as the indicator of best representation because it means that two peaks are correctly located while preserving maximum amount of their energies. In Fig. 2, for the same MP and PP wheezes given in Fig. 1, the two distinct peaks and corresponding p, q, s and J values are presented. It is seen that for MP wheezes high PER values are obtained. In contrast, for PP wheezes, relatively small PER values are obtained. In order to quantify the performance of the proposed method, the chosen PER metrics are employed as features for discriminating MP and PP wheezes. Support Vector Machines (SVM) classifier [16] is used as the learning method with leave one out cross validation method.

3 Experimental Results and Conclusion

In Fig. 3, the percentages (number of samples for a specific parameter set/number of total samples) for the distribution of total, MP and PP wheezes changing with various p, q, s and J values are given. On the left-side the relatively low Q-factor combinations and on the right side relatively higher Q-factor combinations are represented which means frequency resolution increases from left to right. The order of p, q, s and J values used in Fig. 3 is the same with the order of Table 1. For example the first set number in Fig. 3 corresponds to the first column in Table 1 ($p = 2, q = 3, s = 2, J = 8$). It is seen that, in order to achieve the best TF representation, which is obtained with the algorithm given in Section 2.3, a specific parameter set can not be obtained. For almost all parameter sets, except the first set (low Q-factor, low frequency resolution), optimum TF representation for a wheeze sample is achieved. Therefore, it is concluded that an adaptive and automatic system is needed for optimum localization of different peaks due to patient specific TF properties of wheezes. Additionally, the general accuracy of SVM classifier is obtained as 81.4 % when the linear kernel is employed. This shows that PER metric can be used as an indicator for discriminating MP and PP wheezes. In future, to increase the accuracy, different kernels in SVM and other classifiers can be utilized. Moreover, the effect of preprocessing steps, such as de-noising, and ensemble learning methods at the classifier and feature extraction level (with additional TF features) can be explored.

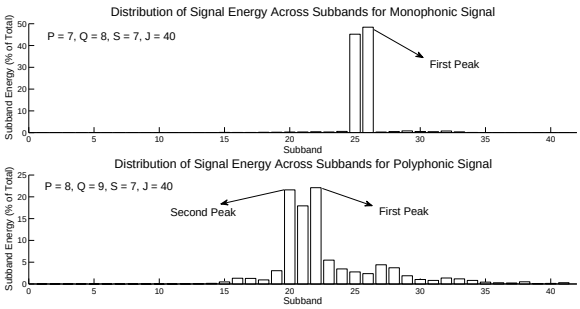

Figure 2: Energy distribution of MP and PP wheezes

Acknowledgements

This work is supported by Boğaziçi University Research Fund under grant number 16A02D2. S. Ulukaya is supported by the Ph.D. scholarship (2211) from Turkish Scientific Technical Research Council (TUBITAK). We would like to thank Sibel Yurt, MD, from Yedikule Chest Disease and Thoracic Surgery Education and Research Hospital and Dr. Ipek Sen for their guidance on data acquisition and labeling of wheeze types.

References

[1] N. Gavriely and D. W. Cugell. *Breath sounds methodology*. CRC Press, 1995.

Table 1: Various p, q, s and J values used in analysis.

Set #	**1**	**2**	**3**	**4**	**5**	**6**	**7**	**8**	**9**	**10**	**11**	**12**	**13**	**14**	**15**	**16**	**17**	**18**	**19**	**20**	**21**	**22**
p	2	3	4	5	5	5	6	6	7	7	7	8	8	8	8	8	9	10	10	10	11	11
q	3	4	5	6	6	6	7	7	8	8	8	9	9	9	9	9	10	11	11	11	12	12
s	2	2	3	4	5	5	5	6	5	6	7	3	4	5	6	7	5	6	7	8	7	8
J	8	10	15	20	25	30	30	35	35	35	40	35	35	35	35	40	35	40	45	50	45	50

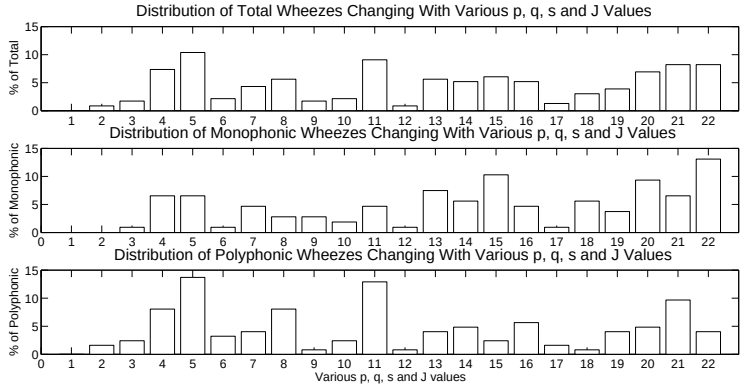

Figure 3: Distribution of total, MP and PP wheezes with respect to various p, q, s and J values

[2] S. Leng et al. The electronic stethoscope. *Biomedical Engineering Online*, 14(1):1–37, 2015.

[3] American Thoracic Society. Updated nomenclature for membership reaction. *Am. Thorac. Soc. News*, 3:5–6, 1977.

[4] A. R. A. Sovijarvi et al. Definition of terms for applications of respiratory sounds. *European Respiratory Review*, 10(77):597–610, 2000.

[5] S. Ulukaya, I. Sen, and Y. P. Kahya. Feature extraction using time-frequency analysis for monophonic-polyphonic wheeze discrimination. In *Engineering in Medicine and Biology Society (EMBC), 37th Annual International Conference of the IEEE*, pages 5412–5415. IEEE, 2015.

[6] N. Meslier, G. Charbonneau, and J. L. Racineux. Wheezes. *European Respiratory Journal*, 8(11):1942–1948, 1995.

[7] R. P. Baughman and R. G. Loudon. Lung sound analysis for continuous evaluation of airflow obstruction in asthma. *CHEST Journal*, 88(3):364–368, 1985.

[8] S. Taplidou and L. J. Hadjileontiadis. Analysis of wheezes using wavelet higher order spectral features. *Biomedical Engineering, IEEE Transactions on*, 57(7):1596–1610, 2010.

[9] P. Forgacs. The functional basis of pulmonary sounds. *CHEST Journal*, 73(3):399–405, 1978.

[10] Y. Nagasaka. Lung sounds in bronchial asthma. *Allergology International*, 61(3):353, 2012.

[11] A. Jain and J. Vepa. Lung sound analysis for wheeze episode detection. In *Engineering in Medicine and Biology Society (EMBC), 30th Annual International Conference of the IEEE*, pages 2582–2585. IEEE, 2008.

[12] F. Jin, S. Krishnan, and F. Sattar. Adventitious sounds identification and extraction using temporal–spectral dominance-based features. *IEEE Transactions on Biomedical Engineering*, 58(11):3078–3087, 2011.

[13] R. Naves, B. H. G. Barbosa, and D. D. Ferreira. Classification of lung sounds using higher-order statistics: A divide-and-conquer approach. *Computer Methods and Programs in Biomedicine*, 129:12–20, 2016.

[14] I. Sen and Y. P. Kahya. A multi-channel device for respiratory sound data acquisition and transient detection. In *Engineering in Medicine and Biology Society (EMBC), 27th Annual International Conference of the IEEE*, pages 6658–6661. IEEE, 2005.

[15] I. Bayram and I. W. Selesnick. Frequency-domain design of overcomplete rational-dilation wavelet transforms. *Signal Processing, IEEE Transactions on*, 57(8):2957–2972, 2009.

[16] C. C. Chang and C. J. Lin. LIBSVM: A library for support vector machines. *ACM Transactions on Intelligent Systems and Technology*, 2:27:1–27:27, 2011.

Address for correspondence:

Sezer Ulukaya

Bogazici University Electrical and Electronics Engineering Department, 34342 Bebek, Istanbul, Turkey

sezer.ulukaya@boun.edu.tr

Effect of body posture on LF/HF in ambulatory ECG

Yutaka Yoshida[1], Yuki Furukawa[1], Hiroki Ogasawara[1],
Emi Yuda[1], Junichiro Hayano[1], ALLSTAR Study Group[2]

[1]Nagoya City University Graduate School of Medical Sciences
[2]Allostatic State Mapping by Ambulatory ECG Repository Study Group

Abstract

LF/HF has been used as a maker of sympathetic predominance in cardiac autonomic activity. Decrease of LF / HF is associated with increased mortality risk. Laboratory studies have reported that LF/HF increases with standing and decreases with lying. Therefor we hypothesized that LF/HF in ambulatory monitoring is associated with the ratio of time in lying position during the monitoring (%lying ratio). Results, the decrease in LF/HF with advancing %lying time quartile was significant (P<0.001). Decreased LF/HF in ambulatory ECG monitoring could be the result at least partly of the fact that patients spent longer time in lying position during the monitoring.

Keywords *Heart Rate Variability, LF/HF, 3-axis accelerometer*

1 Introduction

Low-frequency-to-high-frequency ratio (LF/HF) of heart rate variability (HRV) has been used as a maker of sympathetic predominance in cardiac autonomic activity. In most of major prospective studies on the prognostic value of 24-hr HRV after acute myocardial infarction[1, 2], however, have reported that decrease, rather than increase, in LF/HF is associated with increased mortality risk, which is contrary to the general concept of cardio-protective effects of sympathetic suppression.

Laboratory studies have reported that LF/HF increases with standing and decreases with lying[3]. We therefor hypothesized that decreased LF/HF in ambulatory ECG monitoring is associated with the length of time when patients spent in lying position during the monitoring. We examined this hypothesis with ambulatory ECG big data built by Allostatic State Mapping by Ambulatory ECG Repository (ALLSTAR) project, which has started since 2009 and is gathering >50,000/year of 24-hr ECG data from the entire Japan. Among >300,000 data accumulated, we could estimate patient's posture during the monitoring in 47,624 data recorded with Holter recorders having a built-in 3-axis accelerometer (Cardy 303 pico, Suzuken Co., Japan).

2 Methods

Out of 47,624 ECG data with 3-axis accelerogram, we used 42,483 data that were recorded in patients ≥25 yr and the ECG showed sinus rhythm for >19.2 hr (80% of 24 hr) for this study. These data were recorded between April 2012 and July 2014 in 18,944 men (age, 67 ± 14 yr) and 23,539 women (68 ± 15 yr). From 3-axis accelerograms, we estimated the ratio of time in lying position (%lying time) during the monitoring, by which the patients were divided into four quartile groups (Q1-4, Table). We compared LF/HF and other indices of HRV among the quartile groups.

3 Results

LF/HF decreased progressively with advancing quartile of %lying time. LF/HF correlated negatively with age in both genders (r = -0.50 and -0.43 for men and women, respectively) and %lying time positively with age (r = 0.21 and 0.26 for men and women, respectively). Also, there is significant gender differences in both LF/HF (least-square mean ± SEM adjusted for age,0.59± 0.01, 0.58 ± 0.01 for men and women, respectively; P <0.001) and %lying time (47.4 ± 0.1, 43.7± 0.1; P <0.001). Nevertheless, the decrease in LF/HF with advancing %lying time quartile was significant (P <0.001), even when the effects of age and gender were adjusted.

4 Conclusions

Decreased LF/HF in ambulatory ECG monitoring could be the result at least partly of the fact that patients spent longer time in lying position during the monitoring.

References

[1] Rovere MT, Bigger JT, Jr., Marcus FI, Mortara A, Schwartz PJ, Investigators A. Baroreflex sensitivity and heart-rate variability in prediction of total cardiac mortality after myocardial infarction. Lancet. 1998;351:478-84.

[2] Huikuri HV, Mäkikallio TH, Peng CK, Goldberger AL, Hintze U, Moller M, Grp DS. Fractal correlation properties of R-R interval dynamics and mortality in patients with depressed left ventricular function after an acute myocardial infarction. Circulation. 2000;101:47-53.

[3] Pomeranz B, Macaulay RJ, Caudill MA, Kutz I, Adam D, Gordon D, Kilborn KM, Barger AC, Shannon DC, Cohen RJ, et al. Assessment of autonomic function in humans by heart rate spectral analysis. Am J Physiol. 1985;248(1 Pt 2):H151-3.

On the Heart-Rate Signal Provided by the Zephyr BioHarness 3.0

D. Nepi[1], A. Agostinelli[1], E. Maranesi[1], A. Sbrollini[1], M. Morettini[1], F. Di Nardo[1], S. Fioretti[1], L. Burattini[1]

[1]Department of Information Engineering, Università Politecnica delle Marche, Ancona, Italy

Abstract

The BioHarness 3 system (BH3) by Zephyr is a wearable cardiac sensor specifically designed for training optimization of professional athletes. BH3 records the electrocardiogram (BH3_ECG) and the heart-rate signal (BH3_HRS). Specifically, BH3_HRS is neither the popular tachogram nor the direct not-uniformly sampled heart-rate sequence as function of time. Consequently, the aim of the present study is to gain more insights on BH3_HRS that, if found reliable, would allow a future evaluation of the possibility of a clinical use of the sensor for cardiac risk evaluation. Data were acquired from an amateur athlete (male, 25 years old) during a 5-min rest followed by a 10 min exercise. R-peak detection was performed on BH3_ECG, and the obtained heart-rate signal (HRS) was low-pass filtered using the following six filters: 3-, 4-, and 5-sample averages and 0.30 Hz, 0.35 Hz, and 0.40 Hz 6th order Butterworth low-pass filters. The filtered HRSs were then compared to BH3_HRS in terms of correlation coefficient (ρ), mean square error (MSE), resting heart-rate variability (HRV) and exercise maximum heart rate. Results indicate that the HRS closest to BH3_HRS was obtained with the 3-point average (ρ=0.9688-0.9991, MSE=0.45-0.47 mV^2; comparable resting HRV and exercise maximum heart rate).

Keywords *Heart rate analysis, Sports-related sudden cardiac death, Wearable sensors.*

1 Introduction

Physical activity has beneficial effects on the cardiovascular system [1]. However, high-intensity exercise also associates to malignant cardiac events, including sports-related sudden cardiac death (SRSCD) [2]. SRSCD is defined as a "death occurring during sport or within 1 hour of cessation of sports activity" [3]. In a study on the general population (thus including both competitive and amateur athletes), SRSCD incidence was estimated to be 4.6 cases per million per year, with 6% of cases occurring in young competitive athletes [3]. Although the number of athletic sudden deaths is relatively small, SRSCD represents an important and emotionally charged public health issue [4]. High-intensity exercise may act as a SRSCD trigger in the presence of underlying cardiovascular diseases [5]. Thus, specific screening programs for the identification of cardiovascular abnormalities predisposing to SRSCD in athletes are a priority [6]. Still, recommendations for such screening programs are usually conceived only for competitive athletes, so that amateur athletes are typically left to optional evaluations of their health.

Wearable cardiac monitoring sensors have recently become very popular among athletes. They usually measure the instantaneous heart rate (HR) and sometimes the HR signal (HRS), and they are typically used for training optimization. Several HR and HR-variability (HRV) parameters, easily obtainable from HRS, are universally recognized as indicators of sudden cardiac death [7, 8]. Thus, such wearable cardiac sensors could also be useful for SRSCD risk evaluation if the providing HRSs would result clinically reliable and accurate. The BioHarness 3 system (BH3), promoted by Zephyr, is a commercial advanced wearable sensor for physiological monitoring during sport. It acquires several biological data among which the electrocardiogram (ECG) and HRS. We have observed, however, that HRS by BH3 is neither the popular tachogram nor the direct not-uniformly sampled HR sequence as function of time. Consequently, the aim of the present study is to gain more insights on HRS by BH3 that, if found reliable during both rest and exercise, would allow a future evaluation of the possibility of a clinical use of the sensor (beside its actual training use) for SRSCD prediction.

2 Methods

2.1 The BioHarness 3 by Zephyr

The BH3 wearable monitoring device by Zephyr (www.zephyranywhere.com), now a part of Medtronic, is a lightweight, chest-worn and strap system for real-time wearable physiological monitoring that incorporates, among others, ECG sensors. It may operate in radio frequency transmitting mode for live viewing of data or in logging mode for later download of the data. Among the output signals there are a single-lead ECG tracing (BH3_ECG; mV) sampled at 250 Hz, and a HRS (BH3_HRS; bpm) sampled at 1 Hz.

2.2 Data Acquisition

Data were acquired from an amateur athlete (male, 25 years old) before and during a running test. Particularly, the athlete, after having worn BH3 set in logging mode, stayed still for about 5 minutes for resting data acquisition, and run on a treadmill for 10 minutes at 9.5

Km/h for exercise data acquisition. Rest as well as exercise BH3_ECGs and BH3_HRSs were eventually downloaded on a PC for subsequent processing. The present research was undertaken after obtaining an informed consent from the subject, in compliance with the ethical principles of Helsinki Declaration and approved by the institutional expert committee.

2.3 Signal Processing

Rest and exercise BH3_ECGs were elaborated (Fig.1) in order to get HRSs to be compared to rest and exercise BH3_HRSs. Initially, BH3_ECGs were processed for R-peak detection using the Pan-Tompkins algorithm [9]. By considering that instantaneous HR and RR interval are linked by the following equation:

$$HR = \frac{60}{\text{RR interval}}, \qquad (1)$$

the HR sequences computed from the RR sequences were not-uniformly sampled (being RR-interval not constant) when represented as functions of time. After uniform resampling at 1 Hz, the resampled HRSs (RSMPL_HRS) were submitted to the six low-pass filtering procedures, namely 3-, 4-, and 5-sample finite impulse response averages (AVG3, AVG4 and AVG5, respectively) and 0.30 Hz, 0.35 Hz, and 0.40 Hz infinite impulse response 6th order Butterworth low-pass filters (LPB030, LPB035 and LPB040, respectively) in order to get six HRSs (AVG3_HRS, AVG4_HRS, AVG5_HRS, LPB030_HRS, LPB035_HRS and LPB040_HRS, respectively) to be compared to BH3_HRS. All processing procedures were implemented in MATLAB.

2.4 Signal Comparison

Comparison between rest and exercise BH3_HRS and HRSs was performed by computing a set of parameters (PRM) which included: the correlation coefficient (ρ), the mean square error (MSE; mV^2), a set of HRV parameters measured at rest [7], and maximum HR (maxHR) during exercise [10-12]. The set of HRV parameters measured at rest included:

- meanHR (ms) = mean HR;
- SDNN (ms) = standard deviation of normal RR intervals (NN);
- RMSSD (ms) = root mean square of the successive NN intervals;
- LF/HF ratio: ratio between low-frequency and high-frequency components of the HRS power spectrum.

Eventually, an optimization process based on ρ maximization, MSE minimization, and HRV parameters and maxHR differences minimization was performed in order to identify the HRS closest to BH3_HRS (Fig. 1).

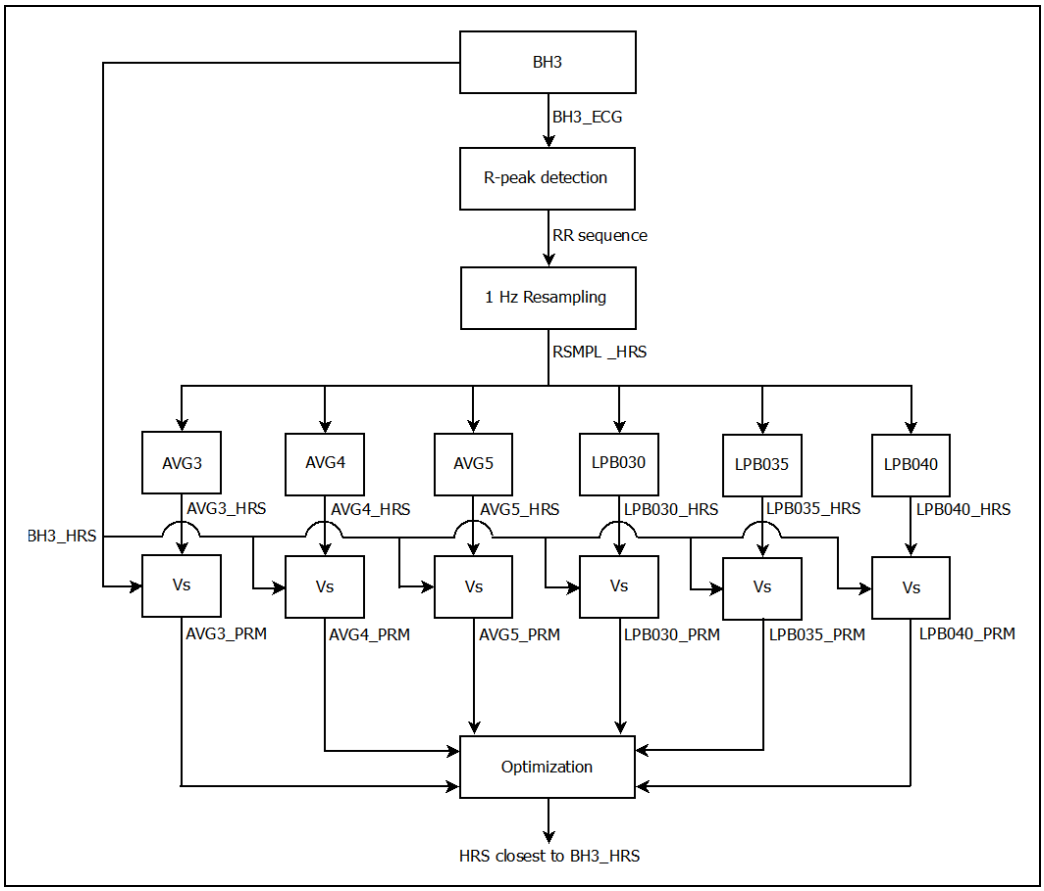

Figure 1. Block diagram of the procedure to find the low-pass filtered HRS closest to BH3_HRS.

3 Results

Already after resampling ρ values, indicating similarities in the signals trends, become quite high (>0.87), with ρ at rest being lower than under exercise (ρ=0.8745 vs ρ=0.9983; Table 1). However, ρ value typically increased after any low-pass filtering (only two exceptions for AVG4_HRS and AVG5_HRS under exercise). Analogously but oppositely, MSE values, indicating signals amplitudes similarities, were maximum after resampling, with rest MSE being much higher than exercise MSE (MSE=18.51 mV^2 vs MSE=0.84 mV^2; Table 1), and tended to decrease after low-pass filtering (only two exceptions for AVG4_HRS and AVG5_HRS under exercise). Thus, according to ρ and MSE only, AVG3_HRS was the closest to BH3_HRS, with resting ρ=0.9688 and MSE=4.47 mV^2, and exercise ρ=0.9991 and MSE=0.45 mV^2.

Comparison of the HRV parameters measured at rest (Table 2) indicates that meanHR was always correctly quantified (93 bpm), while SDNN and RMSSD usually reported differences of few ms (SDNN: 58 ms vs 57-63 ms; RMSSD: 16 ms vs 13-24 ms). Thus, according to these two time-domain parameters, AVG4_HRS was the closest to BH3_HRS, since it provided the same SDNN value (58 ms) and an RMSSD (15 ms) value that differs of only 1 ms from BH3_HRS. AVG3_HRS was also a quite close to BH3_HRS, since provided SDNN (60 ms) and RMSSD (17 ms) values that differ 2 ms and 1 ms, respectively. Instead, according to the frequency-domain HRV LF/HF parameter, AVG3_HRS was the closest to BH3_HRS (2.7 vs 2.9). Eventually, all HRSs provided exercise maxHR values close to that provided by BH3_HRS (maximum difference: 1 bpm; Table 2), with AVG3_HRS and AVG4_HRS matching it (maxHR= 174 bpm). Thus, taking into account all HR parameters, AVG3_HRS was the closest to BH3_HRS (Fig.2).

4 Discussion and Conclusion

The present paper represents a step of a process finalized to clinically validate the signals at the output of BH3 [13]. BH3_HRS is a filtered version of the RR sequence obtained after R-peak detection from BH3_ECG. The knowledge of such filtering procedure would allow an indirect validation of BH3 since the procedure could be applied to large databases of pathological ECGs in order to assess the ability of the processed data (which would result equivalent to the BH3 data) to identify cardiovascular risk. Thus, if the procedure would result reliable, BH3 could be used for clinical investigations in athletes beside training purposes.

According to our results, BH3_HRS is a low-pass filtered version of the RR-sequence and, among the filters considered here, AVG3_HRS is the closest to it, in terms of both morphology (measured in terms of ρ and MSE) and clinical content (measured in terms of HRV parameters at rest and maxHR under exercise).

Recording conditions	HR Signal Processing	ρ	MSE (mV^2)
Resting	RSMPL_HRS	0.8745	18.51
	AVG3_HRS	**0.9688**	**4.47**
	AVG4_HRS	0.9672	4.58
	AVG5_HRS	0.9295	9.78
	LPB03_HRS	0.9614	5.92
	LPB035_HRS	0.9609	6.01
	LPB040_HRS	0.9606	6.06
Exercise	RSMPL_HRS	0.9983	0.84
	AVG3_HRS	**0.9991**	**0.45**
	AVG4_HRS	0.9968	1.69
	AVG5_HRS	0.9923	4.33
	LPB030_HRS	0.9989	0.53
	LPB035_HRS	0.9987	0.62
	LPB040_HRS	0.9985	0.71

AVG: average; LPB: Butterworth low-pass filter.

Table1. Correlation coefficient (ρ) and mean squared error (MSE) values between HRS provided by the BioHarness 3 and the HRS obtained after various signal processing procedures, in both resting and exercise conditions.

It is interesting to observe that BH3_HRS and AVG3_HRS were closer during exercise than during resting (Table 1). This finding could be related to the fact that at rest short-term HRV (that is HR variations within few beats) is higher than exercise short-term HRV (Fig.2) and BH3 may have integrated some constrain that force consecutive RR-intervals to be within some ranges (in Fig. 2 it can be seen that the higher deviations of AVG3_HRS from BH3_HRS occurs in correspondence of strong HR variations of BH3_HRS).

Another cause of discrepancy between BH3_HRS and AVG3_HRS could be related to the occurrence of errors during the R-peak detection phase. If we visually checked the correctness of all R-peaks positions detected from BH3_HRS, the same cannot be done for the R peaks detected by the BH3, since such data is not available. Clearly, difference in R-peak detection will reflect in differences in the computation of the HRS.

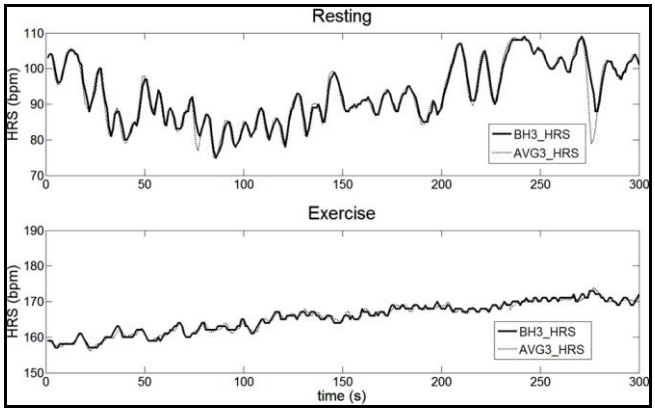

Figure 2. Superimposition of 5-min of BH3_HRS (solid line) and AVG3_HRS(dotted line) in resting (upper panel) and exercise (lower panel) conditions).

HR Signal Processing	**Resting**				**Exercise**
	meanHR (bpm)	***SDNN (ms)***	***RMSSD (ms)***	***LF/HF***	***maxHR (bpm)***
BH3_HRS	93	58	16	2.9	174
RSMPL_HRS	93	63	24	1.8	175
AVG3_HRS	93	60	**17**	**2.7**	**174**
AVG4_HRS	93	**58**	**15**	3.8	**174**
AVG5_HRS	93	57	13	5.7	173
LPB030_HRS	93	60	17	3.3	175
LPB035_HRS	93	61	18	2.6	175
LPB040_HRS	93	61	19	2.2	175

AVG: average; LPB: Butterworth low-pass filter; RMSSD: root mean square of successive NN intervals. SDNN:= NN interval standard deviation

Table2. Values of heart rate variability parameters (meanHR, SDNN, RMSSD, and LF/HF) measured during resting, and maximum HR (maxHR) measured during exercise.

Only one athlete was used in this preliminary study because it allowed a direct (not statistical) comparison between signals. Future studies on a larger set of data are needed to confirm the preliminary finding of this study according to which BH3_HRS is a close approximation of AVG3_HRS.

Reference

[1] S.N. Blair and J.N. Morris. Healthy hearts-and the universal benefits of being physically active: physical activity and health. *Annals of epidemiology*, 19: 253-256, 2009.

[2] D.S. Siscovick, N.S. Weiss, R.H. Fletcher and T. Lasky. The incidence of primary cardiac arrest during vigorous exercise. *The new england journal of medicine*, 311: 874-877, 1984.

[3] E. Marijon, M. Tafflet, D.S. Celermajer, F. Dumas, M.-C. Perier, H. Mustafic, J.F. Toussaint, M. Desnos, M. Rieu, N. Benameur, J.Y. Le Heuzey, J.P. Empana and X. Jouven. Sports-related sudden death in the general population. *Circulation*, 124: 672-681, 2011.

[4] M. S. Link and M. Estes III. Sudden cardiac death in the athlete, bridging the gaps between evidence, policy, and practice. *Circulation*, 125: 2511-2516, 2012.

[5] C.M. Albert, M.A. Mittleman, C.U. Chae, I.M. Lee, C.H. Hennekens and J.E. Manson. Triggering of sudden death from cardiac causes by vigorous exertion *The new england journal of medicine*, 343: 1355-1361, 2000.

[6] S. Sen-Chowdhry and W.J. McKenna. Sudden cardiac death in the young: a strategy for prevention by targeted evaluation. *Cardiology*, 105: 196-206, 2006.

[7] Task force of the european society of cardiology and the north american society of pacing and electrophysiology. Heart rate variability guidelines, standards of measurement, physiological interpretation, and clinical use. *European heart journal supplements*, 17: 354–381, 1996.

[8] S.G. Priori, E. Aliot, C. Blomstrom-Lundqvist, L. Bossaert, G. Breithardt, P. Brugada, A.J. Camm, R. Cappato, S.M. Cobbe, C. Di Mario, B.J. Maron, W.J. McKenna, A.K. Pedersen, U. Ravens, P.J. Schwartz, M. Trusz-Gluza, P. Vardas, H.J. Wellens and D.P. Zipes. Task Force on sudden cardiac death of the European Society of Cardiology. *European heart journal supplements*, 22: 1374-1450, 2001.

[9] J. Pan and W.J. Tompkins. A real-Time QRS detection algorithm. *IEEE Transaction on biomedical engineering*, 32: 230-236, 1985.

[10] S. Atwal, J. Porter and P. MacDonald. Cardiovascular effects of strenuous exercise in adult recreational hockey: the hockey heart study. *Canadian Medical Association Journal*, 166: 303-307, 2002.

[11] G.P. Wandewalle and P. Havette. Heart rate, maximal heart rate and pedal rate. *The American Journal of Sports Medicine*, 27: 205-210, 1987.

[12] I. Astrand. Aerobic work capacity in men and women with special reference to age. *Acta Physiologica Scandinavica*, 49: 1-92, 1960.

[13] D. Nepi, A. Sbrollini, A. Agostinelli, E. Maranesi, F. Di Nardo, S. Fioretti, P. Pierleoni, L. Pernini, S. Valenti, L. Burattini. Validation of the Heart Rate Signal Provided by the Zephyr BioHarness 3.0. *Computing in Cardiology 2016.*

Address for correspondence:

Laura Burattini
Department of Information Engineering, Università Politecnica delle Marche, Ancona, Italy
l.burattini@univpm.it

Ambulatory physical activity monitoring to know healthy life expectancy

E Yuda[1], Y Yoshida[1], H Ogasawara[1], J Hayano[1], ALLSTAR Study Group[2]

1Department of Medical Education, Nagoya City University Graduate School of Medical Sciences, Japan;
2Allostatic State Mapping by Ambulatory ECG Repository (ALLSTAR) project, Executive office, Nagoya City University Graduate School of Medical Sciences, Japan

Abstract

In a physiological big data project named Allostatic State Mapping by Ambulatory ECG Repository (ALLSTAR), we developed a large database of 24-hr physical activities in 19,345 men (age, 65 ± 17 yr) and 23,985 women (67 ± 17 yr) who underwent ambulatory accelerometer and electrocardiographic monitoring in all over Japan. We examined if regional difference in physical activity is associated with the inter-prefecture ranking of healthy life expectancy (HALE) reported by the Japanese Ministry of Health, Labour and Welfare in 2013. Analysis of covariance adjusted for the effect of age revealed that physical activity level decreases progressively in the order of prefectures grouped into upper, middle, and lower tertiles of HALE for both men and women (P <0.001 for both). When the subjects were divided into every 10s yr of age, the correlation between the rankings of physical activity and HALE was observed in 40s to 60s for men and in 50s to 60s for women. Our observations support the putative association between physical activity level and HALE.

Keywords *Physical activity; healthy life expectancy; physiological big data*

1 Introduction

To improve our quality of life in aging societies, we need extend our healthy life expectancy (HALE) close to our average life span. Although reduction in daily physical activity has been proposed as a major risk for shortening HALE, convincing evidence is lacking.

Allostatic State Mapping by Ambulatory ECG Repository (ALLSTAR) Research Group has been accumulating 24-hr Holter ECG and physical activity data since 2009 and has built a big data comprising >300 thousands of data, which are associated with date and geographic data (postal codes)[1]. Among data already collected, 43 thousands were recorded with micro Holter recorders with built-in 3-dimensional accelerometers, which allowed us to analyze the physical activities and body postures in daily life.

In this study, we examined if regional difference in physical activity is associated with the inter-prefecture ranking of HALE reported by the Japanese government.

2 Methods

We studied 3-dimensional acceleration data obtained with Holter ECG recorders (Cardy 303 pico, SUZUKEN CO., LTD) that were collected between April 2012 and July 2014 at three ECG analysis centers (Sapporo, Tokyo, and Nagoya) in Japan. We used data only from subjects >20 yr who have agreed with the usage of their data for this study. The study protocol has been approved by the Research Ethics Committee of Nagoya City University Graduate School of Medical Sciences (No. 709).

The accelerations were measured for left-to-right, caudo-cranial, and postero-anterior axes as X, Y, and Z values, respectively and sampled at 31.25 Hz. Time series of X, Y, and Z were resampled at 10 Hz and combined into a variable, AC (t), with the equation (1). After removing direct current component by a high-pass filter, AC(t) was rectified, averaged over 24 hr, and converted into common logarithmic value, which was used as the index of physical activity (PA).

$$AC(t) = \mathrm{sqrt}(x2(t) + y2(t) + z2(t)) \quad \cdots (1)$$

The data in each gender were divided into 5 groups with subject's age; 20-39, 40-49r, 50-59, 60-64, 65-69 yr. Then, within each age group, data were further divided into the tertiles, upper (L1), middle (L2), and lower (L3), according to the inter-prefecture HALE ranking published by the Japanese Health, Labour, Welfare Ministry [2].

PA was compared among L1, L2, and L3 by ANCOVA using age as covariate. Type 1 error level was set at 0.05 in these analyses. We used Med Calc Ver.14.12.0 for the statistical analysis.

3 Results

Data were obtained from 18875 men (age, 66 ± 14 yr) and 23541 women (69 ± 15 yr) in allover Japan. ANCOVA revealed that PA was highest in the area of highest HALE ranking and lowest in the lowest HALE ranking in both sexes. ANOVA in each age group revealed that associations of PA with HALE ranking exist in all age groups but 20-39 yr in men and in 20-39, 60-64, and 65-69 yr in women (Fig. 1). Additionally,

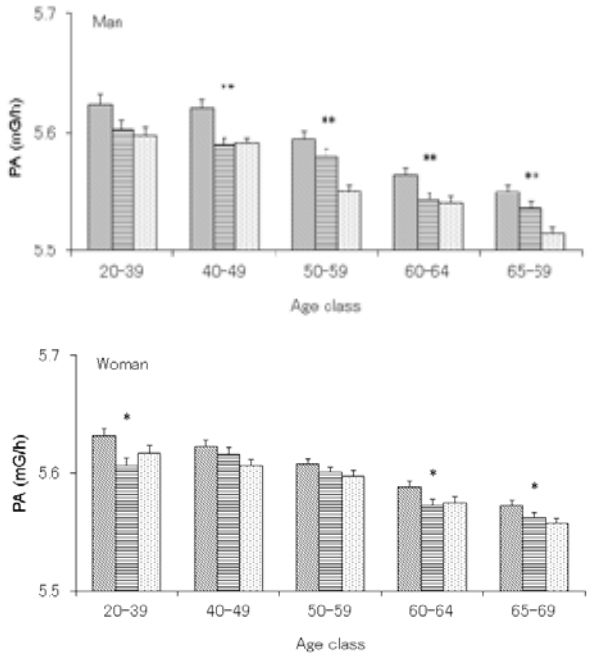

Fig. 1. Physical activity (PA) in the areas divided by the inter-prefecture HALE ranking by gender and age. Fine dotted, horizontal hatched, and coarse dotted bars indicate upper, middle, and lower tertiles of HALE in each age group. Data are mean ± SE. **P <0.01, *P <0.05.

PA was greater in female than in men (P <0.01) and this difference was observed in all age groups (P <0.05).

4 Discussion

We found that PA is greater in women than in men for all age. Also, PA was greater in the areas of higher HALE ranking and this relationship existed >40 yr in men and >60 yr in women. Our findings seem to provide the indirect evidence that supports for the hypothesis that physical activity level is associated with HALE.

In this study, we used physical activity data obtained from patients who underwent Holter ECG for a certain clinical reason. Therefore, there was sampling bias that only those with the clinical reason for ambulatory ECG examination were selected. Nevertheless, we found that they were positively associated with regional difference in HALE. One may speculate that there may be the regional characteristics of physical activity that are less affected by such clinical problems.

We are unable to exclude possibility that the observed association between physical activity and HALE may be mediated by other factors such as regional differences in socioeconomic environment. Because L3 included large cities such as Tokyo and Osaka, there could be differences in residential amenities, economic force, and type of business from areas in L1 and L2, which may cause the differences both in lifestyle and HALE.

5 Conclusions

Regional difference in PA is associated with that in HALE in men after 40 yr and in women after 60 yr of age.

Acknowledgment

A part of this study was reported in the 78th National Convention of IPSJ, 2016 [3,4].

References

[1] Allostatic State Mapping by Ambulatory ECG Repository (ALLSTAR) Research, http://www.med.nagoya-cu.ac.jp/mededu.dir/allstar/

[2] Progress of each goal in Healthy Japan 21 (2nd stage), the Ministry of Health, Welfare, and Labour, http://www.mhlw.go.jp/file/05-Shingikai-10601000-Daijinkanboukouseikagakuka-Kouseikagakuka/sinntyoku.pdf

[3] Yuda, E., Yoshida, Y., Hayano ., ALLSTAR Research Group., Nocturnal Life Style and Short Healthy Life Expectancy: Physiological Big Data Project, Allostatic State Mapping by Ambulatory ECG Repository (ALLSTAR): The 78th National Convention of IPSJ, March 10-12 (2016)

[4] Yuda, E., Yoshida, Y., Hayano, J., ALLSTAR Research Group., Regional Difference in Physical Activity is Associated with the Ranking of Healthy Life Expectancy among Prefectures in Japan: The 78th National Convention of IPSJ, March 10-12 (2016)

Address for correspondence:

Emi Yuda
Department of Medical Education
Nagoya City University Graduate School of Medical Sciences
Emi21@med.nagoya-cu.ac.jp

Estimation Method of Amount of Swallowed Water from Swallowing Sounds

M Imura[1], H Nakafuji[2], S Yoshimoto[2], O Oshiro[2]

[1]School of Science and Technology, Kwansei Gakuin University, Japan;
[2]Graduate School of Engineering Science, Osaka University, Japan;

Abstract

When humans ingest something, swallowing sounds occur at the larynx. Because these swallowing sounds can be measured noninvasively, they can be used to investigate swallowing ability and swallowing habits. The purpose of this study is to estimate how much water is swallowed by analyzing swallowing sounds. In this research, the swallowing sounds were measured on the skin surface of the thyroid cartilage and signal processing methods such as linear prediction analysis and the wavelet transform were applied to the swallowing sounds. The results comprised feature values that may reflect how much water is swallowed, and the number of feature values was reduced by principal component analysis. By using support vector machines, we achieved accurate estimation of amount of swallowed water with a probability more than 60%.

Keywords *Amount of Water, Biomedical Measurement, Sound Signal Processing, Swallowing Sound*

1 Introduction

Human beings take in air, foods, and water through the mouth, thus producing bioacoustic sounds such as masticatory sounds and respiratory sounds. In particular, when something is ingested, swallowing sounds occur at the larynx. Swallowing sounds can be measured noninvasively, and so can be employed to investigate the swallowing function [1]. Several researches of analyzing swallowing sounds have been done [2-4]. However, the quantity of food or beverage swallowed cannot be estimated.

The purpose of this study is to analyze swallowing sounds to estimate how much water is swallowed. If the amount of swallowed water can be measured, the control of water intake can become easier for artificial dialysis patients, by monitoring the amount of swallowed water on a daily basis. In addition, monitoring the amount of swallowed water can reduce the incidence of heat stroke.

We propose an estimation method for the amount of swallowed water. First, swallowing sounds are measured on the surface of the thyroid cartilage. Second, signal processing methods are applied to the swallowing sounds, and feature values, which reflect how much water is swallowed, are extracted. Finally, we examine the relationship between the amount of swallowed water and the feature values.

2 Characteristics of Swallowing Sounds

One swallow is made up of three phases [5]. In the first phase of swallowing, the bolus is formed and transported to the pharynx. In the second phase of swallowing, the bolus moves through the pharynx to the esophagus. In the final phase of swallowing, the bolus is transported to the stomach by peristaltic movement of the esophagus. Swallowing sounds occur during the second phase of swallowing. Swallowing sounds usually have a spectrum between 30 and 1000 Hz.

Videofluoroscopic examination that is used simultaneously with measurement of swallowing sounds revealed that swallowing sounds are composed of three parts [6]. In the first part of swallowing sounds (the first sound), the sound is raised by elevation of the larynx and influx of the bolus to the upper pharynx. In the second part (the second sound), the sound is raised by the influx of the bolus under the pharynx and the opening of the esophagus orifice. In the final part (the third sound), the sound is raised by the descent of the larynx.

Swallowing sounds can be measured noninvasively and easily. However, swallowing sounds are subject to ambient noise or biosounds. Researches have been performed to reduce the influence of such noise and extract swallowing sounds precisely [7].

3 Methods

In this section, the proposed method, which uses swallowing sounds to estimate the amount of swallowed water, is described.

3.1 Overall Process

Fig. 1 shows the flowchart of the proposed method. First, sound signal processing is applied to the measured swallowing sound in order to extract feature values, which may reflect how much water is swallowed. Second, the number of feature values is reduced by principal component analysis (PCA), and swallowing sounds are classified by a support vector machine (SVM), depending on the amount of water swallowed.

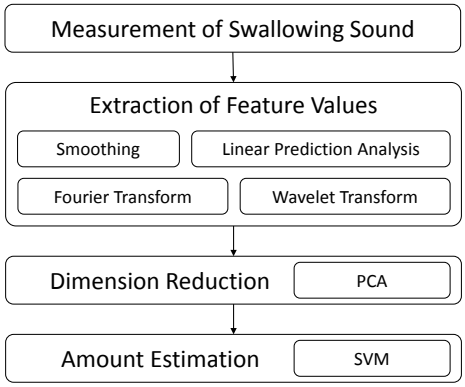

Figure 1: Flowchart of proposed method.

3.2 Measurement of Swallowing Sounds

The swallowing sounds made by three subjects (all men in their twenties) were measured on the skin surface of the thyroid cartilage with a microphone (ECM8000, BEHRINGER) when 5 mL, 10 mL, and 15 mL water were swallowed, respectively, 50 times. The measured swallowing sound signal is fed into the PC through an A/D converter. The sampling rate and resolution were 44,100 Hz and 16 bits, respectively. One swallowing sound signal has 40,000 samples. Fig. 2 shows an example of a swallowing sound signal.

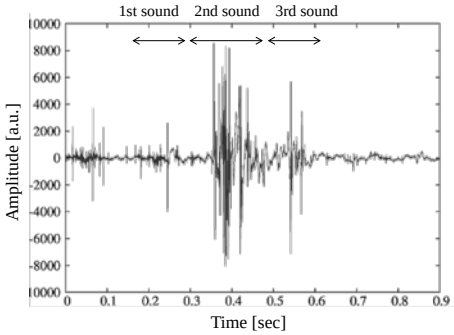

Figure 2: Swallowing sound sample.

3.3 Sound Signal Processing

For the sound signal processing, we employ several methods to extract the feature values.

3.3.1 Smoothing

A swallowing sound signal has N segments $\{x_1, x_2, \cdots, x_N\}$. The signal x_i is smoothed to signal y_i, which can be expressed as

$$y_i = \frac{1}{m+1} \sum_{j=-m/2}^{m/2} x_{i+j} \quad , \tag{1}$$

where $j = 1, 2, \cdots, N$, and m denotes a fixed smoothing size. We adopted two different smoothing sizes; $m = 300$ and $m = 600$. The smoothing with the parameter $m = 300$ can analyze the details of the second sound, and the smoothing with $m = 600$ can examine the relationships between the first, second, and third sounds. Fig. 3 and Fig. 4 show the respective results.

From the results with $m = 300$, two peak values in the second sound, S_1, S_2, and the interval between the two peaks T were extracted as feature values. From the results with $m = 600$, peak values in three sounds and the intervals between the respective peaks $S_a, S_b, S_c, T_a, T_b, T_c$, and the ratios of these values $S_a / S_b, S_b / S_c, S_c / S_a, T_a / T_c$ were also extracted as feature values.

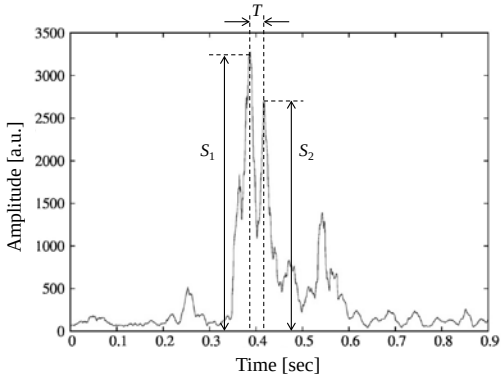

Figure 3: Result of smoothing (m=300).

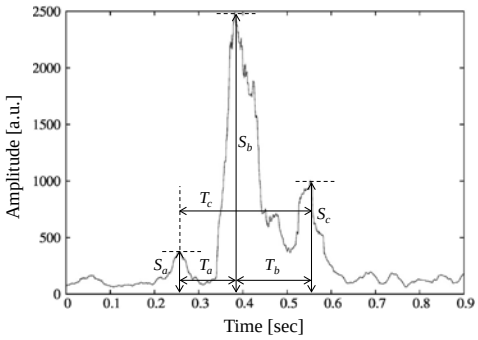

Figure 4: Result of smoothing (m=600).

3.3.2 Linear Prediction Analysis

In linear prediction analysis (LPA), a signal value x_i is estimated by the linear sum of the number μ of adjacent segments $\{x_{i-1}, x_{i-2}, \cdots, x_{i-\mu}\}$. Hence, x_i is

$$x_i + d_1 x_{i-1} + d_2 x_{i-2} + \cdots + d_\mu x_{i-\mu} = e_i \, , \tag{2}$$

where $d_1, d_2, \ldots, d_\mu$ are linear prediction coefficients. The 2nd sound is also analyzed by LPA and linear prediction coefficients are denoted as $d_1', d_2', \ldots, d_\mu'$. The best value of parameter μ was determined to minimize the final prediction error (FPE). FPE(μ) is expressed as

$$\mathrm{FPE}(\mu) = \frac{N+\mu}{N-\mu} \hat{e}^2 \, , \tag{3}$$

where N is the number of data points, and $\hat{e}^2$ is the mean residual. As a result, FPE(μ) takes a minimum value around $\mu = 60$, so we got 120 feature values.

3.3.3 Discrete-Time Fourier Transform

The frequency components of the swallowing sound signals are obtained by the discrete-time Fourier transform (DTFT). The Fourier component X_k is

$$X_k = \sum_{i=0}^{N-1} x_i \exp\left(-j2\pi ik / N\right), \quad (4)$$

where j is the imaginary unit, N is the number of data points, and $k = 0,1,\ldots,N-1$. The DTFT can express at most the half frequency of the sampling rate. The frequency feature values of all the segments are examined by the DTFT.

The rectangular window function w_i was multiplied by the swallowing sound signals x_i, and the DTFT was applied to the signals $w_i x_i$. Fig. 5 shows the typical result of the DTFT. The maximum peak value of the spectrum G, the maximum peak frequency f_1, the sum of powers G_t between 25 Hz and 3200 Hz, and the barycentric frequency f_m were extracted as feature values.

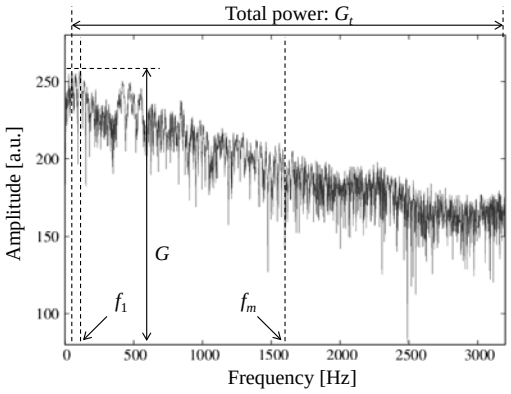

Figure 5: Result of DTFT.

In addition, 1/3 octave analysis is applied to the results of the DTFT. The band between 25 Hz and 3200 Hz is divided into 25 bands every 1/3 octave. The ratios $c_1, c_2, \ldots, c_{21}$ of the sums of powers between the respective band and the sum of powers G_t were also extracted as feature values.

3.3.4 Wavelet Transform

The time-frequency components of the swallowing sound signals are obtained by the wavelet transform. The wavelet transform $W(b,a)$ is

$$W(b,a) = \frac{1}{\sqrt{a}} \sum_{t=0}^{N-1} x_t \bar{\psi}\left(\frac{t-b}{a}\right), \quad (5)$$

where $\psi(t)$ is the mother wavelet, and a and b denote the frequency and the time shift, respectively. In addition, the scalogram $P(b,a)$ is expressed by

$$P(b,a) = \left|W(b,a)\right|^2 . \quad (6)$$

The frequency feature values of the segments at some time are examined by the wavelet transform.

The wavelet transform was applied to the swallowing sound signals. The Gabor wavelet was used as the mother wavelet. Fig. 6 shows the results of the wavelet transform. From the results, the maximum peak value of the scalogram $P_{\max}$ and the maximum peak frequency f_2 were extracted as feature values.

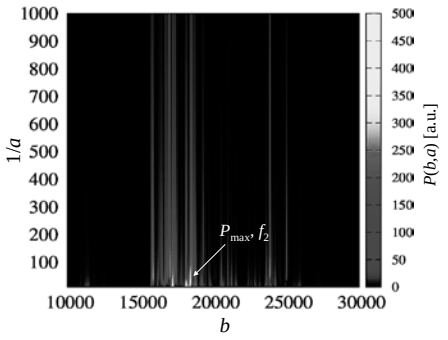

Figure 6: Result of wavelet transform.

3.4 Classification

By the signal analysis methods described in the previous section, we can obtain 160 feature values. To reduce the number of the feature values, PCA is applied. We regard the estimation of amount of swallowed water as a set of 2-class classification problems. Using a support vector machine (SVM), we classify the amount of swallowed water to one of the following classes: 5mL, 10mL or 15mL.

4 Result

In this section, we describe the result of the proposed method.

PCA was applied to the extracted feature values, and the 160 feature values were reduced to 15 values. The cumulative contribution ratio from the 1st component to the 15th component was 91.1%. Table 1 shows the three most affected values in the respective components.

Component	1st	2nd	3rd
1st	d_{43}	d_{44}	d_{45}
2nd	d'_{19}	d'_{20}	d'_{18}
3rd	d'_{12}	d'_{13}	d'_{11}
4th	d_1	d_2	d'_{59}
5th	c_{17}	f_m	c_{20}
6th	c_{19}	d'_1	d'_2
7th	d_{59}	d'_{59}	c_{20}
8th	S_c / S_a	c_{21}	S_c
9th	T_a	G_t	S_c
10th	S_a / S_b	S_b	S_c / S_b
11th	S_c / S_a	S_2	S_c
12th	T_c	T_b	S_a
13th	c_{21}	T_a / T_c	c_9
14th	S_a	T	T_a
15th	T_a / T_c	T_a	T

Table 1: Major feature values for PCA components.

A 2-class soft-margin SVM was applied to 15 feature values for classification between 5 mL and 10 mL, 10 mL and 15 mL, 5 mL and 15 mL. Leave-one-out cross validation was used for the evaluation. We tested the linear kernel, radial basis function (RBF) kernel, and polynomial kernel and the RBF kernel obtained the highest precision.

$$K(x_i, x_j) = \exp\left(-\gamma \left| x_i - x_j \right|\right) \quad (7)$$

Estimation experiments of unknown amount of swallowed water were executed as the evaluation of classifier. We used 30 swallowing sounds which contains 10 sounds each with 5mL, 10mL and 15mL. Table 2 shows the precision of classification results with the best parameters for each subject. Parameter C denotes a control parameter of soft-margin.

Subject	C	γ	Precision
Subject 1	100	0.001	60.0%
Subject 2	100	0.01	66.7%
Subject 3	100	0.01	96.7%

Table 2: Classification results**.**

5 Discussion

In the measurement of swallowing sounds, the precise measured position was not considered. However, the respective swallowing sound signals did not vary greatly, so the swallowing sound signals can be measured independently of the measured position. In addition, swallowing sounds were measured without taking speech or external noise into consideration. These factors may have affected the results negatively, and so the proposed method needs to be improved.

In 15 components that were obtained from PCA and used for SVM, linear prediction coefficients were influential, so the model for swallowing sounds may be different depending on the volume of swallowed water. Further, as the peak values in the three parts of the swallowing sounds and the intervals between the respective peaks were also influential, the movement of the larynx and the pharynx may be different depending on the volume of the swallowed water.

Swallowing sounds made by several subjects were measured and analyzed. The results confirmed that the precision of classification decreased. Thus, the elevation of the larynx, influx of the bolus to the pharynx, and the opening of the esophagus orifice may be different in different individuals. Therefore, the learning of SVM for estimation of the volume of the swallowed water should be done only using data of the subject of interest.

6 Conclusions

In this study, we proposed a method to estimate how much water is swallowed by analyzing swallowing sounds. First, swallowing sounds were measured on the skin surface of the thyroid cartilage. Second, four signal processing methods were applied to the swallowing sounds, and feature values that may reflect how much water was swallowed were extracted. Third, the number of feature values was reduced by PCA. Finally, the swallowing sounds were classified depending on the volume of swallowed water by using SVM. The results showed that swallowed water can be classified with a resolution of 5mL.

Acknowledgements

This work was supported by JSPS KAKENHI Grant Number JP16K00290.

References

[1] M. Aboofazeli and Z. Moussavi. Analysis of temporal pattern of swallowing mechanism. *Proceedings of IEEE Engineering in Medicine and Biology Society*, 5591–5594, 2006.

[2] J. Lee, S. Blain, M. Casas, D. Kenny, and T. Chau. A Radial Basis classifier for the automatic detection of aspiration in children with dysphagia. *Journal of NeuroEngineering and Rehabilitation*, 3(14):1-17, 2006.

[3] N. Tanaka, K. Nohara, K. Okuno, Y. Kotani, H. Okazaki, M. Matsumura, T. Sakai. Development of a swallowing frequency meter using a laryngeal microphone. *Journal of Oral Rehabilitation*, 39(6):411–420, 2012.

[4] S. Masaki, S. Komori, T. Takashima, G. Lopez, S. Tatsuya, and I. Yamada. Wearable eating habit sensing system using internal body sound. *Journal of Advanced Mechanical Design*, 4(1):158–166, 2010.

[5] A. Yadollahi and Z. Moussavi. A model for normal swallowing sounds generation based on wavelet analysis. *Proceeding of Electrical and Computer Engineering*, 827-830, 2008.

[6] S. Shirazi and Z. Moussavi. Acoustical modeling of swallowing mechanism. *IEEE Transaction of Biomedical Engineering*, 58(1):81–87, 2010.

[7] E. Sazonov, O. Makeyev, S. Schuckers, P. Lopez-Meyer, and E. Melanson. Automatic detection of swallowing events by acoustical means for applications of monitoring of ingestive behavior. *IEEE Transaction of Biomedical Engineering*, 57(3):626–633, 2012.

Address for correspondence:

Masataka Imura
School of Science and Technology, Kwansei Gakuin University
m.imura@kwansei.ac.jp

An Integrated Data Format for the Long Term ECG Recordings

H. Nagai [1], T. Shibui[1], Y. Kinukawa[1], S. Wakabayashi[1], K. Yana[1], and T. Ono[2]

[1]Graduate school of Science and Engineering, Hosei University, Tokyo Japan;
[2]Department of Cardiology, Nippon Medical School, Tokyo, Japan;

Abstract

This paper discusses the importance of having the common data format for the long term ECG data recordings aiming at establishing the ECG life log standard. A recommended format consists of two parts, one for the waveform and another for the annotated beat timing data. Modified THEW (Telemetric and Holer ECG Warehouse) format has been examined as a promising candidate for the standard format.

Keywords *Holter ECG, ECG life log, Computational ECG, Health Care, ISHINE, MFER, Biosignal Interpretation.*

1 Introduction

In the for-discussion section of the latest issue of *Methods of Information in Medicine* [1], the vision of Computational Electrocardiography (CECG) has been discussed where continuous ECG data are acquired, stored and processed for the timely user feedback to realize the advanced health care practice. Emerging technologies such as *IoT* or the cloud information systems would be the key to realize this CECG vision. However, more important key issue is to develop the reliable and efficient methods of ECG data processing and interpretation. Although the short term ECG data analysis is thoroughly established for the clinical use, the long term ECG data analysis has to be extensively elaborated for the core functioning of CECG practice [2]. In order to facilitate to realize the vision. As is described in [1], the common standardized data format for the long term ECG recordings will be helpful for the research collaboration. This paper focuses on this issue.

2 Methods

The recommended data format consists of a set of two binary data files for each day. One is for waveform and another is for the beat timing data. The data format is an extended version of the one utilized for the *Telemetric and Holter ECG warehouse* (THEW) of the Rochester University [3]. Two major standardized ECG waveform recording format are known. One is ISHNE [4] and another is MFER, recently approved as an ISO standard [5]. The waveform part of the proposed method basically adopts the ISHINE format, consists of the header followed by the waveform data. The header divided into three blocks, i.e. CRC checksum, the fixed and variable size parameter blocks. The CRC data block checks the validity of the file. Fixed block includes common information of the subjects (subjects' age, sex, sampling frequency etc.). The variable-size block is for some additional information for the users. Users can define the information to be stored. Any data length is allowed. For the efficient waveform data storing, waveform amplitude differences are stored. One byte is used for the waveform amplitude difference. The first bit is used for the overflow flag. If the flag is on, the succeeding byte is interpreted as the additional amplitude data. Annotated RRI interval segment gives a compact yet informative data. It includes the beat to beat information in 2 bytes. (16 bits). The first 4-bit includes the beat annotation and remaining 12-bit is the RR interval. Annotation characterizes each beat by a single character (N: Normal, NG: Artifact, V: Premature ventricular contraction etc.). The subsequent 12-bit describes RR interval. For the long RR interval needs more than 12-bit, the data continuation flag is set to make the following data segment available for getting the correct interval data.

3 Results and Concluding Remarks

Typical data size for the annotated beat timing data achieved by the recommended method is 173KB for 24-hour ECG data if the standard ZIP binary data compression is used together, which requires a half of the data length compared with THEW data format. The format needs 5GB for a typical life-long data recording of 80 years This is a feasible size to own personally. The waveform data will be kept for necessary time span. The CECG vision, once realized, is expected to contribute for extending peoples' healthy life expectancy considerably. The common standardized long term ECG data format will facilitate the research collaborations to realize the goal.

References

[1] Kazuo Yana, "Editorial for Computational Electro-cardiography: Revisiting Holter ECG Monitoring," *Methods Inf. Medicine*. 2016; 55, To appear. DOI: http://dx.doi.org/10.3414/ME15-25-0009

[2] Hansen MM, Miron-Shatz T, Lau AY, Paton C., "Big data in science and healthcare: a review of recent literature and perspectives", Year book Med Inform. 9(1). pp.21-26, 2014.

[3] Rochester University Telemetric and Holer ECG warehouse data format: http://thew-project.org/THEWFileFormat.htm

[4] Fabio Badilini, "The ISHNE Holter Standard Output File Format", *A.N.E.* Vol. 3, No. 3, Part 1. pp.263-266, July 1998.

[5] ISO 22077-1:2015 Health informatics -Medical waveform format Part 1: Encoding rules.

Physiological Variation during Drowsy Driving

Masashi Kitagawa[1], Shima Okada[2]

[1]Graduate School of Science and Engineering, Kindai University, Japan;
[2]Faculty of Science and Engineering, Kindai University, Japan;

Abstract

Recently, drowsy driving has been caused a serious accident. The causes of drowsy driving are the insufficient sleep and fatigue of the driver. Therefore, it is necessary to detect the drowsy state of driver due to preventing the drowsy driving. In this study, we focused on the physiological variation and the head movement during the drowsy state of the driver. As the results, we could confirm that the significant differences in head movement and heart rate between normal and drowsy condition.

Keywords *Drowsy driving, Head movement, Physiological variation, Biological measurement*

1 Introduction

There are some traffic accidents, for example careless driving and drowsy driving. Drowsy driving especially causes a serious accident such as the fatal accident. The causes of drowsy driving, there are insufficient sleep and fatigue of the driver, the time zone of drive, the traffic volume and so on. Therefore, we need to develop the method to detect the drowsy state of driver to prevent the drowsy driving. In this study, we focused on the physiological variation that is related to autonomic nervous system and the head movement during the drowsy state of the driver. We compared the physiological quantities during wake state and drowsy state.

2 Methods

We conducted the driving experiment using a driving simulator during wake state (daytime) and drowsy state (night). Nine healthy males (22-26 years old) took part in this experiment. Fig. 1. shows the experimental image. We measured electroencephalogram (EEG), heart rate, respiratory rate, energy consumption, and head movement of subjects. EEG and heart rate were measured by biological signal measurement device. Respiratory rate and energy consumption were measured by respiratory sensor. Head movement was measured by acceleration sensor. We used EEG for the index of alert level. Subjects drove the traffic lane in the oval course at 100 [km/h] for 60 minutes. If they went out of the traffic lane, they must come back immediately. We finally decide the effective parameter from each physiological quantity to detect the drowsy driving.

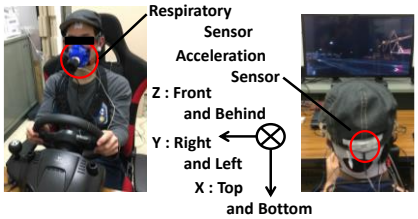

Fig. 1 Experimental image.

3 Results & Discussions

We show the result of head movement in Fig. 2. Amount of head movement increased in drowsy state. We considered that it was difficult to keep the posture by low alert level. Fig. 3. shows the result of each physiological quantity. Heart rate and respiratory rate decreased in drowsy state. We considered that parasympathetic nerve became dominant because of keeping low alert. Energy consumption was seen the unevenness in drowsy state due to increasing the operation of steering wheel. We could confirm that the significant differences in head movement and heart rate between normal and drowsy condition.

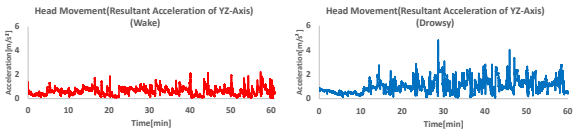

Fig. 2. Result of head movement.

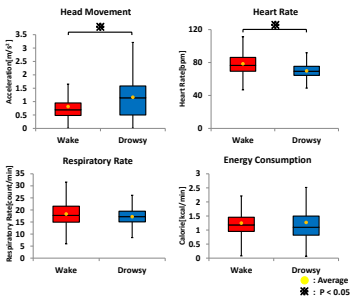

Fig. 3. Box plot of each physiological quantity.

References

[1] H. De Rosario, J.S. Solaz, et al. Controlled inducement and measurement of drowsiness in a driving simulator. *IET Intell. Transp. Syst.,* Vol. 4, Iss. 4, pages 280-288, 2010.

Pharmaceutical Benefit Assessment for Involuntary Exerciser Patient by Image Processing

Masaya KIMACHI [1], Shima OKADA [2]
[1]Guraduate School of Science and Engineering, Kindai University, Japan;
[2]Faculty of Science and Engineering Kindai University, Japan;

Abstract

The system could quantitatively assess the pharmaceutical benefit for involuntary exerciser patients is very important in clinical site. This study we developed the system to assess the pharmaceutical benefit by using image processing to focus on the mouth dystonia. The advantage of this study is noncontact and noninvasive for the patients.

Keywords *Involuntary exercier. Heer-like. Image proceeing.*

1 Introduction

The ratio of elderly people in total population is increasing in Japan. Elderly pepople have some disease. In addition, patients that move the body with difficulty are difficult to go to hospital by themselves. In order to reduce the difficulty for patients, we developed the system for the evaluation of pharmaceutical benefit from the video images that the patient recorded in their home. The study is to evaluate the treatment by paying attention to the mouth dyskinesia found in many involuntary movement's elderly. Mouth dyskinesia is a kind of involuntary movement disorder symptoms to move unconsciously mouth.

2 Evaluation Methods

In order to carry out the evaluation of the treatment, to recognize the movement of the mouth from the video obtained by photographing the involuntary movement's from the front Determining the mouth of a subject by using the Haar-Like features in order to recognize the movement of the mouth.

Haar-Like features : Determining whether the object want to be recognized by capturing the multiple contrast of the image.Feature quantity H (r1, r2) is the average luminance difference between the two regions. It shows an example of the Heer-Like Feature in Fig.1

Fig.1 Example of Haar-Like features

$$H(ri, r2) = S(r1) - S(r2)$$

r1 : The average brightness of the black area.

r2 : The average brightness of the white area.

Evaluation criteria made by learning feature pattern of image of the recognized object and image does not recognize the object.

3 Exprerimental Method

The subjects were older women with involuntary exerciser. In image analysis technique for the evaluation of the treatment using the Haar-Like feature. We were recognition of the mouth in the day 4 and day 8 of the video from the treatment.

3.1 Resurt & Conclusion

In Fig.2, 0 in a) and b) have failed to recognize the mouth, 1 is able to recognize the mouth. a) is the 4 days from treatment ,b) is the 8 days from treatment. Recognition of the mouth cannot be when closed strongly the mouth, move well the mouth, tongue and the tongue is twisted. It is considered to be different from the state of the usual mouth learned by Haar-Like feature. That is, it can be determined that have come up with symptoms of involuntary movements when it is not able to recognize the mouth. In the future, we well evaluation of treatment by results.

a) 4 days after treatment

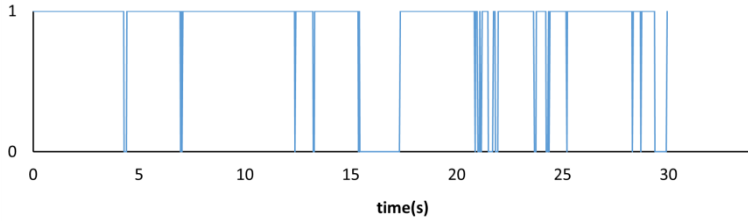

b) 8 days after treatment

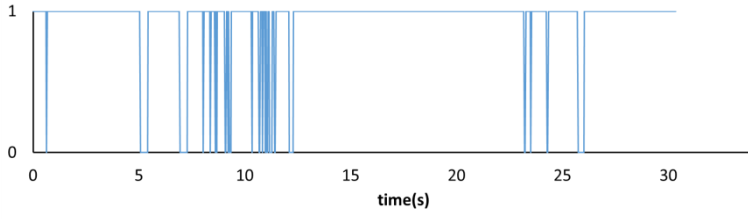

Figure 2: Recognition result of mouth.

References

[1] [1] Etienne Corvee and Frencois Bremond “Haar like and LBP based features for face, head and people detection in video sequences” HAL archives-ouvertes.fr 2011 pp.10

The preliminary study of core temperature estimation with external auditory meatus temperature sensor while exercising.

MyungJun Koh[1], SooYoung Sim[1], KwangMin Joo[1] Kwangsuk Park[2]

[1]Interdisciplinary Program of Bioengineering, Seoul National University, Seoul, Korea
[2]Department of Biomedical Engineering, College of Medicine, Seoul National University, Seoul, Korea
E-mail : bioeng15@bmsil.snu.ac.kr

Abstract

This study shows the preliminary study of estimating core temperature with external auditory meatus temperature sensor while exercising. The exercise consists of 30 minutes of cycling, and treadmill and 30 minutes of rest between each exercise. External auditory meatus (EAM) temperature was measured with high precision NTC thermistors. The highest Correlation coefficient between EAM and core body temperature is 0.8325.

Keywords *Core temperature, External auditory meatus temperature, exercising*

1 Introduction

Estimating core temperature is important to people who work in an extreme environment such as miners, soldiers, firefighters. Every year, many cases of heat stroke and heat injuries have been reported. Physiological Strain Index (PSI) is a good way to determine if the person in the dangerous condition. PSI can be calculated with core temperature and heart rate. It ranges from 0 to 10 and being to 10 is the dangerous situation. [1] Measuring Core body temperature takes ingestible temperature sensing pill which is burdensome, expensive and susceptible to foods and water. Measuring external auditory meatus (EAM) temperature to estimate core body temperature could lead to a better application to people who needs to monitor body temperature. EAM temperature sensor can easily modify into earphones and etc.

2 Methods

3 Subjects volunteered to exercise in a gym. All subjects wore shorts and t-shirts and food and water intake were controlled. High precision NTC thermistors (CANTHERM, MF51E, Canada) were inserted into the 3M foam earplugs The picture of the sensor is shown in Figure 1. The exercise protocol is shown Figure 2.

3 Results

MAE temperature does follow trends of core body temperature while exercising. The mean of the correlation coefficient is 0.7354. Figure 3 and Table 1 shows the results.

Figure 1: Picture of Example of EAM temperature sensor

Time	30min	30min	30min	30min	30min
Activity	Rest	Cycling	Rest	Treadmill	Rest

Table 1: Excercise Protocol

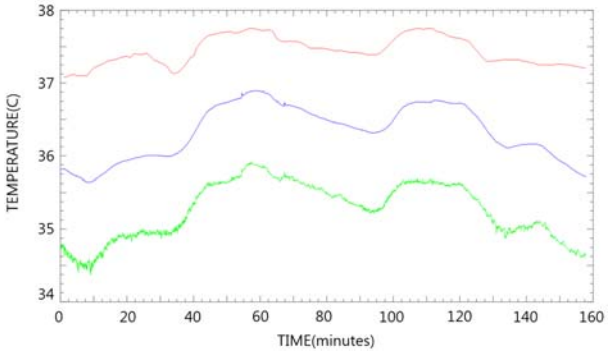

Figure 2: Example of core body temperature of subject 1 comparison with EAM temperature(Red : Core Body Temperature. Green, and Blue : EAM temperature.)

Subjects	Correlation Coefficient
Subject 1	0.6693
Subject 2	0.7046
Subject 3	0.8325
Mean	0.7354

Table 2: Correlation Coefficient of three subjects

4 Conclusions

The results may vary when the type of exercise differ from this study and when the number of subjects was bigger. However, this study shows a good possibility of research that EAM temperature could be an easy way to estimate core body temperature to calculate PSI and other application such as energy expenditure estimation.

References

[1] M. J. Buller and W.A Latzka, A real time heat strain risk classifier using non-invasive measures of heart rate and skin measurement, *Physiological Measurement*, 2008.

Address for correspondence:

MyungJun Koh

Seoul National University
bioeng15@bmsil.snu.ac.kr

Validating Stability of Components Extracted by Nonnegative Matrix Factorization via Clustering

Tianyi Zhou[1,2], Guoqiang Hu[1,2], Reza Mahini[1], Xiao-Feng Gong[3], Qiu-Hua Lin[3], Fengyu Cong[1,2]

[1]Department of Biomedical Engineering, Faculty of Electronic Information and Electrical Engineering, Dalian University of Technology, China
[2]Department of Mathematical Information Technology, University of Jyväskylä, Finland
[3]School of Information and Communication Engineering, Faculty of Electronic Information and Electrical Engineering, Dalian University of Technology, China

Abstract

Nonnegative matrix factorization (NMF) has been widely applied for signal processing and data analysis. The evident drawback of NMF is that the adaptive algorithms of NMF tend to converge to local optimal points, resulting in the demand of validating stability for the extracted components by NMF algorithms. We proposed a straightforward way that after an adaptive NMF algorithm runs for multiple times, all the extracted components can be clustered into the pre-defined number of clusters. And if the inner similarity of each cluster in terms of correlation coefficient between any two memberships of the cluster is closer to 1, the adaptive algorithm yields stable extracted components. Otherwise, the decomposition results would not be acceptable for further analysis. The simulated time-series data decomposed by different NMF algorithms validated the proposed idea. The proposed approach would be very significant for the real-world application, such as, the power spectrum of brain time-series signals.

Keywords *nonnegative matrix factorization, components, coefficients, clustering, stability*

1. Introduction

Nonnegative matrix factorization (NMF) has been widely applied for signal processing and data analysis [1, 2]. Since it was proposed in the 1990s [3-5], many adaptive algorithms have been proposed [2, 6]. Theoretically, NMF is unique with additional and special constraints [2], for example, nonnegativity and sparsity. Despite of the theoretical uniqueness, the adaptive algorithms of NMF tend to converge to the local optimal points in practice. Usually, given an NMF algorithm and a pre-defined number of components, fits of multiple runs with random initialization are examined. If the fits do not vary much across multiple runs of the algorithm, the decomposition is considered to be stable [1]. However, the previous study reported that the fits of two NMF algorithms were similar, but the extracted components by the two NMF algorithms could be different [7].

Another matrix decomposition approach, independent component analysis (ICA) [8], also faces up to the similar problem. It is that the ICA algorithm often converges to the local optimization points in practice although ICA decomposition can be unique in theory [8]. One solution to validate the stability of extracted components by ICA is to run an ICA algorithm multiple times and then clustering all the extracted components [9]. If every found cluster is dense and different clusters are isolated with each other, multiple runs of the ICA algorithm yield the similar sets of ICA components, indicating the ICA decomposition is stable. Otherwise, the different runs of ICA decomposition produce different sets of ICA components.

In this study, we applied the solution for ICA to validate the stability of the extracted components by NMF, and compared classical NMF algorithms and their low-rank approximation derivatives using simulated data.

2. Method

2.1 NMF Algorithms

For a given non-negative data matrix $V \in R^{m\times n}$ and $r \ll \min[m\, n]$. NMF attempts to find non-negative matrices $\mathrm{W} \in R^{m\times r}$ a $H \in R^{r\times n}$ to minimize the function

$$f(\mathrm{W},\mathrm{H}) = \frac{1}{2}\|V - W\ \ \|_F^2 \qquad (1)$$

where W and H are called component matrix and coefficient matrix, The product W is called a NMF of V, although V is not necessarily equal to the product W . Clearly the product W is an approximate factorization of rank at most r. An appropriate decision on the value of r is critical in practice. In most cases, r is usually chosen such that $r \ll m$ $[m,\ n]$ in which case W can be thought as a compressed form of the data in V.

$$V_{m\times n} \approx W_{m\times r}H_{r\times n},\ W \geq 0,\ H \geq 0 \qquad (2)$$

To optimize (1) , a very popular multiplicative update rules were suggested by Lee and Seung [5]

$$\mathrm{H} \leftarrow H.* \frac{V^T W}{HW^T W} \qquad (3)$$

$$\mathrm{W} \leftarrow W.* \frac{V}{WH^T H} \qquad (4)$$

For convenience the algorithm of (3)-(4) is called classical NMF methods, NMF_MU.

Another set of updated formulas has been proposed by Rasmus Bro [10], which is referred to as columnwise method, and later extended as hierarchical alternating least squares （HALS）algorithm[1], where the columns of W and H are updated sequentially by using

$$h_i \leftarrow \frac{1}{w_i^T w_i}[V_i^T w_i] \tag{5}$$

$$w_i \leftarrow \frac{1}{h_i^T h_i}[V_i h_i] \tag{6}$$

$V_i = \mathrm{V} - \sum_{j \neq i} w_j h_j^T$, w_j and h_j are the jth column of W and H, respectively. For each iteration, HALS can only update one column of W and H. Considering that there are R columns in total in W and H, HALS and NMF_MU essentially have equivalent time complexity and space complexity. However, in practice, the HALS often converges faster than MU[11].

When factorizing data with HALS and NMF_MU, we found that the speed of methods convergence is very slow. The major bottleneck is caused by the matrix multiplications with the large matrices V. In the process of updating W and H, the large original data V will be iterated for many times. This process not only converges slowly, but also greatly consumes computer memory. If these large matrices can be replaced by much smaller ones, the efficiency of NMF_MU and HALS can be improved. Motivated by this, low-rank approximation (LRA) based NMF has been proposed [11]:

$$\min_{\widehat{W},\ \widehat{H},\ W,H} F(\widehat{W},\ \widehat{H},\ W,H) = \left\|V - \widehat{W}\widehat{H}^T\right\|_F^2 + \left\|\widehat{W}\widehat{H}^T - WH^T\right\|_F^2 \tag{7}$$

where, $\mathrm{W} \in R_+^{M \times R}$, $\mathrm{H} \in R_+^{R \times N}$, $\widehat{W} \in R_+^{M \times L}$, $\widehat{H} \in R_+^{N \times L}$, $L = p \in M$, and p is a small positive constant.in order to solve (7). Firstly, we need to find the LRA $\min_{\widehat{W},\ \widehat{H},\ W,H} \left\|V - \widehat{W}\widehat{H}^T\right\|_F^2$, where $\widehat{W}$ and $\widehat{H}^T$ are with the low rank L, $L \in M$; Then, optimize $\left\|\widehat{W}\widehat{H}^T - WH^T\right\|_F^2$ with fixed $\widehat{W}^T$ and $\widehat{H}^T$.

The prototypical low-rank NMF algorithms originated with Guoxu Zhou and Andrzej Cichocki [11] is provided below with the mean squared error objective function:

$$\mathrm{H} \leftarrow H.\!*\frac{[\widehat{H}(\widehat{W}^T W)]}{H(W^T W)} \tag{8}$$

$$\mathrm{W} \leftarrow W.\!*\frac{[\widehat{W}(\widehat{H}^T H)]}{W(H^T H)} \tag{9}$$

This is the so-called lraNMF_MU that implements low-rank approximation based multiplicative update (NMF_MU). The first step can be solved efficiently by using principle component analysis (PCA) or truncated singular value decomposition (tSVD) or any other suitable and efficient low-rank approximation algorithms. Now suppose that the optimal $\widehat{W}$ and $\widehat{H}^T$in the first step, i.e., $\mathrm{V} \approx \widehat{W}\widehat{H}^T$. Then optimizing the $\min\left\|\widehat{W}\widehat{H}^T - WH^T\right\|_F^2$ will get above function. At first sight, there is no great difference between (3) and (7). But note that the dimensionality of $\widehat{W}$ a· $\widehat{H}^T$ is much smaller than V. Under the present circumstances, $L = p \in M$, lraNMF_MU has much lower time and space complexity.

Similar to the HALS algorithm, let $V_i = \widehat{W}\widehat{H}^T - \sum_{j \neq i} w_j h_j^T$ and the formulas in (5)-(6) becomes

$$h_i \leftarrow \frac{1}{w_i^T w_i}[\widehat{H}(\widehat{W}^T w_i) - \overline{H_i}(\overline{W_i}^T w_i)] \tag{10}$$

$$w_i \leftarrow \frac{1}{h_i^T h_i}[\widehat{W}(\widehat{H}^T h_i) - \overline{W_i}(\overline{H_i}^T h_i] \tag{11}$$

where $\overline{W_i} \in R^{M \times (R-1)}$ and $\overline{H_i} \in R^{N \times (R-1)}$ are the submatrices of W and H by removing their ith column. The low-rank approximation based HALS is called lraNMF_HALS.

2.2 Hierarchical Clustering

Hierarchical clustering is one of most popular clustering methods. In contrast to partitional clustering, which directly decompose the dataset into a set of disjoint clusters, the hierarchical clustering method is the process for transforming a proximity matrix into a nested partition, which can be graphically represented by a tree called dendrogram. To obtain the number of clusters and the corresponding partitions, we have to cut the dendrogram at a certain level. Cutting it at different levels will lead to different clustering results with different levels[12]. Hierarchical clustering was applied to validate the stability of ICA components [9] here.

Hierarchical clustering algorithms are mainly classified into agglomerative methods (bottom-up methods) and divisive methods (top-down methods). In this study, we select agglomerative methods, where the dendrogram is formed by bottom-up.

Agglomerative methods are as follows:

Step 1) Start with N clustering; basically, each object is a cluster; calculate the proximity matrix for N clusters;

Step 2) Find minimum distance in the proximity matrix and merge the two clusters with the minimal distance;

Step 3) Update the proximity matrix using the new distances between the new cluster and other clusters;

Step 4) Repeat Steps 2 and 3 until all objects are in one cluster.

A conservative cluster quality index Iq in the previous study [9] was defined to reveal the compactness and isolation of a cluster. It is computed as the difference between the average intra-cluster similarities and average extra-cluster similarities:

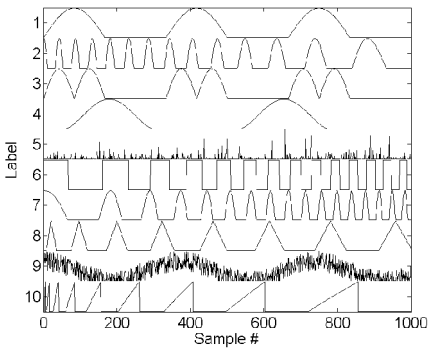

Figure 1: Waveforms of 10 time-series for H in model (1). They are adapted from NMFLAB [1] and called as sources here.

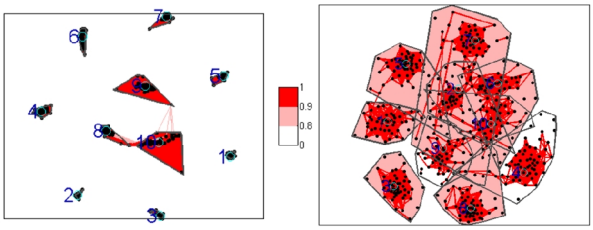

(a) HALS (b) MU

Figure 2: Clustering 500 extracted components from 50 runs of NMF with 10 components in each run: (a) Inner similarity of each cluster for HALS, (b) Inner similarity of each cluster for MU.

$$I_q(C_m)=\frac{1}{|C_m|^2}\sum_{i,j\in C_m}\sigma_i - \frac{1}{|C_m||C_{-m}|}\sum_{i\in C_m}\sum_{j\in C_m}\sigma_i \quad (12)$$

where $C_{-m}=C-C_m$. The range of I_q is from 0 to 1. The closer to 1, the higher stability it is.

2.3 Simulation

Given a signal $H \in R_+^{1\times 1}$ as component matrices shown in Fig. 1, then we generated matrices $W \in R_+^{1\times 6}$. Then we constructed $V^{\circ} = W^T H \in R_+^{6\times 1}$ and $V = V^{\circ} + E$, where E denoted the independent noise and V denoted 64-channel time-series data. We mainly compared the four NMF algorithms' performance (NMF_MU, HALS, lraNMF_MU, lraNMF_HALS) in presence of large noise measured by different signal-to-noise ratio (SNR in decibels).

We used the four NMF algorithms to decompose the data $V \in R_+^{6\times 1}$. In this experiment, 10 components and 10 coefficients are extracted. In order to compare the stability and reliability of decomposed components and coefficients by NMF, we use two steps to solve it:

Step 1): An NMF algorithm runs 50 times. Each time the initialization was random.

Step 2): All extracted components were clustered, respectively, according to their mutual similarities, using agglomerative clustering with average-linkage criterion.

Step 3): The centroid of each cluster was selected as the component extracted by NMF.

3. Results

3.1 Simulated Data with SNR = 20db

For demonstration, when SNR is 20dB, the 10 estimated sources and the clustering results of all 500 components by HALS and MU algorithms are shown in Fig. 2. Ideally, the number of components in each cluster equals to the number of times that NMF is run. Obviously, HALS outperformed MU from the view of the stability of extracted components. In Fig. 2, the denser the cluster is, the better the stability of the components extracted by an NMF algorithm is.

NMF can be regarded as the blind source separation methods. Then, it is necessary to check the estimated source in contrast to the real source. Fig. 3 shows the waveforms of 10 extracted components by two NMF algorithms. By visual inspection, we can come to the conclusion that HALS outperformed MU for estimating the sources.

3.2 Simulated Data with Multiple SNR

In Fig. 2, the SNR is 20dB, which is very high. Fig. 4 demonstrates the results with SNR ranging from -10dB to 20 dB, where four NMF algorithms are applied.

Fig. 4-a shows that fits of four different NMF algorithms were very similar with each other. Fig. 4-b reveals the mean over 10 correlation coefficients of 10 pairs between the source and the estimated source by algorithm for one SNR. The four algorithms yielded different correlation coefficients, which was variable from the fits of the four algorithms. Fig. 4-c presents the mean over 10 Iqs of 10 components extracted by algorithm for one SNT. The stability of four NMF algorithms were very different.

Evidently, bigger correlation coefficient indicating better estimation of sources in Fig. 4-b and the higher Iq implying better stability of extracted components in Fig.

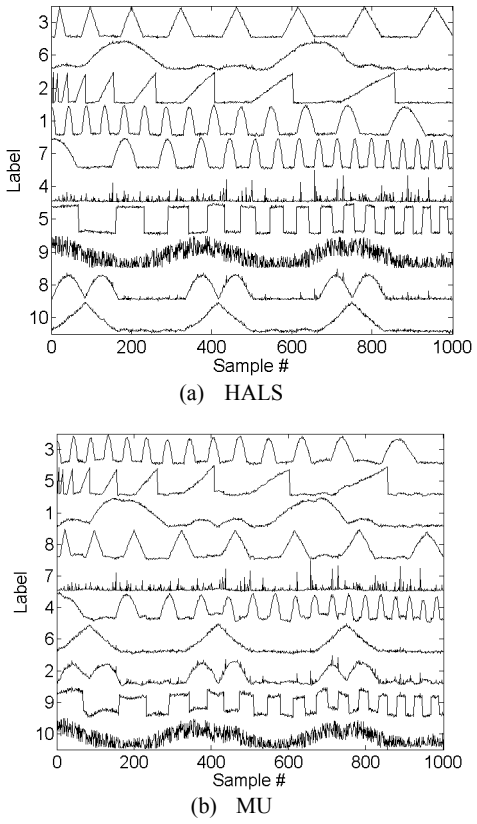

(a) HALS

(b) MU

Figure3: The 10 extracted components by two NMF algorithms.

4-c well correspond to each other. This is reasonable since

if the sources are well extracted by NMF algorithm the stability of the sources can be high as well.

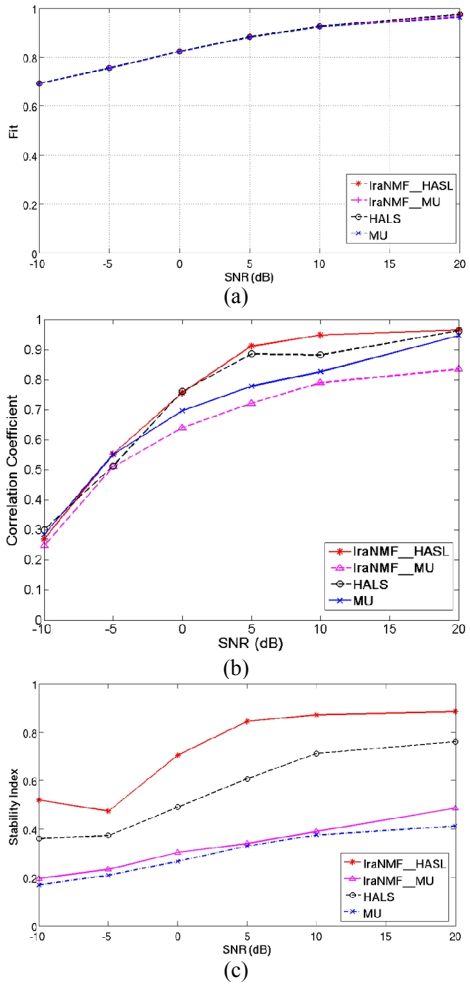

Figure 4: Results of four NMF algorithms with different SNR: (a) fit of NMF model, (b) correlation coefficient between the estimated source and the real source, (c)

4. Conclusions

We proposed an efficient approach in order to validate the stability of extracted components by NMF with clustering the extracted components yielded via multiple runs of one NMF algorithm. In terms of the simulated data, we have found that the higher stability of extracted component by NMF indicates better estimation of the corresponding source. There are variable NMF algorithms in practice and the proposed approach can be applied to choose the appropriate algorithm of NMF to decompose the given dataset. This would be very significant for the real-world application, such as, the power spectrum of brain time-series signals. Moreover, the proposed approach is promising for the multi-way data analysis as well [13]. Due to the limitation of the space, more results will be reported in the future.

Acknowledgements

This work was supported by the Fundamental Research Funds for the Central Universities [DUT16JJ(G)03] in Dalian University of Technology, and National Natural Science Foundation of China (Grant No. 81471742 and 61379012).

References

[1] A. Cichocki, R. Zdunek, A. H. Phan, and S. I. Amari, *Nonnegative Matrix and Tensor Factorizations: Applications to Exploratory Multi-way Data Analysis and Blind Source Separation*: Wiley, 2009.

[2] G. X. Zhou, A. Cichocki, Q. B. Zhao, and S. L. Xie, "Nonnegative Matrix and Tensor Factorizations An algorithmic perspective," *IEEE Signal Processing Magazine,* vol. 31, pp. 54-65, May 2014.

[3] P. Paatero and U. Tapper, "Positive Matrix Factorization - A Nonnegative Factor Model With Optimal Utilization Of Error-Estimates Of Data Values," *Environmetrics,* vol. 5, pp. 111-126, Jun 1994.

[4] P. Paatero, "Least squares formulation of robust non-negative factor analysis," *Chemometrics and Intelligent Laboratory Systems,* vol. 37, pp. 23-35, May 1997.

[5] D. D. Lee and H. S. Seung, "Learning the parts of objects by non-negative matrix factorization," *Nature,* vol. 401, pp. 788-791, Oct 1999.

[6] Y..Wang and Y..Zhang, "Nonnegative Matrix Factorization: A Comprehensive Review," *IEEE Transactions On Knowledge And Data Engineering,* vol. 25, pp. 1336-1353, 2013.

[7] F. Cong, I. Kalyakin, A.-H. Phan, A. Cichocki, T. Huttunen-Scott, H. Lyytinen*, et al.*, "Extract Mismatch Negativity and P3a through Two-dimensional Nonnegative Decomposition on Time-frequency Represented Event-related Potentials," *Lecture Notes in Computer Science (L. Zhang, J. Kwok, and B.-L. Lu (Eds.): ISNN 2010, Part II),* vol. 6064, pp. 385-391, 2010.

[8] A. Hyvarinen, J. Karhunen, and E. Oja, *Independent Component Analysis*: John Wile, 2001.

[9] J. Himberg, A. Hyvarinen, and F. Esposito, "Validating the independent components of neuroimaging time series via clustering and visualization," *Neuroimage,* vol. 22, pp. 1214-1222, Jul 2004.

[10] R. Bro, "Multi-way Analysis in the Food Industry," *Neuroimage,* 1998.

[11] G. Zhou, A. Cichocki, and S. Xie, "Fast Nonnegative Matrix/Tensor Factorization Based on Low-Rank Approximation," *IEEE Transactions on Signal Processing,* vol. 60, pp. 2928-2940, Jun 2012.

[12] B. Abu-Jamous, R. Fa, and A. K. Nandi, Integrative *Cluster Analysis in Bioinformatics*: Wiley Publishing, 2015.

[13] F. Cong, Q. Lin, L. Kuang, X. Gong, P. Astikainen, T. Ristaniemi, "Tensor Decomposition of EEG Signals: A Brief Review", *Journal of Neuroscience Methods*, vol. 248, pp. 59–69, 2015

Address for correspondence: Fengyu Cong, Professor, Department of Biomedical Engineering, Dalian University of Technology, China, cong@dlut.edu.cn

A Simple Method for Monitoring Integration of Pore-Forming Protein into Lipid Bilayer

K Shimba[1,2,3], Y Miyamoto[1], T Yagi[1],

[1]School of Engineering, Tokyo Institute of Technology, Japan;
[2]Japan Society for the Promotion of Science, Japan;
[3]School of Engineering, The University of Tokyo, Japan;

Abstract

Ion channels are important targets for drug development. Although a number of methods are developed for studying ion channels, special equipment for cell culture and microfabrication are needed. Thus, a simple method which does not need any special equipment is helpful for drug discovery and fundamental study. Here, we aimed to develop a simple method for monitoring integration process of pore-forming proteins. In our method, lipid monolayers are formed between the lipid and buffer solution, and between lipid solution and an agar-coated Ag/AgCl electrode. Lipid bilayer is formed by contacting two lipid monolayers. For evaluating pore formation, electrical impedance across the bilayer was measured. Impedance between the agar-coated electrode in the lipid solution and the electrode in the buffer solution was > 10^7 Ω after forming the bilayer. The impedance gradually decreased under the condition with supplementing alpha-hemolysin. These results suggest that our method is suitable to monitor pore-forming process of membrane protein.

Keywords *Lipid bilayer, Impedance measurement, Alpha-hemolysin*

1 Introduction

Ion channels are important therapeutic targets for drug development. A number of study recruited cell lines stably expressing ion channels. For example, Ca^{2+}-activated K^+ channels was examined with the HEK293 cells [1]. Recent progress in microfabrication technology enabled to evaluate functions of ion channels which were formed in artificial lipid bilayer [2]. Although these methods are strong tools, special equipment for cell culture and microfabrication are needed. Thus, a simple method which does not need any special equipment helps drug discovery and fundamental study of ion channel function. In this study, we aimed to develop such a method for monitoring integration process of pore-forming proteins. For evaluating the changes in membrane properties, electrical impedance across the membrane was measured.

2 Materials and Methods

2.1 Bilayer formation

A schematic illustration of the agar-electrode method is shown in Figure 1. In our method, lipid monolayers are formed between the lipid and buffer solution and between lipid solution and an Ag/AgCl electrode. Lipid bilayer is formed by contacting two lipid monolayers (red circle in Figure 1). Electrical properties of the bilayer can be measured with two Ag/AgCl electrodes.

A buffer solution containing 1.0 M KCl and 10 mM HEPES (Dojindo) was prepared. Diphytanoyl glycerol phosphor-choline (DPhPC, Avanti) was diluted in n-hexadecane (Wako) at 10 mg/ml. For a measurement electrode, Ag wires were coated with Ag/AgCl paste, and one of the electrode was covered with agar (Wako). The lipid bilayer was formed as follows. First, the buffer solution was poured in a petri dish, and DPhPC solution was layered on the buffer. Second, an Ag/AgCl electrode with and without agar-coating was set in the DPhPC and buffer solution, respectively. Lipid monolayers were expected to be formed at the boundaries between lipid solution and buffer and between lipid solution and agar. Finally, the agar-coated electrode was manipulated to contact the boundary between the lipid and buffer solution. Alpha- hemolysin (aHL; Sigma), a pore-forming membrane protein, was added to the buffer solution at 20 μg/ml for evaluating the change in impedance. All procedures were performed at room temperature.

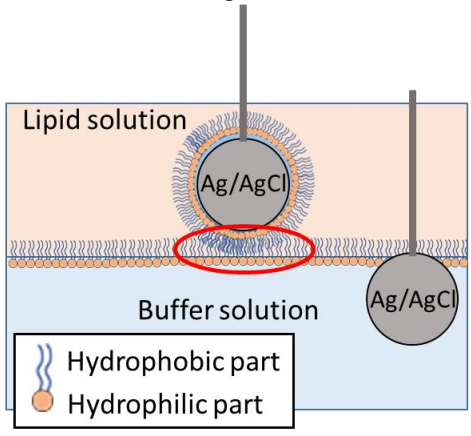

Figure 1: Shcematic illustlation of agar-electrode method.

2.2 Impedance measurement

Impedance of the lipid bilayer at 1 kHz was measured with LCR HiTester (3522-50; Hioki) after forming bilayer with and without aHL. Data were collected every 10 s for more over 15 min. Impedance measurement was performed with a stored program, and the parameters are shown in Table 1. The impedance was normalized by the averaged value within the first 1 min.

3 Results and Discussion

Figure 2 shows the experimental setup. Lipid solution was layered on the buffer solution, and an agar-coated Ag/AgCl electrode touched the boundary. Impedance between the agar-coated electrode in the lipid solution and electrode in the buffer solution was > 10^7 Ω after contacting the agar with boundary between lipid and buffer solution. When both two agar-coated electrodes were set in the buffer solution, impedance between two electrodes was approximately 10^2 Ω. The impedance was consistent with that of previous study [3], suggesting that a lipid bilayer was formed.

Impedance was monitored for 1 hour after forming the bilayer with aHL. Figure 3 shows changes in impedance. Black dots show the impedance under the condition with aHL, and the red shows control. Under the presence of aHL, the normalized impedance gradually decreased to < 0.02. Meanwhile, the impedance did not show such decrease without aHL, suggesting that aHL integrated into the lipid bilayer and formed pores. Additionally, the possible reason for the decrease in impedance is protein pore formed by aHL.

Table 1: Setting of measurement

Parameter	Value
Test frequency	1 kHz
Test voltage	25 mV
Limit for current	Off
Test range	Auto
Open circuit compensation	All
Short circuit compensation	Off
Trigger delay	0 s
Averaging	4 times
Measurement speed	Slow2

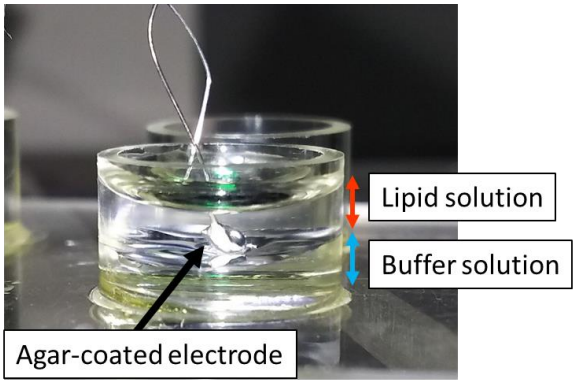

Figure 2: Experimental settings for impedance measurement.

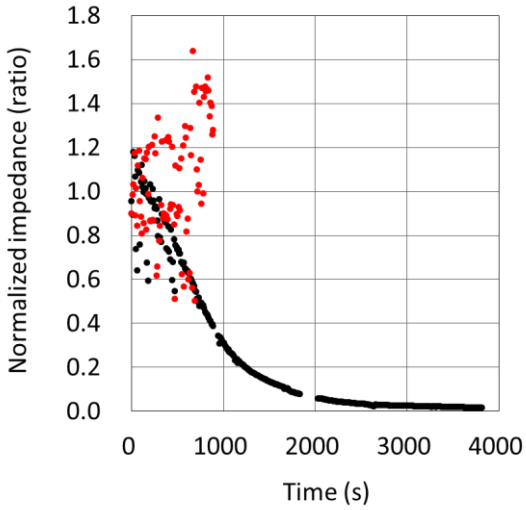

Figure 3: Changes in electrical impedance with and without alpha-meholysin integration.

4 Conclusion

We developed a simple method for evaluating the integration of membrane protein and pore formation. As a result, electrical impedance was gradually decreased after forming bilayer under the condition with aHL. Meanwhile, the impedance did not show such decrease without aHL, suggesting that aHL integrated in the lipid bilayer and formed pores. These results suggest that our simple method is suitable to monitor pore-forming process of membrane protein.

Acknowledgements

This work was partially supported by the Japan Society for the Promotion of Sciences (JSPS) through a Grant-in-Aid for JSPS Fellows (16J7023).

References

[1] C. Hougaard, B. L. Eriksen, S. Jørgensen, T. H. Johansen, T. Dyhring, L. S. Madsen, D. Strøbæk and P. Christophersen, Selective positive modulation of the SK3 and SK2 subtypes of small conductance Ca^{2+}-activated K^+ channels, *British Journal of Pharmacology*, 151:655-665, 2007.

[2] M. A. Czekalska, T. S. Kaminski, S. Jakiela, K. T. Sapra, H. Bayley and P. Garstecki, A droplet microfluidic system for sequential generation of lipid bilayer and transmembrane electrical recording. Lab on a chip, 15:541-548, 2015.

[3] S. Terrettaz, M. Mayer and H. Vogel, Highly Electrically Insulating Tethered Lipid Bilayers for Probing the Function of Ion Channel Proteins, *Langmuir*, 19:5567-5569, 2003.

Address for correspondence:

Kenta Shimba
Tokyo Institute of Technology
shimba.k.aa@m.titech.ac.jp

Assessment of ozone autohemotherapy on patients with multiple sclerosis by time-frequency analysis of near-infrared spectroscopy signals

Xue Han[1], Filippo Molinari[2], Samanta Rossati[2]

[1]School of Mechanical and Electronic Engineering, Wuhan University of Technology, Luoshi Road 122, Hongshan District, Wuhan, Hubei, P. R. China, 430070, hanxue@whut.edu.cn.

[2]Biolab, Department of Electronics, Politecnico di Torino, Corso Duca degli Abruzzi 24, 10129 Torino, Italy, filippo.molinari@polito.it.

Abstract

During the last several decades, the availability of ozone autohemotherapy is gradually being understood through the comprehensive study and clinical experiment. Ozone autohemotherapy is advocated as a form of alternative or combination with orthodox medicine in treating vascular and neurological diseases. In order to study the therapeutic effect of ozone autohemotherapy on multiple sclerosis (MS), we used a near-infrared spectroscopy system to monitor the oxygenhemoglobin (O_2Hb) and dexoygenhemoglobin (CO_2Hb) concentration changes of 6 MS suffer subjects under ozone autohemothearpy for about 150 minutes each.The NIRS-Ozone signals were performed a time-frequency analysis in three time intervals:1)blood removal; 2)blood reinfusion and 3) at the end of the monitoring (a few minutes before the end of the monitoring). By computing and comparing the relative power of O_2Hb and CO_2Hb signals in the very low frequency (VLF) and low frequency (LF) bands during three different recording periods, it can be observed that the VLF power decreases and the LF power increases, which is possible an indication of a clear vascular effect of ozone. From a technical point of view, it is a quantitative assessment of the therapeutic effect of ozone autohemotherapy by means of time-frequency analysis.

Keywords: *Ozone autohemotherapy, near-infrared spectroscopy, time-frequency analysis*

1 Introduction

Ozone is always considered as a harmful gas present in the photochemical smog. Continuous ozone inhalation eventually causes leisions in the respiratory system and extrapulmonary organ because of the releasing of some inflammatory substances [1-2]. However, its toxicity is related to its dosage. In medicine, many studies and clinical application demonstrated that an appropriate ozone dosage with a precise concentration can be used as a treatment [1-2]. Ozone autohemotherapy (OA) achieves the therapeutic result by the reinfusion of the ozonated blood to the patient. When a medical controllable ozone dose reacts with biomolecules present in plasma, there is a biochemistry process that can trigger a precisely calculated minimal oxidative stress which is able to upregulate the antioxidant defenses [1-2]. Thus, the medical ozone therapy has a different result from the oxidative stress induced by continuous inhalation. OA can improve blood circulation, activate antioxidant enzymes and scavenge free radicals [3]. Thanks to the development of dose-adjustable ozone generator, OA as a treatment has been applied in an extensive range of pathologies. Recent studies showed that OA has been already used to treat vascular disease, advanced ischemic diseases and neurological disease [4-8].

This paper introduced the research on the therapeutic effect of OA in multiple sclerosis (MS). NIRS was applied to monitor the changes of cerebral oxygenation level affected by OA on MS patients. The NIRS signals were processed in the time-frequency domain with the method of Choi-Williams Distribution (C-W Distribution). This study is an in-vivo case of investigating the long-term effect of OA in neurological disease.

2 Methods

1.Subjects and Experiment protocol

We enrolled 6 MS patients. All the subjects were instructed about the system and the experimental protocol and signed a written informed consent.

The experiment protocol consisted of three steps: 1) the subjects were drawn 240 grams of blood from the antecubital vein; 2) the blood was mixed with 180ml of a O_2/O_3 gas mixture, which was composed by O_2 at 50%, with an O_3 concentration equal to 40µg/ml (M95, Multioxygen, Gorle, Italy); 3) the blood was slowly reinfused into the subject via the antecubital vein, after being passed through a sterile filter[5]. The ozone therapy experiment were taken under a precise medical observation to see whether they were in comfort and relaxation situation or not during the long-term recording.

2.NIRS recording and NIRS signal processing

Near-infrared spectroscopy (NIRS) is a spectroscopic method to non-invasively monitor the cerebral oxygenation level by detecting changes in hemoglobin concentration associated with neuron activity. The chromophores, oxyhemoglobin (O_2Hb) and deoxyhemoglobin (CO_2Hb), are considered as the main tissue oxygenation parameters [9]. The specific periods of the NIRS monitoring during the OA treatment were applied to assess its therapeutic effect.

The NIRS signals were recorded using a commercially oximeter (NIRO300, Hamamatsu Photonics K.K., Japan) with the sampling rate of 2Hz. Four different wavelength (775, 810, 830 and 910nm) of near- infrared source and a photo-detector were applied to monitor the concentration changes of chromphores. The detecting area is on the forehead 2 cm away from midline and 1cm above the supraorbital ridge [5]. The whole monitoring lasted for about 150 minutes. It was divided into the following stages: 1) baseline condition; 2) blood removal; 3) blood reinfusion; 4) post reinfusion. The NIRS monitoring recorded the concentration changes of O_2Hb and CO_2Hb in the entire process, which reflect the cerebral vasomotor reactivities of the subjects. In this study we limited the observation to 150 minutes, due to the subjects' physiological situation (for example, feeling tired or hungry) and the physiological constraints of the NIRS system.

The nonstationary NIRS-ozone signals were processed by a time-frequency analysis through Choi-Williams Distribution (with σ=0.5) in three time intervals:1) blood removal; 2) blood reinfusion and 3) at the end of the monitoring (a few minutes before the end of the monitoring).

Many studies present the oscillations of cerebral hemodynamics and metabolism in adult human head can be detected by using NIRS, which also provide the possibility of frequency-derived parameters used to assess cerebral autoregulation [10]. These oscillation have been classified within the power spectrum essentially consisting of two different bands: in very low frequency (VLF) (20-40 mHz) and low frequency (LF) band (40-140 mHz), VLFs are thought to be generated by brain stem nuclei, which modulated the lumen of the small intracerebral vessels. LFs reflect the systemic oscillations of the blood pressure and are modulated by the sympathetic system activity[11].

We also computed the time-frequency Squared Coherence Function (SCF) between the O_2Hb and the CO_2Hb concentration signals. Being x(t) the O_2Hb concentration signal and y(t) the CO_2Hb, the SCF between the two signals was defined as

$$SCF_{xy} = \frac{\left|D_{xy}(t,f)\right|^2}{D_{xx}(t,f)\cdot D_{yy}(t,f)}$$

Where, $D_{xy}(t,f)$ is the cross time-frequency C-W representation of the O_2Hb and the CO_2Hb concentration signals, $D_{xx}(t,f)$ is the time-frequency C-W representation of the O_2Hb signal, and $D_{yy}(t,f)$ that of the CO_2Hb signal.

All the auto and cross time-frequency distributions were computed on a suitable time window according to the length of event, with the event centered in the middle part of the window. This value of time window is chosen to keep the experimental protocol sufficiently short.

3 Results

From Figure 1 to Figure 3 respectively, shows the O_2Hb (left) and CO_2Hb(right) concentration changes of one MS subject during the three specific periods.

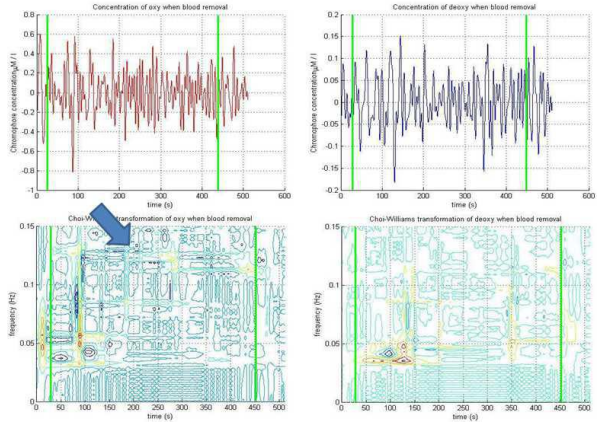

Figure 1: C-W distribution of O_2Hb (left) and CO_2Hb (right) concentration signals during blood removal. The upper panel shows the time course of the O_2Hb and CO_2Hb concentration changes, the lower the C-W distribution (σ=0.5). The vertical green lines mark the onset and offset of blood removal.

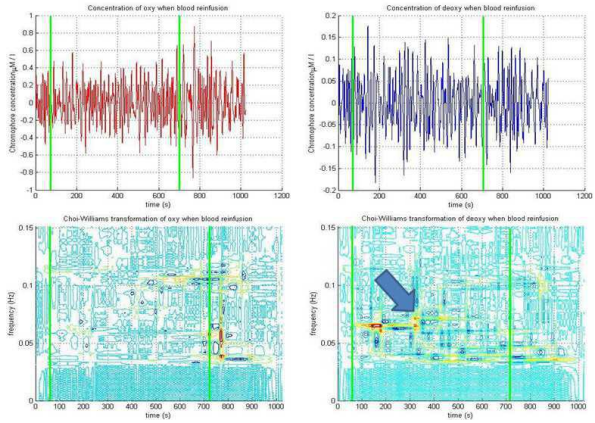

Figure 2. C-W distribution of O_2Hb (left) and CO_2Hb (right) concentration signals during blood reinfusion. The upper panel shows the time course of the O_2Hb and CO_2Hb concentration changes, the lower the C-W distribution (σ=0.5). The vertical green lines mark the onset and offset of blood reinfusion.

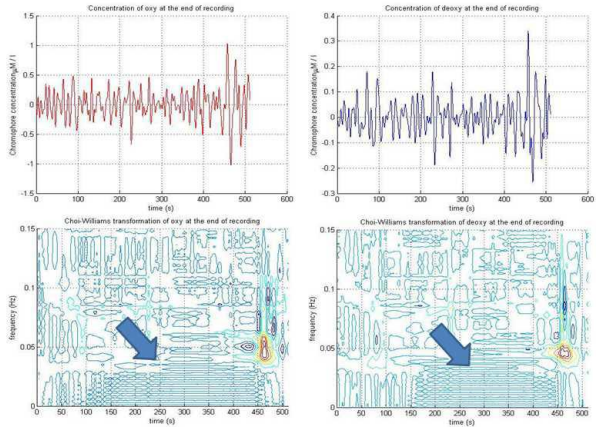

Figure 3. C-W distribution of O_2Hb (left) and CO_2Hb (right) concentration signals during at the end of the monitoring. The upper panel shows the time course of the O_2Hb and CO_2Hb concentration changes, the lower the C-W distribution (σ=0.5).

The results in Figure 1-3 were shown both in time domain (upper) and time-frequency domain(lower).The axes of the upper figures are: horizontal axis is time(s) and the vertical axis is chromphore concentrations (μmol/L). The axes of the lower figures are: horizontal axis is time(s) and the vertical axis is frequency (Hz). Figure 1 showed that power in the LF band, denoting a vagal response due to blood flow perturbation, which is more evident on O_2Hb than on CO_2Hb. Figure 2 showed that there was an increased LF power of CO_2Hb due to cerebral autoregulatioin because the increased oxygen triggered vasoconstriction. Figure 3 showed that there is no power in the VLF band. Oscillations are all in the LF band because it is a long period vascular response.

For each subject, we computed the following variables derived from the Choi-Williams Distribution:

1) The O_2Hb and CO_2Hb power in the VLF and LF bands (P_{VLF} and P_{LF}), during blood removal, blood reinfusion and at the end of the monitoring, for a total of 12 variables.
2) The total power of O_2Hb and CO_2Hb (P_{TOT}), during the same three time intervals, for a total of 6 variables.
3) The O_2Hb and CO_2Hb SCF value in the two bands (SCF_{VLF} and SCF_{LF}) and total (SCF_{TOT}), during the same three time intervals, for a total of 9 variables.
Thus, we organized the data in a matrix containing the 6 subjects as row and 27 measured variables as columns, the total number of variables was 162.

The signal power in the VLF band, LF band and total frequency band were computed by integration of the corresponding time-frequency representation. Since there are three analytical stages, the VLF band and LF band power values were converted into percentage by comparing to the total signal power, see table 1-3.

Variables	P_{VLF}_O_2Hb(%)	P_{LF}_O_2Hb(%)	P_{VLF}_CO_2Hb(%)	P_{LF}_CO_2Hb(%)
Subject 1	30.68867551	61.54420 55	11.619986 47	81.00513 545
Subject 2	16.64811 763	71.5207 9894	17.843588 81	75.33780 148
Subject 3	27.44047 107	63.4708 6868	24.581522 07	65.72830 057
Subject 4	16.87925 651	73.9245 3294	13.479637 92	83.00265 57
Subject 5	11.73696 386	80.6183 4618	15.845336 42	78.30320 422
Subject 6	9.260498 848	81.8244 6692	22.743944 93	70.90363 871
Mean	**18.776**	**72.151**	**17.686**	**75.713**
SD	**8.546**	**8.446**	**5.119**	**6.493**

Table 1. analysis results of power changes of O_2Hb and CO_2Hb during the period of blood removal

Variables	P_{VLF}_O_2Hb(%)	P_{LF}_O_2Hb(%)	P_{VLF}_CO_2Hb(%)	P_{LF}_CO_2Hb(%)
Subject1	25.29527784	69.09768801	11.5624517	82.28847226
Subject2	18.82648998	70.45358962	28.20568403	67.01128425
Subject3	18.03080133	68.17864408	17.59350509	73.14711004
Subject4	18.71469784	76.28820607	17.91248429	77.81918129
Subject5	0.607001994	65.68945505	0.916270821	73.64317435
Subject6	12.86079412	75.04595931	14.84359756	77.66561136
Mean	**15.723**	**70.792**	**15.172**	**75.262**
SD	**8.393**	**4.103**	**8.940**	**5.232**

Table 2. analysis results of power changes of O_2Hb and CO_2Hb during the period of blood reinfusion.

Variables	P_{VLF}_O_2Hb(%)	P_{LF}_O_2Hb(%)	P_{VLF}_CO_2Hb(%)	P_{LF}_CO_2Hb(%)
Subject 1	7.355220366	85.45522974	11.02800894	84.10531039
Subject 2	15.10873463	77.38068006	13.69045667	78.94990268
Subject 3	10.6233097	70.80230521	15.30362044	78.93009618
Subject 4	22.58885968	70.63325517	26.86932401	65.87562301
Subject 5	0.220733154	76.01119815	0.223373446	79.46801936
Subject 6	10.08532773	79.88689619	16.44253697	77.04052917
Mean	**10.997**	**76.695**	**13.926**	**77.395**
SD	**7.505**	**5.645**	**8.625**	**6.114**

Table 3. analysis results of power changes of O_2Hb and CO_2Hb at the end of the recording

According to Table 1-3, it can be observed that the power of O_2Hb and CO_2Hb in the VLF band were progressively reduced during the monitoring. Conversely, the LF power neatly increased for O_2Hb (from 72.151% to 76.695%) and weakly for CO_2Hb (from 75.713% to 77.395%).

The combination of VLF power decrease and LF power increase indicated a clear vascular effect of ozone. In fact, The LF component originates from fluctuations in sympathetic vasomotor control by the central nervous system [12]. This means that we observed a vasomotor activity following OA that lasted about 150 minutes. This numerical result is in accordance to the patients' judgment. Many patients reported that the subjective sensation of overall physical improvement and wellness given by ozone lasted for days after treatment.

4 Conclusions

In conclusion, we applied the Choi-Williams distribution to the NIRS signals to assess the cerebral oxygenation of patients with multiple sclerosis under the ozone autohemotherapy. By computing and comparing the relative power of O_2Hb and CO_2Hb signals in the VLF and LF bands during three different recording periods, it is obvious that the VLF power decreases and the LF power increases. This indicated the endothelial reactivity and showed to be a good result. The time-frequency analysis is an useful tool for characteristics analysis of ozone signals.

Acknowledgements

Grateful acknowledgement is made to my tutor Professor Professor Filippo Molinari who offered me an opportunity to take part in the project and learn and practice the skills on biomedical signal processing. I also appreciate my colleague Samanta Rossati for her suggestions on my work.

References

[1] V.A. Bocci, Scientific and medical aspects of ozone therapy. State of the art, Arch Med Res. 37 (2006) 425-435.

[2] V. A. Bocci, Tropospheric ozone toxicity vs. Usefulness of ozone therapy, Arch Med Res. 38 (2007) 265-267.

[3] A. Larini, L. Bianchi, V. Bocci, The ozone tolerance:I) enhancement of antioxidant enzymes is ozone dose-dependent in jurkat cells, Free Radic Res. 37 (2003) 1163-1168.

[4] V. Bocci, I. Zanardi, V. Travagli, Ozone: a new therapeutic agent in vascular diseases, Am J Cardiovasc drugs. 11 (2011) 73-82.

[5] G. Lintas, F. Molinari, Simonetti V, M. Franzini, W. Liboni, Time and time-frequency analysis of near-infrared signals for the assessment of ozone autohemotherapy long-term effect in multiple sclerosis, Conf Proc IEEE Eng Med Bio Soc. (2013) 6171-6174.

[6] L.Yu, X.J. Lu, H.C. Shi, Q. Wang, Does ozone autohemotherapy have positive effect on neurologic recovery in spontaneous spinal epidural hematoma?, Am J Emerg Med. 32 (2014) 949.e1-949.e2.

[7] A. De Monte, H. van der Zee, V. Bocci, Major ozonated auto-haemotherapy in chronic limb ischemia with ulcerations, J Complement Altern Med. 11 (2005) 363-367.

[8] N. Di Paolo, V. Bocci, D.P. Salvo, G. Palasciano, M. Biagioli, S. Meini, F. Galli, I. Ciari, F. Maccari, F. Cappelletti, M. Di Paolo, E. Gaggiotti, Extracorporeal blood oxygenation and ozonation (EBOO): a controlled trial in patients with peripheral artery disease, Int J Artif Organs. 28 (2005) 1039-1050.

[9] X. Han, M. Bestonzo, F. Molinari, A Near-Infrared Spectroscopy System for Cerebral Oxygenation Monitoring, ICIDM. (2014) 22-27.

[10] F. Molinari, S. Rosati, W. Liboni, E. Negri, O. Mana, G. Allais, C. Benedetto, Time-frequency characterization of cerebral hemodynamics of migraine suffers as assessed by NIRS signals, EURASIP Journal of Advances in Signal Processing. (2010) 1-11.

[11] W. Liboni, F. Molinari, G. Allais, O. Mana, E. Negri, G. Bussone, G. D'Andrea, C. Benedetto, Spectral changes of near-infrared spectroscopy signals in migraineurs with aura reveal an impaired carbon dioxide-regulatory mechanism, Neurol Sci. 30 (2009) S105-S107.

[12] T.B.J.Kuo, C.Ch.Yang, Sh.H.Chan, Selective activation of vasomotor component os SAP spectrum by broad-band stimulation of nucleus reticularis ventrolateralis in the rat, Am J Physiol. 273 (1997) H1291-H1298.

Human Response Delay as a Random Variable: Experiments on Balancing Overdamped Virtual Pendulum

Takashi Suzuki, Ihor Lubashevsky, Shigeru Kanemoto

University of Aizu, Aizu-Wakamatsu, Fukushima, Japan

Abstract

We present the results of our experiments on studying the probabilistic properties of human response delay in balancing virtual pendulum with over-damped dynamics. The overdamping eliminates the effects of inertia and, thereby, reduces the dimensionality of the system under control. The created simulator makes the pendulum (stick) invisible when the angle between it and the upward position is less than 5°. It enables us to measure directly the delay time as the time lag between the moment when the pendulum becomes visible and the moment when a subject starts to move the mouse. It is demonstrated that the response delay time is characterized by a wide distribution sensitive to the particular details of stick balancing process and its possible correlations in the sequence of actions are ignorable. It poses a question about the applicability of standard formalism of delayed differential equations to describing human intermittent control.

Keywords *Human response delay, Human intermittent control, Pendulum balancing, Random variables*

1 Introduction

In the framework of human intermittent control with noise-driven action, the transition from passive to active phases is considered to be probabilistic [1]. It reflects human perception uncertainty and fuzzy evaluation of the current system state before making decision concerning the necessity of correcting the system dynamics. Broadly speaking, during the passive phase the operator accumulates the information about the system state; naturally, this process is not instantaneous but requires some time in addition to the physiological delay in human response. The cumulative effect of the two mechanisms, the accumulation of information about the system state and the physiological delay, can be described by some effective delay time τ. The found stochasticity of human intermittent control in experiments on balancing virtual stick [1] prompts us to expect that this delay time is not a fixed value but a random variable with a relatively wide distribution. To elucidate the probabilistic properties of this cumulative delay in human reaction in controlling unstable mechanical system we have conducted some experiments whose results are reported in the present work.

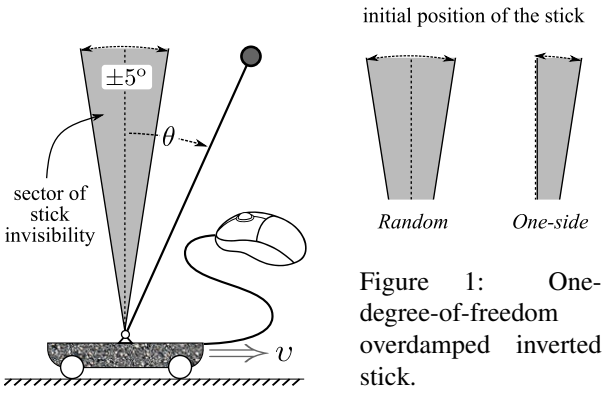

Figure 1: One-degree-of-freedom overdamped inverted stick.

Investigations of response delay in human reactions to various stimuli including visual ones has a relative long history (see, e.g., [2]). Usually in experiments on human visual perception the values of delay time $\tau \gtrsim 100$ ms are detected and they are unimodally distributed within a wide interval; the gamma or Weibull fits are often used to characterize the found results (see, e.g., [3]). During the last decade there has been accumulated some evidence that mental processes contribute substantially to the response delay and such factors as memory load and required attention are essential in this case (e.g., [4, 5]). Taking into account these facts and the possible existence of two mental systems of information processing (see, e.g., reviews [6, 7]) we may expect the response delay time distribution to exhibit complex behavior especially in cases when it is related to decision-making in multifactorial processes like human intermittent control.

2 Methods

As previously [1], the paradigm of balancing an overdamped inverted pendulum was employed. It was implemented via balancing a virtual stick whose dynamics is affected by computer mouse movement (Fig. 1). Namely, the stick dynamics is simulated by numerically solving the ordinary differential equation

$$\tau_\theta \frac{d\theta}{dt} = \sin\theta - \frac{\tau}{l}\vartheta\cos\theta\,, \qquad (1)$$

where θ is the angular deviation of the stick from the vertical position and ϑ is the cart velocity. The parameter τ_θ determines the timescale of the stick motion: the higher the value of τ_θ, the faster the stick falls in the absence of

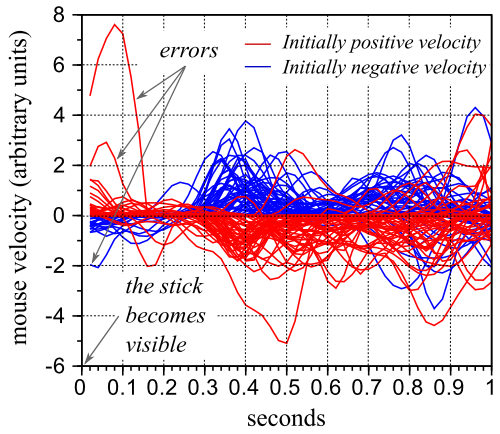

Figure 2: Time pattern of mouse velocity used in measuring the reaction delay time. The origin in this plot is place at the moment when the stick becomes visible for the first time in each balancing trial. The "Random" setup.

human control. The sticks length l determines the characteristic magnitude of the cart displacements required for keeping the stick upright. The cart position was controlled by the operator via a computer mouse. A new feature of this balancing simulator is that the stick becomes invisible within the sector $-5^{\rm o} < \theta < 5^{\rm o}$ (Fig. 1).

The experiments were implemented as a sequence of stick balancing trials. Within one trial the stick is initially placed by the computer inside the sector of invisibility and its further motion is controlled by a subject during the next 5 s or is terminated earlier if the stick has fallen. After the following 3 s designated for subject's rest the system position is restored, the cart is put in the middle of the screen and the stick is automatically returned into the sector of invisibility. Then, the subject again continues the balancing process for the next trial. The total number of trials was about 300 for each subject. Two versions of these experiments were conducted. Within the first one, to be referred to as the "Random" set-up, at the beginning of each trial the stick is placed at an arbitrary chosen position inside the sector of invisibility, whereas within the second "One-side" set-up its initial position can be chosen only from one side of the upward position (Fig. 1). Within the "Random" set-up subjects cannot predict the side on which the stick will appear, whereas for the "One-side" set-up it is determined.

Within one trial the delay time in the human response is measured as the time lag between the moment when the stick becomes visible for the first time and the moment when a subject starts to move the mouse, i.e., when the mouse speed exceeds some threshold introduced to cut-off noise effects. The characteristic time velocity pattern of the mouse motion found in the conducted experiments is shown in Fig. 2.

Eight right-handed healthy male students participated in the experiments. None of them had prior experience in either virtual or real stick balancing. The set of 5-minute exercise sessions enabled them to get familiar with the simulator manipulations before the main experiments.

3 Results and Discussion

Figure 3 demonstrates the characteristic histograms and patterns of the reaction delay time in a sequence of balancing actions; Figure 4 exhibits the corresponding correlation functions of the reaction delay time. In Fig. 3 the data collected within the "One-side"/"Random" set-up are shown in red/blue.

Based on the obtained results we can draw the following conclusions.

(*i*) The human response delay time recorded in these experiments is practically a random variable distributed inside a wide interval. The lower boundary τ_l of this interval can be less than 50 ms (within the obtained accuracy); its upper boundary τ_u is about 500–600 ms. This estimate of τ_l is rather close to the limit response time determined by human physiology (for a resent review see, e.g. [8] and the following discussion), whereas the found value of τ_u is typical for human response delay during complex balancing tasks (see, e.g., [9]).

(*ii*) For different subjects the histograms can exhibit a strong as well as weak dependence on the predictability of the stick motion. Namely, the side on which the stick appears for the first time after the initial system position having been restored. Two subjects, whose actions are illustrated by the diagram shown in the lower right corner in Fig. 3, demonstrated a strong dependence on this factor. Their histograms in the case of the "One-side" set-up are remarkably wider than in the case of the "Random" set-up due to the considerable contribution of the region of small values less than 200–300 ms. This region of rather short response delay may be related to the automatic mechanism of human reaction [9].

(*iii*) The patterns (Fig. 3) and the corresponding correlation functions (Fig. 4) demonstrate the weak correlations (up to their absence) in the response delay time in a stream of subject actions in pendulum balancing. The found correlations for some subjects admits the interpretation, e.g., as certain variations in subject's attention during the balancing task.

During the last decades there have being ongoing debates about the existence of two types of cognitive processes that are fast, automatic, and unconscious and those that are slow, deliberative, and conscious. Moreover they may be assumed to occur from two architecturally (and evolutionarily) distinct cognitive systems. Correspondingly one of these systems must be reflexive, automatic, fast, affective, associative, and primitive, and the second one should be deliberative, controlled, slow, cognitive, propositional, and more uniquely human. Besides, there are accounts assuming the dual-processes to arise parallel and compete with each other, however, there are also arguments against the dual system of decision-making; for a review and discussion of the evidence supporting both sides of the debate a reader may be referred to Refs. [6, 7]. The found dependence of the constructed histograms on subject's individuality argue for the fact that the two cognitive systems are comparable in influence on response delay in human intermittent control. Therefore the re-

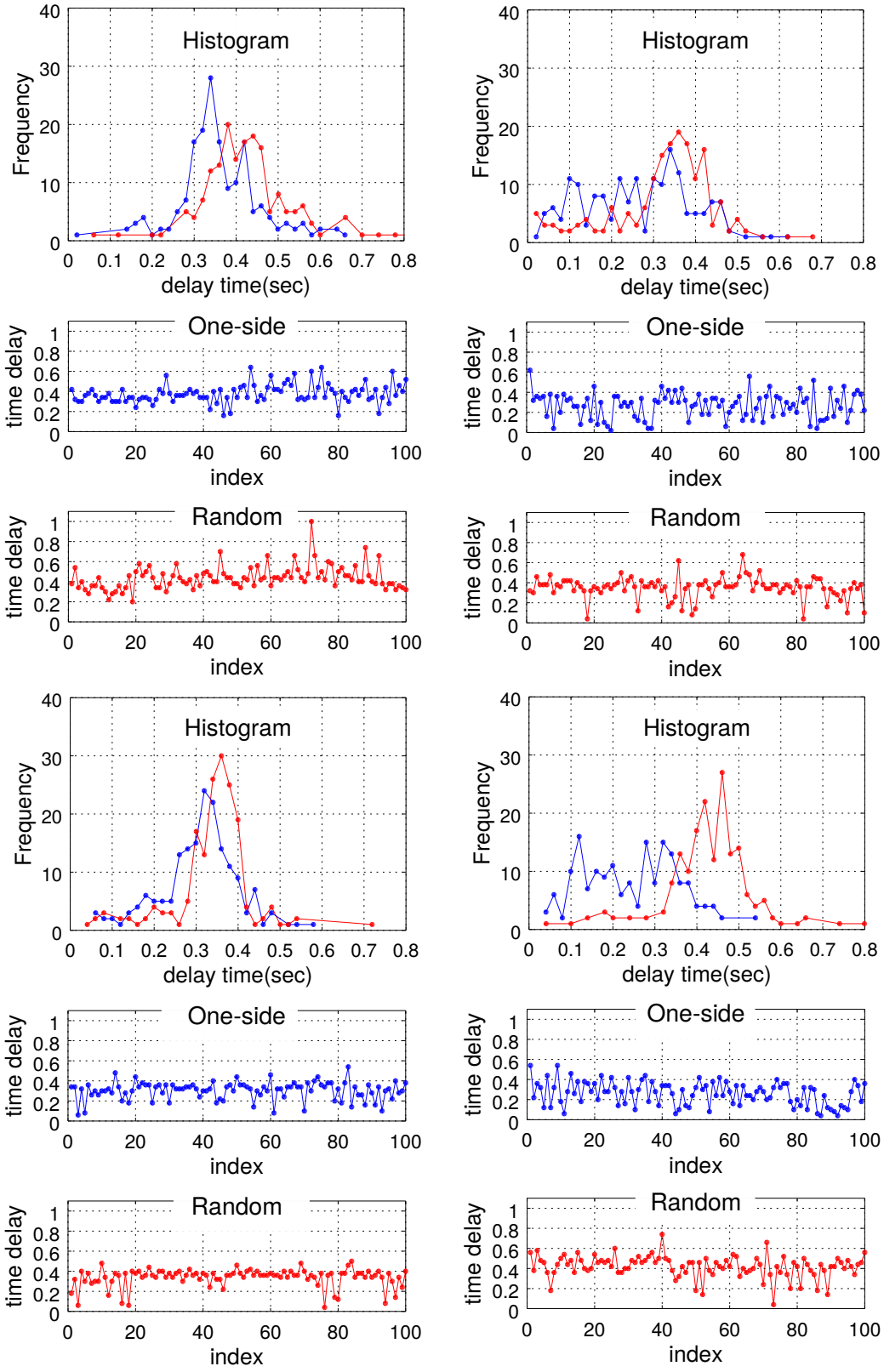

Figure 3: The characteristic histograms and action sequence patterns of response delay time obtained based on the conducted experiments. Blue lines represent the results of the "Random" set-up, red lines match the "One-side" set-up.

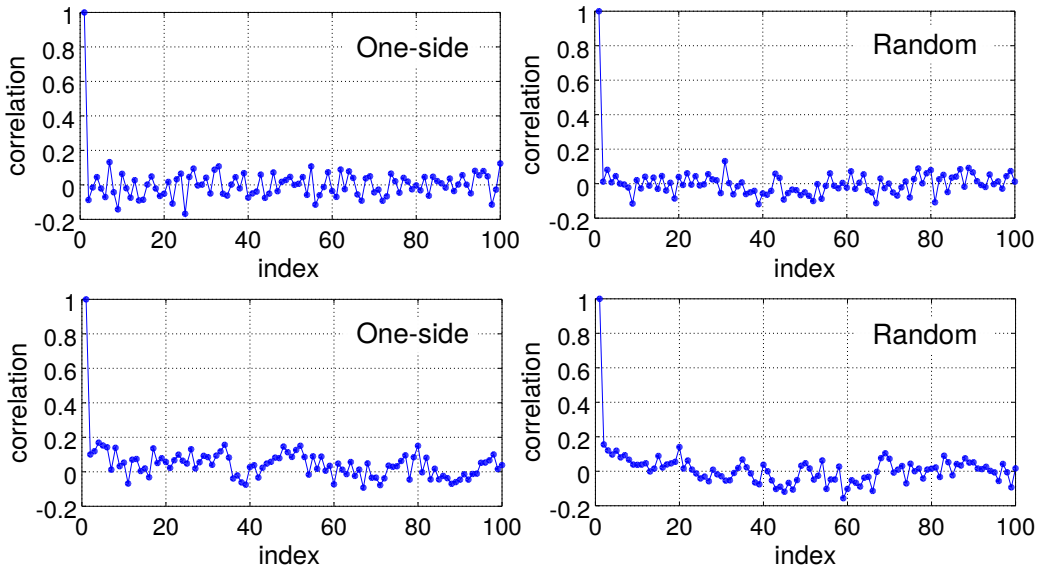

Figure 4: The characteristic correlation functions of the response delay in a sequence of actions in pendulum balancing.

sponse delay must be actually a certain rather complex function of the human state affected by the current situation. It is in a qualitative agreement with the statement that in complex balancing tasks human response may indicate flexible, variable delay and intentional mechanisms associated with central processing [9].

In summary, the demonstrated complex properties of human response delay argue that the delay time, at least in human intermittent control, has to be treated as a random variable which is *simultaneously* characterized by

- a distribution in a wide region,
- the absence of correlations in sequence of actions,
- a dependence on the particular properties of system dynamics and balancing process.

The noted features together allow us to pose a question about the applicability of the standard formalism of delayed differential equations to describing human intermittent control.

References

[1] A. Zgonnikov, I. Lubashevsky, S. Kanemoto, T. Miyazawa, and T. Suzuki: To react or not to react? Intrinsic stochasticity of human control in virtual stick balancing, *Journal of The Royal Society Interface* 11, p. 20140636, 2014.

[2] T. Zandt: Analysis of Response Time Distributions, in: *Stevens' Handbook of Experimental Psychology, Volume 4, Methodology in Experimental Psychology* (H. Pashle and J. Wixted, eds.), pp. 461–516, New York: John Wiley & Sons, Inc, 3rd ed., 2002.

[3] E. Palmer, T. Horowitz, A. Torralba, and J. Wolfe: What are the shapes of response time distributions in visual search?, *Journal of Experimental Psychology: Human Perception and Performance* 37, pp. 58–71, 2011.

[4] E. F. Ester, T. C. Ho, S. D. Brown, and J. T. Serences: Variability in visual working memory ability limits the efficiency of perceptual decision making, *Journal of Vision* 14, no. 4, pp. 2(1–12), 2014.

[5] B. Pearson, J. Raškevičius, P. M. Bays, Y. Pertzov, and M. Husain, "Working memory retrieval as a decision process," *Journal of Vision* 14, pp. 2 (pp. 1–15), 2014.

[6] J. Evans: Dual-processing accounts of reasoning, judgment, and social cognition, *Annual Review of Psychology* 59, pp. 255–278, 2008.

[7] A. Rustichini: Dual or unitary system? Two alternative models of decision making, *Cognitive, Affective, & Behavioral Neuroscience* 8, pp. 355–362, 2008.

[8] R. Nijhawan: Visual prediction: Psychophysics and neurophysiology of compensation for time delays, *Behavioral and Brain Sciences* 31, pp. 179–198, 2008.

[9] I. Loram, M. Lakie, and P. Gawthrop: Visual control of stable and unstable loads: what is the feedback delay and extent of linear time-invariant control?, *The Journal of Physiology* 587, pp. 1343–1365, 2009.

Address for correspondence:

Ihor Lubashevsky
University of Aizu
i-lubash@u-aizu.ac.jp

Mesolevel Intermittency of Human Control: Car-Driving Simulator Experiments

Ryoji Yamauchi, Ihor Lubashevsky, Hiromasa Ando

University of Aizu, Japan

Abstract

Based on the open source engine "TORCS" a rather simple car-driving simulator was created and used to analyze the basic features of human behavior in car-driving within the car-following setup. Eight subjects with different skill in driving real cars participated in these experiments. They were instructed to drive a virtual car without overtaking and losing sight of the lead car driven by computer at a fixed speed. In a series of experiments, the lead car speed was set equal to 60, 80, 100, and 120 km/h. In the present work based on the collected data we single out three characteristic styles of car-driving. Namely, we analyze the statistical properties and time patterns of the car pedal position—the pedal cposition directly reflects subject actions. The discriminated typical styles of driving can be classified as "pulsating," "stationary," and the mixture of the previous two. The latter style admits the interpretation as intermittent transitions between the "pulsating" and "stationary" styles, we call this feature mesolevel intermittency of human control.

Keywords *Human control, Intermittency, Car-driving simulator, Styles of driving*

1 Introduction

During the last decades, a new concept of human actions in stabilizing mechanical systems—called the human intermittent control—was developed (see, e.g., [1]). It considers human operators not to be capable of controlling system dynamics continuously and, as a result, their actions may be conceived of as a sequence of alternate phases of active and passive behavior. The switching between these phases is supposed to be event-driven. The particular mechanism governing the event-driven transitions between the passive and active phases is a matter of ongoing debates. Recently, a novel concept of noise-driven control activation has been developed [2] as a more advanced alternative to the conventional threshold-driven activation. In this concept, the transition from passive to active phases is probabilistic and reflects human perception and fuzzy evaluation of the current system state before making a decision concerning the necessity of correcting the system dynamics. During the passive phase, the control is halted and the system moves on its own. Broadly speaking, during the passive phase the operator accumulates the information about the system state. The individual fragments of active phase can be regarded as open-loop control, which is due to the delay in human reaction (e.g., [1]).

Driving a car in following a lead car is a characteristic example of human control. Recently using the data collected in our preliminary experiments we presented some evidence for that the car-driving should be categorized as a generalized intermittent control with noise-driven activation [3]. In the given work, based on data collected in new series of experiments described below, we analyze the characteristic types of driver actions called car-driving styles. The main attention is focused on a certain "mixed" style admitting interpretation as new class of intermittent phenomena—mesolevel intermittency—whose description is the main goal of the present work.

In the reported experiments, a car-driving simulator based on the TORCS engine (The Open Racing Car Simulator) was used; TORCS is a highly portable multi platform car racing simulator [4] widely used in car racing games as well as academic research. One of the reasons for choosing a car-driving simulator for studying human actions in the car-driving is the possibility of separating the intrinsic human factors from effects of the various heterogeneities of real road structures; the virtual environment is controlled completely.

2 Experiments

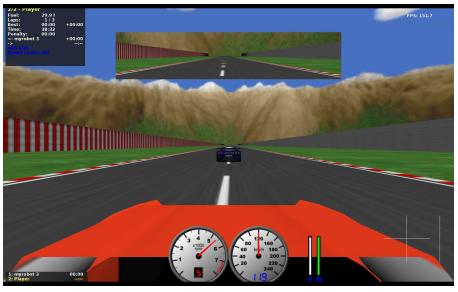

Figure 1: The view of car-following

The conducted experiments were confined to the car-following setup, which is illustrated in Fig. 1. Eight male students of age around 22 and 24 participated in these experiments. Their experience of driving real cars is presented by Table 1. The subjects were instructed to drive

Table 1: Subjects' characteristics and their driving experience.

ID	Driving License; issued	Driving Frequency
1	Yes; 2 months ago	Rarely
2	Yes; 3 years ago	Rarely
3	Yes; 1 year ago	Sometimes
4	Yes; 3 years ago	Often
5	Yes; 4 years ago	Rarely
6	Yes; 2 years ago	Daily
7	Yes; 4 years ago	Rarely
8	Yes; 3 years ago	Daily

a virtual car in any convenient way in following the lead car (driven by a computer at a certain fixed velocity V) without overtaking and losing sight of it. In the series of experiments, the lead car speed was set equal to 60 km/h, 80 km/h, 100 km/h, and 120 km/h. All of the involved subjects participated in these four experimental setups. A detailed description of the virtual car driven by the subjects, the characteristic of car engine, and the track topology can be found in [5].

3 Results

The position of the accelerator and brake pedals directly reflects driver actions and, so, should be included in the list of the phase variables describing the car dynamics. For this reason in the presented analysis the main attention is focused on the characteristic properties of the car pedal position and its time variations showing the driver actions in the active phase of car motion control. The collected experimental data have been used to construct the time patterns and the histograms of pedal position for the accelerator and brake pedals as well as the histograms of their time derivatives. Below this histograms will be refereed to as p-distribution and dp/dt-distribution, respectively.

The characteristic p- and dp/dt-distributions obtained in the conducted experiments are shown in Figs. 2–4. Each of these figures depicts also the corresponding time pattern of the car pedal position, the positive values are related to the acceleration pedal, the negative values represent the brake pedal.

We have singled out three different styles of car-driving using the found characteristic forms of the histograms and the time patterns of pedal position. Let us discuss these styles individually.

Style 1: Pulsating. This style of driving has been demonstrated by subject 3 for the lead car speed $V = 80$–100–120 km/h. The characteristic feature of Style 1 is often transitions between keeping the acceleration pedal pressed near a certain position $p_{\max}$ and releasing it. The brake pedal practically is not used. As a result, the histogram of the pedal position p has two maxima located at $p = 0$, with a clear peak on the histogram, and $p_{\max}$. The histogram of the pedal position time derivative has heavy tails and a sharp peak at the origin.

Style 2: Stationary. This style of driving has been demonstrated by subject 4 for $V = 100$–120 km/h, subject 6 for $V = 80$ km/h, subject 7 for $V = 80$–100–120 km/h, and subject 8 for $V = 120$ km/h. Both the histograms actually are symmetric. Within the given style the time patterns show that the drivers preferred to keep the acceleration pedal pressed continuously.

Style 3: Intermittent. This style of driving has been demonstrated by subject 1 for $V = 60$–80–100 km/h, subject 4 for $V = 60$–80 km/h, subject 5 for $V = 80$–100–120 km/h, subject 6 for the lead car speed equal to 60 and 120 km/h, and subject 8 for $V = 60$–80–100 km/h. Its characteristic feature is practically a unimodal form of the p-distribution except for the one-dot-peak at $p = 0$, this form looks similar to the Laplace distribution. The dp/dt-distribution is essentially non-symmetric, its parts corresponding to the positive and negative values differ substantially in shape. Based on this data it is possible to think that the car braking was implemented via a fast release of the acceleration pedal; in the region of negative values this histogram is characterized by heavy tails. The time pattern looks like a irregular sequence of alternative fragments, when the drivers released the pedals highly often and when they preferred to keep the acceleration pedal pressed for a long time.

Strictly speaking, two additional styles of driving can be singled out [6]. One of them was demonstrated by subject 1 for $V = 120$ km/h, subject 5 for $V = 60$ km/h, and subject 6 for $V = 100$ km/h. Within this style the p-distribution is really symmetric with respect to the point $p_{\max}$ of its maximum and takes the form of the Laplace distribution. However, the dp/dt-distribution is not symmetric remarkably. The other is found in data for subject 4 at $V = 100$–120 km/h, subject 6 at $V = 80$ km/h, subject 7 at $V = 80$–100–120 km/h, and subject 8 at $V = 120$ km/h. Both the corresponding histograms actually are symmetric. Within the given style the time patterns show that the drivers preferred to the acceleration pedal pressed continuously. In the present analysis we regard them as some versions of Style 3.

The shown histograms are ordered according to their symmetry, so Styles 1 and 2 may be treated as some limit cases, whereas Style 3 (and its other versions) may treated as their mixture at the first glance. However, Style 3 possesses individual characteristics not exhibited by Styles 1 and 2 as demonstrated by the p-distribution and dp/dt-distributions, which allows us to regard it as individual style of car driving.

Summarizing the obtained results, the pedal position time patterns found for Style 3 enable us to put forward the concept of *mesolevel intermittency* of human intermittent control. It describes irregular transitions between different modes of behavior acceptable in implementing

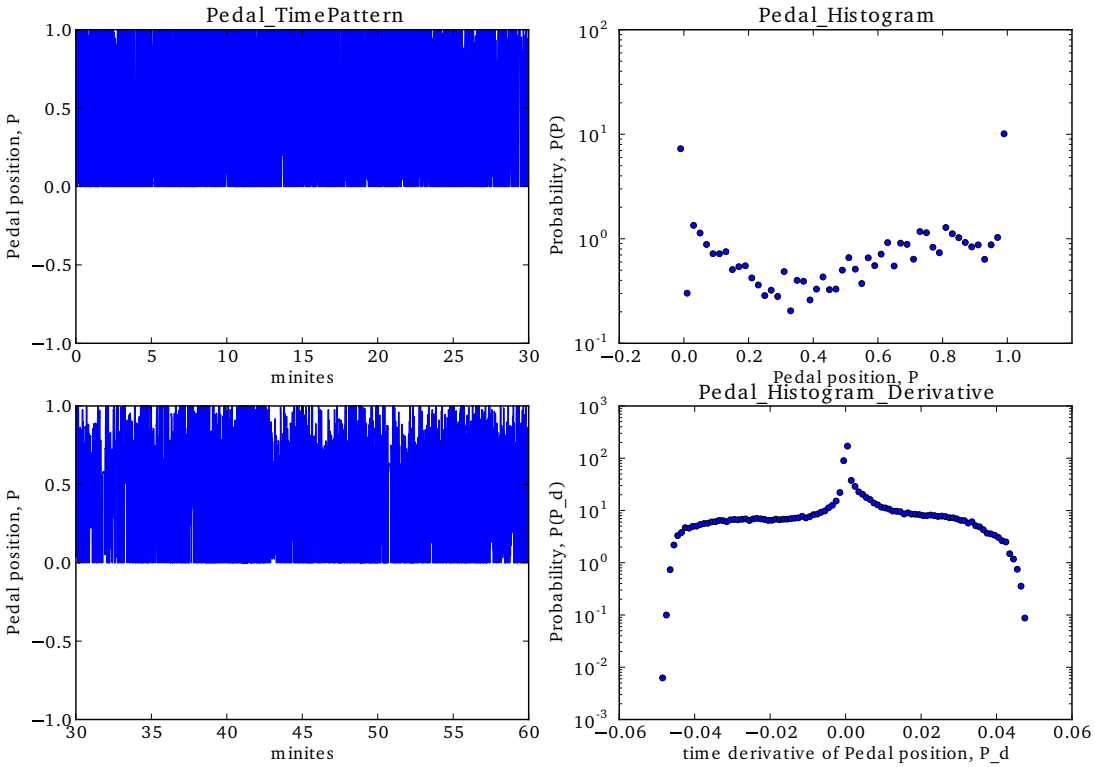

Figure 2: **Style 1**. The time pattern of pedal position and histograms of the pedal position and its time derivative.

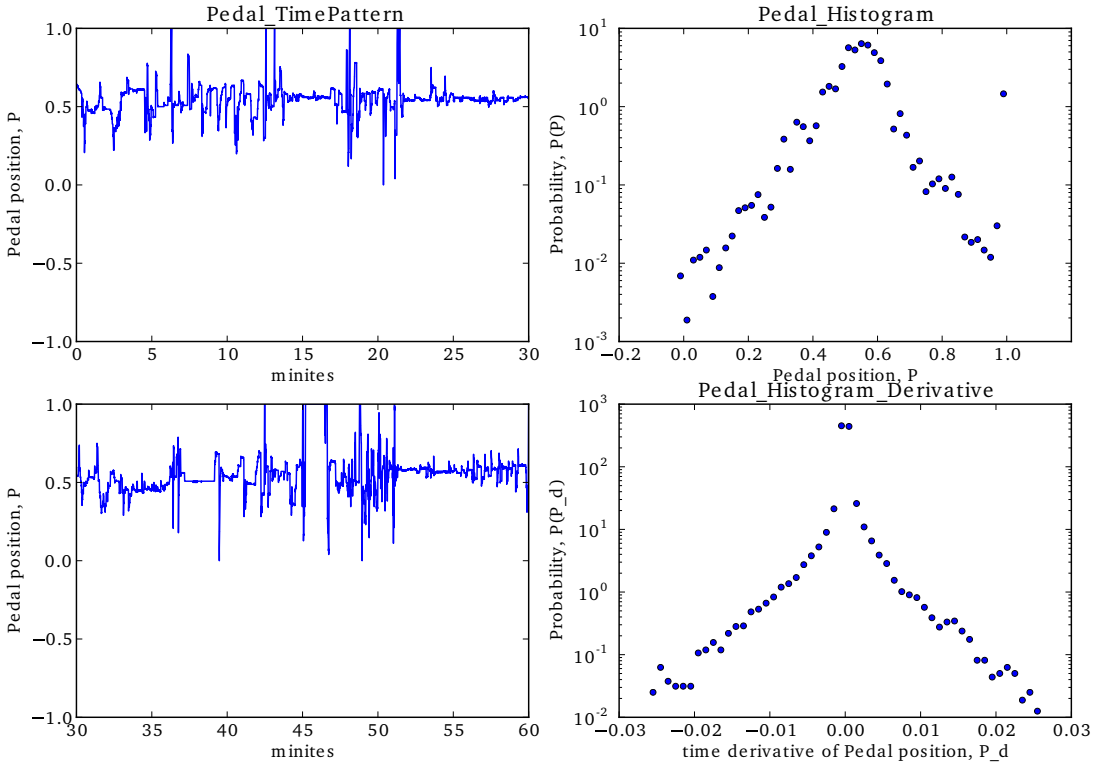

Figure 3: **Style 2**. The time pattern of pedal position and histograms of the pedal position and its time derivative.

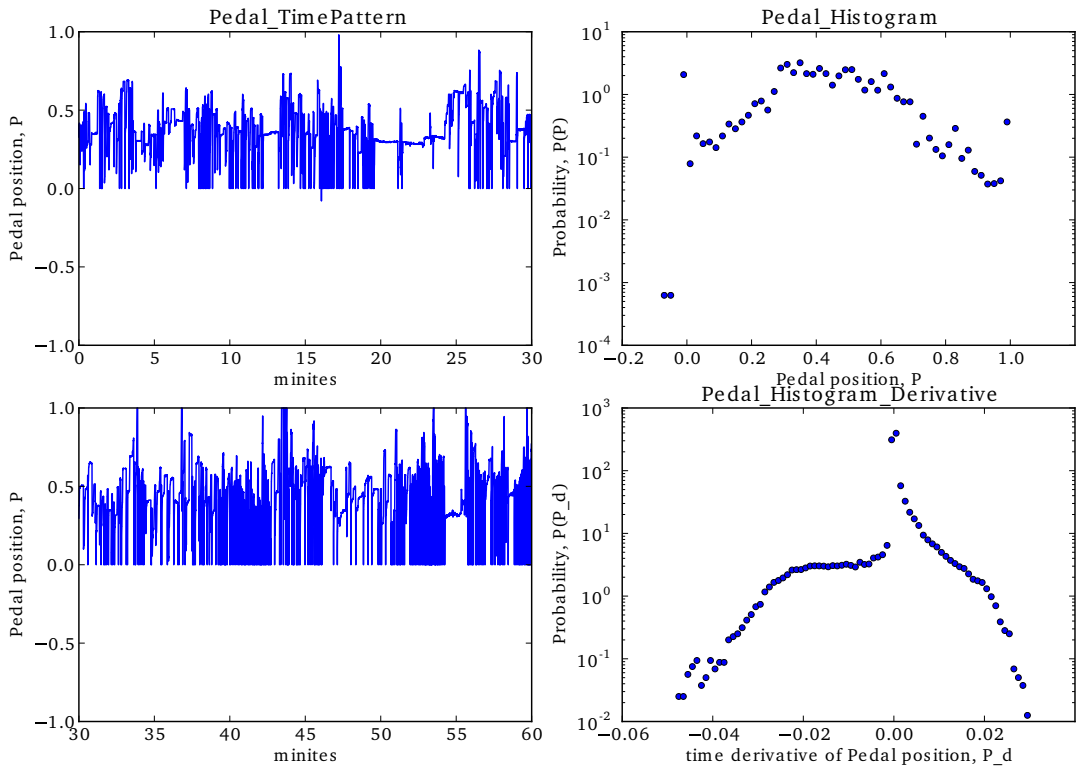

Figure 4: **Style 3**. The time pattern of pedal position and histograms of the pedal position and its time derivative.

some task as, for example, the balancing of inverted pendulum or the car-driving. In the conducted experiments the mesolevel intermittency is instantiated in irregular transitions between Styles 1 and 2. It should be noted that this intermittency characterizes irregular transitions between the basic styles of driving rather than the passive and active phases of the standard (microlevel) intermittent control. Possible mechanisms responsible for the switching between the basic styles of driving is the matter of further research.

Acknowledgements

We thank Maxim Mozgovoy for his help in creating the simulator and the students of Complex Systems Modeling Laboratory (University of Aizu) for their participation in the experiments.

References

[1] Ian D. Loram, Henrik Gollee, Martin Lakie, and Peter J. Gawthrop. Human control of an inverted pendulum: is continuous control necessary? Is intermittent control effective? Is intermittent control physiological? *Journal of Physiology*, 589(2):307–324, 2011.

[2] Arkady Zgonnikov, Ihor Lubashevsky, Shigeru Kanemoto, Toru Miyazawa, and Takashi Suzuki. To react or not to react? Intrinsic stochasticity of human control in virtual stick balancing. *Journal of The Royal Society Interface*, 11:20140636, 2014.

[3] Hiromasa Ando, Ihor Lubashevsky, Arkady Zgonnikov, and Yoshiaki Saito. Statistical Properties of Car Following: Theory and Driving Simulator Experiments. In *Proceedings of the 46th ISCIE International Symposium on Stochastic Systems Theory and Its Applications Kyoto, Nov. 1-2, 2014*, pages 149–155, Kyoto, 2015.

[4] The official site of TORCS. `http://torcs.sourceforge.net/index.php`.

[5] Ihor Lubashevsky and Hiromasa Ando. Intermittent Control Properties of Car Following: Theory and Driving Simulator Experiments. e-print: arXiv:1609.01812 (2016).

[6] Ryoji Yamauchi. Styles of the car-driving as human intermittent control: Experiments with car-driving simulator. Master's thesis, University of Aizu, 2016. Supervized by Prof. Ihor Lubashevsky.

Address for correspondence:

Ihor Lubashevsky
University of Aizu
i-lubash@u-aizu.ac.jp

Reinforcement Learning with Status Quo Bias

K. Hijikata, I. Lubashevsky

Computer Science Division, University of Aizu, Japan

Abstract

We put forward a concept of human intermittent control as a sequence of point-like moments when a subject makes decision on activating or halting the control. These decision-making events are assumed to be driven by the information on the state of system under control the subject accumulate continuously. As the basic formalism of describing this type decision making the generalized model of reinforcement learning with status quo bias is proposed. Numerical simulation demonstrates that the proposed model does possess the required properties of quasi-continuous behavior.

Keywords *Intermittent Control, Reinforcement Learning, Status Quo Bias*

1 Introduction: Model Background

Nowadays intermittent control has become a novel paradigm of human behavior in controlling various unstable systems (see, e.g. [1]). It implies discontinuous control, which repeatedly switches off and on instead of being always active. As a result, human actions in such control form a sequence of alternate phases of passive and active behavior, where the transitions between the phases are governed by event-driven mechanisms.

The threshold mechanism governing the event-driven activation of human control is now widely accepted. It claims that the control is activated when the discrepancy between the goal and the actual system state exceeds a certain threshold. Confining our discussion to conscious actions of humans, we note that the threshold mechanics tacitly assumes human actions to be rather deterministic in nature. Recently [2], based on experimental data on human balancing of virtual overdamped pendulum we put forward a new concept of noise-driving activation of intermittent control which considers human actions highly irregular. In this case human response to the discrepancy between the goal and actual state should be treated as a substantially probabilistic phenomenon.

The individual active phase fragments admit the interpretation as open-loop control (e.g., [1]). It implies that a subject practically does not respond to changes in the system state after the current active phase fragment being initiated and before its termination. In this way we come to the conclusion that the real active behavior of a subject in controlling such systems may be conceived of as a sequence of point-like events when the subject decides to activate the control and, then, to halt its implementation. Between these events his behavior is really passive in spite of the fact that in the active phase the subject executes some actions. We hypothesize that these point-like events can be regarded as the moments when the subject makes decision to change the current control state depending on the information about the system dynamics accumulated between the decision-making moments. This accumulation of information about the system state needs finite time because of the bounded capacity of human cognition and the delay in information processing.

A fairly suitable candidate for describing such processes is the model of reinforcement learning. Unfortunately, this model cannot be applied directly to describing human intermittent control because on time scales much larger than the elementary step in the decision-making the process is strongly discontinuous. The preference for an option is reflected only in the cumulative number of moments when the agent has selected the given option.

The purpose of our research is to generalize the reinforcement learning paradigm to make it applicable to modeling human intermittent control. We turn to the concept of the status quo bias—preference for the current state of affairs—in human behavior [3], for a recent review of status quo bias see, e.g., [4]. Due to status quo bias the agent will select continuously one option for a relatively long sequence of decision-making events, which endows its actions with quasi-continuous dynamics. It opens the gate to describing human intermittent control as (*i*) continuous accumulation of information about the state of controlled system within a certain priority function and (*ii*) and the sequence of events when the subject makes decision on changing the control state in response to the accumulated information.

In the present paper we propose a fairly simple model for reinforcement learning with status quo bias and demonstrate that it does meet the desired property of quasi-continuous dynamics. The gist of this model is the concept of multichannel information processing used previously [5] to describe human learning affected by novelty-seeking (intrinsic motivation).

It should be noted that status quo bias can be seen as a sort of decision inertia implying a perceptual rather than value-based mechanism. Recently [6] a new reinforcement-learning model has been proposed within the classical one-channel paradigm to explain the human decision bias in favor of the same decision as in the previous trial. This model is partly incorporated into the multichannel model to be developed below.

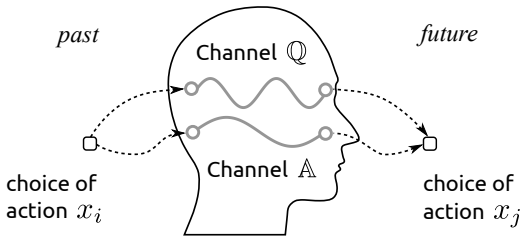

Figure 1: Two channels of information processing. Channel $\mathbb{Q}$, which processes the information about the rewards, continuously interacts with Channel $\mathbb{A}$, which deals with information not directly related to the rewards.

2 Model

An agent is assumed to make repeated choice between finite number of options i, $i = \overline{1, N}$ and to accumulate the information about the chosen options. The accumulated information affects its preferences which, in turn, affects the probability of particular option choice. We consider that the information proceeding is implemented via two independent mental channels. One of them is the deliberate analysis of the obtained rewards, the other is irrational and exhibits status quo bias which can be justified turning to a reason like this. "If just now we have chosen a new option it is not reasonable to choose another option immediately, it could be better to wait until the quality of the chosen option becomes clear." The two channels interact via their cumulative effect on the selection (Fig. 1).

Deliberate Information Processing

Withing the channel $\mathbb{Q}$ each option, first, is associated with the corresponding reward r_i the agent receives each time it has chosen option i; generally the rewards are non-stationary, $r_i = r_i(t)$. Second, the preference of choosing option i is quantified by a value q_i; the value q_i results from the experience the agent gains each time it chooses the corresponding option.

At every time step $t_k = k\tau$ ($k \in \mathbb{N}$, time is measured in units of the time gap between the neighboring decision-making events) the preference values q_i are, first, updated with currently received rewards r_i, and, second, subjected to the memory loss effect, namely,

$$q_i(t_{k+1}) = q_i(t_k) + \delta_{ii_k} r_{i_k}(t_k) - \epsilon_q q_i(t_k)\,, \qquad (1)$$

where the index i_k points to the option i_k chosen at the given time step t_k and the value $0 < \epsilon_q < 1$ quantifies the agent memory capacity. Because of the memory loss effect events in the past separated from the present by time intervals much longer than the time $T_q = 1/\epsilon_q$ practically do not affect the agent behavior. Here the Kronecker delta δ_{ii_k} ($\delta_{ii_k} = 1$ for $i = i_k$ and $\delta_{ii_k} = 0$ for $i \neq i_k$) reflects our assumption that only the for chosen options the preference value is increased by the obtained reward. We accept this assumption because the foregone payoffs may be ignored in the context of the analyzed systems. For the same reason we do not take into account the fact that people usually overweight low-probability events and underweight high-probability events.

Irrational Information Processing

The channel $\mathbb{A}$ allows for the effect of status quo bias on choosing the same option at the next time moment. This effect is taking into account via ascribing some additive preference value $\Delta_i > 0$ to choosing the same option i. The value of $\Delta_i > 0$ gradually decreases as the time interval T_i of keeping the same choice continuously increases

$$\Delta_i(T_i) = \Delta_i^0 \cdot \exp\big(-T_i/T_a\big). \qquad (2)$$

It imitates the human preference to wait a certain time T_a in order to recognize the quality of the made choice.

Decision-Making

Evaluation of events, conscious and unconscious, is relative, for a discussion see, e.g., [7]. Within our model it implies that an arbitrary shift with respect to the quantities evaluating the preferences of agent choice

$$q_i \to q_i + C(t)\,, \qquad (3)$$

where $C(t)$ is some function of time t, should not affect the probability p_i of choosing any option i. In physics a dependence $p(q)$ meeting this condition is well known, it is the Boltzmann or Gibbs distribution written in the form allowing for the status quo bias:

$$p_i(q_i) = \frac{1}{Z} \exp\left\{\beta\left[q_i + \Delta_i \delta_{ii_{k-1}}\right]\right\}. \qquad (4)$$

Here Z is the partition function whose list of arguments comprises the quantities $\{q_j\}$ for all the options $\{j\}$; it has been introduced to normalize the probabilities $\{p_i\}$ to unity. Thereby

$$Z = \sum_{i=1}^{N} \exp\left\{\beta\left[q_i + \Delta_i \delta_{ii_{k-1}}\right]\right\}. \qquad (5)$$

It is worthy of noting that the present model can be described in terms of the probability of choosing option j written as

$$\mathcal{P}_{i\to j} = \frac{1}{Z'} \exp\left\{\beta\left[q_j - q_i\right]\right\},$$

if its previous choice is i ($i \neq j$) and the probability of choosing the same option i given by the expression

$$\mathcal{P}_{i\to i} = \frac{1}{Z'} \exp\left\{\beta\Delta_i\right\}.$$

Here the partition function Z' is related to the previous one, Z, as $Z' = Z \cdot \exp\{\beta q_i\}$. The constant β is a system parameter; its inverse value, $1/\beta$, actually specifies the fuzzy thresholds of the agent perception. When for two options i and $j \neq i$ the corresponding quantities q_i and q_j meet the inequalities $|q_i - q_j| \lesssim 1/\beta$, the agent is not able to distinguish between them in preference, and, consequently, has to regard the two options equivalent, so their choice is practically equiprobable. Measuring the quantities $\{q_i\}$ in the units of $1/\beta$ we may set $\beta = 1$, which will be used below.

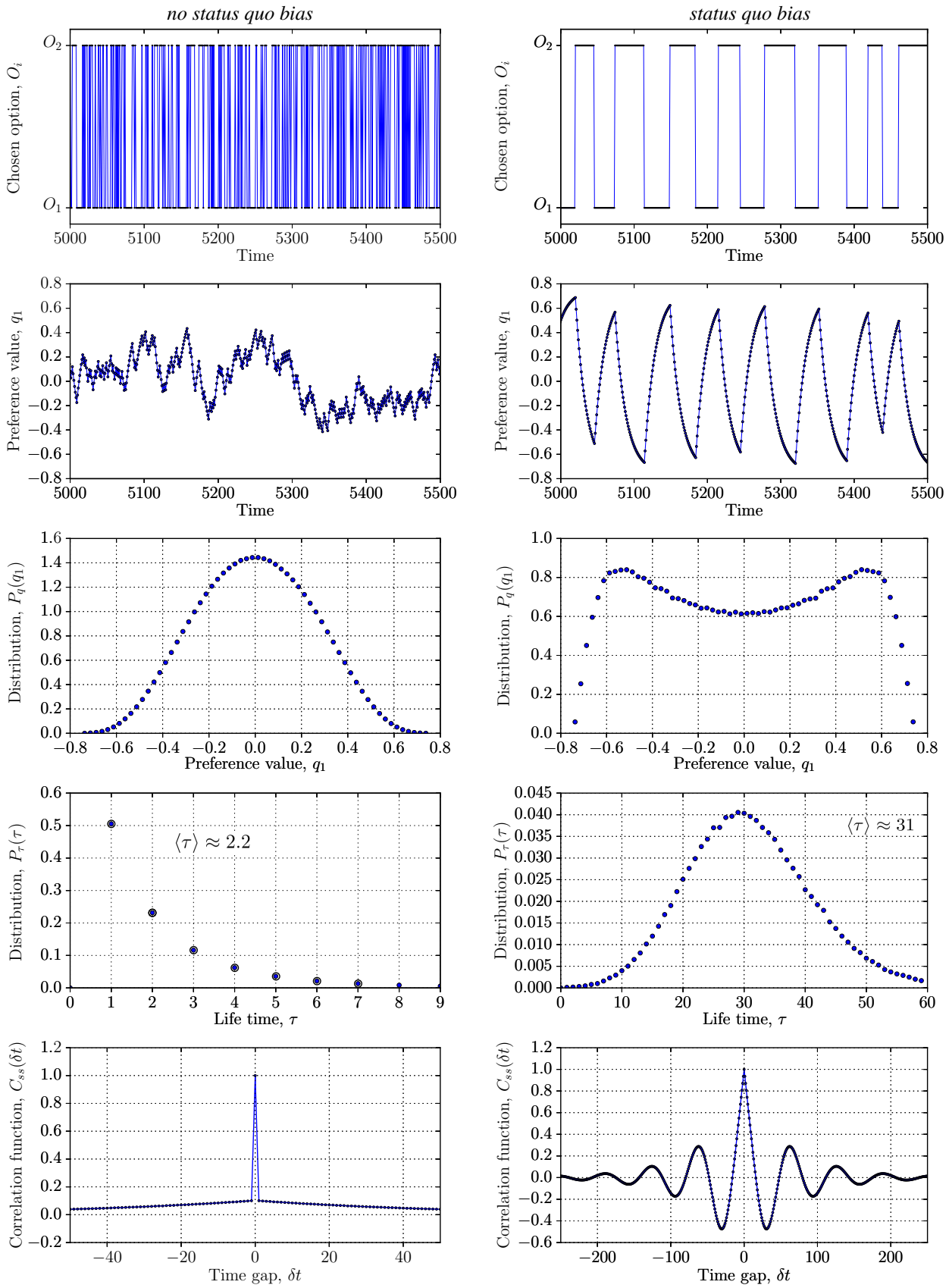

Figure 2: Statistical properties of reinforcement learning for the system with two equivalent options. In simulation the following quantities were used: $T_q = 15$, $T_a = 15$, $r = 0.1$ which corresponds to $q_{\max} = rT_q = 1.5$, $\Delta_0 = 10$. Duration of simulation was 10^6 time units.

Simulated Model

In the dimensionless form the developed model is as follows. At each time moment t_k the preference values of the agent choice are updated according to the equation

$$q_i(t_{k+1}) = (1-\epsilon_q)q_i(t_k) + \left[\delta_{ii_k} - \frac{1}{N}\right] r_{i_k}(t_k)\,, \quad \text{(6a)}$$

where i_k the index of the option chosen at time t_k, the status quo bias effect is governed by the folloiwng equation

$$\Delta_i(t_k) = \Delta_i(t_{k-1})(1-\epsilon_a)\delta_{ii_{k-1}} + \Delta_i^0(1-\delta_{ii_{k-1}})\,, \quad \text{(6b)}$$

where $\epsilon_a = 1/T_a$ and the probability of this choice is

$$p_i(t_k) = \frac{\exp\{q_i(t_k) + \Delta_i(t_k)\delta_{ii_{k-1}}\}}{\sum\limits_{j=1}^{N}\exp\{q_j(t_k) + \Delta_j(t_k)\delta_{ji_{k-1}}\}}\,. \quad \text{(6c)}$$

In deriving equation (6a) we have taken into account the invariance of the given system with respect to transformation (3) and have constructed the function $C(t_k)$ such that the equality

$$\sum_{j=1}^{N} q_j(t_k) = 0$$

hold for all the time moments $\{t_k\}$. At the initial time $t = 0$ ($k = 0$) all the preference values are set equal to zero

$$q_j|_{t=0} = 0 \quad \text{for} \quad \forall j\,. \quad \text{(6d)}$$

Model (6) was studied numerically.

3 Results and Conclusion

To analyze the effect of status quo bias on the continuity of this kind reinforcement learning we have analyzed the choice dynamics for two options equivalent in properties, i.e., $r_i = r$ and $\Delta_i^0 = \Delta$. Results of simulation which allow us to compare the system dynamics with and without status quo bais are shown in Fig. 2. The parameters used in simulation are given in its caption.

The system parameters were chosen such that without the status quo bias effect the two options would be chosen with comparable frequency at any time and the agent does not gain a preference with respect one of them. Thereby the distribution function $P_q(q_i)$ is unimodal and the autocorrelation function $C_{ss}(\delta)$ of the option choice possesses a significant maximum at the time gap equal to zero, $\delta t = 0$. Starting from $\delta t = 1$ the correlations are depressed. The tails of the autocorrelation function propagating over scales about $\delta t \gtrsim 40$ are caused by probabilistic fluctuations of the option preference. They macroscopic, however, cannot be related to smooth variations in the choice dynamics. It is also justified by the estimate of the mean life time of a chosen option.

The situation changes radically in the case of significant status quo bias. The life time of a chosen option becomes macroscopic, which is justified by its distribution, the shown time pattens of the choice dynamics and the preference value variations, as well as the autocorrelation function. In this case the distribution $P_q(q_i)$ of preference values becomes bimodal. It reflects the fact that due to status quo bias the agent is able to evaluate the quality of newly chosen option, which endows the system with quasi-continuous dynamics.

In summary, the obtained results allows us to state that the paradigm of reinforcement learning with status quo bias can provide the desired framework for modeling human intermittent control over mechanical systems.

References

[1] I. D. Loram, H. Gollee, M. Lakie, and P. J. Gawthrop. Human control of an inverted pendulum: is continuous control necessary? Is intermittent control effective? Is intermittent control physiological? *Journal of Physiology*, 589(2):307–324, 2011.

[2] A. Zgonnikov, I. Lubashevsky, S. Kanemoto, T. Miyazawa, and T. Suzuki. To react or not to react? Intrinsic stochasticity of human control in virtual stick balancing. *Journal of The Royal Society Interface*, 11:20140636, 2014.

[3] W. Samuelson and R. Zeckhauser. Status quo bias in decision making. *Journal of Risk and Uncertainty*, 1(1):7–59, 1988.

[4] S. Eidelman and C. S. Crandall. Bias in favor of the status quo. *Social and Personality Psychology Compass*, 6(3):270–281, 2012.

[5] A. Zgonnikov and I. Lubashevsky. Unstable Dynamics of Adaptation in Unknown Environment due to Novelty Seeking. *Advances in Complex Systems*, 17(3 & 4):1450013 (17 pages), 2014.

[6] R. Akaishi, K. Umeda, A. Nagase, and K. Sakai. Autonomous Mechanism of Internal Choice Estimate Underlies Decision Inertia. *Neuron*, 81(1):195–206, 2014.

[7] M. P. Paulus and A. J. Yu. Emotion and decision-making: affect-driven belief systems in anxiety and depression. *Trends in cognitive sciences*, 16(9):476–483, September 2012.

Address for correspondence:

Name Surname: Ihor Lubashevsky
Institution: University of Aizu
email address: i-lubash@u-aizu.ac.jp

Development of a reassemblable robot for automatic ultrasound diagnosis

N Kato[1], S Matsuno[2], M Tateyama[1], Y Ogawa[3], K Kotani[3,4], Y Jimbo[1]

[1]Graduate School of Engineering, The University of Tokyo, Japan;
[2]Graduate School of Frontier Sciences, The University of Tokyo, Japan;
[3]Research Center for Advanced Science and Technology, The University of Tokyo, Japan;
[4]Japan Science and Technology Agency PRESTO, Japan;

Abstract

Ultrasound diagnosis enables us to evaluate lifestyle diseases noninvasively and it is valuable for detection of plaque and obtaining several indices, such as flow mediated dilation. On the other hand, it is difficult to diagnose by using ultrasound device at home or clinic where there is no medical specialist. Previous study proposed a re-assemblable robot with ultrasound diagnosis. However, assuming home or clinical use, the robot must control its probe automatically by itself. In this study, we propose the automatic measurement by using reassemblable robot for ultrasound diagnosis. Firstly, we improve kinematics of the robot and confirm that the influence of noise from sensor was small from simulation. Secondly, we design and create a new phantom for calibration of two probes and we show we can measure with enough accuracy. Finally, assuming measurement for brachial artery, we build an automatic ultrasound diagnosis method and evaluate by phantom. These results show the possibility of an automatic diagnosis by the reassemblable robot.

Keywords *Ultrasound diagnosis, Reassemblable robot, Automatic diagnosis*

1 Introduction

Lifesytle diseases are the leading cause of death in Japan, therefore early diagnosis of them is important. Ultrasound diagnosis can enable to evaluate lifestyle diseases noninvasively. It is valuable for detection of plaque and some index, such as flow mediated dilation (FMD), obtaining from medical ultrasound images. Lifestyle diseases cause us to occur serious symptom unconsciously, thus we need to detect them earlier and spread how to diagnose them widely. Besides, bioinstruments for home use have become more popular associated with trend of health-conscious. Some index from ultrasound diagnosis varies corresponding to lifestyle [1]. Developing simple measurement devices will improve health care at home.

On the other hand, ultrasound diagnosis needs professional skills and enough experiences. Consequently, it is difficult to diagnose where there is no medical specialist. Several robots were developed for direct assistance for manipulating probe and mechanism construction for remote inspection. However, ultrasound diagnosis has many requirements in inspection. Hence, it was desired to build new robots fulfilling those requirements for various inspection. To solve this problem, reassemblable robot with ultrasound diagnosis was proposed for measuring multiple body regions [2], [3]. Assuming home or clinical use, the robot must control its probe automatically, therefore improving mechanism of the robot is desired. In this study, we consider about automatic measurement with the reassemblable robot for ultrasound diagnosis. We establish automatic measure-ment system and evaluate it. Firstly, we consider the robot can be improved. Particularly in kinematics, we implement certain kinematics taken into account constraint condition following reality and estimate about locating the probe. Secondly, we confirm installing another probe is effective for diagnosis and create new phantom for measuring probe location. Thirdly, we investigate space restrictions of probe operation in automatic recognition system in actual measurement. Finally, assuming measurement for brachial artery, we build an automatic ultrasound diagnosis method.

2 Kinematics

2.1 Methods

Iwahashi and Matsuno developed reassemblable robot for home care which has a parallel link construction having six degrees of freedom [2], [3]. The robot has three trays and can move in two directions (Fig. 1). There are two coordinate systems in this robot. First one is top board rectangular coordinate system (System 1) and second one is general rectangular coordinate system (System 2). In system 1, the directions of x axis is determined the directions to the rotation bearing of tray 1 from the center of top board, z axis is determined as normal vector of top board and y axis is orthogonal to x and z axis. In system 2, the origin of coordinate is initial position of tray 3. X and Y axis are the direction of movement of tray and Z axis is determined as opposite direction to gravity. The robot obtains angles between top board and each link with angle sensors, and we defined φ_i (i=1, 2, 3) as the angles from angle sensor values.

The position of each tray (x_i, y_i, z_i) is calculated from φ_i by solving inverse kinematics. Previous study [2] calculated the top board position from an angle and accelerate sensors. However, the kinematics of the previous study [2] was redundant, because it had no

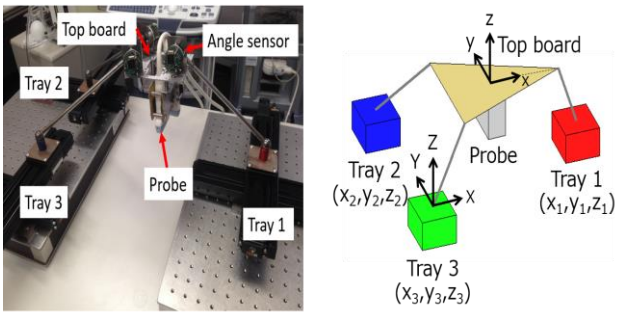

Fig. 1 Schematic of the reassemblable robot

constrains in position information.

We propose a new kinematics including realistic constrains. Because each tray moves on same plane, we can add a constraint condition by the following equations

$$(-y_2z_1+y_2z_3+y_3z_1-y_3z_2)x+(-x_1z_2+x_1z_3+x_2z_1-x_2z_3-x_3z_1+x_3z_2)y \\ +(x_1y_2-x_1y_3+x_2y_3-x_3y_2)z+(-x_1y_2z_3+x_1y_3z_2-x_2y_3z_1+x_3y_2z_1)=0 \quad (1)$$

From each tray position, the normal vector of the tray plane $\vec{n}=(n_1,n_2,n_3)$ can be obtained. Finally, the angle of the top board (θ_X,θ_Y) in system 2 can be calculated by

$$\begin{cases} -\cos\theta_x \sin\theta_y = n_1 \\ \sin\theta_x = n_2 \\ -\cos\theta_x \cos\theta_y = n_3 \end{cases} \quad (2)$$

The rest of the procedures for calculating the operation command of robot movement is same with previous study [2].

The advantage of proposed kinematics is to know the probe position only from angle sensor. When the probe moves, firstly, initial tray position is derived by solving reverse kinematics about initial probe position obtained from angle sensor. Secondly, same calculation about moved tray position is conducted. Finally, the amount of movement about tray is decided. However the output value from angle sensor contains noises, there is an error between measured and calculated value of probe position. We evaluate the accuracy and the robustness to sensor noise in new kinematics by simulation. Firstly, we set initial probe posture using an angle sensor added noise. Secondly, we send movement command to the robot shifting ±50 mm and ±20 degree and compare measured posture and calibration posture derived from forward kinematics. The noise is set from specification of the angle sensor (TS5667N120, Tamagawa seiki co., ltd.). The noise is white Gaussian noise and average is zero and standard deviation is 5.5×10^{-2} degree.

2.2 Results

When the probe moved -50mm to z-direction, each error in location and position was maximum. This was caused by influence of error in angle sensor the most strongly because the angle dramatically changed when the probe moved to z-direction. Next, we moved the probe -50mm to z-direction 100 times which produced the strongest error. This robot was designed as motion resolution of probe was 0.1mm about its location and 0.1 degree about its position. We got the result difference between command and measured result. The error average about location was 0.028 mm and standard deviation was 0.014 mm. About position, the error average was 0.013 degree and standard deviation was 0.01 degree. Each error was smaller than motion resolution, therefore we conclude the new kinematics has enough performance for calculating the probe position against the sensor noise.

3 Probe attachment and calibration

3.1 Methods

We manipulate a probe using information of the latest image in ultrasound diagnosis. The robot also carries out the appropriate calibration and evaluation of probe from image while it moves its probe in diagnosis. However, information from images is limited and there are regions where we cannot obtain information about location and position. To solve this problem, we attach second probe orthogonally (Probe 2) to the original probe (Probe 1). Diagnosis with multiple probes is valuable owing to improvement of inspection efficiency and simplification of tracking target. Moreover, we will be able to evaluate more about calibrating because of additional information from Probe 2.

In order to inspect with multiple probes, we must decide relation between location and position of each probe. We need to build simple calibration method because we attach and calibrate probes according to targets. By the way, measuring a phantom is a simple calibration method. However, it is impossible to measure six degrees of freedom by conventional calibration methods [4], [5], [6].

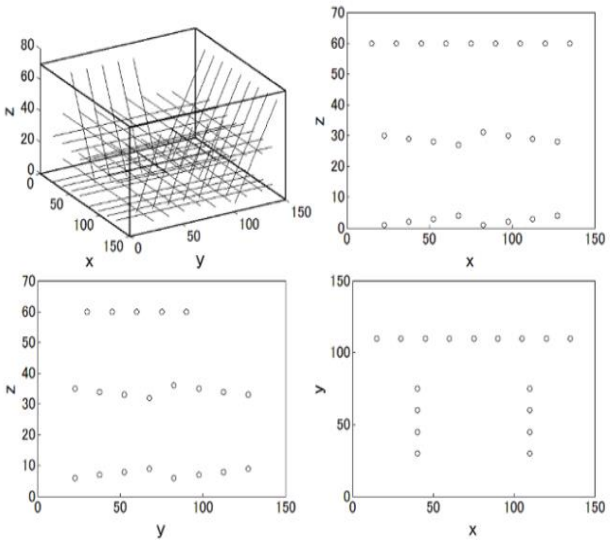

Fig. 2 Phantom design

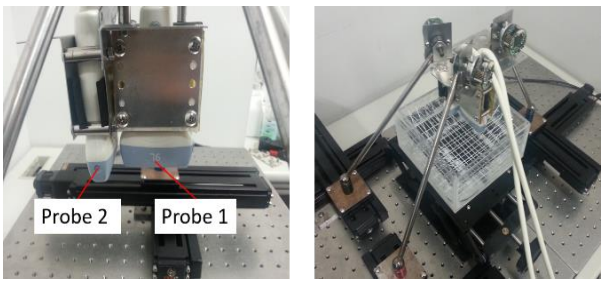

Fig. 3 Setting of multiple probes

In this chapter, we design and create new phantom with which we can measure location and position of probes from ultrasound image. Secondly, we establish calibration method and evaluate it.

Figure 2 shows a conceptual diagram and each cross-sectional view of new phantom. We create the phantom by drilling holes on an acrylic plastic like each cross-sectional view and plastic rods through holes wires like the conceptual diagram. We can calculate location and position of each probe from slope of points of wire, length of line and distance from bottom drawn on ultrasound image. Especially, we can measure x-coordinate from two points of different distance from bottom and y-coordinate from wires put diagonally which convert lateral direction variation into longitudinal one. Regarding θ_y, we determine there is no slope around y-axis when two vertical wires are displayed.

In this method, we can derive a relation between location and position of each probe by the measured images of the phantom. Therefore, when we move and rotate the probe to each direction, we speculate calculated location and position will move similarly. Then, we examine correspondence between measured movement and true movement after the probes were moved and rotated from initial posture to each direction. Figure 3 shows setting of multiple probes and conditions of experiment.

3.2 Results

Figure 4 shows lateral and rotation movement of probe to each direction corresponds to measured probe variation of location and position. Table 1 gives errors about location and position. We evaluated these errors by calculating the diameter of brachial artery which was important index for FMD. Diameter of brachial artery is about 4 mm typically. About an error of x-direction, when we put the probe on 0.52 mm shifted place from the center of blood vessel, the measured diameter of vessel was 3.86 mm assuming blood vessel was a cylinder. In this case, error of FMD was 3.6 %. Similarly, about an error around z-axis, when we put the probe on 0.93° shifted place from the center of blood vessel, vessel diameter was 3.95 mm and the error was 1.3 %. Influence on inspection accuracy of FMD is smaller than 5-10% in each case which is coefficient of variation at hospitals. Thus utilizing this method can calibrate with enough accuracy. For more precise measurement, we need to reconsider the material for phantom and redesign taking into account target for measurement.

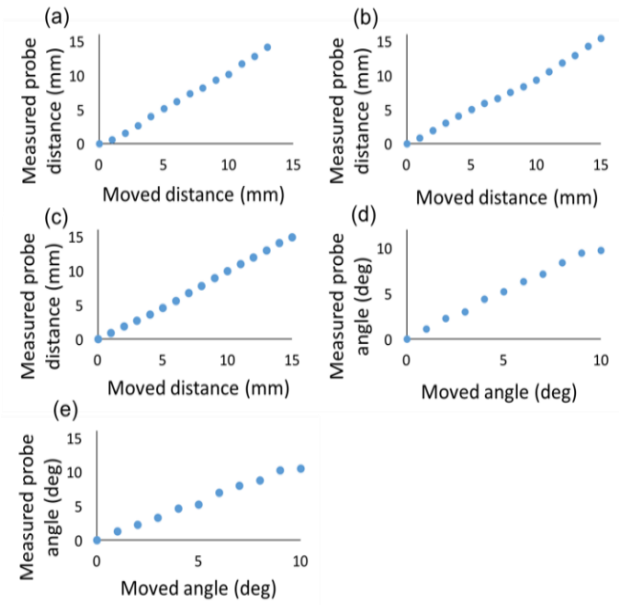

Fig. 4 Measured probe movement versus true probe movement
(a) x (b) y (c) z (d) θ_x (e) θ_z

Table 1 Result of errors in probe movement (mean±std)

x (mm)	y (mm)	z (mm)	θ_x (deg)	θ_z (deg)
0.11±0.41	0.15±0.33	0.16±0.17	0.20±0.22	0.55±0.38

4 The space restrictions of probe operation in automatic recognition system

In actual measurement by using robot, we need to take into consideration of calibration of probe and the space restrictions of probe operation varying in accordance with the target. Thus, we investigated the space restrictions in some artery-measurement situations. We defined targets as the carotid artery and brachial artery, which are popular in medical inspection. We reassembled the robot. The length of links was 464 mm (link 1) and 482 mm (link 2, 3) for the carotid artery. On the other hand, the length of them was 237 mm (link 1) and 264 mm (link 2, 3) for the brachial artery. Figure 5 shows the state of the actual measurements for arteries and ultrasound images of them by using the reassembleable robot. Especially in the carotid artery, it is more complicated to build an automatic recognition system than brachial artery because we need to take into consideration of the restriction of movement territory, as probes may hit against a jaw. Also, we need to consider the involuntary movement caused by breathing. Thus, the proper instructions for controlling the breathing should be given to the patients.

5 Automatic blood vessel recognition

5.1 Methods

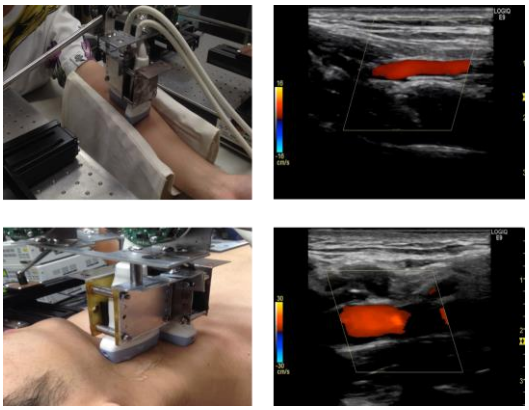

Fig. 5 Measuring the arteries and color Doppler images
(a) Brachial artery, (b) Carotid artery

We discuss about the automatic blood vessel recognition system for brachial artery. We set brachial artery as a target for inspection and identify issues from actual inspection and robot movement. The robot demands automatic target recognition for inspection. We propose a new inspection technique for measuring the blood vessel.

Figure 6 is a schematic of the proposed automatic blood vessel recognition method with two probes for brachial arteries. First, the probes were controlled to downwards until it touched the skin (Fig. 6 (a)). The judgement of touching was evaluated with a rate of brightness variation (contrast) of the probe 1. When the probe is above the skin, the brightness is low. When the probe touches the skin, the brightness is high. Second, the angle of the probe θ_x was adjusted as the probe 1 touches firmly (Fig. 6 (b)). The judgement of firmly touching was evaluated with a ratio of black pixels in the left of the image and those in the right. Third, the probes were moved to the center of the vessel (Fig. 6 (c)). The position was evaluated by the image of the probe 2 as the vessel was on the center of the image. Finally, the angle of the probe 1 was rotated to the correct position (Fig. 6 (d)). The angle was evaluated with a length of the vessel in the image.

We performed following three experiments with Doppler flow phantom (Model 524 Peripheral Vascular Doppler Flow Phantom, ATS Laboratories) in order to detect blood vessel; (a) touching judgement by position z and the contrast, (b) firmly touching judgment by and the ratio of black pixels, and (c) correct rotation by θ_z. The probe recognized that it touched to the target in parallel when a ratio of the number of black pixels is below 1.2 in experiment (b).

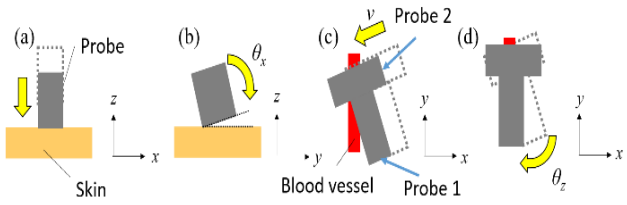

Fig.6 Procedure to automatic detection of the vessel

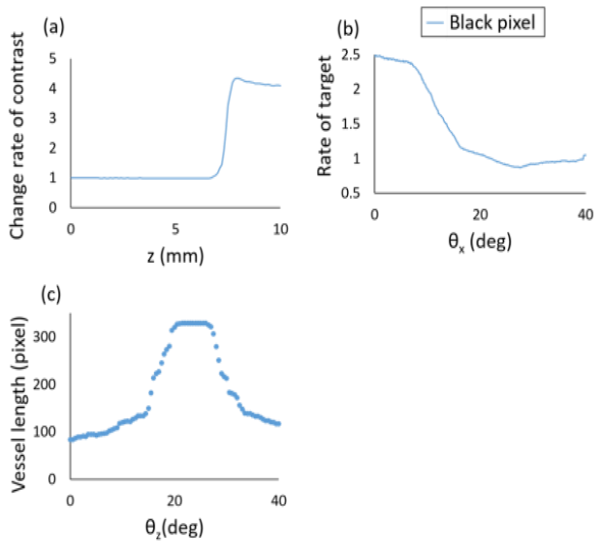

Fig.7 Evaluation of probe contact judgement

5.2 Results

Figure 7 shows results. From the experiment (a), after the amount of movement was over 7 mm variation ratio of brightness was more than four (Fig. 7 (a)). This means probe touched the target. From the experiment (b), initial value in the black pixel was more than two, and we confirmed the value fell to near one when the probe rotated in parallel and judged the probe had contact firmly to the target. From the experiment (c), we confirmed the length of vessel increased as the probe rotated and decreased after the maximum length was detected (Fig. 7 (c)). Figure 7 shows the proposed method can be used for the vessel recognition system.

6 Conclusions

We propose an automatic measurement system using reassemblable robot for automatic ultrasound diagnosis. Firstly, we improved kinematics of the robot. Secondly, we designed and created a new phantom for calibration of two probes. Finally, we performed an automatic blood vessel recognition experiment and evaluation by phantom. We showed the possibility to inspect automatically with this robot.

Acknowledgements

This study was supported in part by KAKENHI (15H05324) and SCOPE.

References

[1] J.D. Allen et al. Time course of improved flow-mediated dilation after short-term exercise training. *Medicine and Science in Sports and Exercise.* 35(5):847-853, 2003.

[2] Y. Iwahashi et al. Development of reassemblable robot for home care with ultrasonic diagnosis. *Proc. of annual conference of Electronics, Information and Systems, IEEJ.* MBE-13-036:61-64, 2013.

[3] S. Matsuno et al. Calibration of reassemblable ultrasonic diagnosis robot for home care. *Proc. of annual conference of Electronics, Information and Systems, IEEJ.* PS4-3:1813-1814, 2014.

[4] J. Kowal et al. On the development and comparative evaluation of an ultrasound B-mode probe calibration method. *Computer Aided Surgery.* 8(3): 107-119, 2003.

[5] D. F. Leotta. An efficient calibration method for freehand 3-D ultrasound imaging systems. *Ultrasound in Medicine & Biology.* 30(7): 999-1008, 2004.

[6] T. K. Chen et al. A real-time freehand ultrasound calibration system with automatic accuracy feedback and control. *Ultrasound in Medicine & Biology.* 35(1): 79-93, 2009.

Address for correspondence:

Naoyuki Kato
Graduate school of Engineering, The University of Tokyo, Japan
kato@neuron.t.u-tokyo.ac.jp

Neurophysiological Evaluation of Visual and Haptic Sense Mechanisms in Grip Movements with Artificial Visual Transmission Delay

Yasushi Fujiwara[1], Kazutomo Yunokuchi[1], Atsuo Maruyama[2], Atsuo Nuruki[1]

1 Graduate School of Science and Engineering, Kagoshima University, Japan;
2 Health Sciences, Niigata University of Health and Welfare, Japan;

Abstract

Prior studies have been performed about weight illusions showing that grip movements can manipulate visual feedback. However, in these experiments, usually only the appearance of the object is changed, such as in the Material-Weight Illusion (MWI) or Size-Weight Illusion (SWI), the most famous among the weight illusions. Here, we confirm the phenomenon of the weight illusion being induced by creating a temporal difference between an object's motion information (lifting) and its visual information (lifted). We used here a virtual reality device with a stereoscopic object gripping system using two haptic devices. We show that it was the manipulation of time that caused the illusion. Still, we could observe neither change of grip force (GF) nor load force (LF) in grip movements of the participants.

Using transcranial magnetic stimulation (TMS), we investigated the activity of the primary motor cortex by examining the excited state of this area during presentation of a visual transmission delay. We observed that the amplitudes of motor evoked potentials were different between various transmission delay times. This result suggests that the weight illusion is associated with activation of the motor cortex and not muscle activity.

Keywords Grip, Transcranial Magnetic Stimulation, Motor Evoked Potentials, Weight Perception, Haptic Device

1 Introduction

Many previous studies about grip movements, such as that by Kinoshita et al[1], suggest that grip force (GF) is influenced by the skin-friction of objects, and many studies have focused on the force on each finger during gripping[2] and the predictive control model of grip[3]. However, the detailed control mechanisms of GF have not yet been revealed.

All humans perceive the weight of an object when they grasp it. Therefore, studies about illusory weight perception caused by visual information have also been conducted. Some typical examples are the Size-Weight Illusion (SWI), which is induced by object size[4][5], and the Material-Weight Illusion (MWI), which is induced by object weight[6]. It has been shown that visual information is a critical factor for the perception of weight, but the exact cause of such illusions is not yet known. There are two theories that hypothesize about the cause. One presumes that it is induced by the difference between the internal motion prediction and real feedback[7]-[11] , and the other that it is induced by the difference between the quantity that is perceived by high level perception, which is independent from the sensorimotor system and is expected [12]-[14].

In this study, we investigated the influence of differences in the time (delay/advance) between visual information and motor information on weight perception. Furthermore, we investigated the electromyogram (EMG) of FDI to check whether they change with GF, as well as brain activity associated with the illusion that is induced by timing differences. We conclude that the primary motor cortex, which is the final output of the motor command system, plays a role.

2 Materials and Methods

2.1 Subjects

All experimental procedures were conducted with the approval of the institutional ethics committee. Our subjects were two right-handed, healthy male adults (Age: 23). All subjects received a description of the experiment and a check of their brain before the experiment. We obtained written informed consent from all subjects.

2.2 Experimental Setting

In this study, we constructed a virtual environment to produce a temporal difference between visual and motor information (Fig.1), and used a 3D-monitor and a half-mirror to produce three-dimensional visual information. Furthermore, two haptic devices (Phantom® Desktop, 3D Systems, Rock Hill, SC, USA) were used for this system in order to interfere with the object in the virtual environment, and each device was mounted on the index finger and thumb. We used a blue cube with a weight of 200 g and a side-length of 5 cm as a gripping object so as not to induce the SWI or MWI.

All subjects lifted the object under a control condition and one of the six test stimuli so as not to be biased by other test stimuli. The control visual-

stimulation had a 0 ms difference in visual information, and the test stimuli had 0 ms, 20 ms, 40 ms, 60 ms, 100 ms, or 160 ms temporal delay-difference. Each test stimulus was presented when the GF exceeded 0.2 N, and was presented a total of 15 times. In addition, control and test stimuli were randomly presented.

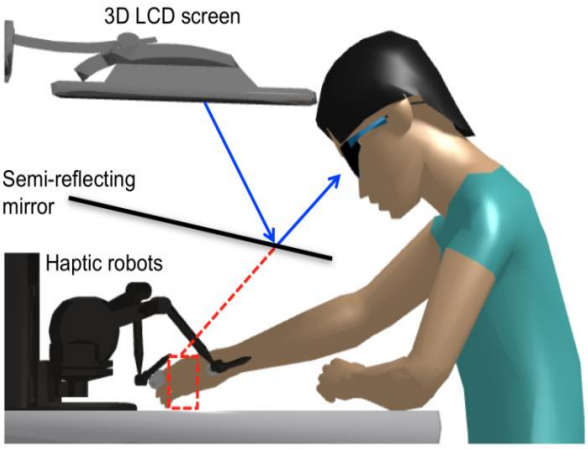

Fig.1: Experiment System

2.3 Transcranial Magnetic Stimulation

We used transcranial magnetic stimulation (TMS) to investigate the effects on weight perception of temporal differences in information, as well as to look at the excitability of primary motor cortex. We measured motor evoked potentials (MEP) from the first dorsal interosseous muscle (FDI). TMS intensity was 110% of the resting motor threshold, which was the minimum stimulation intensity required for an MEP with an amplitude of at least 50 μV to appear with a probability of 50%.

2.4 MEP and Myoelectric Measurement

We used an electromyograph (Neuro pack Σ, Nihon Kohden Corp., Tokyo, Japan) and magnetic stimulator (Magstim200, The Magstim Company Ltd, Carmarthenshire, UK) with a double coil for MEP measurement. The target muscle was FDI, and electromyography data were obtained through an A/D converter (USB-6009, National Instruments, Austin, TX, USA). Electromyographs were measured over 26 ms starting with grip onset until the MEP was induced. Equipment and the target muscle used were the same as for the MEP measurement. In all experiments, MEP and electromyograph were measured and were high- and low-pass filtered at 3000 and 5 Hz, respectively.

2.5 Experimental Task

First, the object was presented 1000 ms after presentation of a fixation point. Then, the subjects were stimulated by TMS as the MEP was recorded. A beep tone was played 300 ms after the object presentation onset. Subjects gripped the object after hearing the beep, and lifted it to a marked position 5 cm away. A second TMS pulse was administered 800 ms after the time delay, and an MEP was recorded. Subjects released the object when the screen became blank after a third beep. This comprised one trial. After odd-numbered trials, subjects immediately performed the next trial. After even numbered trials, however, subjects were given enough time to rest to stabilize their resting muscle potential. TMS was presented a total of 180 times through all experiment tasks. All of the subjects practiced this task without test stimuli and TMS before performing experimental trials.

2.6 Analysis

We analyzed the MEPs by adding, averaging, and calculating the amplification rate of the MEP amplitude, during resting and the visual delay task. For muscle potentials, we calculated iEMG from electromyography data.

3 Results

3.1 The Illusion of Weight Perception

The result of weight perception in the visual delay tasks is shown in Fig.2 The vertical axis and shows the rate at which subjects reported the object as heavier than the reference, and the horizontal axis shows the temporally manipulated delay-time [ms]. Error bars indicate standard error. Repeated measures ANOVA results show significant relation ships($F(5, 54)= 2.386$, $p < 0.01$). After using Sheffe's method of correction for multiple comparisons show there in 0 vs 100 and 160, 20 vs 100 and 160, 40 vs 160, and 60 vs 160 ms .

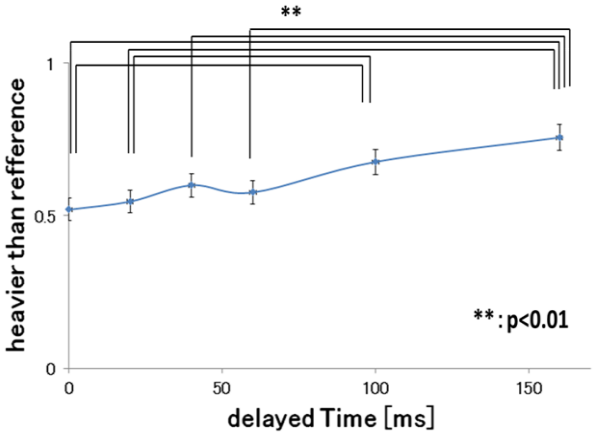

Fig.2: Weight Perception

3.3 GF on Delay and Precede Stimuli

Fig.3 shows the results of GF during the grip movements of subjects for each stimulus condition. The vertical axis shows peak GF during movement (in N)

and the horizontal axis shows the test stimuli. Data were obtained from built-in software in the two haptic devices. Error bars indicate standard error. Repeated measures ANOVA results show no significant relation ships($F(12,182) = 0.04$, $p = 0.99$).

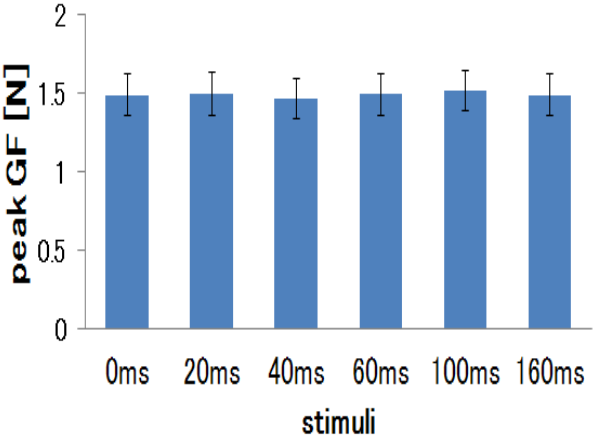

Fig.3: Peak Grip Force

3.4 LF on Delay and Precede Stimuli

Fig.4 shows LF measurements during the grip movements of subjects for each stimulus condition. The vertical axis shows peak LF during movement (in N) and the horizontal axis shows the test stimuli. Error bars represent standard error. A repeated measures ANOVA showed a significant difference between conditions ($F(12, 182) = 4.62$, $p < 0.01$). After using Scheffe's method of correction for multiple comparisons, however, this significance did not remain.

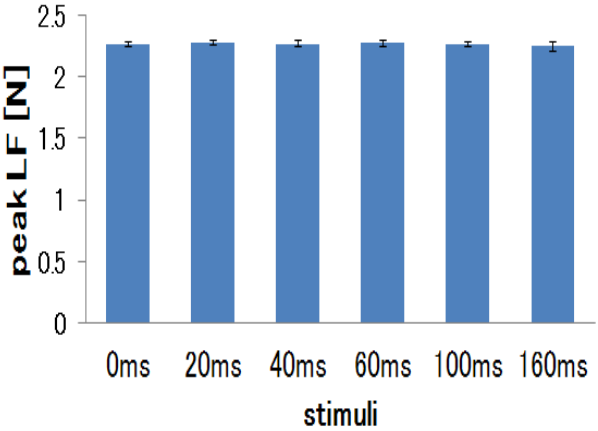

Fig.4: Peak Load Force

3.5 MEP amplification rate

The results of adding, averaging, and comparing MEPs at resting and in each test condition is shown in Fig.5. The vertical axis shows MEP amplitude (in μV) and the horizontal axis shows the test stimuli. The amplification rates of the amplitudes in the various conditions were: control 69.0%, 0 ms 49.1%, 20 ms 71.6%, 40 ms 28.2%, 60 ms 19.5%, 100 ms 38.6%, and 160 ms 57.1%.

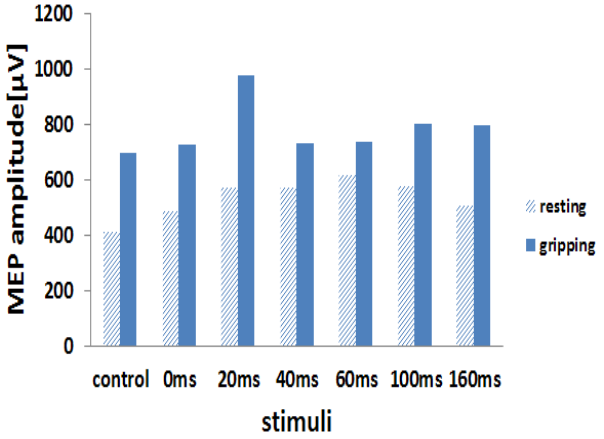

Fig.5: MEP amplitude

3.2 Electromyogram (EMG)

Fig.6 shows integrated electromyogram (iEMG) for each test stimulus in gripping. The vertical axis shows iEMG (in mV) and the horizontal axis shows the test stimuli. Error bars represent standard error.

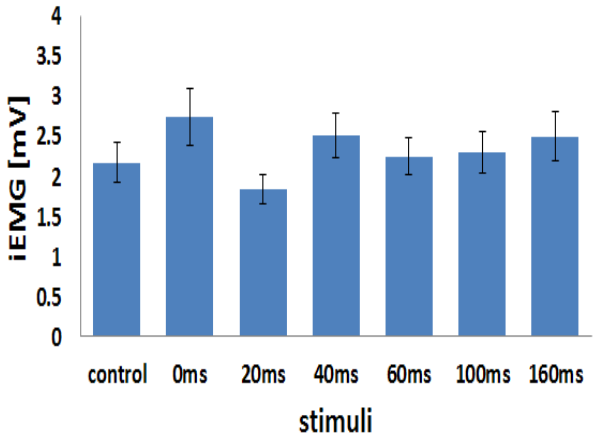

Fig.6: Integrated Electromyogram

4 Discussion

4.1 MEP and iEMG

From our results, we can observe the change of the MEP amplification rate between small and large temporal delays in visual information. We expected to see an increase in the amplification rate as the delay increased, but our obtained data did not show this. In the 20 ms delay condition, however, the rate is larger than in the control and 0 ms conditions. Furthermore, the iEMG was not changed in all the stimulus conditions. This suggests that the illusion that was induced by the 20 ms artificial visual transmission delay is related to primary motor cortex. In the other large-delay stimuli, we could not see any significant effects.

5 Conclusions

In this study, we measured GF, LF, iEMG, and MEPs in order to investigate whether the weight illusion caused by temporal differences in visual information and motor information is reliant on primary motor cortex. As a result, we could see non-significant changes in the GF, the LF and the iEMG in gripping. However, could see large changes in the MEP amplification rate in the 20 ms delay condition, suggesting that the primary motor cortex is involved in the weight illusion induced by artificial visual transmission delay. Although we found that thing, it cannot be certain because we tested only two subjects. Therefore, we need continue to investigate this illusion with a greater number of subjects. In addition, it is necessary to reproduce the same experiment but with an artificial visual transmission advance rather than delay.

Acknowledgements

I would like to express the deepest appreciation to the university bidder, and people who advanced this research by helping as subjects.

This work was supported by JSPS KAKENHI Grant Number 15H03055.

References

[1] Kinoshita H, Kawai S, Ikuta K. : “Contributions and coordination of individual fingers in multiple finger prehension”, Ergonomics, Vol.35, No.3, pp.1212-1230 (1995)

[2] Radwin R. G., Oh S., Jensen T. R., Webster J. G. : “External finger forces in submaximal five finger static pinch prehension”, Ergonomics, Vol.35, No.3, pp. 275-288 (1992)

[3] Takemura N., Inui T., Fukui T. : “Sensorimotor Integration Model for Predictive Control of Reach-to-Grasp”, IEICE technical report. Neurocomputing, Vol.103, No.733, pp.1-6 (2004)

[4] Charpentier A:"Analyse experimentale de quelgues elements de la sensation de poids",Arch. Physiol. Norm. Pathol. Vol.3, pp.122-135 (1891)

[5] Wolfe, H. K:"Some effects of size on judgments of weight",Psychol. Rev. Vol.5, pp.25-54 (1898)

[6] Seashore, C. E : “SoMEPsycho- logical statics: 2.The material weight illusion”, Univ. Iowa Stud. Psychol, Vol.2, pp.36-46. (1899)

[7] Ross, H.E.:"When is weight not illusion?", Quarterly Journal of Experimental Psychology, Vol.21, pp.346-355 (1969)

[8] Christopher M. Davis, William Roberts : "Lifting movements in the size-weight illusion", Perception and Psychophysics, Vol.20, pp.33-36 (1976)

[9] Kim, J., Hong, S., Sato, M., Koike,Y. "Examination of the size-weight-illusion by utilizing the SPIDAR (in Japanese)." Trans Virtual Real Soc Japan, Vol.7, pp.347–354 (2002)

[10] Koike, Y., Kim, J., Shin, D. : "Role of stiffness in weight perception." Japan Psycholgy Reseach, Vol.48, pp.174–187 (2006)

[11] Diedrichsen, J., Verstynen, T., Hon,A., Zhang, Y., Ivry, R.B. (2007)." Illusions of force perception: the role of sensorimotor predictions, visual information, and motor errors." Journal of Neurophysiology, Vol.97, pp.3305–3313 (2007)

[12] Flanagan, J. R., Beltzner, M. A.: "Independence of perceptual and sensorimotor predictions in the size–weight illusion." Nature Neuroscience, Vol.3, pp.737 – 741 (2000)

[13] Flanagan JR, Bittner JP, Johansson RS :"Experience can change distinct size–weight priors engaged when lifting objects and judging their weights." Current Biology Vol.18, pp.1742–1747 (2008)

[14] Brayanov, J. B., Smith, M. A.:"Bayesian and “anti-Bayesian ” biases in sensory integration for action and perception in the size–weight illusion." Journal of Neurophysiology, Vol.103, pp.1518–1531 (2010)

Address for correspondence:

1-21-40, Korimoto, Kagoshima-shi, Kagoshima, 890-0065, Japan

Atsuo Nuruki

Department of Information Science and Biomedical Engineering, Faculty of Engineering, Kagoshima University

nuruki@ibe.kagoshima-u.ac.jp

Skin Motion Artifact in Motion Capturing of Human Bipedal Gait: Characterization and Influence on Joint Torque Estimation

Takuya Inoue[1], Yasuyuki Suzuki[1], Ken Kiyono[1], Taishin Nomura[1]

[1]Graduate School of Engineering Science, Osaka University, Osaka, Japan

Abstract

Optical motion capture systems are widely utilized in human motion analysis, where motions of small markers attached to the body are measured. Skin motion artifacts (SMA), erroneous motions of markers relative to the skeletal links, are one of the major deficits degrading measurement accuracy. Here, we quantitatively characterized the SMA during human bipedal walking. To this end, we measured positions of markers during walking experimentally, and clarified that the SMA during periodic walking was also periodic, which could be approximated by the fourth order Fourier series. We then evaluated how the SMA influences estimation of joint torques in inverse dynamics analysis, and showed that the estimated joint torques was non-negligibly deviated from the true torques, even if the SMA was small.

Keywords *Motion Analysis, Skin Motion Artifact, Posture Estimation, Multi Rigid Link System*

1 Introduction

Experimental measurement using motion capture system is one of the effective methods in human motion analysis [1,2]. Spatiotemporal data of captured markers placed on the human body enable us to reproduce the body motion on a computer, providing a basis for understanding dynamics and mechanisms of human motor control. In a typical procedure of human motion analysis in biomechanics and neurophysiology, the time-series data for the position of the markers are often assimilated into a multi-rigid-link model that approximates the body of experimental subjects in order to represent the human movement, and then joint torques (kinetics) during movement are estimated using the inverse dynamics analysis [3,4]. Accurate estimation of the joint torques is of critical importance, because the joint torques involve various information about the underlying motor control.

In the analysis using motion capture system, skin motion artifacts (SMA), erroneous motions of markers relative to the skeletal links, are one of the major deficits degrading measurement accuracy [5-7]. SMA is caused by deformation of muscles and skins, which induces shift in the marker position relative to skeletal system, leading to erroneous estimation of movement of the skeletal system embedded in the muscular system.

Although there are a number of studies attempting to reduce the influence of SMA, there is no satisfactory solution so far. In this study, we measured positions of markers during walking were experimentally, and characterized SMA during human bipedal walking. We then evaluated how the SMA influences estimation of joint torques in inverse dynamics analysis, and showed that the estimated joint torques was non-negligibly deviated from the true torques, even if the SMA was small.

2 Methods

2.1 Measurement of bipedal walking

Three young healthy adults (mean ± SD, 23 ± 2.83 years old, height 1.73 ± 0.03 m, weight 64.67 ± 6.13 kg) participated in this study. All the subjects provided written informed consent. The experimental procedures were approved by the ethical committee for the human studies at Osaka University.

Subjects were requested to walk on a treadmill with arms folded on their chest. Preferable walking speed was determined individually (1.03 ± 0.21 m/sec). Three trials of 90 seconds were performed. Fourteen infrared reflective markers were placed on the characteristic points on the body of each subject (Fig. 1 and Table 1). Positions of the markers were captured using a motion capture system (SMART-DX, BTC, Italy) with eight infrared cameras and sampling frequency of 300 Hz. Ground reaction force was measured by force sensors embedded in the treadmill with sampling frequency of 1,200 Hz. The time series data of each marker position and ground reaction force were digitally low-pass filtered offline (fourth-ordered Butterworth filter with zero phase lag, cut-off frequency of 10 Hz). Then the marker position was projected on the sagittal plane, where x-axis is anterior-posterior direction of body, and y-axis is superior-inferior direction. The ground reaction force data were resampled with sampling frequency of 300 Hz to align with the marker position data. We detected time instants of every left heel contact from the ground reaction force, and extracted time profiles of the marker positions for every gait cycle, by which we obtained data for 10 cycles from a steady-state walking. In this sequel, we denote the position vector of the markers as $\mathbf{m}_{i,j}[n]=(m^x_{i,j}[n], m^y_{i,j}[n])^{\mathrm{T}}$ (i={HAT, T-L/R, LL-L/R, F-L/R}, j={A, B}, n indicates number of data. See Fig. 1 and Table 1 for details.).

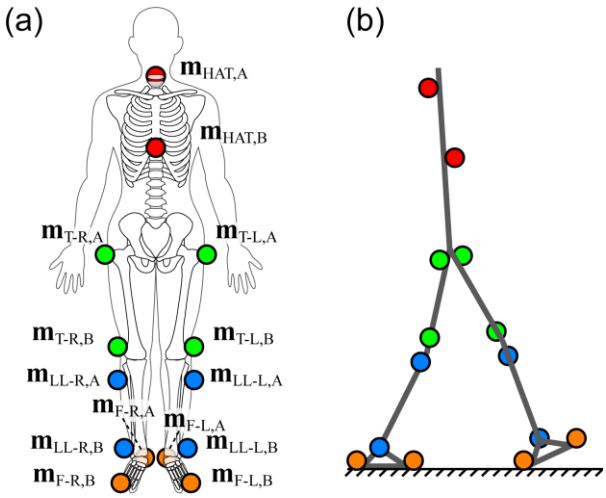

Figure 1: Markar positions during experimental measurement, and seven-rigid-link model of human during bipedal waking. (a) Marker positions. See Table 1 for details. (b) The seven link model which consists of upper body (HAT), left and right thigh (Thigh-L/R), left and right Lower Leg (LowLeg-L/R), and left and right Foot (Foot-LR).

2.2 Posture estimation of human body segment from marker position data

We modeled the human body during walking by a rigid seven-link model, consisting of upper body (Head-Arm-Trunk: HAT), left and right thighs, lower legs, and foots, as in Fig. 1(b). Here, we illustrate how the position and posture of each body segment was estimated from the marker position data. We used a method based on algorithm proposed in the previous study [9]. Since this algorithm was not developed for precise estimation of walking movement, the estimated position and posture of each body segment would be influenced by SMA, which was analyzed in this study.

Let us define a local coordinate fixed on a segment. The origin $\mathbf{o}_i[n]$ (i={HAT, Thigh-L/R, LowLeg-L/R, Foot-L/R}) and the coordinate transformation matrix $\mathbf{A}_i[n]$ of the local coordinate represents the position and the posture of the segment. In this algorithm, the position and the posture of each segment were defined according to position of the joints (hip, knee, and ankle joints) in the global coordinate, where we assume that each joint is fixed on the corresponding segment. To obtain the joint positions, tentative position $\mathbf{o}_i'[n]$ and posture $\mathbf{A}_i'[n]$ of each segment were estimated from the marker position as follows.

Table 1: Marker ID and attached position (j={A,B})

ID	Attached position
$\mathbf{m}_{HAT,j}$	(A) Cervicale (B) Solar plexus
$\mathbf{m}_{T\text{-}L/R,j}$	(A) Left and Right greater trochanter
	(B) Left and Right Femur lateral epicondyle
$\mathbf{m}_{LL\text{-}L/R,j}$	(A) Left and Right Tibia lateral condyle
	(B) Left and Right Lateral malleolus
$\mathbf{m}_{F\text{-}L/R,j}$	(A) Left and Right Pterion
	(B) Left and Right Metatarsal fibular

$$\mathbf{o}_i'[n]=\frac{\mathbf{m}_{i,A}[n]+\mathbf{m}_{i,B}[n]}{2},\ \mathbf{A}_i'[n]=\left(\mathbf{v}_i^x[n]\quad \mathbf{v}_i^y[n]\right), \qquad (1)$$

where $\mathbf{v}_i^x[n]$ is a unit vector directing from a marker A to a marker B on the i-th segment, and $\mathbf{v}_i^y[n]$ is orthogonal to $\mathbf{v}_i^x[n]$. We denote the position of the k-th joint in the local coordinate of the i-th segment as $\bar{\mathbf{J}}_{i,k}$ (i={HAT, T-L/R, LL-L/R, F-L/R}, k={Hip-L/R, Knee-L/R, Ankle-L/R}), each of which is a time-independent constant. The joint position in the global coordinate $\mathbf{J}_{i,k}[n]$ is expressed as $\mathbf{J}_{i,k}[n]=\mathbf{o}_i'[n]+\mathbf{A}_i'[n]\bar{\mathbf{J}}_{i,k}$. For a given joint, its position can be described by two ways. For example, the knee joint position can be described by the local coordinate of thigh and that of shank. If the positions and postures of two adjacent i-th and l-th segments are precisely estimated, the equality $\mathbf{o}_i'[n]+\mathbf{A}_i'[n]\bar{\mathbf{J}}_{i,k}-\mathbf{o}_l'[n]+\mathbf{A}_l'[n]\bar{\mathbf{J}}_{l,k}=0$ holds for the position of the k-th joint connecting these two segments. However, in practice, this equality cannot be satisfied because of the inaccuracy due to SMA. A better estimate of the k-th joint position $\bar{\mathbf{J}}_{i,k}$ in the local coordinate should minimize the following cost function:

$$\sum_n\left|\left(\mathbf{o}_i'[n]+\mathbf{A}_i'[n]\bar{\mathbf{J}}_{i,k}\right)-\left(\mathbf{o}_l'[n]+\mathbf{A}_l'[n]\bar{\mathbf{J}}_{l,k}\right)\right|. \qquad (2)$$

Since we have two optimal $\bar{\mathbf{J}}_{i,k}$ and $\bar{\mathbf{J}}_{l,k}$ that minimize (2) for the k-th joint, we defined the optimal joint position as the midpoint of $\bar{\mathbf{J}}_{i,k}$ and $\bar{\mathbf{J}}_{l,k}$. Moreover, since we consider a model of biped gait in the saggital plane, we defined Hip joint position as midpoint of Hip-L and Hip-R.

Position and posture of each segment were defined as follows: the origin of each of Thigh-L/R and LowLeg-L/R was defined as the midpoint of the proximal and distal joints. The x-axis of the local coordinate was defined by the unit vector directing from the proximal to distal joints. For Foot-L/R and HAT segments, the x-axis of the local coordinate was defined by the unit vector directing from the proximal joint to the midpoint of two marker on the segment, and the origin was set on the x-axis at the mean distance between the joint and the midpoint of two markers.

2.3 Evaluation of Skin Motion Artifact

We defined SMA of a marker on a given segment as a fluctuation of the marker position in the local coordinate of the segment. We referred to the marker position vector in local coordinate as $\bar{\mathbf{m}}_{i,j}[n]=(\bar{m}_{i,j}^x[n], \bar{m}_{i,j}^y[n])$, whose global position is $\mathbf{m}_{i,j}[n]=\mathbf{o}_i[n]+\mathbf{A}_i[n]\bar{\mathbf{m}}_{i,j}[n]$. If there is no SMA, $\bar{\mathbf{m}}_{i,j}[n]$ is a time independent constant vector. However, in practice, $\bar{\mathbf{m}}_{i,j}[n]$ changes in time. $\bar{\mathbf{m}}_{i,j}[n]$ that includes SMA can be obtained as follows:

$$\bar{\mathbf{m}}_{i,j}[n]=(\mathbf{A}_i[n])^{-1}\left(\mathbf{m}_{i,j}[n]-\mathbf{o}_i[n]\right) \qquad (3)$$

$\bar{\mathbf{m}}_{i,j}[n]$ was devided into several segments, each of which spans a gait cycle according to the left heel contact timings, and they were phase-locked averaged. Since $\bar{\mathbf{m}}_{i,j}[n]$ should be a constant if no SMA exists, the fluctuation of $\bar{\mathbf{m}}_{i,j}[n]$ represents the SMA, itself. Under

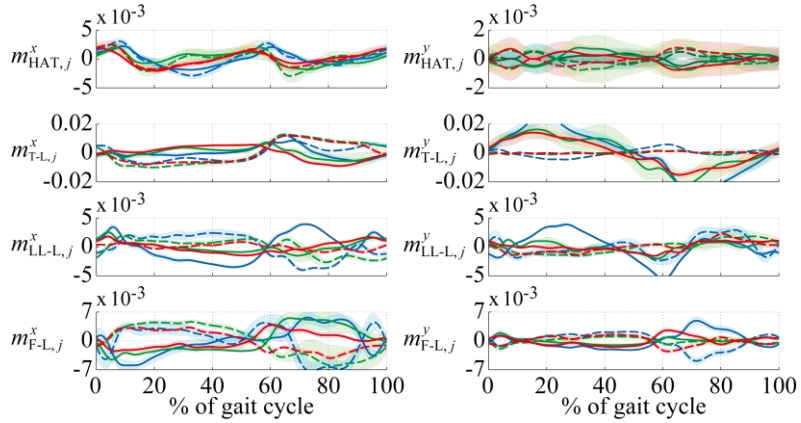

Figure 2: Time series data of estimated skin motion artifact (j={A, B}). In each panel, Horizontal axis is gait phase (0% and 100% correspond to the left heel contact and 50% corresponds to the right heel contact. Solid lines are phase locked average of the skin motion artifact of the marker A, and dashed lines are those of the marker B, which were obtained from 10 gait cycles. Color-bands around the solid curves are the standard deviation. Blue, green, and red colors represent Subjects 1, 2, and 3, respectively.

the assumption that the SMA is a periodic function, $\bar{\mathbf{m}}_{i,j}[n]$ was expanded by Fourier series as follows.

$$\bar{m}^z_{i,j}[n] = c^z_{i,j} + \sum_{k=1}^{K}\left(a^z_{i,j,k}\cos\frac{2\pi kn}{N} + b^z_{i,j,k}\sin\frac{2\pi kn}{N}\right), \quad (4)$$

where z={x,y}, N indicates the data length of one gait cycle, and K is the order of the expansion.

2.4 Influence Evaluation of skin motion artifact on Joint Torque Estimation

We evaluated how the SMA influenced estimation of joint torques during walking. We used a rigid-seven-link model which could establish a stable biped gait in the sagittal plane [3,10]. Through dynamic simulation of the model, we obtained kinematic (position $\tilde{\mathbf{o}}_i[n]$ and posture $\tilde{\mathbf{A}}_i[n]$ of each segment) and kinetic (ground reaction forces and joint torques) data according to the motion equation:

$$\mathbf{M}(\boldsymbol{\theta})\ddot{\boldsymbol{\theta}} + \mathbf{B}\left(\boldsymbol{\theta},\dot{\boldsymbol{\theta}}\right) + \mathbf{K}(\boldsymbol{\theta}) = \mathbf{F} + \boldsymbol{\tau}, \quad (5)$$

where, $\boldsymbol{\theta}$ is vector of position and postures of all segments, $\mathbf{M}$ is the inertia matrix, $\mathbf{B}$ is the centrifugal and Coriolis force, $\mathbf{K}$ is the gravitational force and torque, $\mathbf{F}$ is the ground reaction force, and $\boldsymbol{\tau}$ is the joint torque vector. Subsequently, using the model kinematics and experimental SMA obtained by Eq. (4), we numerically simulated SMA-effected marker positions as follows.

$$\mathbf{m}_{i,j}=\tilde{\mathbf{o}}_i[n]+\tilde{\mathbf{A}}_i[n]\bar{\mathbf{m}}_{i,j}[n]. \quad (6)$$

In this study, we used $\bar{\mathbf{m}}_{i,j}[n]$ obtained from Subject 3. Using the same algorithm in Sec. 2.2, we estimated position and posture of each segment of the model, calculated the SMA-affected joint torques $\boldsymbol{\tau}[n]=(\tau_{\text{Hip-L}},\tau_{\text{Knee-L}},\tau_{\text{Foot-L}},\tau_{\text{Hip-R}},\tau_{\text{Knee-R}},\tau_{\text{Foot-R}})^{\mathrm{T}}$ according to Eq. 5, and to compared them with the non-SMA affected true joint torques.

3 Results

3.1 Experimental Skin Motion Artifacts

Fig. 2 shows the phase-locked averages and standard deviations of SMAs of eight markers during biped gait, which were obtained using 10 gait cycles for each subject. SMA of each subject was qualitatively similar, but not necessarily quantitatively. The standard deviations were relatively small, which means that SMA during periodic motion was also periodic. Cycle length of SMA of markers on HAT was half of walking cycle, while those of markers on the other segments were the same as the gait cycle. In all subjects, amplitude of SMA of the markers on Thigh was large, especially in y-component, which was orthogonal to the line connecting between the hip and knee joints.

Fig. 3 represents the Fourier coefficients of SMAs for the data shown in Fig. 2. In all subjects, the first order Fourier coefficient with gait period (k=1) and the second harmonics were large. The higher order coefficients were much smaller than the first and second components. Indeed, the SMAs were approximated by up to the fourth order Fourier series.

3.2 Influence evaluation of Skin motion artifact on joint torque estimation

Fig. 4 shows the influence of SMAs on the joint torque estimation. In each panel, the joint torques

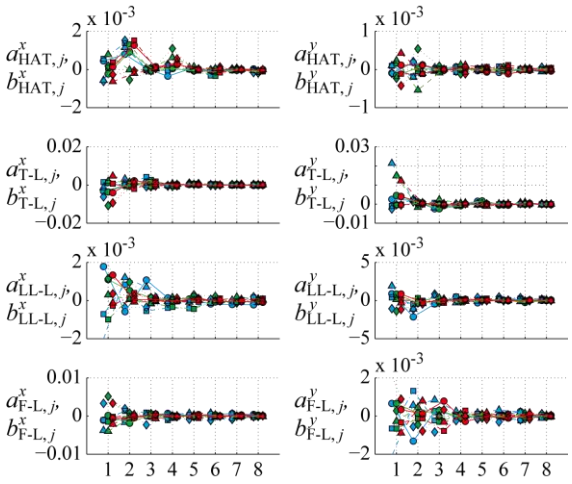

Figure 3: Fourier coefficients of SMAs (j={A, B}). In each panel, horizontal axis is the order of expansion. Circles connected by solid line and triangles connected by dashed line are the coefficients of cos and sin waves of the marker A. Squares connected by chain line and diamonds connected by dotted line are the coefficients of cos and sin waves of the marker B. Blue, green, and red colors are for Subjects 1, 2, and 3, respectively.

estimated from the SMA-affected markers were qualitatively similar to the true non-SMA affected joint torques. However, there are some non-negligible differences, e.g. torque at the left knee joint estimated from the SMA-affected marker position took large values continuously during stance phase of the left leg, and the torques at the right knee and the ankle joints also took larger values than the true torques after the left and the right heel contacts. At the peak of joint torques, the SMA-affected joint torques were about 20% larger than the true joint torques.

4 Discussion and Conclusions

In this study, we analyzed spatiotemporal variations of the markers placed on the human body during bipedal walking, and evaluated the erroneous skin motion artifact (SMA) included in the marker movement. We confirmed that all makers fluctuated periodically with respect to the local coordinate of each body segment, and movement of the markers on thigh was relatively large. By performing the Fourier analysis, we found that the SMAs could be fitted by the fourth order Fourier series, meaning that the SMAs include up to fourth order higher harmonics of the gait cycle. In addition, we evaluated how the SMA influence the joint torque% estimation in the gait analysis, and showed that the joint torques that were calculated by using SMA-affected marker positions could be 20% larger than the actual joint torques.

The analysis in this study showed that differences between the SMAs-affected and the true joint torques could reach 20% in the peak torque amplitude. This error cannot be negligible, implying that a new algorithm of posture estimation, which can reduce the influence of SMA, is required. As shown in this study, SMA during periodic human motion is also periodic. A new algorithm for posture estimation during periodic movements can take this fact into account, where SMA-eliminated postures of the body segments and the SMAs might be better estimated simultaneously.

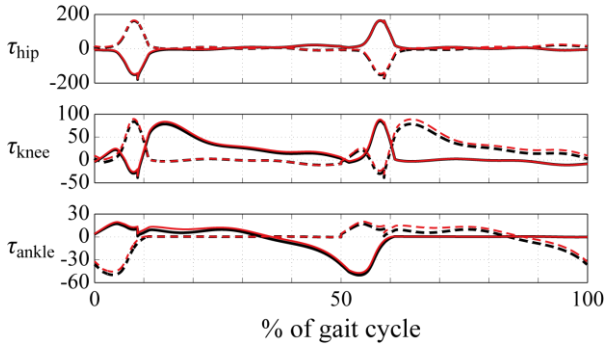

Figure 4: Estimated joint torques of the gait model. In each panel, solid and dashed curves are the joint torques for the left and right legs, respectively (from the top panel; hip, knee, and ankle). Black and red curves are the non-SMA affected and SMA-affected joint torques, respectively.

Acknowledgements

This work was supported by JSPS grants-in-aid (26242041 and 26750147).

References

[1] A. Cappozzo. Gait analysis methodology. *Hum Mov Sci*. 3: 27-50, 1984

[2] B. Dariush, Human motion analysis for biomechanics and biomedicine. *Mach Vis Appl*. 14: 202-205, 2003.

[3] T. Yamasaki, T. Nomura, S. Sato. Possible functional roles of phase resetting during walking. *Biol Cybern*. 88: 468-496, 2003.

[4] Y. Ma, H. Zhang, and S. Jiang. Realistic modeling and animation of human body based on scanned data. *J Comput Sci Technol*, 19(4):529-537, 2004.

[5] A. Cappozzo, F. Catani, A. Leardini, M. Benedetti, U Croce. Position and orientation in space of bones during movement: experimental artefacts. *Clin Biomech*. 11: 90-100, 1996

[6] E Alexander, T. Andriacchi. Correcting for deformation in skin-based marker systems. *J Biomech*. 34: 355-361, 2001.

[7] C. Reinschmidt, A van den Bogert, B Nigg, A. Lundberg, N. Murphy. Effect of skin movement on the analysis of skeletal knee motion during running. *J Biomech*. 30(7): 729-732.

[8] N. Yoshikawa, Y. Suzuki, K. Kiyono, T. Nomura. A Theoretical Study on a Computational Algorithm for Human Posture Estimation Based on Motion Capture of a Small Number of Markers. *Advanced Biomedical Engineering*. 2: 107-116, 2013.

[9] N. Yoshikawa, Y. Suzuki, W. Ozaki, T. Yamamoto, T. Nomura. 4D human body posture estimation based on a motion capture system and multi-rigid link model. *Conf Proc IEEE Eng Med Bio Soci*. 4847-4850, 2012.

[10] C. Fu, Y. Suzuki, K. Kiyono, P. Morasso, T. Nomura. An intermittent control model of flexible human gait using a stable manifold of saddle-type unstable limit cycle dynamics. *J R Soc Interface*. 11: 20140958. 2014.

Address for correspondence:

Yasuyuki Suzuki
Graduate School of Engineering Science, Osaka University, JAPAN
suzuki@bpe.es.osaka-u.ac.jp

Research for Real-time Wireless Bio-Signal detecting System

Hojong Chang *, Hyeongmin Choi [2], Taeyun Lim [3], Suhan Kim [2], Jaeil Kim[3], Cheonyang Lee [2], Hyunduk Kim [1], Gyuseong Cho[1]

[1]* Institute for Information Technology Convergence, KAIST, Korea;
[2] Physionics Co., Ltd, Korea;
[3] Doohaine Co., Ltd., Korea;

Abstract

We designed real-time multi-channel bio-signal measurement system. Photoplethysmography (PPG), and body temperature signal are measured through wireless monitoring system based on Bluetooth Low Energy (BLE). The performance of proposed hardware is compared with reference devices (BIOPAC, Fluke). The experimental results of heart rate and temperature have respectively shown over 90% Reliability.

Keywords : **Photoplethysmography (PPG), Body temperature, Wireless**

1 Introduction

Techniques of the data processing method, which measure and utilize users' bio-signals in their daily life, have been developed. At this time, mobile healthcare available to use the system for anytime and anywhere, based on the wearable device technology. The bio-signal acquisition method used in most of the existing wearable device has a limitation of a motion artifact[1]. So we designed a non-invasive patch type wireless data measurement system which can reduce a motion artifact.

2 Methods

The system developed through in this study is composed of a sensor for measuring the bio-signal and the wireless communication for transmitting and receiving the data. TI Company's TMP007 was used for measuring the users' temperature. Also, the signals coming from the users' heart rate is through LED(530mm, 660mm, 940mm) by utilizing OSRAM Company's SFH7050[2]. Serial communications method was applied for controlling measured multiple signals by I2C(Inter Integrated Circuit) interface which utilizes two signals of SDA(Serial Data) and SCL(Serial Clock). We use Bluetooth 4.0 applied with Bluetooth Low Energy(BLE) for data communication and power consumption. Moreover, it was configured to obtain the data by including basic information such as Device Name, Mac Address and RSSI(Received signal strength indicator) to packets for minimizing the data's security and loss rate.

3 Results

For comparison of the measured data, BIOPAC(MP150) and BIOPAC(BN-TX) was used. We also designed a mobile application which can serving a real time data to user. Figure1 shows a raw data and App screen.

(a) Raw data (b) Measure data

Figure 1 : Measurement signal graph

4 Conclusions

Accuracy of the heart rate is over 97% and the temperature is 91% by comparing with the references. Since the error is due to the field of view(FOV) and distance between the sensor and the surface. To solve this problem it need to redesign a circuit and sensor then we will improve reliability of the data.

Acknowledgements

This study is a result of research conducted by KI institution-specific project(N11160072) of 2016 KAIST's own research projects..

References

[1] Nemati, E., A wireless wearable ECG sensor for long-term applications. IEEE Communications Magazine, 50(1), 36-43, 2012.

[2]Fang, Y.C. Tai, C.-C., Non-invasive multiwavelength photoplethysmography under low partial pressure of oxygen . Journal of Medical Engineering and Technology, 40(6), pp. 315-324, 2016

Address for correspondence:

Name Surname : Chang Hojong
Institution : KAIST
email address : hojoungc@itc.kaist.ac.kr

Invited lecture

Brain computer interfaces for the industrial application of cognitive neuroscience

Fabio Babiloni

University of Rome Sapienza, Italy

Abstract

Are the cognitive neuroscience ready to be used in advanced industrial contexts? In this presentation it will be depicted a possible path for the use of advanced findings in cognitive neuroscience by using the electroencephalogram not only in the medical environment (e.g. to improve the limb rehabilitation path for patients affected by stroke). In particular, applications of advanced EEG signal processing technique will be illustrated in the marketing context (neuromarketing) as well as in the aerospace-aeronautic environment, through the on-line monitoring of the mental workload of pilots, air traffic controllers and other category of professional drivers during their actual operations. Four main areas will be described:

1) Brain Computer Interface. In this part of the talk different applications of the brain computer interfaces (BCI) technology will be first presented. All the applications will be obtained by using the computerized analysis of the electrical activity of the human brain, gathered by a net of electrodes placed on the scalp surface (electroencephalogram, EEG). It will be described how by using the voluntary modulation of EEG activity normal subjects could control external devices such as a cursor on the screen, a mobile robot as well as a wheelchair. Successively, it will be illustrated how the BCI technology could be inserted within the rehabilitation path of the patients suffered of brain strokes. In particular, it will be showed how BCI technologies could enhance the rehabilitation exercise, by including the presentation of the attempt of the movement as early as possible to the patients, although they were not yet able to move their limbs. However, BCI applications could be extended beyond the use in the clinical context, and application in the area of the synthetic telepathy are already investigated by DARPA and by the present research group.
2) Neuromarketing: Application of neuroscience in the evaluation of relevant marketing stimuli will be described. The main cognitive neuroscience indicators for the appreciation of an audiovisual sensory stimuli (e.g. a TV commercials) will be also described. The use of such EEG-based indicators in practical situation will be also illustrated.
3) Online detection of mental workload: Successively, it will be showed different applications of the collection of brain activity in working contexts related to the airplanes pilots. It will be described as it is possible to detect the brain activity related to the insurgence of mental workload. It will be speculated that such detection could be employed in a short future to generate devices able to warn the operators about their perceived workload. Example of such detection of mental workload will be presented in three different conditions: on civil airline pilots, on military pilots and on car drivers.
4) Neuroaestethic: The issue of how we perceive the beauty will be also addressed by the talk, through the presentation of main results obtained by monitoring the EEG activity during the visit of two art galleries with the pictures of Tiziano Vecellio and Jan Veermer.

Conclusions

The possibility to detect in a reliable way the cerebral activity during "real-life" conditions and the possibility to detect brain activity with dry electrodes will be also discussed. Quoting the scientist Martha Farah, the issue is not "if" but "when" the neuroscience will shape our future. We are thinking that such time is arrived.

Wireless Brain-Computer Interface Based on Steady-State Visual Evoked Potential Considering User's Gaze

S Otsuka, J Hori

Graduate School of Science and Technology, Niigata University, Japan;

Abstract

Steady-state visual evoked potential (SSVEP) is widely used to design a brain-computer interface (BCI). To accomplish real-time BCI, that is, if user wants to enter the command at any time, it is necessary to extract user's attentional behavior for visual stimulus. In addition, the wireless EEG system can improve the usability of communication support device used in daily life. In this study, we aim to improve the performance of SSVEP-based BCI by classifying user's state into gazing or resting. Moreover, we compared the performances of two wireless EEG systems. As a result, the accuracy of 73.0 % was obtained by the wireless EEG systems. The number of harmonics that provided the best performance was different in two systems.

Keywords *EEG, Brain-Computer Interface, Steady-State Visual Evoked Potential, Gaze, Wireless EEG System*

1 Introduction

Brain-computer interface (BCI) is a system that allows motor disabilities to communicate with the external world [1]. Among the various EEG signals, steady-state visual evoked potential (SSVEP) is one of the representative EEG responses used for BCI. The SSVEP response is evoked by flickering visual stimulus presented with high repetition rate of 3.5 - 75 Hz [2]. The response synchronized with fundamental frequency and harmonic components of visual stimulus is elicited in the visual cortex. The SSVEP-based BCI has advantages of less user training, and high information transfer rate [3].

In SSVEP-based BCI, user enters the command by gazing the visual stimulus represented on the display or LED panel. In the case of 2-class BCI, 2 kinds of visual stimuli with different frequencies are used. The user is instructed to gaze one of two stimuli. The user's intention is classified using the detected EEG signals. However, to use as the real-time BCI which enables to enter the command at any time, it is necessary to detect the user's intention by distinguishing the gaze from rest. Moreover, the wireless EEG system is superior to conventional wired EEG system in portability and ease of use. Therefore, the wireless EEG system can improve the usability in daily life.

In this study, we aim to improve the performance of SSVEP-based BCI by classifying user's state into gazing or resting for visual stimulus. Furthermore, we compared the results of two wireless EEG systems. The first one was wearable wireless amplifier with pasted active electrodes (Miyuki Giken Polymate Mini AP108). The second was wireless EEG headset (Emotiv EPOC) without paste. To perform the 3-class classification of 2 frequencies and rest, we employed the 2-step discrimination using feature vectors obtained from canonical correlation analysis (CCA) method.

2 Methods

2.1 Subjects

Five healthy male subjects aged 21-23 years participated in the experiment. All subjects gave written informed consents before the experiment. This study was approved by the ethics committee of Niigata University.

2.2 SSVEP-based BCI

2-class BCI based on SSVEP was investigated in this study. Fig. 1 shows visual stimulus used in the experiment. Two reversal check boards were presented on a 23-inch monitor display with a refresh rate of 60 Hz. The distance between the monitor and the subject was 70 cm. The frequencies of the left and right stimulus were set to 4 Hz and 5 Hz, respectively.

Fig. 2 shows the experimental protocol. The experiment was composed of the resting period and the gazing period. The duration of each period was 5 seconds. In the resting period, the subject was instructed to focus on the fixation point at the center of monitor. In the gazing period, left or right arrow was presented at the center, and then subject focused on arrowed stimulus. The trigger for returning to rest was provided by an auditory instruction.

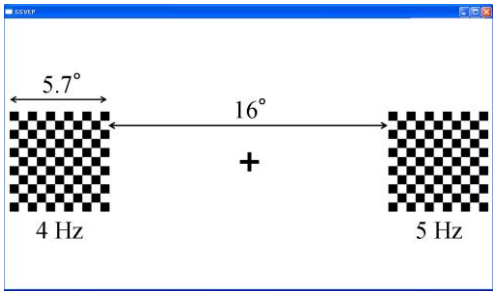

Figure 1: Visual stimulus of 2-class SSVEP-based BCI.

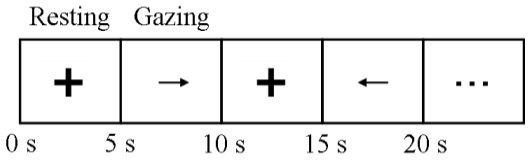

Figure 2: Experimental protocol. The sequence shows the visual indication for the subject.

The experiments were performed with two wireless EEG systems.

Experiment A: wearable wireless amplifier (Miyuki Giken Polymate Mini AP108) is 8ch EEG system with a sampling rate of 500 Hz. To record the EEG signals, active electrodes were put on the scalp surface with paste. In this study, 6 electrodes (O1, O2, PO3, PO4, Oz, and POz) were placed in the occipital region according to the international 10-20 system. The reference electrodes were placed at A1 and A2.

Experiment B: Emotiv EPOC is a wireless EEG headset with a sampling rate of 128 Hz, and records the EEG signals with saline soaked felt pads. EPOC is equipped with 14 recording electrodes and 2 reference electrodes according to the international 10-20 system. In this study, 4 recording electrodes were placed over the visual cortex with rotating the headset by 180˚ in the horizontal plane [4].

Each stimulus was repeated 30 and 100 times in the experiment A and B, respectively. Considering the eye movements, data segments of 1 to 5 s after visual stimuli were used for analysis. The duration of time window that is considered for analysis was set to 1 to 4 s with a step of 1 s.

2.3 Classification

At first, the acquired EEG signals were normalized to zero mean and unit variance. Subsequently, a bandpass filter between 3 to 20 Hz was applied to the signals.

For feature extraction, CCA was applied to the normalized signals. CCA is a method for analyzing correlation between two multi-dimensional variables [5]. CCA can detect the frequency of SSVEP data with high accuracy [6]. Given two sets of variables $\mathbf{X}$ and $\mathbf{Y}$, CCA finds the weight vectors $\mathbf{W}_x$ and $\mathbf{W}_y$ such that the correlation between linear combinations (termed the canonical variables) $\mathbf{x} = \mathbf{X}^T\mathbf{W}_x$ and $\mathbf{y} = \mathbf{Y}^T\mathbf{W}_y$ is maximized as

$$\max_{\mathbf{W}_x,\mathbf{W}_y} \rho = \frac{\mathrm{E}\left[\mathbf{W}_x^T\mathbf{X}\mathbf{Y}^T\mathbf{W}_y\right]}{\sqrt{\mathrm{E}\left[\mathbf{W}_x^T\mathbf{X}\mathbf{X}^T\mathbf{W}_x\right]\mathrm{E}\left[\mathbf{W}_y^T\mathbf{Y}\mathbf{Y}^T\mathbf{W}_y\right]}}. \quad (1)$$

The maximum of correlation coefficient ρ with respect to $\mathbf{W}_x$ and $\mathbf{W}_y$ is the maximum canonical correlation. Here, $\mathbf{X}$ and $\mathbf{Y}$ refer to the multi-channel EEG signals and the reference signals, respectively. The reference signals $\mathbf{Y}_f$ is set as

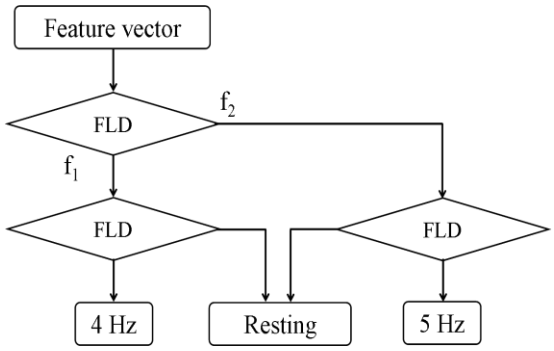

Figure 3: Flowchart of 2-step discrimination.

$$\mathbf{Y}_f = \begin{pmatrix} \sin(2\pi ft) \\ \cos(2\pi ft) \\ \vdots \\ \sin(2\pi N_h ft) \\ \cos(2\pi N_h ft) \end{pmatrix}, \quad (2)$$

where f is the stimulus frequency, t is the time, and the N_h is the number of harmonics including a fundamental. In this study, N_h is set to 1 to 3. The ρ was calculated for each frequency, and 2 dimensional feature vector was obtained.

To classify the subject's state, 2-step discrimination was employed. In each discrimination, Fisher Linear Discrimination (FLD) was applied to feature vectors. Fig. 3 shows the flowchart of discrimination [7]. The class of 4 Hz and 5 Hz were separated easily. However, it was difficult to separate the resting class from combined class of 4 and 5 Hz. Therefore, firstly, feature vectors were discriminated between the class of 4 Hz and 5 Hz. Subsequently, feature vectors were discriminated whether they belonged to resting class.

2.4 Evaluation

At first, the variance ratio among in-class and inter-class variance was calculated to evaluate the feature space. The variance ratio J_σ is given by

$$J_\sigma = \frac{\sigma_B^2}{\sigma_W^2}, \quad (3)$$

where σ^2_W and σ^2_B are the in-class and the inter-class variance, respectively and defined by following equations:

$$\sigma_W^2 = \frac{1}{n}\sum_{i=1}^{L}\sum_{\mathbf{P}\in P_i}(\mathbf{P}-\mathbf{m}_i)^T(\mathbf{P}-\mathbf{m}_i), \quad (4)$$

$$\sigma_B^2 = \frac{1}{n}\sum_{i=1}^{L} n_i(\mathbf{m}_i-\mathbf{m})^T(\mathbf{m}_i-\mathbf{m}), \quad (5)$$

where P_i is the pattern sets in class i, $\mathbf{P}$ is the patterns, n_i is the number of patterns, and $\mathbf{m}_i$ is the mean value over class P_i. Furthermore, n is the number of all patterns, $\mathbf{m}$ is the mean value over all patterns, and L is number of

classes. The larger J_σ, the better class separation.

The leave-one-out cross-validation (LOOCV) was employed to evaluate the classification accuracy. In the LOOCV, one sample is removed from data sets for testing, and remaining data are used for training. All samples are used for testing once, and then the mean accuracy across all trials is calculated.

3 Results

Fig. 4 shows the plots of the correlation coefficients ρ in each number of harmonics. The x and y axes show the correlation coefficient between detected EEG signal and 4 Hz and 5 Hz reference signals, respectively. The blue, red and green spots show the correlation coefficient of 4 Hz, 5 Hz, and resting, respectively. The correlation coefficients considering 3 harmonics were higher than that considering 1 or 2 harmonics in both experiments. In the experiment A, three classes were separated by using only fundamental. On the other hand, in the experiment B, three classes were separated by considering 3 harmonics including fundamental.

Table 1 shows the variance ratios J_σ when changing the number of harmonics. In the experiment A, J_σ tended to be low as number of harmonics increased. On the other hand, in the experiment B, the variance ratios J_σ tended to be large as number of harmonics increased.

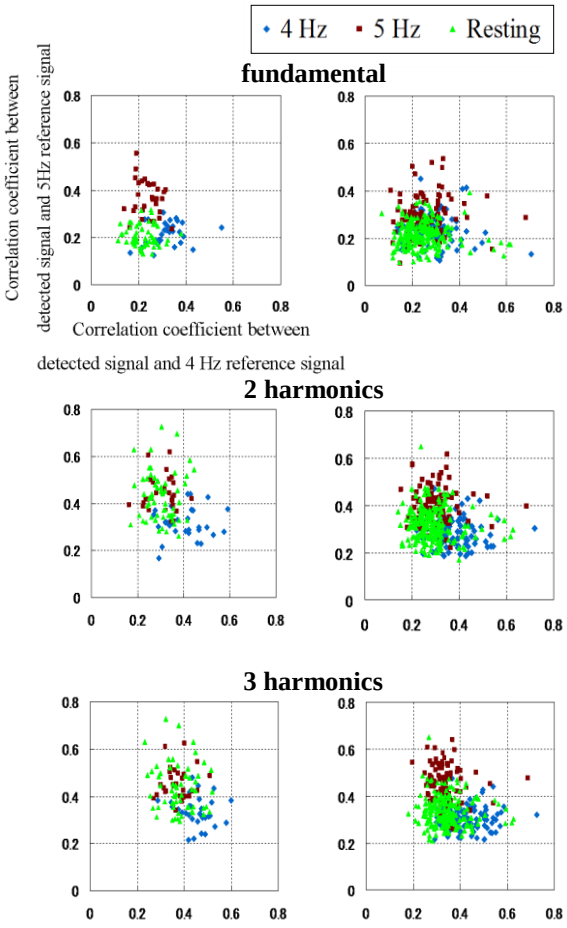

(a) Experiment A (b) Experiment B

Figure 4: Plots of the correlation coefficients when changing the number of harmonics.

Fig. 5 shows the accuracy when changing the number of harmonics as a function of the time window length that is considered for the analysis. In the experiment A, the accuracy considering fundamental was higher than that considering 2 or 3 harmonics. By contrast, in the experiment B, the accuracy using 3 harmonics was higher than that considering fundamental or 2 harmonics. As to the window length, the accuracy in case of long length was high in both experiments. In the case of the experiment A, the accuracy of 73.3 % was obtained with fundamental wave and the window length of 3s. In the experiment B, the accuracy was 73.0 % with 3 harmonics and the window length of 4s.

4 Discussions

The experimental results showed the different tendency between two experiments as to number of necessary harmonics for discrimination. In the experiment A, the class separation and the accuracy as only fundamental wave provided best performance. On the other hand, the results of the experiment B as 3 harmonics were better than others. It was considered that these results due to the signal to noise ratio (SNR) of measured EEG data. The SNR was calculated using the ratio of the power spectrum of the stimulus frequency to that of the neighboring frequencies. Six adjacent frequencies were used with frequency

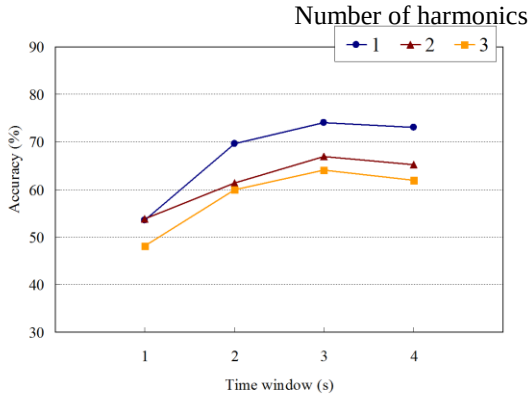

(a) Experiment A

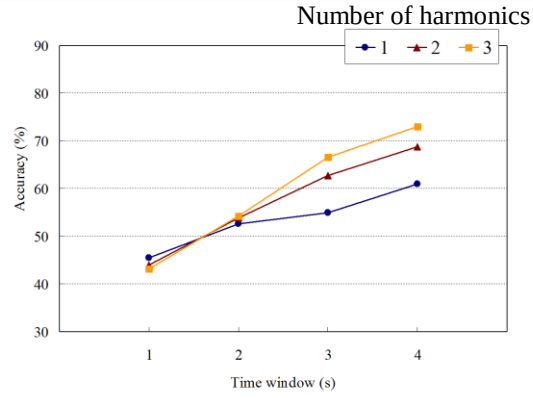

(b) Experiment B

Figure 5: Accuracy when changing the time window length and number of harmonics.

Table 1: The variance ratios J_σ when changing the number of harmonics.

(a) Experiment A

Subject	Discrimination	4 Hz – 5 Hz			4 Hz – Resting			5 Hz – Resting		
	Number of harmonics	1	2	3	1	2	3	1	2	3
1		0.87	0.63	0.66	0.42	0.42	0.30	1.11	0.05	0.01
2		0.72	0.72	0.69	0.61	0.66	0.25	0.94	0.30	0.23
3		0.46	0.36	0.43	0.35	0.47	0.45	0.24	0.08	0.07
4		0.31	0.19	0.17	0.17	0.17	0.11	0.33	0.01	0.01
5		2.40	2.17	2.08	0.83	0.95	0.88	1.98	1.74	1.77
Mean		0.95	0.81	0.80	0.48	0.53	0.40	0.92	0.44	0.42

(b) Experiment B

	Discrimination	4 Hz – 5 Hz			4 Hz – Resting			5 Hz – Resting		
	Number of harmonics	1	2	3	1	2	3	1	2	3
1		0.60	0.84	0.84	0.18	0.25	0.27	0.28	0.39	0.37
2		0.05	0.30	0.41	0.06	0.14	0.17	0.08	0.23	0.25
3		2.23	2.30	2.10	0.85	1.52	0.98	1.57	0.77	0.77
4		0.10	0.42	0.85	0.03	0.19	0.24	0.12	0.17	0.35
5		0.17	0.55	0.79	0.15	0.34	0.41	0.04	0.20	0.31
Mean		0.63	0.88	0.99	0.25	0.49	0.41	0.42	0.35	0.41

resolution of 0.25Hz. Especially, the averaged SNR of fundamental wave in the experiment A (1.97) was higher than that in the experiment B (0.56). While the averaged SNR of 3rd harmonic in the experiment A (1.07) was almost same as that in the experiment B (1.05). Since the SNR of the device used in the experiment A is high, 2nd and 3rd harmonics included alpha band signal (8-13 Hz) that is not necessary for classification. By contrast, in the device used in the experiment B, it was necessary to add harmonics components because of the low SNR. Furthermore, the tendency was the same when changing the number of electrodes.

5 Conclusions

In order to accomplish real-time SSVEP-based BCI, the gazing and resting were classified using CCA. The accuracy of 73.0 % was obtained by using wireless EEG systems. Only fundamental wave was necessary for best performance in the wearable wireless amplifier with pasted active electrodes. On the other hand, 3 harmonics including fundamental was required in the wireless EEG headset without paste. The future work is investigation of other stimulus frequency to improve the accuracy.

Acknowledgements

This work was supported in part by a Grant-In-Aid for Scientific, Research (c) 26350496 from Japanese Society for the Promotion of Science.

References

[1] J.R. Wolpaw, N. Birbaumer, D.J. McFarland, G. Pfurtscheller, and T.M. Vaughan, "Brain-computer interfaces for communication and control," *Clinical Neurophysiology*, 113: 767-791, 2002.

[2] F. Beverina, G. Palmas, S. Silvoni, F. Piccione, and S. Giove, "User adaptive BCIs: SSVEP and P300 based interfaces," *PsychNology Journal*, 1: 331-354, 2003.

[3] F.B. Vialatte, M. Maurice, J. Dauwels, and A. Cichocki, "Steady-state visually evoked potentials: focus on essential paradigms and future perspectives," *Progress in Neurobiology*, 90: 418-438, 2010.

[4] N.V. Manyakov, N. Chumerin, A. Combaz, A. Robben, M.V. Vliet, and M.M. V. Hulle "Decoding SSVEP responses based on PARAFAC decomposition," *International Conference on Bio-inspired Systems and Signal Processing*, 443-447, 2012.

[5] D.R. Hardoon, S. Szedmak, and J. Shawe-Taylor, "Canonical correlation analysis; an overview with application to learning methods," *Neural Computation*, 16: 2639-2664, 2004.

[6] W. Nan, C.M. Wong, B. Wang, F. Wan, P.U. Mak, P.I. Mak, and M.I. Vai, "A comparison of minimum energy combination and canonical correlation analysis for SSVEP detection", *Proceedings of the 5th International IEEE/EMBS Conference on Neural Engineering*, 469-472, 2011.

[7] S. Otsuka, J. Hori, "Classification of the gazing or resting for brain-computer interface using Emotiv EPOC," *Biomedical Engineering Symposium*, 2015.

Address for correspondence:

Shingo Otsuka and Junichi Hori
Graduate School of Science and Technology, Niigata University, Niigata 950-2181, Japan
hori@eng.niigata-u.ac.jp

Development of a mobile and multisensory AR-BCI to operate wheelchair and electrical devices

M Sekimoto[1], Y Kobayashi[2], Y Ogawa[3], K Kotani[3, 4], Y Jimbo[1],

1Graduate School of Engineering, The University of Tokyo, Japan;
2Engineering department, The University of Tokyo, Japan;
3Research Center for Advanced Science and Technology, The University of Tokyo, Japan;
4 PRESTO, Japan Science and Technology Agency, Japan;

Abstract

A Brain-Computer Interface (BCI) enables users who cannot move their own body freely to operate machines. Recently, a system which is a combination of BCI and Augmented Reality (AR) has been proposed. This system can link real machines to augmented markers and realize an intuitive interface. In this study, we propose a mobile and multisensory AR-BCI (mmAR-BCI) system that can operate machines more smoothly, because not only visual stimuli but also auditory stimuli including position information are used to present the choices. We develop a wireless interface which capacitate users for operating wheelchair and electrical devices by using marker information both front and behind users. Also, we evaluate the effectiveness of mmAR-BCI system. The results show the possibility of the mmAR-BCI to operate the machines around the user smoothly and the appropriate stimulus presentation when using mmAR-BCI in many choices of machines.

Keywords *Brain-Computer Interface, Augmented Reality, P300, multisensory, auditory stimuli*

1 Introduction

Brain-Computer Interface (BCI) is an interface which conveys command to devices by analyzing biological signals of the brain. This interface is expected to enable amyotrophic lateral sclerosis patients or severe paralysis patients to communicate others and to operate machines [1]. Most of the BCI use electroencephalogram (EEG) as input of biological signals. Event-related potential (ERP) which is shown as a reaction of thinking and cognitive is known as a typical EEG. P300, which is one of the ERP, has a positive peak voltage after about 300ms when stimuli are given. P300 has larger amplitude than other EEGs and appears as enough distinct reaction without training. So, many researchers use this signals such as a character input system called P300 Speller [2].

The above-mentioned BCI using P300 is necessary to assign the choices beforehand, so the BCI has a problem that it is only used in limited situations such as character input. To solve this problem, using Augmented Reality (AR) is conceivable. AR can add information to surrounding real environment. The general AR systems show the contents corresponding to the markers by recognizing image from two-dimensional code pattern such as AR markers. By utilizing AR-BCI system which is a combination of AR and BCI, users can receive information of the surrounding environment as stimuli.

In previous study, there were AR-BCI systems using visual stimuli as choices of control device [3] [4]. Recently, a system that is named multisensory AR-BCI has been proposed. The multisensory AR-BCI administrated both visual and auditory stimuli to subjects [5]. However, conventional AR-BCI system including multisensory AR-BCI cannot be used for everyday-situation such as wheelchair operation because the system is large and wired each other.

Therefore, in this study, we propose a mobile and multisensory AR-BCI (mmAR-BCI) system that presents marker information as visual stimuli and/or three dimensional stereophonic sounds including position information. The proposed system employs a head-mounted display (HMD) and wireless speakers, and users can receive multisensory stimuli on the wheelchair. Users operate front machines by visual stimuli from HMD and rotate a wheelchair to the direction of behind machines by three dimensional sound stimuli. To evaluate the multisensory AR-BCI system, we measured (1) the rotation accuracy of a wheelchair, (2) discrimination accuracy of three dimensional stereophonic sounds on the wheelchair, and (3) feasibility of parallel task giving visual and auditory stimuli simultaneously.

2 Methods

2.1 Constitution of proposal system

The proposal mobile and multisensory AR-BCI system consisted of two personal computers (PC), an EEG device (g.Nautilus, gtec medical engineering GmbH, Austria), a wheelchair (JWX-1, Yamaha Motor Co., Ltd, Japan), a head-mounted display (HMZ-T2, Sony Corporation, Japan), a USB camera (QcamR Orbit AF, Logicool, Japan), a wireless IP camera (Ai-Ball, BRAVO.Co.,Ltd., Japan), four wireless speakers (VECLOS, THERMOS, Japan), and a stereophonic sound system (Xite-3D Pro, Digital Solutions Inc., Japan). Figure 1 (a) shows the front of multisensory AR-BCI system and (b) shows the back of it. We assumed a virtual cube region whose length is 70 cm and user's head is the center of the cube. Speakers were settled on apex of behind the cube so as to make plane on back of

user. A stereophonic sound system can add the position information like the same situation which each machine generates the sound by controlling the volume of four speakers.

The wireless IP camera, which was mounted on a HMD, recognized the front marker information. The USB camera, which was mounted on a back of wheelchair, recognized the behind maker information.

Figure 2 shows the procedure of the AR-BCI system. The system got the following marker information such as a class of markers (class $\in$ {visual, auditory}), the number of markers, and a marker position from ARToolKit [6] by the cameras reading markers. The system presented users visual stimuli corresponding to the front markers and auditory stimuli added position information corresponding to the behind markers. The front markers presented choices of detailed machine operation, and the behind markers presented position information of extravisual machines. When users want to manipulate extravisual machines, they select the proper choice produced by sound stimuli, and the wheelchair is rotated to the direction of the target machines. When users operate the visible device, they can select detailed choices produced by flash stimuli.

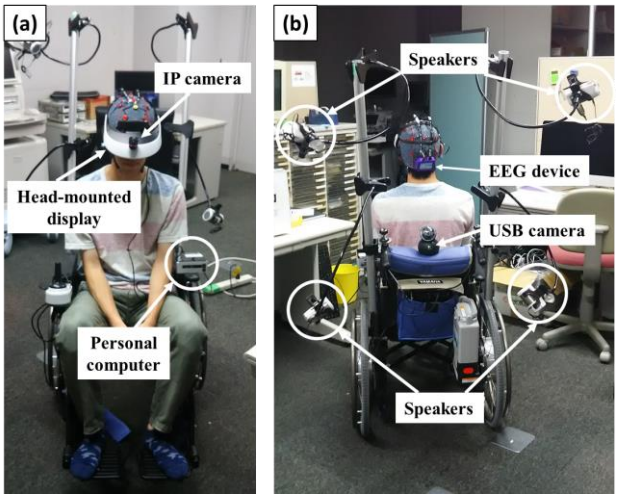

Fig.1: The mobile and multisensory AR-BCI. (a) is the front and (b) is behind the system.

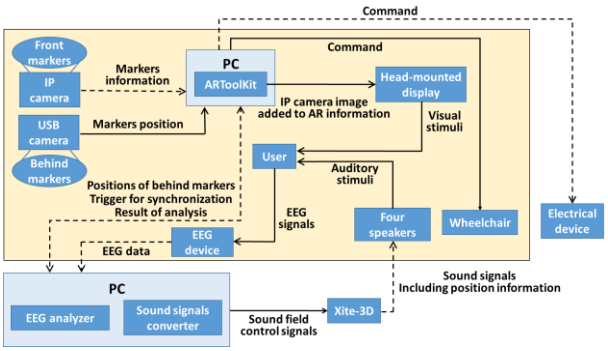

Fig.2: The procedure of the mobile and multisensory AR-BCI. The black broken arrows represent wireless transferring signals. Systems surrounded by the yellow square are movable together with the user.

2.2 Experimental method

To evaluate the mobile and multisensory AR-BCI system we measured (1) the rotation accuracy of a wheelchair, (2) discrimination accuracy of three dimensional stereophonic sounds on the wheelchair, and (3) feasibility of parallel task giving visual and auditory stimuli simultaneously.

2.2.1 Evaluation of the rotation accuracy of the wheelchair

The proposal multisensory AR-BCI system was able to operate behind machine by rotating a wheelchair to the direction of the machine. So, it is necessary for the wheelchair to face the selected marker.

In this experiment, we performed rotating the wheelchair 10 times and evaluated the angel between the wheelchair and the marker. The camera on back of the wheelchair got marker position and PC calculated the rotation angle. Then the wheelchair was rotated depending on the marker position. After the rotation, the camera on the HMD recognized marker position again and wheelchair corrects the rotation angle. The correction of the angles using marker position was carried out until the angle between marker and the wheelchair was less than 3 degrees.

2.2.2 Discrimination of presented position by three dimensional stereophonic sounds

Using the wheelchair mounting stereophonic sound system was the original in this study. So, it was necessary to estimate the possibility of discriminating three dimensional sounds in state of sitting a wheelchair. Four or nine sound stimuli were given to subjects from the back of them using stereophonic sound system. Figure 3 shows the location of the presented sound stimuli. Sound stimuli were single note of 1 kHz. Each stimulus was given 20 times. One trial was consisted 0.5 second of stimuli presentation and 1.5 second of rest. Stimulus presentation positions were settled randomly. Subjects were directed to press the key corresponding to the place of stimuli. Subjects were healthy 4 males (aged 23.25 $\pm$ 0.43 years).

2.2.3 Feasibility investigation of parallel task

In the proposal multisensory AR-BCI, increasing of the number of choices led to decreasing of machine operation speed. To solve this problem, it was conceivable that users performed the choice of task by both visual stimuli and auditory stimuli in parallel. Then we carried out two types of experiment and compared both of them. One type of experiment was that both front choices by visual stimuli and behind choices by auditory stimuli were presented simultaneously. The other type of experiment was that both front and behind stimuli were presented respectively. The former was called parallel task, and the latter was called non-parallel task.

Subjects were seated on a wheelchair and equipped EEG device and HMD. EEG data were measured from eight channel (Fz, Cz, P3, Pz, P4, PO7, Oz, PO8), and all channel ware referenced to right earlobe and grounded to AFz.

Visual stimuli were given from HMD depending on four choices of a humidifier and auditory stimuli were

given from three dimensional stereo phonic sound system depending on assumed four choices. Figure 4 (a) shows the location of auditory stimuli, and Figure 4 (b) shows the screen of the HMD. A humidifier was placed 50cm in front of the subjects. Sound stimuli were single note of 1 kHz. One trial was consisted 0.5 second of presenting stimuli and 0.5 second of rest, and stimuli from the choices of both visual and auditory stimuli were randomly presented. One type of experiment was constructed 8 times experiments. Participants were instructed to attend specified stimuli for each of the stimulus presentation point and to count the number of presenting specified stimuli in their mind. In the parallel task stimuli were given 50 times from each location in an experiment, and in the non-parallel task stimuli were given 25 times form each location in an experiment. So, the both of experimental times were equal. Subjects are healthy 4 males (aged 23.25 $\pm$ 0.43 years).

In the parallel task, flash and sound stimuli were given simultaneously in one trial. However, the orders of flash stimuli and sound stimuli were different. Thus, we could divide choice which subject attended.

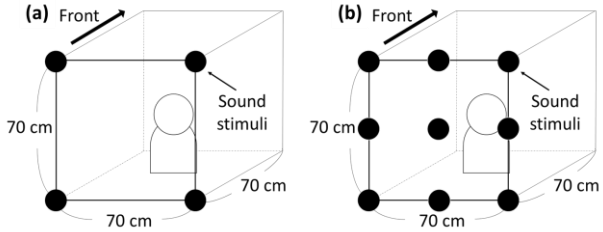

Fig.3: Conceptual diagram of the point of presented sound stimuli. Sound positions are shown in presenting four stimuli (a), and nine stimuli (b).

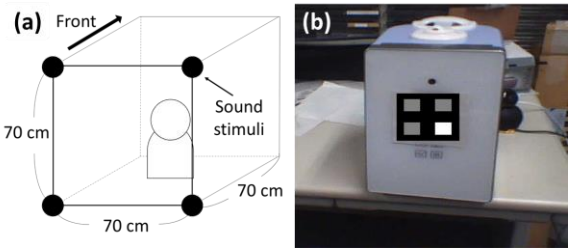

Fig.4: Conceptual diagram of presented stimuli. (a) is sound position, and (b) is the image that was presented to the subjects.

2.3 Analytical method

In this section, we explain analytical method of EEG signals and the derivation of accuracies. The EEG data amplified/digitized at a rate of 250 Hz and passed through an eight-order band-pass filter at between 0.5 Hz and 30 Hz. Data from the 25 samples before presented stimuli were used for baseline correction. We down-sampled 250 samples data after stimuli to 25 samples. We projected down-sampled EEG data to one-dimensional vector by Fisher's linear discriminant [7].
In this research, we divided learning data of reaction to a visual stimuli and auditory stimuli, and we discriminated the data separately visual stimuli and auditory stimuli. Discriminant function was different in the kind of stimuli, so we proposed the method of using probability density function. To get probability density function, we found Gaussian distribution approximation using maximum-likelihood method with the value projected to one-dimensional vector by Fisher's linear discriminant. This function enable us to derive the probability originated form target, and we can identify data using plural discriminant function. We shows the equation of proposal discriminant method (Eq. 1). N is the number of average, i is the number of stimuli, W is a projection vector, $f(x)$ is a feature vector. We used leave-one-out cross validation and $N = 5$.

$$\begin{aligned} &Predected\ Target \\ &= arg\,max\left[P\left(Target\,|W_{class}\cdot\left(\frac{\sum_i^N f(x_i)}{N}\right)\right)\right] \\ &\quad Target \in \{1,2,3,4\} \end{aligned} \tag{1}$$

3 Results

3.1 Evaluation of the rotation accuracy

Figure 5 shows the result of experiment of rotating wheelchair. The wheelchair faced to the marker at the angle of 1.61 ± 0.92 degrees.

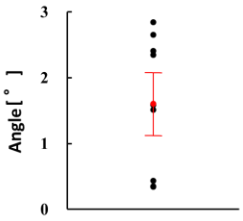

Fig.5: Angles between the wheelchair and the marker. Red point is average and red bar is standard deviation.

3.2 Discrimination of the position of sounds

Table 1 shows the results of discriminant of sounds. Distinction of four sounds was carried out in high percentage of correct answers. On the other hand, discriminant accuracy of nine sounds was low. From the above results, we should change kind of sound in the situation where sounds stimuli located more than three in vertical or horizontal. Moreover, distinct of vertical sound was the most of mistaken in both condition, so we need devise the presenting sounds such as changing the frequency in accordance with the height in the actual use.

Table 1: Accuracy of discriminant of sounds.

Number of discrimination	4 stimuli	9 stimuli
Correct [%]	91.9	29.9
Mistake(Vertical) [%]	8.1	41.8
Mistake(horizontal) [%]	0.0	10.7
Mistake(diagonal) [%]		17.6

3.3 Feasibility of parallel task

Figure 6 shows the averaged EEG waveform of subjects on Pz. In non-parallel task, ERP to attended flash stimuli had a higher positive peak at about 500 ms after presenting stimuli and a lower negative peak at about 700 ms after presenting stimuli than unattended flash stimuli, and ERP to attended sound stimuli had a

higher peak at about 600 ms after presenting stimuli than unattended sound stimuli. In parallel task, ERP to attended flash stimuli had a lower negative peak at about 700 ms after presenting stimuli than unattended flash stimuli, and ERP to attended sound stimuli had a higher positive peak at about 500 ms and 700 ms after presenting stimuli than unattended sound stimuli. The both of ERPs to sound stimuli were smaller than ERPs to flash stimuli.

Figure 7 shows averaged accuracy of subjects. Chance level is 12.5 %. In parallel task accuracy of auditory stimuli was a little lower than in non-parallel task. On the other hand, accuracy of visual stimuli was mostly same in both of tasks.

Figure 8 shows averaged bitrate of subjects. In parallel task bitrate of visual stimuli was higher than in non-parallel task, and bitrate of auditory stimuli was mostly same in both of tasks. These results indicated feasibility and usability of parallel task.

Accuracy and bitrate of sound stimuli were low in spite of the high-accuracy discrimination of sound positions (result of 3.2). Low performance of the auditory stimuli may be caused by the small amplitude of the auditory ERP in Fig. 6. To improve the accuracy and bitrate of the auditory stimuli, we can change the average number of ERP (*N* in Eq. 1) to the variable. And the system continues to present the stimuli until the probability of a target calculated by Eq.1 exceeding some criteria.

In this experiment, we did only experiment under condition that a wheelchair does not move. We will investigate a risk of using HMD when driving wheelchair.

4 Conclusions

In this research, we consisted the mobile and multisensory AR-BCI (mmAR-BCI) system that can operate front machines and move wheelchair toward the behind machine. Moreover, we evaluated the accuracy of rotating wheelchair, the discrimination of the stereophonic sound, and the feasibility of parallel task. The results show the possibility of the mmAR-BCI to operate the machines around the user smoothly and the usability of parallel task when using mmAR-BCI in many choices of machines.

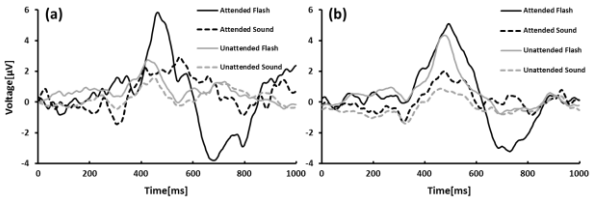

Fig.6 Averaged EEG waveform of the subjects on Pz. (a) is the waveform in non-parallel task, and (b) is the waveform in parallel task. Black solid line is ERP waveform to attended flash stimuli. Black broken line is ERP waveform to attended sound stimuli. Gray lines are waveform to unattended each stimulus, respectively.

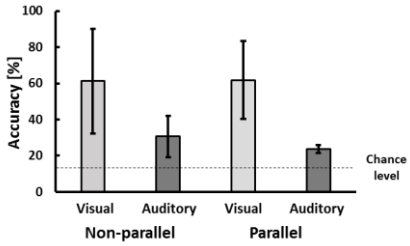

Fig.7 Accuracy for each stimuli and methods.

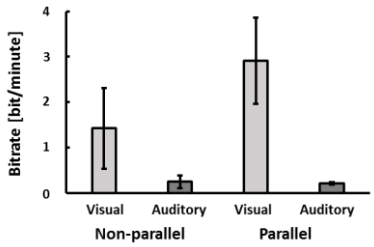

Fig.8 Bitrate for each stimuli and methods.

Acknowledgements

This study was partly supported by Strategic Information and Communications R&D Promotion Programme and KAKENHI (15H05324).

References

[1] J. R. Wolpaw, D. J. McFarland, G. W. Neat, C. A. Forneris: “An EEG-based brain-computer interface for cursor control”, Electroencephalography and clinical Neurophysiology, Vol.78, No.3 pp.252-259, 1991

[2] L. A. Farwell and E. Donchin: “Talking off the top of your head: toward a mental prosthesis utilizing event-related brain potentials”, Electroencephalography and clinical Neurophysiology, Vol.70, No.6 pp.510-523, 1998

[3] K. Kansaku, N. Hata, and K. Takano: “My thoughts through a robot’s eyes: an augmented reality-brain-machine interface”, Neuroscience research, Vol.66, No.2 pp.219-222, 2010

[4] K. Uno, G Naito, Y Tobisa, R Yoshida, Y Ogawa, K Kotani, Y Jimbo: “Basic Investigation of Brain-Computer Interface Combined with Augmented Reality and Development of Improvement Method using the Non-target Object”, The Institute of Electrical Engineers of Japan. C, Vol.133, No.12 pp.2205-2210, 2013

[5] M Sekimoto, Y Shimono, A Akao, T Isomura, Y ogawa, H Qi, K kotani, Y Jimbo: “Basic research for development of a multimodal AR-BCI” The Institute of Electrical Engineers of Japan. C, Vol. 136, No.9, 2016, in press.

[6] H. Kato: “ARToolKit: Library for Vision-based Augmented Reality”, IEIC Technical Report, Vol.101, No.652 pp.79-86, 2002

[7] C. M. Bishop: “Pattern Recognition and Machine Learning”, Springer-Verlag New York, .inc, 2006

Address for correspondence:

Masashi Sekimoto
Graduate School of Engineering, The University of Tokyo, Japan
sekimoto@neuron.t.u-tokyo.ac.jp

Research on Cortical-muscular Responses during Transitions of Sensorimotor States

Qi Huang [1, 2], Li Jiang[1], Masashi Sekimoto [2], Akihiko Akao [2], Kiyoshi Kotani [3, 4], Yasuhiko Jimbo [2],

[1] State Key Laboratory of Robotics and System, Harbin Institute of Technology, China;
[2] Graduate Shool of Engineering, The University of Tokyo, Japan;
[3] Research Center for Advanced Science and Technology, The University of Tokyo, Japan;
[4] PRESTO, Japan Science and Technology Agency, Japan;

Abstract

During myoelectric control, the time delay from the transition electromyography (EMG) signal to force output may influence the control experience and control accuracy. This paper researched the time response between cortical-muscular activity and actual output force during different sensorimotor state transitions. Experimental results revealed the different time course of transitions with increasing muscular contraction levels and decreasing muscular contraction levels. Both the inflection time points of force output and the reaction time of alpha rhythm EEG signals showed significant difference between increasing and decreasing transitions, which indicates the necessity of different time compensation strategy and the possibility of employing EEG signals to shorten the predictive time from EMG to force output and improve prediction accuracy of different transition types.

Keywords *Cortico-muscular Correlation, Electromechanical Delay, EEG*

1 Introduction

EMG based control methods are widely used for robot control [1, 2]. For the EMG based control method, the time delay from the detecting of EMG signal to the executive end has tremendous influence on control stability and experience [3]. To establish a humanoid interaction strategy, it's essential to explore the time course of cortical muscular response during human hand control. A delay of 30~100ms existing between the onset of electrical activity and measurable tension has been found in 1950s [4]. Since then, Cavanagh et al. discovered the significant difference between the delay of isometric contractions and isotonic contractions [5]. However, most of the researches focused on the delay during the onset of contraction, few researches focused on delays during other transitions between different contraction levels.

On the other hand, when people conduct muscular contractions, relevant cortico-muscular synchronization was observed by Conway et al. [6]. After that, Kristeva-Feige et al. researched the beta rhythm coherence during isometric sustained contractions [7], while Mehrkanoon et al. researched the alpha and gamma rhythm coherence when increasing contraction levels [8]. Besides, movement related cortical response was also found during the preparation of movement [9] and after the onset of contraction [10].

This paper is to explore the time course of cortical-muscular response during transitions between different contraction levels.

2 Experimental Setup

2.1 Experimental design

During experimental trials, the subjects were asked to keep steady and pressing a force sensor by conducting isometric muscle contraction of index finger with target contraction levels. Experimental cues and required force levels were displayed through a cue displayer. Within each trial, the subjects were asked to complete the following 4 processes sequentially: 1) two seconds to prepare contraction level Target 1; 2) ten seconds to maintain contraction level Target 1; 3) ten seconds to maintain contraction level Target 2; 4) seven seconds to relax and prepare for next trial. The process of one experimental trial is shown in Fig. 1. During the experiments, the displayer showed the cue of corresponding target contraction level during Process 1 to 3, while showing cross '+' during Process 4. At the same time, a bar on the displayer showed the force level emerged by muscular contraction.

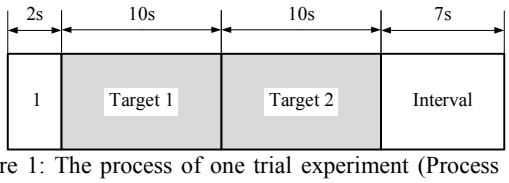

Figure 1: The process of one trial experiment (Process 1 for the preparation of Target 1).

There were three different target contraction levels, resulting in six different transition experimental conditions. Three target contraction levels and their displaying cues are as following:

(1) Non-contraction: completely relax without contraction, with displaying cue as "0";

(2) Low level contraction: contraction to output force within the range of 1.1~1.6N, approximately 20% of maximum voluntary contraction (MVC), with displaying cue as "L";

(3) High level contraction: contraction to output force within the range of 5.2~6.0N, approximately 80% of maximum voluntary contraction (MVC), with display-

ing cue as "H".

After assigning the three target contraction levels to the transition sequence, from Target 1 to Target 2, we get a total of six different transition conditions, as shown in Fig. 2. All the six transition conditions can be categorized into two classes, the incremental class and the decremental class.

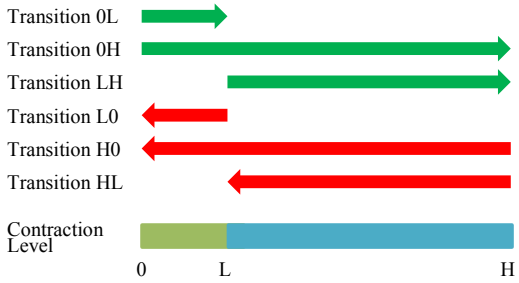

Figure 2: the target contraction levels and transition conditions (green for the incremental class, red for the decremental class)

The experiment on one subject was divided into three sessions. Each session includes 30 trials, 5 trials for each transition condition. To avoid order effects, the order of the trials in one session was pseudo randomized. Each session needs around 14.5 minutes. During the interval of sessions, the subjects could relax and move their limbs slightly. To avoid irrelevant muscular contractions, the subjects were postulated to fit their hands on the desk and contact the pinch meter gently.

2.2 Subjects and Recording

The experiment was run with 4 healthy male subjects, noted as Subject S1~S4. They are right handed, at age 24 ~ 27. All subjects participated with full knowledge of the content and the purpose of the experiment. The experiment was approved by the morality board of the University of Tokyo.

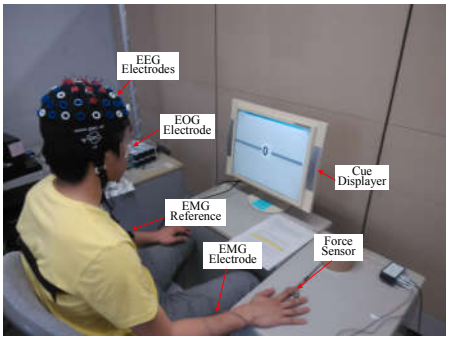

Figure 3: The layout of the devices

To measure the cortico-muscular synchronization activity, the EEG signals and EMG signals were recorded simultaneously. The layouts of the experimental devices are shown in Fig. 3. The EEG signals were recorded with 17 monopolar electrodes and a 32-channel amplifier (band pass filter 2-60Hz, notch filter 50Hz, sampling rate 256Hz, g.USBamp, gtec, Austria). As illustrated in Fig. 4, the electrodes were placed over the sensorimotor cortex (FC3, FC1, FCz, FC2, FC4, C5, C3, C1, Cz, C2, C4, C6, CP3, CP1, CPz, CP2, CP4) according to international 10-20 system. To reduce the artifact of electrooculogram, another channel of the amplifier was used to record the electrooculogram. The EMG was recorded with one bipolar electrode (band pass filter 20~460Hz, sampling rate 1024Hz, SX230-1000, Biometrics, UK) over the flexor digitorum superficialis of the dominant hand. The output force was measured by a pinch meter (P200, Biometrics, UK) with the sampling rate of 1024Hz.

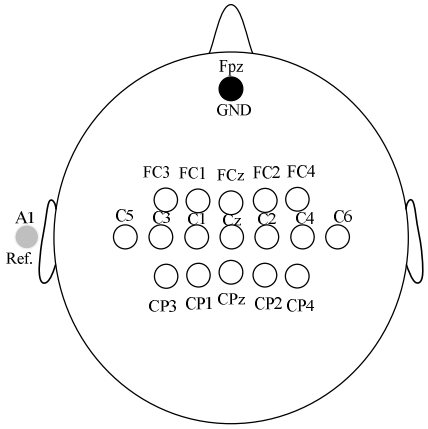

Figure 4: The layout of the EEG electrodes based on international 10-20 system (white electrodes for EEG recoding, black electrode as the ground of the A/D converter, grey electrode as the reference).

3 Methodology

3.1 Processing of Force and EMG signals

To improve the accuracy of the determination of time point, the force signal was fitted to a logistic function after low pass filtered by a 20-order zero phase finite impulse filter (FIR). The fitting function was as following,

$$\tilde{Y} = \frac{A}{1+\exp[-R(t-\tau)]} + I\,, \qquad (1)$$

Where A corresponds to the amplitude of the transition, I corresponds to the initial value before the transition, τ corresponds to the time point with maximum changing rate and R corresponds to the general changing rate of the curve.

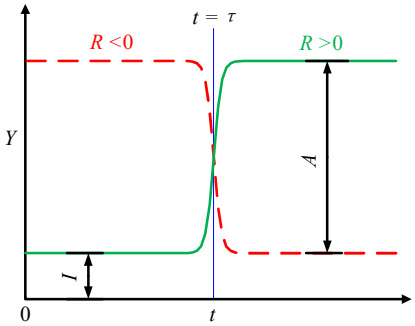

Figure 5: Parameters of logistic function fitting

To compare the time course of different transition conditions, we choose the parameter τ as the inflection time point, and the parameter d=4ln3/|R| to describe the

duration of the transition, which equals the time elapsing from I+0.1A to I+0.9A or the inverse way.

Similar to the processing of force signal, the root mean square (RMS) feature of EMG signal was also fitted to the logistic function. Before fitting, the EMG signal was filtered by a 50Hz zero phase notch filter. For the data series $s(i)$, i=1,2,…l in the one-second long segment, the RMS of the data was computed as:

$$RMS = \sqrt{\frac{1}{l}\sum_{i=1}^{l} s(i)^2} \qquad (2)$$

3.2 Processing of EEG signals

To remove the artifact of electrooculogram, independent component analysis (ICA) was employed [11]. To get the event related change of EEG signals, we mainly focus on the alpha rhythm change. Instantaneous alpha amplitude was normalized after enveloping. The normalized alpha (Na) amplitude is as following

$$Na(t) = \frac{e(t) - e_{Ref}}{e_{Ref}} \qquad (3)$$

Setting the time when the cue of the target changed as t=0 in one trial, where $e(t)$ is the enveloping value of alpha rhythm, e_{Ref} is the mean value of $e(t)$ from -2s to 0. The time point of the largest peak from 0 to +3s of Na(t) is recorded as the reaction time of EEG signals.

Fig. 5 shows the typical trial data after processing.

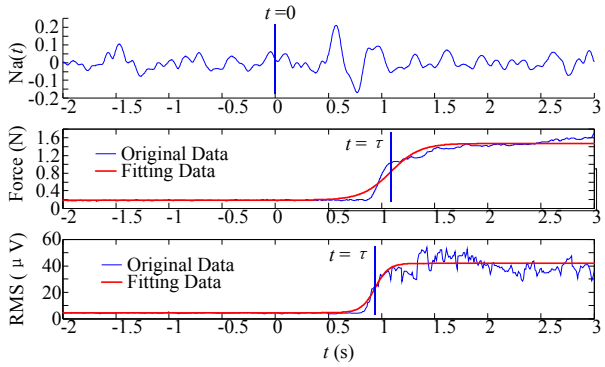

(a) Data of Trial 4, Session 2, Transition 0L, Subject S3

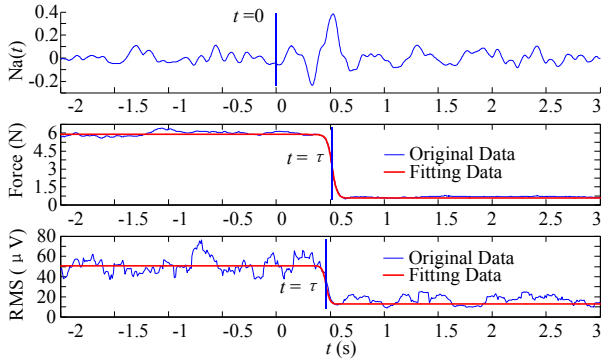

(b) Data of Trial 1, Session 2, Transition H0, Subject S2

Figure 6: Typical trial data after processing

4 Results and Discussions

The inflection time points of the transitions of EMG signals are shown in Fig. 7. The bars in the figures correspond to mean values of the subjects, while the error lines correspond to standard deviation values. The 'average' items correspond to mean values and standard deviation values ignoring the combinations of Target 1 and Target 2. Based on the inflection time points of the transitions of EMG signals, we computed the relative time from EMG time points and to force time points and EEG peaks, positive values corresponding to force time points and EEG peaks after EMG time points and negative values corresponding to force time points and EEG peaks before EMG time points. Similar to Fig. 7, we drew Fig. 8 and Fig. 9 to illustrate the relative time.

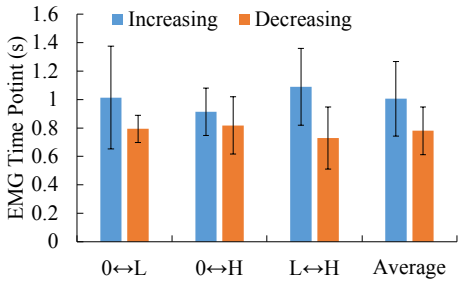

Figure 7: EMG inflection time point after cue

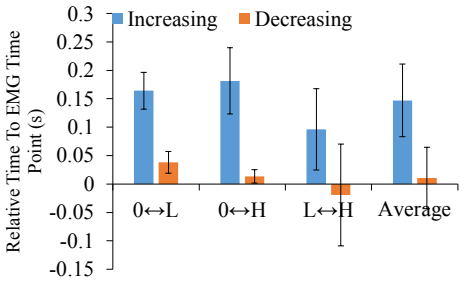

Figure 8: Relative time of force inflection time point to EMG inflection time point

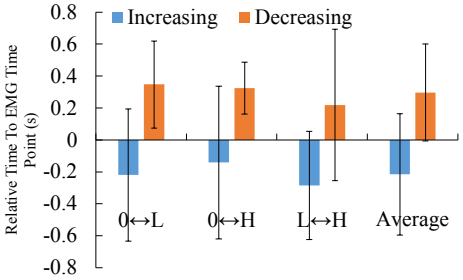

Figure 9: Relative time of EEG peak time point to EMG inflection time point

Repeated measures ANOVA were conducted to verify whether different target combinations (0↔L, 0↔H and L ↔H) have influence on the time indices within same signal source and same changing direction (increasing and decreasing) or not. Results showed no significant influence. And then we saw the target combination difference as a repeated factor like subject difference, and conducted repeated measures ANOVA to verify whether signal sources and changing directions have influence on the time indices or not. Results showed significant influence ($p<0.001$). Then post-hoc multiple comparisons were conducted to get the pair-wise comparing results. Specifically, there was no significant difference between increasing and decreasing EMG time points.

There was significant differences between increasing and decreasing force time points (137ms, $p<0.001$), and increasing and decreasing EEG peaks (-512ms, $p=0.038$).

The durations of force and EMG transitions are shown in Fig. 10 and Fig. 11. Paired wise comparing changing directions, durations of increasing force transitions were 211ms longer ($p<0.001$) than decreasing force transitions while there was no significant difference between increasing and decreasing EMG transitions.

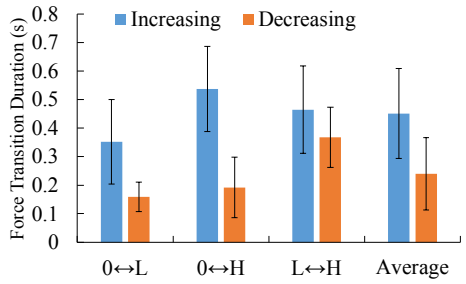

Figure 10: Duration time of force transitions

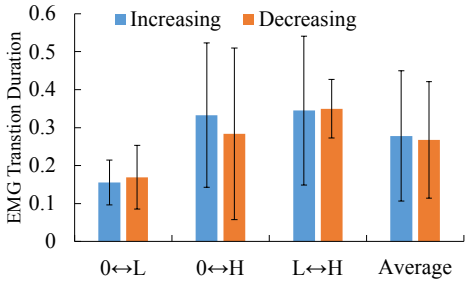

Figure 11: Duration time of EMG transitions

Although we divided the transitions into six classes, the major difference were revealed between transitions with increasing contraction level and transitions with decreasing contraction level. The subjects could not response to the cue transition immediately but with a time delay. When the delay appears in EMG transitions, it was around 900ms. The force and EEG peaks are asynchronous to EMG signals and show significant difference between different transition directions. During increasing transitions, the asynchronization was 147ms later for force but 215ms earlier for EEG peak. During decreasing transitions, the asynchronization was almost zero for force but 296ms later for EEG peak. The variation along transition types indicates the possibility of employing EEG signals to check and modify the predictive model of myoelectric controllers.

The future work is to explore the possibility of employing EEG signals to shorten the predictive time from EMG to force output and improve prediction accuracy of different transition types.

5 Conclusions

This paper researched the time response between cortical-muscular activity and actual output force during different sensorimotor state transitions. Experimental results revealed the different time course of transitions with increasing muscular contraction levels and decreasing muscular contraction levels. Acquired time delay data could be used for better myoelectric control in the future.

Acknowledgement

This work is partly supported by China Scholarship Council (CSC), SCOPE and MEXT/ JSPS KAKENHI Grant Number 15H05324.

References

[1] C. Yang, G. Ganesh, S. Haddadin, S. Parusel, A. Albu-Schaeffer and E. Burdet. Human-like adaptation of force and impedance in stable and unstable interactions. *IEEE transactions on robotics*, 27(5):918-930, 2011.

[2] A. Arash, N. Tsagarakis and A. Bicchi. Tele-impedance: Teleoperation with impedance regulation using a body-machine interface. *The International Journal of Robotics Research*, 0278364912464668, 2012.

[3] B. Hudgins, P. Parker and R.N. Scott. A New Strategy for Multifunction Myoelectric Control. *IEEE Transaction on Biomedical Engineering*, 40(1):82-94,1993.

[4] V.T. Inman, H.J. Ralston, C.M. Saunders, B. Feistein, and E.W. Wright, Relation of human electromyogram to muscular tension. *Electroencephalography and Clinical Neurophysiology*, 4: 187-194, 1952.

[5] P.R.Cavanagh and P.V. Komi, Electromechanical delay in human skeletal muscle under concentric and eccentric contractions. *European journal of applied physiology and occupational physiology*, 42(3): 159-163, 1979.

[6] B.A. Conway, D.M. Halliday, S.F. Farmer, U. Shahani, P. Maas, A.I. Weir, and J.R. Rosenberg. Synchronization between motor cortex and spinal motoneuronal pool during the performance of a maintained motor task in man. *The Journal of Physiology*, 489(3): 917-924, 1995.

[7] R. Kristeva-Feige, C. Fritsch, J. Timmer, and C.H. Lücking. Effects of attention and precision of exerted force on beta range EEG-EMG synchronization during a maintained motor contraction task,*Clinical Neurophysiology*,113(1):124-131, 2002.

[8] S. Mehrkanoon, M. Breakspear, and T.W. Boonstra. The reorganization of corticomuscular coherence during a transition between sensorimotor states. *Neuroimage*, 100: 692-702, 2014.

[9] T. Kajihara, M.N. Anware, M. Kawasaki, Y. Mizuno K. Nakazawa, and K. Kitajoet. Neural dynamics in motor preparation: From phase-mediated global computation to amplitude-mediated local computation. *NeuroImage*, 118: 445-455, 2015.

[10] H. Shibasaki. Cortical activities associated with voluntary movements and involuntary movements. *Clinical neurophysiology*, 123(2): 229-243, 2012.

[11] T.P. Jung, S. Makeig, M. Westerfield, J. Townsend, E. Courchesne, and T.J. Sejnowski. Removal of eye activity artifacts from visual event-related potentials in normal and clinical subjects. *Clinical Neurophysiology*,111(10): 1745-1758, 2000.

Address for correspondence:

Qi Huang
State Key Laboratory of Robotics and System, Harbin Institue of Technology, China
Graduate School of Engineering, The University of Tokyo, Japan
huang@neuron.t.u-tokyo.ac.jp

The estimate of mental workload induced by the use of different processors in a cochlear implant during word recognition in a noisy environment

Giulia Cartocci[1,2*], Anton Giulio Maglione[1,2*], Dario Rossi[1,2], Enrica Modica[1,2], Paolo Malerba[3], Gianluca Borghini[2], Gianluca Di Flumeri[2], Pietro Aricò[2], Fabio Babiloni[1,2]

[1]Department of Molecular Medicine, Sapienza University of Rome, Italy;
[2]BrainSigns srl, Italy;
[3]Cochlear s.r.l. Italy;
*These authors equally contributed to the present paper

Abstract

Advances in the biomedical signal interpretation allow using cerebral signals to assess important cognitive functions in humans, such as the cerebral workload. In fact, the increase in the frontal EEG power spectrum in the theta band and the simultaneous decrease in the parietal EEG power spectrum in the alpha band have been employed in several studies to estimate the mental workload index (IWL). In the present study, the IWL was employed to identify the most appropriate cochlear implant processor among Freedom, CP810 and CP910 (Cochlear Ltd) during a word in noise recognition task. Furthermore, in correspondence of the use of each of the three processors two conditions of noise filtering have been also investigated. The CP910 was the processor inducing the lower IWL among the tested ones. Additionally, the trials in which the Noise filter reduction function was adopted reported the subject's lower IWL values. Results support the capability of identifying the device eliciting less workload level. Such devices would make available user's cognitive resources for additional tasks. The application of the biomedical signal interpretation open the way in a strict future to a new use of cerebral signals to evaluate the impact of several sensors and prosthetic devices.

Keywords *EEG, Theta & Alpha band, Listening effort.*

1 Introduction

Nowadays, we are assisting to continuous improving in performances reported by cochlear implant (CI) users. This observation is tightly related to technological developments and clinical rehabilitation advancements occurring in these years. However, scientific evidences show how fitting CI for optimal speech perception does not necessarily optimize, that is reduce, listening effort. Listening effort level in fact may change between CI processing conditions for which speech intelligibility remains constant [1]. Listening effort has been defined as the proportion of limited cognitive resources engaged in interpreting the incoming auditory signal, so the presence of noise or distortions in a speech signal thus increases cognitive demand and listening effort [2].

Neurophysiological measures have been already employed for assisting the clinical evaluation of hearing impaired subjects in CI candidates [3], CI users [4] and tinnitus [5,6,7]. Generally, the criteria for the choice of the most suitable device is based on subjective measures, but the mental workload level could be estimated through: a) performance evaluation, b) subjective questionnaire and c) physiological measurement. The third modality differentiates from the others since, directly estimated from the electroencephalographic (EEG) signal, it could provide more objective information [8]. Furthermore, the choice of the most appropriate CI fitting is guided by subject's and by clinicians' evaluations and speech intelligibility scores. Speech intelligibility tasks and questionnaires (NASA TLX) were not able to reveal improvements in task execution, despite reaction times measures detected improvement linked to device's spectral resolution increase [1]. Several studies support the EEG spectra modulation corresponding to the variation of the mental workload and to the allocation of mental effort [e.g. 9], and in particular in relation to studies on pilots [10]. At the increase in the frontal EEG power spectra in the theta band (4-7 Hz) and the simultaneous decrease in the parietal EEG power spectra in the alpha band (8-12 Hz) a mental workload increase occurs, known as index of workload (IWL) [8]. Speech in noise recognition produce higher effort and/or stress in hearing impaired subjects in comparison to normal hearing (NH) listeners [11,12,13]. In a recent study, IWL levels have been measured during a forced choice word recognition task in CI children, with the aim of investigating the reaction to different noise conditions [14]. Authors reported a modulation of the IWL in the phase preceding the listening of the word (an IWL increase during the subjects' most challenging noise condition) and in the phase before the word recognition execution (a possible IWL burnout during the same noise condition). A further step from the investigation "environmental challenging features", such as different noise conditions, is the "device challenging features", that is if different versions of cochlear implant devices elicit different measurable levels of mental workload. With this aim, in the present study it has been designed to

investigate three processors versions have been commercializing from 2005 to 2013 by the same company (Cochlear Ltd), so to maintain the same quality standard. To summarize, objective of the present study is to address the following questions: "What cerebral effort is the subject experiencing during the listening, beyond his performances?" and "Is there a way to objectively identify the best device choice for each subject despite behavioral performances?".

2 Methods

The subject was a 43 years old male unilateral CI user, postlingually deaf (probably genetic etiology), implanted at 35 years old in his right side and not aided in his left ear. He was asked to performed a word recognition with and without background babble noise. The selected disyllabic words were taken from a clinical standardized set (Audiometria Vocale. Cutugno, Prosser, Turrini). The experimental conditions were: "No Noise"(NN), with the subject hearing words stimuli in quiet; "Noise without filter reduction" (NwoF) and Noise with filter reduction" (NF). All the auditory experimental conditions were tested using 3 different kind of processors: Freedom, CP810 and CP910 by Cochlear. The signal to noise ratio (SNR) was +5 in all the experimental conditions and the intensity for the stimuli delivery was 65dB. The NN condition was used only to verify the participant's starting level of words comprehension so, reaching the 95% it will not be discussed anymore in the article.
The processors included in the testing were all produced by the same company (Cochlear Italia, Bologna, Italy):

1. Freedom (2005): it uses one omni-directional microphone and a dual post directional microphone. Both microphone systems help the recipient achieve enhanced directionality in front of them. Two of the Freedom's optional functions have been tested in the present work: i) "Beam" allows to focus on the sounds coming from the direction in which the subject is looking, using a dynamic directionality (e.g. when talking with someone in a crowd); ii) "ADRO" is the normal default directionality response.
2. CP810 (2009): presenting speech processing programs with optional functions, among which ADRO (as Freedom) and "Zoom", both tested in the present study. Zoom provides fixed directionality in front of the subject. CP810 uses two omni-directional microphones; the output from the second microphone is electronically delayed and subtracted from the first microphone output to provide directionality.
3. CP910 (2013): it presents an improved dual-system microphone in comparison to the CP810, and a completely automatic processing of the sounds. Also CP910 ADRO function has been tested, along as the "Background Noise Reduction" (SNR-NR). The SNR-NR works by statistically analyzing the incoming signal (irrespective of direction) and estimating the instantaneous SNR of the sound. It assesses the listening environment and detects the background noise level in each frequency channel. It then estimates the SNR in each channel for each analysis frame. The channels with poor SNRs indicative of background noise are attenuated, whereas channels with positive SNRs, typically dominated by speech, are retained [15].

Since it has been shown that hearing-aid-like noise reduction strategies can improve performances on a secondary task, even when no improvement in speech intelligibility is seen [16], a hearing device feature, such as noise reduction, although maybe not relevant when assessed by an intelligibility test, may instead be beneficial leading to a reduction in listening effort. Due to the suggested influence of the background noise on the listening effort of CI recipients, two filters features conditions were tested: 1) No noise filter reduction use, that is the use of ADRO alone; 2) Noise filter reduction use, in other words the use of Beam, Zoom and SNR-NR for the Freedom, CP810 and CP910 respectively.

Consistently in the experimental conditions noise and words stimuli were delivered form 1 front and 1 back loudspeakers, positioned 0° and +180° in relation to the subject. During the trials including the background noise it was emitted continuously. Each experimental condition comprised 20 trials (20 words), each trial lasted up to 8 seconds, varying in length depending on the subject's response time. During the task the subject listened to a word and then was instructed to verbally say only the just heard word.

Subject was sitting on a comfortable chair in a shielded room. A digital ambulatory monitoring system (Bemicro EBNeuro, Italy) was used for the EEG recording. Electrodes were wet and placed according to the international 10-20 system (Fp1,Fp2, F7,F8,F3,F4,Fz,T3,T4,C3,C4,Cz,P7,P8,P3,P4,Pz,O1,O2). Signals were acquired with a sampling frequency of 256 Hz. The EEG recording was filtered with a band pass filter (2-30 Hz) and then the Independent Component Analysis (ICA) was used to manually remove artifacts and blink component from the traces by an experienced researcher. Successively EEG recordings were segmented into epochs of 1 second each, shifted of 0.25 seconds. The Power Spectrum Density (PSD) was calculated for each epoch and channels, observing the EEG PSD values in theta (4-8 Hz) and alpha (8-12 Hz) bands. The index of workload (IWL) was defined as the ratio between the averaged EEG PSD in theta band over the central frontal area (F7,F8,F3,F4,Fz) and the average value of EEG PSD in alpha band over the central parietal area (P7,P8,P3,P4,Pz) as in the following formula:[9]

$$IWL = PSD(\theta F) / PSD(\alpha P) \quad (1)$$

The IWL values were analyzed by the repeated measures Analysis of Variance (ANOVA) in order to compare the different: kinds of processor (Freedom, CP810 and CP910) and the different noise filter conditions of the devices (No noise filter reduction and Noise filter reduction) during the task.

3 Results

Behavioral results were based on the number of words correctly identified within each trial by the

subject. Even without reporting a statistical significance (ANOVA F(5,95)=1.341 p=0.254) a higher percentage of correct responses was obtained in the Noise filter reduction application in comparison to the No noise filter reduction condition (Fig.1). In particular, the best score was obtained for both the Noise filter reduction and the No noise filter reduction during the CP910 sound processor use.

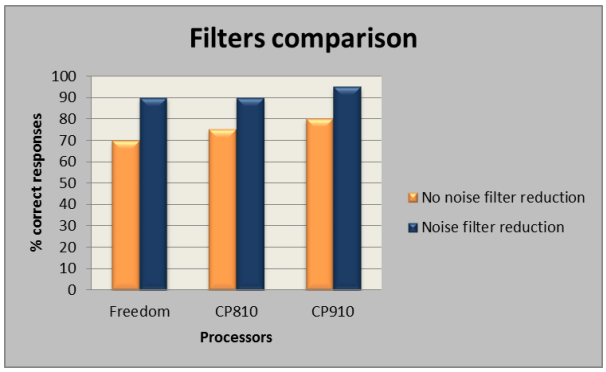

Figure 1: Behavioral scores reported in the comparison among different processors varying the filter modality (without and with noise filter reduction).

The comparison between the IWL values obtained during the testing of the three different kinds of sound processor (Freedom, CP810 and CP910) showed a statistical significant difference (F(2,180) = 3,046 p=0.05), with the lower value reported in the CP910 trial and the higher value in the Freedom trial (Fig.2). Considering the filters features (Fig.3), the trials in which the Noise filter reduction function was adopted reported statistically significantly lower IWL values in comparison to the trials with No noise filter reduction use (F(1,90) = 8,027 p = 0,006).

4. Discussion

The selected sound processors have been already compared in literature on the basis of traditional clinical outcomes: such as speech perception tests. Data showed a significant improvement when using Nucleus 6 (CP910) in comparison to Nucleus 5 (CP810) in adults [17] and children, but circumscribed at the speech in noise perception test [18]. The neurometric approach to the listening effort in CI users has been approached by EEG studies using event related potentials (ERP), reporting a correlation between N2/N4 latencies and rated listening effort [19]. Furthermore, beyond the effort level rating, the above mentioned research by Cartocci et al. [14] showed an increase of IWL values in cochlear implanted children when tested in the most demanding noise condition for them. The results presented in this article shift the focus of the listening effort from the environment-related effort to the device-related listening effort. With regards to the IWL values obtained by the experimental subject while adopting each of the different sound processors, it has been attained the lower workload level in correspondence of the use of the CP910 use.

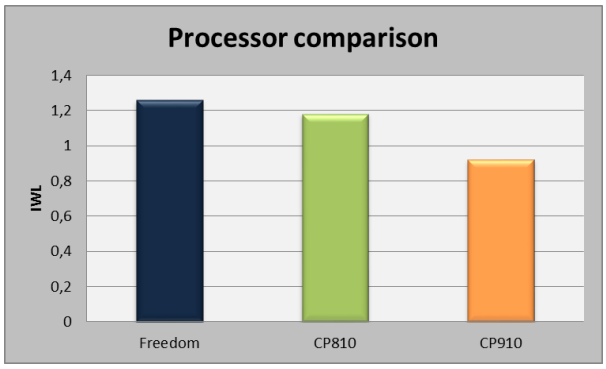

Figure 2: Workload index values reported in the comparison between processor types in a cochlear implant recipient.

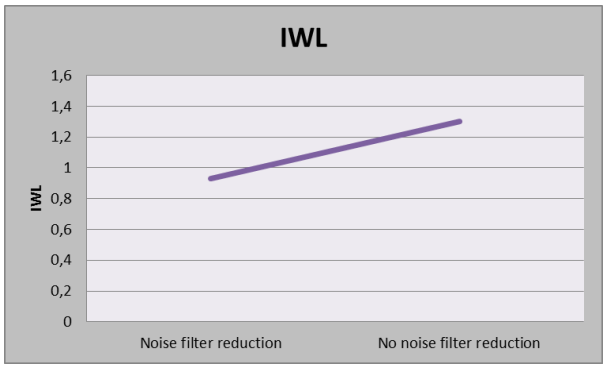

Figure 3: Workload index values reported in the comparison between the Noise filter reduction and the No noise filter reduction condition ($p<0.01$).

The present results are in accord to a very recent study investigating the workload levels induced by an auditory forced choice word recognition task in adult unilateral cochlear implant users [20]. Authors found evidence of a statistical significance of the interaction between kinds of processors and noise filter reduction use, with a trend of lower IWL values in correspondence of the use of the CP910 processors. Some authors hypothesize that Noise Reduction (NR) features in hearing devices reduce listening effort and frees up cognitive resources for other tasks [16]. Hafter and Schlauch [21] proposed that NR algorithms in the processor do not improve speech reception thresholds (SRTs) because performing a function similar to that of the listeners' auditory and cognitive systems. However the same authors suggested that the NR, substituting these physiological functions, may lighten listeners' cognitive load. Therefore, NR might not affect the SRT but may release attentional resources to be used for other, simultaneous tasks. This reduction in cognitive load could be important in natural settings, where multitasking is the norm and cognitive demands are greater. The concept of identifying devices allowing to save cognitive resources appears extremely worthy for facing everyday challenging situations such as noisy environments for cochlear implanted subjects (Fig.2). This observation acquires clear evidence just thinking for example at the requirements for the sustained

attention that children have to generate during their learning processes in the early scholar period of their life. Preschoolers and school-aged children with CI present 2 to 5 times greater risk of clinically significant deficits in comparison to NH children, for instance in the areas of comprehension and conceptual learning and attention [22].Finally, despite the obvious limitation of the single case nature of the present study, data suggest the applicability and usefulness of mental workload estimation for the choice of the most proper biomedical device in patients.

4 Conclusions

The objective of this study was twofold: 1) "What cerebral effort is the subject experiencing during the listening, beyond his performances?" Results suggest that although behavioral results didn't show marked differences among processors, especially when the Noise filter reduction function was activated, EEG results showed a statistical significant difference among IWL values connected to the different processors employment. 2) "Is there a way to objectively identify the best device choice for each subject despite behavioral performances?" Results highlight that the application of the biomedical signal interpretation, open the way to an approach of measuring useful parameters for the best device choice; in this scenario the devices inducing the lower IWL values seem to be preferable because potentially making available cognitive resources for additional demands.

References

[1] C. Pals, et al. Listening effort with cochlear implant simulations. *J. Speech Lang. Hear. Res.*, vol. 56, no. 4, pp. 1075–1084, Aug. 2013.

[2] S. Stenfelt and J. Rönnberg. The Signal-Cognition interface: Interactions between degraded auditory signals and cognitive processes. *Scandinavian Journal of Psychology*, vol. 50, no. 5, pp. 385–393, Oct. 2009.

[3] J. D. Campbell, et al.. Clinical Application of the P1 Cortical Auditory Evoked Potential Biomarker in *Semin Hear*, vol. 32, no. 2, pp. 147–155, May 2011.

[4] A. Sharma, et al.. Developmental and cross-modal plasticity in deafness: Evidence from the P1 and N1 event related potentials in cochlear implanted children. *Int J Psychophysiol*, vol. 95, no. 2, pp. 135–144, Feb. 2015.

[5] G. Cartocci, D. Mannarelli, N. Locuratolo, C. Pauletti, M. Scarpino, L. Antonaci, G. Attanasio, F. Fattapposta, R. Filipo. Serotonin activity in tinnitus: an Intensity Dependence of Auditory Evoked Potentials (IDAP) study. XIX Congresso *SIPF - SOCIETÀ ITALIANA DI PSICOFISIOLOGIA*. Brescia, 14-16 novembre 2011, vol.149, p. S32-S32, 2011..

[6] G. Cartocci, G. Attanasio, F. Fattapposta, N. Locuratolo, D. Mannarelli, and R. Filipo. An electrophysiological approach to tinnitus interpretation. *Int Tinnitus J*, vol. 17, no. 2, pp. 152–157, 2012.

[7] G. Attanasio, F. Y. Russo, R. Roukos, E. Covelli, G. Cartocci, and M. Saponara. Sleep architecture variation in chronic tinnitus patients. *Ear Hear*, vol. 34, no. 4, pp. 503–507, Aug. 2013.

[8] G. Borghini, L. Astolfi, G. Vecchiato, D. Mattia, and F. Babiloni. Measuring neurophysiological signals in aircraft pilots and car drivers for the assessment of mental workload, fatigue and drowsiness. *Neurosci. Biobehav. Rev.* , vol. 44, pp. 58–75, 2014.

[9] W. Klimesch. EEG alpha and theta oscillations reflect cognitive and memory performance: a review and analysis. *Brain Res Brain Res Rev*, vol. 29, no.2-3, pp. 169-95, Apr 1999.

[10] P. Aricò, G. Borghini, I. Graziani, T. Fumihiko, Y. Sun, A. Bezerianos, N. Thakor, F. Cincotti, and F. Babiloni. Towards a multimodal bioelectrical framework for the online mental workload evaluation. 36th Annual International Conference of the IEEE Engineering in medicine and biology society, Chicago, USA, 2014.

[11] F. Asp,,et al.. A longitudinal study of the bilateral benefit in children with bilateral cochlear implants. *Int J Audiol*, vol.54, no.2, pp. 77-88, Feb 2015. Epub 27 Nov 2014.

[12] A. Caldwell and S. Nittrouer. Speech Perception in Noise by Children With Cochlear Implants. *J Speech Lang Hear Res*, vol. 56, no. 1, Feb. 2013.

[13] D. Wendt, et al. Impact of Background Noise and Sentence Complexity on Processing Demands during Sentence Comprehension. *Front Psychol*, vol. 7, Mar. 2016.

[14] G. Cartocci, A. G. Maglione, G. Vecchiato, G. D. Flumeri, A. Colosimo, A. Scorpecci, P. Marsella, S. Giannantonio, P. Malerba, G. Borghini, P. Aricò, and F. Babiloni. Mental workload estimations in unilateral deafened children. *37th Annual International Conference of the IEEE Engineering in Medicine and Biology Society (EMBC)*, 2015, pp. 1654–1657.

[15] S. J. Mauger, et al. Cochlear implant optimized noise reduction. *J Neural Eng*, vol. 9, no. 6, p. 65007, Dec. 2012.

[16] A. Sarampalis,. Objective measures of listening effort: effects of background noise and noise reduction. *J. Speech Lang. Hear. Res.*, vol. 52, no. 5, pp. 1230–1240, Oct. 2009.

[17] S. J. Mauger, et al. Clinical evaluation of the Nucleus® 6 cochlear implant system: Performance improvements with SmartSound iQ. *Int J Audiol*, vol. 53, no. 8, pp. 564–576, Aug. 2014.

[18] A. Plasmans, et al.. A multicentre clinical evaluation of paediatric cochlear implant users upgrading to the Nucleus® 6 system. *International Journal of Pediatric Otorhinolaryngology*, vol. 83, pp. 193–199, Apr. 2016.

[19] M. Finke, et al. On the relationship between auditory cognition and speech intelligibility in cochlear implant users: An ERP study. *Neuropsychologia*, vol. 87, pp. 169–181, Jul. 2016.

[20] A.G. Maglione & G Cartocci et al. Cochlear implant features and listening effort induction: measurement of the mental workload experienced during a word in noise recognition task. *Front. Hum. Neurosci.* Conference Abstract: SAN2016 Meeting. doi: 10.3389/conf.fnhum.2016.220.00043

[21] E.R. Hafter, et al "Cognitive factors and selection of auditory listening bands," in *Noise-induced hearing loss* (pp. 303–310). Philadelphia: B.C. Decker, 1992.

[22] W.G. Kronenberger, et al. Neurocognitive risk in children with cochlear implants. *JAMA Otolaryngol Head Neck Surg*, vol. 140, no. 7, p. 608-15, Jul 2014.

Online detection of auditory attention in a neurofeedback application

Rob Zink[1,2], Annelies Baptist[1,2], Alexander Bertrand[1,2], Sabine Van Huffel[1,2], Maarten De Vos[3]

[1]KU Leuven, Department of Electrical Engineering (ESAT), STADIUS Center for Dynamical Systems, Signal Processing and Data Analytics, Kasteelpark Arenberg 10, 3001 Leuven, Belgium.
[2]iMinds Medical IT, Leuven, Belgium.
[3]Engineering Department, Oxford University, Oxford, United Kingdom.

Abstract

Auditory attention detection (AAD) holds promising potential for usage in auditory-assistive devices. Being able to train subjects in achieving high AAD performance would increase the application potential of AAD. This requires an acceptable temporal resolution and the analysis should take place online. In the current study, we implemented a fully automated closed-loop system that allows for convenient recording outside a lab environment. We achieved high AAD accuracies with a trial length of 10 seconds and provided subjects with visual feedback on their ongoing performance. This exploratory study proves the feasibility of investigating the effect of neurofeedback in such a setting, paving the way for future studies.

Keywords *Auditory Attention Detection, Mobile EEG, Neurofeedback*

1 Introduction

In the past few years, electroencephalography (EEG) has been employed for auditory attention detection (AAD). A pretrained decoder that makes a linear combination of the EEG and delayed versions of it allows to extract a signal with a significantly higher correlation to the attended speaker's envelope as compared to the unattended speaker's envelope [1]. In dual-speaker scenarios, the subject's attention to a specific speaker could be reliably detected with high accuracy in research labs [2, 3, 4]. In addition, several analysis and preprocessing steps have been evaluated to optimize the estimation made by the decoder [5]. The accuracy was found to be dependent on the considered trial length for calculating the decoder and correlations [1, 4]. The temporal resolution of the attention tracking is dependent on the trial length and can therefore be seen as a trade-off between accuracy and temporal resolution. For applications in real-time, shorter trial lengths such as 10s are preferred over the most reported 60s trial length, for example. Online analysis of the attended audio source holds potential for use in assistive audiological devices, such as hearing aids [3, 4] (e.g. to steer a beamformer to the attended speaker).

The effectivity of EEG-based AAD depends, not only on the temporal resolution and differences in speech (i.e. bilabial sounds), but also on the responses of the test subjects themselves. Large differences in accuracy between subjects were observed in the aforementioned studies. It is known for other cognitive paradigms (e.g. such as P300 oddball studies) that subjects' physiological responses can differ substantially, even within subjects when moving from restricted to more real-life scenarios [6]. Providing feedback about the ongoing EEG signals was shown to be beneficial for other EEG paradigms to strengthen the brain responses (e.g., motor imagery [7]). A similar reasoning can be applied for AAD, i.e. training users to elicit stronger brain responses related to the attended speech stream might increase the accuracy. To this end users might experience positive effects from such a neurofeedback training to increase the performance of EEG-based AAD.

In the current study, we explore the application of the AAD in real time. The subjects were recorded in an office environment with mobile EEG hardware and consumer-grade headphones. This is more convenient for the subjects compared to a lab environment. In addition, we apply a neurofeedback scenario to provide a proof-of-concept for a fully automated closed loop system. We implemented an online AAD analysis with a time resolution of 10 seconds. Half of the subjects received visual feedback about their AAD accuracy per time point. We show competitive results compared to existing studies with offline analyses which paves the way to investigate the effect of long term neurofeedback in future studies (e.g. at subjects' home).

2 Methods

2.1 Participants

Twelve native Dutch-speaking subjects (mean age (SD) 22.4 ($\pm$2.1) years, six women) participated in the current experiment. Subjects reported normal hearing and no past or present neurological or psychiatric conditions. All participants signed informed consent forms prior to participation. The ethics committee of the KU Leuven approved the experimental setup.

2.2 Data Acquisition

The acquisition was conducted with a SMARTING mobile EEG amplifier from mBrainTrain (Belgrade, Ser-

bia, www.mbraintrain.com). This amplifier comprises a wireless EEG system running on a notebook computer using a small 24-channel amplifier with similar characteristics to a stationary laboratory amplifier (<1uV peak to peak noise; 500Hz sampling rate). The EEG was measured using 24 Ag/AgCl passive scalp electrodes (Easycap), placed according to the 10-20 standard system with positions: FP1, FP2, Fz, F7, F8, FC1, FC2, Cz, C3, C4, T7, T8, CPz, CP1, CP2, CP5, CP6, TP9, TP10, Pz, P3, P4, O1 and O2. Impedances were kept below 10 kOhm and an abrasive electrolyte gel was applied to each electrode. EEG data were recorded through Openvibe (and stored for offline (reference) analysis) and streamed from Openvibe to Matlab via the labstreaminglayer interface (LSL). The audio stories were played via Openvibe and pre-loaded into Matlab for the online analysis part and synced via the Openvibe audio triggers. Every ten seconds, the data was retrieved from the LSL stream and analyzed in Matlab. Both online and offline analysis used custom-made Matlab scripts.

2.3 Stimuli and Procedure

Audio stimuli consisted of four stories in Dutch (of approximately 13 minutes length), narrated by four different male speakers. Silences were truncated to 500ms and each story was divided into two parts, resulting in 8 sessions of $\pm$6.5 minutes in length. Subjects listened to two stories presented simultaneously through low-cost consumer headphones (Sennheizer mx475). The two audio streams were filtered by head-related transfer functions leading to more realistic perception [2]. Subjects were asked to pay attention to only one story on the left or right side. Afterwards, multiple-choice questions were presented and subjects indicated the difficulty in listening (i.e., indicated on a ten-point scale) and answering some questions about the story. After listening to one full story (2 x 6.5 minutes), subjects switched attention to the opposite side (i.e. left or right speaker). The experimental setup consisted of two blocks of two stories each. The first half of the recordings (24 minutes) were used for estimating the decoder, the latter for evaluation. Half of the subjects received visual feedback (feedback group) on the laptop screen for the second part of the experiment, whereas the other subjects received no feedback (control group). Order effects were avoided by alternating the listening sides among subjects.

2.4 Preprocessing and Analysis

EEG data were bandpass-filtered at 1-8 Hz and consequently down-sampled to 20Hz for each 10s segment of data. The absolute value of the audio waveforms with power-law compression with exponential 0.6 was taken to obtain the audio envelopes, and then an 8Hz low-pass filter was applied [5]. Envelopes were extracted from the clean audio signals for the separate speakers. Offline analysis was done on trial lengths up to 60s, in steps of 10s. Real-time analysis was done on trial lengths of 10s.

The decoder-construction approach followed similar steps as presented in previous publications [1,3]. In short, seven time-shifted versions of the EEG trial were obtained in a 0-300ms range after stimulus onset. All EEG channels and their 7 delayed versions are then linearly combined using a pre-trained linear decoder w. During training, the decoder is optimized such that the resulting output signal has a minimal mean squared error (MMSE) with the attended speech envelope. Thie linear MMSE decoder w can be computed as $w = R^{-1}c$, where R is the covariance matrix over all the EEG channels, and c the cross-correlation vector between the EEG channels and the attended speech envelope [2]. All the Rs and cs computed over the training trials were averaged to create a single average covariance matrix and cross-correlation vector [5]. For each test trial Pearson's correlation coefficient is employed to quantify the decoders' reconstructed envelope to the attended stimulus (CA) and unattended stimulus (CUA). The highest correlation value determines to which of the two speakers the subject was listening at the current trial. The decoders were trained following an (offline) leave-one-trial-out structure on all data. The decoders for the second half of the experiment were computed solely on the training data of the first half of the experiment.

The subjects who received feedback were presented with a colored circle in the center of the screen. After every test trial of ten seconds, the colored circle indicated the performance of the past ten seconds. Four different colors were used for performance indication: Dark red, light red, light green and dark green. Thresholds determining the colors were based on the training set in such a way that the CA and CUA difference would be equally divided for the correct and incorrect trials. Note that trials with a larger CA as compared to CUA (i.e., correct trials) are always green and the incorrect trials are always red. Decoders for analyzing the second half of the dataset were based on the individual training data.

3 Results

3.1 All sessions

Grand average classification accuracy for the 10s window was 81.9% (SD =5.9%). Increasing the window length in the offline analyses raised the accuracy up to 96.9% (SD=3.5%). Figure 1 displays single-subject and grand-average accuracies at different trial lengths. All subjects scored above chance level (>55% at 10s up to >62% at 60s) for all window lengths.

Stable performance was achieved up to removal of 16 channels that contributed the least in the envelope-reconstruction model performance. With a reduced set of 8 channels, an accuracy of 78.8% (SD = 6.5%) was achieved. If we maintained only seven or fewer electrodes, the performance dropped significantly. This is depicted in Figure 2. To evaluate the most discriminative and most redundant channels, we plotted the average number of removal per channel, down to 8 channels. This is illustrated by the left topoplot in Figure 2. The red/yellow colors depict the channels that were re-

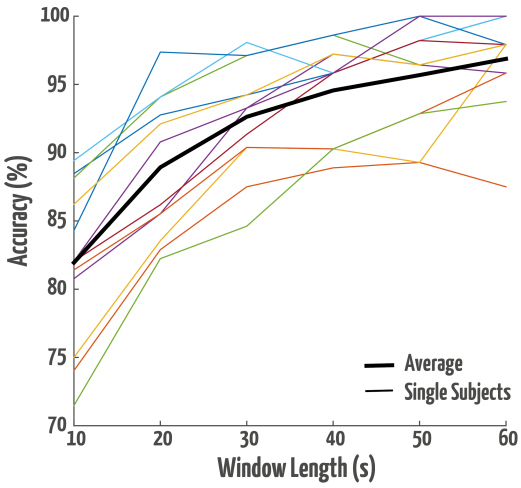

Figure 1: Grand average and subject specific decoding accuracies for different window lengths.

moved without having a large influence on general accuracy. It can be noted that especially the frontal and posterior channels contributed the least to the decoders performance. In contrast, the temporal electrodes (around the ear) are most important, as is depicted by the yellow colors in the right topoplot.

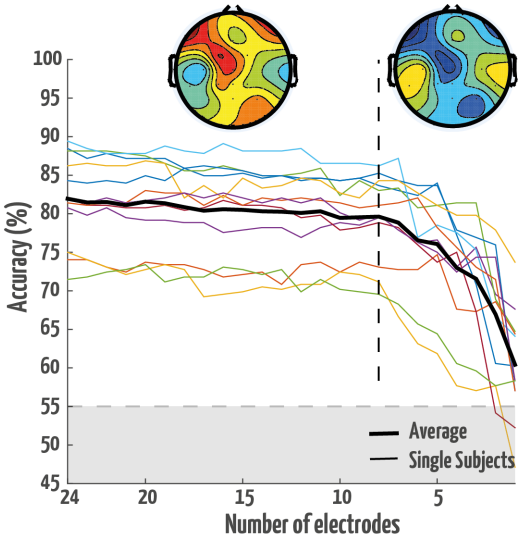

Figure 2: Grand average and subject specific decoding accuracies depending on the number of electrodes for the 10s window length. The channel with the lowest decoder weight (after correction for channel variance differences) is removed in each iteration. Topoplots represent the average distribution for the least discriminative channels on the left and most discriminative on the right. The shaded area indicates the chance level.

3.2 Neurofeedback

Average online classification accuracy in the online decoding of the second half of the data was 79.7% (SD = 7.0%) using the pre-trained decoder. When evaluating the offline leave-one-out decoder, average accuracy was 83.0% (SD = 7.5%). This increase in accuracy was significant (t11=-4.1 $p<0.01$), indicating that additional training data resulted in an increase at the 10s windows. In contrast, this difference was not significant for 60s trial length; both types of decoders achieved equal accuracies: 96.2% and 96.9% for the pre-trained and leave-one-out decoder, respectively.

Comparing the accuracy within the feedback group between the feedback session and the training session revealed a slightly higher accuracy in the feedback session, +4,1 percentage points as calculated with the leave-one-out decoder when averaged over all subjects in the feedback group. Five out of six subjects scored higher in the feedback session, compared to the training session. For the group not receiving feedback, the difference between the second session and the training session was -0.2 percentage points. No effect was found for increased or decreased CA or CUA changes in the feedback group with respect to the training session.

Relative occurrence of the four feedback cues was 41.8% dark green, 40.7% light green, 10.1% light red and 8.7% dark red. We evaluated the temporal patterns at which the cues were evident between the feedback and the hypothetical feedback cues on the training set (i.e., calculated offline with similar thresholds as the feedback session; subjects did not see this feedback.). Entries in Figure 3 indicate, by the colors the relative frequency at which a colorcue in the rows was followed by the colorcues in the columns. It can be noted that, in the feedback session, participants shifted more frequently to dark red after seeing light red. For the training sessions, subjects seem to have less often two consecutive light red trials but more often from light green to light red. Note that the difference in threshold between the light colors is smaller, compared to the dark colors. For example, light green denotes a correct decoding, but with less conficence than in the case of dark green.

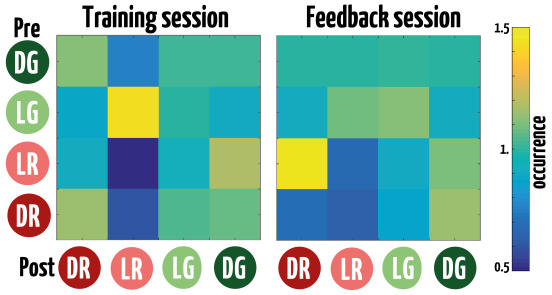

Figure 3: Adjacency matrices for the Training and Neurofeedback session. The entry color indicates the normalized frequencies of a specific color cue (in the rows) that is followed by any other cue (columns). Cues: DG = Dark Green, LG = Light Green, LR = Light Red and DR = Dark Red.

3.3 User Metrics

On average, subjects answered 84.2% (SD = 7.9%) of the questions correctly. We contrasted the number of correct responses of each subject to the general accuracy at the 10s window analysis. This revealed a strong positive correlation ($r = 0.72$, $p < 0.05$). One subject was removed, as its number of correct responses differed more than 2 standard deviations from the mean. Figure 4A displays the individual subjects' accuracy and number of correct responses. A regression line has been added for illustrational purposes. A moderate negative correlation (r

= -0.56, p = 0.059) was found between the average accuracy and the subjects' reported difficulty in answering the questions and overall listening. This correlation is depicted in Figure 4B.

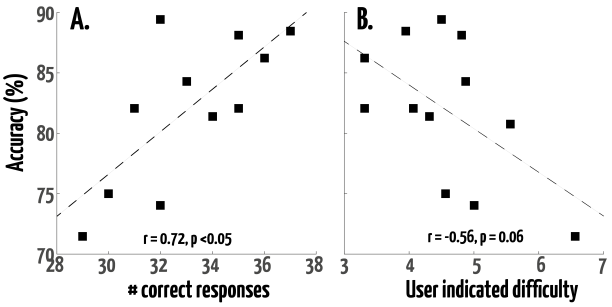

Figure 4: Scatterplots illustrating the correlation between the decoder grand-average accuracy and the number of correct responses after each story in A and the User indicated task difficulty in B. A regression line has been added for illustrational purposes.

4 Conclusion and Discussion

In the current study, we evaluated the possibility of implementing an online closed-loop system for auditory attention detection. With window lengths of 10s, we obtained robust accuracies that, even with a low number of electrodes, are predictive. We provided a fully working feedback system, and the online implementation did not significantly degrade the results. Although a slight improvement in accuracy was observed when using neurofeedback, the effects are not attributed much significance due to the limited number of measurements. Overall the results were similar and competitive to existing lab-studies. This is particularly interesting for future application in long term studies in real-life conditions such as the subjects' home.

The high accuracies in the present work were obtained with 24 electrodes and were found to be stable up to removal of 16 channels. These results are in line with insights presented by [4] and are encouraging for future work in online processing. The neurofeedback results show no clear negative deflection in accuracy due to increased distraction. Nevertheless, subjects who saw light-red feedback were more prone to perform bad in the next trial as well. One explanation may be that when subjects became aware of an error (i.e. shift from green trial to light-red) this leads to a brief surprise effect which lowers the attentional response in the next 10 seconds. In general we conclude that future studies with an increased number of subjects and longitudinal measurements might demonstrate positive effects on the AAD that would be highly valuable for future users of auditory-assistive devices.

A limitation in the current study is the lack of incorporating real-life audio signals. Recently there have been studies evaluating the effect of noisy reference signals and showing a negative impact on performance [3, 8] In addition, real-life scenarios involve frequent switching of attention. This factor is not well reflected in the current paradigm; subjects only switched attention after each story. To this end, it would be interesting to see how a state-space model would perform, as this was shown to have a high temporal resolution [9].

Acknowledgements

Research supported by Research Council KUL: CoE PFV/10/002 (OPTEC); Belgian Federal Science Policy Office: IUAP P7/19/(DYSCO, 20122017), iMinds Medical Information Technologies SBO 2015; Flemish Government, FWO projects: G.0427.10N; EU: (FP7/20072013)/ERC Advanced Grant: BIOTENSORS (nr. 339804). This paper reflects only the authorsFL views, and the Union is not liable for any use that may be made of the contained information.

References

[1] J. A. O'Sullivan, A. J. Power, N. Mesgarani, S. Rajaram, J. J. Foxe, B. G. Shinn-Cunningham, M. Slaney, S. A. Shamma, and E. C. Lalor. Attentional selection in a cocktail party environment can be decoded from single-trial EEG. *Cerebral Cortex*, 25(7):1697–1706, 2015.

[2] N. Das, W. Biesmans, A. Bertrand, and T. Francart. The effect of head-related filtering and ear-specific decoding bias on auditory attention detection. *Internal Report, http://homes.esat.kuleuven.be/ abertran/publications.html*.

[3] S. Van Eyndhoven, T. Francart, and A. Bertrand. EEG-informed attended speaker extraction from recorded speech mixtures with application in neuro-steered hearing prostheses. *arXiv preprint arXiv:1602.05702*, 2016.

[4] B. Mirkovic, S. Debener, M. Jaeger, and M. De Vos. Decoding the attended speech stream with multi-channel EEG: implications for online, daily-life applications. *Journal of neural engineering*, 12(4):046007, 2015.

[5] W. Biesmans, N. Das, T. Francart, and A. Bertrand. Auditory-inspired speech envelope extraction methods for improved EEG-based auditory attention detection in a cocktail party scenario. *IEEE Transactions on Neural Systems and Rehabilitation Engineering*, (in Press), 2016.

[6] R. Zink, B. Hunyadi, S. Van Huffel, and M. De Vos. Mobile EEG on the bike: disentangling attentional and physical contributions to auditory attention tasks. *Journal of Neural Engineering*, 13(4):046017, 2016.

[7] C. Zich, M. De Vos, C. Kranczioch, and S. Debener. Wireless EEG with individualized channel layout enables efficient motor imagery training. *Clinical Neurophysiology*, 126(4):698–710, 2015.

[8] A. Aroudi, B. Mirkovic, M. De Vos, and S. Doclo. Auditory attention decoding with EEG recordings using noisy acoustic reference signals. In *2016 IEEE International Conference on Acoustics, Speech and Signal Processing (ICASSP)*, pages 694–698. IEEE, 2016.

[9] S. Akram, A. Presacco, J. Z. Simon, S. A. Shamma, and B. Babadi. Robust decoding of selective auditory attention from MEG in a competing-speaker environment via state-space modeling. *NeuroImage*, 124:906–917, 2016.

Address for correspondence:

Rob Zink — KU Leuven (Belgium), Department of Electrical Engineering (ESAT), STADIUS Center for Dynamical Systems, Signal Processing and Data Analytics. rob.zink@esat.kuleuven.be

Alpha and low-beta oscillatory patterns extracted with Canonical Polyadic Decomposition relate to LDA classifier performance in real-life Mobile EEG

Rob Zink[1,2], Borbála Hunyadi[1,2], Sabine Van Huffel[1,2], Maarten De Vos[3]

[1]KU Leuven, Department of Electrical Engineering (ESAT), STADIUS Center for Dynamical Systems, Signal Processing and Data Analytics, Kasteelpark Arenberg 10, 3001 Leuven, Belgium.
[2]iMinds Medical IT, Leuven, Belgium.
[3]Engineering Department, Oxford University, Oxford, United Kingdom.

Abstract

The level of attention to cognitive tasks is related to the performance and is therefore likely to also influence the classification accuracy in EEG (auditory) paradigms. Alpha band oscillations (8-12 Hz) in EEG are known to be related to attention and can be quantified through spectral analysis. However, on the channel level, these oscillations are mixed with other brain activity and spatial patterns may vary across tasks. To this end we aim to separate ongoing alpha, theta (4-8 Hz) and low-beta (13-16 Hz) waves in a data driven way and relate it to classifier outcome as obtained by the widely used regularized LDA from a previously recorded outdoor mobile auditory oddball study. The three experimental conditions varied in degree of cognitive load and physical effort. We extract the aforementioned frequency band activity at the single trial level by Canonical Polyadic Decompositon of wavelet-transformed EEG data. Meaningful correlations of the alpha and low-beta-band activity with respect to the subject classification accuracy were found in the two most complex conditions and relate to power band calculations with existing techniques that require electrode selection.

Keywords *Canonical Polyadic Decomposition, Oscillatory patterns, Mobile EEG*

1 Introduction

Recently, mobile EEG has been utilized to investigate attentional paradigms in outdoor conditions (e.g. [1, 2]) Significant differences in task related P300 Event Related Potential (ERP) were identified in real-life ambulatory conditions, as compared to a restricted setup. The influence on the P300 waveform of head and muscle artifacts that arose from being in a fully realistic outdoor biking scenario was found to be minor in previous work [2]. The latter study provided evidence that increased cognitive load in real-life environments is likely to decrease the P300 ERP, which was similar to the thoughts of [1]. Alpha power was found to be diminished in the free biking condition, which may be related to increased attentional demands.

Alpha band activity has been linked to various elements of attentional processing [3]. Low beta components were found to affect attentional processing, as evident through biofeedback training [4]. Theta oscillations were shown to relate to mismatch-negativity responses in MEG data [5]. Being in more demanding scenarios leads to alterations in brain patterns due to automatic (motor) tasks or stronger distractions. For example, significant changes in alpha and beta activation were linked to increasing levels of engagement in virtual reality scenarios [6]. Similar differences might emerge in alpha and beta band characteristics when contrasting real-life recording situations, such as biking outdoors, to more stationary recording environments. Monitoring the alpha and closeby theta and low beta band oscillations on a single-trial basis might reveal additional condition or task-specific effects that are overlooked by the standard analysis which merely focuses on classifier construction and P300 waveform properties [2].

In the current study, we explore the effect of theta (4-8 Hz), alpha (8-12 Hz) and low beta (12-16 Hz) oscillations on classification accuracy as obtained by a widely used regularized Linear Discriminative Analysis (rLDA) classifier. This method was applied to the data from [2], which features three different outdoor mobile recording conditions while the subjects performed a three-class-auditory oddball task. One condition was a completely free ride in an open outdoor environment and can be seen as completely unconstrained.

Canonical Polyadic Decomposition (CPD) is a powerful, data-driven method for extracting ongoing oscillations. CPD was shown to extract relevant alpha sources on a single-trial basis [7]. Decomposing wavelet-transformed EEG data (i.e. Morlet) with CPD, we are able to derive data-driven estimates of the aforementioned oscillations assuming they are present. Each component in the CPD can be characterized by an individual frequency, space and time signature and is classified as theta, alpha and low beta band source if their spectral signature corresponds to the respective frequency bands. In addition, given the nature of CPD, it is possible to remove selected sources. To this end we not only investigate the magnitude of these specific oscillatory components, but also separate them to obtain cleaned EEG datasets.

All in all, we derived meaningful estimates of the

amount of alpha and low beta activity which correlate to the classification accuracy at subject level, without the need for selecting appropriate channels.

2 Methods

2.1 Initial Analysis

The data used in the current study is obtained from [2]. To summarize, fifteen subjects (mean age (SD): 27.1 ($\pm$2.5)) participated in the trial and performed a three-class auditory oddball task. The ethics committee of the KU Leuven approved the experimental setup. The acquisition was conducted with a SMARTING mobile EEG amplifier from mBrainTrain (Belgrade, Serbia, www.mbraintrain.com) with 24 Ag/AgCl passive scalp electrodes (Easycap). Extended Infomax ICA was used to remove EOG activity, and then muscle activity was removed through BSS-CCA. All EEG was band-pass filtered ([0.5-20] Hz). After re-referencing offline, the EEG trials consisted of 22 channels and 500 time-points [-200 to 800ms] with zero being the stimulus onset. In addition, data were down-sampled to 40 Hz. Three different outdoor recording conditions with increasing level of cognitive load were measured. One condition involved sitting completely still on a fixed bike (Still). The second condition involved sitting on the fixed bike while pedaling at a comfortable pace (Pedal). The third involved biking freely around the perimeter (Move). During all sessions, the subjects had to attend the target tone and ignore all other tones and (natural) distractions. For the classification procedure, we followed the approach explained in [2]. Classification accuracies were obtained through regularized LDA based on five-fold cross validation. The average rLDA accuracies for the three conditions were: 77.5%, 72.3% and 66.2% for the Still, Pedal and Move conditions, respectively. Two subjects were excluded, as the accuracy was not above chance level for the Move condition (i.e. $<$55%). Per trial, a continuous wavelet decomposition was applied (i.e. Morlet) with corresponding scales in the 1-16 Hz interval.

2.2 Canonical Polyadic Decomposition

Multidimensional signals can be decomposed by the CPD as a sum of rank-1 terms. For the three-dimensional case, the CPD will decompose a tensor X as follows:

$$X = \sum_{r=1}^{R} a_r \circ b_r \circ c_r + \varepsilon \qquad (1)$$

The number of the components is represented by R, the signatures of all atoms in every mode are represented by a_r, b_r, and c_r, and ε represents the error of the model. Every mode has an individual signature which represents the extracted component characterized; in the three-dimensional tensor, which represents the ERP as a structure of channel $\times$ time $\times$ frequency, c_r would provide the frequency signature, b_r the time courses, and a_r would contain the various atoms' spatial distribution. The CPD model operates on a trilinear basis, i.e. the vectors of each mode are proportional to one another within a component of rank-1. In general terms, when the data follows a structure of rank R, unique decomposition occurs up to permutation and scaling of the extracted components. We computed CPD with the NLS (nonlinear least squares) algorithm in Tensorlab toolbox 3.0, which is available publicly. For an overview of the application of tensor models in biomedical signal analysis, we refer the reader to [8].

2.3 Extracting oscillatory components

Low beta 12-16 Hz, alpha 8-12 Hz and theta 4-8 Hz bands were considered in the CPD decomposition and the corresponding CWT scales were used for the decomposition resulting in a 22 channels $\times$ 40 timepoints $\times$ 17 frequency scales tensor. Rank R was set to 3, as this was shown to be adequate in previous work [7]. The models were randomly initialized and repeated several times to investigate significant differences in output. There were no significant differences, which suggests that the CPD extracted components are stable.

To quantify and select appropriate oscillatory components, we detected the peak in each component's spectral mode and categorized it as theta, alpha or low beta if the index was in one of the corresponding frequency bands. With R=3 CPD will extract 3 components which together explain the most possible variance of the signal. Therefore, if the brain oscillation of interest have low power, it is possible that one or more of the frequency bands of interest are not represented in the components. Figure 1a illustrates a derived single-trial component of subject 1, and the spatial, temporal and spectral modes are depicted from top to bottom, respectively. The source was categorized as an alpha band source, as is evident from the spectral mode. This process was repeated for all trials to obtain, per subject and condition, a number of trials that were categorized into at least one of the three frequency bands. This was in turn correlated to the subject average accuracies as obtained with rLDA.

2.4 Removing selected components

Besides detection, we also reconstruct the frequency band-specific information from the CPD component by multiplying the temporal and spectral mode and scaling it by the channel weight in the decomposition. This process generates per channel a matrix that estimates the source's contribution for a given trial. The result was subtracted from the original wavelet transformed data and an inverse wavelet transform was applied consecutively to obtain cleaned channel $\times$ time data in which the selected component is removed. An example of removing the alpha source from Fig. 1A has been illustrated in Fig. 1B.

2.5 Validation

To validate the data-driven CPD estimates, the frequency estimation process was repeated manually by calculating the normalized band power (based on power spectral density) on three different spatial locations to

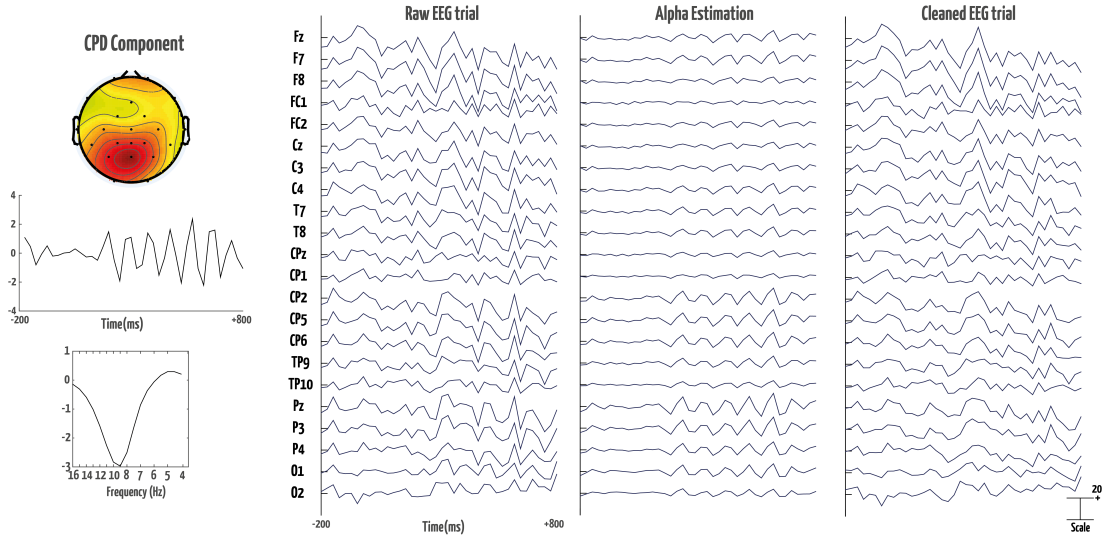

Figure 1: A) A single alpha component of the CPD model of subject 1. From top to bottom, the spatial, temporal and spectral modes are depicted. B) Example of the single-trial EEG data from (a) and the reconstructed alpha patterns by back-reconstructing the CPD component and applying an inverse wavelet transform on the filtered time-frequency matrix provides the cleaned EEG trial.

capture frontal, central and posterior oscillations at channels Fz, Cz and O1 respectively. Removal of these oscillations was achieved by applying a stop-band FIR filter on the selected frequency band on all channels. This will be referred to as the reference method.

3 Results

3.1 Subject-level

A theta band component was detected in nearly all trials: 93.9% in the Still condition, 94.0% in the Pedal condition, and 94.2% in the Move condition. For the alpha band, 74.0%, 72.2% and 70% of the trials were identified to have at least one alpha band component for the Still, Pedal and Move conditions, respectively. Compared to the Pedal (8.7%) and Still (8.5%) conditions we saw an increase in low-beta band quantity in the Move condition, 13.5%. Correlating the subject-average number of alpha trials to the classification accuracy revealed a marginally significant negative correlation (r= -0.51, p = 0.07) in the Pedal condition. Similarly, the low-beta activity correlated marginally with the Pedal condition accuracies as well (r= -0.51, p = 0.08). In addition, a significant correlation was found between the low-beta and rLDA accuracies in the Move condition (r= -0.65, p $<$0.05). These correlations and median spatial plots of the CPD extracted components are illustrated in figure 2. The theta band did not correlate (p $>$0.1) with the rLDA accuracies in any condition. For this reason, results of the theta band and still condition are omitted in the figures, for brevity. Interestingly, no significant correlations between the reference power band estimations on the posterior channel with either band were found. The frontal and central channel estimation of low-beta in the Move condition as extracted by the reference method correlated in similar fashion to the rLDA accuracy as the CPD results (r= -0.72, p $<$0.05) and (r= -0.74, p $<$0.01) respectively. Significant correlation of the reference power bands and the Pedal condition were absent, only similar (negative) trends can be noted.

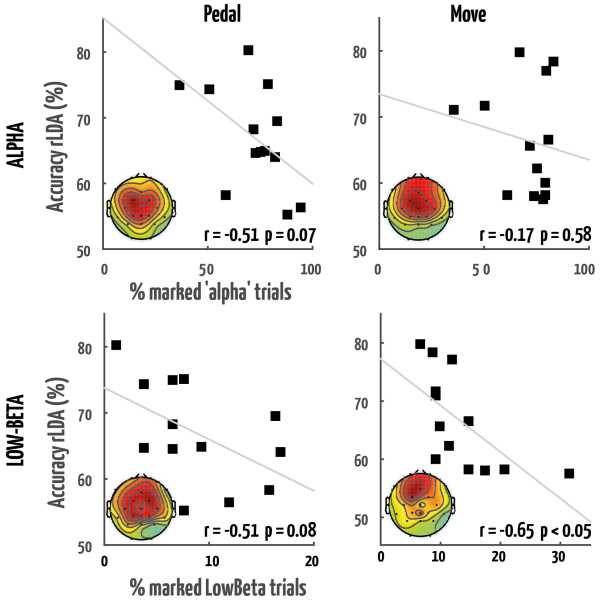

Figure 2: Scatterplots and correlations between the number of trials noted as alpha (top) or low-beta (bottom) by the CPD and the average accuracy. Each data point represents a single subject. The lines are best fit (Least-squares) to the data points and are for illustrative purposes only. The topoplots represent the median spatial mode of the extracted components.

3.2 Removal at Single-Trial level

Finally, we removed the selected oscillatory CPD components per trial from the alpha and low-beta band as these correlated with the average rLDA accuracy. Table 1 represents the grand average classification accuracies for the reference rLDA and for the removal of alpha or low-beta activity on the indicated trials. The accuracy in the move condition improved significantly after removal of the alpha activity (t_{12}=2.65, p $<$0.05). This increase in accuracy was evident for 10 of the 13 subjects. In the other conditions no significant changes can be noted. Ap-

plying the reference stopband filter on the alpha and low-beta bands resulted in similar effects on the classification accuracy as the CPD correction; in the Move condition a slightly higher accuracy was evident (t_{12}=2.21,p <0.05).

Table 1: Average classification accuracies in the Still, Pedal and Move conditions for the regular data (Reference), with removal of alpha activity and low-beta as extracted by the CPD. Significant differences (p <0.05) with respect to the reference are indicated with an asterix.

	Still	Pedal	Move
Initial Accuracy	77.5%	72.3%	66.2%
Alpha Removal	76.9%	72.7%	68.3% *
Low-beta Removal	77.0%	72.4%	66.3%

4 Conclusion and Discussion

We identified meaningful correlations with respect to single-subject performance on the auditory oddball task in the alpha and low-beta band for the Pedal and Move conditions. The extracted theta band activity did not correlate with the classifier performance. Similar results were obtained with existing band power estimation techniques, although the latter requires appropriate selection of spatial location and was less predictive of user rLDA performance in the Pedal condition. This illustrates that the frequency components that were extracted in a data driven way by CPD were meaningful and can be applied in an automated fashion. In addition, removal of the extracted alpha oscillatory activity increased the grand average accuracy in the Move condition. Finally, in all conditions we illustrated that we did not remove discriminative information related to the task.

CPD estimates components' spatial, temporal and spectral characteristics based on the patterns in the data tensor. This way, relevant electrodes that convey similar spectral activity are clustered in a single component. Calculating frequency power on the original [channel $\times$ time $\times$ frequency] tensor requires selection of (a) specific channel(s). For example, posterior channels did not seem to capture predictive alpha and low-beta oscillations whereas the more central and frontal CPD extracted patterns did (Fig. 2). Correcting for the alpha activity increased the classification accuracy in the Move condition. This indicates that the alpha activity, or at least part of it, had a negative effect on the task-related ERP signal. This is a surprising finding, as the alpha power was shown to be low in the Move condition compared to the others [2].

Deriving spectral features that correlate with classifier performance might be a promising addition for evaluating subject differences or tuning classifier characteristics. On a single-trial level, similar derivations have been made in phase-locking value which has been reported to provide valuable information of stimulus-locked oscillations that in turn influence the ERPs of interest [9, 10].

Finally, an extension of the CPD model to a Block Term Decomposition (BTD) might allow for better extraction of the spatio-spectral signatures in our model [11]. A BTD can allow two or more modes to be of higher rank, allowing more variation to be modeled. In the current framework, BTD might be able to capture shifts in phase of the various oscillations over electrodes.

To conclude, the presented work provides exploratory results on the effect of theta, alpha and low-beta oscillations on the classifier performance, contrasting the results between three different outdoor mobile-recorded datasets. Especially in unconstrained or physically engaging scenarios, evaluating these patterns in a data-driven way can provide valuable information on predicted classifier performance.

Acknowledgements

EU: (FP7/20072013)/ERC Advanced Grant: BIOTENSORS (nr. 339804). This paper reflects only the authors' views, and the Union is not liable for any use that may be made of the contained information.

References

[1] M. De Vos, K. Gandras, and S. Debener. Towards a truly mobile auditory brain–computer interface: exploring the p300 to take away. *International journal of psychophysiology*, 91(1):46–53, 2014.

[2] R. Zink et al. Mobile EEG on the bike: disentangling attentional and physical contributions to auditory attention tasks. *Journal of Neural Engineering*, (accepted), 2016.

[3] E. Başar et al. A short review of alpha activity in cognitive processes and in cognitive impairment. *International Journal of Psychophysiology*, 86(1):25–38, 2012.

[4] T. Egner and J. H. Gruzelier. EEG biofeedback of low beta band components: frequency-specific effects on variables of attention and event-related brain potentials. *Clinical Neurophysiology*, 115(1):131–139, 2004.

[5] F. Hsiao et al. Theta oscillation during auditory change detection: an MEG study. *Biological psychology*, 81(1):58–66, 2009.

[6] T. Vogt et al. Effects of exercise in immersive virtual environments on cortical neural oscillations and mental state. *Neural plasticity*, 2015, 2015.

[7] K. Vanderperren et al. Reduction of alpha distortion in event related potentials. In *4th European Conference of the International Federation for Medical and Biological Engineering*, pages 1298–1301. Springer, 2009.

[8] A. Cichocki. Tensor decompositions: A new concept in brain data analysis? *preprint arXiv:1305.0395*, 2013.

[9] A. Mazaheri et al. Asymmetric amplitude modulations of brain oscillations generate slow evoked responses. *The Journal of Neuroscience*, 28(31):7781–7787, 2008.

[10] B. Min et al. The best of both worlds: phase-reset of human EEG alpha activity and additive power contribute to ERP generation. *International Journal of Psychophysiology*, 65(1):58–68, 2007.

[11] B. Hunyadi et al. Block term decomposition for modelling epileptic seizures. *EURASIP Journal on Advances in Signal Processing*, 2014(1):1–19, 2014.

Address for correspondence:

Rob Zink — KU Leuven (Belgium), Department of Electrical Engineering (ESAT), STADIUS Center for Dynamical Systems, Signal Processing and Data Analytics. rob.zink@esat.kuleuven.be

Tracking the poles of an AR time-variant model for EEG studies

G Tacchino[1] and A.M. Bianchi[1]

[1]Department of Electronic, Information and Bioengineering, Politecnico di Milano, Milan, Italy

Abstract

Time-Variant Autoregressive Models (TVAM) can be used to deal with the non-stationarities of electroencephalographic (EEG) signals induced by the performance of cognitive and motor tasks. The model coefficients matrix update on a sample-by-sample basis allows evaluating changes in time of the quantitative indices that describe the directional relationships between different EEG channels. However, these indices are commonly assessed within a fixed frequency range, which does not guarantee that the total power of the brain rhythms under investigation is considered during the performance of the whole task. Here we analyzed EEG data acquired on healthy subjects performing a motor task (i.e., visually guided cue-paced pointing movement). We exploited the time-variant coefficients matrix, as obtained by a bivariate TVAM, to define a time-variant frequency band associated to the sensorimotor mu rhythm from the knowledge of the model poles position in each time instant. The directional interactions between different brain regions (i.e., premotor, motor and posterior parietal cortices) were assessed within these time-variant frequency bands. The contralateral motor cortex was the source of the information flow towards the other areas. The premotor cortex was enrolled after the motor cortex and was found to lead the posterior parietal cortex within a fronto-parietal network.

Keywords *EEG, model poles, Time-Variant Autoregressive Model (TVAM)*

1 Introduction

Changes in the brain activity due to the performance of cognitive and motor tasks can be assessed with an optimal time resolution using electroencephalographic signals (EEG) [1].

In the context of multichannel EEG recordings, directional relationships between different scalp channels can be investigated using multivariate autoregressive models. Specifically, quantitative indices obtained from the model coefficient matrix can be used to describe the directional information flow within the frequency domain [2]. As these indices are derived from autoregressive models, they require the signals stationarity in the time interval to be analyzed. However, the stationarity requirement is generally not fulfilled when brain activity modifications are evaluated during the performance of cognitive and/or motor tasks [1, 3]. To bypass the stationarity requirement, Time-Variant Autoregressive Models (TVAM) allows estimating the model coefficients on a sample-by-sample basis using a Recursive Least Square (RLS) algorithm with an exponential forgetting factor [4–6]. The time-variant coefficient matrix can be easily exploited for the computation of quantitative indices that describe directional relationships between different scalp channels. These quantitative indices are generally evaluated within time-invariant frequency bands. In other words, the index values belonging to a fixed frequency range are averaged together for each time instant. However, it is known from the literature [3] that the frequency of certain brain rhythms is modulated in time by cognitive and sensorimotor processes. Therefore, the index averaging within fixed frequency bands does not guarantee to consider the total power of the brain rhythm under investigation during the performance of the whole task.

In this work we exploit the time-variant coefficients matrix, as obtained by a bivariate TVAM, to identify the position of the model poles in each time instant. The knowledge of the time course of the model poles position is used to define time-variant frequency bands associated to the brain rhythms of interest. We provide an application of this method to EEG data acquired on healthy subjects during the execution of a motor task (i.e., visually guided cue-paced pointing movement). We quantify the existence of directional interactions between different couples of EEG channels through the Normalized Directed Transfer Function (NDTF) [2]. We evaluate this quantitative index within the time-variant frequency band defined from the model poles associated to the sensorimotor mu rhythm.

2 Methods

A) Bivariate Time-Variant Autoregressive Model

A bivariate TVAM [7, 8] of order p can be described by the following matrix form:

$$Y(t) = \sum_{k=1}^{p} A_t(k) Y(t-k) + W(t), \qquad (1)$$

with $Y(t)=[y_1(t)\ y_2(t)]'$ and $W(t)=[w_1(t)\ w_2(t)]'$. The signals $y_1(t)$ and $y_2(t)$ represent the output of the bivariate model, while $w_1(t)$ and $w_2(t)$ are white Gaussian noises with zero mean and variance $\sigma 1$ and $\sigma 2$ respectively. At each time instant t, the model properties are completely described by the coefficients matrix $A_t = [A_t(1)\ A_t(2)\ \ldots\ A_t(p)]$. A_t is updated on a sample-by-sample basis using the RLS identification algorithm with an exponential forgetting factor Λ. The

update in time of the model coefficients matrix allows tracking and following in time the changing properties of the signals under investigation. The RLS algorithm is described by the following equations:

$$A_t = A_{t-1} + K(t)E(t) \quad (2)$$

$$K(t) = \frac{P(t-1)\Phi(t)}{\Lambda + \Phi(t)'P(t-1)\Phi(t)} \quad (3)$$

$$E(t) = Y(t) - \Phi(t)'A_t \quad (4)$$

$$P(t) = \frac{1}{\Lambda}\left[P(t-1) - \frac{P(t-1)\Phi(t)\Phi(t)'P(t-1)}{\Lambda + \Phi(t)'P(t-1)\Phi(t)}\right] \quad (5)$$

According to equation (2) the coefficients matrix at time *t* is updated by summing the coefficients values computed at the previous step (i.e., *t-1*) with an innovation term, which is the product between the prediction errors vector E(t) and the time-variant gain of the model K(t). P(t) is the covariance matrix of data, while Φ(t) represents the observation vector containing the previous p samples of both signals y_1 and y_2. The prediction errors vector E(t) for the two signals is obtained by computing the difference between the actual samples Y(t) and their prediction provided by the model $\Phi(t)'A_t$.

The model poles can be identified at each time instant t by computing the roots of the determinant of (I-A(z)), where I is the identity matrix and A(z) is the transfer function of the bivariate model evaluated at time t [9].

B) Dataset and task description

In this work we analyzed a subset of EEG recordings belonging to a dataset collected for a previous study [10]. In particular, we used data acquired on 7 right-handed healthy subjects (5 males and 2 females; 23.6 ± 3.0 years). Subjects were comfortably seated in front of a touch-screen monitor, with their right arm resting on a table. The experimental protocol was made up of 60 repetitions (trials) of a motor task, which was a cue-paced visually guided pointing movement to be executed with the right upper limb. The protocol was conceived for the investigation of both movement planning and execution phases. Each trial began with the appearance on the monitor of a round cross-shaped sign (CUE stimulus). In this phase of the task the subject was asked to consciously plan the pointing movement. The subject had to stare at the CUE stimulus until a full circle (TARGET stimulus) appeared in the same position. The subject was instructed to touch the TARGET center as quickly and accurately as possible (movement execution phase), and to return in the starting position. After each movement execution the subject received a visual feedback about his/her performance. A more detailed description of the protocol can be found in [10].

C) Data recording and pre-processing

EEG signals were recorded by means of a Sam32 amplifier (MICROMED, Mogliano Veneto, Italy). 19 Ag/AgCl surface electrodes were placed on the scalp according to the 10-20 International System with linked earlobes reference. The ground electrode had a mid-forehead placement. The impedance of each electrode was kept below 5 KΩ. EEG signals were sampled at 1024 Hz.

All data were exported in MATLAB (Mathworks, Natick, MA) environment and offline pre-processed using EEGLAB toolbox [11] and custom scripts. EEG signals were band-pass filtered in the range 0.5 – 45 Hz (finite impulse response filter of order 3000) and down-sampled at 128 Hz. Segments of signals with pronounced non-stereotyped artifacts were removed based on visual inspection. Stereotyped artifacts (e.g. eye blinks, eye movements, cardiac activity and scalp muscles contraction) were removed using independent component analysis. Clean EEG signals underwent surface Laplacian transformation, yielding the estimate of Current Sources Density (CSD). This spatial filtering was performed in order to improve the spatial localization of neuronal activity and to obtain reference-free data. CSD data were used for all subsequent analyses.

D) Data analysis with the bivariate TVAM

The bivariate TVAM analysis was restricted to the electrodes couples F3-C3, C3-P3, F3-P3, C3-C4 since the corresponding brain areas have been shown to be involved in visually guided cue-paced pointing movements [12–14]. For each subject and couple of electrodes, the bivariate model was applied to the continuous CSD signals. The optimal model order was identified through the multivariate Akaike Information Criterion, yielding the value $p = 9$. Trial averaging was performed in the model coefficients domain. In this respect, we identified 8-s-long epochs (1 s before and 7 s after each CUE event) containing the different phases of the motor task: baseline, movement planning phase, movement execution phase and post-movement interval. The model coefficients matrix was averaged over the afore-defined epochs.

For each subject we identified a time-variant frequency band associated to the mu rhythm by tracking the model poles position in each time instant belonging to the 8-s-long epoch (Fig. 1). Since we found two poles associated to the mu rhythm (i.e., $p_{\mu 1}$ and $p_{\mu 2}$), the lower and upper bounds of the time-variant frequency band were defined as $[p_{\mu 1} - 2; p_{\mu 2} + 2]$ Hz.

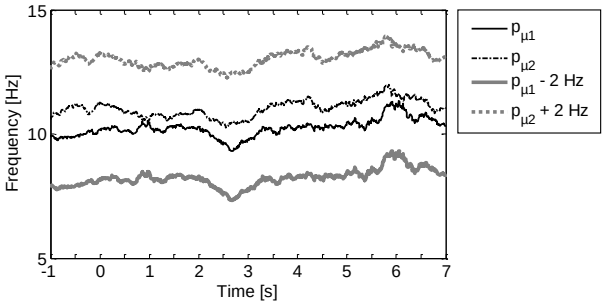

Figure 1: time-variant frequency band associated to the mu rhythm.

The average coefficients matrix was used to estimate the NDTF for each time instant belonging to the 8-s-long epoch. This index, which can assume values between 0 and 1, quantifies the information flow

directed from channel j to channel i at a certain frequency, as described by the following equations:

$$NDTF^2_{j\to i}(t,f)=\frac{|H_{ij}(t,f)|^2}{\sum_{m=1}^{k}|H_{im}(t,f)|^2} \quad (6)$$

$$H(t,f)=(I-\bar{A}(t,f))^{-1}, \quad (7)$$

where $\bar{A}$ is the average coefficients matrix and H represents the transfer matrix of the model.

For each couple of electrodes and time instant t, we computed the following quantitative feature:

$$\Delta NDTF(t)=NDTF^2_{2\to 1}(t)-NDTF^2_{1\to 2}(t), \quad (8)$$

where 1 and 2 represent the first and the second electrode of the couple, while $NDTF^2(t)$ is the average of the NDTF values in the time-variant frequency band for each time instant. The information flow is directed from the first to the second electrode if $\Delta NDTF<0$, while the opposite happens if $\Delta NDTF>0$. Then, we subdivided the time course of $\Delta NDTF$ into 0.5-s-long consecutive and non-overlapping time windows. We used the sign test to statistically evaluate, separately for each window, the existence of a preferential direction of the information flow between channels, with the null hypothesis H_0 representing the absence of a preferential directionality. The significance level of the statistical test was fixed to 5%.

3 Results

Table 1 reports the percentage of subjects showing a statistically significant preferential direction of the information flow between electrodes in the different periods of the motor task.

	BS	Plan	Ex	PM
F3->C3	38	31	37	30
C3->F3	62	69	63	70
C3->C4	22	71	62	31
C4->C3	78	29	38	69
C3->P3	64	58	79	68
P3->C3	36	42	21	32
F3->P3	62	71	63	40
P3->F3	38	29	37	60

Table 1: percentage of subjects showing a statistically significant preferential direction of the information flow between the different couples of electrodes. BS = baseline; Plan = planning; Ex = execution; PM = Post-Movement.

The subdivision of the 8-s-long epoch into the 0.5-s-long time windows used for the statistical analysis is schematically represented in Fig. 2A.

As shown in Fig. 2B, a significant information flow was directed from the contralateral frontal area (i.e., F3 electrode) to the contralateral central area (i.e., C3 electrode) during the whole motor task. With respect to the interaction between the contralateral central and parietal areas (i.e. C3 and P3 electrodes respectively), we observed a significant information flow directed from C3 to P3 electrode. A significant information flow was directed from electrode F3 to P3 during the baseline and during both the movement planning and execution phases. A switch in the directionality of the information flow was instead observed during the post-movement interval.

During the baseline period and during the post-movement interval the information flow was directed from the ipsilateral central area (i.e., C4 electrode) to the contralateral central area (i.e., C3 electrode). A switch in the directionality of the information flow was instead observed during both the movement planning and the movement execution phases, with a significant information flow directed from C3 to C4 electrode.

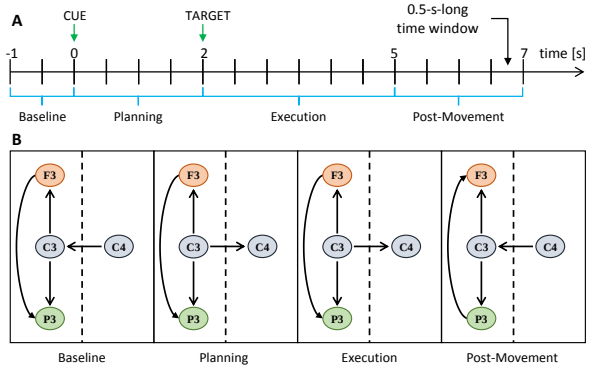

Figure 2: schematic representation of the different periods of the motor task within the 8-s-long epoch (A); statistically significant directional relationships between all electrodes in the different periods of the motor task (B).

4 Discussion

In this work we exploited the coefficients matrix obtained from a bivariate TVAM to quantify the directional relationships between couples of EEG channels during the performance of a motor task. Previous studies also addressed this topic using bivariate/multivariate TVAM [4–6]. In these works, the indices that quantify the coupling between EEG signals were always evaluated within time-invariant frequency bands associated to the rhythms of interest. However, this might not be the proper approach when there is an interest in exploring the evolution in time of a certain phenomenon (e.g., brain activity modifications induced by sensorimotor processes during the performance of a motor task). In fact, it cannot be given for granted that a time-invariant frequency band contain all the power associated to the rhythms of interest during the whole motor task. To overcome this limitation, we quantified the directional relationships between couples of electrodes by evaluating the NDTF within time-variant frequency bands, which were defined from the knowledge of the model poles position in correspondence of each time instant of the motor task.

Our results show that the contralateral motor cortex (i.e. C3 electrode) is the source of the information flow towards the premotor cortex (i.e. F3 electrode) and the posterior parietal cortex (i.e. P3 electrode) during all the

different phases of the motor protocol. Concerning the fronto-central interaction, the information flow is directed from the motor cortex to the premotor cortex. This result is in accordance with findings from Labyt and colleagues, who reported that the enrollment of the premotor cortex in movement planning is secondary to the engagement of the primary motor cortex when cue-paced targeting movements are performed [14]. Concerning the fronto-parietal interaction, the information flow is directed from the premotor cortex to the posterior parietal cortex during both movement planning and execution phases, while a switch of directionality is found during the post-movement period. The former result is in line with findings from the literature, since the premotor cortex has been found to be activated earlier than the posterior parietal cortex when a pointing/reaching movement is planned [12]. We hypothesize that the reversal of the information flow during the post-movement period could be due to the visual feedback received by the subject after movement termination. Our results about directional interactions between C3-P3 and F3-P3 couples are in line with findings from Babiloni and colleagues, who found the posterior parietal cortex receiving peripheral somatosensory and motor information from the primary sensorimotor cortex and from the dorsal premotor cortex during movement preparation and execution [13]. Regarding the inter-hemispheric interaction between left and right motor cortices, the information flow is directed from the contralateral area (i.e. C3 electrode) to the ipsilateral area (i.e. C4 electrode) during movement planning and execution, as also observed by Athanasiou and colleagues during the planning and execution phases of a cue-paced biceps flexion of the forearm [15].

References

[1] G. Pfurtscheller and F. H. Lopes da Silva, "Event-related EEG/MEG synchronization and desynchronization: basic principles," *Clin. Neurophysiol.*, vol. 110, no. 11, pp. 1842–1857, Nov. 1999.

[2] M. J. Kaminski and K. J. Blinowska, "A new method of the description of the information flow in the brain structures," *Biol. Cybern.*, vol. 65, no. 3, pp. 203–210, Jul. 1991.

[3] G. Florian and G. Pfurtscheller, "Dynamic spectral analysis of event-related EEG data," *Electroencephalogr. Clin. Neurophysiol.*, vol. 95, no. 5, pp. 393–396, Nov. 1995.

[4] L. Astolfi, F. Cincotti, D. Mattia, F. De Vico Fallani, A. Tocci, A. Colosimo, S. Salinari, M. G. Marciani, W. Hesse, H. Witte, M. Ursino, M. Zavaglia, and F. Babiloni, "Tracking the Time-Varying Cortical Connectivity Patterns by Adaptive Multivariate Estimators," *IEEE Trans. Biomed. Eng.*, vol. 55, no. 3, pp. 902–913, Mar. 2008.

[5] W. Hesse, E. Möller, M. Arnold, and B. Schack, "The use of time-variant EEG Granger causality for inspecting directed interdependencies of neural assemblies," *J. Neurosci. Methods*, vol. 124, no. 1, pp. 27–44, Mar. 2003.

[6] E. Möller, B. Schack, M. Arnold, and H. Witte, "Instantaneous multivariate EEG coherence analysis by means of adaptive high-dimensional autoregressive models," *J. Neurosci. Methods*, vol. 105, no. 2, pp. 143–158, Feb. 2001.

[7] A. M. Bianchi, T. Locatelli, L. T. Mainardi, M. Cursi, G. Comi, and S. Cerutti, "Event-Related Brain Potentials: Laplacian Transformation for Multichannel Time-Frequency Analysis," *Methods Inf Med*, vol. 39, no. 2, pp. 160–163, 2000.

[8] L. T. Mainardi, A. M. Bianchi, R. Furlan, S. Piazza, R. Barbieri, V. di Virgilio, A. Malliani, and S. Cerutti, "Multivariate time-variant identification of cardiovascular variability signals: a beat-to-beat spectral parameter estimation in vasovagal syncope," *IEEE Trans. Biomed. Eng.*, vol. 44, no. 10, pp. 978–989, Oct. 1997.

[9] G. Baselli, A. Porta, O. Rimoldi, M. Pagani, and S. Cerutti, "Spectral decomposition in multichannel recordings based on multivariate parametric identification," *IEEE Trans. Biomed. Eng.*, vol. 44, no. 11, pp. 1092–1101, Nov. 1997.

[10] E. Molteni, V. Cimolin, E. Preatoni, R. Rodano, M. Galli, and A. M. Bianchi, "Towards a Biomarker of Motor Adaptation: Integration of Kinematic and Neural Factors," *IEEE Trans. Neural Syst. Rehabil. Eng.*, vol. 20, no. 3, pp. 258–267, May 2012.

[11] A. Delorme and S. Makeig, "EEGLAB: an open source toolbox for analysis of single-trial EEG dynamics including independent component analysis," *J. Neurosci. Methods*, vol. 134, no. 1, pp. 9–21, Mar. 2004.

[12] R. A. Andersen and H. Cui, "Intention, Action Planning, and Decision Making in Parietal-Frontal Circuits," *Neuron*, vol. 63, no. 5, pp. 568–583, Sep. 2009.

[13] C. Babiloni, F. Carducci, F. Cincotti, P. M. Rossini, C. Neuper, G. Pfurtscheller, and F. Babiloni, "Human Movement-Related Potentials vs Desynchronization of EEG Alpha Rhythm: A High-Resolution EEG Study," *NeuroImage*, vol. 10, no. 6, pp. 658–665, Dec. 1999.

[14] E. Labyt, W. Szurhaj, J.-L. Bourriez, F. Cassim, L. Defebvre, A. Destée, J.-D. Guieu, and P. Derambure, "Changes in oscillatory cortical activity related to a visuomotor task in young and elderly healthy subjects," *Clin. Neurophysiol.*, vol. 114, no. 6, pp. 1153–1166, Jun. 2003.

[15] A. Athanasiou, C. Lithari, K. Kalogianni, M. A. Klados, and P. D. Bamidis, "Source Detection and Functional Connectivity of the Sensorimotor Cortex During Actual and Imaginary Limb Movement: A Preliminary Study on the Implementation of Econnectome in Motor Imagery Protocols," *Adv Hum-Comp Int*, vol. 2012, pp. 2:2–2:2, Jan. 2012.

Address for correspondence:

Anna Maria Bianchi
Politecnico di Milano
annamaria.bianchi@polimi.it

Automatic artifacts correction: improving on-line EEG analysis

Stefania Coelli[1], Giulia Tacchino[1], Anna Maria Bianchi[1]

[1]Department of Electronics, Information and Bioengineering, Politecnico di Milano, Milano, Italy

Abstract

In this paper an automatic ocular artifacts management procedure for EEG analysis on-line is proposed, composed of a detection algorithm followed by a correction which is based on canonical correlation analysis (CCA). The accuracy of the whole method is tested on simulated signals and its capability of recovering the original signals is shown to be comparable with non-automatic 'gold standard' procedure (independent component analysis - ICA). The method is implemented to be suitable for fast EEG processing to improve on-line signal interpretation. An example on real data is also provided.

Keywords: *canonical correlation analysis; Electroencephalography; ocular artifacts;*

1 Introduction

The Electroencephalography (EEG) is a non-invasive technique used for the measurement of a subject's electrical brain activity directly on the scalp. Since it is characterized by a very high temporal resolution, it results to be suitable for the extraction of information about fast neural changes induced by cognitive and motor processes. Unfortunately, EEG is also characterized by a low signal-to-noise ratio (SNR); indeed, the signal of interest is usually contaminated by a large amount of physiological signals that are not related to cerebral activity (i.e., ocular movements, eye blinks, cardiac activity and muscular activity) and have a much higher amplitude [1, 2]. These non-brain-related electrical activities severely affect the extracted information leading to a wrong interpretation of the neural processes, particularly when an on-line elaboration is performed as, for example, in Brain Computer Interface (BCI) devices [1, 3]. This is particularly true for ocular artifacts (OA) since they cannot be prevented and their amplitude is at least 10 times higher than EEG activity. Several approaches have been proposed in the literature with the aim of removing OA and not simply rejecting them, in order to prevent loss of information [3, 4]. Recently methods such as spatial decompositions (i.e., Principal Component Analysis, PCA [5]) and blind source separation (BSS) (i.e., optimized implementation of Independent Component Analysis (ICA) algorithm [1, 6] and Canonical Correlation Analysis CCA [7-9]) are widely employed in absence of a simultaneous electrooculography (EOG) recording.

CCA approach has been initially proposed only for muscular artifact correction [7] since it is able to order the extracted sources by their autocorrelation coefficient, which usually results to be very low for electromiographic (EMG) components [7, 10]. More recently this approach has been applied also for OA removal both in manual and automatic implementation [2, 9], while its relatively low complexity [4] allows a fast implementation suitable for on-line applications.
Thus, in this work, we propose an artifacts management method for possible on-line applications, which is composed by two steps, i) artifacts detection [11] by using thresholds on four parameters; ii) automatic artifacts correction based on BSS-CCA algorithm [10], validated on simulated data. Finally we show how this method could improve on-line signal interpretation for cognitive task monitoring.

2 Methods

Detection method
The proposed artifacts detection method is based on the 'single-channel, single-epoch' artifacts detection step belonging to the well-known FASTER toolbox, previously proposed by Nolan and coworkers [11], adapted for on-line implementation. We exploited this particular section because it can be applied to short data epochs, and the employed parameters are intuitive and fast to compute. Since the detection method is based on parameters thresholding, a sufficient number of signal windows has to be collected to serve as baseline segments on which, after a classical amplitude thresholding (max<100μm min>-100 μm), the mean, the variance and the standard deviation are computed [11]. After that, for each channel and baseline window the following parameters are computed during the whole training period: i) the variance; ii) the median of the gradient; iii) the amplitude range of the channel and iv) the deviation of the mean amplitude from the channel mean amplitude.
Thus, the thresholds are computed through the 'three sigma rule' formula [12] at the end of this training step. The above-described four parameters are computed for each new 2-s-long window in input and their values are compared with the thresholds. An artifact is detected if N (1 to 4) parameters contemporary cross their thresholds for at least one channel.

Artifact correction
We employed the classical canonical correlation analysis as blind source separation algorithm as proposed by several authors [2, 7–10].
The CCA is a statistical approach to solve the BSS problem. In particular when the two sets of signals are

the observed data X(t) and their one-sample delayed version Y(t), the CCA finds two sets of basis vectors such that the correlation matrix between the described signals is a diagonal matrix in the new basis [2, 10]. After removing the mean of each row from the data matrices X(t) and Y(t), the linear combinations $a = w^{T}_{a}$ X and $b = w^{T}_{b}$Y, of the components in X and Y are called 'canonical variables', where w_a and w_b are the canonical weights vectors. CCA finds the weight vectors by maximizing the correlation ρ (Eq.1) between the variables *a* and *b*,

$$\rho = \frac{w^{T}{}_{a} C_{XY} w_b}{\sqrt{(w^{T}{}_{a} C_{XX} w_a)(w^{T}{}_{b} C_{YY} w_b)}} \quad (1)$$

where C_{XX} and C_{YY} are the nonsingular covariance matrices of X and Y, while C_{XY} is covariance matrix between the two sets.

BSS-CCA extracts sources that are uncorrelated with each other, but maximally auto-correlated and orders them by decreasing ρ values[7].

Finally, the BSS problem is solved by computing the time series $a_i(t)$ corresponding to the signal sources $S_i(t)$. In this work we adapted the Matlab function implemented by [7] and freely downloadable.

Every time an artifact is detected, the BSS-CCA algorithm is executed to identify M sources (M = number of channels). A source of the S(t) matrix is automatically labeled as an artifact source based on a thresholding method applied to three parameters (i.e., the kurtosis [1], the amplitude and the correlation coefficient (ρ) [8]) computed on each obtained source. A source of artifact is identified if:

- its amplitude and kurtosis values contemporary exceed their thresholds, meaning that a high amplitude artifact is present;
- the amplitude remains higher than the threshold for at least 100 ms, identifying a blink artifact;
- the correlation coefficient is lower than a selected level, meaning that the source, having a very low autocorrelation value, mainly resembles an EMG artifact [7, 8].

In particular, the amplitude and kurtosis thresholds are automatically computed as mean value + standard deviation; a minimum level for the correlation coefficient is manually empirically selected on the data since correlations coefficients are sorted in a descendent order. To finally correct the artifact, the weights associated to the identified artifact source are set to zero and the clean data are computed as $X_{clean}(t) = W_{clean} * S(t)$.

Simulated data

In order to create realistic simulated signals corrupted by artifacts, we selected real EEG signals from our database in order to provide both clean EEG background and artifacts source.

In particular we selected signals recorded on subjects performing a two minutes rest recording with eyes open. EEG signals were recorded by means of a Sam32 amplifier (MICROMED, Mogliano Veneto, Italy), 19 Ag/AgCl surface electrodes were placed on the scalp according to the 10-20 International System with reference on the right earlobe. The impedance of every electrode was kept below 10kΩ. The sampling frequency was set to 256 Hz, an antialiasing low-pass filter and a notch filter were set at 120 Hz and 50 Hz respectively. Data were then digitally band-pass filtered in the range 1 - 70 Hz by means of a finite impulse response filter (FIR).

125 2-s-long EEG epochs from subject 1 and 95 epochs of the same duration from subject 2 were selected as underlying clean EEG background, since no muscular or blink artifacts were present according to visual inspection. The clean windows were stored as two 3-D matrices (number of channels x number of samples x number of windows), one for each 'clean' EEG background source (2 subjects).

We obtained a real distribution of blink and eye movement artifacts over the EEG electrodes by applying ICA (INFOMAX)[13] to the signals belonging to other subjects from the same database in order to remove the sources of EEG activity, while maintaining only the evident artifacts sources [7] (blink source from 2 subjects). We reproduced the realistic artifacts distribution over the EEG channels by back-propagation [9]; then the obtained signals were segmented into 2-s-long windows. To remove any possible EEG-related activity, the blink artifacts were band-pass filtered between 2 and 7 Hz (second order Butterworth) and finally stored in two separated matrices called 'BLINK1' and 'BLINK2'. The final step of the simulation was the summation of the randomly selected artifact windows from 'BLINK1' or 'BLINK2' matrices to the clean' EEG background windows [5, 9].

Real data

From the same database, we selected an EEG recorded on a subject performing 2 minutes of mathematical computations and 2 minutes of rest with eyes open, exactly with the same set-up and pre-processing steps described above.

We exploited this recording to simulate an on-line extraction of an attention measure (β-power/α-power) [14] with and without the OA correction.

3 Results

Simulation results

In our study we employed two clean datasets on which artifacts were randomly added. The results presented here are obtained by computing the detection thresholds on 30 baseline windows and by setting the number of contemporary exceeded thresholds equal to 2 (see section 2). Concerning the correction, we empirically set the correlation threshold at 0.55. As regards the detection performances, since for the simulated datasets the relative ground truth was available, we computed the detection accuracy (ACC), sensitivity (SE) and specificity (SP) [12]. On our four datasets we obtained a mean ACC of 0.90 (±0.03), SE and SP values respectively of 1 and 0.65 (±0.18).

The method was able to detect all the inserted artifacts, while the low SP values can be due both to the selected number of thresholds to be contemporary exceeded and to the effective low number of artifact-free windows inserted in each dataset.

In Fig.1 an example of correction on a 2-s-long window, in which the presence of a blink was detected, is presented. Fig.1A reports the extracted CCA components and the three parameters considered to automatically reject the artifact source (correlation, kurtosis and amplitude). In this example the first two sources are removed because they both exceed the kurtosis and amplitude thresholds and furthermore, the first component also presents an amplitude higher than the threshold for at least 100 ms. The correction result is shown in panel B. In order to quantitatively measure the capability of the correction method of maintaining the underlying EEG signals, as in [2, 6, 9] the correlation coefficient CC between the original clean signals and the respective corrected signals was employed.

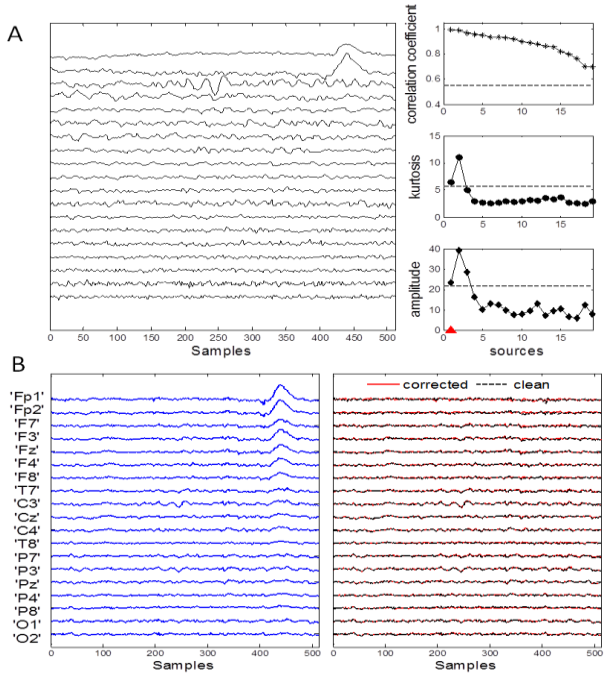

Figure1. A) example of extracted CCA components and relative computed parameters (ρ, kurtosis and amplitude); B) correction result.

The mean and standard deviation values of CC computed on each electrode across the 233 corrected 2-s-long epochs were computed (EEG epochs correctly identified as clean are not included, in order not to artificially enhance correction method performances) and compared with the CC result obtained on the same signals after correction employing ICA (INFOMAX) [13] on the whole signal and removing by visual inspection only the blink component (only the 1st component was removed).

As expected the more affected electrodes are the frontal ones (Fp1, Fp2, F7, F3, Fz, F4, F8) which reach a mean CC values of 0.834, while the central (T7, C3, Cz, C4, T8) and the posterior electrodes (P7, P3, Pz, P4, P8, O1, O2) result less corrupted by the correction method with a mean CC of 0.955 and 0.971 respectively. Despite being obtained on short windows of signals without the operator direct control on the number of components removed, these values result to be comparable with the performances obtained employing classical ICA method with manual correction (i.e. 0.854, 0.988 and 0.997). To finally check the feasibility of the proposed method for possible application in real-time elaboration, we measured the elapsed time for the complete processing of a 2-s-long window (detection and correction) obtaining a mean elapsed time of 0,012 (±0,013) ms.

Cognitive task results

The attention measure employed was the ratio between beta and alpha power, extracted from frontal electrodes (F3/F4, F7/F8) in 2-s-long signal windows. Since the frontal electrodes are known to be the most affected by OAs, misleading information is obtained when an OA occurs. In fact, as shown in Fig.2, the presence of a non-corrected blink could artificially increase alpha waves amplitude, while beta results to be almost unaffected. Since false increments of power in alpha and lower frequency bands could be interpreted as a decrease of attention [14] correction is very important. Fig.2A-B-C respectively represent the signal (F7) before (blue) and after (red) correction and the corresponding extracted alpha and beta waves. Boxplots in panel D show the distribution of the measured beta/alpha ratio with and without correction during 2 minutes of mathematical calculations and 2 minutes at rest, on windows of 2 seconds (50% overlap). In both conditions (Math and Rest) the measured values, when computed after OA correction, are increased and also the difference of the median of the two conditions (Math-Rest) is increased after correction (54% with correction, 40% without correction).

4 Conclusion

This study addressed the challenge of automatic management of ocular artifacts in EEG recordings, with particular attention to on-line applications. Thus we proposed a two steps approach (detection and BSS-CCA based correction) in order to improve on-line signal interpretation. The method was tested on simulated data and quantitatively evaluated by computing detection accuracy [12] and comparing the correction results with classical ICA approach [2]. Despite an initial optimal parameters selection was needed, the detection step showed good accuracy and high sensitivity values on our simulated datasets.

Correction results were found to be comparable with classical ICA and visual inspection approach, thus supporting this method as effective for OA management. We also showed that, during a cognitive task the employed attention index calculation is more reliable after blink artifact removal.

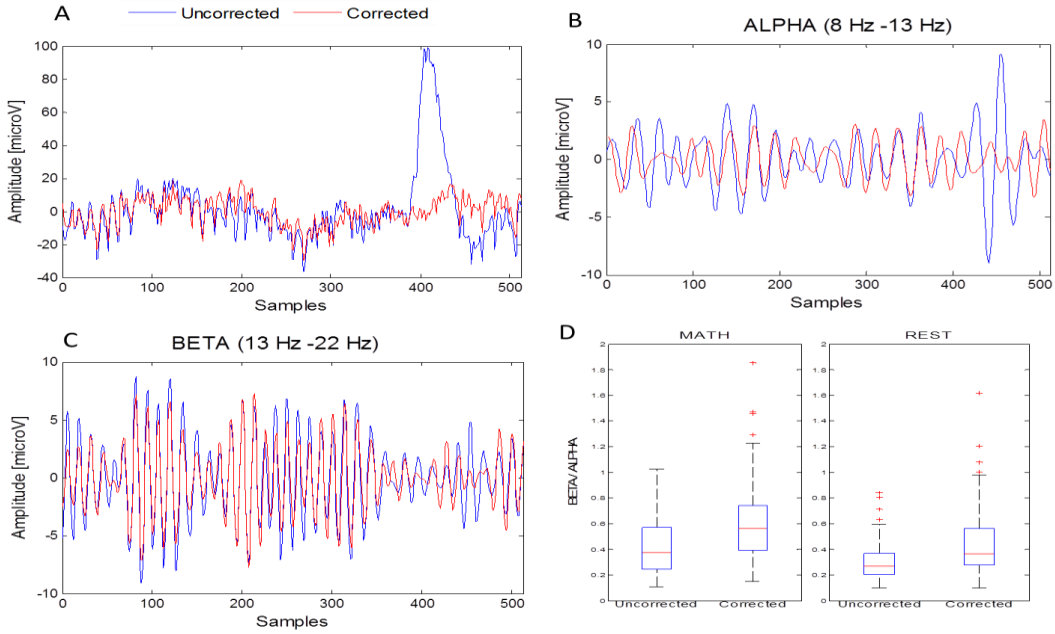

Figure 2. A) signal (F7) before (blue) and after (red) correction and the corresponding (B) alpha and (C) beta waves. D) boxplot of distribution of the measured beta/alpha values with and without correction during mathematical computations and rest.

As future work, the proposed approach should be tested on different window lengths and muscular artifacts should also be considered. Finally, the actual on-line feasibility should be rigorously tested.

Acknowledgment

This work was partially supported by the Think and Go project funded by Regione Lombardia POR FSE 2007/2013, and Fondazione Cariplo.

References

[1] I. Daly, R. Scherer, M. Billinger, and G. Müller-Putz, "FORCe: Fully Online and Automated Artifact Removal for Brain-Computer Interfacing," *IEEE Trans. Neural Syst. Rehabil. Eng.*, vol. 23, no. 5, pp. 725–736, Sep. 2015.

[2] M. H. Soomro, N. Badruddin, and M. Z. Yusoff, "Comparison of blind source separation methods for removal of eye blink artifacts from EEG," in *2014 5th International Conference on Intelligent and Advanced Systems (ICIAS)*, 2014, pp. 1–6.

[3] M. Fatourechi, A. Bashashati, R. K. Ward, and G. E. Birch, "EMG and EOG artifacts in brain computer interface systems: A survey," *Clin. Neurophysiol. Off. J. Int. Fed. Clin. Neurophysiol.*, vol. 118, no. 3, pp. 480–494, Mar. 2007.

[4] D. Safieddine, A. Kachenoura, L. Albera, G. Birot, A. Karfoul, A. Pasnicu, A. Biraben, F. Wendling, L. Senhadji, and I. Merlet, "Removal of muscle artifact from EEG data: comparison between stochastic (ICA and CCA) and deterministic (EMD and wavelet-based) approaches," *EURASIP J. Adv. Signal Process.*, vol. 2012, no. 1, p. 127, 2012.

[5] S. Casarotto, A. M. Bianchi, S. Cerutti, and G. A. Chiarenza, "Principal component analysis for reduction of ocular artefacts in event-related potentials of normal and dyslexic children," *Clin. Neurophysiol. Off. J. Int. Fed. Clin. Neurophysiol.*, vol. 115, no. 3, pp. 609–619, Mar. 2004.

[6] J. F. Gao, Y. Yang, P. Lin, P. Wang, and C. X. Zheng, "Automatic removal of eye-movement and blink artifacts from EEG signals," *Brain Topogr.*, vol. 23, no. 1, pp. 105–114, Mar. 2010.

[7] W. De Clercq, A. Vergult, B. Vanrumste, W. Van Paesschen, and S. Van Huffel, "Canonical correlation analysis applied to remove muscle artifacts from the electroencephalogram," *IEEE Trans. Biomed. Eng.*, vol. 53, no. 12 Pt 1, pp. 2583–2587, Dec. 2006.

[8] J. Gao, C. Zheng, and P. Wang, "Online removal of muscle artifact from electroencephalogram signals based on canonical correlation analysis," *Clin. EEG Neurosci.*, vol. 41, no. 1, pp. 53–59, Jan. 2010.

[9] C. Zhao and T. Qiu, "An automatic ocular artifacts removal method based on wavelet-enhanced canonical correlation analysis," in *2011 Annual International Conference of the IEEE Engineering in Medicine and Biology Society*, 2011, pp. 4191–4194.

[10] M. Borga and H. Knutsson, "A Canonical Correlation Approach to Blind Source Separation," *ResearchGate*.

[11] H. Nolan, R. Whelan, and R. B. Reilly, "FASTER: Fully Automated Statistical Thresholding for EEG artifact Rejection," *J. Neurosci. Methods*, vol. 192, no. 1, pp. 152–162, Sep. 2010.

[12] X. Yong, M. Fatourechi, R. K. Ward, and G. E. Birch, "Automatic artefact detection in a self-paced brain-computer interface system," in *2011 IEEE Pacific Rim Conference on Communications, Computers and Signal Processing (PacRim)*, 2011, pp. 403–408.

[13] A. Delorme and S. Makeig, "EEGLAB: an open source toolbox for analysis of single-trial EEG dynamics including independent component analysis," *J. Neurosci. Methods*, vol. 134, no. 1, pp. 9–21, Mar. 2004.

[14] F. G. Freeman, P. J. Mikulka, L. J. Prinzel, and M. W. Scerbo, "Evaluation of an adaptive automation system using three EEG indices with a visual tracking task," *Biol. Psychol.*, vol. 50, no. 1, pp. 61–76, May 1999.

Address for correspondence:
Anna Maria Bianchi
Politecnico di Milano, Italy
email: annamaria.bianchi@polimi.it

Cluster Aggregation for Analyzing Event-Related Potentials

Reza Mahini[1], Tianyi Zhou[1,2], Peng Li[3], Asoke Nandi[4], Hong Li[3], Fengyu Cong[1,2]

[1]Department of Biomedical Engineering, Faculty of Electronic Information and Electrical Engineering, Dalian University of Technology, China;
[2]Department of Mathematical Information Technology, University of Jyvaskyla, Finland;
[3]College of Psychology and Sociology, Shenzhen University, Shenzhen China;
[4]Department of Electronic and Computer Engineering, Brunel University, London, UK;

Abstract

Topographic analysis are references independent for Event-Related Potentials (ERPs), and thus render statistically unambiguous results. This drives us to develop an effective clustering approach to finding temporal samples possessing similar topographies for analysing the temporal-spatial ERPs data. The previous study called CARTOOL used single clustering method to cluster ERP data. Indeed, given a clustering method, the quality of clustering varies with data and the number of clusters, motivating us to implement and compare multiple clustering algorithms via using multiple distance functions. By finding the minimum distance among the various clustering methods and selecting the most selected clustering algorithms with other methods via voting the proposed method, a most suitable algorithm showing a considerable performance for a given dataset can be found. This cluster aggregation approach assists to use the most suitable founded cluster for each dataset. We demonstrated the effectiveness of the proposed method by using ERP data for cognitive neuroscience research.

Keywords *Cluster Aggregation, Cognitive Neuroscience, ERP Data Analysis, Spatial, Temporal.*

1 Introduction

Event-related potentials (ERPs) are important tools for cognitive neuroscience by analyzing peak measurements [1]. Usually, the mean amplitude of an ERP over a certain time range is measured as the peak amplitude for statistical analysis [1]. The underlying assumption of this approach is that the topographies over that certain time range do not change. In order to validate the assumption, the clustering has been applied the temporal-spatial ERP data to find the temporal samples sharing the similar spatial topographies [2].

In the latest version of CARTOOL software 3.55 (2014), it is possible to use one of the two Clustering methods named; K-means and Hierarchical clustering with some good selective options [2]. It could be considerable that clustering algorithm selection and the quality of clustering would be affected by different conditions such as, dataset types, quality of data and etc. In this study, we demonstrate that for given dataset the proposed method can find a suitable clustering algorithm among various ones in a reliable way.

The following of the study is structured into 3 Sections; we start with data mining technique clustering in Section 2 and the cluster aggregation method is described, Section 3 provides experimental results and discussion about the results and Section 4 includes conclusions and future works.

2 Method

Indeed, in clustering analysis, one solution to the question above is the use of numerical clustering validation algorithms and assessing the quality of clustering results in terms of many criteria. Since it is also true that no single clustering validation algorithm has been claimed to impartially evaluate the results of any clustering algorithm, the use of clustering validation is not an overwhelmingly reliable solution [4]. In this study, the two-way clustering is applied. Since the multi-way analysis is significant for ERP data analysis [5], it is worth extending the two-way clustering to the multi-way clustering. Consequently, we propose a new approach for that how to use cluster aggregation aim to deal with uncertainty in datasets and clustering algorithms, using multiple clustering methods and multiple distance functions for cluster aggregation to achieve reliable analysis.

2.1 Clustering Methods

In this study, five popular clustering algorithms are used and they are briefly introduced as the following:

- *K-means Clustering*; which for Given a dataset with N data objects in an M-dimensional feature space, this algorithm determines a partition of K groups or clusters which detailed in [6].
- *Hierarchical Clustering*; Basically Hierarchical clustering algorithms are mainly classified into methods (bottom-up methods) and divisive agglomerative methods (top-down methods), based on how the hierarchical divide or merge is formed [3].
- *Fuzzy C-means (FCM)*; Dunn developed fuzzy k-partition algorithms which minimize certain fuzzy extensions of the k-means least-squared-error

criterion function [7]. Eventually, the generalised algorithm was named fuzzy c-means (FCM) [8].

- *Self-Organizing Map (SOM);* Clustering in the neural network literature is generally based on competitive learning (CL) model, Kohonen made particularly strong implementation of CL in his work on learning vector quantisation (LVQ) and self-organising maps (SOM) also known as self-organising feature maps (SOFM) [9].
- *Diffusion Maps Spectral Clustering*; Spectral clustering is an algorithm which is very close to the graph cut clustering algorithm. It requires the computation of the first k eigenvectors of a Laplacian matrix; Diffusion map is a dimensionality reduction method that embeds the high-dimensional data to a low-dimensional space. Clustering is performed within the low-dimensional space [10].

2.2 Distance Functions

Partition–Partition (P–P) Comparison approaches, equivalent to median partition approaches, attempt to provide the solution of an optimization problem, which maximizes the total similarity to the given partitions [4]. In Eq.1 and Eq. 2, which R is the number of clustering algorithms and C^* is the clustering with maximum similarity with the other clusterings and minimum dissimilarity with them [4], There are several distance functions for measuring similarity or dissimilarity between partitions. More details have explained in [4].

$$C^* = a \qquad p\in\mathbb{P}_x \sum_{j=1}^{R} \Gamma(C, C_j) \tag{1}$$

$$C^* = a \qquad p\in\mathbb{P}_x \sum_{j=1}^{R} \mathcal{M}(C, C_j) \tag{2}$$

We used a number of distance functions aim to cluster aggregation. Briefly, we describe them in below;

- *Fowlkes and Mallows distance function*

The Wallace distance of two clustering algorithms *C, C'* is;

$$W_I(C, C') = \frac{N_1}{\sum_k n_k(n_k-1)/2} \tag{3}$$

$$W_{I'}(C, C') = \frac{N_1}{\sum_k n'_k(n'_k-1)/2} \tag{4}$$

Where N_{11} is The number of pairs of objects that were clustered in the same clusters in *C* and *C'*. They represent the probability that a pair of points which are in the same cluster *C, C'*.

$$\mathcal{F}(C, C') = \sqrt{W_I(C, C')W_{I'}(C, C')} \tag{5}$$

The index is used by subtracting the base-line and normalizing by the range, so that the expected value of the normalized index is 0 while the maximum (attained for identical clustering algorithms) is [11].

- *Rand distance function*

$$\mathcal{R}(C, C') = \frac{N_1 + N_0}{n(n-1)/2} \tag{6}$$

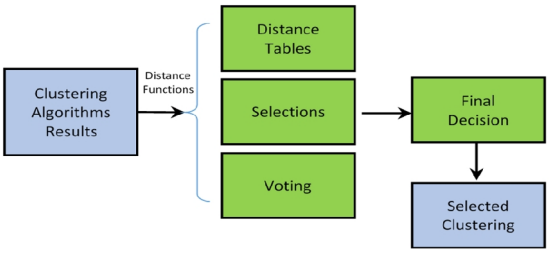

Figure 1: The cluster aggregation model.

And N_{00} is The number of pairs of objects that were clustered in separate clusters in *C* and also *C'*. A similar transformation was introduced for Rand index and Adjusted Rand Index.

- *Adjust Rand distance function*

$$A\ (C, C') = \frac{R(C, C') - E[R]}{1 - E[R]} = \frac{\sum_{i,j}\binom{n_{i,j}}{2} - \left[\sum_i \binom{n_i}{2}\sum_j \binom{n_j}{2}\right] \Big/ \binom{n}{2}}{\frac{1}{2}\left[\sum_i \binom{n_i}{2} + \sum_j \binom{n_j}{2}\right] - \left[\sum_i \binom{n_i}{2}\sum_j \binom{n_j}{2}\right] / \binom{n}{2}} \tag{7}$$

The main motivation for adjusting indices like *R* and *F* is the observation that the unadjusted *R, F* do not range over the entire [0, 1] interval (i.e. min $R > 0$, min $F > 0$). There are other criteria in the literature, to which the above discussion applies. For instance, the Jaccard index in [11].

- *Jaccard distance function*

Jaccard index for two clustering algorithms C, C' is;

$$\mathcal{J}(C, C') = \frac{N_1}{N_1 + N_0 + N_1} \tag{8}$$

2.3 Cluster Aggregation

Clustering comparison can be useful for examining whether the structures of the clusters match to some predefined classification of the instances. In fact, researchers use different distance algorithms, even clustering ensemble causes to obtain good results most of the time, but we tried aggregation with acceptable workload. The consensus clustering problem is considered as an NP-hard problem [11] yet, we are still able to provide approximation guarantees for many of the algorithms we propose via using a combination of different distance functions. Fig. 1 illustrates the proposed aggregation algorithm model.

Clustering algorithms results can be compared together with the mentioned distance functions. To compare the clustering algorithm results and eventually to make distance table, we have used the distance functions' results. This means that, the clustering algorithms are selected with a maximum value of similarity by the other algorithms in the distance tables. Next voting assisted to find which clustering has selected more than the others. The final decision is made based on the voting table to find a suitable clustering algorithm.

3 Experimental Results and Discussion

We implemented the proposed algorithm by using five clustering algorithms and four distance functions. First, because these algorithms are standard and also we need to control the number of clusters in proposed algorithm. In this study, ERP data which have been published in [12] for the gamboling task is used. We just selected one subject and one stimulus data randomly and the size was 500 temporal samples by 58 electrodes (features for each sample). Absolutely, we applied it to all the subjects' data to find group behavior which is very important in cognitive neuroscience. The main goal is to find ERP components using the proposed method. Fig. 2 presents the 5 algorithms clustering performance for the sample dataset. Indeed, we considered the CARTOOL proposed algorithms (k-means and Hierarchical Clustering) as it is shown in this figure. We applied clustering algorithms for this dataset with 6 clusters according to eigenvalues distribution and the explained variance value diagram. Due to the limited space, they are not shown here.

Fig. 3 demonstrates distance function tables based on 4 distance functions (Rand, Adjusted Rand, Fowlkes and Mallow and Jaccard indices) and for five clustering algorithms in the order with: K-means (1), Hierarchical (2), FCM (3), SOM (4) and Diff-Spec (5). Moreover, Table 1 and Table 2 illustrate aggregation algorithm results. Table 2 shows that the K-means have been selected 8 times by the other clustering methods, as a result K-means is used as the suitable method after comparison.

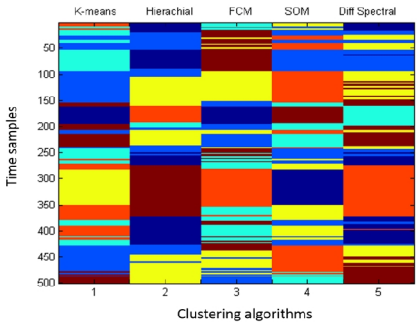

Figure 2: The 5 clustering algorithms membership

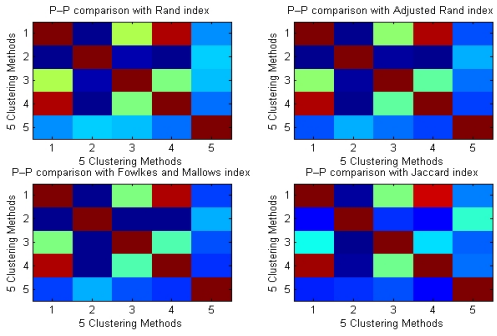

Figure 3: Four Distance function tables for 5 clustering algorithms.

Comp. No.	Distance Func.	Clustering Meth.	Selected Meth.	Similarity Value
1	1	1	4	0.9912
2	1	2	5	0.8768
3	1	3	1	0.9162
4	1	4	1	0.9912
5	1	5	2	0.8768
6	2	1	4	0.9721
7	2	2	5	0.6136
8	2	3	1	0.7261
9	2	4	1	0.9721
10	2	5	2	0.6136
11	3	1	4	0.9776
12	3	2	5	0.6931
13	3	3	1	0.7781
14	3	4	1	0.9776
15	3	5	2	0.6931
16	4	1	4	0.9415
17	4	2	5	0.6221
18	4	3	1	0.6032
19	4	4	1	0.9712
20	4	5	3	0.4763

Table 1: How the clustering algorithms select similar one for them based on distance functions.

K-means	Hierarchical	FCM	SOM	Diff_Spec
8	3	1	4	4

Table 2: Voting table for the selected methods.

Inner similarity of objects inside clusters is presented in Fig. 4, reasonable correlation in order to objects in each cluster is appeared. Fig. 5 shows the inter-cluster correlation and it means that the clusters are enough separated. Moreover, it would be very important to recognize important time windows corresponding to related ERP waveform. This concept is shown in Fig. 6. Fig. 7 presents the topography of these clusters according

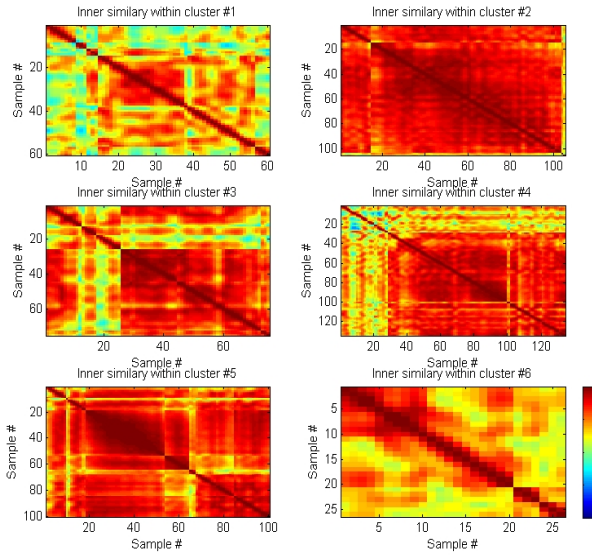

Figure 4: Correlation between 6 clusters.

to 6 clusters. It is clearly seen that there are 6 different topography results for 6 clusters and it means that all the time points in each cluster have same topography and we could treat them as a point, this advantage assists us to find the reasonable time range to average the amplitudes for the ERP peak measurement, providing a reliable and objective way for cognitive neuroscience research. Due to the length limitation of the study, we will report the results of the full ERP dataset in the future study.

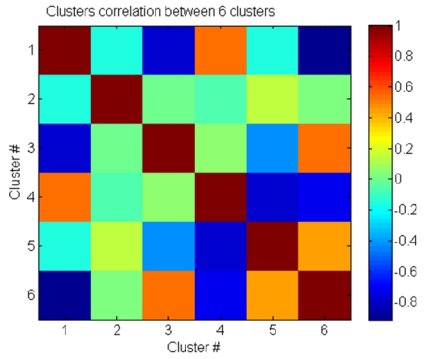

Figure 5: Correlation coefficient among centriods in clusters.

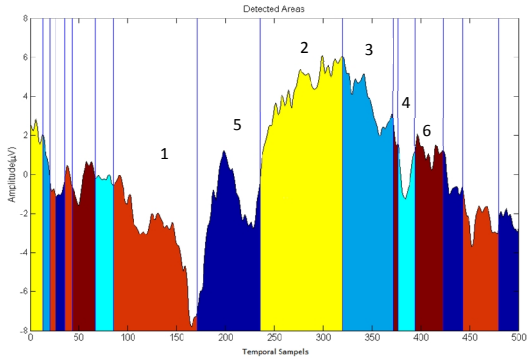

Figure 6: Detected components for ERP waveform clustered into six clusters.

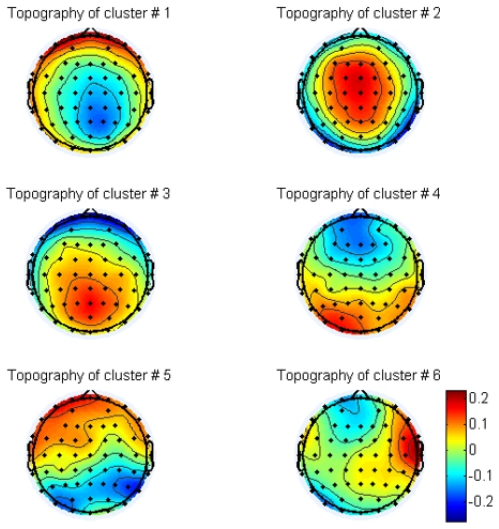

Figure 7: Topographies of centroids of the six clusters.

4 Conclusions and Future Works

In this study, we have proposed an effective approach to finding the temporal samples sharing similar topographies of ERPs for cognitive neuroscience research. Using several distance functions to find a better algorithm for clustering makes this method more reliable and suitable for processing ERP data. In future works, we are going to improve the method for brain signal processing by using clustering ensemble and consider other different datasets for processing.

5 Acknowledgement

This work was supported by the Fundamental Research Funds for the Central Universities [DUT16JJ(G)03] in Dalian University of Technology in China, and National Natural Science Foundation of China (Grant No. 81471742).

References

[1] S. J. Luck. *An Introduction to the Event-Related Potential Technique*, second edition, SBN 978-0-262-52585-5 MIT Press 2014.

[2] D. Brunet, M. M. Murray, and C. M. Michel, Spatiotemporal analysis of multichannel EEG: CARTOOL. *Computational intelligence and neuroscience*, ID. 813870-813870, 2011.

[3] P.N. Tan, M. Steinbach and V. Kumar. *Introduction to Data Mining*, Pearson, On-line Supplement, ISBN-13: 9780321335661, 2006

[4] B. Abu-Jamous, R. Fa and A. K. Nandi. *Integrative cluster analysis in bioinformatics*. John Wiley & Sons, Ltd, ISBN 978-1-118-90653-8, 2015.

[5] F. Cong, Q.H. Lin, L.D. Kuang, X.F. Gong, P. Astikainen and T. Ristaniemi, Tensor Decomposition of EEG Signals: *A Brief Review, Journal of Neuroscience Methods* 248 59–69, 2015.

[6] S. Yu, L.C. Tranchevent, X. Liu, et al. Optimized data fusion for kernel K-means clustering. *IEEE Transactions on Pattern Analysis and Machine Intelligence*, vol. 34, no. 5, pp. 1031–1039, 2012.

[7] J.C. Dunn, Well-separated clusters and optimal fuzzy partitions. *Journal of Cybernetics*, 4(1), pp. 95–104, 1974.

[8] J.C. Bezdek, Pattern Recognition with Fuzzy Objective Function Algorithms, *Kluwer Academic Publishers*, Alphen aan den Rijn. 1981.

[9] T. Kohonen, The self-organizing map. *Proceedings of the IEEE*, 78(9), pp. 1464–1480. 1990.

[10] T. Sipola, F. Cong, T. Ristaniemi, V. Alluri, P. Toiviainen, E. Brattico, et al., Diffusion Map for Clustering fMRI Spatial Maps Extracted by Independent Analysis, *in Proceeding of IEEE International Workshop on Machine Leaning on Signal Provessing*, 2013.

[11] M. Meila, Comparing clusterings - an information based distance. *Journal of Multivariate Analysis*, vol. 98, pp. 873-895, May 2007.

[12] C. Han, P. Li, C. Warren, T. Feng, J. Litman, and H. Li. Electrophysiological evidence for the importance of interpersonal curiosity. *Brain Research, vol. 1500,* pp. 45-54, 2013.

Author Index